The Journal of Heat Transfer (ISSN 0022-1481) is published quarterly for $90 per year by The American Society of Mechanical Engineers, 345 East 47th Street, New York, N Y 10017. Second class postage paid at New York, NY and additional mailing offices. POSTMASTER: Send address changes to The Journal of Heat Transfer, c/o THE AMERICAN SOCIETY OF MECHANICAL ENGINEERS, P.O. Box 3199, Grand Central Station, New York, NY 10163.
CHANGES OF ADDRESS must be received at Society headquarters seven weeks before they are to be effective. Please send old label and new address.
PRICES: To members, $36.00, annually; to nonmembers, $90.00.
Add $6.00 for postage to countries outside the United States and Canada.
STATEMENT from By-Laws. The Society shall not be responsible for statements or opinions advanced in papers or . . . printed in its publications (B7.1, para. 3).

INDEXED by the Engineering Index, Inc.

Journal of Heat Transfer

Published Quarterly by The American Society of Mechanical Engineers

VOLUME 106 • NUMBER 3 • AUGUST 1984

ANNOUNCEMENTS

TECHNICAL PAPERS

(Contents continued)

TECHNICAL NOTES

Simulation of Rapid Heating in Fusion Reactor First Walls Using the Green's Function Approach

A. M. Hassanein
Argonne National Laboratory,
Fusion Power Program.
Argonne, Ill. 60439

G. L. Kulcinski
University of Wisconsin,
Nuclear Engineering Department,
Madison, Wis. 53706

The solution of the heat conduction probem in moving boundary conditions is very important in predicting accurate thermal behavior of materials when very high energy deposition is expected. Such high fluxes are encountered on first wall materials and other components in fusion reactors. A numerical method has been developed to solve this problem by the use of the Green's function. A comparison is made between this method and a finite difference one. The comparison in the finite difference method is made with and without the variation of the thermophysical properties with temperature. The agreement between Green's function and the finite difference method is found to be very good. The advantages and disadvantages of using the Green's function method and the importance of the variation of material thermal properties with temperature are discussed.

1 Introduction

Large energy deposition and intense heat fluxes are encountered on fusion reactor first wall components either due to x-ray and ion debris in Inertial Confinement Fusion (ICF) reactors or during a plasma dump in magnetic fusion reactors. Sizeable temperature excursions, resulting in melting and in some cases evaporation of the metallic components, have been observed [1, 2]. Although the analysis in this paper could be applied to any system where large energy deposition in short times is expected, the relation to fusion reactors is of particular importance to the design of the vacuum chamber. Recently a model has been developed by the authors [3] to accurately solve the heat conduction equation for this problem by finite difference methods. In this model, the surface temperature is determined by both the boundary conditions as well as by the kinetics of the evaporation process. The correct boundary condition entails partitioning of the incident energy flux into conduction, melting, evaporation, and radiation. Consequently, the heat conduction problem is one involving two moving boundaries, one being the melt-solid interface, and the other the surface receding as a result of evaporation. The kinetics of evaporation establish the connection between the surface temperature and the net atom flux leaving the surface, taking recondensation into account.

In this paper, the solution of this heat conduction problem in moving boundary conditions is presented by the use of the Green's function method. The Green's function method provides an easy and fast way of calculating the temperature rise within a reasonable range of accuracy. The finite difference approach consumes large computer time because of the limitations on both the maximum time step and zone thickness required for the stability of the solution. A comparison between the Green's function solution and the finite difference one developed in previous work [3] is also presented. This comparison with the finite differnece methods is made with and without the variation of the material thermal properties with temperature.

Although the results presented for carbon in this paper only consider one moving boundary at the surface because of vaporization (since carbon does not melt), the analysis is presented generally for the two moving boundaries to give a complete description of the possible transformations that can take place during rapid heating of wall materials.

2 Formulation of the Heat Conduction Problem

Consider the first wall or the area of deposition as a semi-infinite medium. This is reasonable in view of the short heat penetration depth during a plasma disruption in magnetic fusion rectors or target debris deposition in ICF reactors. Under a heat flux $F(t)$, the temperature distribution $T(x,t)$ must then satisfy the heat conduction equation

$$\rho c \frac{\partial T}{\partial t} - \nabla \cdot k \nabla T = \dot{q}(x, t) \tag{1}$$

where

ρ = density
c = specific heat
k = thermal conductivity
$\dot{q}(x, t)$ = volumetric energy deposition rate

All the thermophysical properties are functions of the local temperature. Initially the temperature is assumed to be constant throughout the material. The boundary conditions are that the back temperature, i.e., T_{back} = constant for large distances x and at any time t, and on the surface the heat flux is given by

$$F(t) = -k(T_v)\frac{\partial T}{\partial x} + \rho(T_v)L_v v(T_v) + \sigma\epsilon(T_v^4 - T_0^4) \tag{2}$$

where $T_v(t) = T(0, t)$, L_v is the heat of vaporization, and $v(T_v)$ is the velocity of the receding surface. This velocity is a function of the instantaneous surface temperature and other material parameters. Furthermore, the radiative heat transfer term contains the Stefan-Boltzmann constant σ; ϵ is the emissivity of first wall material; and T_0 is the surface temperature of the cold portion of the first wall inside the reactor cavity. For the radiative heat loss, it is assumed that parts of the first wall (mainly in magnetic fusion reactors) not struck by the plasma dump remain at the steady-state temperature T_0. Thus radiation heat flow is assumed from hot regions (T_v) where disruptions occur to the colder parts (T_0) of the unaffected areas. In ICF reactors, this term goes to zero since a microexplosion reaction is assumed to be symmetrical and the temperature will be the same everywhere.

The general heat-conduction equation with constant thermal properties can be written as

Contributed by the Heat Transfer Division for publication in the JOURNAL OF HEAT TRANSFER. Manuscript received by the Heat Transfer Division November 22, 1982.

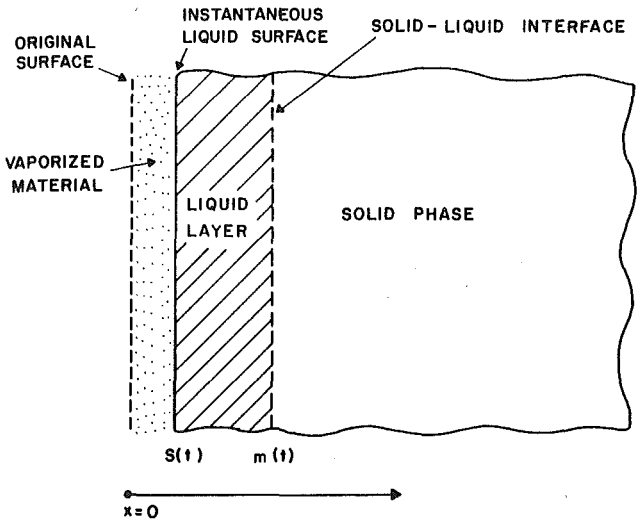

Fig. 1 Schematic representation of solid-liquid-vapor interfaces

$$\rho c\frac{\partial T}{\partial t} - k\nabla^2 T = \dot{q}(x, t) \tag{3}$$

where ρ, c, k are independent of temperature. For a semi-infinite medium, the Green's function is given by

$$G(x, t, x', t') = \frac{1}{2\sqrt{\pi\alpha(t-t')}}\{e^{-\frac{(x-x')^2}{4\alpha(t-t')}} + e^{-\frac{(x+x')^2}{4\alpha(t-t')}}\} \tag{4}$$

where α is the thermal diffusivity. The general solution for the temperature rise due to any deposition function is given by [4]

$$T(x, t) = \int_{t'}\int_{x'} \frac{1}{\rho c}\dot{q}(x', t')G(x, t, x', t')dx'dt' \tag{5}$$

Once melting occurs, the condensed phase consists of two regions

(*a*) $s(t) \le x \le m(t)$ for the melt layer
(*b*) $m(t) \le x$ for the solid phase

where

$s(t)$ is the instantaneous distance of the melted surface.
$m(t)$ is the distance of the melted layer from the surface (as shown in Fig. 1).

The boundary conditions are now that at $x = m(t)$

$$T_s(m(t), t) = T_l(m(t), t) = T_m \tag{6a}$$

and

$$-K_l\frac{\partial T_l}{\partial x}\bigg|_{m(t)} = -K_s\frac{\partial T_s}{\partial x}\bigg|_{m(t)} + \rho_s L_f w(t) \tag{6b}$$

where T_m is the melting temperature; the subscripts s and l refer to solid and liquid regions, respectively; L_f is the latent heat of fusion; and

$$w(t) = \frac{dm}{dt} \tag{7}$$

is the velocity of the melt-solid interface.

If the heating is continued long enough and at a sufficiently high rate, significant vaporization may occur from the surface, assuming that the melting material stays in place. It is necessary to account for the receding surface at the interface between vapor and solid or liquid. This can be done by introducing a moving coordinate system

$$z(t) = x - s(t) \tag{8}$$

for which the surface always remains at $z = 0$. Transforming the heat conduction equation (1) or (3) to this moving frame gives

$$\rho c\left(\frac{\partial T}{\partial t} + \frac{\partial T}{\partial z}\cdot\frac{dz}{dt}\right) - \nabla\cdot k\nabla T = \dot{q}(z, t) \tag{9}$$

where

$$\frac{dz}{dt} = -\frac{ds(t)}{dt} = -v(t) \tag{10a}$$

$v(t)$ = velocity of the receding surface. This velocity is a highly nonlinear function of the surface temperature. Models to calculate surface velocity and evaporation are given in detail in (3). In these models, the surface velocity is given by

$$v(t) = 5.8\times 10^{-2}\frac{x\sqrt{A}P_v(T_v)}{\rho(T_v)\sqrt{T_v}}[0.8 + 0.2e^{-t/10\tau_c}]\text{cm/s} \tag{10b}$$

where

x = sticking probability (usually = 1)
A = atomic mass number
P_v = vapor pressure (Torr)
τ_c = vapor collision frequency (s^{-1}).

The kinetics of evaporation establish the connection between the surface temperatures and the net atom flux leaving the surface. Since the maximum temperature will be at the surface, no boiling phenomena is assumed to take place. Consequently, there is no specific temperature where a phase change from liquid to vapor phase can occur. Rather there is a continuous flow of vaporized atoms in which the rate of material removal depends only on the surface temperature, the corresponding vapor pressure, and the type of wall material.

Substituting equation (10*a*) into equation (9) gives

$$\rho c\frac{\partial T}{\partial t} - \rho c v(t)\frac{\partial T}{\partial z} - \nabla\cdot k\nabla T = \dot{q}(z,t) \tag{11}$$

The main difference in this equation is that it includes the convective term $v(t)\partial T/\partial z$. This term is important in the case of intensive evaporation if we are to obtain accurate calculations of the temperature. The surface boundary condition is then given by

$$F(t) = -k\frac{\partial T}{\partial z}\bigg|_{z=0} + \rho L_v v(t) + \sigma\epsilon(T_v^4 - T_0^4) \tag{12}$$

where

$v(t)$ is again the velocity of the receding surface
$F(t)$ is the incident heat flux

Equation (11) can be written as

$$\rho c\frac{\partial T(z, t)}{\partial t} - k\nabla^2 T(z, t) = \dot{q}(z, t) + \rho c v(t)\frac{\partial T(z, t)}{\partial z} \tag{13}$$

The right-hand side of equation (13) consists of the volumetric energy deposition function and a convective term $\rho c v(t)\ \partial T/\partial z$, which could be treated as a part of the deposition function. Then equation (13) can written as

$$\rho c\frac{\partial T(z, t)}{\partial t} - k\nabla^2 T(z, t) = \dot{q}'(z, t) \tag{14}$$

where

$$\dot{q}'(z, t) = \dot{q}(z, t) + \rho c v(t)\frac{\partial T(z, t)}{\partial z} \tag{15}$$

The solution for the temperature rise due to the modified deposition function given by equation (15) and boundary condition in equation (12) is given by [5]

$$T(z,t)=\int_{t'}\int_{x'}\frac{1}{\rho c}\dot{q}'(z',t')G(z,t.\,z',t')dz'dt'$$

$$-\alpha\int_{t'}dt'G(z,t,0,t')\frac{\partial T(0,t')}{\partial z} \tag{16}$$

From equation (12) the gradient of the temperature can be represented by

$$k\frac{\partial T(0,t)}{\partial z}=\rho L_v v(t)+\sigma\epsilon(T_v^4-T_0^4)-F(t) \tag{17}$$

Substituting equation (17) and (15) into equation (16) yields

$$T(z,t)=\frac{1}{\rho c}\int_{t'}\int_{x'}(\dot{q}(z',t')+\rho c v(t')\nabla T(z',t'))$$
$$G(z,t,z',t')dz'dt' \tag{18}$$
$$+\frac{1}{\rho c}\int_{t'}G(z,t,0,t')(F(t')-\rho L_v v(t')-\sigma\epsilon(T_v^4-T_0^4))dt'$$

where

$$\nabla T(z,t) = \frac{\partial T(z,t)}{\partial z}$$
$$T_v = T(0,t)$$

The difficulty in calculating the temperature rise from equation (18) is that both $v(t)$ and $\nabla T(z,t)$ are functions of the current temperatures, which are unknown. This is also true for the radiative heat transfer term in the second integral of equation (18). Although calculating the surface velocity, $v(t)$, requires only the knowledge of the surface temperature, the term $\nabla T(z,t)$ requires the current temperature distribution throughout the entire space.

A good approximation for the solution of equation (18) is to use the numerical techniques developed in [6]. In these techniques, space and time are divided into many divisions forming mesh points. The integrals over the time in equation (18) are replaced by a summation over the discrete values of time. The integration over the time is carried out from the initial time ($t = 0$) up to the time where the temperature is needed (i.e., T_n). The integration over space is carried out over the entire space. Each time integral term in equation (18) is replaced by two parts. The first part is a summation from the initial time and up to the time before the last (i.e., t_{n-1}). The second part is when the time approaches the time at which the temperature is needed (i.e., t_n). Then the solution for the temperature increase (at any point x_n and at time t_n) can be written as

$$T(x_n,t_n)=\sum_{t_i'=0}^{t_{n-1}}w_i\Delta t_i\int_0^\infty\frac{1}{\rho c}[\dot{q}(x',t_i')+\rho c v(t_i')\nabla T(x',t')]$$
$$G(x_n,t_n,x',t_i')\,dx'$$
$$+w_n\Delta t_n\operatorname{Lim}_{t_i'\to t_n}\int_0^\infty\frac{1}{\rho c}[\dot{q}(x',t_i')+\rho c v(t_i')\nabla T(x',t_i')]$$
$$G(x_n,t_n,x',t_i')dx'$$
$$+\frac{1}{\rho c}\sum_{t_i'=0}^{t_{n-1}}\Delta t_i[F(t_i')-\rho L_v v(t_i')-\sigma\epsilon(T^4(0,t_i')-T_0^4)]$$
$$G(x_n,t_n,0,t_i')$$
$$+\frac{1}{\rho c}\Delta t_n[F(t_n)-\rho L_v v(t_n)-\sigma\epsilon(T^4(0,t_n)$$
$$-T_0^4)]\frac{1}{2\sqrt{\pi\alpha\Delta t_n}}e^{-(x_n^2/4\alpha\Delta t_n)} \tag{19}$$

where

$T(x_n,t_n)$ is the temperature at any point x_n and time t_n.

w_i is a weighting factor depending on the method of integration.

Δt_i is the incremental time step.

In the second part of the first integral of equation (19), the Green's function possesses a singularity when $t_i' \to t_n$. To avoid this singularity, the last time step is made to be much smaller compared to any other time step, i.e.,

$$\Delta t_n << \Delta t_i \tag{20}$$

where

$$t_{n-1}=t_n-\Delta t_n \tag{21}$$

It can easily be shown that [6]

$$\operatorname{Lim}_{\epsilon\to 0}\frac{1}{2\sqrt{\pi\alpha\epsilon}}e^{-\frac{(x-x')^2}{4\alpha\epsilon}}\to\delta(x-x') \tag{22}$$

where $\delta(x-x')$ is the cronial δ-function. Using this result the last term of the first integral in equation (19) can now be written as

$$w_n\Delta t_n\int_0^\infty\frac{1}{\rho c}[\dot{q}(x',t_i')+\rho c v(t_i')\nabla T(x',t_i')]\operatorname{Lim}_{t_i'\to t}$$
$$G(x_n,t_n,x',t_i')\,dx'$$
$$=w_n\Delta t_n\int_0^\infty\frac{1}{\rho c}[\dot{q}(x',t_i')+\rho c v(t_i')\nabla T(x',t_i')][\delta(x-x')$$
$$+\delta(x+x')]dx'$$

It can also be shown that [4]

$$\left.\begin{aligned}\int f(x',t)\delta(x-x')dx'=f(x,t)\\ \int f(x',t)\delta(x+x')dx'=f(-x,t)\end{aligned}\right\} \tag{23}$$

Then substituting equation (22) in equation (19) and using the result from equation (23), the temperature rise in equation (19) reduces to

$$T(x_n,t_n)=\ldots+w_n\Delta t_n\frac{1}{\rho c}[\dot{q}(x_n,t_n)+\rho c v(t_n)\nabla T(x_n,t_n)]$$
$$+\frac{1}{\rho c}\sum_{t_i'=0}^{t_{n-1}}\Delta t_i[F(t_i')$$
$$-\rho L_v v(t_i')-\sigma\epsilon(T^4(0,t_i')-T_0^4)]G(x_n,t_n,0,t_i')$$
$$+\frac{1}{\rho c}[F(t_n)-\rho L v(t_n)-\sigma\epsilon(T^4(0,t_n)-T_0^4)]\frac{1}{2\sqrt{\pi\alpha}}e^{-(x_n^2/4\alpha\Delta t_n)}\sqrt{\Delta t_n} \tag{24}$$

where

$$\int_0^\infty dx'\,\dot{q}(x',t_n)\delta(x_n-x')=\dot{q}(x_n,t_n)$$

and

$$\int_0^\infty dx'\,\nabla T(x',t_n)\delta(x_n-x')=\nabla T(x_n,t_n)$$

since

$$\dot{q}(-x_n,t_n)=0$$

and

$$\nabla T(-x_n,t_n)=0$$

Again the R.H.S. of equation (24) contains terms that are functions of the current unknown temperatures. These can be

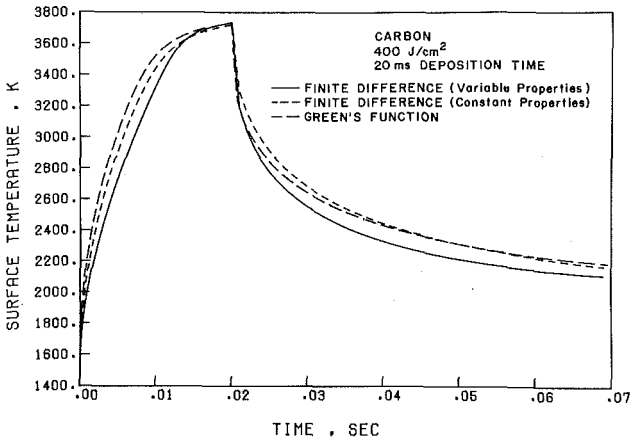

Fig. 2 Comparison of surface temperature rise for carbon for 400 J/cm^2 deposited in 20 ms by different methods

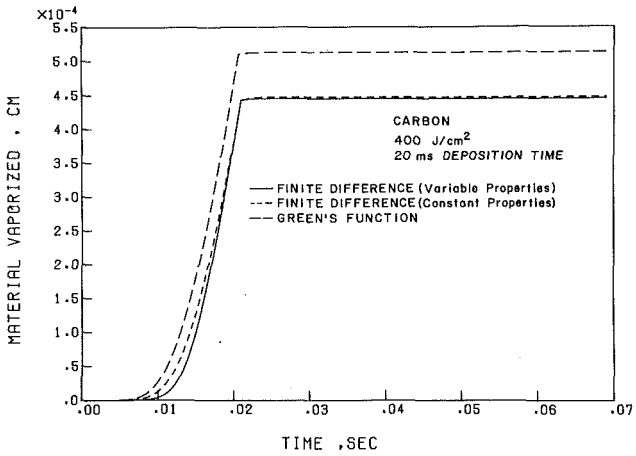

Fig. 4 Evaporated material from carbon by different methods

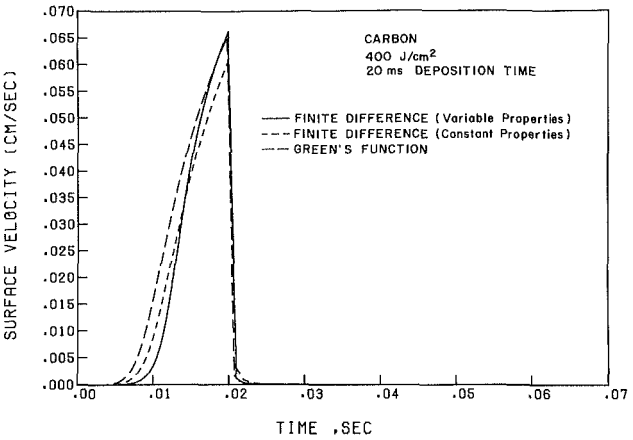

Fig. 3 Carbon surface velocity for 400 J/cm^2 deposited in 20 ms by different methods

approximated by using the temperatures from the previous time step which are known. By choosing the increments between time steps small enough, the solution of equation (24) yields an accurate approximation to the integral equation (18). These choices always involve a compromise between accuracy and computer time. However, the required time step for these calculations is found to be much larger than the one required by the finite difference methods to solve the same problem.

The solution of equation (24) is implemented in the computer code A*THERMAL [7]. This equation can be used to determine the thermal response of fusion first walls both in inertial and in magnetic confinement reactors due to any kind of incident radiation, such as laser, x-rays, heat flux, or ions (light or heavy) for inertial confinement and plasma ions in magnetic confinement reactors.

3 Test Case

To test the accuracy of the solution for the moving boundary problem developed in this study, a comparison with the finite difference method is made. An example of the plasma disruption case [3] is considered where 400 J/cm^2 of plasma energy is deposited in a carbon first wall in 20 ms duration when the plasma suddenly and for unkown reasons becomes unstable. Carbon does not melt so only one moving boundary at the surface is considered in the solution of the heat conduction equation. The comparison is made between the finite difference with and without the variations of the thermal properties with temperature. In the Green's function method, it is assumed that the thermal properties are constant and equal to those of the finite difference with constant properties. The thermophysical properties used in these calculations are given in [8]. Perturbation methods to account for the variation of thermal properties with temperature in the Green's function method are developed in [6]. A solution for the two moving boundaries problem where the material could change phase beside the surface moving boundary is also implemented in the computer code A*THERMAL.

4 Results and Discussion

The surface temperature as a function of the deposition time for the three methods, i.e., finite difference with variable properties, finite difference with constant properties, and the Green's function is shown in Fig. 2. The agreement between the Green's function and the finite difference with constant properties is very good as seen from Fig. 2. The little difference between the two methods, which is less than 3 percent, could be explained by the size of the time step chosen for each method. Although the Green's function method seems to require more calculations than the finite difference, its time step is much larger and its calculation is more straightforward than that for the finite difference approach. The effect of the variation of thermal properties on the surface temperature can also be seen from Fig. 2. The constant thermal properties chosen for Green's function and the finite difference were an average over a high temperature range. Because the lower the temperature, the higher the conductivity for carbon, the finite difference with variable properties has lower temperature than the other two methods either at earlier times in the pulse or at longer times after the end of the disruption.

The velocity of the receding surface, $v(t)$, as a function of time for the three methods of calculation is shown in Fig. 3. The lower surface velocity at earlier times for the finite difference with variable properties is due to the lower surface temperature because of higher thermal conductivity. The difference between the finite difference with constant properties and Green's function is also illustrated in Fig. 3. The agreement between the two methods is considered very good. The slightly higher velocity predicted by Green's function is due to the slightly higher surface temperature. Because of the highly nonlinear dependence of the surface velocity on the surface temperature, the difference between the surface velocity calculation by Green's function and by the finite difference methods is larger than the difference in calculating the surface temperature.

The amount of the total material vaporized can be

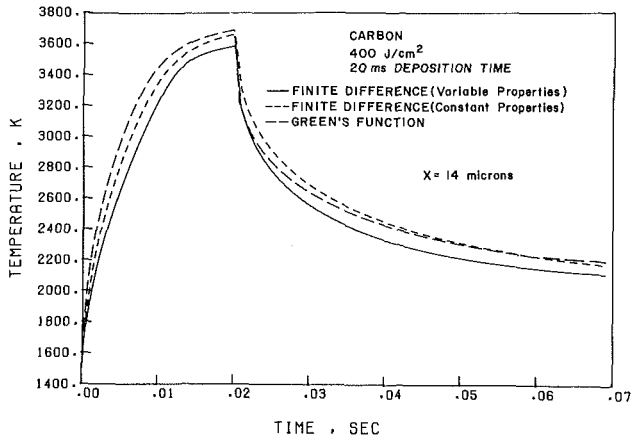

Fig. 5 Comparison of temperature rise for carbon for 400 J/cm² deposited in 20 ms by different methods at x = 14 microns

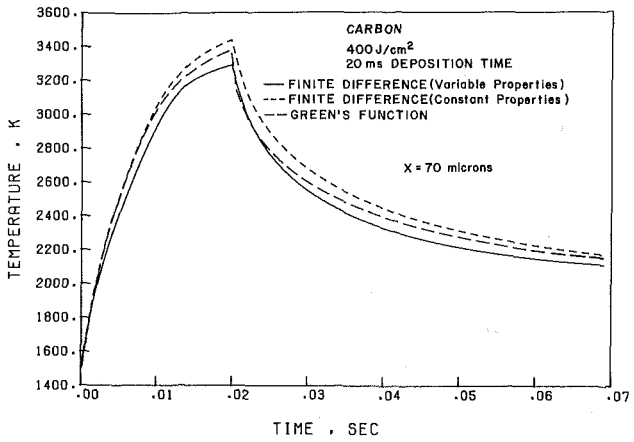

Fig. 6 Comparison of temperature rise for carbon for 400 J/cm² deposited in 20 ms by different methods at x = 70 microns

estimated by integrating the velocity of the receding surface over the pulse duration time. Figure 4 shows the amount of carbon varporized as calculated by the three different methods. The good agreement between both the finite difference methods, i.e., with and without the variation of thermal properties, is not because of the insignificance of the variation of the thermal properties with temperature, but rather because of the chosen value for the constant properties. This can be seen from Fig. 3, where although the velocity of the surface for the variable properties is lower at earlier times of the pulse, it becomes higher than the velocity for the constant properties near the end of the pulse. This incidentally has the effect of producing almost equal material vaporized from carbon for these two methods. On the other hand, Fig. 4 also shows about 10 percent higher total material vaporized by Green's function methods than the finite difference with constant properties. Although the surface temperature calculated using Green's function is only slightly higher than that calculated by the finite difference, and even lower after the end of the disruption time, the strong dependence of the evaporated material on the surface temperature and the integration of the surface velocity over all the pulse duration causes larger differences. After the end of the pulse the temperature drops very fast to where there is no significant vaporization occurring. So the slightly lower surface temperature calculated by Green's function after the end of the pulse will not affect the total material evaporated.

The temperature distribution inside the bulk of the first wall material is also calculated using the three methods. Figures 5 and 6 show the temperature distribution of carbon at distance x = 14 and 70 microns from the surface. Because of the lower temperature inside the material, the difference (at x = 14 and 70 microns) between the finite difference with variable properties is larger than the difference between the other two methods. The larger the distance into the material, the lower the temperature and the larger the effect of the variation of the thermal properties. The agreement between Green's function and the finite difference with constant properties at larger distances into carbon is still very good, as can be seen from Figs. 5 and 6.

5 Conclusions

A method has been developed to solve the heat conduction problem with moving boundaries and other boundary conditions by the use of Green's function. The agreement of this solution with the method of the finite difference to solve the same problem is seen to be very good. The advantage of using the Green's function method is that it provides an easy and fast way of calculating the temperature rise in the material. This is because of no limitations on the time step or the mesh size used for the calculations. However, for more accurate results, the finite difference method is recommended, especially when evaporation is to be evaluated from these temperatures. The variation of the thermal properties with temperature can be very important in calculating accurate temperatures, especially in the case of very high energy depositions or if the material undergoes a change of phase, This is because of the larger differences between the solid- and liquid-phase properties. Because of the highly nonlinear dependence of the receding surface velocity on the surface temperature, a small change in calculating the surface temperature could result in large differences in the surface velocity, and consequently larger differences in calculating the total material removed from the surface by evaporation.

Acknowledgment

Support for this work has been partially provided by the U.S. Department of Energy.

References

1 Cohen, S. A., et al., "Mechanisms Responsible for Topographical Changes in PLT Stainless Steel and Graphite Limitors," *Nuclear Fusion*, Vol. 21, 1981, pp. 233-249.

2 Sabado, M. M., et al., "*Doublet III Limiter Performance and Implications for Mechanical Design and Material Selection for Future Limiters*," General Atomic Report GA-A15633, Oct. 1979.

3 Hassanein, A. M., Kulcinski, G. L., and Wolfer, W. G., "Vaporization and Melting of Materials in Fusion Devices," *J. Nucl. Mat.*, Vol. 103 & 104, 1981, pp. 321-326.

4 Carslaw, H. S., and Jaeger, J. C., *Conduction of Heat in Solids*, 2d ed., Oxford, 1959.

5 Ozisik, M. N., *Heat Conduction*, Wiley-Interscience, New York, 1980.

6 Hassanein, A. M., and Kulckinski, G. L., "Numerical Methods for Calculating the Temperature Increase in ICF First Walls," University of Wisconsin Fusion Engineering Program Report UWFDM-397, Nov. 1980.

7 Hassanein, A. M., "Thermal Effects and Erosion Rates Resulting from Intense Deposition of Energy in Fusion Reactor First Walls," University of Wisconsin Fusion Engineering Program Report UWFDM-465, Ph.D. thesis, Mar. 1982.

8 Rasor, N. S., and McClelland, J. D., "Thermal Properties of Graphite, Molybdenum and Tantalum, to Their Destruction Temperatures," *J. Phys. Chem. Solids*, Vol. 15, 1959, pp. 17-26.

Adaptive Collocation Method for Simultaneous Heat and Mass Diffusion With Phase Change[1]

T. C. Chawla
Mem. ASME

D. R. Pedersen

G. Leaf

W. J. Minkowycz[2]
Mem. ASME

A. R. Shouman[3]
Mem. ASME

Reactor Analysis and Safety Division,
Argonne National Laboratory,
Argonne, Ill. 60439

In post-accident heat removal applications, the use of a lead slab is being considered for protecting a porous bed of steel shot in an ex-vessel cavity from direct impingement of molten steel or fuel as released from the reactor vessel following a hypothetical core disassembly accident in an LMFBR. The porous bed is provided to increase the coolability of the fuel debris by the sodium coolant. The present study is carried out to determine melting rates of a lead slab of various thicknesses in contact with sodium coolant and to evaluate the extent of the penetration and the mixing rates of molten lead into liquid sodium by molecular diffusion alone. The study shows that these two calculations cannot be performed simultaneously without the use of adaptive coordinates which cause considerable stretching of the physical coordinates for mass diffusion. Because of the large difference in densities of these two liquid metals, the traditional constant density approximation for the calculation of mass diffusion cannot be used for studying their interdiffusion. The use of the orthogonal collocation method along with adaptive coordinates produces accurate results, which are ascertained by comparing with the existing analytical solutions for concentration distribution for the constant density approximation and for melting rates of infinite lead slab. The analysis further shows that the melting rate progressively increases as the thickness of lead slab decreases. The mixing of two liquid metals by molecular diffusion is extremely slow and the molten lead is likely to stay separated from the sodium coolant unless free convection exists in the sodium. Before any significant mixing takes place, the lead, upon melting, will sink to the bottom of the porous bed and not participate in removing heat from fuel debris lying on the top of the porous steel bed.

Introduction

In postaccident heat removal (PAHR) considerations, following a failure of pressure vessel in a hypothetical LMFBR core disassembly accident, the release of molten core debris into ex-vessel cavity is of major concern. To protect the ex-vessel cavity floor from failure, numerous designs are under consideration. In one such consideration, a slab of lead in the range of 10-20 cms in thickness is placed over a porous bed of stainless steel shots (provided for improved heat transfer by sodium coolant) lying over the ex-vessel cavity floor (see Fig. 1). The slab of lead is expected to protect the porous bed of stainless shots against direct impingement of molten steel or fuel as released from the pressure vessel. Since the ex-vessel cavity is considerably larger in diameter than the pressure vessel, it is expected that sodium coolant will be in direct contact with the lead slab in the outer (relative to pressure vessel) part of the ex-vessel cavity. It is therefore of interest to determine: (*i*) the rate at which lead will melt upon contact with the pool of sodium and (*ii*) the rate and the extent of penetration by molecular diffusion of molten lead into sodium. Molten lead is completely miscible in liquid sodium; however, because of large density differences, initially the only mechanism available for mixing of molten lead into sodium coolant is molecular diffusion or possibly by natural convection in the sodium pool in the presence of heat sources such as due to a layer of fuel debris lying on the lead slab. The effect of natural convection in the sodium pool is outside the subject matter of the present study. In the present study, we will merely evaluate the rate and the extent of mixing molten lead into sodium by molecular diffusion and develop an adaptive collocation method for solving one-dimensional phase change problems involving simultaneous heat and mass tranfer.

The study of simultaneous molecular diffusion of heat and mass in a liquid-liquid system especially with large density differences such as between molten lead and sodium presents a considerable challenge in view of the following two considerations: (*i*) the rate of molecular mass diffusion is considerably slower than that for heat diffusion, and therefore, the extent of the penetration of mass diffusion at any given time is significantly smaller than that for heat diffusion, and (*ii*) owing to large density difference between sodium and lead, constant mixture density approximation for mass

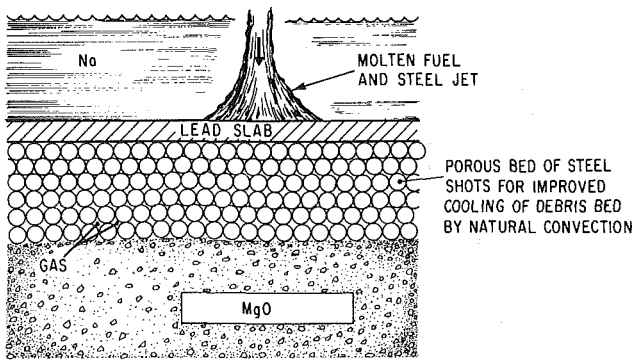

Fig. 1 The schematic of the physical problem analyzed

[1]This work was performed under the auspices of the U.S. Department of Energy.

[2]Presently at the Department of Mechanical Engineering, University of Illinois at Chicago, Chicago, Ill. 60680

[3]Presently at the Department of Mechanical Engineering, New Mexico State University, Las Cruces, N.M. 88003

Contributed by the Heat Transfer Division for publication in the JOURNAL OF HEAT TRANSFER. Manuscript received by the Heat Transfer Division January 24, 1983.

diffusion is not valid, and therefore, an analytical solution though available for constant density approximation is not applicable to lead-sodium diffusion. As will be demonstrated, a constant density approximation leads to a significant error in the solution of mass diffusion problem for the system under consideration. Consequently, a solution of the problem has to be pursued numerically. However, because of the foregoing considerations, a solution by numerical methods presents a considerable challenge. The enormous difference in the diffusion rates for heat and mass introduces stiffness in the system of ODEs resulting from spatial discretization of the PDEs governing these two diffusion processes. Therefore, finite differencing with respect to time requires special handling. Significant difference in penetration distances of heat and mass diffusion results in an extremely poor spatial resolution for mass diffusion if the same mesh distribution is used in physical coordinates for calculating simultaneously both of these processes.

Since the width of the field for mass diffusion is considerably smaller than that for the heat diffusion, the mesh distribution will correspondingly have to be very closely spaced in the field where computations of mass diffusion are required. With the conventional methods, the number and the density of meshes required for the calculations of simultaneous heat and mass diffusion greatly exceed those that are theoretically necessary for normal engineering accuracy. To circumvent these difficulties, we have devised a special coordinate system to span the field in which mass diffusion is important. Coupled with this coordinate system, we will utilize a collocation method with Hermite splines as approximatling functions and Gaussian quadrature points as the collocation points. This method is known (see for example [1] and [2]) for very high accuracy, both for moving boundary problems and problems that contain very sharp variation of dependent variables or shock fronts.

For the problem just described, there does not appear to be any analytical solution available; however, Rubinstein [3] and Lunardini [4] discuss solutions of a number of simplified moving boundary problems involving simultaneous heat and mass transfer.

Formulation of Model and Governing Equations

Consider a slab of lead of finite thickness L at room temperature brought suddenly into contact with hot liquid sodium pool of very large height. The initial temperature of sodium is such that upon contact, lead begins to melt immediately. The molten lead, which is completely miscible in all proportions in sodium liquid, begins to diffuse into sodium and sodium into molten lead. However, the mass diffusion process is considerably slower than the melting rate of lead; therefore, at all times ample molten lead is available for diffusion. The lower side of lead is in contact with a porous bed with porosity exceeding 50 percent and is filled with gases. For simplicity in modeling, the lower side of the slab has been assumed to have negligible cooling. Both lead and sodium extend sufficiently far enough laterally such that heat and mass transfer can be assumed to be one-dimensional through the thicknesses of these materials. Figure 2 shows schematically the geometry of this system. Although, for better physical appeal, the discussion is centered around the sodium-lead system, the succeeding treatment of this physical problem is sufficiently general to have applicability to a wide variety of heat and mass diffusion problems with similar characteristics.

The physical coordinate x is placed at the interface between lead and sodium as shown in Fig. 2. This figure also shows schematically temperature and concentration distributions following contact at $x = 0$. The melt interface between solid and molten lead is located at $x = \delta(t)$. The equations governing one-dimensional heat and mass diffusion and the motion of molten interface are given as

$$\frac{\partial T}{\partial t} = \alpha \frac{\partial^2 T}{\partial x^2} \tag{1}$$

$$\frac{\partial C}{\partial t} = \frac{D}{\rho} \frac{\partial}{\partial x}\left(\rho \frac{\partial C}{\partial x}\right) \tag{2}$$

Nomenclature

A = coefficient matrix in equation (40)
C = mass concentration of lead in sodium-lead mixture
C_p = specific heat at constant pressure
D = diffusion coefficient
F = dependent variable or function
G = right-hand side of equation (40)
ΔH = latent heat of fusion
K = thermal conductivity
k = order of hermite splines
L = thickness of lead slab
l_p = number of intervals in pth region
N_p = number of unknown coefficients for a given PDE in a pth region
Se = $C_{pM}(T_\infty - T_M)/\Delta H$
T = temperature
T_0 = initial temperature of lead slab
T_M = melting temperature for lead
T_∞ = initial temperature of sodium coolant
t = time
x = physical coordinate as shown in Fig. 1
Y = unknown vector of coefficients of expansion and melt interface position used in equation (40)
α = thermal diffusivity
β = stretching or contraction parameter for coordinate transformation
γ = $\rho_N^{-1} - \rho_M^{-1}$
Δ = δ/L, nondimensional position of melt interface
δ = position of melt interface
δ_∞ = position of melt interface for the case of infinite lead slab
η = nondimensional coordinate for heat diffusion
η_c = nondimensional coordinate for mass diffusion
θ = $(T - T_\infty)/(T_M - T_\infty)$, nondimensional temperature for liquid sodium
μ = proportionality parameter for melt interface position
ρ = density of mixture of lead and sodium
ρ_M = density of pure molten lead
ρ_N = density of pure sodium coolant
$\sigma^p_{j,q}$ = position of Gauss-Legendre quadrature point of order q used as a collocation point in jth interval and pth region
τ = $t\alpha_M/L^2$, nondimensional time
ϕ = $(T - T_\infty)/(T_M - T_\infty)$, nondimensional temperature for solid lead
ϕ_0 = $(T_0 - T_\infty)/(T_M - T_\infty)$, initial nondimensional temperature for solid lead
ψ = $(T - T_\infty)/(T_M - T_\infty)$, nondimensional temperature for molten lead
ω = mass concentration for lead in lead-sodium mixture in the molten lead region (see Fig. 2)

Subscripts

M = molten lead
N = sodium coolant
p = pth region, $1 \le p \le 3$
S = solid lead

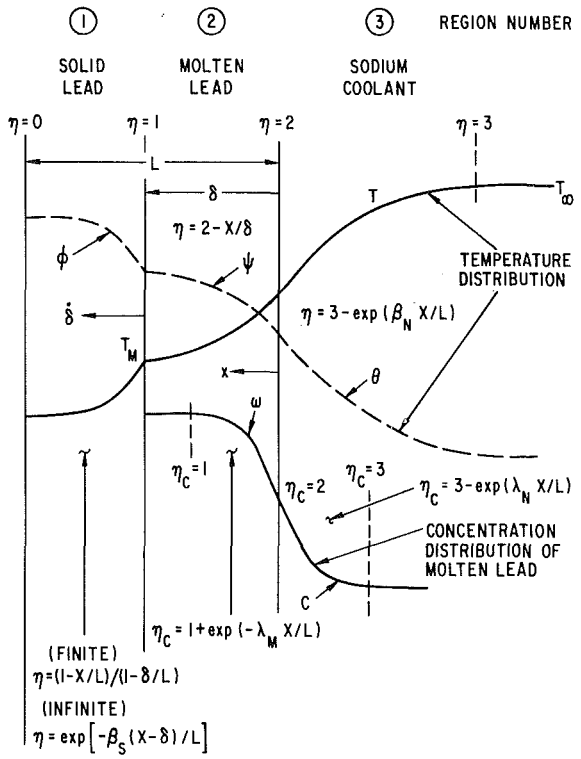

Fig. 2 Schematic of lead melting and diffusion in sodium following their contact

$$\rho\Delta H\frac{d\delta}{dt}=K_s\frac{\partial T}{\partial x}\Big|_{\delta^+}-K_M\frac{\partial T}{\partial x}\Big|_{\delta^-} \tag{3}$$

with boundary conditions as

$$K_s\frac{\partial T}{\partial x}\Big|_L=0 \tag{4}$$

$$T(\delta,t)=T_M \tag{5}$$

$$T(0^+,t)=T(0^-,t) \tag{6}$$

$$K_M\frac{\partial T}{\partial x}\Big|_{0^+}=K_N\frac{\partial T}{\partial x}\Big|_{0^-} \tag{7}$$

$$T(-\infty,t)=T_\infty \tag{8}$$

$$C(\delta,t)=1 \tag{9}$$

$$C(0^+,t)=C(0^-,t) \tag{10}$$

$$D_M\frac{\partial C}{\partial x}\Big|_{0^+}=D_N\frac{\partial C}{\partial x}\Big|_{0^-} \tag{11}$$

$$C(-\infty,t)=0 \tag{12}$$

and initial conditions as

$$T(x,0)=T_0,\ C(x,0)=1 \text{ for } x>0 \tag{13}$$

$$T(x,0)=T_\infty,\ C(x,0)=0 \text{ for } x<0 \tag{14}$$

$$\delta(0)=0 \tag{15}$$

Density, ρ of the mixture occurring in equation (2) is related to densities ρ_M and ρ_N of pure lead and sodium through

$$\frac{1}{\rho}=\frac{1-C}{\rho_N}+\frac{C}{\rho_M}. \tag{16a}$$

The foregoing expression clearly shows that if ρ_N and ρ_M were nearly equal, the mixture density ρ will be nearly constant; however, $\rho_M \simeq 13\ \rho_N$, implying that the mixture density ρ cannot be assumed constant. As will be demonstrated subsequently, the usual assumptions of constant ρ in solving mass diffusion problem leads to significant errors in the calculation of concentration C from equation (2). Further, we notice that for liquids $\alpha/D \sim 10^4-10^5$, this implies that the boundary layer (or penetration) thickness (which varies as square root of diffusivity and is a measure of the extent of diffusion) for mass diffusion, L_D is at least 10^{-2} times smaller than the boundary layer thickness for heat diffusion, L_α. Furthermore, $\delta \sim \sqrt{\alpha_m t}$ (for an infinite lead slab), it then follows that $(L_D/\delta) \sim 10^{-2}$. This discussion implies that the thickness of the molten region is always about two orders of magnitude greater than mass diffusion boundary layer thickness. Consequently, boundary conditions (9) need not be applied at $x = \delta$. As will be seen subsequently, the penetration thickness for mass diffusion is on the order of millimeters over the time span of interest. Thus for all practical purposes, boundary conditions (9) can be modified to read

$$C(\infty,t)=1 \tag{16b}$$

It follows from the previous discussion that field width of interest for the calculation of mass concentration is considerably smaller than that for the heat diffusion. Furthermore, boundary conditions (16*b*) and (12) imply that for all practical purposes both molten lead and sodium can be considered media of infinite thicknesses for the purpose of calculating mass concentration. In writing equations (1) and (2), we have implicitly assumed that properties are constant, i.e., independent of temperature or concentration field. As will be seen subsequently, the penetration thickness of the concentration both in lead and sodium is extremely small compared to the field width for heat diffusion; thus, for all practical purposes, mass diffusion is confined in the neighborhood of interface between sodium and lead. It then follows that the properties of the two media for heat diffusion are independent of concentration over almost all the field width. Similarly, it follows that diffusion coefficients for these media are also independent of temperature fields. It also follows that the mesh distribution in physical coordinates is not suitable for the calculation of concentration as it must be adaptive to account for extreme narrowness of the field width for the concentration. In other words, we must stretch the field width by using a coordinate transformation of the form

Lead:

$$\eta_c=1+\exp(-\lambda_M x/L) \tag{17a}$$

Sodium:

$$\eta_c=3-\exp(\lambda_N x/L) \tag{17b}$$

where $\lambda_M >> 1$ and $\lambda_N >> 1$ are the stretching parameters. These parameters allow us to stretch the widths to any desired degree. Futhermore, meshes with these transformations are much more closely spaced in the neighborhood of interface where the variation of concentration is the sharpest. Clearly, these transformations change an infinite domain in physical coordinates into a finite domain in the transformed coordinates.

In order to track the moving melt interface, it is convenient to introduce the following coordinate transformations

Solid lead (region #1):

for a slab of finite thickness,

$$\eta=\frac{1-x/L}{1-\Delta},\ \Delta=\delta/L \tag{18a}$$

for a slab of infinite thickness,

$$\eta=\exp\left[-\beta_s\left(\frac{x}{L}-\Delta\right)\right] \tag{18b}$$

Molten lead (region #2):

$$\eta = 2 - \frac{x/L}{\Delta} \tag{19}$$

Sodium coolant:

$$\eta = 3 - \exp(\beta_N x/L) \tag{20}$$

The transformation (18) allows the transformed coordinate η to vary from 0 to 1 in the solid lead region, both for finite and infinite slabs. The transformation (19) for molten lead allows η to vary between 1 and 2. The transformation (20) for sodium allows η to vary between 2 and 3. The boundaries of these coordinates are shown in Fig. 2. In these transformed coordinates, the melt interface always lies at $\eta = 1$ and consequently appears immobilized in these coordinates. We may note that transformation (17) for the concentration also vary from 1 to 2 in molten lead region and from 2 to 3 in sodium. By maintaining these boundary values of the transformed coordinates, we can use the same mesh distributions for concentration in transformed coordinates as used for heat diffusion in molten lead and sodium, respectively. This, in turn, will allow us to use the same set of approximating functions for both heat and mass diffusion.

Using transformation (17–20) in equations (1–12) and (16*b*) gives

Solid lead:

finite slab,

$$\frac{\partial \phi}{\partial \tau} = -\frac{\dot{\Delta}}{1-\Delta}\eta\frac{\partial \phi}{\partial \eta} + \frac{(\alpha_s/\alpha_M)}{(1-\Delta)^2}\frac{\partial^2 \phi}{\partial \eta^2} \tag{21a}$$

$$\left.\frac{\partial \phi}{\partial \eta}\right|_{\eta=0} = 0 \tag{21b}$$

$$\phi(1, \tau) = 1 \tag{21c}$$

infinite slab,

$$\frac{\partial \phi}{\partial \tau} = -\beta_S \eta \dot{\Delta}\frac{\partial \phi}{\partial \eta} + (\alpha_s/\alpha_M)\beta_s^2 \eta\left(\frac{\partial \phi}{\partial \eta} + \eta\frac{\partial^2 \phi}{\partial \eta^2}\right) \tag{22a}$$

$$\phi(0, \tau) = \phi_0 \tag{22b}$$

$$\phi(1, \tau) = 1 \tag{22c}$$

Molten lead:

$$\frac{\partial \psi}{\partial \tau} = -(2-\eta)\frac{\dot{\Delta}}{\Delta}\frac{\partial \psi}{\partial \eta} + \frac{1}{\Delta^2}\frac{\partial^2 \psi}{\partial \eta^2} \tag{23a}$$

$$\psi(1, \tau) = 1 \tag{23b}$$

$$\psi(2^-, \tau) = \theta(2^+, \tau) \tag{24}$$

$$\frac{\partial \omega}{\partial \tau} = \lambda_M^2(\eta-1)\left(\frac{D_M}{\alpha_M}\right)\left[\gamma\rho(\eta-1)\left(\frac{\partial \omega}{\partial \eta}\right)^2 + \frac{\partial \omega}{\partial \eta} + (\eta-1)\frac{\partial^2 \omega}{\partial \eta^2}\right] \tag{25a}$$

$$\omega(1, \tau) = 1 \tag{25b}$$

$$\omega(2^-, \tau) = C(2^+, \tau) \tag{25c}$$

Sodium:

$$\frac{\partial \theta}{\partial \tau} = \beta_N^2(\eta-3)\left(\frac{\alpha_N}{\alpha_M}\right)\left[\frac{\partial \theta}{\partial \eta} + (\eta-3)\frac{\partial^2 \theta}{\partial \eta^2}\right] \tag{26a}$$

$$\frac{K_M}{\Delta}\left.\frac{\partial \psi}{\partial \eta}\right|_{\eta=2^-} = K_N\beta_N\left.\frac{\partial \theta}{\partial \eta}\right|_{\eta=2^+} \tag{26b}$$

$$\theta(3, \tau) = 0 \tag{26c}$$

$$\frac{\partial C}{\partial \tau} = \lambda_N^2(\eta-3)\left(\frac{D_N}{\alpha_M}\right)\left[\gamma\rho(\eta-3)\left(\frac{\partial C}{\partial \eta}\right)^2 + \frac{\partial C}{\partial \eta} + (\eta-3)\frac{\partial^2 C}{\partial \eta^2}\right] \tag{27a}$$

$$D_M\lambda_M\left.\frac{\partial \omega}{\partial \eta}\right|_{\eta=2^-} = D_N\lambda_N\left.\frac{\partial C}{\partial \eta}\right|_{\eta=2^+} \tag{27b}$$

$$C(3, \tau) = 0 \tag{27c}$$

Here, in mass diffusion equations (25*a*) and (27*a*), we have omitted the use of subscript c on η with a view to using the same mesh distribution both for η and η_c.

Melt interface:

finite lead slab,

$$\dot{\Delta} = \mathrm{Se}\left\{\frac{(K_S/K_M)}{1-\Delta}\left.\frac{\partial \phi}{\partial \eta}\right|_{\eta=1} - \frac{1}{\Delta}\left.\frac{\partial \psi}{\partial \eta}\right|_{\eta=1}\right\} \tag{28a}$$

infinite lead slab,

$$\dot{\Delta} = \mathrm{Se}\left[(K_S/K_M)\beta_S\left.\frac{\partial \phi}{\partial \eta}\right|_{\eta=1^-} - \frac{1}{\Delta}\left.\frac{\partial \psi}{\partial \eta}\right|_{\eta=1^+}\right] \tag{28b}$$

Collocation Method

We shall seek an approximate solution of equations (21–28) by a collocation method using cubic Hermite spline basis functions as approximating functions in the spatial variable η for $F(\eta, \tau)$ (where F denotes a dependent variable). More specifically, let the interval $[p-1, p]$ pertaining to a pth region ($1 \le p \le 3$) be divided by a set of points called break points as

$$p-1 = \eta_1 < \eta_2 < \ldots < \eta_{l+1} = p, \; h_i = \eta_i - \eta_{i-1}$$

A convenient basis for generating Hermite splines is the set

$$\{V_i(\eta), S_i(\eta)\}_{i=1}^{l+1} \text{ where}$$

$$V_i(\eta) = \begin{cases} 3\left(\frac{\eta-\eta_{i-1}}{h_i}\right)^2 - 2\left(\frac{\eta-\eta_{i-1}}{h_i}\right)^3 & \text{for } \eta_{i-1} \le \eta \le \eta_i \\ \left(1-\frac{\eta-\eta_i}{h_{i+1}}\right)^2\left[1+2\left(\frac{\eta-\eta_i}{h_{i+1}}\right)\right] & \text{for } \eta_i \le \eta \le \eta_{i+1} \\ 0 \text{ otherwise} \end{cases} \tag{29a}$$

$$S_i(\eta) = \begin{cases} h_i\left[-\left(\frac{\eta-\eta_{i-1}}{h_i}\right)^2 + \left(\frac{\eta-\eta_{i-1}}{h_i}\right)^3\right] & \text{for } \eta_{i-1} \le \eta \le \eta_i \\ h_{i+1}\left(\frac{\eta-\eta_i}{h_{i+1}}\right)\left(1-\frac{\eta-\eta_i}{h_{i+1}}\right)^2 & \text{for } \eta_i \le \eta \le \eta_{i+1} \\ 0 \text{ otherwise} \end{cases} \tag{29b}$$

It is assumed that the functions $V_i(\eta)$ and $S_i(\eta)$ vanish to the left of η_1 and functions $V_{l+1}(\eta)$ and $S_{l+1}(\eta)$ vanish to the right of η_{l+1}. In addition, we note the following properties of the basis functions:

1 Each $V_i(\eta)$ and $S_i(\eta)$ is continuous, together with its derivative, in the domain $[p-1,\ p]$ with degree of smoothness, $\nu = 2$.

2 Each V_i and S_i is a cubic (i.e., order $k = 4$) polynomial in each subinterval, and they vanish outside the interval $[\eta_{i-1}, \eta_{i+1}]$.

3
$$\begin{matrix} V_i(\eta_j)=\delta_{ij} & V_i'(\eta_j)=0 \\ S_i(\eta_j)=0 & S_i'(\eta_j)=\delta_{ij} \end{matrix} \qquad 1 \le i, j \le l+1$$

In terms of these basis functions, a dependent variable $F(\eta, t)$ can be approximated as

$$F(\eta, \tau) = \sum_{i=1}^{l+1} [F_i(\tau) V_i(\eta) + F_i'(\tau) S_i(\eta)] \tag{30a}$$

where the coefficients of expansion F_i (τ), F_i' (τ) (as follows from property 3 of Hermite splines) are, respectively, the unknown values of the function $F(\eta,\ \tau)$ and its spatial derivative at the break point η_i with $1 \le i \le l+1$; i.e., $F_i(\tau) = F(\eta_i,\ \tau)$, $F_i'(\tau) = F'(\eta_i,\ \tau)$. In view of property 2 of these splines, expansion (30*a*) becomes

$$F(\eta, \tau) = \sum_{i=j}^{j+1} [F_i(\tau) V_i(\eta) + F_i'(\tau) S_i(\eta)] \text{ for } \eta \epsilon (\eta_j,\ \eta_{j+1})$$
$$\text{with } 1 \le j \le l \tag{30b}$$

The use of expansion (30) in equations (21–28) gives, respectively, for finite slab

$$\sum_{i=j}^{j+1} [\dot\phi_i V_i(\eta^1) + \dot\phi_i' S_i(\eta^1)] = -\frac{\dot\Delta}{1-\Delta}\eta^1 \phi'(\eta^1) + \frac{1}{(1-\Delta)^2}\phi''(\eta^1) \tag{31a}$$

$$\dot\phi_1' = 0 \tag{31b}$$

$$\dot\phi_{l+1} = 0 \tag{31c}$$

for infinite slab,

$$\sum_{i=j}^{j+1} [\dot\phi_i V_i(\eta^1) + \dot\phi_i' S_i(\eta^1)] = -\beta_S \eta^1 \dot\Delta \phi'(\eta^1) + \beta_S^2 \eta^1 [\phi'(\eta^1) + \eta\phi''(\eta^1)] \tag{32a}$$

$$\dot\phi_1 = 0 \tag{32b}$$

$$\dot\phi_{l+1} = 0 \tag{32c}$$

$$\sum_{i=j}^{j+1} [\dot\psi_i V_i(\eta^2) + \dot\psi_i' S_i(\eta^2)] = -(2-\eta^2)\frac{\dot\Delta}{\Delta}\psi'(\eta^2) + \left(\frac{\alpha_M/\alpha_S}{\Delta^2}\right)\psi''(\eta^2) \tag{33a}$$

$$\dot\psi_1 = 0 \tag{33b}$$

$$\dot\psi_{l+1} - \dot\theta_{l+1} = 0 \tag{33c}$$

$$\sum_{i=j}^{j+1} [\dot\omega_i V_i(\eta^2) + \dot\omega_i' S_i(\eta^2)] = \lambda_M^2(\eta^2-1)\left(\frac{D_M}{\alpha_S}\right) \{\gamma\rho(\eta^2-1)[\omega'(\eta^2)]^2 + \omega'(\eta^2) + (\eta^2-1)\omega''(\eta^2)\} \tag{34a}$$

$$\dot\omega_1 = 0 \tag{34b}$$

$$\dot\omega_{l+1} - \dot C_1 = 0 \tag{34c}$$

$$\sum_{i=j}^{j+1} [\dot\theta_i V_i(\eta^3) + \theta_i' S_i(\eta^3)] = \beta_N^2(\eta^3-3)\left(\frac{\alpha_N}{\alpha_S}\right)[\theta'(\eta^3) + (\eta^3-3)\theta''(\eta^3)] \tag{35a}$$

$$\dot\psi_{l+1}' - (K_N/K_M)\Delta\beta_N\dot\theta_1' = (K_N/K_M)\beta_N\theta_1'\dot\Delta \tag{35b}$$

$$\dot\theta_{l+1} = 0 \tag{35c}$$

$$\sum_{i=j}^{j+1} [\dot C_i V_i(\eta^3) + \dot C_i' S_i(\eta^3)] = \lambda_N^2(\eta^3-3)\left(\frac{D_N}{\alpha_S}\right)\{\gamma\rho(\eta^3-3)[C'(\eta^3)]^2 + C'(\eta^3) + (\eta^3-3)C''(\eta^3)\} \tag{36a}$$

$$\dot\omega_{l+1}' - \left(\frac{D_N}{D_M}\right)\left(\frac{\lambda_N}{\lambda_M}\right)\dot C_1' = 0 \tag{36b}$$

$$\dot C_{l+1} = 0 \tag{36c}$$

finite lead slab,

$$\dot\Delta = Se\left[\frac{1}{1-\Delta}\phi_{l+1}' - \frac{(K_M/K_S)}{\Delta}\psi_1'\right] \tag{37a}$$

infinite lead slab,

$$\dot\Delta = Se\left[\beta_S\phi_{l+1}' - \frac{(K_M/K_S)}{\Delta}\psi_1'\right] \tag{37b}$$

Here η^P denotes η pertaining to pth region $(1 \le p \le 3)$ and

$$F'(\eta^p) = \sum_{i=j}^{j+1} [F_i V_j'(\eta^p) + F_i' S_i'(\eta^p)] \tag{38a}$$

$$F''(\eta^p) = \sum_{i=j}^{j+1} [F_i V_i''(\eta^p) + F_i' S_i''(\eta^p)] \tag{38b}$$

which hold for $\eta^p \epsilon (\eta_j^p,\ \eta_{j+1}^p)$ with $1 \le j \le l_p$ and $1 \le p \le 3$. For later convenience in obtaining a solution, we have taken the time derivative of the boundary condition after using expansion (30) in them.

Each of these equation sets (equations (31–36)) contain $N_p = 2(l_p + 1)$ with $1 \le p \le 3$ unknown coefficients of expansion. The two boundary conditions associated with each set naturally allow us to determine two coefficients. The remaining unknown coefficient equal to $2l_p$ in each set are determined by evaluating or collocating these PDEs at $2l_p$ collocation points in each region. According to approximation theory [5, 6], optimum collocation points for Hermite splines as the approximating functions are the Gauss-Legendre quadrature points of order 2 for each interval

$$\sigma_{j,q}^p = \frac{1}{2}(\eta_j^p + \eta_{j+1}^p) + (-1)^q \frac{\eta_{j+1}^p - \eta_j^p}{2\sqrt{3}} \quad 1 \le j \le l_p,\ 1 \le q \le 2 \tag{39}$$

The evaluation of each of the PDEs in the set of equations ((31–36)) at the aforementioned collocation points leads to a set of ODEs. These equations, when combined with their boundary conditions and equation (37) for melt interface, give the following set of ODEs written compactly as

$$A(Y, \tau)\dot Y = G(Y, \tau) \tag{40}$$

where Y is an $5N_p + 1$ $(1 \le p \le 3)$ dimensional vector of $5N_p$ unknown coefficients and the position of melt interface. By virtue of the local or piecewise basis of the approximation functions, the coefficient matrix $A(Y, \tau)$ is banded matrix of bandwidth equal to $2(2k-1) + 1$.

Computational Details

The solution of eqauation (40) is obtained by the standard library routine LSODI [7]. It solves the initial value problem

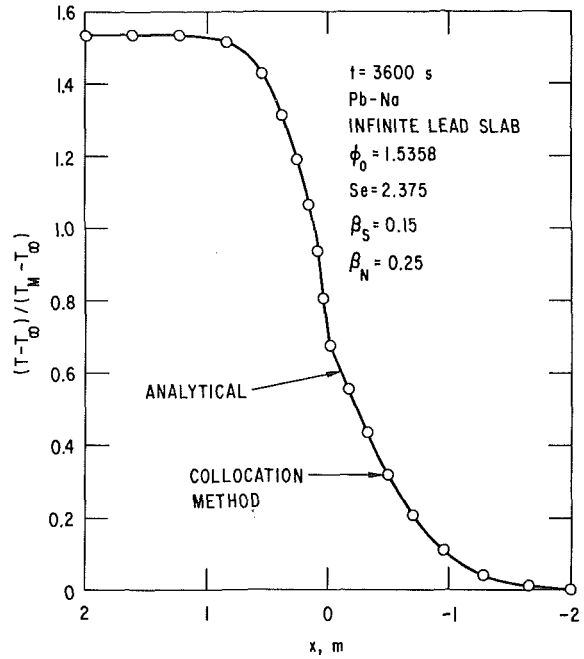

Fig. 3 A comparison of analytical and numerical solutions for temperature profile for the case of infinite lead slab

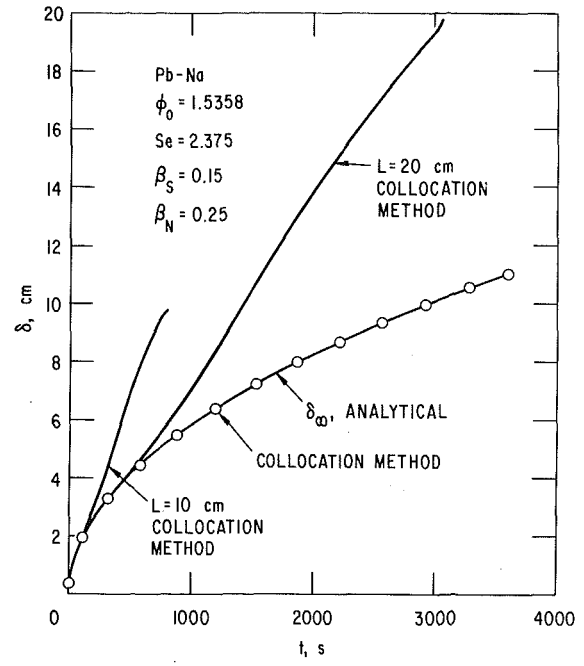

Fig. 4 The position of melt interfaces as a function of time for various thicknesses of the lead slab

with banded coefficient matrix by using Gear's so-called backward multistep differentiation formulas suitable for stiff system. The size of time step is controlled automatically by specified error tolerance for the integrator.

For the system of equations (equations (31-37)), it is clear that at time $\tau = 0$, the system is singular; consequently, we must provide a starting solution that is approximately valid in the neighborhood of $\tau = 0$. One can readily observe that finite lead slab behave like an infinite slab during the short time after it is brought into contract with the sodium pool. Consequently, one can use an analytical solution available [8] for describing temperature profiles and the position of the melt interface subsequent to contact between two infinite slabs initially at uniform but different temperatures. This solution is given as

$$\phi(x,t) = \phi_0 + \frac{1-\phi_0}{\operatorname{erfc}(\mu\sqrt{\alpha_M/\alpha_S})}\operatorname{erfc}\left(\frac{x}{2\sqrt{\alpha_S t}}\right) \tag{41a}$$

$$\psi = \frac{K_M\sqrt{\alpha_N} + K_N\sqrt{\alpha_M}\operatorname{erf}\left(\frac{x}{2\sqrt{\alpha_M t}}\right)}{K_M\sqrt{\alpha_N} + K_N\sqrt{\alpha_M}\operatorname{erf}(\mu)} \tag{41b}$$

$$\theta = \frac{K_M\sqrt{\alpha_N}}{K_M\sqrt{\alpha_N} + K_N\sqrt{\alpha_M}\operatorname{erf}(\mu)}\operatorname{erfc}\left(-\frac{x}{2\sqrt{\alpha_N t}}\right) \tag{41c}$$

$$\delta_\infty = 2\mu\sqrt{\alpha_M t} \tag{41d}$$

$$\frac{K_N\sqrt{\alpha_M}e^{-\mu^2}}{K_M\sqrt{\alpha_N} + K_N\sqrt{\alpha_M}\operatorname{erf}(\mu)} - \frac{K_S\sqrt{\alpha_M}\phi_0\exp[-(\alpha_M/\alpha_S)\mu^2]}{K_M\sqrt{\alpha_S}\operatorname{erfc}(\mu\sqrt{\alpha_M/\alpha_S})} = \frac{\mu\sqrt{\pi}}{Se} \tag{41e}$$

The starting solution for concentration is provided by analytical solution obtained by assuming $\gamma = 0$, i.e., constant mixture density and is given as

$$\omega = 1 - \frac{\sqrt{D_N}}{\sqrt{D_N} + \sqrt{D_M}}\operatorname{erfc}\left(\frac{x}{2\sqrt{D_M t}}\right) \tag{42a}$$

$$C = \frac{\sqrt{D_M}}{\sqrt{D_N} + \sqrt{D_M}}\operatorname{erfc}\left(-\frac{x}{2\sqrt{D_N t}}\right) \tag{42b}$$

This solution is significantly different (as will be demonstrated subsequently) from the solution for the case of variable mixture density with widely different densities. However, the numerical solution of equations (25) and (27) converges asymptotically to the "true" solution, which does not depend on the starting solution. This is an expected behavior of this class of problems relating to infinite media.

Results

Assuming the lead slab to consist of infinite thickness, Fig. 3 shows a comparison between the analytical and numerical solution obtained by collocation method for temperature profile. The two solutions agree extremely well with no discernable difference between them. Figure 4 shows the position of the melt interface as a function of time for $L \to \infty$, $L = 0.2$ m, and $L = 0.1$ m. The comparison of the calculated solution for case of $L \to \infty$ agree again with the analytical solution with no discernible difference between the two. For cases $L = 0.2$ m and $L = 0.1$ m, the calculated solutions, as expected, agree well for short times with analytical solution for the case of $L \to \infty$. Approximate finite slab solutions are also discussed by Lunardini [4]. After the temperature boundary layer penetrates the thickness of the lead slab, i.e., as the whole thickness of the solid lead begins to heat up, melt interfaces for these two cases begin to move significantly faster than the melt interface for the case $L \to \infty$. As expected for the melt rate for $L = 0.2$ m is slower than that for $L = 0.1$ m.

Figure 5 shows a plot of concentration profiles as a function of position both for the cases of constant and variable mixture densities. This figure clearly shows that a significant difference exists between the two profiles, implying that it would not be valid without incurring significant error to use constant density approximation for Pb-Na, liquid-liquid system. In this figure, we have also compared the analytical solution with the calculated solution for the case of constant density approximation. These solutions are in excellent agreement. One may, however, note that the penetration thickness for both the variable and the constant cases are nearly identical. By comparison of Fig. 3 with Fig. 5, one can

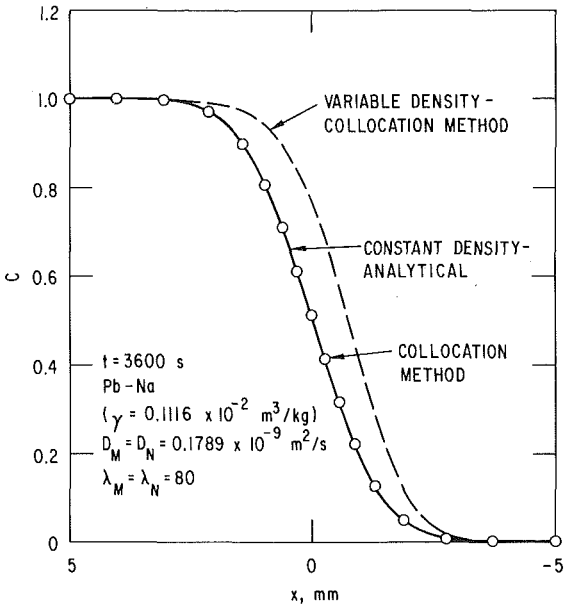

Fig. 5 A comparison of concentration distributions for constant and variable density cases

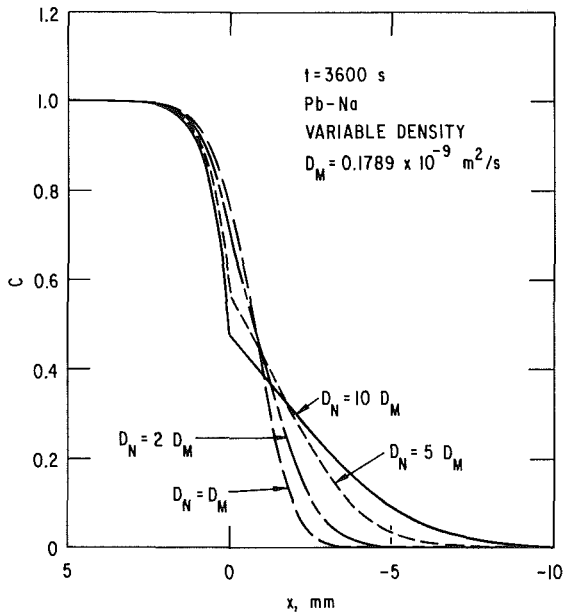

Fig. 6 The effect of varying diffusion coefficient in sodium on concentration profiles

conclude very readily that penetration thickness for interdiffusing liquids is extremely small as compared to that for temperature. Thus it is clear that the computations for mass diffusion in liquids require the use of very special adaptive coordinates which must cause significant stretching of the physical coordinates.

We have also studied tha effect of a difference in diffusion coefficients for the two interdiffusing liquids. This difference can arise if the diffusion coefficients are allowed to depend on concentration and temperature. Figure 6 shows plots of concentration profiles for various values of diffusion coefficients for sodium. The value for the lead is kept fixed at its calculated nominal value. As expected, penetration thickness in sodium increases with increasing diffusion coefficient, however, these increases are still very modest, even when the diffusion coefficient in sodium is increased tenfold. It would then appear that liquid-liquid diffusion cannot be relied upon to cause any significant mixing between lead and sodium. The two liquid metals will stay separated unless some convective mechanism for mass transport is brought into play. Thus, it is clear that before any significant mixing takes place, lead will sink to the bottom of the steel shot bed upon complete melting and will not participate to any significant extent in removing heat by natural convection from the fuel debris lying on the top of the steel shot bed.

Conclusions

Simultaneous calculations of mass and heat transfer in a liquid-liquid system cannot be carried out in physical coordinates without using a number of meshes that far exceeds the number that is theoretically necessary for normal engineering accuracy. The introduction of the adaptive coordinates that cause considerable stretching of the physical coordinates allows the calculation of mass diffusion simultaneous with the heat diffusion and phase change. A comparison of the calculated results with analytical solutions for heat diffusion and melt interface position for the case of infinite lead slab show an excellent agreement. The calculation of the melt interface shows that rates of melting increase significantly with decreasing thickness of lead. For the case of constant mixture density, the analytical solution for concentration profile agrees extremely well with the calculated results.

The calculations for concentration profiles show that constant density approximation is not a valid approximation for liquid-liquid diffusion in a binary system such as lead and sodium which have exceedingly different densities. Liquid-liquid mass diffusion is an extremely poor mechanism for causing mixing of one liquid into another and, therefore, cannot be relied upon without some convective mechanism to achieve any degree of mixing between lead and sodium in PAHR applications.

Acknowledgments

The authors greatly appreciate the skill offered by James Bingle in preparing computer plots of the computational results. This work was performed under the auspices of the U.S. Department of Energy.

References

1 Chawla, T. C., Leaf, G., and Chen, W., "A Collocation Method Using B-Splines for One-dimensional Heat or Mass Transfer-Controlled Moving Boundary Problems," *Nucl. Eng. Des.*, Vol. 35, 1975, pp. 163-180.

2 Chawla, T. C., Leaf, G., and Minkowycz, W. J., "A Collocation Method for Convection Dominated Flows," *International Journal for Numerical Methods in Fluids*, Vol. 4, 1984, pp. 271-281.

3 Rubinstein, L. I., *The Stefan Problem*, American Mathematical Society, Providence, R.I. 1971.

4 Lunardini, V. J., *Heat Transfer in Cold Climates*, Van Nostrand Reinhold Co., New York, 1981.

5 Douglas, J., and Dupont, T., "A Finite Element Collocation Method for Quasilinear Parabolic Equation," *Math. Comput.*, Vol. 27, 1973, pp. 17-18.

6 DeBoor, C., and Swartz, B., "Collocation at Gaussian Points," *SIAM* (Soc. Ind. Appl. Math), *J. Numer. Anal.*, Vol. 10, 1973, pp. 582-606.

7 Hindmarsh, A. C., "Two New Initial Value Ordinary Differential Equations Solvers," *ACM-SIGNUM Newsletter*, Vol. 15, 1980, pp. 10-11.

8 Carslaw, H. S., and Jaeger, J. C., *Conduction of Heat in Solids*, 2d ed. Oxford University Press, London, 1959.

Ice-Formation Phenomena for Water Flow Between Two Cooled Parallel Plates

N. Seki
Professor.

S. Fukusako
Associate Professor.

G. W. Younan
Graduate Student.
Department of Mechanical Engineering,
Faculty of Engineering,
Hokkaido University,
Sapporo 060, Japan

Experiments have been performed to investigate the ice-formation phenomena and the heat transfer characteristics for water flow between two horizontal parallel plates. The experiments were carried out under the condition that the upper and lower plates were cooled at the same uniform temperature, which was less than the freezing and the temperature of the water. The temperature of the plates ranged from -7 to $-14°C$ with inlet-water temperature varied from 2 to 5°C. The cooling-temperature ratio θ_c ranged from 1.4 to 7.0. By using three different values of height H, 16, 30, and 40 mm between the horizontal parallel plates, the Reynolds number Re_H were varied from 3.8×10^3 to 3.2×10^4. As a result of the present investigation, two different types of ice-formation were observed. One was transition ice-formation type, and the other was smooth ice-formation type. It was found that the transition ice-formation type occurred for $Re_H/\theta_c^{0.741} < 10^4$, while the smooth ice-formation type occurred for $Re_H/\theta_c^{0.741} > 10^4$. The relation equations for the ice-transition position and the heat transfer coefficients along the water-ice interface were extensively determined.

Introduction

Ice-formation phenomena are observed in many diverse processes, such as the freezing of water in pipes, the blockage of chemical process line, and the freezing of liquid metals in heat exchangers.

A number of theoretical and experimental studies have been directed at this objective. All the theoretical studies [1–4] have considered the laminar water flow of several degrees above its phase-change temperature entering a section of duct, pipes or two parallel plates, in which the duct-wall temperature is below the phase-change temperature. The experimental studies [5, 6] for laminar flow have treated the ice-formation phenomena only for short distances. In these studies, increase in ice-layer thickness along the length of the duct was predicted until the steady-state ice profile was attained. On the other hand, in the prediction for turbulent flow [7–12], the treatment of the ice-formation phenomena have assumed that the ice-layer thickness is thin enough so that as a first approximation it does not affect the flow characteristics. Therefore, these studies also have not predicted any change in the ice-layer thickness throughout the water-flow passage. But, in fact, when the duct has enough length and the rate of ice formation is relatively high, an occurrence of the transition in the ice-layer thickness may be predicted. A few studies [13, 14] for the transition of ice formation on flat plate have been conducted. Also it was observed in [15, 16] that the ice-layer profile steady-state condition did not show the uniformly tapered flow passage as have been predicted by the previous theoretical studies [1–4]. Moreover, the visual observation [15, 16] of the development of ice waves in internal solidification were used to fix the limitations of solution for the prediction of the onset of freeze-shut in pipe containing turbulent flow studied in [17]. This means that under some condition of the water-flow velocity and the ice-deposit rate, a laminar boundary layer will form along the ice-water interface, even though the main water flow is initially turbulent flow. From the standpoint of hydrodynamics, this laminar boundary layer is usually unstable, then it will be changed to turbulent boundary layer at a certain position in the flow passage. This results in an enhancement of local heat-transfer coefficient, and then a transition in the ice-layer thickness may occur.

From the foregoing literature survey, it is apparent that no data pertaining to the location of the ice-layer transition and to the heat transfer characteristics in the water flow between two parallel plates where ice formation exists have hitherto been published.

The purpose of this paper is to present the results of an experimental study into the ice-layer transition position and the heat transfer characteristics along the water–ice interface formed between two horizontal parallel plates. In particular, the effects of the cooled-wall temperature, the inlet-water temperature, the duct height, and the inlet-water velocity on the ice-layer transition position and the heat transfer at the water-ice interface are extensively discussed.

Experimental Apparatus and Procedure

Experimental Apparatus. The schematic diagram of the current apparatus is presented in Fig. 1. The main parts of the experimental apparatus consisted of a test section and two closed flow loops having the control systems of temperature and flow rates. These flow loops were the main water-flow and coolant-flow ones, respectively.

Figure 2 depicts the test section. The test section was made as different values of height between the parallel plates to take into account the effect of length–height ratio L/H on the ice-transition phenomena. The upper and lower plates were made of copper and were 5 mm in thickness. The heights between these plates were 16, 30, and 40 mm with rectangular cross sections having widths of 120, 120, and 216 mm, respectively. All parts of the test section were designed to have the same length of 1200 mm in order to give the ratios of length to height L/H ranging from 30 to 75. The temperatures of the upper and lower copper-plate surfaces were measured by 24 copper-constantan thermocouples, 0.3 mm in diameter. The thermocouple junctions were inserted at the center of the plates in line. In order to achieve the uniform temperatures of the plates, the upper and lower back side spaces of the test section were divided into six independent chambers, through which the temperature controlled coolants were independently circulated.

Contributed by the Heat Transfer Division for publication in the JOURNAL OF HEAT TRANSFER. Manuscript received by the Heat Transfer Division June 30, 1983.

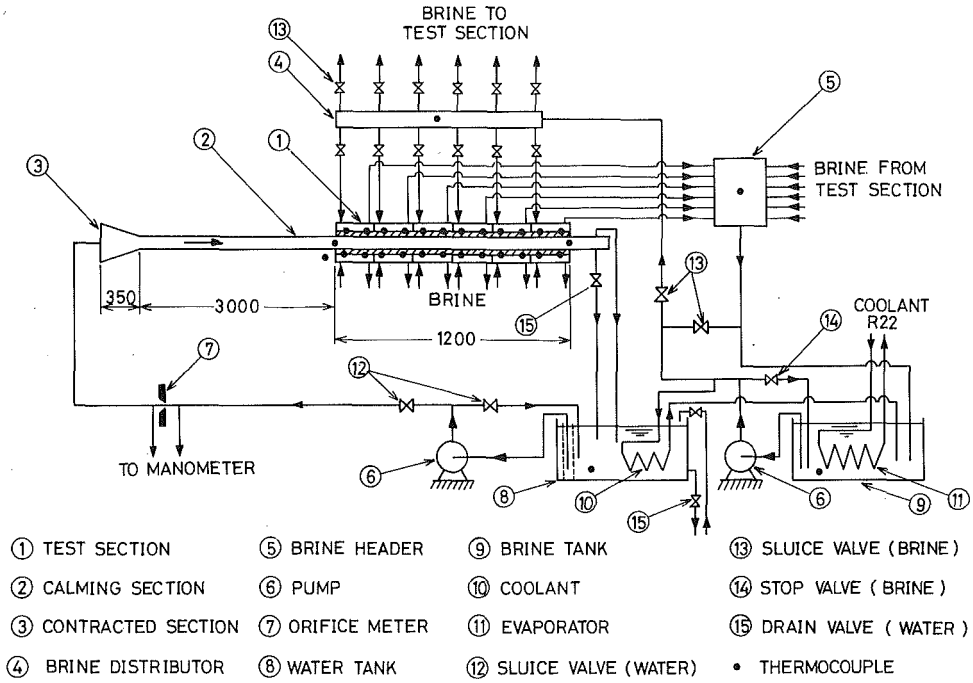

Fig. 1 Schematic drawing of experimental apparatus

For observation and measurement of the transient and steady-state ice-layer thicknesses, the front and back sides of the test section were made from transparent lucite plate, 15 mm in thickness. The main water-flow consisted of a main water tank, a heat exchanger, a centrifugal pump, controlling valves, an orifice meter, a contracted duct, a calming section, and thermometric measuring instruments, as is shown in Fig. 1.

Brine was used as the coolant fluid. As can be seen in Fig. 1, the main parts of the coolant-flow loop consisted of an evaporator connected with refrigerating unit, a large brine tank, a centrifugal pump, a brine distributor connected with 12 adjustable valves, a brine returning header, and thermometric measuring instruments. A camera system, consisting of two cameras, screens and lights, was employed to measure the ice-layer thickness during the transient growth period and at the steady state.

Experimental Procedure. The main water flow was driven by a centrifugal pump, whose flow rate controlled by the controlling valves and whose discharge was measured by the calibrated orifice meter. The flow entered the test section as a fully developed turbulent flow through the calming section 3000 mm in length. Just before the main flow entered the test section, the inlet-water temperature T_∞ was measured with three thermocouples, as shown in Fig. 2. In order to achieve the uniform temperatures of upper and lower plates, the coolant fluid was driven by a centrifugal pump through the chambers, which were installed at the back sides of the horizontal parallel plates of the test section. The temperatures of brine and main water flow at the test section were con-

Nomenclature

a = constant
b = constant
B_f = freezing parameter, defined in equation (10)
C = constant
f = function
h_m = mean heat transfer coefficient
h_x = local heat transfer coefficient
H = height between horizontal parallel plates
L = length of test section
L_f = heat fusion of ice
Nu_m = mean Nusselt number, defined in equation (14)
Nu_x = local Nusselt number, defined in equation (9)
Pr = Prandtl number, evaluated at T_∞
Re_H = Reynolds number, defined in equation (1)
$\mathrm{Re}_{x\mathrm{on}}$ = onset Reynolds number, defined in Fig. 7
t = time
T_f = freezing temperature
T_∞ = inlet-water temperature
Tw_c = cooling-plate temperature
U_∞ = average velocity of main water flow at inlet of test section
x = distance from inlet of test section
X_{tr} = distance of ice-transition position from inlet of test section
X_{tr}/H = dimensionless ice-transition position
α = ice thickness parameter, defined in Fig. 7
$\delta_{i,x}$ = local ice-layer thickness
θ_c = cooling-temperature ratio, defined in equation (2)
λ_i = thermal conductivity of ice, evaluated at $(Tw_c + T_f)/2$
λ_∞ = thermal conductivity of water, evaluated at T_∞
ν_∞ = kinematic viscosity of water, evaluated at T_∞
ρ_i = density of ice, evaluated at $(Tw_c + T_f)/2$

Subscripts

on = onset condition
st = steady-state condition
tr = transition

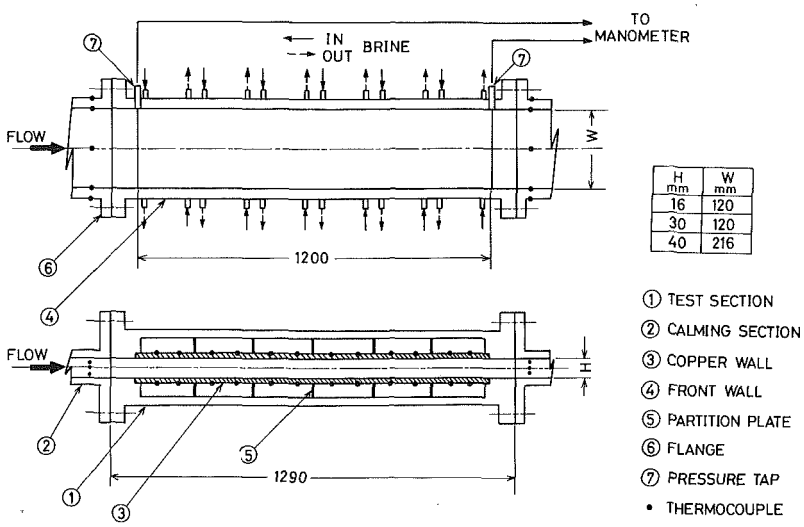

H mm	W mm
16	120
30	120
40	216

Fig. 2 Details of test section

trolled by the evaporator and brine-water heat exchanger, respectively. Time was measured ice flashs on the plate surfaces. The static pressures across the test section were recorded during the experimental runs in the predetermined time intervals. All of the data were recorded when the steady-state conditions were established. It was assumed that the steady state was attained when all of the readings remained constant for more than one hour. A series of still photographs were taken continuously at predetermined time intervals during the growth period of the ice layer. The negative films were developed to large sizes and so that the ice-layer thicknesses could be accurately measured from them.

Results and Discussion

Visual Observation. Visual observations were made in order to study the effects of both the Reynolds number Re_H and cooling-temperature ratio θ_c on the ice-layer profiles formed along the upper and lower plates of the test section. The photographs in Figs. 3(*a-d*) show the development characteristics of the ice layers normally observed. In each photograph, the horizontal dark areas near the upper and lower plates are ice layers, while the horizontal white areas between the drak areas is the waterflow passage. In photographs of Fig. 3(*a*), at time $t = 0$ ice growth is seen to have been initiated. A short time after the initiation of ice growth, the transition in the upper and lower ice-layer thicknesses are observed. With time, the ice-layer thicknesses upstream the transition position increase and they tend to have a uniform taper from the inlet of the test section to the ice-transition positions. Moreover, the ice-transition positions migrated upstream until they reached steady-state positions.

As shown in Fig. 3(*b*), the steady-state, ice-transition positions tended to approach the inlet of the test section with increasing Reynolds number. Furthermore, for $\mathrm{Re}_H = 2.9 \times 10^4$ and $\theta_c = 3.67$, any transition in the ice-layer thickness throughout the test section was not observed, as shown in Fig. 3(*b*)-5.

The transition in the ice-layer thickness may be due to the transition from laminar boundary layer formed at water-ice interface to a turbulent boundary layer, as is later discussed. Thus this kind of ice formation will be called "transition ice-formation type." On the other hand, at high values of the Reynolds number, the convective heat-transfer coefficient will significantly higher and the ice thickness may become thin and smooth. There may be, in short, little or no chance for the existence of any laminar boundary layer at the water-ice interface. Essentially, the boundary layer along the water–ice interface appears to become a turbulent boundary layer from the starting point of ice formation ($x = 0$) to the exit of the test section. Therefore, this kind of ice formation is hereinafter called "smooth ice-formation type."

For the transition ice-formation type, the behavior of the ice-transition point appears to be very similar to the transition behavior from a laminar boundary layer to a turbulent one as is observed during ice growth on a flat plate [13, 14]. The existence of a recirculating separation of flow stream behind the downstream face of the transition point was confirmed by the injection of dye into the main water-flow, as shown in the sequence of photographs of Figs. 3(*c*) and 3(*d*). Also it was observed in the experimental runs that the ice-transition position at steady-state condition will tend to approach the inlet of the test section by increasing the values of cooling-temperature ratio θ_c.

Criterion for Two Types of Ice Formation. As a result of the present experiments, the main parameters that are relevant in correlating and evaluating the type of the ice formation were found to be the Reynolds number Re_H and the cooling temperature ratio θ_c, which is defined as

$$\mathrm{Re}_H = 2HU_\infty/\nu_\infty \tag{1}$$

$$\theta_c = (T_f - Tw_c)/(T_\infty - T_f) \tag{2}$$

It was generally found that the transition ice-formation type occurred at relatively low values of Re_H and high values of θ_c, while the smooth ice-formation type occurred at higher values of Re_H and lower values of θ_c than the transition ice-formation type. In order to determine the criterion for these two types of the ice-formation, the data obtained in the present experiments are given in dimensionless form in Fig. 4. In Fig. 4, Reynolds number Re_H was plotted as a function of the cooling-temperature ratio θ_c for both ice-formation regions.

In Fig. 4, it appears that the criterion for the transition ice-formation region may be defined as

$$\mathrm{Re}_H/\theta_c^{0.741} < 10^4 \tag{3}$$

while the criterion for the smooth ice-formation region may be denoted in the following form

$$\mathrm{Re}_H/\theta_c^{0.741} > 10^4 \tag{4}$$

Transition Ice-Formation Type and Ice-Transition Position. As pointed out earlier, when the water flows between two parallel plates at certain values of Re_H and θ_c, a laminar boundary layer will form along water–ice interface even if the main inlet-water is initially a fully developed

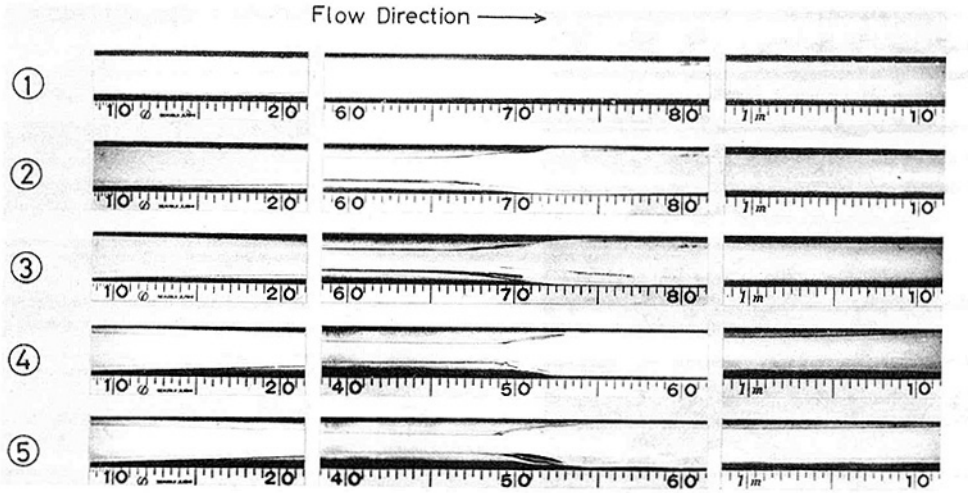

Fig. 3(*a*) Transient development of ice-layer thickness for transition ice-formation type at $Re_H = 1.1 \times 10^4$, $\theta_c = 3.5$ and H = 30 mm: (1) 10 min passed, (2) 50 min passed, (3) 90 min passed, (4) 210 min passed, (5) 280 min passed

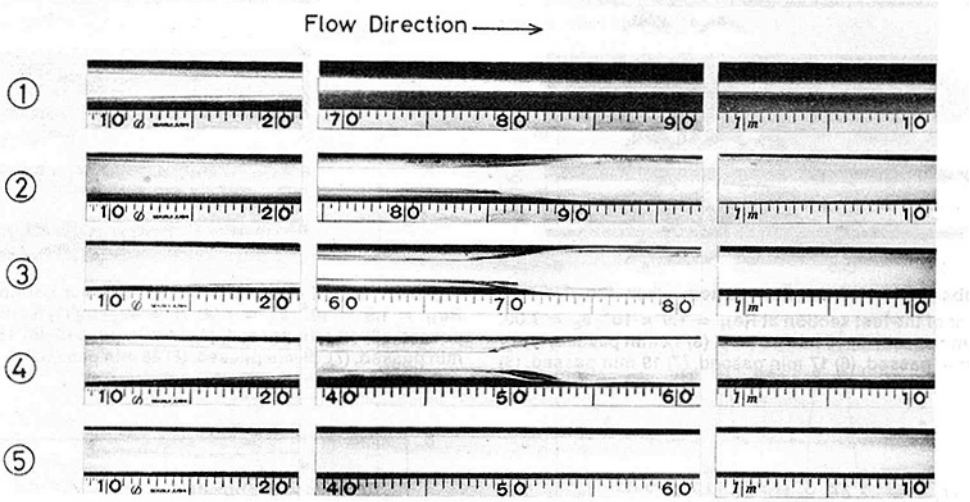

Fig. 3(*b*) Effect of flow and temperature parameters on steady-state, ice-layer profile for H = 30 mm: (1) no ice transition throughout test section $Re_H = 4.1 \times 10^3$, $\theta_c = 3.5$; (2) transition ice-formation type $Re_H = 6.6 \times 10^3$, $\theta_c = 2.29$ and $(X_{tr})_{st} = 86.5$ cm; (3) transition ice-formation type $Re_H = 8.2 \times 10^3$, $\theta_c = 3.67$ and $(X_{tr})_{st} = 68.0$ cm; (4) transition ice-formation type $Re_H = 1.1 \times 10^4$, $\theta_c = 3.50$ and $(X_{tr})_{st} = 49.0$ cm; (5) smooth ice-formation type $Re_H = 2.9 \times 10^4$, $\theta_c = 3.67$

turbulent flow [18, 19], as shown in photographs of Fig. 3(*d*)-1. From the stand point of hydrodynamics, this laminar boundary layer is usually unstable and will be changed to a turbulent boundary layer at a certain position in the flow passage, as observed in [13, 14]. This transition appears to be associated with flow separation at the transition point, as shown in photographs of Figs. 3(*c*)-3 and 3(*d*)-3. Therefore, this separation will give rise to the heat transfer rate from the water to the ice surface. Consequently, the transition in the ice-layer thickness will occur at certain position $(X_{tr})_{on}$, (Figs. 3(*c*)-5 and 3(*d*)-5 show that this position will be at about $x =$ 40.0 cm for $Re_H = 1.9 \times 10^4$ and $\theta_c = 7.0$), and then it will move to the upstream until it reaches to a steady-state position $(X_{tr})_{st}$.

In case of the transition ice-formation type, it was found that the main parameters influencing the dimensionless ice-transition position at the onset and steady-state conditions were the Reynolds number Re_H and the cooling-temperature ratio θ_c.

From the characteristics mentioned above, it appears that the dimensionless ice-transition position (X_{tr}/H) at the onset and steady-state conditions may be evaluated as follows

$$(X_{tr}/H)_{on}, (X_{tr}/H)_{st} = C\mathrm{Re}_H^a \theta_c^b \tag{5}$$

where the constant C, a, and b could be determined from the experimental results.

By using the present experimental results for the three different values of the heights of 16, 30, and 40 mm between the horizontal parallel plates, the constants of equation (5) were determined, and the experimental relation formulae were written as

$$(X_{tr}/H)_{on} = 6.95 \times 10^5 \, \mathrm{Re}_H^{-1.10} \theta_c^{-0.123} \tag{6}$$

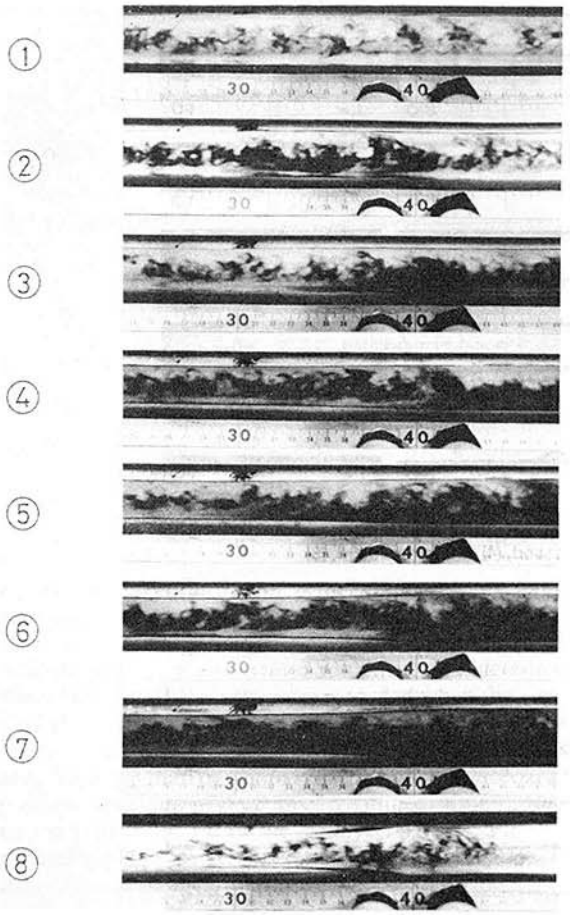

Fig. 3(c) Visual observation of the flow pattern when the dye was injected at the center of the test section at $Re_H = 1.9 \times 10^4$, $\theta_c = 7.00$, $H = 40$ mm: (1) 5 min passed, (2) 10 min passed, (3) 12 min passed, (4) 14 min passed, (5) 15 min passed, (6) 17 min passed, (7) 19 min passed, (8) 28 min passed

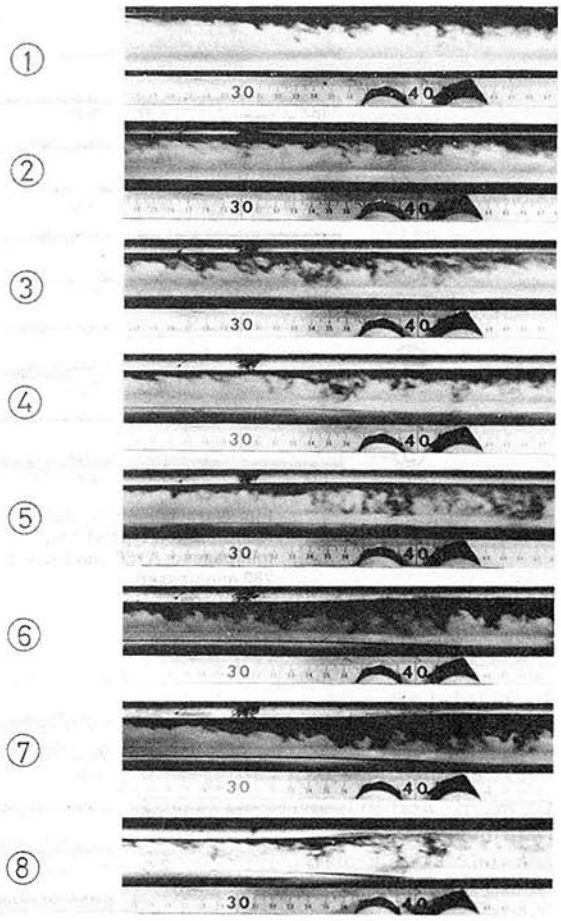

Fig. 3(d) Visual observation of the laminar boundary layer pattern at $Re_H = 1.9 \times 10^4$, $\theta_c = 7.00$, $H = 40$ mm, (1) 5 min passed, (2) 10 min passed, (3) 12 min passed, (4) 14 min passed, (5) 15 min passed, (6) 17 min passed, (7) 19 min passed, (8) 28 min passed

and

$$(X_{tr}/H)_{sl} = 2.46 \times 10^5 \mathrm{Re}_H^{-1.02} \theta_c^{-0.113} \qquad (7)$$

Figures 5 and 6 show that equations (6) and (7) relate reasonably the present experimental results within the scattered values of about ±20 and ±25 percent, respectively. The reason that the power indices in equation (6) and (7) are different from those in Fig. 5 and 6, respectively, is due to the fact that the slope of the experimental relation lines in these figures does not exactly equal one. Also it should be noted that equations (6) and (7) could be used under the criterion of equation (3).

It is relevant to consider comparison between the current results and those of Hirata et al. [13]. In [13], the experiments were carried out under the condition that the water flows along a uniform temperature flat plate. A comparison using the ice thickness parameter α and onset Reynolds number $Re_{x,on}$ is made in Fig. 7 for $H = 16$, 30, and 40 mm. As will be seen in this figure, the present experimental results are quantitatively different from those of [13]. Of interest is that most of the data for $H = 16$ mm decrease below the value of the correlation line in [13], while the data for $H = 40$ mm approach this correlation line. Namely, it can be noted that the greater H becomes, the greater α becomes in the almost region of $Re_{x,on}$. Therefore, one can note that the ice-formation phenomena on a flat plate is a limiting one of a variety of ice-formation phenomena between parallel plates, because flow over a flat plate can be attained when the distance between the parallel plates H approach infinity.

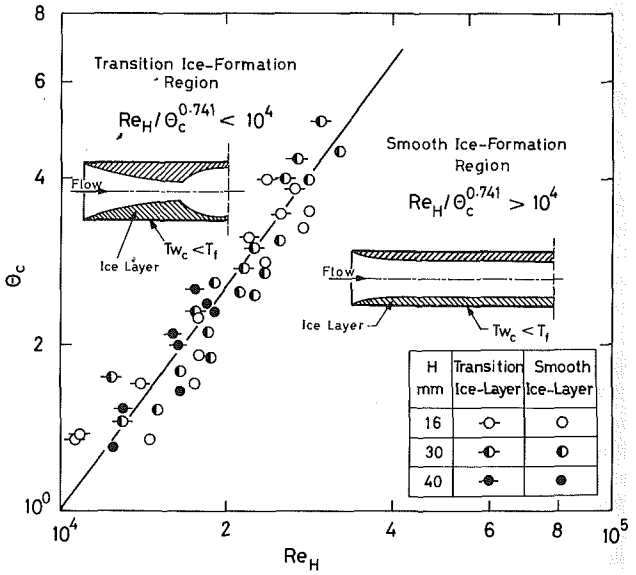

Fig. 4 Different region of ice-formation

Heat Transfer Characteristics at Water–Ice Interface. In order to calculate the local convective heat transfer coefficient h_x along the water–ice interface, an experimental analysis will be considered for the transiently freezing water along the test

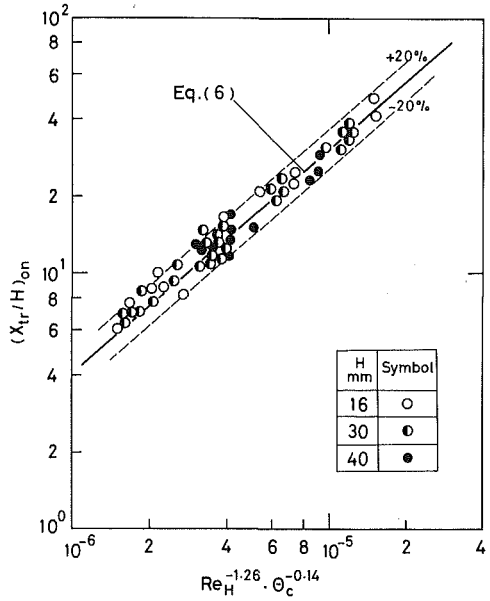

Fig. 5 Correlation of dimensionless ice-transition position at onset condition

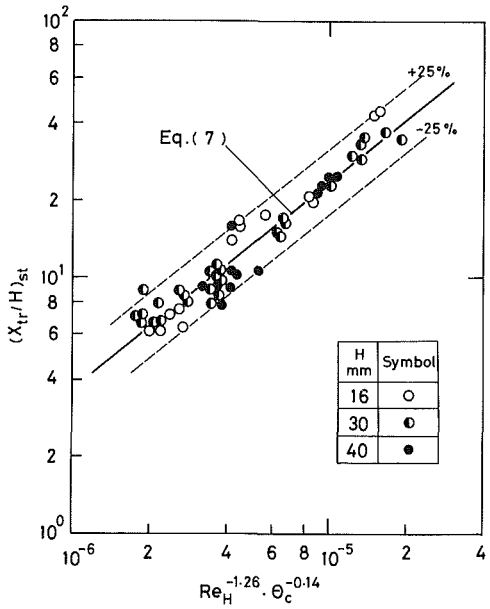

Fig. 6 Correlation of dimensionless ice-transition position at steady-state condition

section plates. The following assumptions were used in the analysis: (*a*) the transient and steady-state ice-layer thicknesses along the upper and lower test section plates are symmetrical; (*b*) the axial heat conduction in the ice layer can be neglected; and then (*c*) the variation of the temperature within the ice-layer thickness is linear at any position of the test section.

Under these assumptions, the distribution of local heat-transfer coefficient h_x can be written as

$$h_x = \lambda_i(T_f - Tw_c)/\delta_{i,x}(T_\infty - T_f) - \rho_i L_f(\partial\delta_{i,x}/\partial t)/(T_\infty - T_f) \quad (8)$$

where λ_i is thermal conductivity of ice layer; ρ_i, density of ice layer; L_f, heat fusion of ice; t, time; $\delta_{i,x}$, local ice-layer thickness; T_f, freezing temperature; T_∞, inlet-water temperature; and Tw_c, cooled-plate temperature.

By introducing the local Nusselt number Nu_x and the freezing parameter B_f, equation (8) may be written as

$$Nu_x = h_x 2H/\lambda_\infty = 2HB_f/\delta_{i,x} - \rho_i L_f(\partial\delta_{i,x}/\partial t)/(T_\infty - T_f) \quad (9)$$

where the freezing parameter B_f is defined as

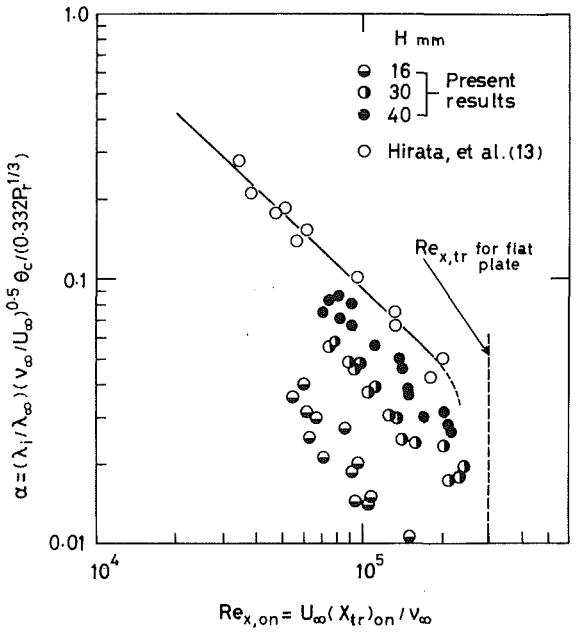

Fig. 7 Comparison of the experimental results between flat plate and two parallel plates

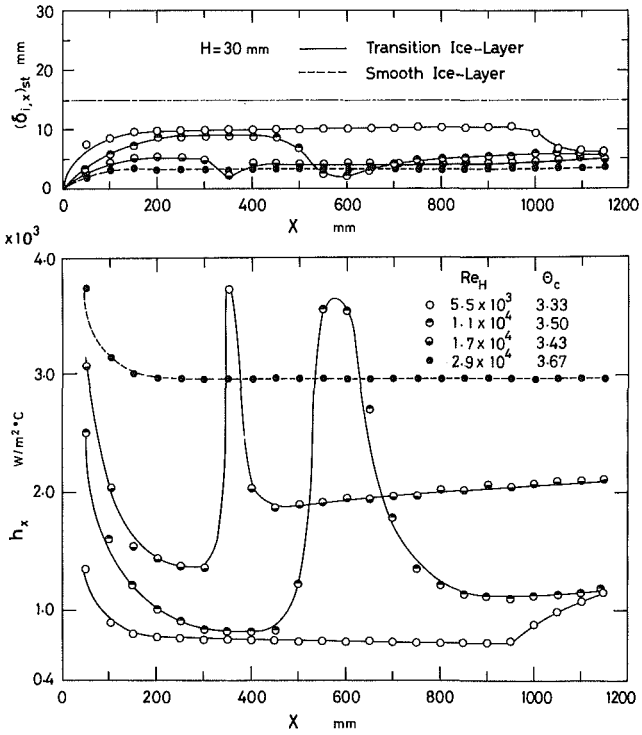

Fig. 8 Variation of ice-layer thickness and local heat transfer coefficient for two different ice-formation types

$$B_f = \lambda_i(T_f - Tw_c)/\lambda_\infty(T_\infty - T_f) \quad (10)$$

When the steady-state condition is established, the term $(\partial\delta_{i,x}/\partial t)$ in equation (9) will disappear. Then the local Nusselt number can be expressed in the form

$$Nu_x = 2HB_f/(\delta_{i,x})_{st} \quad (11)$$

where $(\delta_{i,x})_{st}$ is the local ice-layer thickness at the location x for the steady-state condition.

The typical convective local heat transfer coefficient h_x along the water-ice interface corresponding to the values of $(\delta_{i,x})_{st}$ for two types of the ice-formation are presented in Fig. 8.

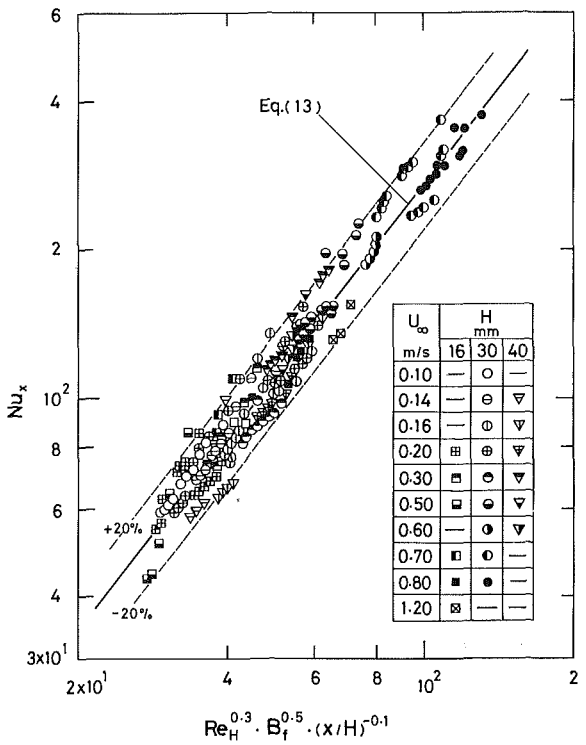

Fig. 9 Relationship of local Nusselt number for transition ice-formation type

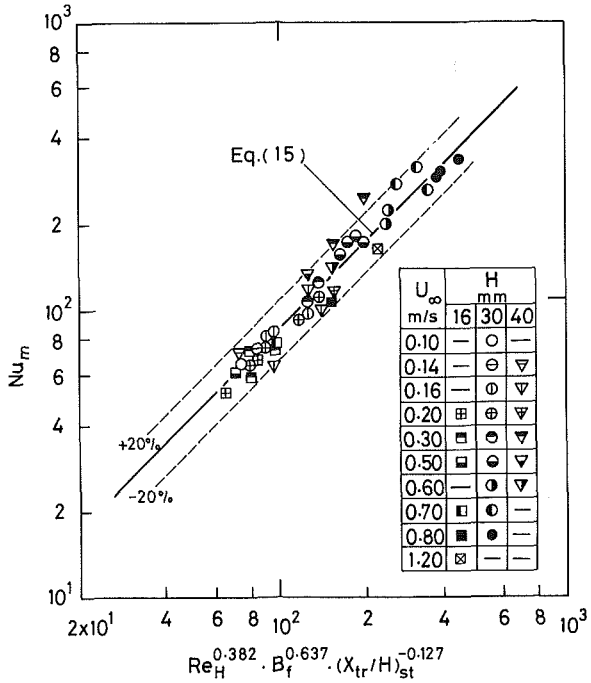

Fig. 10 Relationship of mean Nusselt number for transition ice-formation type

From an inspection of Fig. 8, it is evident that in case of the transition ice-formation type the values of h_x decrease abruptly at the inlet region of the test section and then gradually to the ice-transition position $(X_{tr})_{st}$, while in case of the smooth ice-formation type the value of h_x is nearly constant throughout the test section except the region near the inlet of the test section, thus yielding the characteristics of the thermal entrance region. Also it can be seen from Fig. 8 that the values of h_x for the smooth ice-formation type are higher than those for the transition ice-formation type throughout

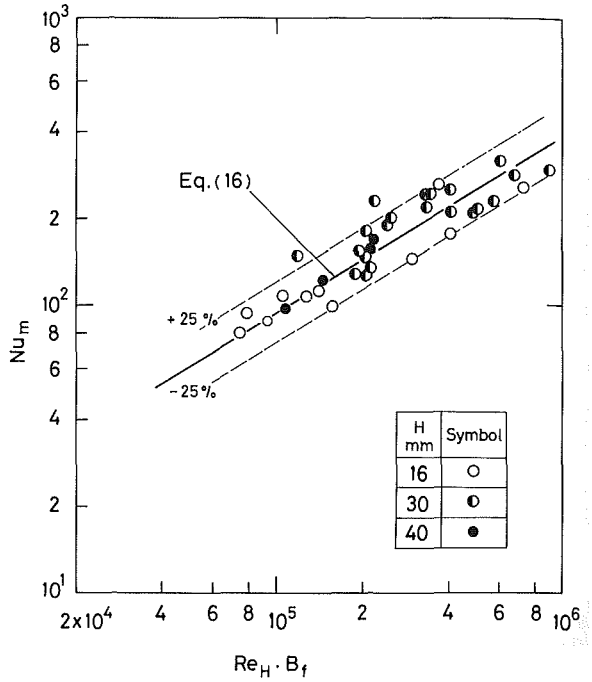

Fig. 11 Relationship of mean Nusselt number for smooth ice-formation type

the test section except the region just downstream the ice-transition position.

Local and Mean Nusselt Numbers for Transition Ice-Formation Type. Attention will at first be turned to the relationship of local heat transfer coefficient, along the water-ice interfce upstream the ice-transition to $(X_{tr})_{st}$. As a result of the present experiments, it was found that for the range studied the local heat transfer coefficient may be expressed by the following relationship among dimensionless groups.

$$\mathrm{Nu}_x = f(\mathrm{Re}_H, B_f, x/H) \tag{12}$$

The experimental heat transfer data for the region upstream the ice-transition position are plotted in terms of the aforementioned dimensionless groups in Fig. 9. By employing the least-square technique, equation (12) may be given as

$$\mathrm{Nu}_x = 0.764\ \mathrm{Re}_H^{0.382}\ B_f^{0.637} (x/H)^{-0.127} \tag{13}$$

Equation (13) may reasonably correlate the full range of the experimental data for the transition ice-formation type within an average deviation less than ±20 percent, as will be shown in Fig. 9. The reason that the power indices in equation (13) are different from those in Fig. 9 is because the slope of the experimental relationship line in this figure is greater than one.

In the present study, the mean Nusselt number Nu_m is defined as

$$\mathrm{Nu}_m = h_m 2H/\lambda_\infty, \quad h_m = 1/(X_{tr})_{st} \int_0^{(X_{tr})_{st}} h_x dx \tag{14}$$

where $(X_{tr})_{st}$ is the steady-state ice-transition position. Consequently, the relation equation of the mean Nusselt number for the transition ice-formation type may be obtained as the following form

$$\mathrm{Nu}_m = 0.875\ \mathrm{Re}_H^{0.382}\ B_f^{0.637}\ (X_{tr}/H)_{st}^{-0.127} \tag{15}$$

Figure 10 shows that equation (15) is in good agreement with the present experimental results within an average deviation of ±20 percent.

Mean Nusselt Number for Smooth Ice-Formation Type. Attention will finally be turned to the relationship of

the mean Nusselt number, for the smooth ice-formation type with both of Reynolds number Re_H and freezing parameter B_f. From Fig. 8, it can be seen that the local heat transfer coefficient h_x for the smooth ice-formation type will tend to take a constant value, except for the region very near the inlet of the test section, as pointed out earlier. From all of the experimental results obtained for the smooth ice-formation type, it is also revealed that there may be the thermal-entrance characteristics only in the region of the dimensionless distance x/H, ranging from 3 to 5. Consequently, by neglecting the thermal entrance effect mentioned above, the values of the mean Nusselt number Nu_m for the smooth ice-formation type at the steady-state condition are plotted as a function of $Re_H B_f$ in Fig. 11 and are reasonably expressed in the following form

$$Nu_m = 7.37 \times 10^{-2} (Re_H B_f)^{0.624} \quad (16)$$

It appears from Fig. 11 that all of the data obtained for the smooth ice-formation type may be well correlated by equation (16) within an average deviation less than ±25 percent.

Conclusions

According to the experimental results of the present investigation concerning the freezing of water flow between horizontal parallel plates, the following major conclusions may be drawn:

1 Although the main flow is initially a fully developed turbulent flow, the ice-layer thickness will be abruptly changed at a certain location within the water-flow passage under the operating conditions given by equation (3).

2 The main parameters governing the freezing phenomena for the present system are the Reynolds number $Re_H = 2HU_\infty/\nu_\infty$ and the cooling-temperature ratio $\theta_c = (T_f - Tw_c)/(T_\infty - T_f)$.

3 Two different types of ice-formation are observed to exist; the one is the transition ice-formation type and the other the smooth ice-formation type.

4 In case of the transition ice-formation type, the ice-layer transition may occur due to instability of the laminar boundary layer which will be formed along the water-ice interface. The transition position of ice-layer thickness will approach the steady-state ones depending on the Reynolds number and the cooling-temperature ratio.

5 The smooth ice-formation type probably occurs because the laminar boundary layer nearly vanishes under the condition of equation (4), causing the ice-layer thickness to become quite thin throughout the water-flow passage.

References

1 Zerkle, R. D., Sunderland, J. E., "The Effect of Liquid Solidification in a Tube Upon Laminar-Flow Heat Transfer and Pressure Drop," ASME JOURNAL OF HEAT TRANSFER, Vol. 109, 1968, pp. 183–190.

2 Özisik, M. N., and Mulligan, J. C., "Transient Freezing of Liquid in Forced Flow Inside Circular Tube," ASME JOURNAL OF HEAT TRANSFER, Vol. 91, 1966, pp. 385–389.

3 Stephan, K., "Influence of Heat Transfer on Melting and Solidification in Forced Flow," *International Journal of Heat and Mass Transfer*, Vol. 12, 1969, pp. 199–214.

4 Richard, T. B., and Alan, J. C., "Freezing of Fluids in Forced Flow," *International Journal of Heat and Mass Transfer*, Vol. 12, 1967, pp. 1581–1587.

5 Mulligan, J. C., and Jones, D. D., "Experiments on Heat Transfer and Pressure Drop in Horizontal Tube with Internal Solidification," *International Journal of Heat and Mass Transfer*, Vol. 19, 1976, pp. 213–219.

6 Hirata, T., Gilpin, R. R., and Cheng, K. C., "The Steady State Ice Layer Profile on a Constant Temperature Plate in Forced Flow-I. The Laminar Regime," *International Journal of Heat and Mass Transfer*, Vol. 22, 1979, pp. 1425–1433.

7 Arora, A. P., and Howell, J. C., "An Investigation of the Freezing of Super-Cooled Liquid in Forced Turbulent Flow Inside Circular Tube," *International Journal of Heat and Mass Transfer*, Vol. 16, 1973, pp. 2077–2085.

8 Shibani, A. A., and Özisik, M. N., "Freezing of Liquids in Turbulent Flow Inside Tubes," *The Canadian Journal of Chemical Engineering*, Vol. 55, 1977, pp. 672–677.

9 Thomason, S. B., Mulligan, J. C., and Everhart, J., "The Effect of Internal Solidification on Turbulent Flow Heat Transfer and Pressure Drop in Horizontal Tube," ASME JOURNAL OF HEAT TRANSFER, Vol. 100, 1978, pp. 387–394.

10 Thomason, S. B., and Mulligan, J. C., "Experimental Observations of Flow Instability During Turbulent Flow Freezing in Horizontal Tube," ASME JOURNAL OF HEAT TRANSFER, Vol. 102, 1980, pp. 782–784.

11 Shibani, A. A., and Özisik, M. N., "A Solution of Freezing of Liquids of Low Prandtl Number in Turbulent Flow Between Parallel Plates," ASME JOURNAL OF HEAT TRANSFER, Vol. 99, 1977, pp. 20–24.

12 Chul, C., and Özisik, M. N., "Transient Freezing of Liquids in Turbulent Flow Inside Tubes," ASME JOURNAL OF HEAT TRANSFER, Vol. 101, 1979, pp. 465–468.

13 Hirata, T., Gilpin, R. R., and Cheng, K. C., "The Steady State Ice Layer Profile on Constant Temperature Plate in Forced Convection Flow-II. The Transition and Turbulent Regimes," *International Journal of Heat and Mass Transfer*, Vol. 22, 1979, pp. 1435–1443.

14 Gilpin, R. R., Hirata, T., and Cheng, K. C., "Wave Formation and Heat Transfer at an Ice-Water Interface in the Presence Turbulent Flow," *Journal of Fluid Mechanics*, Vol. 99, 1980, pp. 619–640.

15 Gilpin, R. R., "The Morphology of Ice Structure in a Pipe at or near Transient Reynolds Number," *Heat Transfer—AIChE Symposium Series 189*, Vol. 75, 1979, San Diego, Calif., pp. 89–94.

16 Gilpin, R. R., "Ice Formation in Pipe Containing Flow in the Transition and Turbulent Regimes," ASME JOURNAL OF HEAT TRANSFER, Vol. 103, 1981, pp. 363–368.

17 Epstein, M., and Cheung, F. B., "On the Prediction of Pipe Freeze-Shut in Turbulent Flow," ASME JOURNAL OF HEAT TRANSFER, Vol. 104, 1982, pp. 381–384.

18 Knudsen, J., and Katz, D., *Fluid Dynamics and Heat Transfer*, McGraw-Hill, 1958.

19 Mill, A. E., "Experimental Investigation of Turbulent Heat Transfer in the Entrance Region of Circular Conduit," *Journal of Mechanical Engineering Science*, Vol. 4, No. 1, 1962, pp. 63–77.

Two-Region Analysis of Interface Shape in Continuous Casting With Superheated Liquid

R. Siegel
NASA Lewis Research Center,
Cleveland, Ohio 44135
Fellow ASME

A slab ingot is being formed as a continuous casting by withdrawal from a mold with parallel walls. The sides of the ingot below the mold are cooled to remove heat of fusion and energy transferred to the solidification interface by superheated liquid metal in the mold. A two-region analysis is made to determine the non-uniform heat conduction from the liquid metal to the interface, and then from the interface to the cooled ingot sides. The solidification interface shape is found that is compatible with the removal of fusion energy and nonuniform heating from the liquid. The solution is obtained by two applications of a Cauchy boundary value method.

Introduction

An important metal fabrication technique is the continuous casting of an ingot by pulling it from a mold with parallel sides while cooling the ingot below the mold to remove heat of solidification and energy due to liquid metal superheat. The metallic crystal structure is influenced by the heat flows at the solidification interface and by the interface shape. By proper control, a strengthened composite structure can be formed by directional solidification of a eutectic; this has application in casting turbine blade sections. The solidification interface is an unknown "free" boundary and its shape adjusts to the heat transfer conditions. In [1] and [2], the interface shape during casting of a slab was analyzed by a conformal mapping technique. Since the background of the casting problem was given in those papers, it is not necessary to repeat it here. In [1] and [2], the ingot interface shape was obtained for the liquid metal either at the solidification temperature or transferring a uniform heat flux to the interface. The complexity of the conformal transformations required in the mapping method made it difficult to treat other types of interface heating conditions.

In [3], a Cauchy boundary value method was devised that provided a more convenient solution for the problem in [2]. This method has been used here to study the effect of liquid superheat on the interface shape, and in particular how nonuniform heat transfer from the liquid influences distortions of a nearly flat interface. Interfaces that are kept flat within a certain tolerance are important to form certain types of crystal structures as discussed in [1]. The Cauchy boundary value method is applied in two parts. First the heat transfer in the ingot is analyzed, and the interface shape is found to satisfy heat removal from the interface due to the latent heat of fusion and a generalized nonuniform heat transfer from the superheated liquid. Then for a particular type of mold, the Cauchy method is applied a second time to obtain the heat conduction from the liquid metal to the solidification interface. This result is used in the ingot solution to yield the interface shape.

Analysis

The geometry is shown in Fig. 1(*a*) and consists of an ingot of width $2a$ being cast by withdrawal at constant velocity $\bar{u}$ from a mold with insulated sides of height h. Above h, the wall is uninsulated, and heat can be added to maintain a superheated liquid metal ($t_l > t_f$). The liquid transfers a local heat flux $q_l(s)$ to the solidification interface. For constant $\bar{u}$ the latent heat of fusion to be removed locally along the interface is $\bar{u}\rho\lambda\partial x/\partial s$. To remove heat from the interface, the ingot sides below the mold are cooled to temperature t_c. At the interface, the boundary condition for heat conduction into the solid is

$$k_s \frac{\partial t}{\partial n}\bigg|_s = \bar{u}\rho\lambda \frac{\partial x}{\partial s} + q_l(s) \tag{1a}$$

and the temperature is equal to the solidification temperature

$$t_s = t_f \tag{1b}$$

Along the insulated mold sides

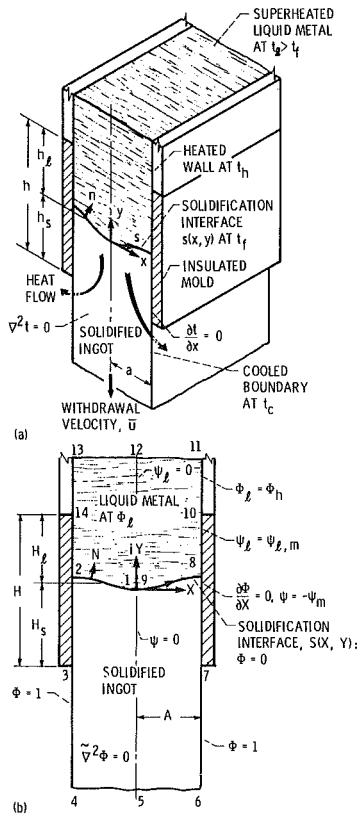

Fig. 1 Slab ingot being withdrawn from mold in continuous casting: (*a*) physical geometry; (*b*) geometry and boundary conditions in dimensionless physical plane

Contributed by the Heat Transfer Division for publication in the JOURNAL OF HEAT TRANSFER. Manuscript received by the Heat Transfer Division April 22, 1983.

$$\frac{\partial t}{\partial x} = 0 \tag{2}$$

and along the cooled boundaries

$$t = t_c \tag{3}$$

The boundary conditions for heat conduction in the liquid will be given later for determining $q_l(s)$.

The analysis will deal with slow withdrawal rates so that the heat transport $\rho \bar{u} c_p \partial t/\partial y$ is neglected relative to conduction within the ingot of the heat supplied at the interface by both fusion and heat conduction through the liquid (see discussion in [1]). The temperature distribution in the solid is then governed by the heat conduction equation

$$\frac{\partial^2 t}{\partial x^2} + \frac{\partial^2 t}{\partial y^2} = 0 \tag{4}$$

The shape of the solidification interface is to be found that is consistent with equation (4) and the boundary conditions (1-3). As discussed in [1], with regard to ingot crystal structure, it is desired in some casting processes to maintain a nearly planar solidification interface. This analysis will examine the effect of the variation of $q_l(s)$ on the deviation of the interface from being flat.

Solution Method Using Potential Plane. Heat transfer is first considered for the solid; the liquid will be treated in a later section. The temperature is expressed in terms of a potential Φ (see Nomenclature) and all lengths are non-dimensionalized relative to γ. Then within the solid

$$\frac{\partial^2 \Phi}{\partial X^2} + \frac{\partial^2 \Phi}{\partial Y^2} = 0 \tag{5}$$

At the solidification interface the $q_l(s)$ is dividend into a uniform component $\bar{q}_l$ and a spatially varying component $F(s)$ so that from (1*a*)

$$-\frac{\partial \Phi}{\partial N}\bigg|_s = \frac{\partial X}{\partial S} + \frac{\bar{q}_l}{\bar{u}\rho\lambda} + \frac{F(S)}{\bar{u}\rho\lambda} \tag{6a}$$

$$\Phi = 0 \tag{6b}$$

at the cooled boundaries

$$\Phi = 1 \tag{7}$$

and at the insulated mold sides

$$\frac{\partial \Phi}{\partial X} = 0 \tag{8}$$

(see Fig. 1(*b*)). For conditions that will yield rather flat interfaces, the $F(s)$ is small compared with $\bar{u}\rho\lambda + \bar{q}_l$.

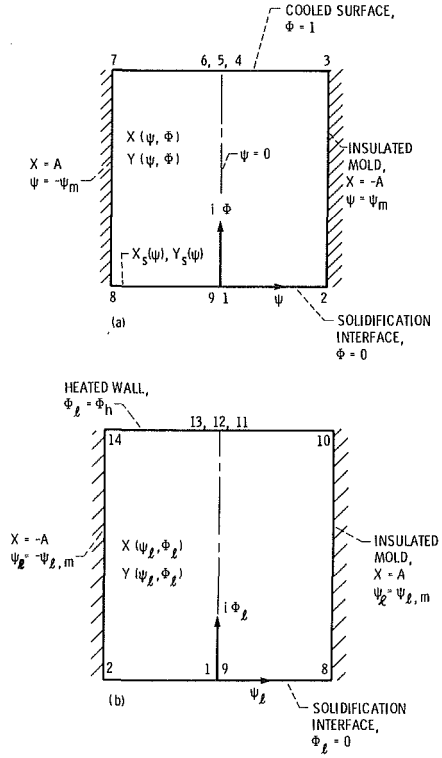

Fig. 2 Regions in potential plane: (*a*) solid region; (*b*) liquid region

Equations (6*b*-8) show that the ingot is bounded by two constant Φ boundaries and two boundaries normal to the Φ lines; hence the region occupies a rectangle in the $\Psi - \Phi$-plane as shown in Fig. 2(*a*). The coordinates Ψ is a heat flow function orthogonal to Φ. In [3], a method was given for obtaining the unknown interface during ingot casting with the liquid metal not superheated. The solution was obtained by solving for X and Y in terms of Ψ and Φ as independent variables. Let the X and Y values along $\Phi = 0$ in Fig. 2(*a*) (the solidification interface) be denoted as $X_s(\Psi)$, $Y_s(\Psi)$. If these functions of Ψ were known, then throughout the rectangle the X and Y are equal to

$$X(\Psi,\Phi) = \mathrm{Re}X_s(\Psi + i\Phi) - \mathrm{Im}Y_s(\Psi + i\Phi) \tag{9a}$$

$$Y(\Psi,\Phi) = \mathrm{Im}X_s(\Psi + i\Phi) + \mathrm{Re}Y_s(\Psi + i\Phi) \tag{9b}$$

Nomenclature

A = dimensionless parameter and dimensionless length, $a\bar{u}\rho\lambda/k_s(t_f - t_c) = a/\gamma$
a = half-width of slab ingot
B_o, B_n, C_n = coefficients in Fourier series
D_n = coefficients in Fourier series
F = liquid heat flux variation
h = height of insulated mold; $H = h/\gamma$
k = thermal conductivity
n = outward normal to interface
q = heat flux
$\bar{q}_l$ = uniform portion of liquid heat flux at interface
s = coordinate along interface
t = temperature
$\bar{u}$ = casting velocity of ingot
x,y = coordinates in physical plane; $X = x/\gamma$, $Y = y/\gamma$
X_s, Y_s = coordinates of solidification interface

Greek Symbols

γ = length scale parameter, $k_s(t_f - t_c)/\bar{u}\rho\lambda$
λ = latent heat of fusion per unit mass of solid
ρ = density of solidified material
Φ = potential function in solid, $(t_f - t)/(t_f - t_c)$
Φ_l = potential function in liquid, $(t_l - t_f)/(t_f - t_c)$; $\Phi_h = (t_h - t_f)/(t_f - t_c)$
Ψ = heat flow function orthogonal to Φ

Subscripts

c = at cooled boundary
f = at solidification temperature
l = liquid
m = maximum value
s = at solidification interface; solid

Interface Shape for Arbitrary Heating Variations at Interface. Before considering the coupled liquid-solid solution, consider how the interface responds to a generalized $F(S)$ heating function that is symmetric about the Y-axis. Since small deviations from a flat surface are being analyzed, the $\partial X/\partial S$ is approximated by unity. The heating function in equation (6*a*) can then be expanded into a Fourier series (compatible with the liquid conduction solution found later), and a Cauchy-Riemann equation is used to change the Φ derivative to a Ψ derivative; this yields from (6*a*)

$$-\frac{\partial \Psi}{\partial X}\bigg|_s = 1 + \frac{\bar{q}_l}{\bar{u}\rho\lambda} + \frac{1}{\bar{u}\rho\lambda}\sum_{n=1}^{\infty} C_n \cos\frac{n\pi X_s}{A} \tag{10}$$

Since $\Psi = 0$ along $X = 0$, integration yields along S

$$\Psi(X_s) = -\left(1 + \frac{\bar{q}_l}{\bar{u}\rho\lambda}\right)X_s - \frac{1}{\bar{u}\rho\lambda}\frac{A}{\pi}\sum_{n=1}^{\infty}\frac{C_n}{n}\sin\frac{n\pi X_s}{A} \tag{11}$$

At the side wall $X_s = -A$ the Ψ has a maximum value, Ψ_m, equal to

$$\Psi_m = \left(1 + \frac{\bar{q}_l}{\bar{u}\rho\lambda}\right)A \tag{12}$$

Then equation (11) becomes

$$\frac{\Psi}{\Psi_m} = -\frac{X_s}{A} - \frac{1}{\pi}\sum_{n=1}^{\infty}\frac{1}{n}\frac{C_n}{\bar{u}\rho\lambda + \bar{q}_l}\sin\frac{n\pi X_s}{A} \tag{13}$$

For the condition of small spatial heating variations, $C_n/(\bar{u}\rho\lambda + \bar{q}_l) << 1$ and the zeroth order approximation to equation (13) is $X_s/A \approx -\Psi/\Psi_m$. The summation in (13) is small relative to the other terms, so the zeroth approximation can be made in the summation to yield second order accuracy. Then solving for X_s

$$\frac{X_s(\Psi)}{A} = -\frac{\Psi}{\Psi_m} + \frac{1}{\pi}\sum_{n=1}^{\infty}\frac{1}{n}\frac{C_n}{\bar{u}\rho\lambda + \bar{q}_l}\sin n\pi\frac{\Psi}{\Psi_m} \tag{14}$$

$$(-1 \le \Psi/\Psi_m \le 1)$$

This provides the $X_s(\Psi)$ needed for the solution in equations (9).

The unknown $Y_s(\Psi)$ is represented by a Fourier series expansion as in [3]

$$Y_s(\Psi) = B_o + \sum_{n=1}^{\infty} B_n \cos n\pi\frac{\Psi}{\Psi_m} \tag{15}$$

Equations (14) and (15) are substituted into (9*a*,*b*) to yield

$$X(\Psi,\Phi) = -A\frac{\Psi}{\Psi_m} + \frac{A}{\pi(\bar{u}\rho\lambda + \bar{q}_l)}\sum_{n=1}^{\infty}\frac{C_n}{n}\sin n\pi\frac{\Psi}{\Psi_m}\cosh n\pi\frac{\Phi}{\Psi_m} + \sum_{n=1}^{\infty} B_n \sin n\pi\frac{\Psi}{\Psi_m}\sinh n\pi\frac{\Phi}{\Psi_m} \tag{16a}$$

$$Y(\Psi,\Phi) = -A\frac{\Phi}{\Psi_m} + \frac{A}{\pi(\bar{u}\rho\lambda + \bar{q}_l)}\sum_{n=1}^{\infty}\frac{C_n}{n}\cos n\pi\frac{\Psi}{\Psi_m}\sinh n\pi\frac{\Phi}{\Psi_m} + B_o + \sum_{n=1}^{\infty} B_n \cos n\pi\frac{\Psi}{\Psi_m}\cosh n\pi\frac{\Phi}{\Psi_m} \tag{16b}$$

To find the B_n, apply the conditions that $\Phi = 1$ and $X = -A$ along boundary 3-4. Then from equation (16*a*)

$$\sum_{n=1}^{\infty} B_n \sin n\pi\frac{\Psi}{\Psi_m}\sinh\frac{n\pi}{\Psi_m} = -A + A\frac{\Psi}{\Psi_m} - \frac{A}{\pi(\bar{u}\rho\lambda + \bar{q}_l)}\sum_{n=1}^{\infty}\frac{C_n}{n}\sin n\pi\frac{\Psi}{\Psi_m}\cosh\frac{n\pi}{\Psi_m} \tag{17}$$

Using $0 \le \Psi \le \Psi_m$ along 3-4, the B_n can be found from (17) in the usual manner of determining Fourier coefficients

$$B_n = -\frac{A}{\pi}\frac{2}{n\sinh\dfrac{n\pi}{\Psi_m}}\left[1 + \frac{C_n}{2(\bar{u}\rho\lambda + \bar{q}_l)}\cosh\frac{n\pi}{\Psi_m}\right] \tag{18}$$

It is convenient to express the local height of the interface as the distance from the bottom edge of the mold, $Y_s - Y_3$, where Y_3 is found from equation (16*b*) at $\Psi = \Psi_m$ and $\Phi = 1$. Then by substituting equation (18) into equation (16*b*)

$$\frac{Y_s(\Psi) - Y_3}{A} = \frac{1}{\Psi_m} - \frac{2}{\pi}\ln 2 + \frac{1}{\pi}\sum_{n=1}^{\infty}\frac{C_n}{\bar{u}\rho\lambda + \bar{q}_l}\frac{1}{n\sinh\dfrac{n\pi}{\Psi_m}}\left[(-1)^n - \cosh\frac{n\pi}{\Psi_m}\cos n\pi\frac{\Psi}{\Psi_m}\right] - \frac{2}{\pi}\sum_{n=1}^{\infty}\frac{1}{n\sinh\dfrac{n\pi}{\Psi_m}}\left[\cos n\pi\frac{\Psi}{\Psi_m} - (-1)^n e^{-n\pi/\Psi_m}\right]\left(-1 \le \frac{\Psi}{\Psi_m} \le 1\right) \tag{19}$$

Equations (14) and (19) determine the solidification interface. The Ψ_m is related to physical quantities by equation (12). With Ψ_m and $C_n/(\bar{u}\rho\lambda + \bar{q}_l)$ specified as parameters, various Ψ/Ψ_m from 0 to 1 are inserted to compute the interface shape. Results are given in Fig. 3 and will be discussed later.

Two-Region Problem. In the previous section, the spatial variation of heating of the interface by the liquid was considered to be a known function. This function will now be obtained for a two-region geometry as shown in Figs. 1(*a*) and 1(*b*). The vertical walls above the insulated mold are heated to $t_h > t_f$. Convection in the liquid is neglected, so heat is

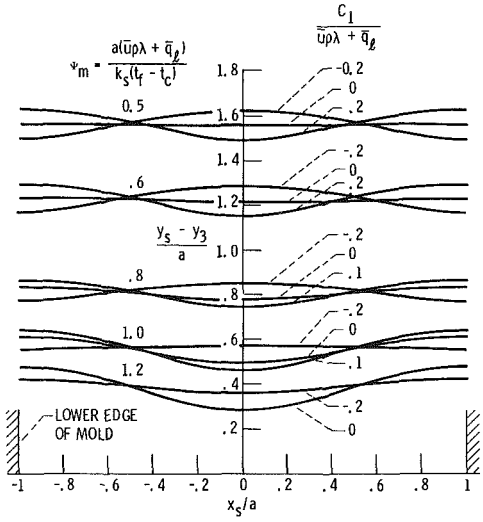

Fig. 3 Effect on interface shape of heating by liquid in the form, $\bar{q}_l + C_1 \cos(\pi x_s/a)$

transferred by conduction through the liquid metal from the heated boundaries to the solidification interface. For the cases of interest here the interface is down within the mold so that the heat flow paths through the liquid depend primarily on the height-width ratio h_l/a and are influenced only in a very secondary fashion by the small interface curvature. Hence to determine $q_l(x)$, the interface is allowed to be flat. In the liquid at the interface $q_l(x)=k_l(\partial t_l/\partial y)_s$. Putting this in dimensionless form and using a Cauchy-Riemann equation yields

$$\frac{\partial \Phi_l}{\partial Y}\bigg|_s = \frac{\partial \Psi_l}{\partial X}\bigg|_s = \frac{k_s}{k_l}\frac{q_l(X)}{\bar{u}\rho\lambda} \tag{20}$$

Let the unknown relation between X_s and Ψ_l be represented by a Fourier series; then

$$X_s(\Psi_l) = A\frac{\Psi_l}{\Psi_{l,m}} + \sum_{n=1}^{\infty} D_n \sin n\pi \frac{\Psi_l}{\Psi_{l,m}} \tag{21a}$$

$$Y_s(\Psi_l) = 0 \tag{21b}$$

Note that $X_s=0$ at $\Psi_l=0$, and $X_s=\pm A$ at $\Psi_l=\pm\Psi_{l,m}$; the $\Psi_{l,m}$ is unknown at this point.

Equations (21) are substituted into equations (9) to obtain X and Y in the rectangle of Fig. 2(*b*)

$$X(\Psi_l,\Phi_l) = A\frac{\Psi_l}{\Psi_{l,m}} + \sum_{n=1}^{\infty} D_n \sin n\pi \frac{\Psi_l}{\Psi_{l,m}} \cosh n\pi \frac{\Phi_l}{\Psi_{l,m}} \tag{22a}$$

$$Y(\Psi_l,\Phi_l) = A\frac{\Phi_l}{\Psi_{l,m}} + \sum_{n=1}^{\infty} D_n \cos n\pi \frac{\Psi_l}{\Psi_{l,m}} \sinh n\pi \frac{\Phi_l}{\Psi_{l,m}} \tag{22b}$$

Along boundary 10–11, $\Phi_l=\Phi_h$, $X=A$ and Ψ_l goes from 0 to $\Psi_{l,m}$. Using equation (22*a*) the D_n are found as Fourier coefficients in the same fashion as the B_n in equation (18)

$$D_n = \frac{2A}{\pi}\frac{1}{n\cosh(n\pi\Phi_h/\Psi_{l,m})} \tag{23}$$

The unknown $\Psi_{l,m}$ is related to the height H_l of the mold above the interface. The H_l will be needed to relate it to the known height H in Fig. 1(*b*). From point 10 in Figs. 1(*b*) and 2(*b*), the $H_l = Y(\Psi_{l,m},\Phi_h)$; then from equations (22*b*) and (23), after rearrangement to improve convergence

$$\frac{H_l}{A} = \frac{\Phi_h}{\Psi_{l,m}} - \frac{2}{\pi}\left[\ln 2 + 2\sum_{n=1}^{\infty}\frac{(-1)^n}{n}\frac{e^{-2n\pi\Phi_h/\Psi_{l,m}}}{1+e^{-2n\pi\Phi_h/\Psi_{l,m}}}\right] \tag{24}$$

This will be used later to determine $\Psi_{l,m}$ from the mold geometry. Note that $\Psi_{l,m}$ only appears in the ratio $\Phi_h/\Psi_{l,m}$.

The heating at the interface by the liquid, $q_l(X_s)$, is given by equation (20). The $\partial\Psi_l/\partial X|_s$ is found from X_s obtained by evaluating equation (22*a*) at $\Phi_l=0$ with D_n from (23)

$$\frac{X_s}{A} = \frac{\Psi_l}{\Psi_{l,m}} + \frac{2}{\pi}\sum_{n=1}^{\infty}\frac{1}{n}\frac{\sin(n\pi\Psi_l/\Psi_{l,m})}{\cosh(n\pi\Phi_h/\Psi_{l,m})} \tag{25}$$

Now consider the solid region. The interface boundary condition for the ingot is from equations (10) and (20)

$$-\frac{\partial\Psi}{\partial X}\bigg|_s = 1 + \frac{q_l(X)}{\bar{u}\rho\lambda} = 1 + \frac{k_l}{k_s}\frac{\partial\Psi_l}{\partial X}\bigg|_s \tag{26}$$

Integrating from $\Psi=0$ to Ψ_m as X goes from 0 to $-A$ yields the maximum value Ψ_m in the solid (note that at $X=-A$, $\Psi_l=-\Psi_{l,m}$),

$$\frac{\Psi_m}{A} = 1 + \frac{k_l}{k_s}\frac{\Phi_h}{A}\frac{\Psi_{l,m}}{\Phi_h} \tag{27}$$

To find $X_s(\Psi)$ for use in the solution in equations (9), equation (25) is differentiated to obtain $\partial X/\partial\Psi_l|_s$, this is inserted into equation (26), and the result integrated to obtain

$$\Psi = -X_s - \frac{k_l}{k_s}\frac{\Psi_{l,m}}{A}\int_0^{X_s}\frac{dX}{1+2\sum_{n=1}^{\infty}\dfrac{\cos(n\pi\Psi_l/\Psi_{l,m})}{\cosh(n\pi\Phi_h/\Psi_{l,m})}} \tag{28}$$

As will be shown in Table 1, for mold heights H/A such as 2 or 3, the $\Phi_h/\Psi_{l,m}$ obtained from equations (24) (and (33) given later) are greater than about 1.5 so that $\cosh(n\pi\Phi_h/\Psi_{l,m})$ is large. The summation in (28) is thus dominated by the first term, which is much smaller than unity and can be brought into the numerator by $(1+\epsilon)^{-1}\approx 1-\epsilon$ for $\epsilon<<1$. After integration, rearrangement and use of equation (27)

$$\frac{X_s}{A} = -\frac{\Psi}{\Psi_m} + 2\frac{k_l}{k_s}\frac{\Psi_{l,m}}{\Psi_m}\frac{1}{A}\int_0^{X_s}\frac{\cos(\pi\Psi_l/\Psi_{l,m})}{\cosh(\pi\Phi_h/\Psi_{l,m})}dX \tag{29}$$

Since the cosh terms in (25) and (29) are large, the zeroth-order approximations are that $X_s/A=\Psi_l/\Psi_{l,m}$ and $X_s/A=-\Psi/\Psi_m$. These approximations are used in the integral of equation (29) to generate the next order approximation; this yields little error (accurate to second order) since the integral term is small

$$\frac{X_s(\Psi)}{A} = -\frac{\Psi}{\Psi_m} - \frac{2}{\pi}\left(1-\frac{A}{\Psi_m}\right)\frac{\sin(\pi\Psi/\Psi_m)}{\cosh(\pi\Phi_h/\Psi_{l,m})} \tag{30}$$

Equation (30) is now compared with equation (14) in the solution for general nonuniform heat addition at the interface. The equations are of the same form where

$$\frac{C_1}{\bar{u}\rho\lambda+\bar{q}_l} = -2\left(1-\frac{A}{\Psi_m}\right)\frac{1}{\cosh(\pi\Phi_h/\Psi_{l,m})} \tag{31}$$

and $C_n=0$ for $n\geq 2$. The $Y_s(\Psi)$-coordinates are then obtained directly from equation (19) as

$$\frac{Y_s(\Psi)-Y_3}{A} = \frac{1}{\Psi_m} + \frac{2}{\pi}\left\{-\ln 2 + \left(1-\frac{A}{\Psi_m}\right)\frac{1}{\cosh(\pi\Phi_h/\Psi_{l,m})}\frac{1+\cosh(\pi/\Psi_m)\cos(\pi\Psi/\Psi_m)}{\sinh(\pi/\Psi_m)} - \sum_{n=1}^{\infty}\frac{1}{n\sinh\dfrac{n\pi}{\Psi_m}}\left[\cos n\pi\frac{\Psi}{\Psi_m} - (-1)^n e^{-n\pi/\Psi_m}\right]\right\} \tag{32}$$

To obtain the average height H_s in Fig. 1(*b*)

$$\frac{H_s}{A} = \frac{1}{A}\int_0^A \frac{Y_s(X/A)-Y_3}{A}dX \approx \int_0^1 \frac{Y_s(\Psi/\Psi_m)-Y_3}{A}d(\Psi/\Psi_m)$$

which gives

$$\frac{H_s}{A} = \frac{1}{\Psi_m} + \frac{2}{\pi}\left\{-\ln 2 + \left(1-\frac{A}{\Psi_m}\right)\frac{1}{\cosh(\pi\Phi_h/\Psi_{l,m})\sinh(\pi/\Psi_m)} + \sum_{n=1}^{\infty}\frac{(-1)^n}{n}\frac{e^{-n\pi/\Psi_m}}{\sinh(n\pi/\Psi_m)}\right\} \tag{33}$$

To calculate interface shapes the parameters k_l/k_s, Φ_h and A are chosen. Then a trial value of $\Phi_h/\Psi_{l,m}$ is selected and H_l/A is calculated from equation (24), and Ψ_m from (27). The H_s/A is then obtained from (33) and $H/A=H_l/A+H_s/A$. Various $\Phi_h/\Psi_{l,m}$ are tried until the desired H/A is obtained. Then Ψ/Ψ_m values from 0 to 1 are inserted into equations (30) and (32) to obtain the interface coordinates. Results are given in Fig. 4 and the corresponding parameters are in Table 1.

Table 1 Parameters and results for two-region analysis; $k_l/k_s = 1$

Φ_h	A	$\Phi_h/\Psi_{l,m}$	Ψ_m	H_l/A	H_s/A	H/A
0.5	0.4	1.5134	0.7304	1.0722	0.9278	2.000
0.5	0.6	1.7537	0.8851	1.3124	0.6876	2.000
0.5	0.8	1.9404	1.0577	1.4991	0.5009	2.000
1.0	0.4	1.8281	0.9470	1.3868	0.6132	2.000
1.0	0.6	1.9815	1.1047	1.5402	0.4598	2.000
1.0	0.8	2.1071	1.2746	1.6658	0.3342	2.000
0.5	0.4	2.2703	0.6202	1.8290	1.1710	3.000
0.5	0.6	2.6187	0.7909	2.1774	0.8226	3.000
0.5	0.8	2.8588	0.9749	2.4175	0.5825	3.000
0.5	1.0	3.0300	1.1650	2.5887	0.4113	3.000
1.0	0.4	2.6068	0.7836	2.1655	0.8345	3.000
1.0	0.6	2.8347	0.9528	2.3934	0.6066	3.000
1.0	0.8	3.0048	1.1328	2.5635	0.4365	3.000
1.0	1.0	3.1353	1.3190	2.6940	0.3060	3.000

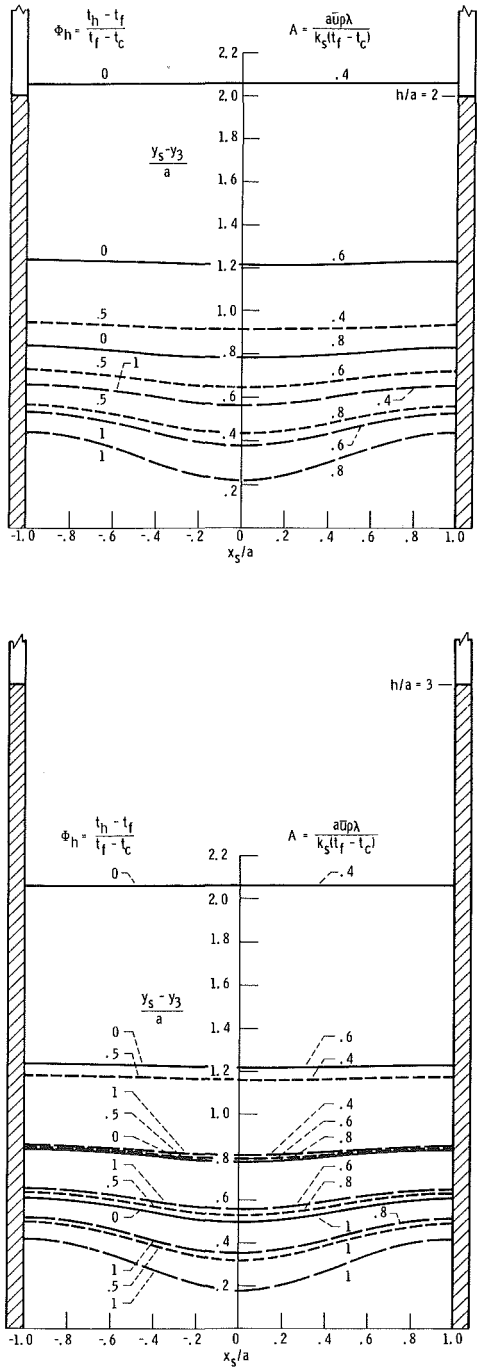

Fig. 4 Interface shapes for two-region solution: (*a*) insulated mold height, *h*/*a* = 2; (*b*) insulated mold height, *h*/*a* = 3

Results and Discussion

In the first section of the analysis, the shape of the solidification boundary was obtained for heating at the interface by the superheated liquid in the form

$$\bar{q}_l + \sum_{n=1}^{\infty} C_n \cos(n\pi x_s/a),$$

which was assumed known from an auxiliary analysis or experiment. The interface coordinates, nondimensionalized by the ingot half-width, are given by equations (14) and (19), and they depend on the parameter $\Psi_m = a(\bar{u}\rho\lambda + \bar{q}_l)/k_s(t_f - t_c)$ and the coefficients $C_n/(\bar{u}\rho\lambda + \bar{q}_l)$. To illustrate the results, interfaces were calculated for a single cosine variation ($C_n = 0$ for $n \neq 1$) and results are in Fig. 3.

First consider the curves where $C_1 = 0$ and hence the heating from the liquid is uniform over the interface. The results agree with [1] where that special case was analyzed; the analysis was carried out here by an entirely different method. For small Ψ_m, associated with slow withdrawal rates $\bar{u}$ and small liquid heating $\bar{q}_l$, the interface position is high within the mold. As the withdrawal rate or heating is increased, the interface drops down to provide the required smaller resistance for heat flow to the cooled boundaries. The interface becomes curved, being lower in the center; the interface is a constant temperature boundary and its shape adjusts to be normal to the heat flow lines.

For a positive C_1, there is nonuniform heating along the interface with larger heating in the central section. This causes the interface to dip down more in the center so that the additional heating in this region can be conducted to the cooled ingot sides.

A negative C_1 has the opposite effect; the decreased heating in the central region raises the solidification interface in the central portion, thus counteracting the central depression associated with ingot withdrawal. This is desirable for casting processes in which the interface is to be kept flat. By having a negative C_1 heating distribution, the withdrawal rate could be increased and still have a flat interface. For example, when $C_1 = 0$, the interface is quite flat for $\Psi_m = 0.6$. By having nonuniform heating with $C_1 = -0.1$ or -0.2, the interface is kept flat while Ψ_m is increased; if the average heating component $\bar{q}_l$ can be kept small (note that $\bar{q}_l$ must be

$$\geq \sum_{n=1}^{\infty} C_n$$

since $\bar{q}_l$ is positive for all x_s), this would permit an increase in ingot withdrawal rate $\bar{u}$. The heating distribution could be supplied by a heating grid in the liquid above the interface.

To obtain a flat interface, equation (15) shows that $B_n = 0$ so that from equation (18) the heating coefficients are $C_n/(\bar{u}\rho\lambda + \bar{q}_l) = -2/\cosh(n\pi/\Psi_m)$. For the one-term ap-

proximation (Fig. 3) this yields, for example, $C_1/(\bar{u}\rho\lambda+\bar{q}_l)=-0.079$ and -0.173 to yield a flat interface for $\Psi_m=0.8$ and 1.0.

Now consider the two region analysis for the conditions in Fig. 1. The mold walls above height h are heated to t_h and energy is conducted through the liquid to the solidification interface. The interface coordinates are given by equations (30) and (32), and their evaluation is outlined in the analysis. Results were carried out for two insulated wall heights, $h/a=2$ and 3, and the interfaces are in Fig. 4. The conductivity ratio is $k_l/k_s=1$, and values for other ratios are easily carried out as the series generally converge rapidly. Less than five terms were needed for the calculations here. The significant quantities for the cases shown are in Table 1; all of the $\Phi_h/\Psi_{l,m}$ are large enough so that the restrictions in the analysis are valid.

Each part of Fig. 4 has curves for the two temperature ratios, $\Phi_h=(t_h-t_f)/(t_f-t_c)=0.5$ and 1.0. For comparison, results from [1] are shown for $\Phi_h=0$; in this instance, the liquid is all at t_f, and the interface is not heated by the liquid. Increasing Φ_h causes the interface to move to a lower position in the mold in order to transfer away the additional energy supplied by conduction. Increasing $A=a\bar{u}\rho\lambda/k_s(t_f-t_c)$ has the same effect, since this corresponds to an increased amount of solidification energy that must be removed. The two-region analysis predicts how the factors such as liquid heating, casting rate, and insulated mold height influence the interface shape and location within the mold. The analytical results can be easily evaluated for other values of the parameters than those shown. The solution shows how the interface in continuous casting adjusts itself to accommodate to the various parameters that can be used to regulate the solidification process.

References

1 Siegel, R., "Shape of Two-Dimensional Solidification Interface During Directional Solidification by Continuous Casting," ASME JOURNAL OF HEAT TRANSFER, Vol. 100, Feb. 1978, pp. 3-10.

2 Siegel, R., "Analysis of Solidification Interface Shape During Continuous Casting of a Slab," *International Journal of Heat and Mass Transfer*, Vol. 21, Nov. 1978, pp. 1421-1430.

3 Siegel, R., "Cauchy Method for Solidification Interface Shape During Continuous Casting," ASME JOURNAL OF HEAT TRANSFER, Vol. 105, Aug. 1983, pp. 667-671.

A Numerical Heat Transfer Analysis of Strip Rolling

A. A. Tseng
Staff Engineer,
Martin Marietta Laboratories,
Baltimore, Md. 21227
Mem. ASME

The lack of a practical mathematical model to simulate thermal behavior of the metal rolling process has forced mill operators and designers to rely on plant experience and testing, which is time consuming and expensive. An effective finite difference model has been developed to study the temperature profiles of the work roll and the strip. Several finite difference techniques have been successfully employed to cope with the special characteristics of the rolling process, such as very high velocity, high temperature variation in a very thin layer, curved boundary, and bimaterial interface. Typical rolling conditions were analyzed to provide temperature information on the roll and strip. Both cold and hot rollings were considered, and the effect of changing velocities was also studied. Good correspondence is found when present results are compared with either analytical solutions under simplified rolling conditions or measured data.

Introduction

The metal rolling process involves extremely high pressures and velocities, which create a large amount of heat from deformation and friction. The adequate cooling of the roll and the rolled products is of considerable concern to mill designers and operators. Improper or insufficient cooling not only can lead to shortened roll life, due to spalling caused by thermal stresses, but it can also significantly affect the shape or crown of the roll and result in buckled strips or belted edges. In order to study the influence of cooling practices on the roll and strip, a good understanding of the thermal aspects of the process is essential. Also, knowledge of roll and strip temperatures can contribute to insights about the metallurgical structure of the workpiece and the lubricant behavior, and eventually lead to better control of the material properties and surface conditions.

Considerable work has been done on modeling the thermal behavior of the rolling processes. The scope of the work ranges from a highly simplified approach yielding approximate closed-form solutions [1] to complex numerical methods giving more accurate predictions [2–6]. In the numerical approaches, Parke and Baker [2] developed a two-dimensional (plane), finite difference model to investigate transient roll behavior. Without presenting details, Poplawski and Seccombe [3] reported that they extended the plane model to include a third dimension. Wilmotte and Mignon [4] studied the mean axial temperature variation to the roll through an axisymmetric finite difference approach. On the other hand, Zienkiewicz, Onate, and Heinrich [5] predicted the strip temperature by using a finite element technique. Lahoti, Shah, and Altan [6] developed a model that included the strip and also a small wedge of roll.

Most of the foregoing models [2–5] simulated either the roll or the strip alone. However, the rolling process involves the deformation heat generated in the strip, the friction heat at the roll–strip interface, and the heat removed from the rolls by coolant and ambient air. Therefore, the strip and the roll should be considered together. Although Lahoti et al. [6] considered the strip and the roll together, they did not model the portion of the roll where cooling impinges; therefore, their model cannot be used to study the influence of changing cooling practices, and an artificial condition must be assumed along the radial boundary of the portion. Moreover, their finite difference formulation requires an orthogonal type mesh, but the mesh actually was arranged nonorthogonally in the deformed strip region. Current numerical models are, therefore, either inefficient or have distinct limitations.

The purpose of this study was to effectively analyze the thermal behavior of the rolling process by considering the roll and strip simultaneously. A Eulerian formulation was employed in order to minimize the number of grid points required. An upwind differencing scheme was selected to overcome the numerical instability resulting from the high velocity involved in the rolling process. Also, a generalized finite difference scheme was employed to allow use of a nonorthogonal mesh in the deformed strip region and the roll-strip interface area. Typical rolling conditions have been investigated. Both cold and hot rollings were considered, as was the effect of changing velocities.

Formulation

As observed for long and wide strip rolling [1, 3, 7, 8], the mills often operate near quasi- or cyclic steady-state conditions and the axial heat flow is usually not significant. In the present analysis, the cyclic steady-state and planar simplifications will be employed to analyze both the work roll and strip.

Work Roll. With respect to a fixed Eulerian reference frame, the basic equation governing the temperature field T for a homogeneous and isotropic roll is

$$\omega/\alpha\ \partial T/\partial\theta = \partial^2 T/\partial r^2 + 1/r\,\partial T/\partial r + 1/r^2\,\partial^2 T/\partial\theta^2 \qquad (1)$$

where r and θ are the radial and circumferential directions, respectively; ω is the angular velocity; and α is the thermal diffusivity of the roll.

In general, a thin liquid/scale film is presented at the roll–strip interface. Since tremendous rolling pressure builds up in the interface, the film is very thin, on the order of microns [10]. Therefore, in the present study, the thermal resistance of the film can be neglected and the surface temperatures of the roll and of strip approach the same value:

$$T|_{br} = T|_{bs} \qquad (2)$$

where subscripts br and bs represent the roll and strip boundaries, respectively. Also the net interface heat flux into the strip and the roll must equal the heat generated by friction, i.e.,

$$k\left(\frac{\partial T}{\partial r}\right)_{br} + k_s\left(\frac{\partial T}{\partial n}\right)_{bs} - q_f = 0 \qquad (3)$$

where $\partial/\partial n$ represents differentiation along the normal of the strip boundary (positive outward); k and k_s are the thermal

Contributed by the Heat Transfer Division for publication in the JOURNAL OF HEAT TRANSFER. Manuscript received by the Heat Transfer Division July 25, 1983.

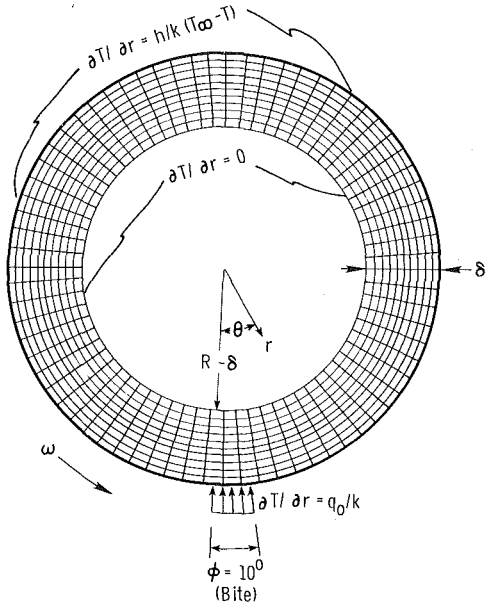

Fig. 1 Roll mesh boundary conditions for simplified rolling process

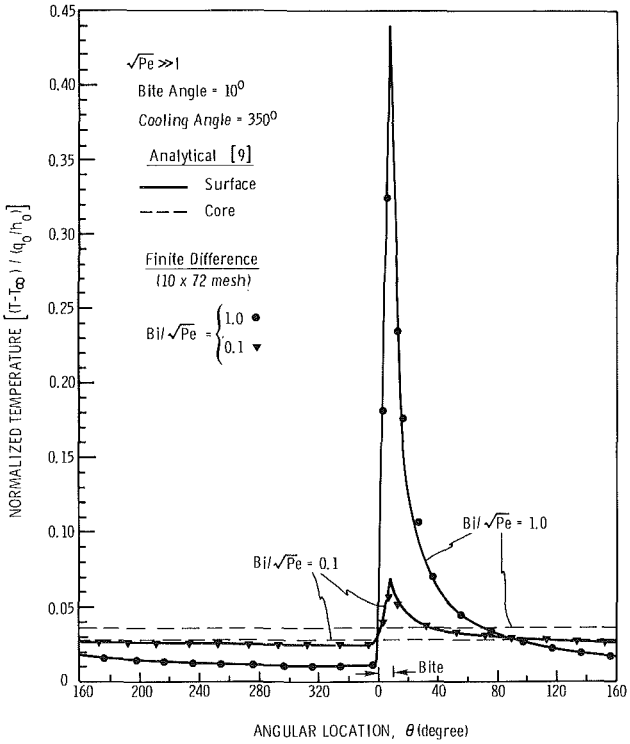

Fig. 2 Roll temperature for simplified rolling condition

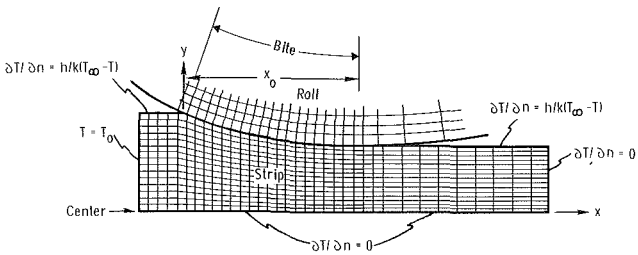

Fig. 3 Typical mesh for strip and interface region

conductivities of the roll and strip, respectively; and q_f is the friction heat generated at the interface. The boundary condition for the remaining portion of the roll circumference is

$$-k\partial T(R,\theta)/\partial\theta = h(\theta)\{T(R,\theta) - T_\infty\} \quad (4)$$

where h is the heat transfer coefficient or the contact conductance, representing the heat loss by convection to the coolant or by conduction to the backup roll; T_∞ is the ambient or the backup roll temperatures; and R is the radius of the roll.

Since the roll is rotated rapidly, and all temperatures vary within a very thin layer near the surface, only the thin layer needs to be modeled. The interior boundary condition becomes

$$\partial T(R-\delta,\theta)/\partial r = 0 \quad (5)$$

here δ is the depth of the skin layer.

Following an order of magnitude analysis of individual terms in equation (1), δ/R can be found as a function of the Peclet number Pe, $R^2\omega/\alpha$. Alternately, following Patula [9], $\delta/R \le 4.24/\sqrt{\text{Pe}}$, when $\sqrt{\text{Pe}} >> 0$, a condition satisfied in most commercial strip rolling. Based on a numerical study [11], $\delta/R = 7/\sqrt{\text{Pe}}$ is large enough for the numerical model and is used in the analysis.

The governing equation, equation (1), is approximated by using second-order central differencing for the conduction terms (right side) and first-order upwind differencing [11, 12] for the convection term (left side); the latter eliminates the numerical instability resulting from the high Peclet number. Since at the interface region, the mesh needed in the roll should match with that of the strip, the differencing equations that allow a nonuniform mesh in the θ-direction are adopted. Solution of this difference equation has been carried out by an iteration (successive relaxation) scheme.

To illustrate some specific thermal behaviors of the work roll, a simplified rolling process that a rotating roll is subjected to – constant heat input (q_0) over 10 deg of the circumference and uniform convective cooling (h_0) is applied over the remaining area – is first studied (Fig. 1). This problem has recently been solved analytically by Patula [9]. Because the skin depth is very thin for the Peclet numbers of interest, the parameters R, ω, α, k, and h_0 can be combined into a single dimensionless group, $\text{Bi}/\sqrt{\text{Pe}}$, where Bi is the Biot number, h_0R/k. Then the temperature profiles become identical in a plot of the normalized temperature, $(T-$

Nomenclature

Bi = Boit number ($=hR/k$)
e = deformation heat density rate
h = convective heat transfer coefficient
k = thermal conductivity
l,m = distances in the x- and y-directions, respectively
n = outward normal to the boundary
Pe = Peclet number ($=R^2\omega/\alpha$)
q_f = friction heat flux
r = radial coordinate
R = radius of the roll
t = strip thickness
T = temperature
u,v = velocities in the x- and y-directions, respectively
V = roll surface velocity
x,y = Cartesian coordinates
α = thermal diffusivity
δ = skin layer depth
θ = circumferential coordinate
ω = angular velocity of the roll

Subscripts

br = roll boundary
bs = strip boundary
i = neighboring points
n = neutral plane
s = strip
∞ = ambient condition
0 = uniform or original quantities

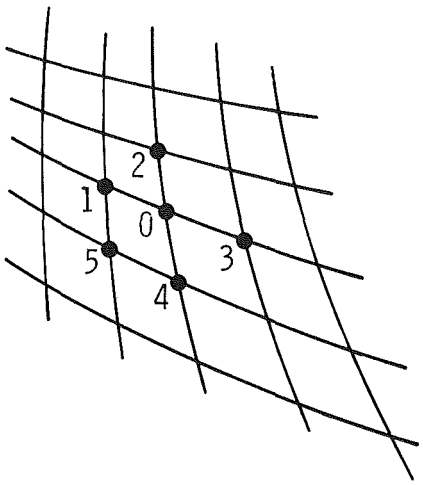

Fig. 4 Neighboring point arrangment of generalized finite difference scheme

$T_\infty)/(q_0/h_0)$, against $(R-r)/\delta$ for any fixed $\mathrm{Bi}/\sqrt{\mathrm{Pe}}$, which will certainly simplify further parametric study.

The normalized roll temperatures obtained by the present numerical scheme and by the analytical approach [9] are compared in Fig. 2 for the $\mathrm{Bi}/\sqrt{\mathrm{Pe}}=0.1$ and 1.0, the conditions at which most modern mills operate. A 11 (radial) × 72 (circumferential) uniform mesh is used. The dimensionless parameter $\mathrm{Bi}/\sqrt{\mathrm{Pe}}$ can be regarded as the Biot number based on the skin depth, $h_0\delta/k$. Also the accuracy of the numerical results for the scheme used is dependent on $\mathrm{Bi}/\sqrt{\mathrm{Pe}}$ rather than on the Peclet number alone, which was reported in other analysis using the upwind scheme [12]. As shown in the figure, the finite difference results follow the analytical solutions very well for the mesh used.

Strip. During rolling, the temperature changes within the strip result from the heat generated by the work of deformation and by the friction between roll and strip interface. The governing equation for heat flow in the x and y-directions (Fig. 3) for a moving medium is

$$u\partial T/\partial x + v\partial T/\partial y = \alpha_s(\partial^2 T/\partial x^2 + \partial^2 T/\partial y^2) + e\alpha_s/k_s \quad (6)$$

where u and v are the velocities in the x- and y-direcitons, respectively; α_s is the thermal diffusivity of the strip; and e is the deformation heat generation rate. The velocity distributions u and v used in the study are obtained by assuming $u = V_r t_n/t$, where V_r is the roll surface velocity; t_n is the thickness of the strip at the neutral plane (where the strip and roll velocities are equal); and t is the thickness of the strip. When the continuity equation is satisfied, then $v = V_r(t_n/t^2)(dt/dx)y$.

Since the strip velocity (or, more precisely, the strip Peclet number $(V_r t_n/\alpha_s)$ is high, the conduction term, $\partial^2 T/\partial x^2$, becomes small in comparison with the convection term, $u\partial T/\partial x$. Thus the temperature at a short distance upstream of the initial contact point should be the initial strip temperature T_0. The boundary condition at some distance downstream (e.g., the contact length) from the exit contact point may be assumed to be $\partial T/\partial x = 0$; i.e., the temperature variation in the x-direction should no longer be sensitive to the location of the boundary.

The strip has a curved boundary associated with a very complicated interface condition, and here a nonorthogonal mesh is convenient. Therefore, a generalized finite difference (GFD) method is used. This method has been successfully applied to many heat transfer problems [13, 14]. It calculates the needed derivatives by using a two-dimensional Taylor series expansion about a point (x_0,y_0) up to second-order terms. One has

Table 1 Operational parameters for Coil 45 [3]

Strip material:	Mild Steel[a]
Roll material:	Cast Steel[a]
Coolant:	Water
Entry gauge:	0.15 cm (0.0589 in.)
Exit gauge:	0.114 cm (0.045 in.)
Roll speed:	1146.6 cm/s (2257 fpm)
Forward slip:	0%
Strip width:	63.5 cm (25 in.)
Work-roll diameter:	50.8 cm (20 in.)
Total input energy:	3694 kW(4954 HP)
Strip entry temp.:	65.6°C (150°F)

[a]Both roll and strip have the following thermal properties:

Thermal conductivity:	0.4587 W/cm-°C
Thermal diffusivity:	0.1267 cm^2/s

$$T = T_0 + (\partial T/\partial x)_0 l + (\partial T/\partial y)_0 m + 1/2(\partial^2 T/\partial x^2)_0 l^2 + 1/2(\partial^2 T/\partial y^2)_0 m^2 + (\partial^2 T/\partial x\partial y)_0 lm \quad (7)$$

where $T = T(x,y)$, $T_0 = T(x_0,y_0)$, $l = x - x_0$, and $m = y - y_0$. Five independent equations, similar to equation (7), can be obtained by using five arbitrarily located neighboring points; $(x_i,y_i), i = 1 \ldots 5$ are shown in Fig. 4. Letting $T_i = T_i(x_i,y_i)$, one has $l_i = x_i - x_0$ and $m_i = y_i - y_0$. The five spatial derivatives $\partial T/\partial x \ldots \partial^2 T/\partial x\partial y$ at point (x_0,y_0) can be computed in terms of the functional values at the five neighboring points, $T_1 \ldots T_5$. Substituting these expressions into the governing equation (equation (6)) yields an algebraic equation for the temperature of the point of interest in terms of the five neighboring points. The advantage of this method is that it allows use of a nonorthogonal mesh chosen for compatibility with the shape of the strip–roll interface.

However, when (x_0,y_0) is a central point (Fig. 4), solution of these GFD equations, like their central difference counterpart in the conventional finite difference (CFD) method used for modeling the work roll, displays nonphysical spatial oscillation at a high Peclet number. Following a remedy similar to that used in the CFD method, one-sided approximations are used for the convection terms to achieve numerical stability. A detailed description of this method can be found in [14]. As indicated in this reference, very good accuracy can be achieved for a reasonably fine mesh at very high Peclet numbers.

Heat Generation by Plastic Deformation and Friction. In principle, information on heat generated by plastic deformation and friction can be analytically predicted [1, 3, 5, 6] or directly measured [1, 3, 15]. However, the greatest uncertainty in the analytical approach is in modeling friction behavior, which still is not completely understood. This uncertainty greatly affects predicting not only the friction energy but also the neutral point and consequently the velocities and the deformation heat generation rate. As pointed out in a recent study of aluminum rolling [16], based on the Coulomb friction law, the numerical predictions of the roll separating force can match the measured data reasonably well, but there is more than a 100 percent difference in predicted and measured torques (or energies). On the other hand, if the torques match well, the difference in predicted and measured forces can be more than 100 percent. Because of the aforementioned inconsistency, in the present analysis, the input data of the heat generated by deformation and friction will be obtained from the direct measurements of power. The uncertainty in using the measurement approach is in allocating the total energy measured to various sources of energy consumption.

Cold Rolling

As an illustration, a rolling condition recorded from one of the Bethlehem Steel's cold tandem mills [3] is analyzed by the

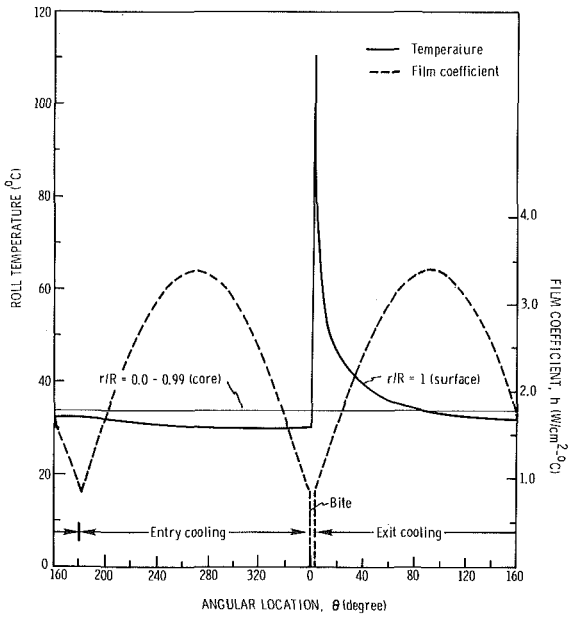

Fig. 5 Film coefficient and roll temperature for cold rolling case

present finite difference scheme. The operational parameters recorded are summarized in Table 1.

In the rolling process, most of the power input goes to deform the strip and to overcome the friction resistance at the roll-strip interface. The remaining power is dissipated as friction energy in the mill stand, particularly in the backup bearings. To roll a mild steel at the speed presently considered, Bentz and Roberts [15] found that about 90 percent of the total power is consumed in the deformation of the workpiece and in the friction loss at the interfaces. In the present analysis, we will use this 90 percent estimate and also follow Bethlehem's prediction [3] that 6.5 percent of the 90 percent total power is dissipated as friction heat at the interface. Moreover, according to Farren and Taylor's observation [17], for steel, 86.5 percent of the deformation energy is converted into heat. Using the foregoing numbers, the resulting values of heat generated by deformation and interface friction are 2689 and 217 kW, respectively; they have also been assumed to be uniformly distributed in the deformed region and the interface.

As indicated in the Bethlehem study [3], the convective heat transfer coefficient for a typical water cooling spray varies from 0.85 $W/cm^2 - °C$ to 3.4 $W/cm^2 - °C$. The heat coefficient, as represented in Fig. 5 by a dotted line, varies as a half sine curve to simulate both the entry and exit coolings. The corresponding strip Pe becomes 1036. The mean value of Bi and the value of Pe for the roll are 137 and 2.3×10^5, respectively, or $Bi/\sqrt{Pe} = 0.29$.

As shown in Fig. 3, 45×15 mesh was selected for the strip in which 20×15 was within the bite region; the mesh in the y-direction is uniformly distributed over the local thickness of the strip, and the mesh is also chosen to match the uniform spacing along the circumference of the roll. In the upstream region, the mesh is uniform in both x- and y-directions. In the downstream region, the mesh spacing is equal in y, but gradually increases in x. A 72 (circumferential) $\times$ 15 (radial) mesh was used for the roll. The roll mesh was refined near the bite region to match that used in the strip.

Based on this mesh arrangement, the computed temperatures of the roll and strip are shown in Figs. 5 and 6, respectively. The surface temperature of the roll peak or the strip exit is 110.4°C, which agrees well with the measured value, 112.8°C [3], despite the simplified input assumptions. Results based on a mesh with a doubled number of grid points in the strip (30×20 in the bite region) are also shown in Fig. 6, as circles which closely agree with those based on the foregoing model with less grid points. This agreement indicates that in the mesh range considered, the results are not sensitive to the mesh and therefore should be reliable.

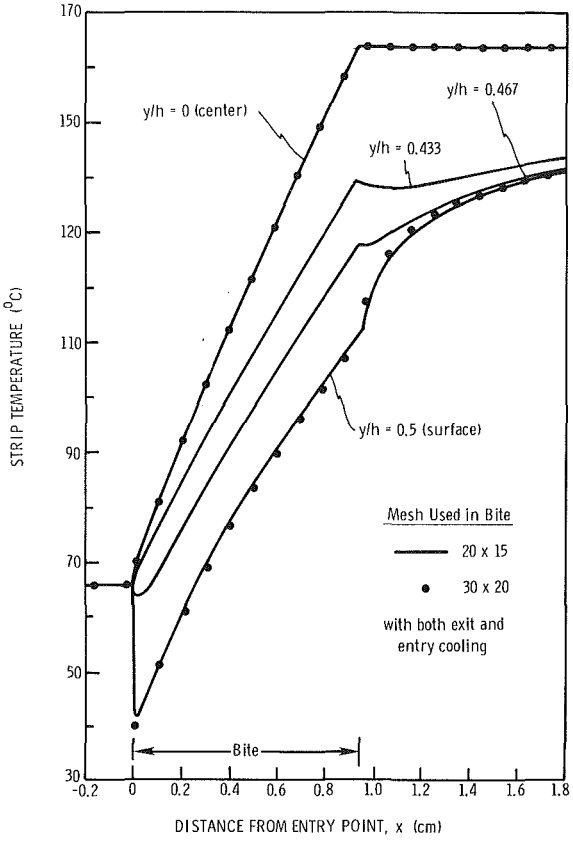

Fig. 6 Strip temperature for cold rolling case

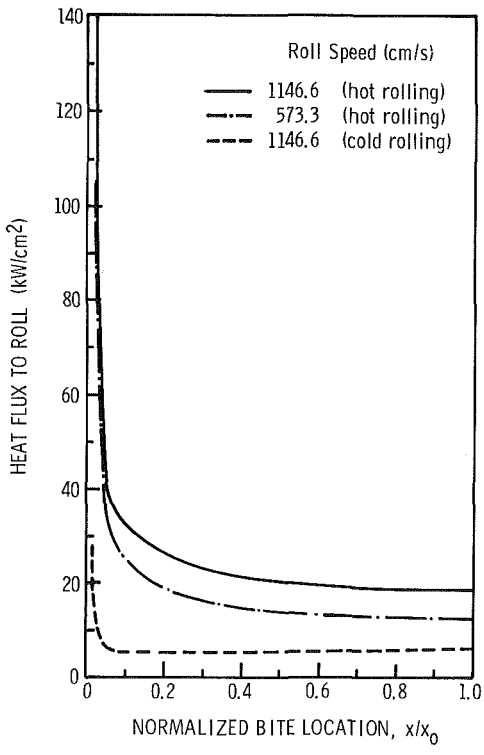

Fig. 7 Interface heat flux to roll

Figure 5 indicates that the roll temperature variations are limited within a very thin layer, about 1 percent of the radius,

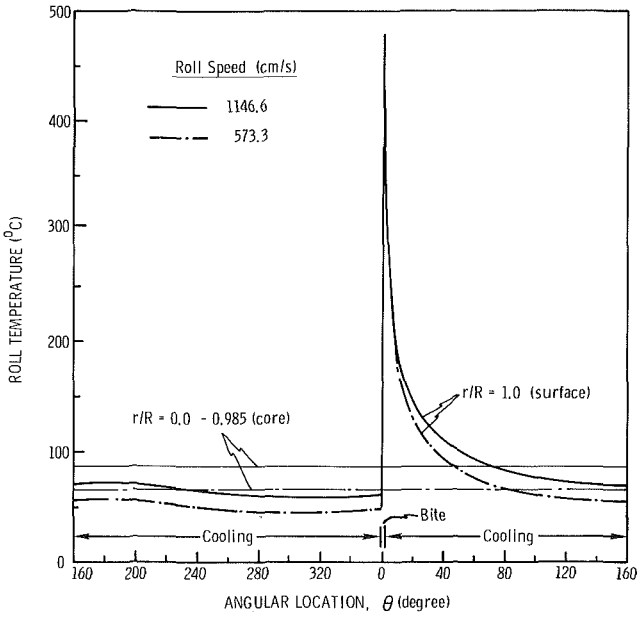

Fig. 8 Roll temperature for hot rolling cases

which is consistent with the associated boundary condition, equation (5). The surface temperature rapidly increases at the bite due to great heat generated by the friction and transferred from the strip. As the roll leaves the bite, the surface temperature immediately decreases due to heat convection to the coolant and heat conduction into the immediate subsurface layer. Although detailed comparison is not possible, in general, the foregoing results are similar to the reported measured behaviors [3, 8, 18, 19]. On the other hand, Lahoti et al. [6] predicted a very uniform temperature along the interface and a quite large thermal layer in the roll. Their result appears to be distorted by the aforementioned artificial boundary condition.

Figure 6 indicates that while the strip is under deformation, the bulk temperatures inside the strip increase continuously; this is largely controlled by the deformation energy. On the other hand, the strip surface temperaure changes much more drastically and is mainly controlled by the friction heat and the roll temperature. Because the roll is heavily cooled by the coolant, it acts like a heat sink. Thus, as soon as the strip hits the roll, its surface temperature drops. Since considerable friction and deformation heat are created along the interface and transferred from the neighboring sublayer, the surface temperature picks up rapidly.

Beyond the bite (Fig. 6), the strip temperature tends to become uniform. In this region, the heat convected to the air has been assumed to be negligible. For high-speed rolling, the strip temperature behaves parabolically rather than elliptically, as implied by equation (6). In other words, the boundary conditions assumed in the downstream region should not have a noticeable effect on the bite region. Figure 7 shows a plot of the heat flux transferred to the roll versus the normalized interface location (where x_0 and x are defined in Fig. 3). The dotted line represents the case currently discussed. At the initial contact stage, as anticipated, a very large amount of heat is transfered to the roll. In fact, the roll surface temperature is about 35°C lower than that of the strip (Figs. 5 and 6). To satisfy the boundary condition, equation (2), a step change of surface temperature is expected to occur at the initial contact point ($x=0$) The induced heat flux to the roll at $x=0$ mathematically could approach to infinite (Fig. 7). Away from the contact area, the heat flux to the roll increases slowly. The corresponding heat flux transferred from the strip is the roll heat flux less than uniform friction heat flux which is 3.62 kW/cm^2.

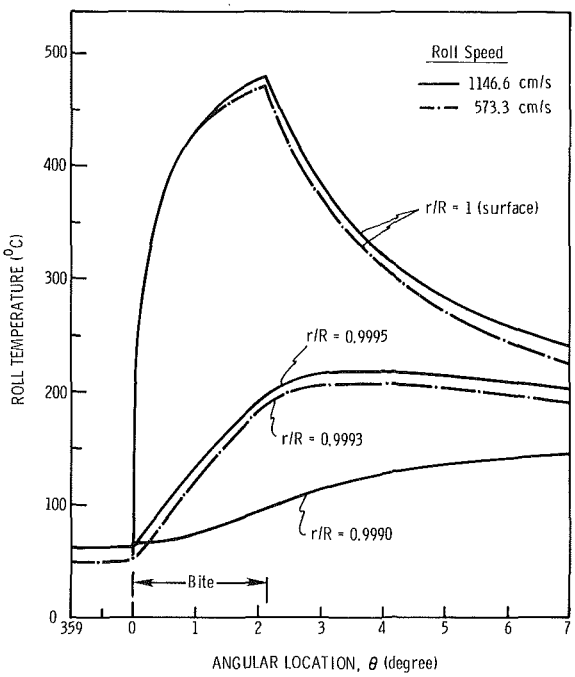

Fig. 9 Roll temperature near the bite

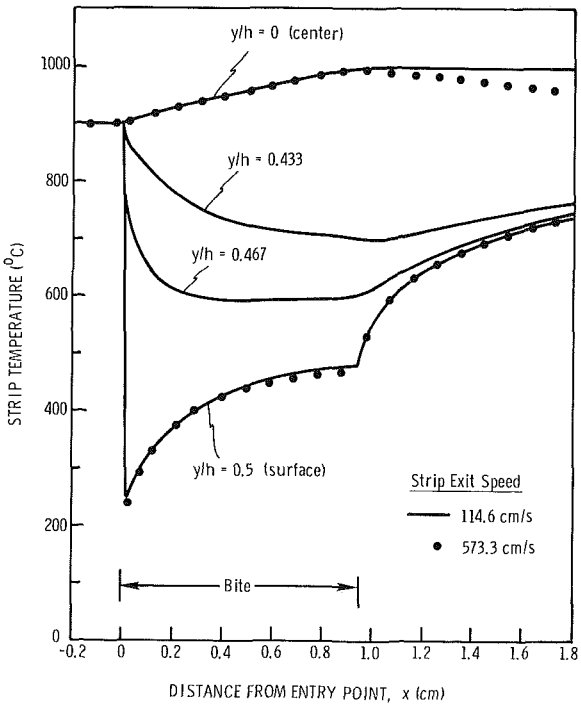

Fig. 10 Strip temperature for hot rolling cases

It is believed that in those measurement studies previously cited [18, 19], the strip initial temperatures were close to that of the roll. Therefore, the strip is not expected to have a temperature drop at the initial contact stage. However, it is noteworthy that at very high rolling speeds, measuring the local temperature change in the bite could be a big challenge. For instance, for the case considered, the total time that the strip passes through the bite lasts about 0.8 ms. A pyrometer response time less than a 100 microseconds is required to detect this type of temperature changes. For the best commercially available pyrometers, the response time is on the order of 1 ms. Similarly, in numerical analyses, if the mesh used in the bite area is relatively coarse, the temperature drop described before could also be difficult to predict.

Moreover, in the cited numerical studies, Zienkiewicz et al. [5] predicted that the strip surface temperature gradually increases in the bite for both cold and hot rollings. Since they considered the strip alone, a specified convective boundary condition was imposed in the interface region. This did not allow a very large amount of heat flux transferring to the roll at the initial contact stage and led to a result, as expected, of no temperature drop at the interface. Lahoti et al. [6] predicted a rather uniform temperature along the strip surface, which is believed largely due to the imposed boundary condition mentioned before.

Hot Rolling

In hot rolling, the strip is normally rolled at elevated temperatures at which recrystallization proceeds faster than work hardening. In addition, the hot strip is generally rolled at thicker gauge and lower speed than that of the cold strip. Since the gauges specified in Table 1 are still suitable for hot rollings, these gauges will also be used for the hot rolling analysis. Two cases are considered. The first focuses on the effect of changing the working temperature by raising the strip entry temperature to 900°C, which is frequently encountered in hot rolling. The second case shows the effect of changing velocity by slowing the roll speed from 1146.6 to 573.3 cm/s. The other operating conditions are similar to those discussed for cold rolling.

Figure 8 depicts the roll temperature distributions for the two hot rolling cases considered. A comparison of Fig. 8 with Fig. 5 indicates that the temperature profile change between the hot and cold rollings is mainly in magnitude but not in shape. The temperature magnitude is governed by both the interface heat flux and the speed. As shown in Fig. 7, at a speed of 1146.6 cm/s, the heat flux increases about four times from the cold to hot rolling. The corresponding increase of temperature is also found to be about fourfold (Figs. 5 and 8).

Figure 8 shows that, except in the bite region, the roll temperature is reduced about 15 percent with the speed is slowed 50 percent. As indicated in Fig. 9, the difference in the bite region is much smaller. For example, the corresponding decrease of the peak temperature is less than 2 percent. The temperature decrease due to slowing the speed is mainly due to decrease of the heat flux (Fig. 7). Actually, when keeping constant heat flux, slowing the speed will increase the temperaure as noted in Fig. 2. Figure 9 also shows that near the bite, very large temperature variations are within a very thin layer. The layer thickness, consistent with the previous finding, is dependent on the speed, or more precisely, the roll Pecelt number.

The strip temperatures for the two hot rolling cases are presented in Fig. 10. In the bite region, the strip temperature, similar to the roll temperatures, is not noticeably affected by changing the speed within the range considered. In the downstream region ($x > x_0$), the stip center temperature drops faster in the slower strip. By contrast, the surface temperatures are not sensitive to the speeds considered. This figure also indicates the temperature drop in the initial contact stage is much larger than its counterpart for the cold strip, as shown in Fig. 6. When the strip entry temperature rises from 65.6°C to 900°C, the temperature drop increases approximately from 25°C to 650°C, reflecting the great increase in the temperature difference between strip and roll ahead of the bite. The larger the temperature drop in the bite region, the greater may be the impact on lubricant behavior.

Finally, note that for the same amount of thickness reduction, the power requirement for hot rolling generally is less than that for cold rolling. However, in view of the uncertainty of the friction behavior and the deformation energy publications noted before, it was not considered worthwhile to explore in the present study either the effects of changing friction energy of variability due to deformation energy.

Concluding Remarks

The heat transfer behavior of the rolling process has been studied for cold and hot conditions. Because the heat generation occurs in the strip or at the strip-roll interface while heat removal is at the roll surface, both the strip and roll should be considered together and analyzed at the same time. The results show that the extremely large temperature variations are found in both roll and strip near the bite (interface) region. Such high temperature variation could create very large thermal stresses within the thin layer and in turn, controls the rate of roll wear or roll failure. Proper control of this stress could significantly extend the roll life [1, 8]. A large temperature drop could also be found in the strip surface at the initial contact stage. In hot rolling, for example, the strip surface temperature can drop from 900°C, the entry temperature, to less than 250°C at the initial contact stage.

The present study also shows by comparing the present results with published findings tht utilize either analytical methods or direct measurements that the computational scheme used is effective and reliable. However, it is believed that the greatest uncertainly in analyses will arise not from the numerical scheme, but from the input data, in particular, the friction energy, the neutral point (or the forward slip), and the heat transfer coefficient of coolant.

References

1 Roberts, W. L., *Cold Rolling of Steel*, Marcel Dekker, New York, 1978.

2 Parke, D. M., and Baker, J. L., "Temperature Effects of Cooling Work Rolls," *Iron and Steel Engineer*, Vol. 49, 1972, pp. 83-88; also published as a report by the Association of Iron and Steel Engineers, Pittsburgh, Pa.

3 Poplawski, J. V., and Seccombe, D. A., Jr., "Bethlehem's Contribution to the Mathematical Modeling of Cold Rolling Tandem Mills," *Iron and Steel Engineer*, Vol. 57, 1980, pp. 47-58.

4 Wilmotte, S., and Mignon, J., "Thermal Variations of the Camber of the Working Rolls During Hot Rolling," *Metallurgical Reports CRM*, No. 34, 1973, pp. 17-34.

5 Zienkiewicz, O. C., Onate, E., and Heinrich, J. C., "A General Formulation for Coupled Thermal Flow of Metals Using Finite Elements," *International Journal for Numerical Methods in Engineering*, Vol. 11, 1981, pp. 1497-1514.

6 Lahoti, G. D., Shah, S. N., and Altan, T., "Computer-Aided Analysis of the Deformations and Temperatures in Strip Rolling," ASME *Journal of Engineering for Industry*, Vol. 100, 1978, pp. 159-166.

7 Tereshko, A. K., Polukin, V. P., Nikolaev, V. A., Terkhov, V. N., and Titarenko, L. A., "Experimental Investigation of Work Roll Temperature Distribution During Cold Rolling," *Steel in the U.S.S.R.*., 1970, pp. 218-220.

8 Stevens, P. G., Ivens, K. P., and Happer, P., "Increasing Work- Roll Life by Improved Roll-Cooling Practice," *Journal of the Iron and Steel Institute*, Vol. 209, 1971, pp. 1-11.

9 Patula, E. H., "Steady-State Temperature Distribution in a Rotating Roll Subject to Surface Heat Fluxes and Convective Cooling. " ASME *Journal of Heat Transfer*, Vol. 13, 1981, pp. 36-41.

10 Wilson, W. R. D., Walowit, J. A., "An Isothermal Hydrodynamic Lubrication Theory for Strip Rolling with Front and Back Tension," *Tribology Convention 1971*, Inst of Mech Eng, London, pp. 164-172.

11 Tseng, A. A., "Finite-Difference Solutions for Heat Transfer in a Roll Rotating at High Speed," *Numerical Heat Transfer*, Vol. 7, 1984, pp. 113-125.

12 Roache, P. J., *Computational Fluid Dynamics*. Hermosa Publishers, Albuquerque, N.M., 1972, pp. 64-82.

13 Chung, K. C., "A Generalized Finite-Difference Method for Heat Transfer Problems of Irregular Geometries," *Numerical Heat Transfer*, Vol. 4, 1981, pp. 345-357.

14 Tseng, A. A., "A Generalized Finite-Difference Scheme for Convection-Dominated Metal Forming Problems," *International Journal for Numerical Methods in Engineering*, Vol. 20, 1984, in press.

15 Bentz, R. J., and Roberts, W. L., "Predicting Rolling Forces and Mill Power Requirements for Tandem Mills," *Blast Furnace and Steel Plant*, Vol. 58, 1970, pp. 559-568.

16 Saeed, U., and Lenard, J. G., "A Comparison of Cold Rolling Based on the Equilibrium Approach," ASME *Journal of Engineering Materials and Technology*, Vol. 102, 1980, pp. 223-228.

17 Farren, W. S., and Taylor, G. I., "The Heat Developed During Plastic Extension of Metal," *Proceedings of the Society of London*, Series A, Vol. 107, 1925, pp. 422-429.

18 Kannel, J. W., and Dow, T. A., "The Evolution of Surface Pressure and Temperature Measurement Techniques for Use in the Study of Lubrication in Metal Rolling," ASME *Journal of Lubrication Technology*, Vol. 96, 1974, pp. 611-616.

19 Jeswiet, J., and Rice, W. B., "Measurement of Strip Temperature in Roll Gap During Cold Rolling," *CIRP Annals*, Vol. 24, 1975, pp. 153-156.

Condensation Heat Transfer on Laminar, Falling Film

V. D. Rao
Department of Chemical Engineering.

P. K. Sarma
Department of Mechanical Engineering.

Andhra University,
Visakhapatnam-530003
India

The process of condensation of vapors on a laminar, falling film of immiscible liquid is formulated within the framework of certain assumptions for a laminar, two-film model. The numerical solutions are presented for a wide range of parameters, and it is observed that the dynamics of the falling film has a profound influence on the condensation heat transfer rates. The condensation heat transfer coefficient is found to be a function of the modified Graetz number, subcooling parameter, and the heat capacity ratio of coolant-to-condensate. Further, shorter liquid film lengths would yield considerably high condensation heat transfer rates in comparison with the Nusselt analysis.

Introduction

Studies [1] on direct-contact heat transfer are of paramount importance in the design of low-pressure, regenerative feedwater heaters for thermal power plants and desalination-cum-power generation plants. The regenerative, direct-contact, low-pressure feedwater heaters have the clear-cut advantages of higher heat transfer rates, trouble-free maintenance, and less initial capital outlay in comparison with the conventional heat exchangers. The present state-of-the art in direct-contact heat transfer investigations is given by Sideman [2] in his review article. The breakdown of the continuous liquid phase into discrete liquid particles interacting with the continuous phase of the relatively cold or hot fluid provides more contact area, and this phenomenon serves as an augmentative technique for better transport of thermal energy from the hot to cold with or without phase transformation taking place during the heat exchange. Further, in situations where abundant supply of the coolant is limited due to geographically arid conditions prevailing at the plant location, it is pointed out by Merte [3] that condensation of vapors on disintegrated liquid droplets in the jet condensers could be a viable proposition to conserve energy and at the same time to recycle the preheated feed water. Hasson et al. carried out theoretical [4] and experimental [5] investigations relating to the phenomena of condensation of vapors on laminar liquid jets. Their analysis considered three forms of liquid jets, viz., (*i*) cylindrical, (*ii*) uniformly thick, and (*iii*) fan spray liquid sheets. The experimental investigation by Hasson et al. [5] mainly concerned the evaluation of the average Nusselt as a function of modified Graetz away from the tip of the nozzle for the fan spray jet. Acceptng a random error of ± 35 percent, the average Nusselt for condensation of steam in the asymptotic region of the fan spray sheet where fringes are absent was given as 5, the evaluation of Nusselt being carried out taking the hydraulic diameter of the sheet as the characteristic dimension. Murty and Sastri [6] investigated the problem of condensation of vapors on accelerating liquid jets issuing out from a nozzle and the variation of condensation heat transfer along the jet for various Prandtl numbers and subcooling parameters was reported. The subsequent instability in the jet would alter the flow configuration to droplet breakdown, and the process of condensation of vapors takes place on the surface of the droplets. Tamir and Rachmilev [7] experimentally studied the problem of condensation of immiscible vapors on a laminar film of water spread over a spherical surface. The average interfacial heat transfer coefficients are arrived at with the aid of a theoretical model with certain simplifying assumptions. The process of condensation of vapors on droplets was studied by Brown [8], Weinberg [9], and Syhre [10]. It is essentially observed by all that the average heat transfer coefficients for condensation on drops are much higher than those for filmwise condensation. Ford and Lekic [11] conducted experiments, to observe the rate of condensation of saturated steam on water droplets.

Another possible configuration of the coolant is a thin laminar film on a vertical or an inclined surface maintained at a temperature lower than the saturation temperature of the vapors to be condensed on the coolant film. Various aspects relating to the dynamics of the falling films have been investigated in several studies [12–17]. The heat transfer studies from the wall surface to the laminar falling liquid films with or without evaporation at the vapor-liquid interface drew the attention of many investigators [18–21].

The present article considers another aspect, viz., the condensation of vapors on the surface of a laminar falling film of immiscible liquid, and numerical results are presented to bring out the influence of various parameters on the condensation heat transfer rates.

Physical Model and Formulation

The flow of the liquid coolant takes place from a slit in the form of a thin film down an inclined plane with a prescribed velocity profile at the exit of the slit, i.e., at $x = 0$. The coolant surface exposed to the condensing vapors is assumed to be smooth and free from waves, thus excluding the effects of surface tension on the condensation heat transfer. Diabatic condition of heat flow is assumed at the coolant-condensate interface. While solving the condensation of binary-vapor mixtures on a vertical surface, it was ponted out [22] that the analysis can be accomplished by assuming either a separated or a homogeneous flow model. The separated flow model consideres the constitutive equations of the two immiscible phases separately, with the inclusion of matching boundary conditions and the phase transformation peculiarities at the relevent interfaces. The homogeneous model is based on the averaged physical properties of the two immiscible liquid phases. The separated or two-film model is assumed in the foregoing analysis. The condensate film occupies a preferential segregated position and is essentially distributed evenly over the falling immiscible coolant film. The phenomenon of breakdown of the condensate film into discrete droplets is mainly characterized by the relative magnitudes of the molecular cohesive forces and densities of

Contributed by the Heat Transfer Division for publication in the JOURNAL OF HEAT TRANSFER. Manuscript received by the Heat Transfer Division. June 2, 1983.

the condensate and coolant films. Such a situation of film disintegration of the condensate is precluded in the analysis undertaken. The condenser surface ($y = 0$) is maintained under isothermal conditions at a specified temperature T_0, far lower than the saturation temperture of the condensate, corresponding to the system pressure. The conservation of energy in the coolant film is accomplished in two successive stages. During the thermally developing state, development of thermal penetration thickness into the coolant film takes place commencing with $\delta_t = 0$ at $x = 0$ and ending with $\delta_t = \delta_1$ at $x = x_1$ (say). The second stage for $x \geq x_1$ is termed as the thermally developed state. During this stage, the enthalpy of the coolant rapidly increases due to the condensation of vapors taking place. Thus, in the absence of non-condensible gases in the quiescent medium of vapors and for the configuration shown in Fig. 1, the governing equations can be written as follows:

Conservation of mass in the coolant film

$$\int_0^{\delta_1} \rho_1 u_1 dy = \int_0^{h_0} \rho_1 u_1 dy = \dot{m} = \text{constant} \tag{1}$$

Conservation of momentum in the coolant film

$$\frac{d}{dx}\int_0^{\delta_1} \rho_1 u_1^2 dy = \mu_1 \frac{\partial u_1}{\partial y}\bigg|_0^{\delta_1} + \rho_1 g_0 \delta_1 \tag{2}$$

Conservation of momentum in the condensate film

$$\frac{d}{dx}\int_{\delta_1}^{\delta_1+\delta_2} \rho_2 u_2^2 dy - U_i \frac{d}{dx}\int_{\delta_1}^{\delta_1+\delta_2} \rho_2^2 u_2 dy$$

$$= -\mu_2 \frac{\partial u_2}{\partial y}\bigg|_{\delta_1} + \rho_2 g_0 \delta_2. \tag{3}$$

Equations (2) and (3) consider the inertial forces and the shear at the interface of coolant condensate films. For the physical model under consideration, when the coolant film is an accelerating one, the term related to inertia force plays significant role [17] in the region $x \to 0$ (i.e., near the exit of the slit) because of its prominance relative to the viscous and body forces. The shear at the condensate-vapor interface is not of primary importance [3] in problems of condensation when $\Pr \geq 1$, and hence it is excluded in equation (3). Further, the earlier [3] experience shows that in the case of thick condensate films, inclusion of inertia terms would yield accurate predictions over a wide range of Prandtl numbers and subcooling parameters. The integral equations of the conservation of energy in the coolant film during the thermally developing and developed stages, respectively, are as follows:

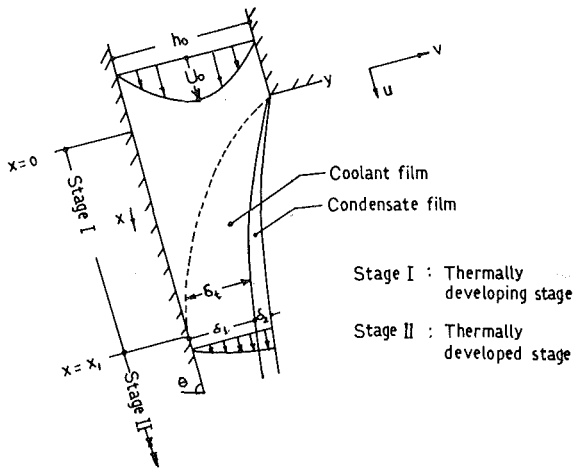

Fig. 1 Physical model and coordinate system

$$\frac{d}{dx}\int_{\delta_1-\delta_t}^{\delta_1} u_1(T_1 - T_0)dy = \alpha_1 \frac{\partial T_1}{\partial y}\bigg|_{y=\delta_1} \tag{4a}$$

$$\frac{d}{dx}\int_0^{\delta_1} u_1(T_1 - T_0)dy = \alpha_1 \frac{\partial T_1}{\partial y}\bigg|_0^{\delta_1} \tag{4b}$$

Conservation of energy in the condensate film

Nomenclature

C = specific heat
f = variable defined in equation (15*b*)
F = ratio of thickness of thermal boundary layer-to-thickness of coolant film, δ_t/δ_1
g_0 = gravitational constant, $g \sin\theta$
h_0 = size of the slit
h_{fg} = latent heat of condensing vapors
h_x = local heat transfer coefficient defined in equation (24*a*)
h_x^* = local heat transfer coefficient from Nusselt's analysis
k = thermal conductivity
k^* = thermal conductivity ratio of coolant to condensate, k_1/k_2
L = length of the plate or wall
Nu_x = local Nusselt number defined in equation (24*b*), $h_x L/k_2$
$\dot{m}$ = mass flow rate at the exit of the slit ($x=0$) per unit width of the wall as defined in equation (1).
$\Pr$ = Prandtl number
Re_0 = Reynolds number, $4\dot{m}/\mu_1$
S = subcooling parameter, $C_2(T_s - T_0)/h_{fg}$
T = temperature
T_i = variable temperature at the coolant-condensate interface
u = x-component of velocity
u_i = velocity at the coolant-condensate interface
U_i = velocity at the condensate-vapor interface
U_0 = maximum velocity at the exit of the slit, i.e., at $x = 0$
v = y-component of velocity
x,y = position coordinates
x^* = dimensionless distance from the exit of the slit, x/L

Greek Symbols

α = thermal diffusivity
β = gravitational force parameter, $g_0 L^3/\nu_1^2$
γ = heat capacity ratio parameter, $\rho_1 C_1/\rho_2 C_2$
δ_1 = variable thickness of the coolant film
δ_2 = variable thickness of the condensate film
δ_t = variable thickness of the thermal penetration in the coolant film
Δ_1 = δ_1/h_0
Δ = δ_2/δ_1
ν = kinematic viscosity
ρ = density
ρ^* = ρ_1/ρ_2
μ = dynamic viscosity
μ^* = μ_1/μ_2
θ_i = dimensionless temperature at the coolant-condensate interface, $(T_i - T_0)/(T_s - T_0)$
θ = inclination of the plate to horizontal
ϕ = dimensionless variable defined in equation (18)
ψ = dimensionless variable defined in equation (17*b*)

Subscripts

0 = at the exit of the slit ($x = 0$)
1 = coolant
2 = condensate
s = saturation

$$\frac{d}{dx}\int_{\delta_1}^{\delta_1+\delta_2} u_2(T_1-T_2)dy=\alpha_2\frac{\partial T_2}{\partial y}\Big|_{\delta_1}^{\delta_1+\delta_2} \tag{5}$$

The heat balance at the vapor-condensate interface is as follows

$$\frac{d}{dx}\int_{\delta_1}^{\delta_1+\delta_2} u_2 dy=\frac{k_2}{\rho_2 h_{fg}}\frac{\partial T_2}{\partial y}\Big|_{y=\delta_1+\delta_2}. \tag{6}$$

Thus, it is imminent that proper choice of velocity and temperature profiles in the coolant and condensate films is a prerequisite to utilize equations (1-6).

The boundary conditions for the above set of governing equations and the possible velocity and temperature fields in the coolant and condensate films are as follows: For $x \le 0$

$$y=0,\ u_1=0,\ y=h_0,\ u_1=0,\ \text{and}\ y=h_0/2,\ u_1=U_0. \tag{7}$$

For $x \ge 0$

$$y=0,\ u_1=0,\ \text{and}\ T_1=T_0=\text{constant} \tag{8}$$

$$y=\delta_1,\ u_1=u_2=u_i\ \text{and}\ T_1=T_2=T_i \tag{9}$$

$$y=\delta_1,\ \mu_1\frac{\partial u_1}{\partial y}=\mu_2\frac{\partial u_2}{\partial y} \tag{10}$$

$$y=\delta_1,\ k_1\frac{\partial T_1}{\partial y}=k_2\frac{\partial T_2}{\partial y} \tag{11}$$

$$y=\delta_1,\rho_1\left(v_1-u_1\frac{d\delta_1}{dx}\right)=\rho_2\left(v_2-u_2\frac{d\delta_1}{dx}\right)=0. \tag{12}$$

Boundary condition (12) signifies that mass exchange across the coolant-condensate interface is absent.

$$y=\delta_1+\delta_2,\ u_2=U_i,\ T_2=T_s\ \text{and}\ \frac{\partial u_2}{\partial y}=0 \tag{13}$$

$$y=\delta_1-\delta_t,\ T_1=T_0\ \text{and}\ \frac{\partial T_1}{\partial y}=0 \tag{14}$$

Choice of velocity and temperature profiles: The velocity profile for the coolant film is adopted from [17] which is as follows:

$$x\le 0,\ u_1=4U_0\left[\left(\frac{x}{h_0}\right)-\left(\frac{y}{h_0}\right)^2\right] \tag{15a}$$

$$x\ge 0,\ u_1=\frac{4U_0h_0}{f\delta_1}\left[\frac{f+2}{3}\left(\frac{y}{\delta_1}\right)-\left(\frac{y}{\delta_1}\right)^2\right] \tag{15b}$$

where $f=f(x)$ and $1 \le f \le 4$

The variable f attains an asymptotic value 4 away from the slit to degenerate to original profile as suggested by Nusselt in his classical paper. The velocity profile in the condensate film is obtained as shown below, satisfying the relevant boundary conditions, viz., equations (9, 10, 13, 15b).

$$u_2=\frac{U_0h_0}{\delta_1}\left[\frac{4(f-1)}{3f}-\frac{2}{3}\frac{\mu_1}{\mu_2}\frac{\delta_2}{\delta_1}(4-f)(2\xi-\xi^2)\right]. \tag{16}$$

where $\xi=(y-\delta_1)/\delta_2$

The temperature profiles for the coolant film during the thermally developing and developed stages are respectively as follows

$$x\le x_1,\ \frac{T_1-T_0}{T_i-T_0}=\left[\frac{y-\delta_1+\delta_t}{\delta_t}\right]^2 \tag{17a}$$

where $\delta_t=\delta_t(x)$ and $0 \le \delta_t \le \delta_1$

$$x\ge x_1,\ \frac{T_1-T_0}{T_i-T_0}=\psi\left(\frac{y}{\delta_1}\right)+(1-\psi)\left(\frac{y}{\delta_1}\right)^2. \tag{17b}$$

where $\psi=\psi(x)$ and $0 \le \psi \le 1$

The temperature distribution in the condensate film is given by the following expression

$$\frac{T_2-T_i}{T_s-T_i}=\phi\xi+(1-\phi)\xi^2 \tag{18}$$

where $\phi=\phi(x)$ and $0 \le \phi \le 1$

In the problem under investigation, the five dependent variables that are functions of the flow direction can be listed as δ_1, δ_2, f, ϕ, and δ_t (or ψ). Manipulation of the equations (1-6) would result in the following set of first order simultaneous differential equations in dimensionless form

$$\frac{d\Delta_1}{dx^*}=-\frac{(G_4G_7+G_5G_6)(G_5b_1-G_2b_2)+G_2G_4(G_7b_2-G_5b_3)}{(G_4G_7+G_5G_6)(G_1G_5-G_2G_3)+G_2G_3G_4G_7} \tag{19}$$

$$\frac{d\Delta}{dx^*}=\frac{G_5b_1}{G_2G_4}-\frac{b_2}{G_4}-\frac{(G_1G_5-G_2G_3)}{G_2G_4}\frac{d\Delta_1}{dx^*} \tag{20}$$

$$\frac{df}{dx^*}=\left(b_1+G_1\frac{d\Delta}{dx^*}\right)/G_2 \tag{21}$$

$$\frac{d\phi}{dx^*}=\left[G_{15}b_4-G_{11}b_5+(G_8G_{15}-G_{11}G_{12})\frac{d\Delta}{dx^*}-(G_9G_{15}-G_{11}G_{13})\frac{df}{dx^*}\right]/(G_{10}G_{15}-G_{11}G_{14}) \tag{22}$$

$$\frac{dF}{dx^*}\left(\text{or}\ \frac{d\psi}{dx^*}\right)=\left(b_4+G_8\frac{d\Delta}{dx^*}-G_9\frac{df}{dx^*}-G_{10}\frac{d\phi}{dx^*}\right)/G_{11}. \tag{23}$$

where

$$G_1 = (10f^2-5f+4)/f;\ G_2=\Delta_1(5f-8)/f^2$$

$$b_1 = \frac{360}{\text{Re}_0}\left(\frac{L}{h_0}\right)\left[\frac{f}{3}\frac{\beta}{\text{Re}_0}\left(\frac{h_0\Delta_1}{L}\right)^3-1\right]$$

$$G_3 = \frac{2}{f^2\Delta_1}[15(f-1)^2+10\mu^*\Delta f(f-1)(4-f)+4\mu^{*2}\Delta^2f^2(5f^2-4f+8)]$$

$$G_4 = \frac{\mu^*}{f}(4-f)[10(f-1)-3\mu^*\Delta f(4-f)]$$

$$G_5 = [30(f-1)+5\mu^*\Delta f(2f^*-3f-12)+16\mu^{*2}\Delta^2f^3(5f-2)]/f^3.$$

$$b_2 = \frac{60}{\text{Re}_0}\left(\frac{L}{h_0}\right)\left[\frac{\rho^*\Delta(4-f)}{\Delta_1}+\frac{2\beta}{\text{Re}_0}\left(\frac{h_0}{L}\right)^3\Delta_1{}^2\Delta\right]$$

$$G_6 = \frac{3(f-1)}{f}-2\mu^*\Delta(4-f)$$

$$G_7 = \Delta(3+\mu^*\Delta f^2)/f^2$$

The other variables during the thermally developing ($x \le x_1$) and thermally developed ($x \ge x_1$) stages, respectively, are as follows:

Thermally developing stage, $0 \le F \le 1$:

$$b_3 = \frac{6S\gamma}{k^*\text{Re}_0\text{Pr}_1}\left(\frac{L}{h_0}\right)\frac{(1-\theta_i)(2-\phi)}{\Delta_1\Delta}$$

$$G_8 = 2k^*\theta_ig_1/\phi f$$

$$G_9 = 2(3F^2-10F+10)/f^2$$

$$G_{10} = 2k^*\Delta\theta_ig_1/\phi^2$$

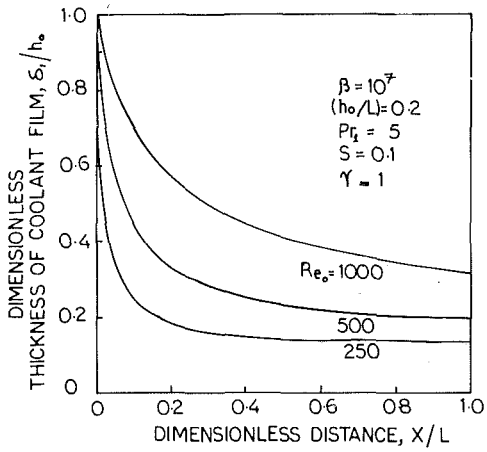

Fig. 2 Variation of coolant film thickness with distance from the exit of the slit

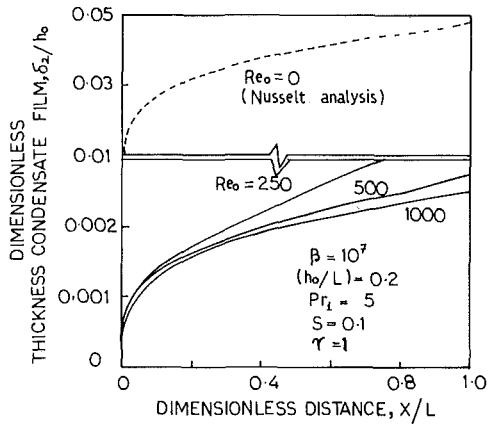

Fig. 3 Variation of the thickness of the condensate film with distance from the exit of the slit

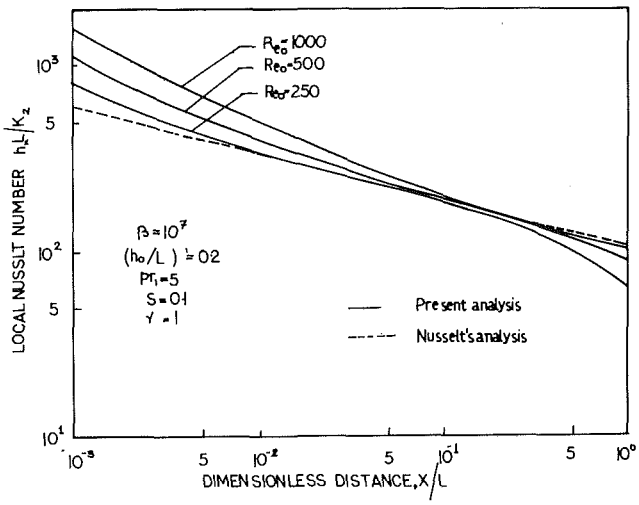

Fig. 4 Effect of inlet Reynolds number of the coolant on local Nusselt number

$$G_{11} = \frac{2}{f}\left[\frac{k^*\Delta\theta_i g_1}{\phi F} + 10(f-1) + 5F(4-f) - 9F^2\right]$$

$$b_4 = \frac{240}{\mathrm{Re}_0\mathrm{Pr}_1\Delta_1 F}\left(\frac{L}{h_0}\right)$$

$$G_{12} = \frac{2(1-\theta_i)}{f}g_3 + \frac{2k^*\Delta\theta_i^2}{\phi f F}g_2$$

$$G_{13} = \Delta(1-\theta_i)[80+\mu^*\Delta(22-7\phi)]/f^2$$

$$G_{14} = \Delta(1-\theta_i)[20-7\mu^*\Delta(4-f)] - 2k^*\Delta^2\theta_i^* g_2/\phi^2 fF$$

$$G_{15} = 2k^*\Delta^2\theta_i^2 g_2/\phi f F^2$$

$$b_5 = \frac{480\gamma}{k^*\mathrm{Re}_0\mathrm{Pr}_1}\left(\frac{L}{h_0}\right)\frac{(1-\theta_i)(1-\phi)}{\Delta_1\Delta}$$

where

$$\theta_i = \phi F/(\phi F + 2k^*\Delta)$$

(From the boundary condition (11) using relevant temperature profiles)

$$g_1 = 20(f-1) + 5F(4-f) - 6F^2$$

$$g_2 = 20\phi f - 80(f-1) + \mu^*\Delta f(4-f)(22-7\phi)$$

$$g_3 = 10\phi f - 40(f-1) + \mu^*\Delta f(4-f)(22-7\phi)$$

Thermally developed stage ($0 \le \psi \le 1$):

$$b_3 = \frac{6S\gamma}{k^*\mathrm{Re}_0\mathrm{Pr}_1}\left(\frac{L}{h_0}\right)\frac{(1-\theta_\theta)(2-\phi)}{\Delta_1\Delta}$$

$$G_8 = k^*(2-\psi)\theta_i g_1/\phi f$$

$$G_9 = (6-\psi)/f^2$$

$$G_{10} = k^*\Delta(2-\psi)\theta_i g_1/\phi^2 f$$

$$G_{11} = k^*\Delta\theta_i g_1/\phi f + (5f+1)/f$$

$$b_4 = \frac{240}{\mathrm{Re}_0\mathrm{Pr}_1}\left(\frac{L}{h_0}\right)\frac{(1-\psi)}{\Delta_1}$$

$$G_{12} = 2(1-\theta_i)g_3/f + k^*\Delta(2-\psi)\theta_i^2 g_2/\phi f$$

$$G_{13} = \Delta(1-\theta_i)[80+\mu^*\Delta(22-7\phi)]/f^2$$

$$G_{14} = \Delta(1-\theta_i)[20-7\mu^*\Delta(4-f)] - k^*\Delta^2(2-\psi)\theta_i^2 g_2/\phi^2 f$$

$$G_{15} = k^*\Delta^2\theta_i^2 g_2/\phi f$$

$$b_5 = \frac{480\gamma}{k^*\mathrm{Re}_0\mathrm{Pr}_1}\left(\frac{L}{h_0}\right)\frac{(1-\theta_i)(1-\phi)}{\Delta_1\Delta}$$

where

$$\theta_i = \phi/[\phi + k^*\Delta(2-\psi)]$$

$$g_1 = 5\psi f + 15f + \psi - 6$$

$$g_2 = 20\phi f - 80(f-1) + \mu^*\Delta f(4-f)(22-7\phi)$$

$$g_3 = 10\phi f - 40(f-1) + \mu^*\Delta f(4-f)(22-7\phi)$$

Local heat transfer coefficients:
Evaluation of local heat transfer coefficients is of practical importanct. Local heat transfer coefficient h_x is defined by the equation

$$k_2\left.\frac{\partial T_2}{\partial y}\right|_{y=\delta_1+\delta_2} = h_x(T_s - T_0) \qquad (24a)$$

For the temperature profile chosen, i.e., equation (18), the local Nusselt number is given by

$$\mathrm{Nu}_x = \left(\frac{L}{h_0}\right)(1-\theta_i)\,(2-\phi)/\Delta_1\Delta \qquad (24b)$$

Thus equations (19 to 23) are solved during the thermally developing ($0 \le F \le 1$) and thermally developed ($0 \le \psi \le 1$) stages, respectively, employing fourth-order, Runge-Kutta numerical scheme on a digital computer with the initial condition that at $x = 0$, $\Delta_1 = f = 1$ and $\Delta = \phi = F = 0$. The matching condition for the two stages is that at $x = x_1$ (say), $F = 1$ and $\psi = 0$. Local Nusselt numbers are computed from equation (24*b*). The salient results are further outlined.

Discussion of Results

The variation of the thickness of the coolant film and that of the condensate film along the surface are shown in Figs. 2

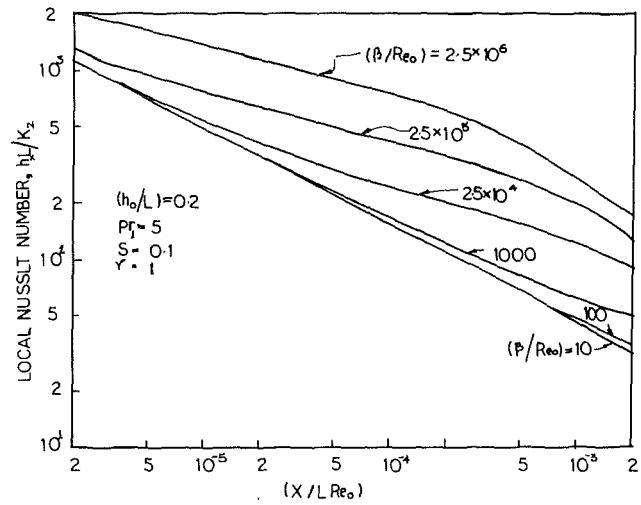

Fig. 5 Effect of the parameter (β/Re_0) on local Nusselt number

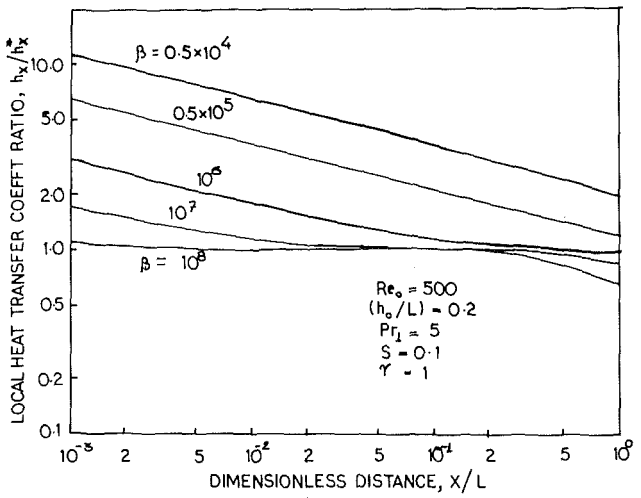

Fig. 6 Effect of parameter β on condensation heat transfer coefficient ratio, (h_x/h_x^*)

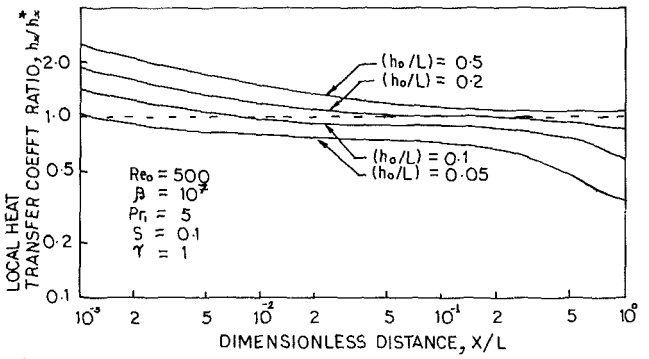

Fig. 7 Effect of (h_0/L) ratio on condensation heat transfer coefficient ratio (h_x/h_x^*)

and 3, respectively. Figure 2, while substantiating the previous observations [17], reveals that the Reynolds number of the coolant film is a major variable that would determine its thickness. For a given location on the wall surface, as the Reynolds number increases the thickness of the coolant film increases. Figure 3 gives the effect of the coolant film Reynolds number on the thickness of the condensate film and as one would expect the thickness of the condensate film is decreasing with increasing Reynolds number of the coolant when the major system parameters β, (h_0/L), Pr_1, S are kept

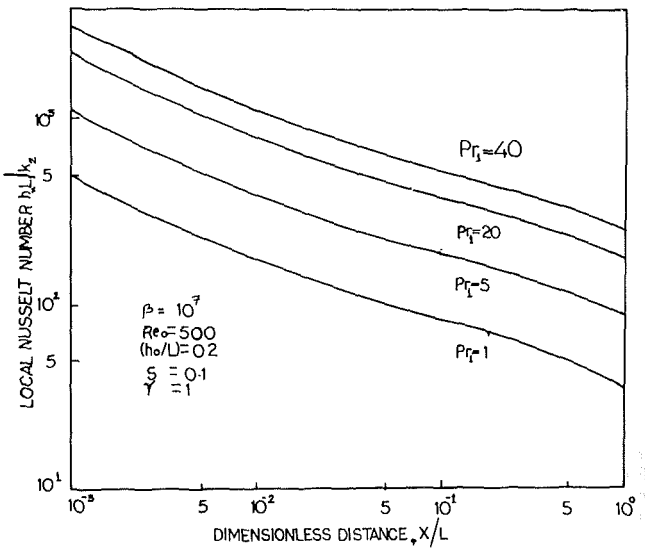

Fig. 8 Effect on Prandtl number of the coolant on local Nusselt number

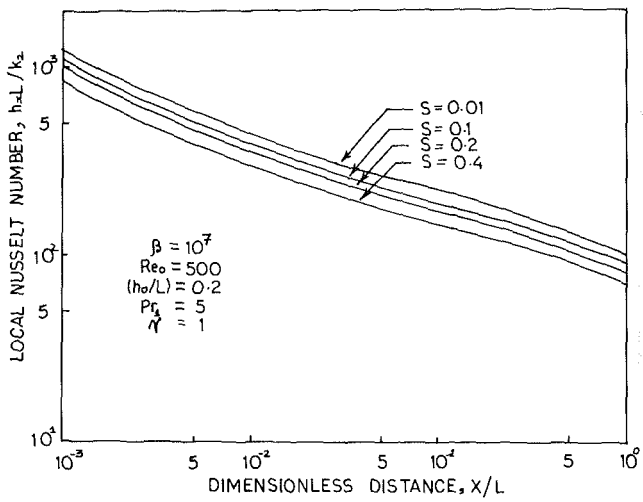

Fig. 9 Effect of subcooling parameter S on local Nusselt number

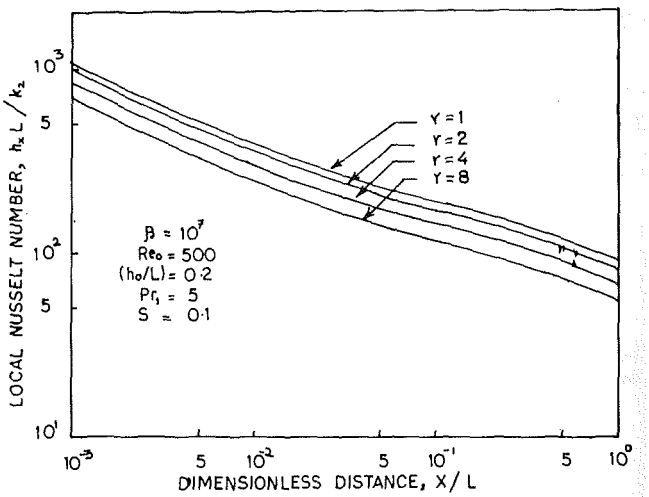

Fig. 10 Effect of heat capacity ratio of coolant-to-condensate on local Nusselt number

constant. The decrease in the thickness of the condensate film with increase in the thickness of the coolant film may mainly be attributed to the pronounced effect of inertial forces in the

developing zone of the coolant film on the condensate film. The important aspect of the analysis is the study of the variation of local Nusselt numbers with the distance from the exit of the slit. Typical Figs. 4–10 indicate the influence of various system parameters on condensation heat transfer coefficients. Figure 4 clearly shows the influence of Reynolds number of the coolant film on Nusselt numbers. As Reynolds number increases, the Nusselt modulus increases due to the decrease in the thermal resistance of the condensate film, as can be inferred from Fig. 3. Local Nusselt numbers according to Nusselt are shown dotted in Fig. 4. It is observed that at farther locations from the exit of the slit the augmentation in condensation heat transfer rates over the Nusselt's type of condensation is marginal. In the thermally developed stage (i.e., $x \geq x_1$), especially for low Reynolds numbers, the enthalpy of the coolant film rapidly increases with substantial increase in the temperature at the coolant-condensate interface along the flow direction. As a result, the Nusselt numbers fall monotonically during the thermally developed stage. Figure 5 is plotted to bring out the influence of the inclination of the plate (signifying the change in the body force component) on the condensation heat transfer rate. The dimensionless parameter (β/Re_0) physically signifies the ratio of body force-to-viscous force, or in other words, the orientation of the surface for a given coolant-condensate system. Obviously, for a given location on the plate the vertical orientation of the wall is the best suited and gives higher heat transfer coefficients. Figure 6 reveals that as β decreases the condensation augmentation ratio h_x/h_x^* increases. Figure 7 unfolds an important aspect, namely, the limitation to be imposed on the length of the coolant film to derive economically higher rates of condensation. The variation of $0.05 \leq (h_0/L) \leq 0.5$ depicts that for a given value of the slit dimension h_0, the decrease in the effective length of the film would give high condensation heat transfer rates or in otherwords the graph indirectly suggests that shorter film lengths of the coolant in the direct contact heat exchangers would give better performance. Figure 8 gives the effect of Prandtl number of the coolant on condensation heat transfer. The increase in Prandtl number is accompanied by a substantial increase in condensation heat transfer. This is mainly due to the decrease in the thermal penetration thickness in the coolant film with the increase in the Prandtl number of the coolant film. Approximately the results indicate that $h_x \propto \mathrm{Pr}_l^{0.5}$. The effect of the subcooling parameter $C_2(T_s - T_0)/h_{fg}$) on local Nusselt numbers is shown in Fig. 9. It is observed that as in the classical Nusselt's analysis the subcooling parameter has a decreasing effect on condensation heat transfer rates. In the case of Nusselt's analysis $h_x^* \propto S^{-0.25}$ where as in the present case $h_x \propto S^{-0.1}$. This observation reveals that the overall performance of the direct-contact condenser in comparison with the conventional condenser working under identical thermal potentials is far superior, since the augmentation that can be achieved, i.e., $(h_x/h_x^*) \propto (\Delta T)^{0.15}$, where h_x and h_x^* are the heat transfer coefficients in the present analysis and that of Nusselt, respectively, and ΔT in the thermal potential. Figure 10 gives the effect of the heat capacity ratio of coolant-to-condensate on local Nusselt number. It is observed that with increase in the heat capacity ratio there is decrease in the condensation heat transfer coefficients. The results of the present theoretical analysis when compared with those of Murty and Sastri [6] revealed more or less the same orders of magnitude of the Nusselt numbers for identical parameters. However, it may be noted that the results of the present analysis need not necessarily coincide with those of either Hasson et al. [4, 5] or Murty and Sastri [6] in view of the fact that the physical model considered herein is different from either of those in the references cited above. No attempt is made to bring out a comparison between the present investigation and that of Tamir and Rachmilev [7] since their interfacial heat transfer measurements are intimately tied to their theoretical analysis which differs substantially from the present theoretical investigation.

Conclusion

The theoretical study undertaken has revealed that the direct contact condensers with shorter coolant film lengths would be highly effective in as much as the condensation heat transfer rates would be greater by far than those evaluated from Nusselt analysis. The low-pressure feedwater heaters in thermal power plants or desalination plants can be conceived with proper design of multiple tray or packed bed system enabling the formation of effective coolant films in successive stages of a single module.

Acknowledgments

The authors thank the University Grants Commission – New Delhi for their support.

References

1 Bilders, Z. P., Kishnevshkii, Y., Lebedev, N., and Taubman, E. I., "Use of Direct-Contact Condensers in Combined Power and Fresh Water Plants With Gas Turbines," *Thermal Engng.* Vol. 18, Nos., 1971, p. 126.

2 Sideman, S., "Direct-Contact Heat Transfer Between Immiscible Liquids," *Advances in Chemical Engineering*, Vol. 6, Academic Press, New York, 1965.

3 Merte Jr., "Condensation Heat Transfer," *Advances in Heat Transfer*, Vol. 9, 1973, pp. 181–272.

4 Hasson, D., Luss, D., and Peck, R., "Theoretical Analysis of Vapor Condensation on Laminar Liquid Jets," *International Journal of Heat and Mass Transfer*, Vol. 7, 1964, pp. 969–981.

5 Hasson, D., Luss, D., and Navon, U., "An Experimental Study of Steam Condensation on a Laminar Water Sheet," *International Journal of Heat and Mass Transfer*, Vol. 7, 1964, pp. 983–1001.

6 Murty, N. S., and Sastri, V. M. K., "Condensation on a Falling Laminar Liquid Sheet," *Can. J. Chem. Engg.*, Vol. 54, 1976, pp. 633–635.

7 Tamir, A., and Rachmilev, I., "Direct-Contact Condensation of an Immiscible Vapor on a Thin Film of Water," *International Journal of Heat and Mass Transfer*, Vol. 17, 1974, pp. 1241–1251.

8 Brown, G., "Heat Transmission by Condensation of Steam on a Spray of Water Drops," *Proceedings of General Discussion on Heat Transfer, Inst. of Mech. Eng.*, 1951, pp. 49–52.

9 Weinberg, S., "Heat Transfer to Low-Pressure Sprays of Water in Steam Atmosphere," *Proc. Instn. Mech. Engrs.*, 167B, 1952, pp. 240–253.

10 Syhre, H., *Energie-technik*, Vol. 11, 1961, p. 401

11 Ford, J. D., and Lekic, A., "Rate of Growth of Drops During Condensation," *Int. Journal of Heat and Mass Transfer*, Vol. 16, 1973, pp. 61–64.

12 Fulford, G. S., "The Flow of Liquids in thin Films," *Advances in Chemical Engineering*, Vol. 5, Academic Press, New York, 1964, pp. 151–236.

13 Hasson, A., "Laminar Flow Along a Vertical Wall," ASME *Journal of Applied Mechanics*, Vol. 34, 1967, pp. 535.

14 Murty, N. S., and Sastri, V. M. K., "Accelerating Laminar Liquid film along an Inclined Plane," *Chem. Eng. Sci.*, Vol. 28, 1973, pp. 869.

15 Stucheli, A., and Ozisik, M. N., "Hydrodynamic Entrance Lengths of Laminar Falling Films," *Chem. Eng. Sci.*, Vol. 31, 1976, pp. 369.

16 Narayanamurthy, V., and Sarma, P. K., "A Note on Hydrodynamic Entrance Lengths of Non-Newtonian Laminar Falling Liquid Films," *Chem. Eng. Sci.*, Vol. 32, 1977, pp. 566–567.

17 Narayanamurthy, V., and Sarma, P. K., "Dynamics of Developing Laminar Non-Newtonian Falling Liquid Films With Free Surface," ASME *Journal of Applied Mechanics*, Vol. 45, 1978, pp. 19–24.

18 Narayanamurthy, V., and Sarma, P. K., "A Note on Thin Film Evaporation-Prediction of Heat Transfer Rates," *Journal of Chemical Engineering of Japan*, Vol. 6, 1973, pp. 457–459.

19 NarayanaMurthy, V., and Sarma, P. K., "Falling Film Evaporators—A Design Equation for Heat Transfer Rates," *Can J. Chem. Engg.*, Vol. 55, 1977, pp. 732.

20 NarayanaMurthy, V., and Sarma, P. K., "Heat Transfer to Non-Newtonian Laminar Falling Liquid Films With Smooth Wave Free Gas-Liquid Surface," *Int. J. Multi-Phase Flow*, Vol. 4, 1978, pp. 413–425.

21 Sarma, P. K., Al-Jubouri, S. A., and Narayana Murthy, V., "Evaporation for Accelerating Laminar Liquid Films," *Can. J. Chem. Eng.*, Vol. 56, 1978, pp. 639–642.

22 Sykes, J. A., and Marchello, J. M., "Condensation of Immiscible Liquids on a Horizontal Tube," *Ind. Eng. Chem. Process Des. Develop.*, Vol. 9, 1970, pp. 63–71.

W. C. Lee
Research Engineer,
GEC Energy Systems Ltd.,
Leicester.

S. Rahbar
Graduate Student.

J. W. Rose
Reader in Mechanical Engineering.

Department of Mechanical Engineering,
Queen Mary College,
University of London.
England

Film Condensation of Refrigerant-113 and Ethanediol on a Horizontal Tube—Effect of Vapor Velocity

Heat transfer measurements are reported for condensation of refrigerant-113 and ethanediol (ethylene glycol) on a single horizontal tube with vertical downflow. For refrigerant-113, vapor velocities up to around 6 m/s were obtained, while for ethanediol, velocities in excess of 100 m/s were obtained at low pressure. The results are compared with those of earlier investigators and with theory.

Introduction

In recent years, several theoretical studies of the problem of forced convection condensation on horizontal tubes have been undertaken [1–20]. The approaches have been along the same broad general lines but, since they use different assumptions and approximations, are of varying degrees of complexity. A basically sound, but relatively simple, analysis is that of Shekriladze and Gomelauri [2], who used the asymptotic (infinite condensation rate) expression for the shear stress at the condensate surface to obtain, for the case of vertical vapor downflow (see Fig. 1), the following expression for the mean Nusselt number

$$\mathrm{Nu}/\tilde{\mathrm{R}}\mathrm{e}^{1/2} = 0.64\{1+(1+1.69F)^{1/2}\}^{1/2} \tag{1}$$

By adopting the asymptotic surface shear stress expression, the problem of vapor boundary-layer separation was avoided. Fujii et al. [4] have obtained more complete solutions by matching the shear stress at the vapor-condensate interface and using an approximate integral treatment of the vapor boundary layer.

The form of the assumed vapor velocity profile was such that the surface shear stress was always positive so that the problem of boundary-layer separation again did not arise. The solutions of Fujii et al. [4] were summarized by the approximate equation

$$\mathrm{Nu}/\tilde{\mathrm{R}}\mathrm{e}^{1/2} = X(1+0.276F/X^4)^{1/4} \tag{2}$$

where

$$X = 0.9(1+G^{-1})^{1/3} \tag{3}$$

Equation (1) gives smaller Nusselt numbers than equation (2), since the asymptotic shear stress is less than the actual shear stress and leads to a thicker condensate film. With increasing condensation rate (increasing values of G) equations (1) and (2) give similar results. The two equations virtually coincide for $G >$ about 5, and for $G > 1$ the difference between the two results is of comparable magnitude with typical scatter of experimental data.

The fact that experimental data at relatively high vapor velocity (low F) have indicated lower values of Nu (see Fig. 2) has led to the suggestion that vapor boundary layer separation (not taken account of in equations (1) and (2)) may have an appreciable effect. Fujii and co-workers [15, 17] obtained solutions wherein the angle at which separation of the vapor boundary layer occurs was calculated and the surface shear stress set to zero beyond this point. As pointed out by Lee and Rose [20], the resulting Nusselt numbers do not differ greatly from those given by equation (2).

Attempts have also been made to explain the discrepancy between experiment and theory on the basis that the theoretical models [2, 4] used the condition of uniform tube-wall temperature. Theoretical solutions, using instead the condition of uniform wall heat flux [15, 17], gave lower mean heat transfer coefficients, i.e., apparently more in line with data at high velocities. It was pointed out [20], however, that the mean Nusselt number in this case involves the integral of the condensate film thickness over the tube surface (as compared with its reciprocal in the case of uniform tube wall temperature). Thus, in evaluating the theoretical mean Nusselt number, greatest weight is given to the rear part of the tube, where the calculation is least reliable, and least weight is given to the forward part of the tube where most of the heat transfer takes place. The fact that predicted mean Nusselt numbers were in better agreement with experimental data was considered fortuitous [20].

In addition to the low (with respect to equation (2)) experimental heat transfer coefficients at high vapor velocity, coefficients in excess of the theoretical values have recently been reported by Honda et al. [19] for refrigerant-113 (see Fig. 2 (*f*)).

Some measure of success has been achieved in predicting overall heat transfer from vapor to coolant [12–14, 18, 26]. The most recent and complete work is that of Fujii and co-workers [18, 26], where a solution of the condensate problem along the lines indicated above [15, 17] was combined with a solution for conduction in the tube wall and prescribed coolant-side condition. These solutions indicate

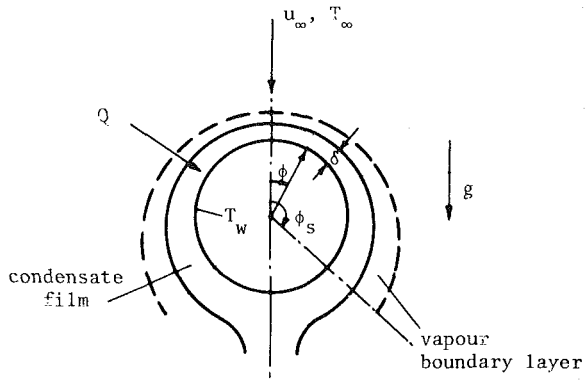

Fig. 1 Physical model

Contributed by the Heat Transfer Division for publication in the JOURNAL OF HEAT TRANSFER. Manuscript received by the Heat Transfer Division August 9, 1984.

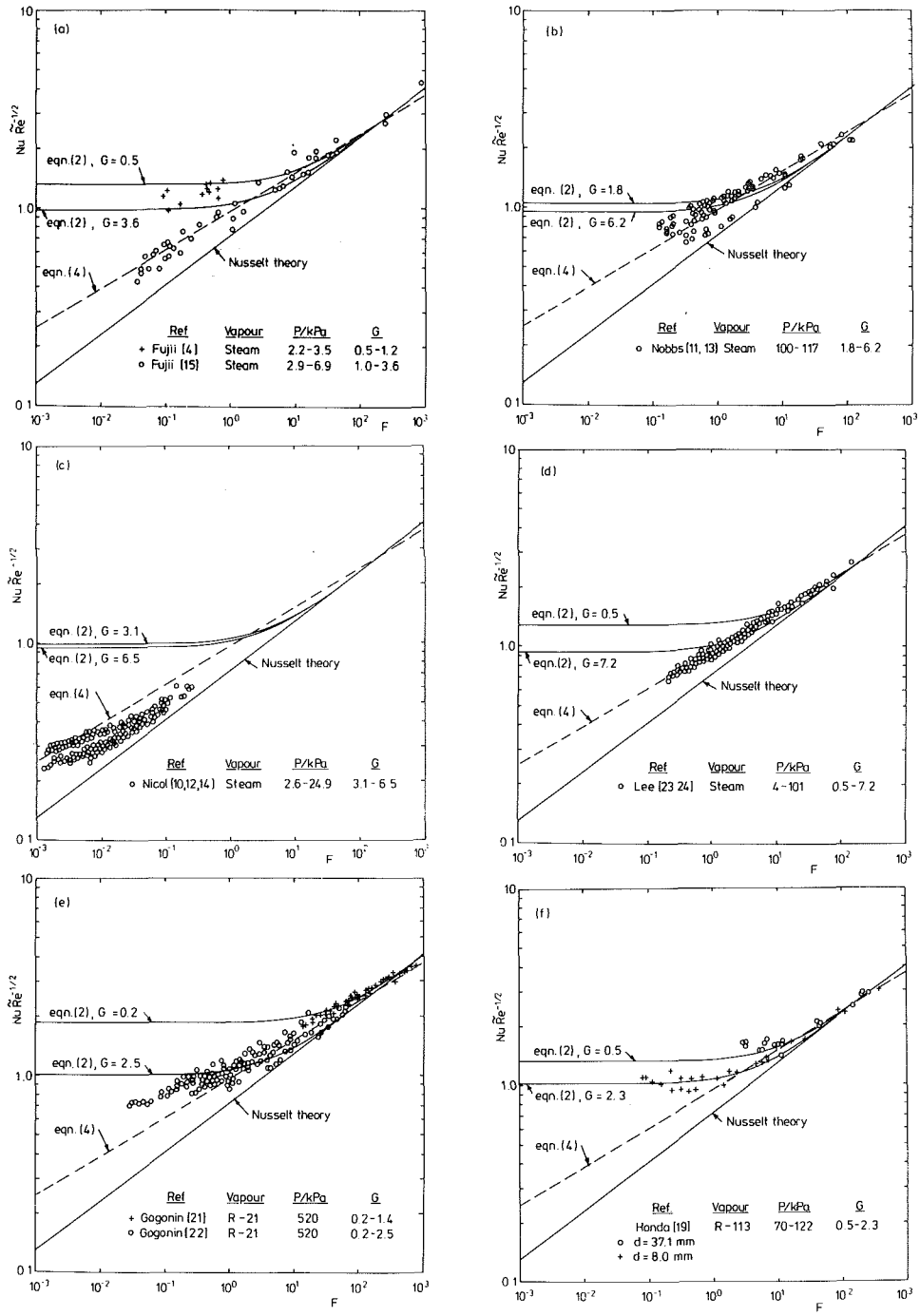

Fig. 2 Results of earlier investigations

Nomenclature

c_{Pv} = isobaric specific heat capacity of vapor
d = outside tube diameter
F = $g\,d\,\mu\,h_{fg}/u_\infty^2\,k\,\bar{\Delta T}$
G = $(\Delta T\,k/\mu\,h_{fg})(\rho\,\mu/\rho_v\,\mu_v)^{1/2}$
g = gravitational acceleration
h_{fg} = specific enthalpy of evaporation
k = thermal conductivity of condensate
Nu = $Q\,d/k\,\bar{\Delta T}$
P = vapor pressure
Q = mean heat flux
$\tilde{\mathrm{Re}}$ = $u_\infty\,\rho\,d/\mu$
$T_{\mathrm{sat}}(P)$ = saturation temperature at P
T_∞ = vapor temperature
T_w = local wall temperature
$\bar{T}_w$ = mean wall temperature
u_∞ = free-stream velocity of vapor
X = defined in equation (3)
ΔT = local temperature difference across condensate film, $T_{\mathrm{sat}}(P) - T_w$
$\bar{\Delta T}$ = mean temperature difference across condensate film, $T_{\mathrm{sat}}(P) - \bar{T}_w$
δ = thickness of condensate film
η = recovery factor
μ = dynamic viscosity of condensate
μ_v = dynamic viscosity of vapor
ρ = density of condensate
ρ_v = density of vapor
ϕ = angle measured from vertical, see Fig. 1.
ϕ_s = value of ϕ at vapor boundary-layer separation point

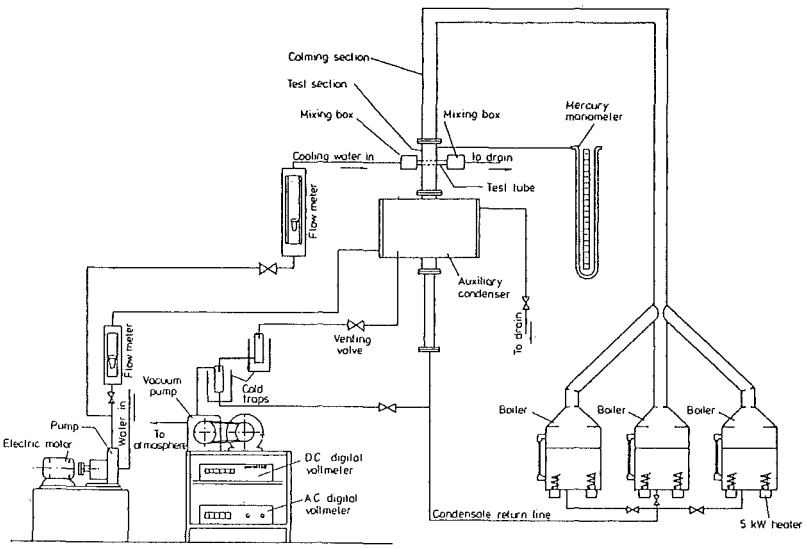

Fig. 3 Apparatus

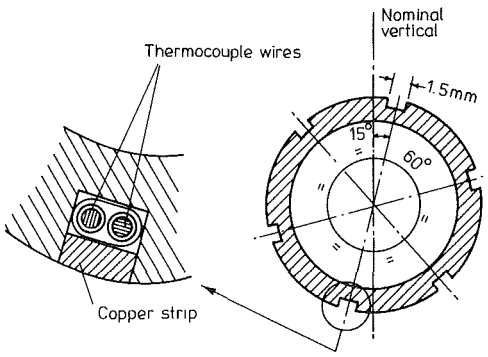

Fig. 4 Location of thermocouples in condenser tube

lower mean vapor-side heat transfer coefficients at the higher vapor velocities. They do not, however, explain the higher coefficients for R-113. While the method of solution, i.e., treating condensate, tube wall, and coolant side simultaneously, is undoubtedly sound, it is not entirely satisfactory for making detailed comparisons for the condensate film, particularly in cases where the coolant-side resistance dominates.

To summarize, significant discrepancies exist between theory and experiment at high velocity and, for a refrigerant, at moderate vapor velocity. These may be due to inaccuracies in the experiments or deficiencies in the theory or both. In order to shed more light on these issues, new measurements have been made with ethanediol (ethylene glycol), whose properties are such that high vapor velocities (low values of F) can be obtained under convenient operating conditions, and also with refrigerant-113.

Apparatus and Procedure

Referring to Fig. 3, vapor was generated in three stainless steel boilers, each fitted with two 5-kW electric immersion heaters. Two heaters (in different boilers) were supplied via variable transformers. The vapor flowed vertically downwards via a calming section (1 m) to the test section (dia 76 mm) where the horizontal condenser tube was located. Vapor and condensate from the test condenser tube passed into the auxiliary condenser located directly beneath the test section. The condensate was returned by gravity to the boiler. The auxiliary condenser was vented via a cold trap and vacuum pump. The boiler, vapor supply duct, and test section were thermally well insulated. For some tests with ethanediol, the test section was fitted with a window so that the condenser tube could be observed.

The copper condenser tube (i.d. 7.5 mm, o.d. 12.5 mm) was fitted with six wall thermocouples. The thermocouples (28 s.w.g. twin laid) were located in longitudinally machined grooves (1.5 mm $\times$ 1.5 mm) and enclosed by tightly fitting soldered copper strips. The junctions were located midway along the tube. The relative angular locations of the junctions are given in Fig. 4. The condenser tube was insulated from the body of the test section by ptfe bushes. The coolant inlet and exit temperatures were measured by thermocouples, the exit temperature being measured after a well-insulated mixing section. The inlet-to-exit temperature difference was also observed with a six-junction, series-connected differential thermocouple. The two measurements of the coolant temperature rise generally agreed to better than 0.1 K. Care was taken to ensure adequate isothermal immersion of the thermocouple leads and the coolant channel was thermally well insulated at inlet to and exit from the test section. The thermocouple calibration procedure was as described in [27], giving an estimated accuracy of $\pm$ 0.05 K.

The vapor temperature was measured by two thermocouples located approximately 65 mm above the test condenser tube. A pressure tapping to a mercury manometer with a vernier scale was also located at this position.

The vapor flow rate was obtained from the precisely measured power input to the boilers with due allowance for the small thermal losses from the apparatus. An equation giving the losses in terms of the vapor and ambient temperatures was established by preliminary experiments of two types, one in which all of the condensate was collected and compared with that calculated on the basis of the power input (for details see [23]) and a second in which the minimum power to maintain the vapour temperature was determined.

At the high vapor velocities, obtained with ethanediol, temperatures significantly higher than the saturation temperature were found, owing to "temperature recovery" on the thermocouple probe. Account was taken of this in the vapor velocity calculation using a recovery factor of 0.95 in an

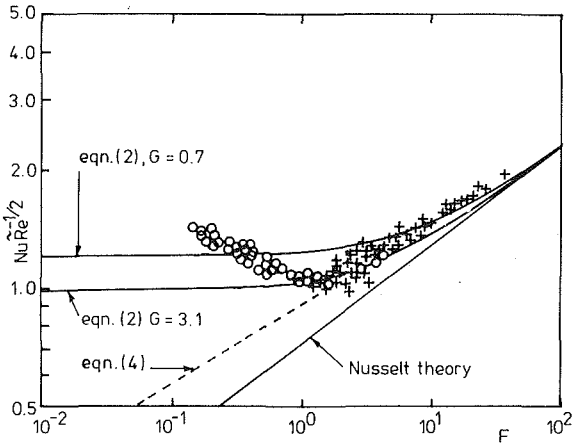

Fig. 5 Comparison of present results for R-113 with [23, 24] and with equation (2)

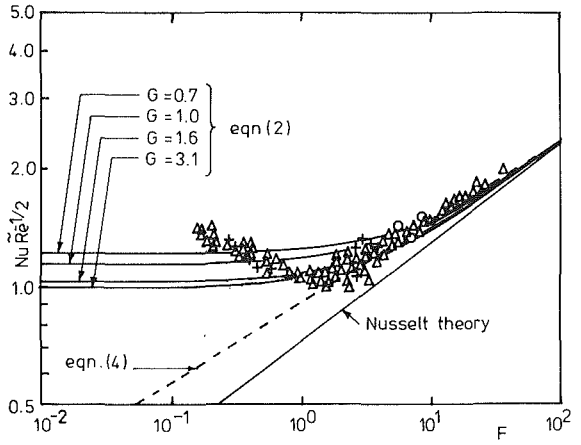

Fig. 7 Data of Fig. 5 with ranges of G distinguished: ○ $G \leq 1$, + $1 < G \leq 1.6$, △ $G > 1.6$

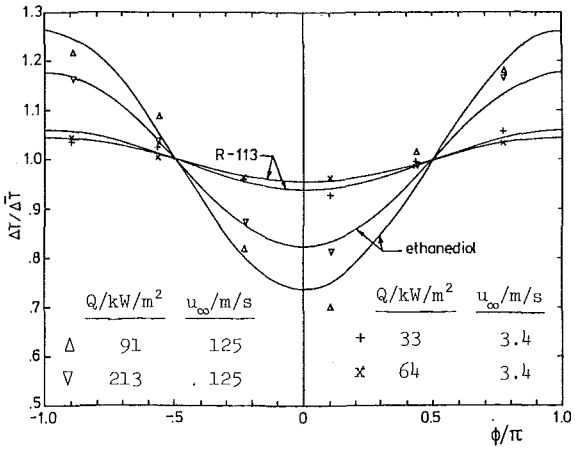

Fig. 6 Typical temperature profiles around the condenser tube. The lines are cosine fits.

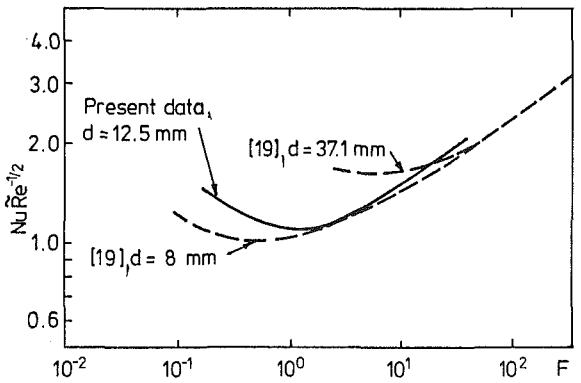

Fig. 8 Condensation of R-113. Comparison of present data with [19].

iterative calculation which gave both vapor velocity and true vapor temperature.[1]

Except for the high vapor velocity tests with ethanediol, the pressure and temperature of the vapor corresponded closely with saturation values indicating that the vapor was essentially free of noncondensing gases. (The apparatus, when empty, could readily be pumped down to a pressure of around 2 mm Hg, and the overnight pressure rise, when isolated, was less than 10 mm Hg.)

The mean heat flux to the condenser tube was obtained from the coolant flow rate and temperature rise. In preliminary tests [23], when arrangements for condensate collection were incorporated, the two heat flux measurements agreed to within 5 percent. The tube wall temperatures were obtained from the embedded thermocouples. A small correction for the depth of the junctions below the tube surface was made.

The apparatus was operated with the vent valve from the auxiliary condenser fully open. Tests were carried out for a range of boiler input powers, at each of which tests were carried out for several coolant flow rates for the test condenser tube and with a fixed coolant flow rate for the auxiliary condenser.

Results and Discussion

Refrigerant-113. For these measurements the test section was not fitted with a window and the condenser tube could not be viewed. The apparatus was operated with the vent valve from the auxiliary condenser open to atmosphere so that all tests were conducted at essentially atmospheric pressure. Vapor velocities in the approximate range 1–6 m/s were obtained.

Figure 5 compares, on the basis of the parameters of equation (2) the present results and the earlier data of Lee and Rose [23, 24] (obtained with the same apparatus as used in the present investigation but with a larger diameter test section). It may be seen that the two data sets agree satisfactorily where they overlap ($1 < F < 5$). The present data, however, show an unexpected (on a theoretical basis) upturn with decreasing values of F (higher vapor velocities). As may be seen from Fig. 6, the measured temperature profiles around the tube are relatively flat so that the uniform wall temperature model should not be greatly in error. Lines given by equation (2) for the extreme experimental values of G are also shown in Fig. 5. It is seen that the data and theory are in fair general agreement. However, the low F data with higher values of $\tilde{Nu}\tilde{Re}^{-1/2}$ generally have the higher G values (see Fig. 7) so that the upturn of the data at low F values is not explained on the basis of equation (2).

In Fig. 8, a mean line through the data shown in Figs. 5 and 7 is compared with mean lines through the R-113 data of

[1] A value of 0.95 was chosen for η, having regard to the probe Reynolds number and the Mach number of the vapor flow. The maximum calculated stagnation temperature rise, $\eta u_\infty^2/2c_{p_v}$ was around 5 K. The vapor specific volume, and hence velocity, are essentially proportional to the (absolute) thermodynamic temperature so that the value of u_∞ is not sensitive to that of η.

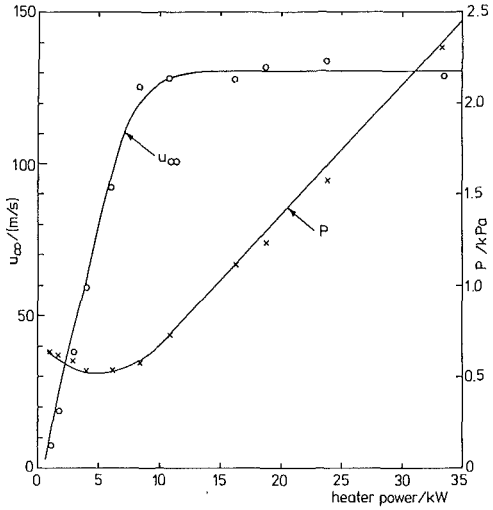

Fig. 9 Condensation of ethanediol. Dependence of vapor velocity and pressure on boiler heater power.

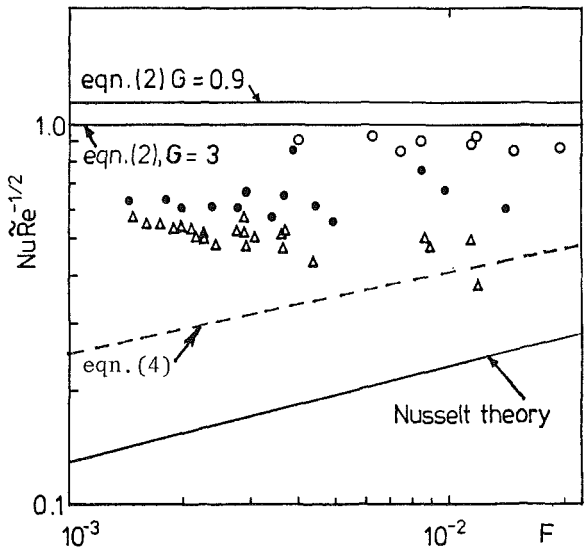

Fig. 10 Condensation of ethanediol. Results obtained before modifications to apparatus. For all data $0.9 < G < 3$.

Honda et al. [19] (see Fig. 2*f*)). The two data sets are evidently in good general agreement and both exhibit the trend to higher values of $\tilde{Nu}\tilde{Re}^{-1/2}$ at high velocity (low F). The data of Honda et al. [19] show an effect of tube diameter (not predicted by theory). The position of the line representing the present data (tube dia. 12.5 mm) in relation to the lines of Honda et al. for tube diameters of 8 mm and 37.1 mm is consistent with the dependence on diameter found by the previous workers.

In summary, the present results, together with [19, 23, 24] show, at higher vapor velocities, a stronger rate of increase of heat transfer coefficient with vapor velocity than indicated by theory. The data also show a dependence on tube diameter not predicted by theory.

Ethanediol. For the initial measurements the test section was not fitted with a window. In later tests a window was fitted so that the test condenser tube could be observed. For all tests, the auxiliary condenser vacuum pump was operated and the apparatus allowed to attain an equilibrium pressure level that depended on the power input to the boiler heaters as shown in Fig. 9. It is also seen in Fig. 9 that the vapor

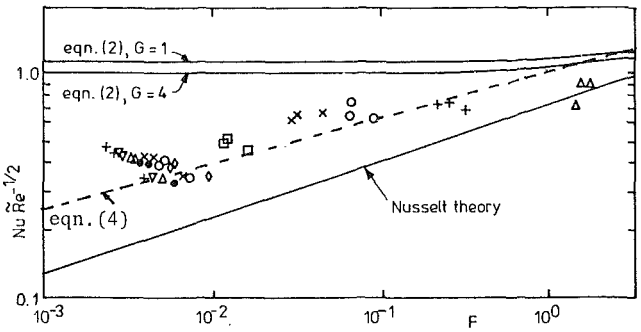

Fig. 11 Condensation of ethanediol. Results obtained after modification to apparatus. The different symbols denote different boiler heater powers. For all data $1 < G < 4$.

velocity attains a steady value where the increase in vapor density with increase in pressure accommodates the increasing vapor mass flow rate. This behavior may be due to "choking" of the flow following the right-angle bends between the boiler and the test section.

A sample of the results obtained in the initial tests (no window) is given in Fig. 10. As may be seen, somewhat inconsistent data were obtained on different occasions. In a few cases, relatively high values of $\tilde{Nu}\tilde{Re}^{-1/2}$, close to those given by equation (2), were found with little or no evidence of dependence on heater power (vapor velocity) or coolant flow rate (condensation rate). More usually, lower values of $\tilde{Nu}\tilde{Re}^{-1/2}$ were obtained with evidence of increase at low values of F (high vapor velocity) and at the higher coolant flow rates. On other occasions, results intermediate between these extremes were found. Figure 10 shows results for the extreme cases, together with a data set exhibiting intermediate behavior. All of the data shown in Fig. 10 are for relatively high vapor velocity, since both heaters in one of the boilers are supplied directly (i.e., not via a variable transformer), and the minimum power input, with all boilers operating, was around 6 kW.

Modifications were then carried out so that one heater in each of the three boilers was supplied via a variable transformer. At the same time the test section was fitted with a window. Following these modifications and with the condenser tube newly cleaned (with fine emery cloth) a further set of measurements was made extending to low vapor velocities (the lowest boiler input power used was about 1 kW when the vapor velocity was about 7 m/s). Film condensation was observed throughout these tests. The results are shown in Fig. 11. At low F, overlapping the range of the earlier tests, the values of $\tilde{Nu}\tilde{Re}^{-1/2}$ are in general agreement with the lower values found formerly. At the high vapor velocities, increase of $\tilde{Nu}\tilde{Re}^{-1/2}$ with increase in coolant flow rate (condensation rate) was evident.

Following a period of several days during which the apparatus was not operated, it was noticed that the condensate remaining on the tube had the appearance of poor quality dropwise or mixed condensation. When the boilers were switched on, and vapor passed over the tube, quite good quality dropwise condensation (small, rapidly moving drops) was observed over the upper two-thirds of the tube surface. This persisted for several hours until the apparatus was shut down. No heat transfer data were taken on this occasion. The tube was removed and cleaned, following which film condensation was reestablished. No further occurrences of dropwise condensation have yet been observed. It is considered that the higher values of $\tilde{Nu}\tilde{Re}^{-1/2}$ in Fig. 10 (obtained when the condenser tube could not be observed) may relate to dropwise or mixed condensation conditions. It was, however, also noted that the higher values of $\tilde{Nu}\tilde{Re}^{-1/2}$

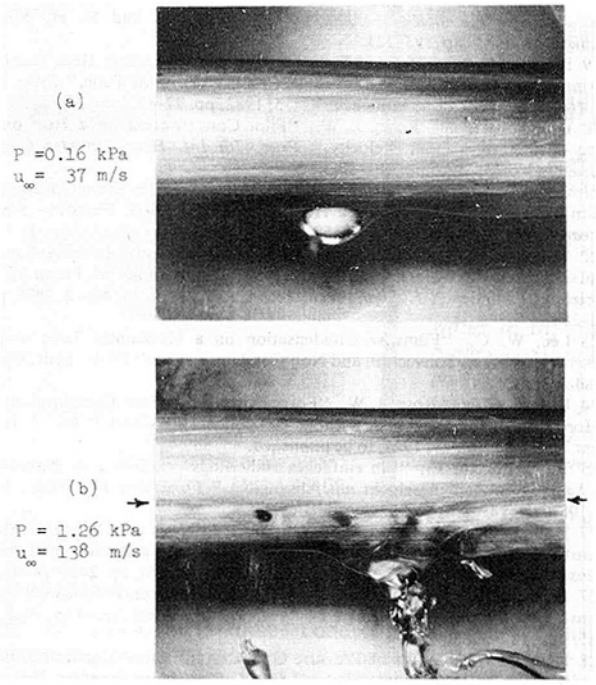

Fig. 12 Condensation of ethanediol. The arrows indicate the position of the "ridge" in the condensate film.

tended to occur at the higher vapor pressures (the vapor pressure range varied somewhat from run to run) so that this may also be a contributory factor.

The present results for film condensation of ethanediol, shown in Fig. 11, may be compared with the earlier data for other fluids by reference to the correlation of steam data given by Fujii et al. [15]

$$\mathrm{Nu}\bar{\mathrm{R}}\mathrm{e}^{-1/2} = 0.96F^{1/5} \tag{4}$$

which is also shown on Figs. 2, 5, 7, and 10. It may be seen that equation (4) is in quite good general agreement with the earlier data for steam at moderate velocities (see Figs. 2(*a*), 2(*b*), and 2(*d*)), while the present high-velocity data for ethanediol show rather higher values of $\mathrm{Nu}\bar{\mathrm{R}}\mathrm{e}^{-1/2}$ (see Fig. 11) and the high-velocity steam data (see Fig. 2(*c*)) indicate somewhat lower values. For the refrigerants (see Figs. 2(*e*), 2(*f*), and 5), equation (4) underestimates the values of $\mathrm{Nu}\bar{\mathrm{R}}\mathrm{e}^{-1/2}$ at the higher velocities.

After fitting the window, two phenomena, illustrated in Fig. 12, were observed during condensation of ethanediol. At relatively high vapor velocities (> about 80 m/s) an abrupt thickening of the condensate film was seen on the lower half of the tube. (Similar behavior has been noted by other investigators [19] and attributed to vapor boundary layer separation). It was observed in the present investigation that, as the vapor velocity was raised, the "ridge" in the condensate film was first discernible near the lower edge of the tube, moved upward with increasing vapor velocity and downward somewhat with increase in coolant flow rate (condensation rate). Also, at the higher vapor velocities, it was observed that condensate leaving the tube was supported for some time in agglomerations, by upward vapor flow in the wake. These agglomerations moved erratically both upward (sometimes reattaching to the condensate film) and downward as well as parallel to the tube axis, and remained suspended for several seconds.

Concluding Remarks

Discrepancies between theory and experiment for R-113 found earlier [19] have been confirmed in the present investigation. At the higher vapor velocities the observed heat transfer coefficients significantly exceed the predicted values, and the rate of increase of the coefficient with velocity is greater than indicated by theory. These discrepancies may be due to onset of turbulence in the condensate film, which, in turn, may be associated with instability caused by the reverse pressure gradient over the lower half of the tube as discussed in [28].

At high vapor velocity, the variation of vapor pressure (and corresponding saturation temperature) around the tube may have a significant effect. Attention has earlier been drawn to this by Butterworth [29], who indicated that the associated effective temperature drop would be of the order of $T_\infty u_\infty^2/h_{fg}$. For the present ethanediol data this quantity had a maximum value of around $0.4\,\widetilde{\Delta T}$ at the highest vapor velocities.

For ethanediol, the lower mean heat transfer coefficients may also be due in part, to the relatively strong temperature variation around the tube (see Fig. 6) as indicated by Fujii [18]. Calculations have been carried out by the present authors on the basis of uniform wall heat flux rather than uniform wall temperature. The analytical treatment of the condensate film was as described by Fujii et al. [15, 17], and the surface shear stress was evaluated by the method of Truckenbrodt [25] as well as by the method of Truckenbrodt as modified by Fujii et al [15, 17]. These calculations gave mean Nusselt numbers closer to the experimental values. Detailed comparisons, however, showed that the calculated temperature drop across the condensate film was, for most of the tube (prior to the calculated vapor boundary layer separation point), much smaller than observed (by factors of 2 to 4). Beyond the vapor boundary layer separation point, the theoretical temperature drop was much larger than the measured value. As indicated earlier, theoretical vapor-to-coolant solutions [18, 26] are not suitable for detailed study of the condensing side when the coolant-side resistance is appreciable.

Finally it should be noted that, in cases where ΔT varies appreciably around the tube (as is the case with the present experimental data for ethanediol), a mean heat transfer coefficient, $Q\sqrt{\Delta T}$, may be inappropriate for evaluating an overall vapor-to-coolant coefficient by summing resistances, since the validity of this technique requires essentially isothermal inner and outer tube wall temperatures. The theoretical vapor-to-coolant calculations of Fujii [18], however, imply that the error may, in some cases, be quite small.

Acknowledgment

This work was carried out as part of the HTFS general research program funded by the Chemicals and Minerals Requirements Board of the U.K. Department of Industry.

References

1 Sugawara, S., Michiyoshi, I., and Minamiyama, T., "The Condensation of Vapor Flowing Normal to a Horizontal Pipe," *Proc. 6th Japan Nat. Congr. Appl. Mech.*, 1956, pp. 385-388.

2 Shekriladze, I. G., and Gomelauri, V. I., "Theoretical Study of Laminar Film Condensation of a Flowing Vapour," *Int. J. Heat Mass Transfer*, Vol. 9, 1966, pp. 581-591.

3 Denny, V. E., and Mills, A. F., "Laminar Film Condensation on a Horizontal Cylinder at Normal Gravity," ASME *Journal of Heat Transfer*, Vol. 91, 1969, pp. 495-501.

4 Fujii, T. Uehara, H., and Kurata, C., "Laminar Filmwise Condensation of Flowing Vapor on a Horizontal Cylinder," Int. J. Heat Mass Transfer, Vol. 15, 1972, pp. 235-246.

5 Denny, V. E., and South III, V., "Effects of Forced Flow, Noncondensables and Variable Properties on Film Condensation of Pure and Binary Vapors at the Forward Stagnation Point of a Horizontal Cylinder," *Int. J. Heat Mass Transfer*, Vol. 15, 1972, pp. 2133-2142.

6 Ferreira, S. M. M., "Forced Convection Condensation of Vapor Flowing Around a Cylinder," *Chem. Engg. Journal*, Vol. 6, 1973, pp. 81-90.

7 Ferreira, S. M. M., "Forced Convection Condensation of Vapour Flowing Around a Circular Cylinder," *Chem. Engg. Journal*, Vol. 7, 1974, pp. 253–256.

8 Honda, H., and Fujii, T., "Effect of the Direction of Oncoming Vapour on Laminar Filmwise Condensation on a Horizontal Cylinder," *Proc. 5th Int. Heat Transfer Conf.*, Tokyo, Vol. 3, 1974, pp. 299–303.

9 Nicol, A. A., and Wallace, D. J., "The Influence of Vapour Shear Force on Condensation on a Cylinder," *Inst. Chem. Engrs., Symp. Ser.*, No. 38, 1974, pp. 1–19.

10 Wallace, D. J., "A Study of the Influence of Vapour Velocity Upon Condensation on a Horizontal Tube," Ph.D. thesis, University of Strathclyde, Glasgow, 1975.

11 Nobbs, D. W., "The Effect of Downward Vapour Velocity and Inundation on the Condensation Rates on Horizontal Tubes and Tube Banks," Ph.D. thesis, University of Bristol, 1975.

12 Nicol, A. A., and Wallace, D. J., "Condensation with Appreciable Vapour Velocity and Variable Wall Temperature," *Symp. on Steam Turbine Condensers*, NEL Report No. 619, 1976, pp. 27–38.

13 Nobbs, D. W., and Mayhew, Y. R., "Effect of Downward Vapour Velocity and Inundation on Condensation Rates on Horizontal Tube Banks," *Symp. on Steam Turbine Condensers*, NEL Report No. 619, 1976, pp. 39–52.

14 Nicol, A. A., Bryce, A., and Ahmed, A. S. A., "Condensation of a Horizontally Flowing Vapour on a Horizontal Cylinder Normal to the Vapour Stream," *Proc. 6th Int. Heat Transfer Conf.*, Toronto, Vol. 2, 1978, pp. 401–406.

15 Fujii, T., Honda, H., and Oda, K., "Condensation of Steam on a Horizontal Tube," *Condensation Heat Transfer*, ASME, New York, 1979, pp. 35–43.

16 Gaddis, E. S., "Solution of the Two-Phase Boundary-Layer Equations for Laminar Film Condensation of Vapour Flowing Perpendicular to a Horizontal Cylinder," *Int. J. Heat Mass Transfer*, Vol. 22, 1979, pp. 371–382.

17 Fujii, T., and Honda, H., "Forced Convection Condensation on a Horizontal Tube," (in Japanese), *Trans. Japan Soc. Mech. Engrs.*, Vol. 45, 1980, pp. 95–102.

18 Fujii, T., "Vapor Shear and Condensate Inundation," *Power Condenser Heat Transfer Technology*, edited by, P. J. Marto, and R. H. Nunn, Hemisphere, 1981, pp. 193–223.

19 Honda, H., Nozu, S., and Fujii, T., "Vapour-to-Coolant Heat Transfer During Condensation of Flowing Vapour on a Horizontal Tube," *Proc. 7th Int. Heat Transfer Conf.*, München, Vol. 5, 1982, pp. 77–82.

20 Lee, W. C., and Rose, J. W., "Film Condensation on a Horizontal Tube—Effect of Vapour Velocity," *Proc. 7th Int. Heat Transfer Conf.*, München, Vol. 5, 1982, pp. 101–106.

21 Gogonin, I. I., and Dorokhov, A. R., "Heat Transfer From Condensing Freon-21, Vapour Moving Over a Horizontal Tube," *Heat Transfer—Soviet Research*, Vol. 3, No. 6, 1971, pp. 157–161.

22 Gogonin, I. I., and Dorokhov, A. R., "Experimental Investigation of Heat Transfer With Condensation of the Moving Vapour of Freon-21 on Horizontal Cylinders," *J. Appl. Mech. Techn. Phys.*, Vol. 17, No. 2, 1976, pp. 252–257.

23 Lee, W. C., "Filmwise Condensation on a Horizontal Tube in the Presence of Forced Convection and Non-Condensing Gas," Ph.D thesis, Univ. London, 1982.

24 Lee, W. C., and Rose, J. W., "Forced Convection Film Condensation on a Horizontal Tube With and Without Noncondensing Gases," *Int. J. Heat Mass Transfer*, Vol. 27, 1984, to be published.

25 Truckenbrodt, E., "Ein einfaches Näherungsverfahren zum Berechnen der Laminaren Reibungschicht mit Absangung," *Forschung Ing. Wes.*, Vol. 22, 1956, pp. 147–157.

27 Honda, H., and Fujii, T., "Numerical Analysis of Conjugate Heat Transfer During Condensation of a Flowing Vapour on a Horizontal Tube," *Trans. Jap. Soc. Mech. Engrs.*, (in Japanese), Vol. 46, 1980, pp. 2420–2429.

27 Le Fevre, E. J., and Rose, J. W., "An Experimental Study of Heat Transfer by Dropwise Condensation," *Int. J. Heat Mass Transfer*, Vol. 8, 1965, pp. 1117–1133.

28 Rose, J. W., "Effect of Pressure Gradients in Forced Convection Film Condensation on a Horizontal Tube," *Int. J. Heat Mass Transfer*, Vol. 27, 1984, pp. 39–47.

29 Butterworth, D., "Developments in the Design of Shell-and-Tube Condensers," ASME Paper No. 77-WA/HT-24, 1977.

S. Mochizuki

Y. Yagi

R. Tadano

Department of Mechanical Engineering,
Tokyo University of Agriculture
and Technology,
Koganei-City, Tokyo, Japan

Wen-Jei Yang

Department of Mechanical Engineering
and Applied Mechanics,
The University of Michigan,
Ann Arbor, Mich. 48109
Fellow ASME

Convective Filmwise Condensation of Nonazeotropic Binary Mixtures in a Vertical Tube

Complete condensation of binary mixtures of R11-R114 refrigerants is experimentally and theoretically studied. The test apparatus consists of two concentric tubes, with the vapor mixture flowing downward in the inner tube and the cooling water in the annular space in countercurrent direction. The composition of the binary-component mixtures is varied. An empirical equation is derived to correlate condensation heat transfer performance. A semitheoretical model is developed to predict laminar- and turbulent-film condensation on a vertical surface. Theory compares well with experiments. The vapor-coolant temperature difference remains practically constant throughout the entire flow passage, thus reducing the exergy loss to a minimum. The device is particularly attractive in extracting the available energy from geothermal and ocean thermal energy sources.

Introduction

It is well-known that condensation heat transfer deteriorates in the presence of noncondensable gases or vapors. Therefore, prevention of foreign substances from entering a condenser becomes an important task in maintaining the performance of the heat transfer device. In condensers using pure vapors, the vapor temperature remains generally constant during the process of phase change. This implies that the vapor-coolant temperature difference increases along the direction of vapor flow in counterflow type heat exchangers. It thus creates a situation in which the available excess energy is maximum at the coolant entrance and reduces toward the coolant exit. The situation is not the best from the viewpoint of utilizing the available excess energy. One can enhance the utilization of the available energy by maintaining the vapor-coolant temperature difference at the vapor entrance throughout the coolant passage. The process can be realized by running the condensing vapor and the coolant in counterflow direction with the vapor temperature falling along its passage. The use of pure vapors cannot achieve the goal. It is feasible, at least in principle, that certain nonazeotropic binary mixtures may serve the purpose. However, the presence of a foreign vapor, although condensable, would certainly trigger a reduction in the condensation heat transfer of an otherwise pure vapor.

The present study is motivated by the selection of an appropriate heat engine cycle and working substances in order to extract as much available energy as possible from geothermal and ocean thermal energy sources. If a heat exchanger is employed for extracting the available energy (i.e., exergy) from a source of low thermal potential, the change in the temperature difference between the warm and cold fluids must be kept as small as possible in order to reduce the exergy loss in the heat exchanger. The study serves two main purposes: one is to examine the feasibility of operating a condenser in which the vapor temperature falls along the path of condensation by the use of nonazeotropic binary mixtures; the other is to provide more information on condensation heat transfer characteristics of binary vapor mixtures. The information is rather scarce in comparison with the references available for the condensation of pure vapors and the effects of noncondensable gases. References [1] and [2] briefly discuss the condensation of binary vapor mixtures. Recently, Westwater [3] presented a comprehensive review of the state of knowledge on condensation. He indicated that little is known about condensing mixed vapors inside tubes—particularly at very high flow rates. Van Es and Heertjes [4] studied theoretically and experimentally the natural convective condensation of the nonazeotropic vapor mixtures of benzene and toluene in a vertical tube. The vapor mixtures did not completely condense in the tube and the theory included the solution for turbulent flow of the vapor mixtures.

This paper deals with convective filmwise condensation of binary vapor mixtures of R11 and R114 flowing downward inside a vertical tube being cooled by water in counterflow. An empirical equation is derived to correlate test data. Theory is compared with experiments.

Experimental Apparatus

The test section consisted of a 3080 mm-long concentric pipe placed in a vertical position, as shown in Fig. 1. The

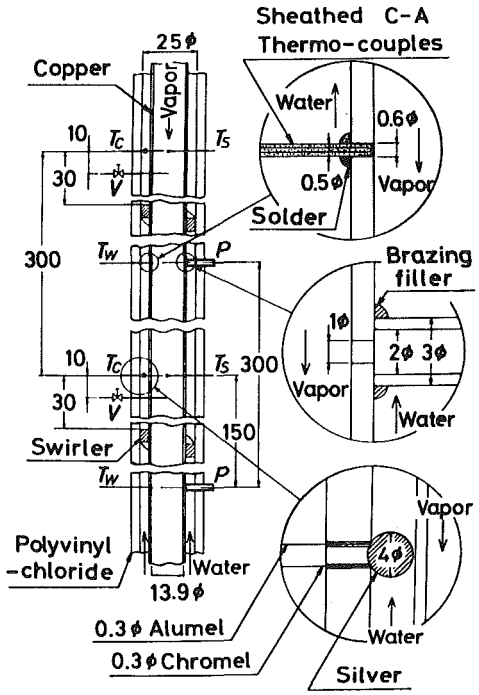

Fig. 1 Test section

Contributed by the Heat Transfer Division for publication in the JOURNAL OF HEAT TRANSFER. Manuscript received by the Heat Transfer Division August 10, 1983.

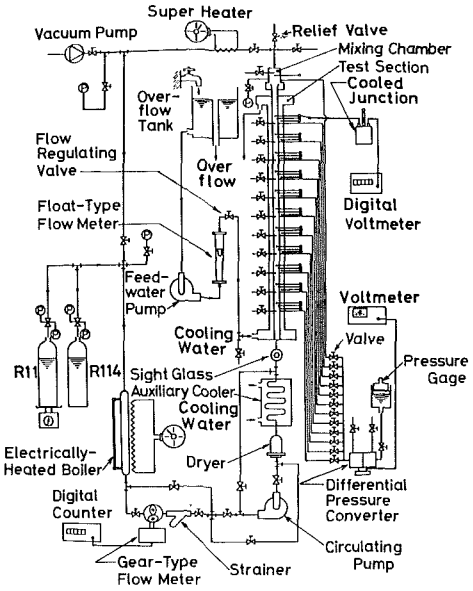

Fig. 2 A schematic of test apparatus

inner tube was made of copper with 13.9-mm i.d. and 16-mm o.d., while the outer tube was made of polyvinyl chloride with 25-mm i.d. and 32-mm o.d. A mixed vapor of refrigerants R11 and R114 (more volatile) entered at the top end and flowed downward into the inner tube. Water was used as the coolant, which entered at the lower end and flowed upward through the annular space.

Sheathed (with 0.5-mm o.d. thin stainless-steel tubing.) chromel-alumel thermocouples were used for measuring the temperatures of the mixed vapor and the condensing surface. They were flexible and could be freely bent. The outer tube was cut axially into two half-pieces and could be removed for installing thermocouples. Each thermocouple was wound one turn around the inner tube before it was inserted into the tube wall. The temperature-measuring tip surface of the sheathed thermocouple was soldered and flushed with the inner surface of the test tube. Hence the temperature gradient along the thermocouple wires was reduced to a minimum, and the fin effect of the wires may be considered negligible. Eleven thermocouples, as indicated by T_s in Fig. 1, were installed at 300 mm intervals along the centerline of the inner tube to measure the local vapor temperautre. Ten thermocouples indicated by T_w were used to measure the inside surface temperatures of the copper tube at 300 mm intervals along the tube axis. In order to determine the distributions of the static vapor pressure, the composition of the mixed vapor, and the coolant temperature at 300 mm intervals along the tube axis, 10 1-mm-i.d. static-pressure holes (indicated by P in Fig. 1), 11 0.5-mm-o.d. vapor-sampling capillary tubes (attached with valves), and 11 0.3 mm-dia chromel-alumel thermocouples (indicated by T_c) were also installed on the test section. Details of the installation are available in Fig. 1.

Figure 2 illustrates a schematic diagram of the entire test setup. The mixed vapor generated in the electrically heated boiler was fed into the vertical test section after flowing through the superheater and the mixing chamber. The condensate then flowed through the sightglass, the auxiliary condenser (where the liquid was subcooled in order to prevent the occurrence of cavitation in the pump), the dryer, the pump, the strainer, the gear-type flow meter, and back into the boiler. The volumetric flow rate $\dot{V}$ of the condensate was determined by the flowmeter with the aid of the digital counter. The cooling water from the overflow tank was fed into the test section by the feedwater pump. Its flow rate, which was regulated by the valve, was measured by the float-type flow meter.

The vapor-pressure distribution in the test section was measured by 10 pressure taps, see Fig. 1. Each pressure tap was connected to the high-pressure side of the strain-gage type differential pressure converter through a 2-mm-i.d. capillary tube which was filled with the working substance in liquid phase. Each capillary tube was equipped with a valve. The low-pressure side of the converter was hooked up to a source

Nomenclature

A = constant defined by equation (12)
a = vapor temperature gradient
B = constant defined by equation (12)
b = coolant temperature gradient
C_p = constant-pressure specific heat, kJ/kg°C; C_{pl}, of condensate; C_{ps}, of vapor
C_v = constant-volume specific heat, kJ/kg°C; C_{vs}, of vapor
d = inside diameter of condensation tube, m
E_l,E_{cr} = parameters defined by equation (35)
F = function defined by equation (22)
f = Fanning friction factor
Ga = dimensionless parameter as defined by equation (14)
g = gravitational acceleration, m/s^2
H = dimensionless parameter as defined by equation (2)
h = local condensation heat transfer coefficient, W/m^2°C; $h_{\exp}$, empirical value; h_f, in laminar film; h_t, in turbulent film; h_{th}, theoretical value
$\bar{h}$ = average value of h; $\bar{h}_f$, in condensate film; $\bar{h}_t$, in turbulent film; $\bar{h}_o$, in combined laminar and turbulent regions as defined by equation (36)
j = heat transfer factor
k_l = thermal conductivity of condensate, W/m°C
l = length of condensing region in the test section, m
$\dot{M}$ = $\dot{m}_l/\dot{m}_{si}$; $\dot{M}_l$, of condensate; $\dot{M}_s$, of vapor; $(\dot{M}_l)_{cr}$, $\dot{M}_l$ at transition
$\dot{m}$ = mass flow rate, kg/s; $\dot{m}_c$, of coolant; $\dot{m}_l$, of condensate; $\dot{m}_s$, of vapor; $\dot{m}_{si}$ of vapor at tube inlet
Nu = Nusselt number; Nu_f, defined by equation (17) for laminar film; Nu_t, defined by equation (33) for turbulent film; Nu_o, defined by equation (37) for combined laminar and turbulent regions
P = static vapor pressure, Pa
Pr_l = Prandtl number of condensate
q = rate of heat flow, W; q_c, of coolant; q_s, of vapor
q'' = local heat flux, W/m^2
R = dimensionless parameter as defined by equation (2)
Re = Reynolds number; Re_δ, of the condensation film as defined by equation (23); $(\mathrm{Re}_\delta)_{cr}$, Re_δ, at transition as defined by equation (24); Re*, defined by equation (2); Re_l, defined by equation (14); $(\mathrm{Re}_l)_{cr}$, Re_l, at transition
T = temperature, °C; T_c, of coolant; T_{ci}, of coolant at inlet; T_{ce} of coolant at exit; T_l, of condensate; T_s, of

Table 1 Range of condensation experiments of R11, R114 and their mixtures

Working substance	R-11	R-114	R-11 + R-114
$\dot{m}_c$ kg/h	239 ~ 246	239 ~ 240	210 ~ 246
T_c °C	17.0 ~ 18.0	17.1 ~ 18.0	16.0 ~ 20.4
$\dot{m}_{si}$ kg/h	15.2 ~ 60.9	21.6 ~ 71.2	12.9 ~ 51.9
U_i m/s	3.16 ~ 10.2	1.63 ~ 5.41	1.79 ~ 6.46
T_{sat} °C	34.3 ~ 58.8	32.1 ~ 44.1	29.6 ~ 44.6
$Re_l \times 10^{-7}$	1.38 ~ 12.3	0.98 ~ 7.04	0.58 ~ 7.50
$\bar{h}$ kW/m^2 °C	0.70 ~ 1.35	0.64 ~ 1.09	0.61 ~ 1.03
$Nu_l = \bar{h}\, l/k_l \times 10^{-4}$	1.01 ~ 4.95	1.50 ~ 5.43	0.86 ~ 4.29
H	0.06 ~ 0.15	0.085 ~ 0.185	0.05 ~ 0.146
Pr_l	3.77 ~ 4.09	5.66 ~ 5.71	4.37 ~ 5.60
$R = (\rho_l \mu_l / \rho_s \mu_s)^{0.5}$	49.6 ~ 79.6	37.3 ~ 47.3	41.4 ~ 69.9
[a] $5.6 \times 10^3 (R/Pr_l)^{8/3} x^{10/3} \times 10^{-5}$	6.85 ~ 24.7	1.34 ~ 3.20	2.01 ~ 13.5
$l\,m$	1.13 ~ 3.08	1.43 ~ 3.08	0.83 ~ 3.08
P_i N/m$^2 \times 10^{-5}$	1.44 ~ 2.97	2.67 ~ 3.77	1.64 ~ 3.28
y_{1i}(R-114)mol − %	0	1	0.2 ~ 0.9

[a] $x = 0.45(1.20 + Pr_l/RH)^{1/3}$

with known pressure. By opening one valve at a time, the pressure difference on both sides of the converter was read on the pressure gage. The static pressure of each pressure tap was corrected by the corresponding static head.

Samples of the nonazeotropic binary vapor mixture in the test section were collected by 11 stainless capillary tubes with minivalves. Each sample, after being liquefied, was analyzed using a chromatograph for its composition.

Experimental Results

The mixtures of R11 and R114 of various compositions were tested as nonazeotropic binary component working fluids. The physical properties of pure R11 and R114 fluids in [5] were used. The working fluid was introduced after all parts of the test apparatus were evacuated to approximately 10^{-4} Torr or 1.33×10^{-2} N/m^2 by means of a vacuum pump. Table 1 lists the range of condensation experiments on R-11, R114, and their mixtures in the present study.

Since complete condensation took place in the test section, the rate of condensation heat transfer was determined as $q_s = \dot{m}\lambda$. The variation of λ with the composition and temperature of the vapor mixture was determined using the method of Reid et al. [5]. The integrated mean value of λ along the axial direction was used in the correlation of test results. On the coolant side, the mass flow rate and temperatures at the entrance (the end of condensation to be exact) and exit (the beginning of condensation) to the test section $\dot{m}_c$, T_{ci}, and T_{ce}, respectively, were measured. The enthalpy change of the coolant inside the test section q_c was evaluated by $q_c = (\dot{m} C_p)_c (T_{ce} - T_{ci})$. The deviation between q_s and q_c in each test

Nomenclature (cont.)

vapor; T_{sat}, at saturated state; T_{si}, of vapor at inlet; T_{se}, of vapor at the end of condensation; T_w, of tube wall

$\overline{\Delta T}$ = mean temperature difference between vapor and tube wall ($T_s - T_w$), °C

U_i = inlet vapor velocity, m/s

u = velocity inside condensate layer, m/s

X = mole fraction of a component in condensate; X_1, of more volatile component; X_2, of less volatile component

x = vapor quality as defined by equation (1)

Y = mole fraction of a component in vapor phase; Y_1, of more volatile component; Y_2, of less volatile component; Y_{1i}, Y_1, at inlet

y = distance from tube wall, m

Z = z/d; Z_{cr}, at transition

z = axial distance measured from the beginning of condensation, m; z_{cr}, at transition

α = dimensionless parameter as defined by equation (7)

β = dimensionless parameter as defined by equation (7)

Δ = δ/d

δ = condensate thickness, m; δ_{cr}, at transition; δ_f, in laminar region; δ_t, in turbulent region

ϵ = function defined by equation (34)

η = l/d

λ = latent heat of condensation, kJ/kg; λ', as defined by equation (38)

μ = absolute viscosity, kg/sm; μ_l, of condensate; μ_s, of vapor

ν_l = kinematic viscosity of condensate, m^2/s

ρ = density, kg/m^3; ρ_l, of condensate; ρ_s, of vapor

ϕ = dimensionless parameter as defined by equation (21)

ψ = dimensionless parameter as defined by equation (2)

τ_s = vapor shear stress at the liquid-vapor interface, N/m^2

Subscripts

c = coolant

cr = transition from laminar to turbulent film

e = at condenser exit

exp = empirical value

f = laminar condensate layer

i = at condenser inlet

l = condensate

o = combined laminar and turbulent regions

p = under constant pressure

s = vapor

sat = saturated state

t = turbulent condensate layer

th = theoretical value

v = under constant volume

1 = more volatile component

2 = less volatile component

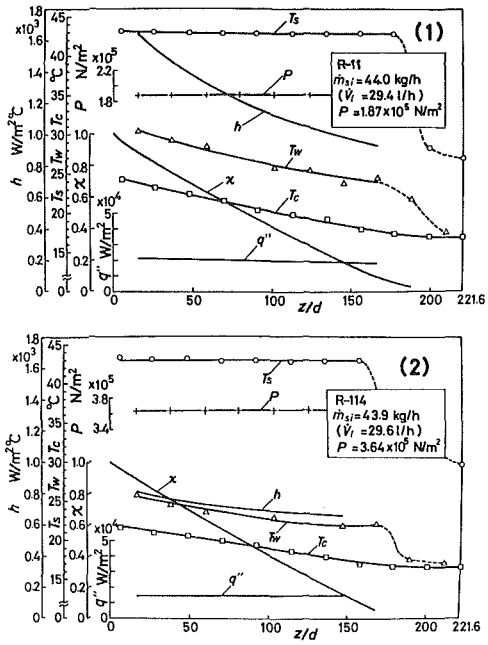

Fig. 3 Typical test results using R11 and R114

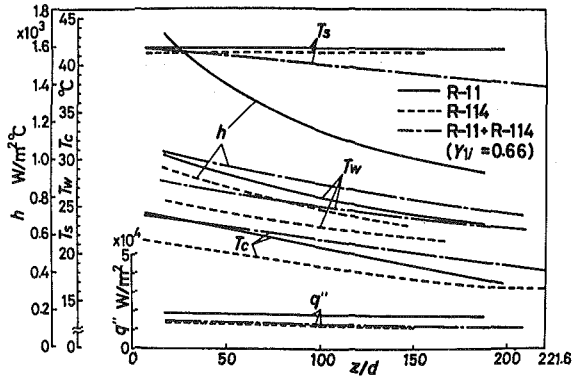

Fig. 4 Test results of R11-R114 binary mixture with inlet vapor component Y_{1i} = 0.66 and mass flow rate $\dot{m}_i$ = 45 kg/h

was within ± 5 percent, indicating the adequacy of insulating the test apparatus as well as high accuracy in the measurements of flow rates and temperatures.

The vapor, tube wall, coolant temperatures (T_s, T_w, T_c), and the static vapor pressure (P) along the flow path in the test section were measured. After using the least-square method to smooth the temperature and pressure distributions, q'', h, and x were determined using the expressions

$$q'' = -\frac{(\dot{m}\, C_p)_c}{\pi d}\left(\frac{dT_c}{dz}\right), \quad h = \frac{q''}{T_s - T_w};$$

$$x = 1 - \frac{\pi d}{\dot{m}_{si}\lambda}\int_o^z q''\, dz \tag{1}$$

The physical quantities T_s, T_w, T_c, P, q'', h, and x were then plotted against the z in the test section.

In the interest of brevity, only two representative results are presented in Figs. 3 and 4. Figure 3 illustrates the test results for pure working fluids R11 and R114, while the performance of the R11–R114 binary mixtures is shown in Fig. 4 for Y_{1i} = 0.66. Therefore, pure R11 nd R114 in Fig. 3 can be considered corresponding to Y_1 = 0 and 1.0, respectively.

In Fig. 3, because the vapor entering the test section was slightly superheated (by 5 to 6°C), T_s, near the entrance, dropped slightly along the flow. However, during the process

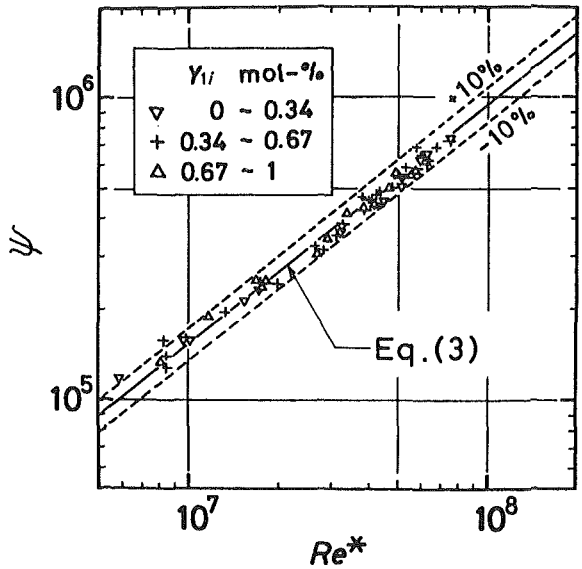

Fig. 5 Correlations of all test results of R11-R114 binary mixtures and empirical equation (3)

of condensation, T_s, P, and q'' all remained constant. T_s dropped abruptly following the completion of the condensation process, due to the subcooling of the condensate. The location of $x = 0$ obtained by an extrapolation of the x curve coincided with the location of an abrupt fall in T_s.

In the case of a condensing R11–R114 vapor mixture, Fig. 4 revealed that both T_s and T_c vary linearly with z while both P and q'' remained essentially constant during the process of condensation. The vapor mixture and the coolant flowed in a countercurrent direction. It was also observed that both h and T_w decreased with z. The experimental results for the vapor mixtures were correlated in Fig. 5 by plotting ψ against Re*, wherein

$$\left.\begin{aligned} &\psi = \mathrm{Nu}(R/\mathrm{Pr}_l)^{0.8} H^{0.3\eta 0.3}; \quad \eta = l/d; \quad \mathrm{Nu} = \frac{\bar{h} l}{k_l} \\ &\mathrm{Re}^* = \frac{U_i l}{\nu_l}; \quad R = \left(\frac{\rho_l \mu_l}{\rho_s \mu_s}\right)^{1/2}; \quad H = \frac{C_{p_l}\overline{\Delta T}}{\lambda} \end{aligned}\right\} \tag{2}$$

It is seen that irrespective of Y_{1i}, the condensation heat transfer performance can be correlated by the empirical equation

$$\mathrm{Nu} = 0.38(\eta H)^{-0.3}(\mathrm{Re}^* \mathrm{Pr}_l/R)^{0.8} \tag{3}$$

Its accuracy is about ± 10 percent for Re* between 5.8 × 10^6 and 7.5 × 10^7 and η ranging from 60 to 222.

Theory

It is desirable to predict thermodynamic equilibrium characteristics and condensation heat transfer performance of a nonazeotropic vapor mixture in a vertical tube. The following theoretical model is proposed: assuming an ideal binary mixture, the use of Raoult's law yields the temperature-composition diagram at constant pressure P = 2.53 × 10^5 N/m^2 for the R11–R114 mixture in Fig. 6. During the process of condensation, the temperature-composition relationship of the vapor phase follows the condensation-point curve, while that of the liquid phase follows the boiling-point curve in the direction indicated by the arrow sign. The relationship ($T_{si} - T_{se} = T_{li} - T_{le}$) is obvious. Figure 7 is a plot of (temperature change $T_{si} - T_{se}$) versus Y_{1i} obtained using Raoult's law for two pressure levels, 9.31 × 10^4 N/m^2 and 3.92 × 10^5 N/m^2 in solid lines. The experimental

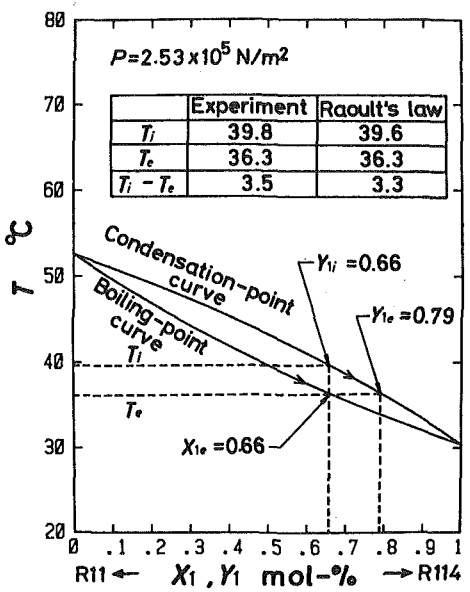

Fig. 6 Temperature-composition equilibrium diagram for R11-R114 binary mixtures at pressure of 2.53 × 10^5 N/m^2

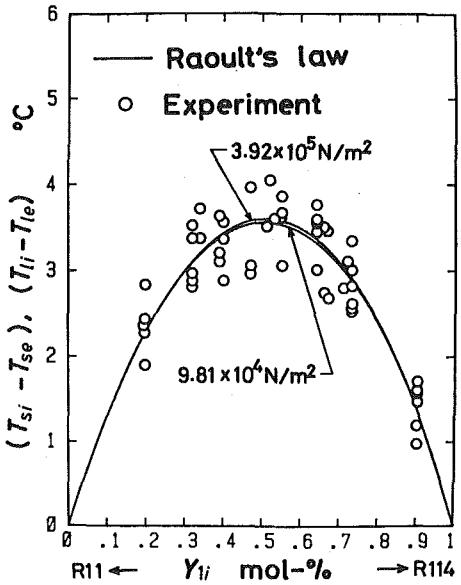

Fig. 7 Comparison between Raoult's law and experimental results of temperature drop-inlet vapor composition relationship for R11-R114 saturated vapor mixtures

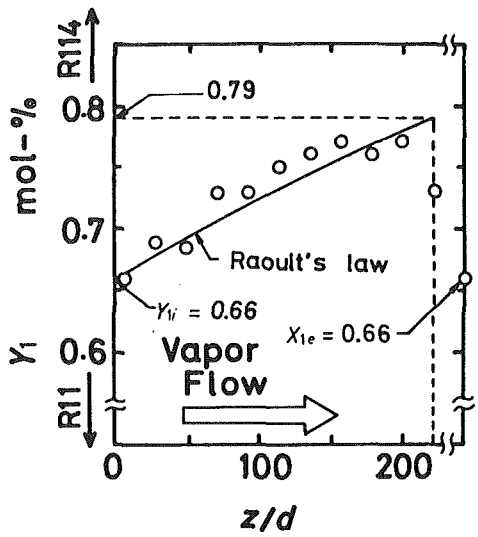

Fig. 8 Comparison between Raoult's law and measurements of change in vapor compositions along flow passage

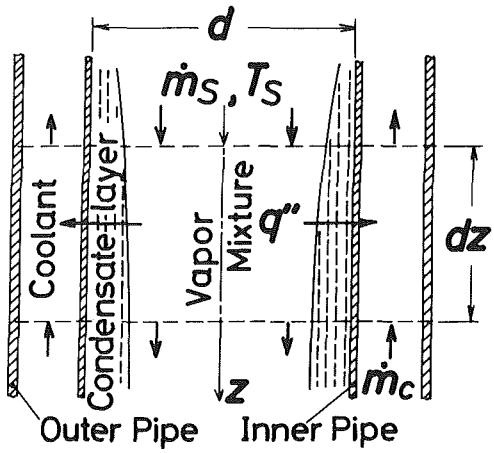

Fig. 9 Control volume defined for theoretical analysis

measurements of $(T_{si} - T_{se})$ are superimposed on Fig. 7 for comparison with the theoretical prediction. Theory and experiments agree well over a substantial range of Y_{1i}: from 20 to 90 percent. Figure 7 also shows that irrespective of the vapor pressure, the temperature difference takes a maximum value, about 3.5°C in the range of $Y_1 = 0.5$ to 0.6.

Figure 8 is a plot of Y_1 versus z based on the linear $T_s - z$ relationship observed in Fig. 4. Test results indicated by circles agree very well with the theoretical prediction (in a solid line) during the process of condensation. One may then conclude that R11-R114 mixtures behave like an ideal nonazeotropic binary mixture.

Next, a semitheoretical model is proposed to determine the heat transfer performance during the condensation of an ideal nonazeotropic binary vapor mixture flowing downward inside a vertical tube. The physical system consists of vertical concentric pipes with the vapor mixture flowing downward inside the inner tube while the cooling fluid is flowing upward in the annular space. Figure 9 shows the control volume defined for the semitheoretical model. Both laminar and turbulent films are considered and are combined to give analytical results for the case of laminar flow in the upper portion of a tube surface and turbulent flow on the lower portion.

The model is developed based on two empirical observations: linear variations of T_c and T_s with z as depicted in Figs. 3 and 4. A linear variation of T_c with z implies a constant temperature gradient $(dT_c/dz) = -b$, where b is a positive constant. A simple heat balance for the differential volume of the coolant in Fig. 9 yields $q'' \pi d\, dz = -(\dot{m}\, C_p)_c\, dT_c$. It leads to

$$q'' = -\frac{(\dot{m}\, C_p)_c}{\pi d}\frac{dT_c}{dz} = \frac{b(\dot{m}\, C_p)_c}{\pi d} = \text{constant} \qquad (4)$$

which agrees with the test results in Figs. 3 and 4.

The linear $T_s - z$ relationship gives $T_s = T_{si} - az$. Although λ varies with z, its mean value is employed as mentioned in the previous section. Now a heat balance on the differential volume of (diameter d and length dz) of the working fluid yields

$$(\dot{m}\, C_p T)_s + (-\lambda d\dot{m}_s) = q'' \pi d\, dz + (\dot{m}_s + d\dot{m}_s) C_{ps} (T_s + dT_s)$$

With the substitution of $dT_s/dz = -a$, one gets

$$\frac{d\,\dot{m}_s}{q''\pi d-(\dot{m}\,C_p)_s a}=-\frac{dz}{\lambda+C_{ps}(T_{si}-az)} \tag{5}$$

The equation is integrated from $z = 0$, where condensation begins, to $z = z$. With rearrangement in dimensionless form, one gets

$$\dot{M}_s=\beta-\frac{\alpha(\beta-1)}{\alpha-Z} \tag{6}$$

in which

$$\dot{M}_s=\frac{\dot{m}_s}{\dot{m}_{si}};\quad Z=\frac{z}{d};\quad \beta=\frac{q''\pi d}{\dot{m}_{si}a\,C_{ps}};\quad \alpha=\frac{\lambda+C_{ps}T_{si}}{C_{ps}a\,d} \tag{7}$$

The nondimensional condensate flow rate $\dot{M}_l$ $(=\dot{m}_l/\dot{m}_{si})$ is obtained by

$$\dot{M}_l=1-\dot{M}_s=\frac{(\beta-1)Z}{\alpha-Z} \tag{8}$$

(a) **Laminar Film.** Consider the control volume defined in the condensate film in Fig. 9. For the laminar flow case, neglecting of momentum effects, a balance of the shear, gravity, and pressure forces on the control volume yields the expression for the condensate velocity along the tube wall u as [6].

$$u=\frac{(\rho_l-\rho_s)g}{\mu_l}\left(y\delta_f-\frac{y^2}{2}\right)+\frac{\tau_s}{\mu_l}y \tag{9}$$

The continuity requires

$$\frac{\dot{m}_l}{\pi d}=\rho_l\int_0^{\delta_f}u\,dy=\frac{(\rho_l-\rho_s)\rho_l g\,\delta_f^3}{3\mu_l}+\frac{\rho_l\tau_s\delta_f^2}{2\mu_l} \tag{10}$$

which is a modified Nusselt analysis for condensation inside a circular tube, including the effect of vapor shear stress at the interface. It can be shown that if τ_s is less than $(6\dot{m}_l\mu_l\rho_l g^2/\pi d)^{1/3}$, the cubic equation (10) has only one real root and two conjugate imaginary roots. With the simplification of $\rho_l - \rho_s \cong \rho_l$ the real root is found to be

$$\delta_f=A+B-\frac{\tau_s}{2\rho_l g} \tag{11}$$

wherein

$$\left\{\begin{matrix}A\\B\end{matrix}\right\}=\left\{\frac{1}{\rho_l^2 g}\left[\frac{1}{2}\left(-\frac{\tau_s^3}{4\rho_l g^2}+\frac{3\dot{m}_l\mu_l}{\pi d}\right)\right.\right.$$

$$\left.\left.\pm\left[\frac{3\dot{m}_l\mu_l}{4\pi d}\left(\frac{3\dot{m}_l\mu_l}{\pi d}-\frac{\tau_s^2}{2\rho_l g^2}\right)\right]^{1/2}\right]\right\} \tag{12}$$

When the incoming vapor velocity is low, τ_s becomes negligibly small. Equation (11) is then reduced to

$$\delta_f=\left(\frac{3\dot{m}_l\mu_l}{\pi d\rho_l^2 g}\right)^{1/3}\quad\text{or}\quad\Delta=\left(\frac{3\mathrm{Re}_l\dot{M}_l}{4\,Ga}\right)^{1/3} \tag{13}$$

where

$$\Delta_f=\frac{\delta_f}{d};\quad \mathrm{Re}_l=\frac{4\dot{m}_{si}}{\pi d\mu_l};\quad Ga=\frac{gd^3}{\nu_l^2} \tag{14}$$

Re_l is related to Re^* by

$$\mathrm{Re}_l=\mathrm{Re}^*\left(\frac{\rho_s}{\rho_l}\right)\Big/\eta \tag{15}$$

The local value of the laminar heat transfer coefficient h_f is determined as

$$h_f=\frac{k_l}{\delta_f}=\frac{k_l}{d}\left[\frac{4Ga(\alpha-Z)}{3\mathrm{Re}_l Z(\beta-1)}\right]^{1/3} \tag{16}$$

The condensation mean Nusselt number is defined as

$$\mathrm{Nu}_f=\frac{\bar{h}_f l}{k_l} \tag{17}$$

Here, $\bar{h}_f$ is the integrated average value of h

$$\bar{h}_f=\frac{1}{l}\int_o^l h_f dz \tag{18}$$

The condensation length l can be determined by

$$l=\frac{\dot{m}_{si}\lambda}{b(\dot{m}\,C_p)_c}\quad\text{or}\quad\eta=\frac{\dot{m}_{si}\lambda}{bd(\dot{m}\,C_p)_c} \tag{19}$$

Equations (16–19) are combined to yield

$$\mathrm{Nu}_f=\left[\frac{4Ga}{3\mathrm{Re}_l(\beta-1)}\right]^{1/3}\alpha\left\{\frac{[\eta^2(\alpha-\eta)]^{1/3}}{\alpha}\right.$$

$$\left.-\frac{1}{6}\ln\left|\frac{[(\alpha-\eta)^{1/3}+\eta^{1/3}]^3}{\alpha}\right|\right.$$

$$\left.-\frac{1}{\sqrt{3}}\arctan\left[\frac{2(\alpha-\eta)^{1/3}-\eta^{1/3}}{\sqrt{3}\,\eta^{1/3}}\right]+\frac{\pi}{2\sqrt{3}}\right\} \tag{20}$$

The expression can be rewritten as

$$\phi=\bar{h}\left(\frac{\nu_l^2}{k_l^3 g}\right)^{1/3}=F/\mathrm{Re}_l^{1/3} \tag{21}$$

where F is functions of α, β, and η and is defined as

$$F=\left[\frac{4}{3(\beta-1)}\right]^{1/3}\left(\frac{\alpha}{\eta}\right)\left\{\frac{[\eta^2(\alpha-\eta)]^{1/3}}{\alpha}\right.$$

$$\left.-\frac{1}{6}\ln\left|\frac{[(\alpha-\eta)^{1/3}+\eta^{1/3}]^3}{\alpha}\right|\right.$$

$$\left.-\frac{1}{\sqrt{3}}\arctan\left[\frac{2(\alpha-\eta)^{1/3}-\eta^{1/3}}{\sqrt{3}\,\eta^{1/3}}\right]+\frac{\pi}{2\sqrt{3}}\right\} \tag{22}$$

For complete condensation, Nusselt's theoretical result for filmwise condensation of pure vapor on vertical surfaces gives $F = 1.47$, for Re_l not exceeding 2100 [7].

(b) **Transition From Laminar to Turbulent Film.** With film condensation of vapor mixture on a tall vertical tube, one can easily obtain condensation rates such that the condensate film Reynolds number

$$\mathrm{Re}_\delta=4\dot{m}_l/(\pi d\mu_l)=\mathrm{Re}_l\dot{M}_l=\dot{M}_l\mathrm{Re}^*\rho_s/(\eta\,\rho_l) \tag{23}$$

exceeds the critical value (1800 with $\tau_v = 0$, based on a freely falling film [7]) at which turbulence begins. Substituting the transition Reynolds number

$$(\mathrm{Re}_\delta)_{cr}=(\mathrm{Re}_l\dot{M}_l)_{cr}=1800 \tag{24}$$

into equation (13), one obtains

$$\delta_{cr}=\left(\frac{1350\,\nu_l^2}{g}\right)^{1/3}\quad\text{or}\quad\Delta_{cr}=\left(\frac{1350}{Ga}\right)^{1/3} \tag{25}$$

where δ_{cr} is the film thickness at the transition from laminar to turbulent films. The substitution of equation (24) into equation (8) yields

$$Z_{cr}=\frac{\alpha}{1+\dfrac{(\beta-1)\mathrm{Re}_v}{1800}} \tag{26}$$

(c) **Turbulent Film.** For turbulent flow of the condensate layer, the friction factor f in conduits was used for flow of liquid layers, while the analogous heat transfer factor j was employed for the heat flow across δ_t [8, 9]. f can be expressed as

$$\frac{1}{2}f=\frac{\delta_t^3\rho_l^2 g}{(\dot{m}_l/\pi d)^2} \tag{27}$$

This expression is combined with the $f-j$ relationship for turbulent flow in conduits, i.e., $j=f/2$, to give

$$\delta_l=\left[\frac{j}{\rho_l^2 g}\left(\frac{\dot{m}_l}{\pi d}\right)^2\right]^{1/3} \quad \text{or} \quad \Delta_l=\left(\frac{j}{16\,Ga}\mathrm{Re}_\delta^2\right)^{1/3} \tag{28}$$

The definition of j produces

$$h_l=\frac{j\,C_p\dot{m}_l}{\pi\,d\,\delta_l \mathrm{Pr}_l^{2/3}} \tag{29}$$

while the empirical expression in [9] reads

$$j=0.027\ \mathrm{Re}_\delta^{-0.2} \tag{30}$$

The substitution of equations (28) and (30) into equation (29) is followed by the incorporation of equation (8). One then obtains the local heat transfer coefficient in the turbulent condensate layer as

$$h_l=0.0509\frac{k_l}{d}(Ga\ \mathrm{Pr}_l)^{1/3}[\mathrm{Re}_l(\beta-1)]^{0.2}\left(\frac{Z}{\alpha-Z}\right)^{0.2} \tag{31}$$

The average value of h_l over the range of $z_{cr}\le z\le l$ can be determined by

$$\bar{h}_l=\frac{1}{l-z_{cr}}\int_{z_{cr}}^{l}h_l dz \tag{32}$$

The mean Nusselt number is

$$\mathrm{Nu}_l=\frac{\bar{h}_l l}{k_l}=0.0793\,\eta\frac{(\mathrm{Pr}\ Ga)^{1/3}}{\eta-Z_{cr}}[\mathrm{Re}_l(\beta-1)]^{0.2}\epsilon \tag{33}$$

in which

$$\epsilon=\alpha\Bigg\{-\frac{E_l}{1+E_l^5}+\frac{E_{cr}}{1+E_{cr}^5}+\frac{1}{4}\ln\left|\frac{E_l+1}{E_{cr}+1}\right|$$

$$-\frac{1}{20}\ln\left|\frac{E_l^5+1}{E_{cr}^5+1}\right|$$

$$+\frac{1}{4\sqrt{5}}\ln\left|\frac{[2E_l^2+(\sqrt{5}-1)E_l+2][2E_{cr}^2-(\sqrt{5}+1)E_{cr}+2]}{[2E_l^2-(\sqrt{5}+1)E_l+2][2E_{cr}^2+(\sqrt{5}-1)E_{cr}+2]}\right|$$

$$+\frac{1}{10}\Bigg[\sqrt{10+2\sqrt{5}}\ \arctan\frac{4E_l-1+\sqrt{5}}{\sqrt{10+2\sqrt{5}}}$$

$$+\sqrt{10-2\sqrt{5}}\arctan\frac{4E_l-1-\sqrt{5}}{\sqrt{10-2\sqrt{5}}}$$

$$-\sqrt{10+2\sqrt{5}}\arctan\frac{4E_{cr}-1+\sqrt{5}}{\sqrt{10-2\sqrt{5}}}$$

$$-\sqrt{10-2\sqrt{5}}\arctan\frac{4E_{cr}-1-\sqrt{5}}{\sqrt{10-2\sqrt{5}}}\Bigg]\Bigg\} \tag{34}$$

and

$$E_l=\left(\frac{\eta}{\alpha-\eta}\right)^{1/5};\quad E_{cr}=\left(\frac{Z_{cr}}{\alpha-Z_{cr}}\right)^{1/5} \tag{35}$$

(d) Overall Heat Transfer Performance. The average heat transfer coefficient in the combined laminar and turbulent regions over the entire condensate layer is evaluated by

$$\bar{h}_o=\frac{\bar{h}_f z_c+\bar{h}_t(l-z_c)}{l} \tag{36}$$

It can be written in dimensionless form as

$$\mathrm{Nu}_o=\frac{\bar{h}_o l}{k_l}=\frac{\mathrm{Nu}_f Z_{cr}}{\eta}+\mathrm{Nu}_t\left(1-\frac{Z_{cr}}{\eta}\right) \tag{37}$$

(e) Effect of Superheated Vapor and Subcooled Condensate. It is important to take the effects of superheated vapor and subcooled condensate into account in the determination of heat transfer performance. When the wall temperature is below saturation and film condensation occurs, the condensation rate is increased by greater superheating. Rohsenow and Choi [5] suggested modifying the analysis only by accounting for the larger enthalpy change from the superheated vapor to the subcooled condensate. This is accomplished by replacing λ with λ' in equations (2) and (7), where

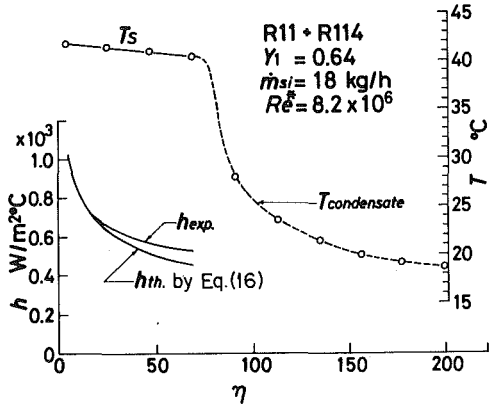

Fig. 10 Comparison between theoretical prediction and test results for local condensation heat transfer coefficient distribution in laminar condensate film

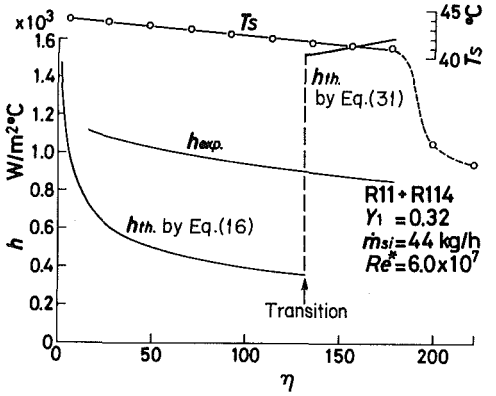

Fig. 11 Comparison between theoretical prediction and test results for local condensation heat transfer coefficient distribution in laminar-turbulent condensate film

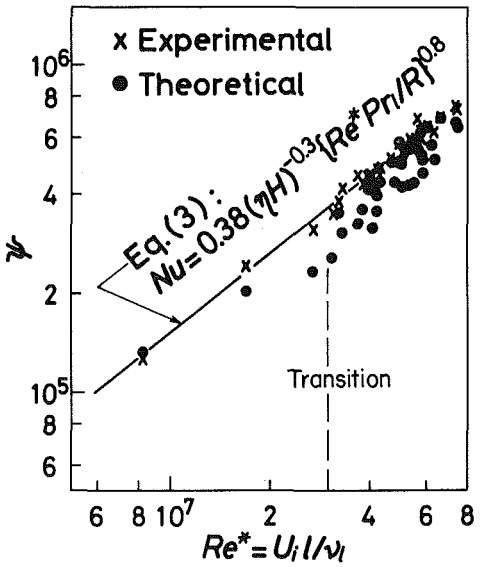

Fig. 12 Comparison between theoretical and experimental results of average condensation heat transfer performance

$$\lambda' = C_{vs}(T_s - T_{sat}) + \lambda + \frac{3}{8} C_{pl}(T_{sat} - T_w) \quad (38)$$

Comparison Between Theory and Experiments

Equations (16) and (31) for the axial distribution of local condensation heat transfer coefficients are graphically depicted as the solid line indicated by h_{th} in Figs. 10 and 11 for laminar and turbulent condensate film flows, respectively. Figure 10 corresponds to the laminar condensation of a vapor mixture with $Y_1 = 0.64$, and at a relatively low mass flow rate of 18 kg/h, as well as shorter condensation length of $\eta \cong 72$. In contrast, a mixture with $Y_1 = 0.32$, but at a relatively high mass flow rate of 44 kg/h and a higher value of $\eta \cong 180$, is depicted in Fig. 11. The condensate film flow underwent a transition at $\eta = 128$. The experimental results of the local condensation coefficient h_{exp} are superimposed in the figures for comparison with theory. Also plotted is the measured results of the vapor temperature T_s as dotted lines. In Fig. 10, theory underpredicts but compares well with experiments, especially at low values of z/d. However, at high flow rate in Fig. 11, test results surpass theoretical predictions in the laminar condensate flow regime due to the neglect of effects of steam flow velocity. The discrepancy between theory and experiments in the turbulent region is originated in the application of the $f = 2j$ relationship. The theoretical and experimental curves in the laminar range are practically parallel starting from η of approximately 30. h decreases with η in the laminar flow region due to an increase in δ, while the increase in h in the turbulent flow regime was attributed to an increase in the condensate flow rate along the condensation path.

Theoretical prediction of the average condensation heat transfer performance, using equations (20) and (37) for laminar and combined flows, respectively, is compared with test data in Fig. 12. The empirical expression (3) is superimposed in the figure. The transition from laminar to turbulent flows occurs at Re^*_{cr} of about 3.0×10^7, corresponding to $(Re_\delta)_{cr} = 1800$. Theoretical prediction agrees well with test results in both the laminar and turbulent flow regimes. If, however, the empirical coefficient of 0.027 for tube flows in equation (30) were replaced by 0.0295 for flows over a plate [11], one would obtain an excellent agreement between theory and experiments in the combined flow range.

An examination of equations (20) and (33) reveals that condensation heat transfer performance as measured by Nu is a function of five dimensionless parameters Ga, Re_l, β, α, and η in the laminar condensate film and six parameters Ga, Re_l, β, α, η, and Pr_l in the turbulent case. The value of Nu increases linearly with $Ga^{1/3}$ in both the laminar and turbulent condensate films. However, it decreases with $[(\beta - 1)Re_l]^{1/3}$ in the laminar case but increases with $Re^{0.2}$ in the turbulent case. At transition, the condensate film thickness Δ_{cr} varies inversely with $Ga^{1/3}$, while the location shifts linearly with α and inversely with $(\beta - 1)Re_l$.

Conclusions

The condensation of R11–R114 vapor mixtures in a vertical tube in countercurrent flow with the coolant is studied experimentally and theoretically. It is concluded that:

1 R11–R114 mixtures behave like ideal nonazeotropic binary mixtures.

2 The vapor temperature falls linearly along the flow path during the condensation process, and the vapor-coolant temperature difference remains fairly constant throughout the flow passage.

3 The condensation heat flux is constant along the flow path in most countercurrent flow cases.

4 The empirical equation (3) correlates test data for condensation of ideal nonazeotropic binary mixtures and can also be applied to the condensation of pure vapors.

5 The semitheoretical equations (20) and (37) for heat transfer performance in the laminar and combined flows, respectively, correlate well with experiments. However, theoretical prediction for the axial distribution of local condensation heat transfer coefficients by equations (16) and (31) is less satisfactory at high flow rates.

Future studies should refine the theoretical models to take into account the effects of steam flow velocity (namely shear stress at the vapor–liquid interface), inertia and energy convection in the laminar flow regime, and to use a more sophisticated condensation heat transfer model for the turbulent flow region.

References

1 Collier, J. G., *Convective Boiling and Condensation*, McGraw-Hill, U.K., London, ch. 10, 1972.

2 Van Stralen, S. J., *Boiling Phenomena*, Vol. 1, McGraw-Hill, New York, 1979, pp. 384–385.

3 Westwater, J. W., "Condensation," *Heat Transfer in Energy Problems*, edited by T. Mizushina and Wen-Jei Yang, Hemisphere Publishing, Washington, D.C., 1983, pp. 81–92.

4 Van Es, J. P., and Heertjes, P. M., "On the Condensation of a Vapour of a Binary Mixture in a Vertical Tube," *Chem. Eng. Sci.*, Vol. 5, 1956, pp. 217–225.

5 Reid, R. C., Prausnitz, J. M., and Sherwood, T. K., *The Properties of Gases and Liquids*, 3d ed., McGraw-Hill, New York, 1977.

6 Rohsenow, W. M., and Choi, H. Y., *Heat, Mass, and Momentum Transfer*, ch. 10, Prentice-Hall, Englewood Cliffs, N.J., 1961.

7 McAdams, W. H., *Heat Transmission*, ch. 13, 3d ed., McGraw-Hill, New York, 1954.

8 Cooper, C. M., Drew, T. B., and McAdams, W. H., "Isothermal Flow of Liquid Layers," *Industrial and Engineering Chemistry*, Vol. 26, 1934, pp. 428–431.

9 Rohsenow, W. H., Webber, J. H., and Ling, A. T., "Effect of Vapor Velocity on Laminar and Turbulent Film Condensation," ASME *Transactions*, Vol. 78, 1956, pp. 1637–1644.

10 Jakob, M., *Heat Transfer*, Vol. 1, Wiley, New York, 1949, p. 682.

11 Kays, W. M., *Convective Heat and Mass Transfer*, ch. 10, McGraw-Hill, New York, 1966.

C. W. Sohn
U.S. Army CERL,
Champaign, Ill. 61820
Assoc. Mem. ASME

M. M. Chen
Department of Mechanical Engineering,
University of Illinois
at Urbana-Champaign,
Urbana, Ill. 61801
Mem. ASME

Heat Transfer Enhancement in Laminar Slurry Pipe Flows With Power Law Thermal Conductivities

Generalized theoretical results for heat transfer in laminar pipe flow with power law varying thermal conductivities are presented. The study is motivated by experimental observations that above a threshold shear rate the effective thermal conductivity for disperse two-phase mixtures increases with shear rate. Using a relatively general three parameter power law model for conductivity as a function of shear rate, heat transfer results for short and long pipes as well as with developing thermal profiles were obtained for both the uniform wall heat flux and uniform wall temperature conditions. The results show that significant enhancement in heat transfer coefficient could be obtained from the microconvective effects.

1 Introduction

A number of communications have reported on the evidence of shear-enhanced heat and mass transfer in flowing slurries and in flowing blood [1-4]. The phenomenon was systematically investigated by Sohn and Chen [5]. Their results showed that the thermal conductivity of a dispersed two-phase mixture increases with shear rate when the particle Peclet number ($\mathrm{Pe} = ed^2/\alpha$) is sufficiently high. Here e is the local shear rate, d the particle diameter, and α the heat diffusivity. The nature of the Peclet number dependence shown by the data, as well as a theoretical model formulated to explain the phenomenon [6,7], indicates that the enhancement is due to particle-scale microconvection associated with particle-fluid interactions in the shear field.

The phenomenon suggests a new approach to the enhancement of convective heat transfer. The enhancement of conductivity is strongly dependent on the particle diameter. On the other hand, the apparent viscosity of suspensions is known to be relatively insensitive to the particle diameter. Thus, with a proper choice of parameters, significant increase in heat transfer coefficients may be possible without excessive pressure drop penalties. The objective of the present communication is to provide theoretical heat transfer coefficients based on a general three-parameter conductivity model, which can be readily fitted to either observed or predicted data on the shear dependent thermal conductvity.

For the purpose of calculating heat transfer coefficients in laminar slurry pipe flows, it will be assumed that the particle diameters are small relative to the pipe diameter, so that the slurry can be treated as a single-phase fluid with a given viscosity and thermal conductivity. It is known that for sufficiently large solid volume fractions, the interaction of the solids generally leads to a relatively uniform distribution of solids through the radius of the pipe, with the exception of a thin particle-depleted layer in the vicinity of the wall. The thickness of this layer is of the order of the particle diameter [8]; thus, in the limit of small d/R, it is also justified to neglect the presence of the particle-depleted layer as part of the continuum assumption.

A parabolic velocity distribution will be assumed in the present analysis for simplicity of analysis. Studies on suspension rheology have shown that at low rates of shear, slurries may exhibit non-Newtonian behavior. At higher shear rates, including those corresponding to the higher flow rates encountered in engineering applications, suspensions containing granular particles (in contrast to filaments or fibers) tend to be Newtonian [9]. It is also reported that suspensions of noninteracting spheres are usually Newtonian up to a volume concentration of 25 percent or higher [10]. Observation of parabolic velocity profiles for suspensions of neutrally buoyant particles is also reported [11]. Accordingly, the parabolic velocity profile should be valid for a large number of conditions of interest. General trends of the results should also be applicable to fully developed flows of non-parabolic velocity distribution, whose analysis poses no significant difficulties and promises no significant insight.

2 Model

The theoretical model for present analysis is shown in Fig. 1. Neglecting the axial conduction as in most high-Peclet-number convection studies, the energy equation is

$$2\rho c_p U\left\{1-\left(\frac{r}{R}\right)^2\right\}\frac{\partial T}{\partial x}=\frac{1}{r}\frac{\partial}{\partial r}\left\{rk(r)\frac{\partial T}{\partial r}\right\} \qquad (1)$$

This problem differs from the usual laminar convection problem [12] in that the thermal conductivity k is now a function of radial position due to its dependence on the local shear rate. In view of the data cited above [5], a relatively general yet simple three-parameter model of the thermal conductivity-shear rate dependence shall be assumed (see Fig. 1)

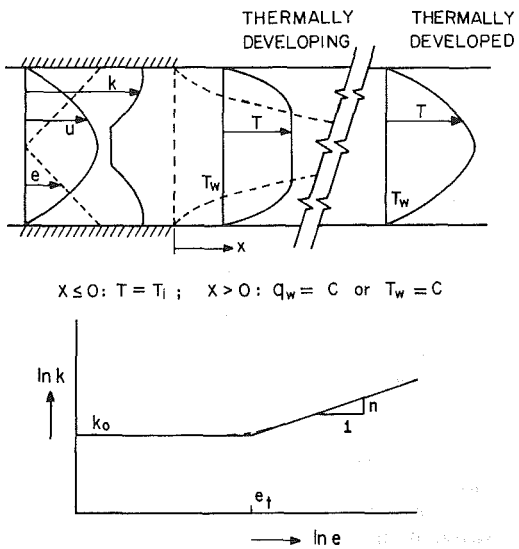

Fig. 1 Schematic illustration of theoretical model for heat transfer in pipe flow

Contributed by the Heat Transfer Division for publication in the JOURNAL OF HEAT TRANSFER. Manuscript received by the Heat Transfer Division December 15, 1982.

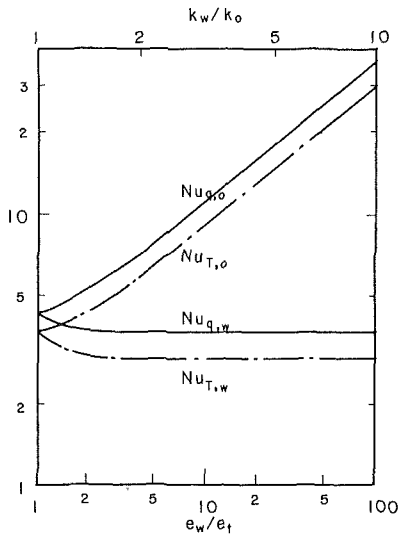

Fig. 2 Variation of Nusselt number for fully developed flow with respect to shear rate ratio and conductivity ratio for $n = 0.5$

$$k = k_o \qquad \text{for } e < e_t \tag{2a}$$

$$k = k_o (e/e_t)^n \qquad \text{for } e \geq e_t \tag{2b}$$

where e_t denotes the threshold shear rate below which there is little enhancement, k_o the unenhanced thermal conductivity, and n the experimental exponent. Admittedly, the discontinuity at $e = e_t$ is not too realistic. However, no significant error is expected to result from such an assumption especially when $k_w >> k_o$ as will be discussed later. The power law form of equation (2) was motivated not only by the experimental trend shown in [5], but also by the fact that for $k_w/k_o >> 1$ the normalized equation and the results depend on the exponent n only. Furthermore, the model is relatively general; by varying the three parameters k_o, e_t, and n, very faithful matching to any experimentally observed curve can be made.

For a parabolic velocity distribution, the rate of shear is proportional to r. Thus the dependence of k on r can be expressed in the following form

$$k/k_w = (r/R)^n \qquad \text{for } r \geq r_t \tag{3a}$$

$$k/k_w = (r_t/R)^n \qquad \text{for } r < r_t \tag{3b}$$

where k_w, the conductivity at the wall, and r_t, the threshold radius, can be evaluated from k_o and e_t using the relationship

$$k_w = k_o (4U/(e_t R))^n \tag{4a}$$

$$r_t = (e_t R^2)/(4U) \tag{4b}$$

For equation (4), we have restricted our attention to the nontrivial case when k_w is greater than k_o. It will be found that k_w rather than k_o is more convenient as the reference quantity in dimensionless parameters. The quantities k_w and k_o can be easily converted into each other by equation (4).

3 Results

Solutions to equation (1) are obtained with the following sets of boundary conditions.

(*a*) Uniform wall heat flux:

$$(\partial T/\partial r)_{r=R} = -q_w/k; \quad (\partial T/\partial r)_{r=0} = 0; \quad T(r, x=0) = T_i \tag{5a,b,c}$$

(*b*) Uniform wall temperature:

$$T(r=R, x) = T_w; \quad (\partial T/\partial r)_{r=0} = 0; \quad T(r, x=0) = T_i \tag{6a,b,c}$$

In the following, the solutions for the limiting cases of very long and very short pipes as well as the solution for thermally developing profiles are presented.

3.1 The Limiting Case of Very Long Pipe With Uniform Wall Heat Flux. The Nusselt number for a fully developed flow is given by

$$\mathrm{Nu}_{q,w} = \left(\frac{(n^2 - 18n + 88)}{2(4-n)(6-n)(8-n)} - \frac{n}{2(4-n)} \left(\frac{r_t}{R}\right)^{4-n} - \frac{n}{3(6-n)} \left(\frac{r_t}{R}\right)^{6-n} - \frac{n}{16(8-n)} \left(\frac{r_t}{R}\right)^{8-n} \right)^{-1} \tag{7}$$

where $\mathrm{Nu}_{q,w}$ denotes the Nusslet number defined on the basis of k_w. Thus, as k_w increases, there is a continued increase of the heat transfer coefficient even as $\mathrm{Nu}_{q,w}$ approaches a constant asymptotic value. To illustrate this, $\mathrm{Nu}_{q,w}$ ($= hD/k_w$) and $\mathrm{Nu}_{q,o}$ ($= hD/k_o$) are both plotted in Fig. 2 as functions of e_w/e_t and k_w/k_o. It is seen that for e_w greater than $3e_t$, $\mathrm{Nu}_{q,w}$ is essentially a constant ($\mathrm{Nu}_{q,w} = 3.64$) whereas $\mathrm{Nu}_{q,o}$ continues to increase as k_w/k_o is increased. For this reason, it is more convenient to present the results in terms of Nusslet numbers based on k_w. For $e_w/e_t = k_w/k_t = 1$, the solution reduces to the well-known solutions for uniform conductivity [12–14].

3.2 The Limiting Case of Very Long Pipes With Uniform Wall Temperature. The asymptotic solution for fully developed temperature profile is in the form

$$T - T_w = Cf(r) \exp(-mx/R) \tag{8}$$

This solution, in fact, corresponds to the first term of the eigenfunction expansion presented in section 3.4.2. For the case of $n = 0.5$, the Nusselt number is

$$\mathrm{Nu}_{T,w} = \lambda_1/2 = 2.88 \quad \text{for } e_w >> e_t \tag{9}$$

$\mathrm{Nu}_{T,w}$ and $\mathrm{Nu}_{T,o}$ are plotted in Fig. 2 as functions of e_w/e_t and k_w/k_o. Again it is seen that $\mathrm{Nu}_{T,w}$ is essentially constant

Nomenclature

C = coefficient of eigenfunction series expansion
c_p = specific heat at constant pressure
d = particle diameter
e = shear rate
h = heat transfer coefficient
k = thermal conductivity
n = experimental exponent for a power-law relationship
Nu = Nusselt number
Pe = Peclet number
q = heat flux
R = pipe radius or eigenfunction
Re = Reynolds number
r = radial coordinate
r^* = r/R
T = temperature
U = bulk velocity
x = axial coordinate
x^* = $(\alpha_w/UD)(x/R)$

Greek Symbols

α = heat diffusivity
ρ = density
λ = eigenvalue

Subscripts

i = quantity at the inlet of the pipe
o = quantity at the unenhanced state
q = related to uniform wall heat flux condition
t = quantity at the threshold shear rate
T = related to unifrm wall temperature condition
w = quantity at the wall

Table 1 First three eigenvalues and constants

N		T_w = const $n=0.5$	$n=0.4$	$n=1/3$		q_w = const $n=0.5$	$n=0.4$	$n=1/3$
1	λ	5.76	6.07	6.28	λ	16.0	17.7	18.9
	C	1.72	1.66	1.62	C	.744	.651	.598
	$R'(1)$	−.637	−.709	−.758	$R(1)$	−.307	−.341	−.365
2	λ	27.4	30.5	32.6	λ	48.2	54.4	58.3
	C	−1.32	−1.18	−1.10	C	−4.03	−.334	−.297
	$R'(1)$	.631	.749	.833	$R(1)$	.206	.238	.261
3	λ	65.5	74.0	79.9	λ	97.0	110.	120.
	C	1.16	.997	.909	C	.286	.231	.202
	$R'(1)$	−.626	−.768	−.872	$R(1)$	−.159	−.188	−.209

for e_w/e_t greater than 3, corresponding to k_w/k_o greater than 1.73. The values of λ_1 for different values of n are shown in the Table 1. It is noted that, as in the case of uniform heat flux, the Nusselt number hD/k_w is essentially independent of k_w/k_o for $k_w/k_o > 2$.

3.3 The Limiting Case for Very Short Heated Lengths. For a pipe with a fully developed velocity profile and a very short heated length, the thermal boundary layer is very thin relative to the pipe radius. Within the thermal boundary layer, the variation of shear rate could be neglected and the thermal conductivity can be approximated to the value corresponding to the wall shear rate. The problem is now reduced to the classical Leveque problem [15], which can be solved analytically through similarity transformations.

3.3.1 Uniform Wall Heat Flux Solution. The Nusselt number along the axial direction is given by

$$\mathrm{Nu}_{q,w} = hD/k_w = 1.6404x^{*(-1/3)} \tag{10}$$

3.3.2 Uniform Wall Temperature Solution. The Nusselt number along the axial direction is given by

$$\mathrm{Nu}_{T,w} = hD/k_w = 1.3566x^{*(-1/3)} \tag{11}$$

3.4 General Problem. Between the two limiting cases, the problem can be viewed as a modified Graetz problem with variable thermal conductivity. Solutions are obtained by separation of variables [12] for both wall boundary conditions.

3.4.1 Uniform Wall Heat Flux Solution. The local Nusselt number is given by

$$\mathrm{Nu}_{x,q,w} = 2/\left(\sum_{n=1}^{\infty} C_n \exp(-\lambda_m x^*) R_n(r^*=1,\lambda_n) + 2/\mathrm{Nu}_{q,w}\right) \tag{12}$$

where $\mathrm{Nu}_{q,w}$ is the Nusselt number for the fully developed case given in equation (7).

3.4.2 Uniform Wall Temperature Solution. The local Nusselt number is

$$\mathrm{Nu}_{x,T,w} = \left(\sum_{n=1}^{\infty} C_n \exp(-\lambda_n x^*) R_n'(r^*=1,\lambda_n)\right) \Big/ \left(2\sum_{n=1}^{\infty} (C_n/\lambda_n)\exp(-\lambda_n x^*) R_n'(r^*=1,\lambda_n)\right) \tag{13}$$

The asymptotic value of the local Nusselt number is the solution for a fully developed flow given in equation (9).

The shooting method was employed to solve the eigenvalue equations resulted in the separation of variables for equation (1). Details of the calculation can be found in [16]. The fourth-order Runge-Kutta method is used for integration of the differential equations. For the evaluation of coefficients in the eigenfunction expansion, the extended Simpson's rule is used for numerical integration.

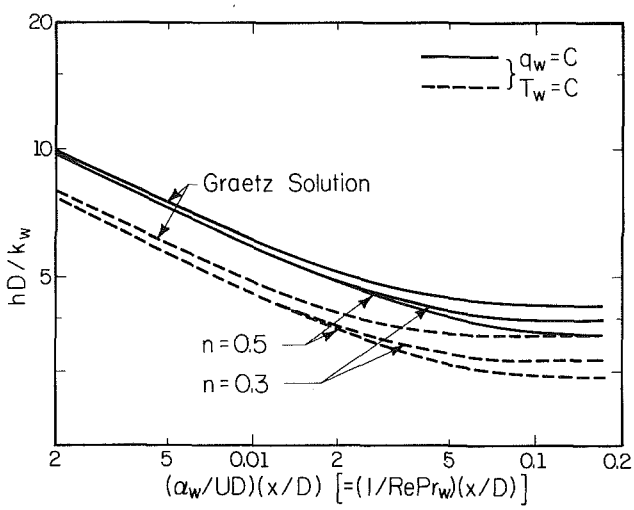

Fig. 3 The Nusselt number ($\mathrm{Nu}_{x,w}$) based on wall conductivity as a function of Graetz number ($(\alpha_w/UD(x/D)$) compared to the Graetz solution with uniform conductivity

The local Nusselt numbers based on the thermal conductivity at the wall ($\mathrm{Nu}_{x,w}$) for both wall conditions can be calculated from equations (12), (13), and Table 1 (which contains the first three eigenvalues). Up to the tenth eigenvalues and associated quantities are given in [16]. The heat transfer results for $n=0.5$ and 0.3 are shown in Fig. 3. As expected, the local Nusselt numbers approach the fully developed solutions (equations (7) and (9)) when x^* is large, and the Graetz solutions when x^* is very small. The latter means that across the thinner thermal boundary layer the shear rate approaches the wall shear rate, and the results approach the solutions for constant thermal conductivity. It should be noted that the Nusslet numbers in Fig. 3 are based on the wall thermal conductivity, which would be increased from the unenhanced value k_o to the value k_w predicted by equation (4*a*) as the shear rate is increased.

4 Discussion

For both the thermally developed and developing cases considered above, $\mathrm{Nu}_{T,w}$ and $\mathrm{Nu}_{q,w}$ are essentially independent of k_w/k_o for $k_w/k_o > 2$. This suggests that the heat transfer behavior is primarily sensitive to the wall conductivity k_w and n. The latter can be shown to be equal to $(d\ \ln(k)/d\ \ln(r))_w$, and hence describes the variation of k with respect to r near the wall. On the other hand, at k_o the unenhanced conductivity of the fluid near the centerline is seen to play a very insignificant role. This is, of course, not unexpected, since by far the most important heat conduction process takes place near the wall. For similar reasons, the use of the discontinuous model, equation (2), instead of a more continuous expression, to approximate the $K(e)$ relationship is also justified for $k_w/k_o > 2$. For $k_w/k_o < 2$, a more detailed analysis would be necessary if precise results are desired. This discussion suggests that in the attempt to approximate an

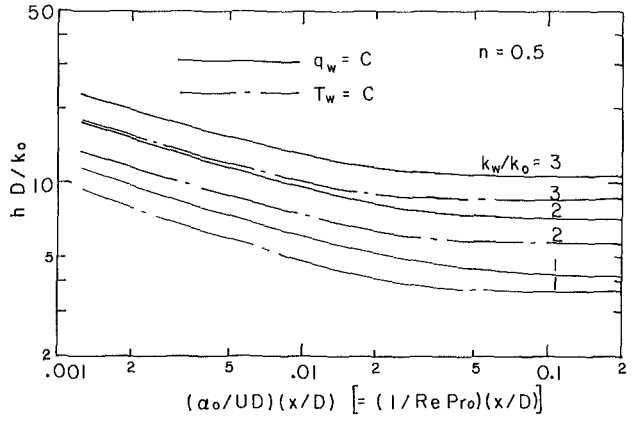

Fig. 4 The Nusselt number ($Nu_{x,o}$) as a function of ($\alpha_o/UD(x/D)$ for several conductivity ratios, $n = 0.5$

Table 2 Theoretical enhancement ratios for thermal conductivity and heat transfer coefficients in slurry pipe flows[a]

		Thermal conductivity enhancement ratios		Heat Transfer coefficient enhancement ratios	
Velocity (m/s)	Particle diameter	Tube diameter		Tube diameter	
	(mm)	3mm	10mm	3mm	10mm
	0.1	—	—	—	—
0.1	0.3	—	—	—	—
	1.0	3.0	1.6	2.5	1.4
	0.1	—	—	—	—
1.0	0.3	2.8	1.6	2.4	1.3
	1.0	9.4	5.2	7.9	4.3
	0.1	3.0	1.6	2.5	1.4
10.	0.3	8.9	4.9	7.5	4.1
	1.0	30.	16.	25.	14.

[a]For fully developed flows with $n=1/2$, $Pe_t=300$ [5], $\alpha=10^{-7}$ m^2/s, and $q_w=$const.

experimentally observed $k(e)$ relationship by a power law, efforts should be directed toward obtaining a good fit near the wall shear rate e_w. The parameters n, e_t, and k_o can be evaluated from the known function $k=k(e)$ using the following expressions

$$n=(e_w/k_w)\,(dk/de)_{e=e_w} \tag{14a}$$

$$k_o=k(0) \tag{14b}$$

$$e_t=e_w\,(k_o/k_w)^{1/n} \tag{14c}$$

For design calculations and parameteric studies, scaling laws are convenient. These can be obtained for the very long and very short pipes by substituting $e\sim U/D$ and equation (4) into the respective results. The results are

For very long pipes:

$$h\sim k_w/D\sim (Ud^2)^n k_o^{\,1-n} D^{-1-n} \tag{15a}$$

For very short pipes:

$$h\sim k_w/D\sim (Ud^2/D)^{2n/3} k_o^{\,2(1-n)/3}\,(U/D)^{1/3} \tag{15b}$$

No such simple scaling law is possible for the general case of thermally developing flows. It is expected that for this general case, the dependence of h on the parameters would lie some where between those of the two limiting cases.

One of the values of the present analysis is to provide a glimpse of the extent of heat transfer enhancement that might be possible from the use of slurries as heat transfer fluids. To this end, Fig. 4 shows a comparison between the heat transfer coefficients, expressed in Nusslet numbers based on k_o, for several values of k_w/k_o with $n=0.5$. Significant increase in heat transfer coefficients for the case of enhanced thermal conductivity is noted. As a more physical illustration, the estimated increases of thermal conductivity and heat transfer coefficient in slurry flow in pipes for several combinations of particle sizes, pipe diameters, and velocities are shown in Table 2. It is seen that rather dramatic increases of the heat transfer coefficient are predicted for some range of conditions. Because the present analysis neglects the particle-depleted layer and other complexities of slurry flows, it is not known whether the predicted high heat transfer coefficents can actually be realized in practice. Experimental studies to verify these predictions would be desirable.

The thought of using slurries as heat transfer fluids might strike some engineers as being too radical. After all, conventional pumps and fluid handling equipments may no longer be suitable. However, one must admit that potential rewards in high heat transfer rates are tantalizing. Furthermore, slurries have at least another potential advantage, i.e., their natural antifouling properties. On the other hand, the use of suitable liquid–liquid, two-phase mixtures may lead to heat transfer enhancement without the handling difficulties. These possibilities suggest exciting frontiers worthy of further exploration.

Acknowledgment

The authors wish to acknowledge their appreciation to the Heat Transfer Program, National Science Foundation, for its support through Grant No. ENG-78-15692.

References

1 Keller, K. H., "Effects of Fluid Shear on Mass Transport in flowing Blood," *Fed. Proc.*, Vol. 30, 1971, pp. 1591–1599.

2 Turritto, V. T., Venis, A. M., and Leonard, E. F., "Platelet Diffusion in flowing Blood, *I/E Chem. Fundam.*, Vol. 11, 1972, pp. 216–223.

3 Ahuja, A. S., "Augmentation of Heat Transport in Laminar Flow of Polystyrene Suspensions: I. Experiments and Results," *J. Appl. Phys.*, Vol. 46, 1975, pp. 3408.3416.

4 Eckstein, E. C., Bailey, D. G., and Shapiro, A. H., "Self-Diffusion of Particles in Shear Flow of a Suspension," *J. Fluid Mech.*, Vol. 79, 1977, pp. 191–208.

5 Sohn, C. W., and Chen, M. M., "Microconvective Thermal Conductivity in Disperse Two-Phase Mixtures as Observed in a Low Velocity Couette Flow Experiment," ASME JOURNAL OF HEAT TRANSFER, Vol. 103, 1981, pp. 47–51.

6 King, D., and Chen, M. M., "A Simple Theoretical Model for Shear Enhanced Transport in Disperse Two-Phase Mixtures," presented at the 1982 ASME WAM, Phoenix, Ariz. 1982, Paper No. 82-WA/HT-46.

7 Chen, M. M., "On Continuum Formulation of Platelet and Related Transport pertaining to Thrombogenesis," Paper No. 4a, presented at the AIChE Natl. Mtg., June 2–5, 1974, Pittsburg, Pa.

8 Vand, V., "Viscosity of Solutions and Suspensions," *J. Phys. Coll. Chem.*, Vol. 52, 1948, pp. 277–299.

9 Goldsmith, H. L., and Mason, S. G., "The Microrheology of Dispersions," *Rheology-Theory and Applications*,. Vol. 4, eidted by F. R. Eirich, Academic Press, New York, 1967, pp. 82–250.

10 Rutgers, Ir. R., "Relative Viscosity of Suspensions of Rigid Spheres in Newtonian Liquids," *Rheol. Acta*, Band 2, 1962, pp. 202–210.

11 Karnis, A., Goldsmith, H. L., and Mason, S. G., "The Kinetics of Flowing Dispersions, I. Concentrated Suspensions of Rigid Particles," *J. Colloid Sci.*, Vol. 22, 1966, pp. 531–553.

12 Shah, R. K., and London, A. L., *Laminar Flow Forced Convection in Ducts*, Advances in Heat Transfer, Supplement 1, Academic Press, New York, 1978.

13 Sellars, J. R., Tribus, A., and Klein, J. S., "Heat Transfer to Laminar Flow in a Round Tube for Flat Conduit-The Graetz Problem Extended," ASME Transactions, Vol. 78, 1956, pp. 441–448.

14 Siegel, R. E., Spparow, E. M., and Hallman, T. M., "Steady Laminar Heat Transfer in a Circular Tube with Prescribed Wall Heat Flux," *Appl. Sci. Res.*, Ser. A, Vol. 7, 1958, pp. 386–392.

15 Leveque, M. A., "Les lois de la Transmission de Chaleur par Convention," *Ann. Mines*, Vol. 13, 1928, pp. 210–239.

16 Sohn, C. W., "Heat Transfer in Laminar Solid-Fluid Supsension Flow," Ph. D. thesis, University of Illinois, Urbana, Ill., 1980.

Simplified Analysis of Air-Bubble Plumes in Moderately Stratified Environments

N. A. Hussain
Associate Dean.
Mem. ASME

B. S. Narang
Professor of Aerospace Engineering.

College of Engineering,
San Diego State University,
San Diego, Calif. 92182

This paper is concerned with the behavior of buoyant plumes driven by rising gas bubbles through a moderately stratified liquid environment. A two-phase mathematical model is proposed for calculating the induced turbulent vertical liquid flow and its temperature. Simultaneous numerical solutions of the continuity, momentum, and energy equations are obtained for the two cases of an axisymmetric and a two-dimensional air jet submerged in water. Water pumping rates, liquid velocities, plume radii (widths), and temperatures are obtained as a function of air flow rates, depth of submergence, and the assumed temperature profile of the water in the region far away from the jet. Effects of temperature stratification in the liquid region far away from the jet resulted in increased liquid flow rates as well as increased plume cross-section areas. Comparisons are made with the experimental information available in the literature.

Introduction

Buoyant plumes driven by a source of gas bubbles have found a number of successful applications over the years. Bubble plumes have been used to prevent parts of the surface of a river or a lake from freezing over [1-2]. Oil slicks on water surfaces can be contained by bubble plumes [3]. Bubble plumes have also been used as barriers against saltwater intrusion in rivers and lakes, and for aeration in water purification and waste treatment plants. Protection from underwater explosion damage is another application.

In recent year, some analytical work has been done aimed at defining models of isothermal buoyant plumes. Cederwall and Ditmars [4] suggested a model that is based on the similarity of bubble plumes and buoyant plumes. The bubble distribution is then represented by a Gaussian density distribution across the plume and a virtual origin of 0.8 m below the injection plate is necessary to fulfill the boundary conditions of zero momentum flux and mass flux of water at the position of the virtual origin. This allows a starting solution presented for that of a simple plume to be used which leads to a solution that is only valid well above the injection point. Kobus [5] presented a model which is similar to that of [4]. The relative bubbble velocity was assumed to be negligible compared to the water velocity for small air rates and the entrainment coefficient was adjusted in terms of the slip velocity in order to find an appropriate solution. A second approximate solution was found for large air rates when the averaged bubble velocity is considered constant. Kobus's experimental results were in agreement with these two hypotheses.

Hussain and Siegel [6], based on observations of a stream of air bubbles rising through liquid water, treated the plume as double-zoned liquid jet in which the inner zone consisted of a single row of big bubbles with their wakes rising from a single orifice. The outer zone consisted only of entrained liquid. The key parameter in this model is again the entrainment coefficient. The value for a single phase jet was used as a basis, corrected for the gas liquid density ratio and for the relative bubble motion in the inner zone.

Most recently Milgram [13] presented experimental data obtained for an axisymmetric bubble plume in an isothermal environment. Milgram's experiments took place in Bugg Spring, which is a natural sinkhole spring located at Okalumpka, Florida. Experiments for measuring velocity profiles were conducted with a gas outlet depth of 50 m and gas flow rates up to 0.59 normal m^3/s. Based on these experimental data, Milgram developed a numerical model based on the integral formulation of the conservative equations. Gaussian velocity profiles were used and the entrainment coefficent was taken to be a variable that depends on both the gas flow rate and the depth. Hussain and Narang [7] extended the analysis of the axisymmetric jet model, developed by Hussain and Siegel [6], to the two-dimensional case. The axisymmetric air-bubble plumes will exist when air is released from a single orifice submerged in water. The two-dimensional air-bubble plumes will exist when the air is released from either a perforated tube or a tube with longitudinal slot submerged in water. Top-hat velocity profiles were employed by Hussain et al. [6-7], in contrast to Guassian velocity distributions that were employed by [4, 5, 13]. McDougall [10] reported on the behavior of bubble plumes in highly stratified environments. McDougall's experimental observations led him to develop a model very much similar to the one developed earlier by Hussain and Siegel [6]. The numerical results reported by McDougall indicate that the rate of spreading of the plume increases with increasing stratification level in the liquid. McDougall's theoretical model employs top-hat velocity and temperature profiles.

In all the aformentioned investigations, the bubble plumes were assumed to be isothermal and thus no stratification effects were considered. Recently Goossens [8] presented a study of reservoir destratification with bubble columns. The plume model suggested by Goossens [8] has three stages of development. The first stage is where the liquid moves only in the bubble wakes. This region is of negligible height. The second stage starts with a short contraction, which is followed by an entraining region. The third stage is located near the water surface, the liquid ceases entraining and flows off radially. The entrainment coefficient for the second stage was determined experimentally.

The purpose of the present investigation is to extend the analysis of Hussain et al. [6, 7], to include the effect of temperature stratification for both the axisymmetric jet as well as the two-dimensional jet.

Analysis

(i) Axisymmetic Air-Bubble Plumes. The axisymmetric,

Contributed by the Heat Transfer Division for publication in the JOURNAL OF HEAT TRANSFER. Manuscript received by the Heat Transfer Division August 29, 1983. Paper No. 83-HT-69.

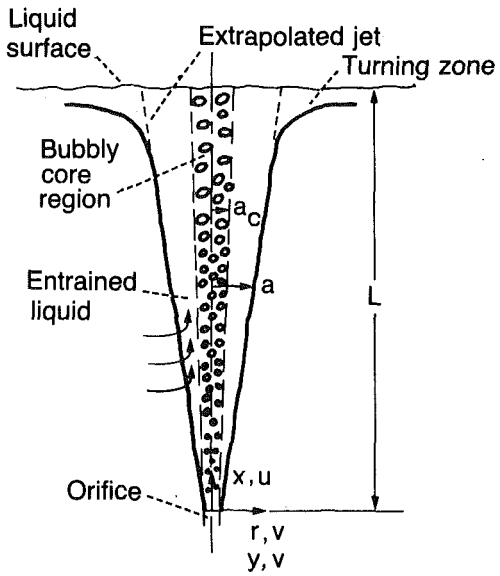

Fig. 1 Configuration of liquid jet induced by rising column of gas bubbles

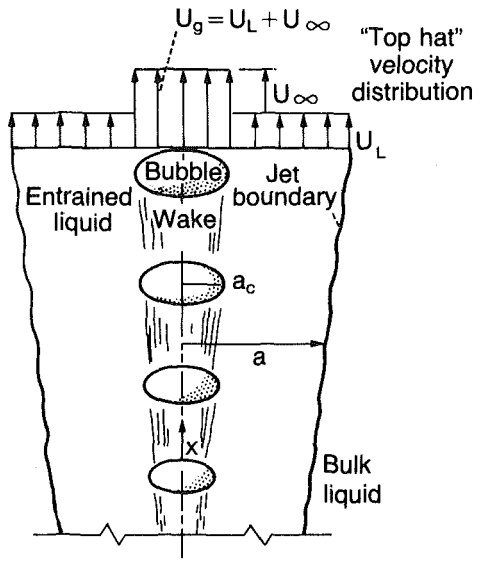

Fig. 2 Details of the proposed mathematical model for studying the two-phase jet

two-phase jet considered here is essentially that of Hussain and Siegel [6] and is shown in Fig. 1. The flow field is assumed to be steady and fully turbulent. The liquid field is nonisothermal, and therefore, the liquid density is considered to be a function of temperature. The gas density is assumed to vary according to the ideal gas law. In the present investigation no attempt has been made to analyze the jet's turning zone when it reaches the liquid surface. It is also assumed that the gas leaves the submerged orifice with negligible upward momentum. The bubbles are assumed to be sufficiently large so that their drag is fully turbulent, and hence they rise at a constant terminal velocity relative to the liquid. The local bubble velocity is assumed equal to the local liquid velocity plus the bubble terminal velocity.

It is important to note that the present two-phase plume is different from the single-phase buoyant plume in a stratified environment. Morton [9] has indicated that a height is reached where the plume stops rising and starts spreading out due to the decrease in the buoyancy forces. For a bubble plume in a moderately stratified environment, the bubbles in the inner region of the plume obviously will continue to rise to the liquid surface where they burst out. However, the rising entrained liquid, in both the inner and the outer region of the plume, will turn at the liquid surface and move horizontally outward as shown in Fig. 1. McDougall [10] observed that some of the liquid in the outer part of a bubble plume in a highly stratified environment can leave the plume and spread out horizontally at its own density level.

Gas Continuity. It is assumed that in the central region of the jet, bubbles are rising in a chain bubble fashion and that $1/(K+1)$ of the vertical height is occupied by the gas bubble and $K/(K+1)$ is occupied by the liquid wake. This is shown in Fig. 2. For a fixed gas flow rate, the mass flow rate, M_g, of the gas at any depth x can be written as

$$M_g = \int_o^{a_c} \frac{2\pi r}{k+1} \rho_g U_g dr = \text{Constant} \tag{1}$$

Where the gas density is given by the ideal gas law

$$\rho_g = \frac{1}{RT}[P_a + \rho_l (L-x)] \tag{2}$$

Liquid Continuity. The following equation accounts for the liquid carried into the liquid region and also into the bubble wakes of the jet by the turbulent entrainment

$$\frac{d}{dx}\left[\frac{k}{(k+1)}\int_o^{a_c} 2\pi\rho_l r U_g dr + \int_{a_c}^{a} 2\pi r \rho_l U_l dr\right]$$

$$= -(2\pi\rho_l r v)_{r\to\infty} = 2\pi E a \rho_{lo} U_l \tag{3}$$

Nomenclature

a = radius or half width of jet, as appropriate, m
a_c = radius (or half width) of inner zone of jet, m
C_{pg} = specific heat capacity of gas at constant pressure, J/K kg
C_{vl} = specific heat capacity of liquid at constant volume, J/K kg
E = entrainment coefficient
E_0 = entrainment constant
F_D = drag force (see equation (4))
g_c = universal gravitational constant, 1.0 kgm/Ns^2
h_g = specific enthalpy of gas, J/kg
h_{li} = specific enthalpy of the liquid inside the jet, J/kg
h_{lo} = specific enthalpy of the liquid outside the jet, J/kg
k = ratio of wake volume to bubble volume
L = depth of gas source below liquid surface, m
M_g = mass flow rate of gas, kg/s (kg/s m for two-dimensional jet)
M_l = mass flow rate of liquid pumped, kg/s (kg/s m for two-dimensional jet)
P_a = atmospheric pressure, 1.0132 $\times 10^5$ N/m^2
Q_l = volumetric flow rate of liquid pumped, m^3/s
r = radial coordinate for the axisymmetric plume
ρ_g = gas density kg/m^3
ρ_l = liquid density kg/m^3
ρ_{lo} = jet's ambient liquid density kg/m^3
T_g = gas temperature, K
T_{lo} = ambient liquid temperature, K
U_∞ = bubble terminal velocity, m/s
U_g = gas velocity, m/s
U_l = liquid velocity, m/s
x = depth of fluid, m
y = transverse coordinate for the two-dimensional plume
σ = surface tension, N/m

Gas and Liquid Momentum. The upward buoyancy force of the bubble is balanced by a small change of bubble momentum and a large drag force F_D of the liquid on the bubbles:

$$\int_o^{a_c} \frac{g}{k+1}(\rho_l-\rho_g)2\pi r\,dr=\frac{d}{dx}\left[\int_o^{a_c}\frac{1}{k+1}2\pi r\rho_g U_g^2 dr\right]+F_D \tag{4}$$

Where $F_D=\dfrac{d}{dx}\left[\int_o^{a_c}\dfrac{k}{k+1}2\pi r\rho_l U_g^2 dr+\int_{a_c}^{a}2\pi r\rho_l U_l^2 dr\right]$

Gas and Liquid Energy Equation. The body of water containing the plume is assumed to be infinite and to have no ambient flow pattern. This limits the present model to regions very close to the jet. Although the gas may emerge at a temperature different from the water temperature at that location, the heat transfer between the water and the gas bubble will soon ensure that the bubbles are at the same temperature as that of water. This has been shown to be true by McDougall [10]. Consequently, one can assume that the thermal gradients are small and therefore energy transport by conduction can be ignored compared to that caused by the adiabatic turbulent mixing. Based on this assumption, the energy equation may be written as

$$\frac{d}{dx}\left[\frac{2\pi}{k+1}\left\{\int_o^{a_c} rU_g\rho_g h_g dr+\int_o^{a_c} r\rho_g\frac{U_g^3}{2g_c}dr+\int_o^{a_c} r\rho_g U_g\frac{g}{g_c}x\,dr\right\}\right.$$
$$\left.+\frac{2\pi k}{k+1}\left\{\int_o^{a_c} r\rho_l U_g h_{li}\,dr+\int_o^{a_c} r\rho_l\frac{U_g^3}{2g_c}dr+\int_o^{a_c} r\rho_l U_g\frac{g}{g_c}x\,dr\right\}\right.$$
$$\left.+2\pi\left\{\int_{a_c}^{a} r\rho_l U_l h_{li}dr+\int_{a_c}^{a} r\rho_l\frac{U_l^3}{2g_c}dr+\int_{a_c}^{a} r\rho_l U_l\frac{g}{g_c}x\,dr\right\}\right]$$
$$=2\pi a\rho_{lo}U_l E\left[h_{lo}+\frac{\bar{v}_l^2}{2g_c}+\frac{g}{g_c}x\right] \tag{5}$$

Where $\bar{v}_l$ is the average local velocity of the liquid that is being entrained by the jet at $r = a$, which has to be determined.

The total mass that is being entrained by the two-phase jet at any x is given in equation (3) and is equal to $2\pi Ea\rho_{lo}U_l\,dx$.

Since this entrained mass has to enter the jet through its outer boundary, then it is plausible to write that this entrained mass is also equal to $2\pi a\rho_{lo}\bar{v}_l dx$. Therefore, $\bar{v}_l$ may be written as

$$\bar{v}_l = E\,U_l. \tag{6}$$

Many previous researchers [4, 5, 8] have assumed that the average vertical velocity profile could be represented by a Gaussian velocity profile given by

$$U(r,x)=U(x)\exp\left(-\frac{r^2}{b^2}\right)$$

where b is an effective radius of the plume. This has some experimental support in unstratified surroundings as shown by Kobus [5], but in any case the exact form of the profile is not important in determining the physics of the model; the only essential assumption is that the profiles are similar at all heights. Therefore, for the integration of equations (1), (3), (4), and (5), "top hat" velocity and temperature profiles have been assumed for convenience. This has yielded good results for free convection plumes [9].

$$U_g(x,r)=U_g(x)\quad 0\le r\le a_c(x) \tag{7a}$$

$$U_l(x,r)=\begin{cases}U_l(x) & a_c(x)<r\le a(x)\\ 0 & r>a(x)\end{cases} \tag{7b}$$

$$T_g(x,r)=T_{li}(x,r)=T(x)\ \text{for}\ 0\le r\le a(x) \tag{7c}$$

$$T_l(x,r)=T_{lo}(x)\quad r>a(x) \tag{7d}$$

U_g and U_l are related by

$$U_g(x)=U_l(x)+U_\infty \tag{8}$$

where U_∞ is the terminal velocity of a single bubble rising in a large region of quiesecent liquid.

Expression for Entrainment Coefficient. The term $2\pi\rho_{lo}aU_lEdx$ represents the total mass being physically entrained at the jet's boundary. For a single-phase jet, when the density in the plume is the same as that of the surrounding fluid, E is taken as a constant. Ricou and Spalding [11] suggest that for the case of a single-phase axisymmetric jet, the value of E should be modified by a multiplicative factor of $(\rho_g/\rho_l)^{1/2}$. Based on the concept that the entrainment depends on the square root of the excess momentum flux in the jet, Hussain and Siegel [6] further suggest that the entrainment also depends on the velocity of jet relative to its surroundings and on the interfacial area between the jet and the surrounding region.

Accordingly, the expression for entrainment can be written as

$$E=E_o\left[1+\left(\frac{k}{k+1}\right)\left(\frac{a_c}{a}\right)\left(\frac{U_\infty}{U_l}\right)+\left(\frac{\rho_g}{\rho_{lo}}\right)^{1/2}\frac{1}{k+1}\left(\frac{a_c}{a}\right)\left(\frac{U_\infty}{U_l}\right)\right] \tag{9}$$

Equations (2–8), and (9), together with equations (1, 3–5) and by expressing $h_l = C_{vl}T + P/\rho_l$ and $h_g = C_{p_g}T$ result in the following

$$M_g=\frac{\pi a_c^2}{k+1}\rho_g U_g=\text{Constant} \tag{10}$$

$$\begin{bmatrix}C_1 & C_1 & C_3\\ M_1 & M_2 & M_3\\ E_1 & E_2 & E_3\end{bmatrix}\begin{bmatrix}\dfrac{dT}{dx}\\ \dfrac{dU_l}{dx}\\ \dfrac{da}{dx}\end{bmatrix}=\begin{bmatrix}C_4\\ M_4\\ E_4\end{bmatrix} \tag{11}$$

Where C_i, M_i, and E_i are given in the Appendix.

Now the system of equations (11) is solved to give

$$\frac{da}{dx}=\frac{C_1M_2E_3-C_1M_4E_2-C_2M_1E_4+C_2M_4E_1+C_4M_1E_2-C_4M_2E_1}{C_1M_2E_3-C_1M_3E_2-C_2M_1E_3+C_2M_3E_1+C_3M_1E_2-C_3M_2E_1}$$
$$=F(U_l,a,T,x) \tag{12}$$

$$\frac{dU_l}{dx}=\frac{C_1M_4E_3-C_1M_3E_4-C_4M_1E_3+C_4M_3E_1+C_3M_1E_4-C_1M_4E_1}{C_1M_2E_3-C_1M_3E_2-C_2M_1E_3+C_2M_3E_1+C_3M_1E_2-C_3M_2E_1}$$
$$=G(U_l,a,T,x) \tag{13}$$

and

$$\frac{dT}{dx}=\frac{C_4M_2E_3-C_4M_3E_2-C_2M_4E_3+C_2M_3E_4+C_3M_4E_2-C_3M_2E_4}{C_1M_2E_3-C_1M_3E_2-C_2M_1E_3+C_2M_2E_1+C_3M_1E_2-C_3M_2E_1}$$
$$=H(U_l, a, T, x) \tag{14}$$

The differential equations (12-14) may be solved simultaneously by using the Runge-Kutta method for any given M_g and any given temperature distribution T_o (x) and the associated density distribution ρ_{lo} (T) in the liquid region far away from the jet.

At $x = 0$, $a = a_c$, $T = T_o$ $(x = 0)$, and $U_l = 0$, so that $U_g = U_\infty$. Then the initial conditions at $x = 0$ to begin the integration are from equation (10)

$$a(x=0)=\left[\frac{(k+1)M_g}{\pi U_\infty \rho_g}\right]^{1/2}$$

The latter condition, $U_l(0) = 0$, however, causes starting difficulty in the integration, since it is in the denominator of a few terms, so a small value of U_l was used ($U_l(0) = .001$). The calculations using values smaller than 0.001 made no significant difference.

***(ii)* Two-Dimensional Air-Bubble Plumes.** The two-dimensional, two-phase jet considered here is similar to that shown in Fig. 1 except that the circular orifice is replaced by a slot or a row of orifices. Employing analysis very much similar to the analysis of the previous section, the governing equations of continuity, momentum, and energy, respectively, are

$$M_g=\int_o^{a_c}\frac{2}{(k+1)}u_g\rho_g dy=\text{constant} \tag{15}$$

$$\frac{d}{dx}\left[\int_o^{a_c}\frac{k}{(k+1)}\rho_l u_g dy+\int_{a_c}^{a}\rho_l U_l dy\right]=E\rho_{lo}U_l \tag{16}$$

where

$$\rho E=E_o\left[1+\frac{k}{k+1}\frac{U_\infty}{U_l}+\frac{1}{k+1}\left(\frac{\rho_g}{\rho_{lo}}\right)^{1/2}\frac{U_\infty}{U_l}\right] \tag{17}$$

$$\int_o^{a_c}\frac{g}{k+1}(\rho_l-\rho_g)dy=\frac{d}{dx}\left[\int_o^{a_c}\frac{1}{k+1}\rho_g U_g^2 dy+\int_o^{a_c}\frac{k}{k+1}\rho_l U_g^2 dy+\int_{a_c}^{a}\rho_l U_l^2 dy\right] \tag{18}$$

$$\frac{d}{dx}\left[\frac{1}{k+1}\left\{\int_o^{a_c}\rho_g U_g h_g dy+\int_o^{a_c}\rho_g U_g\frac{U_g^2}{2g_c}dy+\int_o^{a_c}\rho_g U_g\frac{g}{g_c}x dy\right\}+\frac{k}{k+1}\left\{\int_o^{a_c}\rho_l U_g h_{li}dy+\int_o^{a_c}\rho_l U_g\frac{U_g^2}{2g_c}dy+\int_o^{a_c}\rho_l U_g\frac{g}{g_c}x\,dy\right\}+\int_{a_c}^{a}\rho_l U_l h_{li}dy+\int_{a_c}^{a}\rho_l U_l\frac{U_l^2}{2g_c}dy+\int_{a_c}^{a}\rho_l U_l g_c x\,dy\right]=Eo_{lo}U_l\left[h_{lo}+\frac{\tilde{v}^2}{2g_c}+\frac{g}{g_c}x\right] \tag{19}$$

where

$$\tilde{v}=E_o\left[U_l+\frac{k}{k+1}U_\infty+\frac{1}{k+1}\left(\frac{\rho_g}{\rho_{lo}}\right)^{1/2}U_\infty\right]$$

The following "top-hat" velocity and temperature profiles are assumed:

$$U_g(x,y)=U_g(x)\quad 0\le y\le a_c(x)$$

$$U_l(x,y)=\begin{cases}U_l(x) & a_c(x)<y\le a(x)\\ 0 & y>a(x)\end{cases}$$

$$T_g(x,y)=T_{li}(x,y)=T(x)\ \text{for}\ 0\le y\le a(x)$$

$$T_l(x,y)=T_{lo}(x)\quad \text{for}\ y>a(x) \tag{20}$$

the U_g and U_l are related as before by

$$U_g(x)=U_l(x)+U_\infty$$

Again, equations (2) and (20), together with (15-19), result in

$$M_g=\frac{2}{k+1}\rho_g a_c U_g \tag{21}$$

and

$$\begin{bmatrix}C_1' & C_2' & C_3'\\ M_1' & M_2' & M_3'\\ E_1' & E_2' & E_3'\end{bmatrix}\begin{bmatrix}\frac{dT}{dx}\\ \frac{dU_l}{dx}\\ \frac{da}{dx}\end{bmatrix}=\begin{bmatrix}C_4'\\ M_4'\\ E_4'\end{bmatrix} \tag{22}$$

Where C_i', M_i', and E_i' are given in the Appendix.

Solving the system of equations (22) for da/dx, dU_l/dx, and dT/dx result in identical relations to those which are given in equations (12), (13), and (14), except that each and every C, M, and E is replaced by C', M', and E'. These equations may be integrated by using the Runge-Kutta method as in the case of axisymmetric jet.

Again, at $X = 0$, $a = a_c$, $T = T_{lo}(X = 0)$, and $U_l = 0$ so that $U_g = U_\infty$. The initial conditions at $X = 0$ to begin the integration are from equation (21)

$$a(X=0)=\frac{(k+1)M_g}{2\rho_g U_\infty}$$

and $U_l(0) = 0$. For reasons mentioned earlier, U_l (0) is taken to be equal to 0.001.

Results and Discusssion

A number of quantities must be specified in order to compute the induced liquid flow and temperature of the liquid in the jet regions. The terminal velocity U_∞ of a single bubble in undisturbed fluid could be obtained from [12]

$$U_\infty=1.53\left[\frac{\sigma g(\rho_l-\rho_g)}{\rho_l^2}\right]^{1/4} \tag{23}$$

which yields a $U_\infty = 0.252$ m/s for air bubbles in water. A value of $E_o = 0.08$ for the axisymmetric two-phase jet and $E_o = 0.09$ for the two-dimensional, two-phase jet are recommended as is the case in [6, 7].

For given values of $T_{lo}(x)$, $\rho_{lo}(x)$, and L, one may solve for a (L), $U_l(L)$ and T (L) by integrating equation (12), (13), and (14) using the Standard IBM Library Subroutine on Runge-Kutta method. For the case of a two-dimensional jet, equation (12), (13), and (14), in which every C, M, and E is replaced by C', M', and E', are also integrated to $X = L$ to obtain a (L), U_l (L), and T (L).

The upward flow of liquid M_l pumped by the rising gas bubbles can be determined from the following equations:

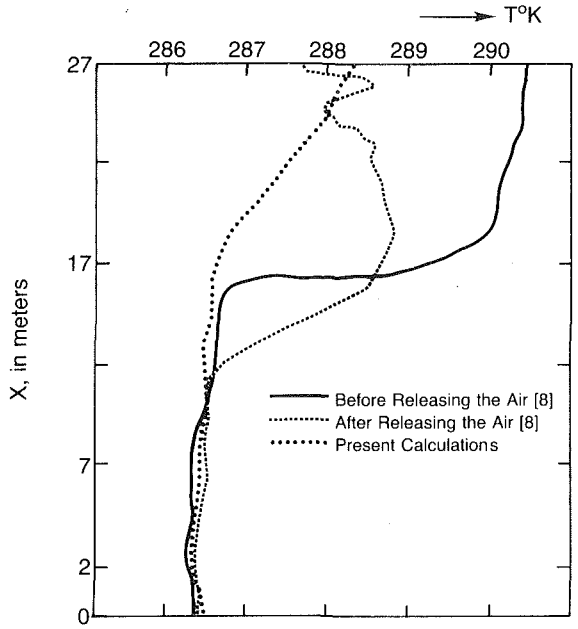

Fig. 3 Comparison of the performance of the present model with the experimental results of Goossens [8]

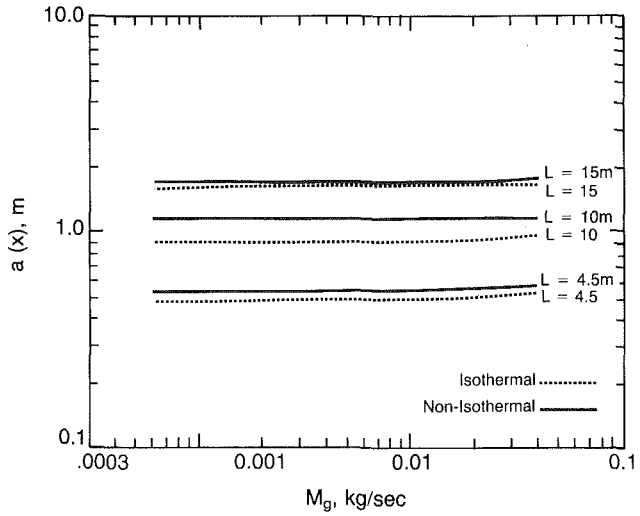

Fig. 4 Radius of rising jet at water surface versus mass flow rate of air

$$M_l = \pi (a^2 - a^2{}_c)\,\rho_l U_l + kM_g \frac{\rho_l}{\rho_g} \text{ (axisymmetric)} \qquad (24)$$

and

$$M_l = 2(a - a_c)\,\rho_l U_l + kM_g \frac{\rho_l}{\rho_g} \text{ (two-dimensional)} \qquad (25)$$

where the a_c in the foregoing two equations is obtained from equation (10) and (21), respectively.

In order to establish some level of confidence in the proposed analysis, it is imperative that the results obtained by means of the present model be comparable to those obtained experimentally. Unfortunately, the available experimental data in the literature are very limited. This is especially true for the case of measurement of thermal profiles associated with air-bubble plumes in water. Goossens's [8] study appears to be the only one which gives experimental measurements of temperature data associated with air-bubble plumes. Goossens gathered his data in the Hondered-en-Dertig reservoir in Holland. That reservoir has an area of 2km^2 and

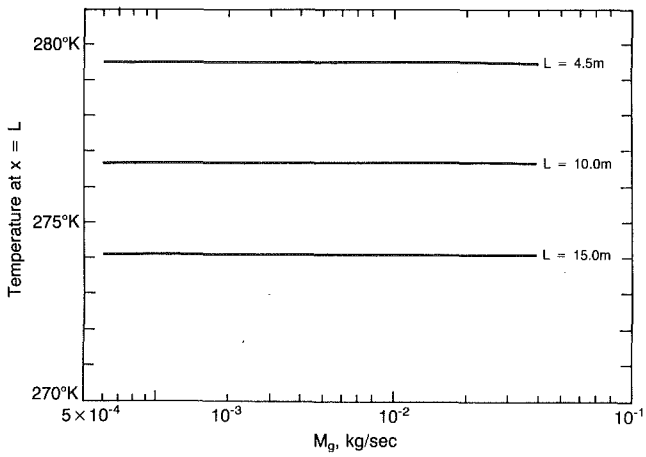

Fig. 5 Temperature of water being pumped to the surface versus mass flow rate of air for the symmetric jet

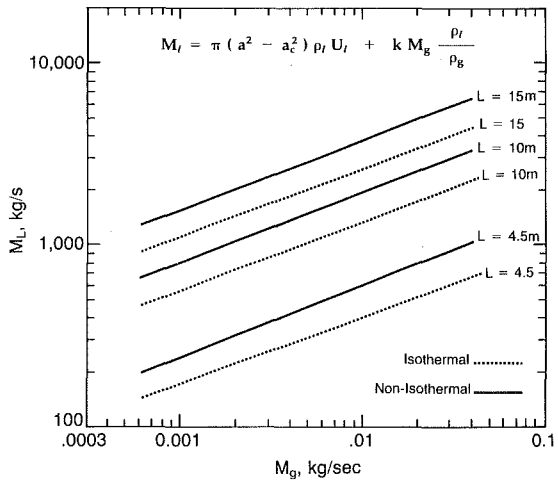

Fig. 6 Liquid pumped to the surface versus mass flow rate of air for the axisymmetric jet

a depth of 27 m. Goossens measured the temperature distribution in the reservoir as a function of depth prior to and after the onset of the air injection which was released at the bottom of the reservoir from a circular orifice at a gas flow rate of 12 m^3/min.

Using the above gas flow rate and the initial temperature distribution reported by Goossens, calculation are made to obtain the axial temperature distribution in the plume. Goossens's temperature distribution could be very closely approximated by the following relations:

$$T_{lo}(x) = \begin{cases} 0.02x + 286.3 & \text{for } 0 \le x < 16 \text{ m} \\ 1.13x + 268.53 & \text{for } 16 \le x < 19 \text{ m} \\ 0.06x + 188.8 & \text{for } 19 \le x \le 27 \text{ m} \end{cases}$$

The values of $E_o = 0.08$ and $U_\infty = .252$ m/s are used. The results of the present calculations are shown in Fig. 3.

Comparing the numerical results with those of Goossens, one can see that the maximum difference between the presently calculated data and those measured by Goossens is about 48 percent. In the region near the water surface, the calculated results are within 13 percent of the experimental data. These calculations are based on using the maximum overall temperature difference of 4.25°K between $x = 0$ and $x = 27$ m as the normalizing characteristic temperatrue. These results are very encouraging since the present model considers a very simplified mode of analysis. More experimental data

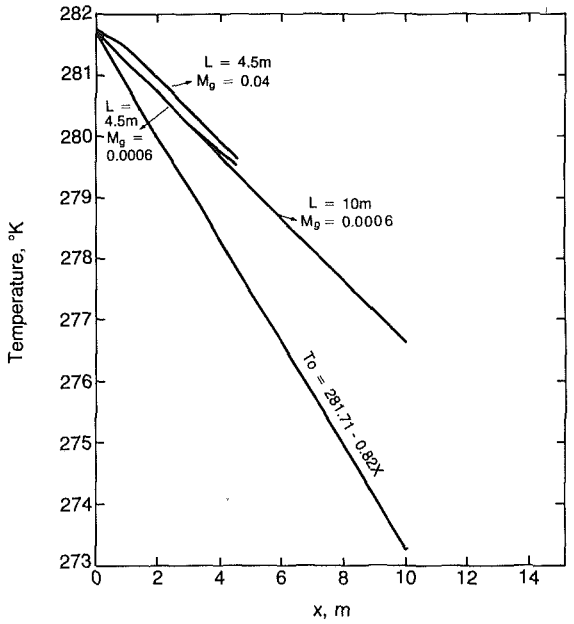

Fig. 7 Temperature distribution in axisymmetric jet

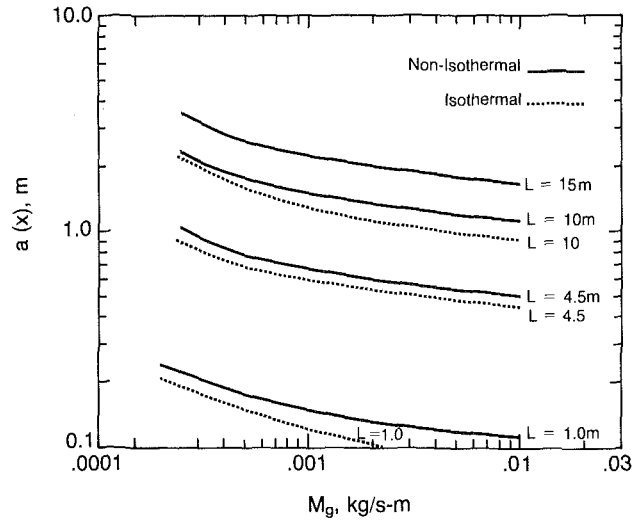

Fig. 8 Half-width of jet at liquid surface versus mass flow rate of air

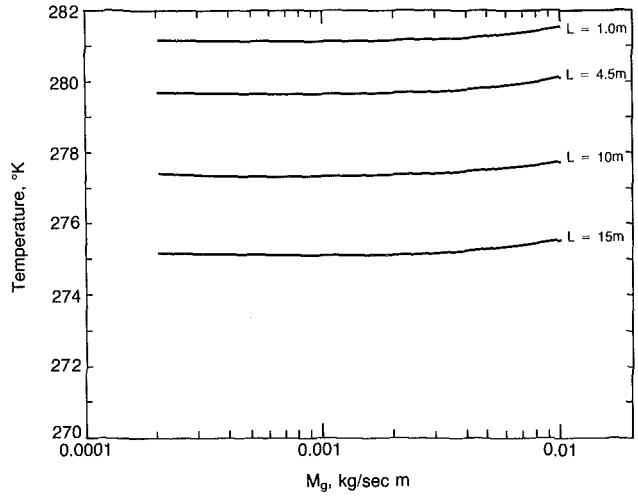

Fig. 9 Temperature of water being pumped to the surface versus mass flow rate of air for the two-dimensional jet

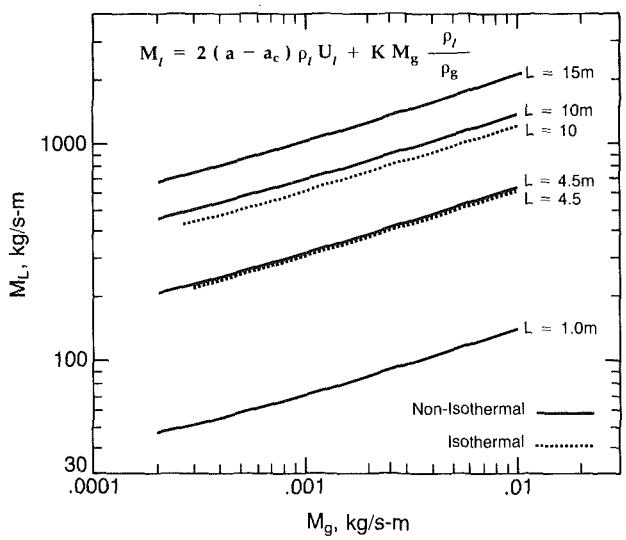

Fig. 10 Liquid pumped to the surface versus mass flow rate of air for the two-dimensional jet

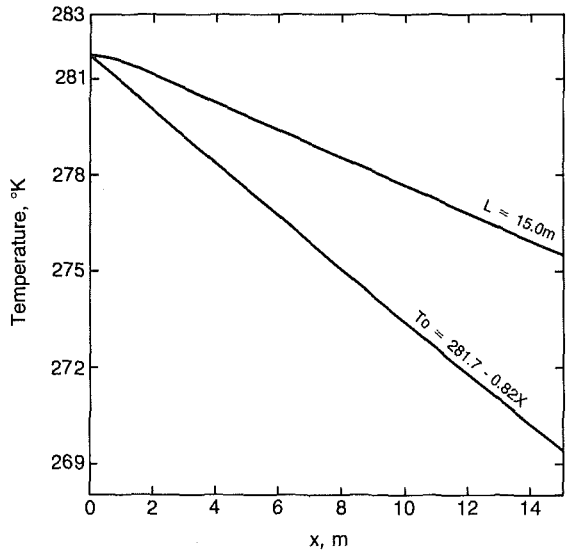

Fig. 11 Temperature distribution in a two-dimensional jet

are naturally needed before any further refinements are warranted. No liquid mass flow rates were reported by Goossens and, therefore, no comparison could be made here for this particular case.

Since the main purpose of the present investigation is to study the effects of the temperature stratification in water on the performance of the two phase plume, it is, therefore, important to compare the nonisothermal results which are obtained using the present analysis with those obtained previously by Hussain et al for the isothermal case.

The results presented below are with regard to the prevention of ice formation in lakes by raising warm bottom water to the surface. For some small lakes, the water temperature profiles under ice cover may be represented by a linear profile $T_{lo}(x) = 281.7 - 0.82$ x [1], Using this temperature distribution in the water surrounding the jet, calculations are made to predict $a(x)$, $U_l(x)$, $M_l(x)$, and $T(x)$. These results are presented in Figs. 4-6 for the axisymmetric jet, and in Fig. 8-10 for the two-dimensional case. Some of the comparisons between the jet's temperature distribution with the ambient water temprature distribution are shown in Fig. 7 for the axisymmetic jet, and in Fig. 11 for

the two-dimensional jet. It is worthwhile to mention that for the temperature distribution in the liquid considered here, the maximum change in the water density is only 0.128 percent. Therefore, the liquid density, with a good degree of approximation, could be considered as constant.

It is interesting to note that the results of the nonisothermal and the isothermal analysis exhibit the same general behavior: For the axisymmetric jet, the rates of liquid pumped to the surface, when temperature stratification is considered, are generally larger by as much as 37 percent than those obtained when the liquid is considered to be at a uniform temperature [6].

The liquid mass flow rates that are being pumped to the liquid surface may be obtained by the following approximate relation

$$M_l = 286.28\, M_g^{.367}\, L^{1.57} \tag{26}$$

Table 1 shows comparison of the present study with that of [6] and with the limited data of Kobus [5]. A comparison between the reported experimental results of Milgram [13] and the present numerical model for a rising axisymmetric bubble plume in an iosthermal environment is shown in Table 2.

The effects of the temperature stratification on the analysis of two-dimensional jets are less noticeable. The increase in the liquid mass flow rates is within 5 percent of those of Hussain and Narang [7] for the isothermal case. It is interesting that the present results for the two-dimensional jet may be predicted as follows

for

$$M_g < .001 \text{ kg/s m}$$
$$M_l = 332.57\, M_g^{.23}\quad L^{.994} \tag{27}$$

and for

$$M_g > .001 \text{ kg/s m}$$
$$M_l = 594.6\, M_g^{.313}\quad L^{.996} \tag{28}$$

Another effect of the temperature stratification appears to be wider plumes at the liquid surface as compared to the isothermal cases [6, 7]. The two-dimensional plumes are as much as 26 percent wider while the axisymmetric plumes are 12 percent larger.

Although it is true that the present results are limited in their applicability to the assumed ambient liquid temperature distribution surrounding the jet, the present paper has presented a simplified mode of analysis by which one can estimate the liquid pumping rates and the temperature of the liquid that is being pumped to the surface. With this information one can accurately calculate the amount of surface ice which can be melted for a given gas mass flow rate.

Conclusions

A simplified analysis of air bubble plumes in a moderately stratified water environment is presented. The mathematical model of Hussain et al. [6, 7] is extended to include the effects of moderate stratification in the temperature of the liquid. The results of the present analysis indicate that the rate of liquid carried upward in an axisymmetric jet driven by a rising stream of gas bubbles is very much affected by the degree of stratification originally present in the liquid environment. However, in the case of a two-dimensional jet driven by rising gas bubbles, the rate of liquid carried upward is not significantly affected by the stratified liquid environment.

The effect of temperature stratification are noticeable on the plume radius for the axisymmetric case and the plume's half-width for the two-dimensional case. The plume sizes are

Table 1 Volumetric pumping rates in an axisymmetric jet at a location 3.3 m above orifice submerged 4.5 m below surface

Air flow standard conditions	$\frac{\text{Volume water pumped}}{\text{Volume air release d}} = \frac{Q_l}{Q_g}$		
Q_g, m^3/s	Kobus [5]	Isothermal environment [6]	Stratified environment (present work)
.00255	86	73	91.7
.00420	67	54	67.7
.00620	62	42	53.6

Table 2 Comparison between the experimental data of Milgram [13] and the present numerical model for an axisymmetrical bubble plume in an iosthermal environment

	Milgram experimental data [13]			Present work (isothermal environment)			
x (m)	a (m)	U_l (m/s)	Q_l (m^3/s)	a (m)	U_l (m/s)	Q_l (m^3/s)	M_g (Kg/s)
1.98	.15	1.127	.077	0.285	1.029	.2546	
16.47	1.572	0.506	3.929	1.75	.5521	5.306	
25.82	1.967	.477	5.797	2.656	.4823	10.68	0.0294
37.81	2.466	.562	10.725	3.806	.4332	19.70	
43.90	2.895	.553	14.555	4.291	.4202	24.28	
46.95	3.191	.516	16.503	4.674	.411	28.23	
1.98	.257	1.542	.306	0.3616	1.546	0.5827	
16.47	1.732	.863	8.124	1.797	.9745	9.838	
25.82	2.476	.823	15.834	2.698	.858	19.57	
37.81	3.621	.838	34.475	3.841	.7765	35.92	0.1447
43.90	4.384	.743	44.811	4.323	.7547	44.23	
1.98	.328	1.74	0.552	.4445	1.821	.9896	
16.47	2.359	1.109	19.351	1.851	1.314	14.00	
25.82	3.583	0.971	39.102	2.751	1.164	27.53	0.347
37.81	5.365	0.906	81.840	3.894	1.057	50.16	
43.90	6.393	0.861	110.436	4.375	1.028	61.64	
46.95	6.955	0.823	124.919	4.756	1.009	71.52	
1.98	.412	2.105	1.041	.5513	2.025	1.617	
16.47	2.488	1.316	25.493	1.920	1.675	19.10	
25.82	3.615	1.188	48.652	2.821	1.493	37.00	
37.81	5.296	1.184	104.145	3.966	1.360	66.83	0.723
43.90	6.343	1.162	146.677	4.449	1.324	81.93	
46.95	6.944	1.129	170.688	4.830	1.301	94.91	

uniformly larger than those obtained under isothermal conditions.

From the present analysis one can calculate not only the mass flow rate of the liquid that is being pumped to the surface but also the temperature of the liquid as it arrives at the surface. More experimental data are needed to further check the accuracy of the analysis presented here.

References

1 Williams, G. P., "Winter Water Temperature and Ice Prevention by Air Bubbling," *The Engineering Journal*, Vol. 44, No. 3, Mar. 1961, pp. 79-84.

2 Baines, W., "The Principles of Operation of Bubbling Systems," *Proceedings Symposium on Air Bubbling*, National Research Council (Canada), May 1961, pp. 12-22.

3 Jones, W. T., "Air Barriers as Oil Spill Containment Devices," *Society of Petroleum Engineers Journal*, Apr. 1972, pp. 126-142.

4 Cederwall, K., and Ditmars, J. D., "Analysis of an Air Bubble Plume," W. M. Keck Lab. of Hydraulics and Water Resources, Div. of Engng. and Appl. Sci., Cal. Inst. of Techn., Report No. KH-R-24.

5 Kobus, H. E., "Analysis of the Flow Induced by Air Bubble Systems," *Coastal Engineering Conference*, Vol. II, ch. 65, London 1968, pp. 1016-1031.

6 Hussain, N. A., and Siegel, R., "Liquid Jet Pumped by Rising Gas Bubbles," ASME *Journal of Fluids Engineering*, Vol. 98, No. 1, Mar. 1976, p. 49.

7 Hussain, N. A., and Narang, B. S., "Analysis of Two-Dimensional Air-Bubble Plumes," *AIChE Journal*, Vol. 23, No. 4, July 1977, p. 596.

8 Goossens, L., "Reservoir Destratification with Bubble Columns," Ph.D. thesis, Laboratorium Voor Fysische Technologie, Technische Hogeschoof Delft, Delft University of Technology, 1979.

9 Morton, B. R., Taylor, G. I., and Turner, J. S., "Turbulent Gravitational Convection from Maintained and Instantaneous Sources," *Proc. Roy. Soc.*, A 234, 1956, pp. 1-23.

10 McDougall, T. J., "Bubble Plumes in Stratified Environments," *Journal of Fluid Mechanics*, Vol. 85, Part 4, 1978, pp. 655-672.

11 Ricou, F. P., and Spalding, D. B., "Measurements of Entrainment by Axisymmetrical Turbulent Jets," *Journal of Fluid Mechanics*, Vol. II, pt. 1, Aug. 1961, pp. 21-32.

12 Zuber, N., and Findley, J. A., "Average Volumetric Concentration in Two-Phase Flow Systems," ASME JOURNAL OF HEAT TRANSFER, Series C, Vol. 87, No. 4, Nov. 1965, pp. 453-468.

13 Milgram, J. H., "Mean Flow in Round Bubble Plumes," *Journal of Fluid Mechanics*, Vol. 133, 1983, pp. 345-376.

APPENDIX

$$C_1 = \frac{\rho_l M_g}{\pi \rho_g T}\left[k-(k+1)\frac{U_l}{U_g}\right]+\left[\frac{kM_g}{\pi\rho_g}+U_l\left\{a^2-\frac{M_g(k+1)}{\pi\rho_g U_g}\right\}+\frac{g}{g_c}\frac{M_g\rho_l}{RT\rho_g^2}(L-x)\left\{\frac{(k+1)U_l}{\pi U_g}-k\right\}\right]\frac{d\rho_l}{dT}$$

$$C_2 = \rho_l a^2 \frac{\rho_l M_g (k+1)}{\pi\rho_g U_g}\left(\frac{U_l}{U_g}-1\right)$$

$$C_3 = 2a\rho_l U_l$$

$$C_4 = 2\rho_{lo}E_o\left[aU_{lo}+\frac{k}{k+1}a_c U_\infty+\frac{a_c U_\infty}{k+1}\left(\frac{\rho_g}{\rho_{lo}}\right)^{1/2}\right]+\frac{gM_g\rho_l^2}{2g_c\rho_g^2 RT}\left[(k+1)\frac{U_l}{U_g}-k\right]$$

$$M_1 = \left[\frac{kU_gM_g}{T}\frac{\rho_l}{\rho_g}-\frac{(k+1)M_gU_l^2}{TU_g}\left(\frac{\rho_l}{\rho_g}\right)\right]+\left(\frac{kM_gU_g}{\pi\rho_g}+U_l^2(a^2-\frac{M_g(k+1)}{\pi\rho_g U_g}\right)+\frac{gU_g}{g_c}\frac{M_g(L-x)}{RT\rho_g}\left\{1-\frac{1}{k+1}-\frac{k}{k+1}\left(\frac{k_l}{\rho_g}\right)+\frac{\rho_l}{\rho_g}\left(\frac{U_l}{U_g}\right)^2\right\}\left]\frac{d\rho_l}{dT}\right.$$

$$M_2 = \left[M_g+3kM_g\frac{\rho_l}{\rho_g}+(k+1)M_g\left(\frac{U_l}{U_g}\right)^2\frac{\rho_l}{\rho_g}+2\pi a^2\rho_l U_l-2(k+1)^*M_g\frac{\rho_l u_l}{\rho_g U_g}\right]$$

$$M_3 = 2\pi\rho_l a U_l^2$$

$$M_4 = \frac{gM_g}{U_g}\left(\frac{\rho_l}{\rho_g}-1\right)-\frac{g}{g_c}\frac{kM_gU_g}{RT}\left(\frac{\rho_l}{\rho_g}\right)^2+\frac{g}{g_c}(k+1)^*\frac{M_gU_l^2}{RTU_g}\left(\frac{\rho_l}{\rho_g}\right)^2$$

$$E_1 = M_gC_{pg}+2kC_{vl}M_g\left(\frac{\rho_l}{\rho_g}\right)+\frac{kM_gP_a}{RT}+\frac{kM_gLg\rho_l}{g_cT\rho_g}+\frac{k\rho_lM_gU_g^2}{2g_c\rho T}+\pi\rho_lU_la^2C_{vl}-\frac{(k+1)\rho_lU_lC_{vl}M_g}{\rho_gU_g}-\frac{(k+1)\rho_lU_lM_g}{\rho_gTU_g}\left(C_{vl}T+\frac{U_l^2}{2g_c}+\frac{P_a}{\rho_l}+\frac{g}{g_c}L\right)+\frac{d\rho_l}{dT}\left[\left\{\left(\pi a^2-\frac{M_g(k+1)}{\rho_gU_g}\right)\left(U_lC_{vl}T+\frac{U_l^3}{2_{g_c}}+L\frac{g}{g_c}U_l\right)\right\}-\frac{M_g(L-x)}{RT\rho_g^2}\left\{\left(kC_{vl}\rho_lT+\frac{g}{g_c}kP_a+k\left(\frac{g}{g_c}\right)^2\rho_lL+\frac{gk\rho_lU_g^2}{2g_c^2}\right)-\frac{U_l}{U_g}(k+1)\left(\rho_lC_{vl}T+\frac{g\rho_lU_l^2}{2g_c^2}+\frac{g}{g_c}P_a+\rho_lL\left(\frac{g}{g_c}\right)^2\right)\right\}-\frac{kM_gP_a}{\rho_l\rho_g}\right]$$

$$E_2 = \frac{M_gU_g}{g_c}+\frac{k\rho_lM_gU_g}{g_c\rho_g}+\frac{\pi\rho_lU_la^2}{g_c}-\frac{\rho_lU_l^2(k+1)M_g}{g_c\rho_gU_g}+\frac{(k+1)M_g\rho_lU_l}{\rho_gU_g^2}\left(C_{vl}T+\frac{U_l^2}{2g_c}+\frac{P_a}{\rho_l}+L\frac{g}{g_c}\right)+\pi\rho_la^2\left(C_{vl}T+\frac{U_l^2}{2g_c}+\frac{P_a}{\rho_l}+L\frac{g}{g_c}\right)-\frac{\rho_l(k+1)M_g}{\rho_gU_g}\left(C_{vl}T+\frac{U_l^2}{2g_c}+\frac{P_a}{\rho_l}+L\frac{g}{g_c}\right)$$

$$E_3 = 2\pi a\rho_lU_l\left(C_{vl}T+\frac{U_l^2}{2g_c}+\frac{P_a}{\rho_l}+L\frac{g}{g_c}\right) \text{ and}$$

$$E_4 = 2\pi E_o\rho_{lo}\left[aU_l+kU_\infty\left\{\frac{M_g}{(k+1)\pi\rho_gU_g}\right\}^{1/2}+U_\infty\left\{\frac{M_g}{(k+1)\pi\rho_lU_g}\right\}^{1/2}\right]\left[C_{vl}T_{lo}+\frac{P_a}{\rho_l}+\frac{g}{g_c}L+\frac{E_o^2}{2g_c}*\left\{U_l+\frac{U_\infty}{a}\left(\frac{M_g}{\pi(k+1)\rho_gU_g}\right)^{1/2}\left(k+\left(\frac{P_g}{\rho_l}\right)^{1/2}\right)\right\}^2\right]-\frac{g}{g_c}M_g-\frac{kC_{vl}M_g}{R}\left(\frac{\rho_l}{\rho_g}\right)^2-\frac{\rho_l}{RT\rho_g^2}\left(\frac{g}{g_c}kM_gP_a+k\rho_lM_gL\left(\frac{g}{g_c}\right)^2+\frac{g\rho_lU_g^2M_g}{2g_c^2}\right)+\frac{g}{g_c}\frac{(k+1)M_gU_l}{RTU_g}\left(\frac{\rho_l}{\rho_g}\right)^2\left(C_{vl}T+\frac{U_l^2}{2g_c}+\frac{P_a}{\rho_l}+\frac{g}{g_c}L\right)$$

$$C_1' = \frac{M_g\rho_l}{2\rho_gT}\left[k-(k+1)\frac{U_l}{U_g}\right]+\frac{gk\rho_l(L-x)M_g}{2\rho_g^2g_cRT}+\frac{kM_g}{2\rho_g}+\left\{a-\frac{(k+1)M_g}{2\rho_gU_g}\right\}U_l\left]\frac{d\rho_l}{dT}\right.$$

$$C_2' = \rho_l\left\{a-\frac{(k+1)M_g}{2\rho_gU_g}\left(1-\frac{U_l}{U_g}\right)\right\};\quad C_3' = U_l\rho_l$$

$$C_4' = \rho_{lo} E_o U_l \left[1 + \frac{k}{k+1} \frac{U_\infty}{U_l} + \frac{1}{k+1} \frac{U_\infty}{U_l} \left(\frac{\rho_g}{\rho_{lo}} \right)^{1/2} \right] + \frac{M_g}{2RT} \frac{\rho_l^2}{\rho_g^2} \left[(k+1) \frac{U_l}{U_g} - k \right]$$

$$M_1' = \frac{U_g M_g k \rho_l}{2\rho_g T} \left[1 - \frac{k+1}{k} \frac{U_l^2}{U_g^2} \right] + \left[\frac{k}{2} \frac{M_g U_g}{\rho_g} + \frac{M_g U_g}{2RT} \frac{g}{g_c} \frac{\rho_l}{\rho_g^2} (L-x) \left\{ (k+1) \left(\frac{U_l}{U_g} \right)^2 - k \right\} + U_l^2 \left\{ a - \frac{(k+1)}{2} * \frac{M_g}{\rho_g U_g} \right\} \right] \frac{d\rho_l}{dT}$$

$$M_2' = \frac{M_g \rho_l}{2\rho_g} \left(k + \frac{\rho_g}{\rho_l} \right) + 2aU_l \rho_l - \frac{(k+1) M_g U_l \rho_l}{\rho_g U_g} \left(1 - \frac{U_l}{U_g} \right)$$

$$M_3' = \rho_l U_l^2$$

$$M_4' = \frac{\rho_l g M_g}{2\rho_g U_g} \left(1 - \frac{\rho_g}{\rho_l} \right) - \frac{k}{2} \frac{U_g M_g \rho_l^2}{\rho_g^2 RT} + \frac{(k+1) M_g U_l^2 \rho_l^2}{2\rho_g^2 U_g RT}$$

$$E_1' = \left[\frac{1}{2} M_g C_{pg} + k M_g C_{vl} \frac{\rho_l}{\rho_g} + \frac{kRM_g}{2} + \frac{kM_g}{4g_c} \frac{\rho_l}{\rho_g} \frac{U_g^2}{T} + \frac{gkM_g \rho_l x}{2g_c \rho_g T} + \left\{ a - \frac{(k+1) M_g}{2\rho_g U_g} \right\} \rho_l C_{vl} U_l - \frac{(k+1) M_g}{2} \frac{\rho_l}{\rho_g} \frac{U_l}{U_g} C_{vl} - \frac{(k+1) RM_g}{2} \frac{U_l}{U_g} - \frac{(k+1) M_g}{4g_g} \frac{\rho_l}{\rho_g} \frac{U_l^3}{U_g T} - \frac{(k+1) M_g}{2} \frac{g}{g_c} \frac{\rho_l}{\rho_g} \frac{U_l}{U_g} \frac{x}{T} \right] + \left[\frac{kM_g}{2\rho_g} \left(C_{vl} T + \frac{U_g^2}{g_c} + \frac{g}{g_c} x \right) + \left(a - \frac{(k+1) M_g}{2\rho_g U_g} \right) * \left(C_{vl} U_l T + \frac{U_l^3}{2g_c} + \frac{g}{g_c} x U_l \right) - \frac{(L-x)}{2RT} \frac{k\rho_l M_g g}{\rho_g^2 g_c} \left(C_{vl} T + \frac{U_g^2}{2g_c} + \frac{g}{g_c} x \right) \right] \frac{d\rho_l}{dT}$$

$$E_2' = \left[\frac{M_g U_g}{2g_c} + \frac{kM_g \rho_l U_g}{2g_c \rho_g} + \left\{ a - \frac{(k+1) M_g}{2\rho_g u_g} \right\} \left(C_{vl} \rho_l T + R\rho_g T + \frac{3}{2g_c} \rho_l U_l^2 + \frac{g}{g_c} \rho_l x \right) + \frac{M_g (k+1)}{2\rho_g U_g^2} \rho_l U_l C_{vl} T + \frac{M_g (k+1)}{2U_g^2} RTU_l + \frac{M_g (k+1)}{4\rho_g U_g^2} \frac{\rho_l U_l^3}{g_c} + \frac{M_g (k+1)}{2\rho_g U_g^2} \frac{g}{g_c} \rho_l U_l x \right]$$

$$E_3' = \rho_l U_l C_{vl} T + R\rho_g U_l T + \frac{\rho_l U_l^3}{2g_c} + \frac{g}{g_c} \rho_l U_l x$$

$$E_4' = \left[E_o \rho_{lo} \left\{ C_{vl} T_{lo}(X) + \frac{P_a}{\rho_{lo}} + (L-X) \frac{g}{g_c} \right\} \left\{ U_l + \frac{kU_\infty}{k+1} + \frac{U_\infty}{k+1} \left(\frac{\rho_g}{\rho_{lo}} \right)^{1/2} \right\} + \frac{\rho_{lo} E_o^3}{2g_c} \left\{ U_l + \frac{kU_\infty}{k+1} + \frac{U_\infty}{k+1} \left(\frac{\rho_g}{\rho_{lo}} \right)^{1/2} \right\}^3 + \frac{g}{g_c} E_o \rho_{lo} x \left\{ U_l + \frac{kU_\infty}{k+1} + \frac{U_\infty}{k+1} \left(\frac{\rho_g}{\rho_{lo}} \right)^{1/2} \right\} - \frac{gM_g}{2g_c} - \frac{gk\rho_l^2 C_{vl} M_g}{2g_c R\rho_g^2} - \frac{g}{4g_c^2} \frac{kM_g}{RT} U_g^2 \left(\frac{\rho_l}{\rho_g} \right)^2 - \frac{g}{2g_c} kM_g \frac{\rho_l}{\rho_g} - \frac{g^2 kM_g}{2g^2 RT} \times \left(\frac{\rho_l}{\rho_g} \right)^2 + \frac{g}{g_c} \frac{(k+1)}{2} \frac{\rho_l M_g}{\rho_g^2 U_g RT} (\rho_l U_l C_{vl} T + RT\rho_g U_l + \frac{\rho_l U_l^3}{2g_c} + \rho_l U_l \frac{g}{g_c} x) \right]$$

Analysis of Laminar Mixed Convective Plumes Along Vertical Adiabatic Surfaces

K. V. Rao

B. F. Armaly
Mem. ASME

T. S. Chen
Mem. ASME

Department of Mechanical and Aerospace Engineering
University of Missouri-Rolla,
Rolla, Mo. 65401

Laminar mixed forced and free convection from a line thermal source imbedded at the leading edge of an adiabatic vertical surface is analytically investigated for the cases of buoyancy assisting and buoyancy opposing flow conditions. Temperature and velocity distributions in the boundary layer adjacent to the adiabatic surface are presented for the entire range of the buoyancy parameter $\xi(x) = Gr_x/Re_x^{5/2}$ from the pure forced ($\xi(x) = 0$) to the pure free ($\xi(x) = \infty$) convection regime for fluids having Prandtl numbers of 0.7 and 7.0. For buoyancy-assisting flow, the velocity overshoot, the temperature, and the wall shear stress increase as the plume's strength increases. On the other hand, the velocity overshoot, the wall shear stress, and the temperature decrease as the free-stream velocity increases. For buoyancy opposing flow, the velocity and wall shear stress decrease but the temperature increases as the plume's strength increases.

Introduction

A plume arising from a heated element is a problem of considerable interest in several engineering applications, e.g., hot-wire anemometry, and flows that arise in fire studies, and cooling of electronic circuitry. Free plumes from a line or a point thermal source have been the subject of numerous investigations and a detailed survey was reported by Gebhart [1]. Wall plumes have received substantially less attention, and the development of wall plumes due to thermal line sources has been reported by Jaluria and Gebhart [2], Liburdy and Faeth [3], and Afzal [4]. The development of wall plumes induced by a heated surface of finite extent was reported by Jaluria [5] and by Sparrow et al. [6], while measurements were reported by Mollendorf and Carey [7] and by Zimin and Lyakhov [8].

It has been well established [9, 10] that the thermal buoyancy force plays a significant role in forced convection when the flow velocity is relatively low and the temperature difference between the surface and the free stream is relatively large. Under these conditions, mixed convection analysis is needed because the pure forced-convection or the pure free-convection analysis fails to predict the flow or heat transfer characteristics accurately. Most of the reported work on plumes treats only the case of pure free-convection flows. However, Afzal [11] has examined the case of mixed convection from a free plume arising from a thermal line source using a series expansion method for the solution, while Jaluria [5] has considered the case of mixed convection from wall plumes induced by a heated surface of finite extent by using the finite difference method of solution. A lack of studies, along with limited range of available results on mixed convection wall plumes, has motivated the present study. Its objective is to examine the development of wall plumes arising from a thermal line source imbedded at the leading edge of an adiabatic vertical surface over the entire mixed convection regime.

In order to generate results that cover the entire mixed convection regime, it is necessary to obtain two solutions to the same governing equations. One solution represents a perturbation to the pure forced-convection regime (i.e., weakly buoyant plumes) and the other solution represents a perturbation to the pure free-convection regime (i.e., strongly buoyant plumes). This approach was selected because the accuracy of either solution deteriorates as the perturbation parameter, $\xi(x)$ or $\xi_1(x)$, increases. The forced convection variables, $\eta = y(u_\infty/\nu x)^{1/2}$ and $\xi(x) = Gr_x/Re_x^{5/2}$, were used to transform the governing equations into a set of partial differential equations to examine the regime of the weakly buoyant plumes. Similarly, the free-convection variables, $\eta_1 = (y/x)Gr_x^{1/5}$ and $\xi_1(x) = Re_x/Gr_x^{2/5}$, were used to transform the same governing equations to examine the regime of the strongly buoyant plumes. The two sets of transformed equations were then solved by the local similarity and the local nonsimilarity methods as a function of the buoyancy parameter, $\xi(x)$ or the forced convection parameter $\xi_1(x)$. Results from the two solutions were then combined to cover the entire range of mixed convection regime, from pure forced convection to pure free convection. To the authors' knowledge, such a study on adiabatic wall plumes arising from a line thermal source has not been conducted.

Analysis

The geometry considered in this study, shown in Fig. 1, is equivalent to a line thermal source imbedded at the leading edge of an adiabatic vertical plane surface. The forced flow is along the plane surface and the direction of the forced convection velocity can be either assisting or opposing the buoyancy-induced convective velocity. For this simplified, two-dimensinal flow geometry, the governing equations, under Boussinesq approximation, are given by

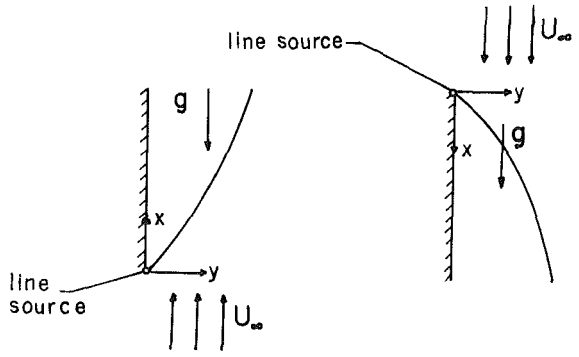

Fig. 1 Schematic of geometry under consideration

Contributed by the Heat Transfer Division for publication in the JOURNAL OF HEAT TRANSFER. Manuscript received by the Heat Transfer Division April 4, 1983.

$$\frac{\partial u}{\partial x} + \frac{\partial v}{\partial y} = 0 \tag{1}$$

$$u\frac{\partial u}{\partial x} + v\frac{\partial u}{\partial y} = \nu\frac{\partial^2 u}{\partial y^2} \pm g\beta(T - T_\infty) \tag{2}$$

$$u\frac{\partial T}{\partial x} + v\frac{\partial T}{\partial y} = \alpha\frac{\partial^2 T}{\partial y^2} \tag{3}$$

The positive and negative signs in front of the last term in equation (2) correspond to upward forced-flow (buoyancy assisting) and downward forced-flow (buoyancy opposing) conditions, respectively. The boundary conditions for equations (1-3) are

$$u = v = 0; \quad \frac{\partial T}{\partial y} = 0 \text{ at } y = 0$$

$$u \to u_\infty, T \to T_\infty \text{ as } y \to \infty \tag{4}$$

The conservation of energy requires that at any position $x > 0$, the convective energy is equal to the energy released by the line heat source, Q. Thus

$$Q = \rho C_p L \int_0^\infty u(T - T_\infty)dy \tag{5}$$

Weakly Buoyant Plumes. To examine the effect of buoyancy force on the forced flow for a weakly buoyant plume, the governing system of equations, equations (1-5), are transformed from the (x,y)-coordinates to the $(\xi(x), \eta(x,y))$-coordinates

$$\xi(x) = \frac{\mathrm{Gr}_x}{\mathrm{Re}_x^{5/2}}; \quad \eta(x,y) = y\left(\frac{u_\infty}{\nu x}\right)^{1/2} \tag{6}$$

In addition, a reduced stream function $F(\xi,\eta)$ and a dimensionless temperature $\theta(\xi,\eta)$ are defined, respectively, as

$$F(\xi,\eta) = \frac{\psi(x,y)}{(\nu u_\infty x)^{1/2}}; \quad \theta(\xi,\eta) = \frac{(T - T_\infty)}{T^*}\mathrm{Re}_x^{1/2} \tag{7}$$

where $\psi(x,y)$ is the stream function that satisfies equation (1) with $u = \partial\psi/\partial y$ and $v = -\partial\psi/\partial x$, and the equivalent line source temperature T^* is defined by

$$T^* = \frac{Q}{\rho C_p \nu L} \tag{8}$$

The resulting system of transformed equations are given by

$$F''' + \frac{1}{2}FF'' \pm \xi\theta = \frac{1}{2}\xi(F'G' - F''G) \tag{9}$$

$$\frac{1}{\mathrm{Pr}}\theta'' + \frac{1}{2}(F\theta)' = \frac{1}{2}\xi(F'\phi - \theta'G) \tag{10}$$

in which the primes denote partial derivatives with respect to η. Using the familiar local nonsimilarity approach [12, 13], the governing equations for $G(\xi,\eta)$ and $\phi(\xi,\eta)$ are given by

$$G''' + GF'' + \frac{1}{2}FG'' \pm (\theta + \xi\phi) - \frac{1}{2}F'G' = \frac{1}{2}\xi(G'G' - G''G) \tag{11}$$

$$\frac{1}{\mathrm{Pr}}\phi'' + \frac{1}{2}G'\theta + G\theta' + \frac{1}{2}F\phi' = \frac{1}{2}\xi(G'\phi - \phi'G) \tag{12}$$

The boundary conditions for the above four coupled differential equations are

$$F(\xi,0) = F'(\xi,0) = \theta'(\xi,0) = G(\xi,0) = G'(\xi,0) = \phi'(\xi,0) = 0 \tag{13a}$$

$$F'(\xi,\infty) = 1, \quad G'(\xi,\infty) = 0 \tag{13b}$$

Conservation of energy requires that for any ξ, the following integrals must be satisfied.

$$\int_0^\infty F'\theta d\eta = 1; \quad \int_0^\infty (F'\phi + G'\theta)d\eta = 0 \tag{13c}$$

The above ten independent boundary conditions, equations (13a-c), are sufficient [14] for solving the governing equations (9-12). The use of these boundary conditions automatically satisfy the conditions of $\theta(\xi,\infty) = \phi(\xi,\infty) = 0$.

The local similarity solution for this case consists of solving only equations (9) and (10) when the right-hand sides of these equations are replaced by zero. On the other hand, the local nonsimilarity method requires the solution of the four coupled partial differential equations, equations (9-12). It has been shown in the past [10] that the local nonsimilarity solution method provides more accurate results than the local similarity solution method, particularly at larger magnitudes of the perturbation parameter, ξ.

Strongly Buoyant Plumes. To examine the case of a strongly buoyant plume and the influence of forced convection on its development, it is convenient to transform the original system of governing equations, equations (1-5), from the (x,y)-coordinates to the $(\xi_1(x), \eta_1(x,y))$-coordinates

$$\xi_1(x) = \frac{\mathrm{Re}_x}{\mathrm{Gr}_x^{2/5}}; \quad \eta_1(x,y) = \frac{y}{x}\mathrm{Gr}_x^{1/5} \tag{14}$$

In addition, a reduced stream function $F_1(\xi_1,\eta_1)$ and a dimensionless temperature $\theta_1(\xi_1,\eta_1)$ are defined as

Nomenclature

C_f = $\tau_w / \frac{1}{2}\rho u_\infty^2$ friction coefficient
C_p = specific heat of the fluid
F = reduced stream function, equation (7)
F_1 = reduced stream function, equation (15)
g = gravitational acceleration
G = $\partial F/\partial\xi$
G_1 = $\partial F_1/\partial\xi_1$
Gr_x = $g\beta T^* x^3/\nu^2$, local Grashof number
L = length of thermal line source
Pr = Prandtl number
Q = strength of thermal line source
Re_x = $u_\infty x/\nu$, local Reynolds number
T = fluid temperature
T_w = wall temperature
T_∞ = free-stream temperature
T^* = equivalent temperature of thermal line source, equation (8)
u = axial velocity component
u_∞ = free-stream velocity
v = normal velocity component
x = axial coordinate
y = transverse coordinate
α = thermal diffusivity
β = volumetric coefficient of thermal expansion
δ_u = plume width, velocity field
δ_T = plume width, temperature field
η = pseudo-similarity variable, equation (6)
η_1 = pseudo-similarity variable, equation (14)
θ = dimensionless temperature, equation (7)
θ_1 = dimensionless temperature, equation (15)
μ = dynamic viscosity
ν = kinematic viscosity
ξ = $\mathrm{Gr}_x/\mathrm{Re}_x^{5/2}$, buoyancy parameter
ξ_1 = $\mathrm{Re}_x/\mathrm{Gr}_x^{2/5}$, forced convection parameter
ρ = density of the fluid
τ_w = wall shear stress
ϕ = $\partial\theta/\partial\xi$
ϕ_1 = $\partial\theta_1/\partial\xi_1$
ψ = stream function, equation (7)

Superscript

$'$ = partial derivative with respect to either η or η_1

$$F_1(\xi_1,\eta_1)=\frac{\psi(x,y)}{(\nu \mathrm{Gr}_x^{1/5})};\quad \theta_1(\xi_1,\eta_1)=\frac{(T-T_\infty)}{T^*}\mathrm{Gr}_x^{1/5} \tag{15}$$

The resulting transformed set of equations are given by

$$F_1'''+\frac{3}{5}F_1F_1''-\frac{1}{5}(F_1')^2\pm\theta_1=\frac{1}{5}\xi_1(F_1''G_1-F_1'G_1') \tag{16}$$

$$\frac{1}{\mathrm{Pr}}\theta_1''+\frac{3}{5}(F_1\theta_1)'=\frac{1}{5}\xi_1(\theta_1'G_1-F_1'\phi_1) \tag{17}$$

in which the primes in the foregoing equations now denote partial derivatives with respect to η_1. By using the local nonsimilarity method, the governing equations for $G_1(\xi_1,\eta_1)$ and $\phi_1(\xi_1,\eta_1)$ become equivalent to

$$G_1'''+\frac{2}{5}F_1''G_1+\frac{3}{5}F_1G_1''-\frac{1}{5}F_1'G_1'\pm\phi_1=\frac{1}{5}\xi_1(G_1''G_1-G_1'G_1') \tag{18}$$

$$\frac{1}{\mathrm{Pr}}\phi_1''+\frac{3}{5}G_1'\theta_1+\frac{4}{5}F_1'\phi_1+\frac{2}{5}G_1\theta_1'+\frac{3}{5}F_1\phi_1'=\frac{1}{5}\xi_1(\phi_1'G_1-G_1'\phi_1) \tag{19}$$

The boundary conditions for the above set of equations, equations (16–19), are given by

$$F_1'(\xi_1,0)=F_1(\xi_1,0)=\theta_1'(\xi_1,0)=G_1'(\xi_1,0)=G_1(\xi_1,0)=\phi_1'(\xi_1,0)=0 \tag{20a}$$

$$F_1'(\xi_1,\infty)=\xi_1;\quad G_1'(\xi_1,\infty)=1 \tag{20b}$$

In addition, conservation of energy requires that for any value of ξ_1, the following integrals must be satisfied

$$\int_0^\infty F_1'\theta_1\,d\eta_1=1;\quad \int_0^\infty(G_1'\theta_1+F_1'\phi_1)d\eta=0 \tag{20c}$$

The use of these boundary conditions automatically satisfy the conditions of $\theta_1(\xi_1,\infty)=\phi_1(\xi_1,\infty)=0$.

The local similarity solution for this case consists of solving only equations (16) and (17) when the right-hand sides of these equations are replaced by zero. On the other hand, the local nonsimilarity method requires the solution of the four coupled partial differential equations, equations (16–19). As stated previously, the local nonsimilarity solution method is expected to provide more accurate results than the local similarity solution method, particularly at larger magnitudes of the perturbation parameter, ξ_1.

Results for the weakly buoyant plume and for the strongly buoyant plume were generated to cover the entire regime of mixed forced and free convection. The variables used in the strongly buoyant plume case are related to the ones used in the weakly buoyant plume case by the following expressions

$$\eta_1=\frac{\eta}{\xi_1^{1/2}};\quad \xi_1=\xi^{-2/5} \tag{21a}$$

$$F_1(\xi_1,\eta_1)=F(\xi,\eta)\xi_1^{1/2};\quad \theta_1(\xi_1,\eta_1)=\theta(\xi,\eta)\xi_1^{-1/2} \tag{21b}$$

The velocity, temperature, and shear stress can be evaluated utilizing either the weakly buoyant or the strongly buoyant plume results by using the following relations

$$u(x,y)=u_\infty F'(\xi,\eta)=u_\infty F_1'(\xi_1,\eta_1)\xi_1^{-1} \tag{22a}$$

$$T(x,y)-T_\infty=\frac{\theta(\xi,\eta)Q}{\rho C_p\nu L\mathrm{Re}_x^{1/2}}=\frac{\theta_1(\xi_1,\eta_1)Q\xi_1^{1/2}}{\rho C_p\nu L\mathrm{Re}_x^{1/2}} \tag{22b}$$

$$\tau_w(x)=\rho u_\infty^2F''(\xi,0)\mathrm{Re}_x^{-1/2}=\rho u_\infty^2F_1''(\xi_1,0)\xi_1^{-3/2}\mathrm{Re}_x^{-1/2} \tag{22c}$$

It should be pointed out that equations (9) and (10) are identical with the ones developed by Afzal [11] for examining weakly buoyant free plumes, and equations (16) and (17) should also be identical with his equations for strongly buoyant free plumes. The authors believe that a typographical error exists in the publication [11] where a minus sign is missing from the right-hand side of the strongly buoyant free plume equations.

Results and Discussion

Results over the entire range of mixed convection for the adiabatic wall plume were obtained by solving the two sets of governing equations, equations (9–13) for weakly buoyant plumes and equations (16–20) for strongly buoyant wall plumes. The results for the pure free-convection wall plume $\xi_1(x)=0$ were generated and used to initiate the calculations for the strongly buoyant wall plume regime. Similarly, the results for the pure forced convection wall plume $\xi(x)=0$ were generated and used to initiate the calculations for the weakly buoyant wall plume regime. The buoyancy parameter $\xi(x)$ and the forced convection parameter $\xi_1(x)$ were then increased and solutions were obtained at different values of these parameters. A fourth-order, Runge-Kutta integration scheme with Nachtsheim-Swigert iterative shooting technique was employed to obtain the solutions. In the numerical solution, a check was made to confirm that smoothness conditions at the edge of the boundary layer were satisfied ($F''(\xi,\infty)=\theta'(\xi,\infty)=G''(\xi,\infty)=\phi'(\xi,\infty)=0$ for the weakly buoyant plume and $F_1''(\xi_1,\infty)=\phi_1'(\xi_1,\infty)=G_1''(\xi_1,\infty)=\phi_1'(\xi_1,\infty)=0$ for the strongly buoyant plume). An integration step size, $\Delta\eta$ or $\Delta\eta_1$, of 0.01 and a value of η_∞, the edge of the boundary layer, ranging from 8 to 12 for different buoyancy parameters, were found to be adequate to satisfy a convergence criterion of 10^{-4} at η_∞.

Results for the weakly buoyant wall plume are presented for values of the buoyancy parameter of $0\le\xi(x)\le50$. Similarly, the results for the strongly buoyant wall plume are presented for forced convection parameter of $0\le\xi_1(x)\le1$. The combined range of these results covers the entire mixed forced and free convection regime. The dimensionless velocity and temperature distributions are presented in Figs. 2–5 for buoyancy assisting flow conditions for fluids having Prandtl numbers of 0.7 and 7.0 (such as air and water). The dimensionless velocity distribution, $u/u_\infty=F'(\xi,\eta)=F_1'(\xi_1,\eta_1)/\xi_1$, for the weakly buoyant and for the strongly buoyant wall plumes, are presented in Figs. 2 and 3, respectively. When the line source strength Q increases, the plume velocity and the velocity overshoot increase. In addition, the location of the maximum velocity moves closer to the adiabatic wall, thus causing an increase in the wall shear stress. On the other hand, as the free-stream velocity increases the plume velocity increases but the velocity overshoot decreases, and this change is accompanied by a decrease in the wall shear stress. The plume width (velocity boundary layer thickness, δ_u) decreases as the source velocity increases.

The present results for the pure free-convection wall plume, $\xi_1(x)=0$, compare very well (within 1 percent) with the values published by Jaluria and Gebhart [2], who used a slightly different transformation and the local similarity method for solving this problem. Results for other regimes are currently not available in the literature for comparison with the present results. For the same parameters (i.e., fixed u_∞, T_∞, x, and Q), it can be deduced that fluids with a higher Prandtl number experience a lower velocity, lower velocity overshoot, smaller buoyancy parameter (ξ), smaller plume width (δ_u), smaller friction coefficient (c_f), but a higher wall shear stress (τ_w).

The dimensionless temperature distributions for assisting flow in a weakly buoyant wall plume $\xi\theta(\xi,\eta)$ and in a strongly buoyant wall plume, $\theta_1(\xi_1,\eta_1)$ are presented in Figs. 4 and 5, respectively. The dimensionless quantity $\xi\theta(\xi,\eta)$ is used to examine the influence of source strength Q on the temperature

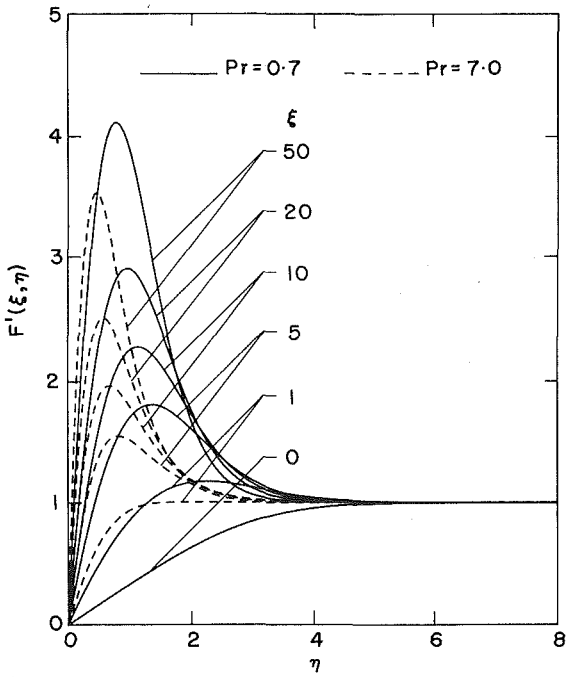

Fig. 2 Velocity profiles for weakly buoyancy-assisted plumes

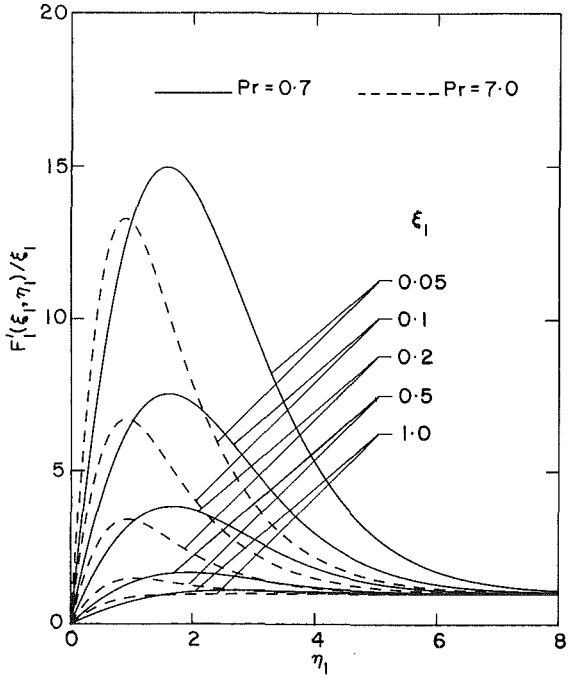

Fig. 3 Velocity profiles for strongly buoyancy-assisted plumes

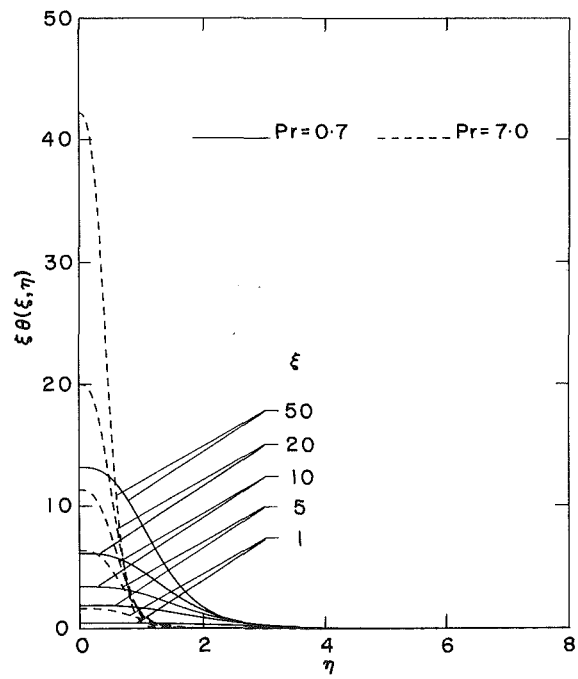

Fig. 4 Temperature profiles for weakly buoyancy-assisted plumes

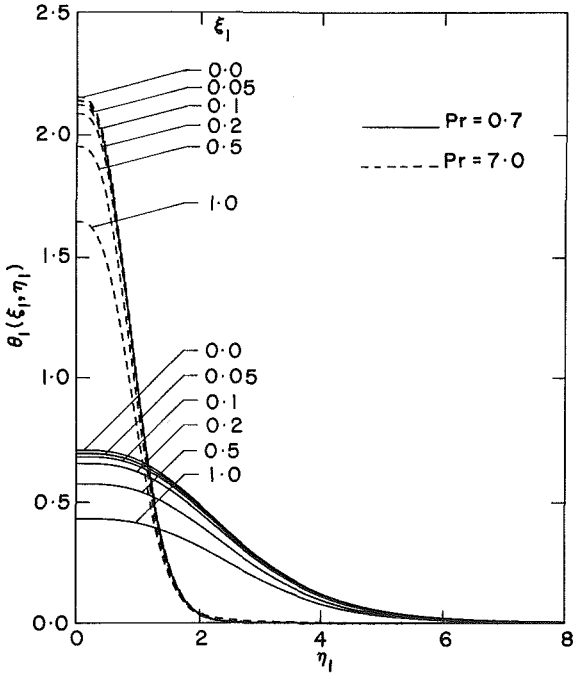

Fig. 5 Temperature profiles for strongly buoyancy-assisted plumes

distribution for fixed values of axial position x, and free-stream velocity u_∞, because under these conditions the quantity $\xi\theta(\xi,\eta)$ is proportional to $(T - T_\infty)$. The dimensionless quantity $\theta_1(\xi_1,\eta_1)$ is used to examine the influence of free-stream velocity on the temperature distribution for fixed values of axial position x and source strength Q, because under these conditions the quantity $\theta_1(\xi_1,\eta_1)$ is proportional to $(T - T_\infty)$. The wall temperature decays with the distance x, and the rate of this decrease is a function of the line source strength. It varies between the pure free-convection wall plume behavior $(T_w - T_\infty) \sim x^{-0.6}$ and the pure forced-convection wall plume behavior $(T_w - T_\infty) \sim x^{-0.5}$, depending on the relative strength of the line source. As the free-stream velocity increases for a fixed x and Q, the temperature of the plume decreases, Fig. 5, and as the source strength Q increases for a fixed x and u_∞, the temperature of the plume increases, Fig. 4. It can be seen that for the same buoyancy parameter, fluids with a higher Prandtl number experience a smaller plume width δ_T and a higher value of dimensionless wall temperature $\xi\theta(\xi,0)$ or $\theta_1(\xi_1,0)$. It should be noted, however, that due to differences in thermophysical properties (i.e., ρ, c_p, ν, and β), a higher Prandtl number fluid will result in a much smaller magnitude for T^* and ξ for the same source strength Q. This implies that a higher Prandtl number fluid will experinece a lower wall temperature difference $(T_w - T_\infty)$ for the same source strength Q.

The dimensionless wall temperature $\theta(\xi,\eta)$ and the wall shear stress $F''(\xi,0)$ for assisting flows are presented in Figs. 6

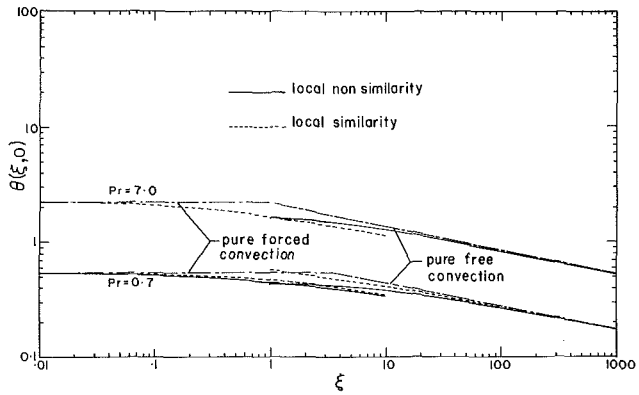

Fig. 6 Wall temperature variation for buoyancy-assisted plumes

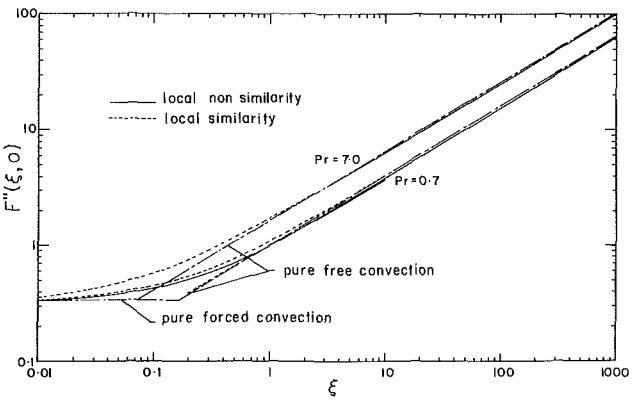

Fig. 7 Variation of $F''(\xi,0)$ for buoyancy-assisted plumes

and 7, respectively, over the entire mixed convection regime. The results in these figures represent both the solution of the weakly buoyant plumes, equations (9–13), for $.01 \le \xi \le 10$ and the solution of the strongly buoyant plumes, equations (16–20), for $.063 \le \xi_1 \le 1$ or its equivalent $1 < \xi < 1000$. The results from the strongly buoyant plumes solution $F_1''(\xi_1,0)$, $\theta_1(\xi_1,0)$, and ξ_1 were converted to the weakly buoyant plumes variables $F''(\xi,0)$, $\theta(\xi,0)$, and ξ, by utilizing equations (21) and (22). For comparison, the local similarity results are presented along with the local nonsimilarity values for Prandtl number of 0.7. As indicated previously, when the perturbation parameter ξ or ξ_1 increases, the accuracy of the solution decreases, and the local nonsimilarity method of solution should provide more accurate results than the local similarity method. It appears that in the weakly buoyant wall plume regime, $0.01 < \xi(x) < 10$, the agreement between the two solution methods is very good. On that basis, the results that are presented for Prandtl number of 7.0, in the weakly buoyant wall plume regime were generated by using the local similarity solution method.

The good agreement between the local similarity and the local nonsimilarity methods of solution deteriorates when these methods are used to solve the strongly buoyant plumes, equations (16–20). As can be seen from Fig. 6, the two solution methods for $\theta_1(\xi_1,0)$ start to deviate from each other when $\xi_1 > 0.23$ or $\xi < 4$. For that reason, the local nonsimilarity solution method, which is expected to be the more accurate solution, is utilized for the strongly buoyant plume solution, equations (16–20), for Prandtl number of 0.7 and 7 for the range of $0 < \xi_1 < 1$, which is equivalent to $\infty > \xi > 1$. Since the solution scheme is based on perturbing the pure forced- and the pure free-convection limits, and since the accuracy of these solutions deteriorates as the perturbation parameter increases, it is recommended that the local nonsimilarity results be used from the weakly buoyant plume solution for the region between $0 \le \xi \le 1$ and from the strongly buoyant plume solution for the region between $0 \le \xi_1 < 1$ to extract results in the entire mixed convection regime. Asymptotes describing the pure free-convection and the pure-forced-convection wall plumes are also presented in Figs. 6 and 7. They identify the region where both the pure free- and the pure forced-convection results deviate from the predicted mixed convection values. This region, $.01 < \xi < 100$, can be defined as the mixed-convective regime for the adiabatic wall plume. The magnitude of $F''(\xi,0)$ increases and the magnitude of $\theta(\xi,0)$ decreases as the buoyancy parameter increases. Values of $F''(\xi,0)$, $\theta(\xi,0)$, $F_1''(\xi_1,0)$, and $\theta_1(\xi_1,0)$ are also listed in Tables 1 and 2 for weakly buoyant and strongly buoyant regime, respectively.

Table 1 Weakly buoyant plumes

		Pr = 0.7		Pr = 7.0	
ξ	ξ_1	$F''(\xi,0)$	$\theta(\xi,0)$	$F''(\xi,0)$	$\theta(\xi,0)$
0.0	∞	0.3321	0.5373	0.3321	2.2676
0.01	6.3095	0.3424	0.5362	0.3620	2.2425
0.02	4.7818	0.3526	0.5347	0.3902	2.2197
0.03	4.0659	0.3627	0.5336	0.4169	2.1989
0.05	3.3145	0.3824	0.5295	0.4669	2.1619
0.07	2.8971	0.4014	0.5258	0.5132	2.1295
0.1	2.5119	0.4288	0.5201	0.5775	2.0877
0.2	1.9037	0.5121	0.5033	0.7622	1.9833
0.3	1.6186	0.5865	0.4899	0.9192	1.9092
0.5	1.3195	0.7190	0.4714	1.1870	1.8050
0.7	1.1533	0.8374	0.4584	1.4178	1.7314
1.0	1.0000	0.9983	0.4447	1.7217	1.6509
2.0	0.7579	1.4553	0.4191	2.5425	1.4907
3.0	0.6444	1.8305	0.3999	3.2104	1.3978
5.0	0.5253	2.4600	0.3739	4.3223	1.2838
7.0	0.4592	2.9994	0.3565	5.2657	1.2115
10.0	0.3981	3.7100	0.3384	6.4980	1.1376
20.0	0.3017	5.6347	0.3041	9.7983	1.0032
30.0	0.2565	7.2095	0.2851	12.4703	0.9305
50.0	0.2091	9.8435	0.2621	16.9080	0.8451
70.0	0.1828	12.0910	0.2477	20.6685	0.7927
100.0	0.1585	15.0408	0.2332	25.5770	0.7403

Table 2 Strongly buoyant plumes

		Pr = 0.7		Pr = 7.0	
ξ_1	ξ	$F_1''(\xi_1,0)$	$\theta_1(\xi_1,0)$	$F_1''(\xi_1,0)$	$\theta_1(\xi_1,0)$
0.0	∞	1.0150	0.7082	1.6397	2.1533
0.001	3.1623×10^7	1.0148	0.7079	1.6397	2.1530
0.002	5.5902×10^6	1.0147	0.7076	1.6397	2.1528
0.003	2.0286×10^6	1.0145	0.7074	1.6397	2.1525
0.005	5.6569×10^5	1.0143	0.7068	1.6397	2.1518
0.007	2.4392×10^5	1.0140	0.7063	1.6397	2.1513
0.01	1.0000×10^5	1.0136	0.7055	1.6398	2.1504
0.02	1.7677×10^4	1.0123	0.7027	1.6399	2.1473
0.03	6.4150×10^3	1.0109	0.7000	1.6400	2.1442
0.05	1.7889×10^3	1.0083	0.6945	1.6402	2.1379
0.07	7.7136×10^2	1.0058	0.6891	1.6404	2.1314
0.1	3.1623×10^2	1.0021	0.6809	1.6408	2.1214
0.2	5.5907×10^1	0.9908	0.6535	1.6422	2.0852
0.3	2.0286×10^1	0.9812	0.6260	1.6437	2.0448
0.5	5.6569	0.9682	0.5720	1.6464	1.9512
0.7	2.4392	0.9582	0.5125	1.6485	1.8404
1.0	1.0	0.9618	0.4270	1.6509	1.6436

The velocity and temperature distributions for the buoyancy opposing flow conditions are presented for Pr = 0.7 and Pr = 7, respectively, in Figs. 8 and 9. The results for this case were obtained from the solution of the equations describing the weakly buoyant wall plume, but the negative sign replaces the positive sign in front of the buoyancy term in equations (9) and (11). As the source strength increases, the temperature and the plume width increase, but the velocity and wall shear stress decrease (see Figs. 8 and 9). The solution terminates when the velocity gradient at the wall becomes close to zero, indicating an approach to flow separation. Flow separation occurs at $\xi = 0.1534$ for Pr = 0.7 and at $\xi = 0.0601$ for Pr = 7.0. For a given source strength, a higher

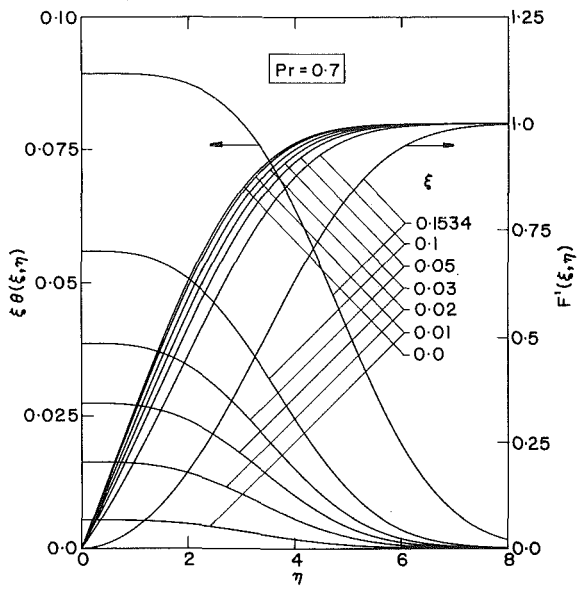

Fig. 8 Velocity and temperature profiles for buoyancy-opposed plumes

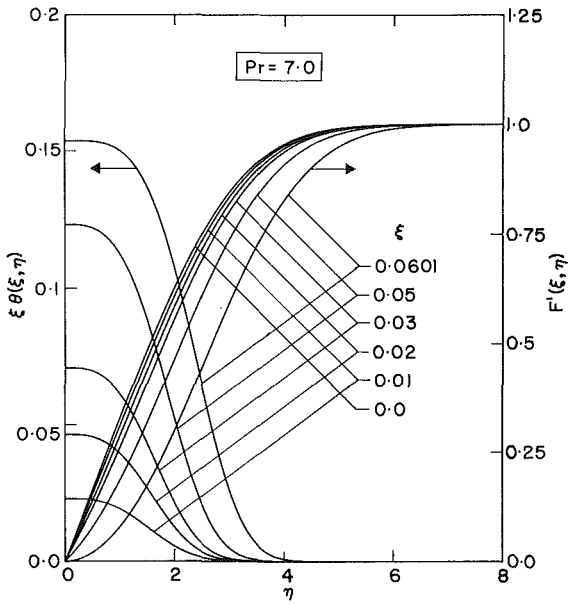

Fig. 9 Velocity and temperature profiles for buoyancy-opposed plumes

Prandtl number fluid causes a large reduction in the magnitude of the bouyancy parameter due to differences in thermophysical properties and thus causes a decrease in the plume width and in the wall temperature difference ($T_w - T_\infty$) and an increase in the velocity and in the wall shear stress.

Conclusion

The development of a laminar mixed forced- and free-convection plume from a line thermal source imbedded at the leading edge of an adiabatic vertical plane surface is analyzed for the cases of buoyancy-assisting and buoyancy-opposing flow conditions. New results for the velocity, temperature, and wall shear stress are presented for fluids having Prandtl numbers of 0.7 and 7.0 for the entire regime of mixed convection, from pure forced ($\xi = 0$) to pure free ($\xi_1 = 0$) convection regime. The results clearly show that in the region where $.01 < \xi < 100$ mixed convection significantly influences the development of the wall plume. Outside that range the development of the wall plume could be approximated by either the pure forced-convection or the pure free-convection analysis of a wall plume. For buoyancy-assisting case, an increase in the source strength causes the velocity overshoot, wall shear stress, and wall temperature difference to increase, but causes the plume's width to decrease. When the free-stream velocity increases, the velocity overshoot, the wall shear stress, and the wall temperature difference decrease. For a given source strength Q, a higher prandtl number causes the buoyancy parameter, the velocity overshoot, the wall temperature difference, and the plume's width to decrease, but causes the wall shear stress to increase. For the buoyancy-opposing case, an increase in plume's strength causes the velocity and wall shear stress to decrease, but the wall temperature difference and the plume's width to increase. For a given source strength, a higher Prandtl number fluid will cause the buoyancy parameter, the plume width, and the wall temperature difference to decrease but the velocity and the wall shear stress will increase.

Acknowledgment

This study was supported in part by grants from the National Science Foundation (NSF CME 79-19459 and NSF MEA 8111673). The funds for numerical computation were provided by the University of Missouri-Rolla.

References

1 Gebhart, B., "Natural Convection Flows and Stability," in *Advances in Heat Transfer*, Vol. 9, 1973, pp. 297-301.

2 Jaluria, Y., and Gebhart, B., "Buoyancy-Induced Flow Arising From a Line Thermal Source on an Adiabatic Vertical Surface," *International Journal of Heat and Mass Transfer*, Vol. 20, 1977, pp. 153-157.

3 Liburdy, J. A., and Faeth, G. M., "Theory of a Steady Laminar Thermal Plume Along a Vertical Adiabatic Wall," *Letters in Heat and Mass Transfer*, Vol. 2, 1975, pp. 407-418.

4 Afzal, N., "Convective Wall Plume: Higher Order Analysis," *International Journal of Heat and Mass Transfer*, Vol. 23, 1980, pp. 505-513.

5 Jaluria, Y., "Mixed Convection in Wall Plumes," ASME Paper No. 81-HT-37, presented at the *ASME/AIChE National Heat Transfer Conference*, Milwaukee, Wis., Aug. 2-5, 1981.

6 Sparrow, E. M., Patankar, S. V., and Abdul-Wahed, R. M., "Development of Wall and Free Plumes Above a Heated Vertical Plate," ASME JOURNAL OF HEAT TRANSFER, Vol. 100, 1978, pp. 184-190.

7 Carey, V. P., and Mollendorf, J. C., "The Temperature Field Above a Concentrated Heat Source on a Vertical Adiabatic Surface," *International Journal of Heat and Mass Transfer*, Vol. 20, 1977, pp. 1059-1067.

8 Zimin, V. D., and Lyakhov, Y. N., "Convective Wall Plume," *Zhurnal Prikhadnoi Mekhaniki i Teknicheskoi Fiziki*, Vol. 11, No. 3, 1970, pp. 159-161.

9 Mucoglu, A., and Chen, T. S., "Mixed Convection on Inclined Surfaces," ASME JOURNAL OF HEAT TRASNFER, ASME Vol. 101, 1979, pp. 422-426.

10 Ramachandran, N., Armaly, B. F., and Chen, T. S., "Mixed Convection Over a Horizontal Heated Flat Plate," ASME JOURNAL OF HEAT TRANSFER, Vol. 105, 1983, pp. 420-423.

11 Afzal, N., "Mixed Convection in a Two-Dimensional Buoyant Plume," *Journal of Fluid Mechanics*, Vol. 105, 1981, pp. 347-368.

12 Sparrow, E. M., Quack, H., and Boerner, C. J., "Local Nonsimilarity Boundary-Layer Solutions," *AIAA Journal*, Vol. 8, 1970, pp. 1936-1942.

13 Minkowycz, W. J., and Sparrow, W. M., "Local Nonsimilar Solutions for Natural Convection on a Vertical Cylinder," ASME JOURNAL OF HEAT TRANSFER, Vol. 96, 1974, pp. 178-183.

14 Fujii, T., "Theory of the Steady Laminar Natural Convection Above a Horizontal Line Heat Source and a Point Heat Source," *International Journal of Heat and Mass Transfer*, Vol. 6, 1963, pp. 597-606.

An Experimental Investigation of Combined Convection From a Short Vertical Cylinder in a Crossflow

A. M. Clausing
Associate Professor.

K. C. Wagner
Graduate Research Assistant.

R. J. Skarda
Graduate Research Assistant.

Department of Mechanical and Industrial Engineering, University of Illinois at Urbana-Champaign, Urbana, Ill. 61801

An experimental investigation of combined convective heat transfer from a smooth, isothermal vertical cylinder to a surrounding gas medium is described. The study was motivated by the desire to predict the convective heat loss from the 10-MW_e pilot plant solar receiver in Barstow, California. Hence emphasis is placed on the supercritical (Reynolds number Re greater than 10^5, turbulent (Rayleigh number Ra_L greater than 10^9) regime. The influences of the Reynolds number, the Rayleigh number, the Richardson number, and T_w/T_∞—the ratio of the surface temperature, T_w to the ambient air temperature T_∞—are deduced. Large ranges of these dimensionless parameters are covered with a single model by using a variable ambient temperature, cryogenic wind tunnel over the temperature range 80 K $\leq T_\infty \leq$ 300 K. The cryogenic facility also enables the simultaneous generation of large Rayleigh numbers and large Reynolds numbers.

Introduction

This experimental investigation of combined convective heat transfer was motivated by the desire to predict the convective heat loss from the 10-MW_e pilot plant solar receiver in Barstow, California. The convective heat exchange from large objects, such as the pilot plant solar receiver, buildings, solar collectors, components of industrial processing plants, etc., often occurs in regimes where both buoyancy and interia forces must be considered. Although buoyancy influences are always present, they are usually of negligible consequence for small objects. Large characteristic lengths, on the other hand, result in large buoyancy forces even if the temperature of the surface T_w is not vastly greater than the ambient temperature T_∞. Convective heat transfer processes in which both inertia and buoyant forces must be considered are referred to as combined or mixed convection.

Heated or cooled objects with characteristic lengths of the order of 10 m in a wind with a velocity V of several meters per second have several unusual characteristics which do not permit an accurate estimate of the convective heat exchange and simultaneously make experimental investigations difficult. Specifically:

1 The Reynolds numbers Re for the crossflow over the object due to the wind are of the order of 10^6. These Reynolds numbers lie beyond nearly all the available data and the capability of most wind tunnels.

2 The Grashof numbers Gr_L that characterize the buoyant flow are also large—on the order of 10^{13}. Since the Grashof number is proportional to L^3, it is difficult to attain large Grashof numbers in controlled laboratory studies of scaled-down models.

3 The buoyant forces are of the same magnitude as the interia forces; thus, the problems of interest are combined convection phenomena. Almost all available data are for either pure free or pure forced convection.

The pilot plant solar receiver is an external receiver that is cylindrical in shape. This study is concerned with the determination of the average heat transfer coefficients over smooth, vertical, right circular cylinders with solid, adiabatic ends and with a height to diameter ratio, L/D, of 2—an approximation of the pilot plant receiver. Even with these simplifications, one finds:

1 Nearly all available pure forced convection data are applicable only if $L/D >> 1$.

2 Most of the analytical and experimental investigations of combined convection phenomena are for parallel, attached boundary layer flows. The only studies of combined convection in crossflow are in a completely different flow regime, $Re_D < 10^4$ and $Gr_L < 10^7$ (see, e.g., [1–3]).

3 The influence of variable properties in combined convection is unknown. Available data lie mostly in the range of $0.8 < T_w/T_\infty < 1.4$ whereas solar receivers typically operate in the range $1.5 < T_w/T_\infty < 4$.

One reason for the absence of data in the regime of interest is the difficulty of simultaneously generating both large Reynolds numbers and large Grashof numbers. Another problem is obtaining large values of T_w/T_∞ without masking the results by radiative heat transfer. A variable ambient temperature cryogenic facility was constructed at the University of Illinois at Urbana-Champaign (UIUC) for these reasons. The investigation was conducted in this facility.

Experimental Apparatus and Procedure

The UIUC facility is a variable ambient temperature tunnel which can operate with test section temperatures between 350 and 80 K. The cryogenic tunnel provides a means of obtaining, simultaneously, large increases in the Reynolds number and the Grashof number. The variable T_∞ feature enables one to cover large ranges of the relevant dimensionless groups such as T_w/T_∞, Re, Gr, and Ri (the Richardson number) without changing models and without the results being masked by the radiative mode. The influence of T_∞, ΔT, L, etc., on these dimensionless parameters and the advantages of the use of a cryogenic environment are described in detail in [4]. The tunnel, which is illustrated in Fig. 1, has a rectangular test section with a height of 1.2 m and a width of 0.6 m. It has liquid-nitrogen-cooled walls, and gaseous nitrogen is used as the working fluid. It is a variable speed, recirculating tunnel with a maximum velocity of 8 m/s at 80 K. The turbulence intensity in the test section is 2.3 percent.

Contributed by the Heat Transfer Division and presented at the ASME-JSME Joint Thermal Engineering Conference, Honolulu, Hawaii, March 1983. Manuscript received by the Heat Transfer Division January 17, 1983.

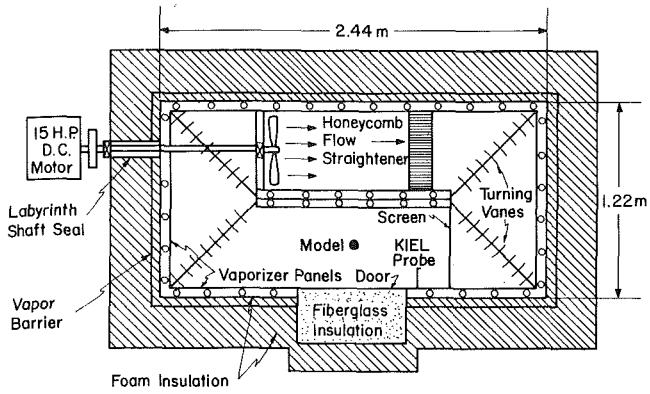

Fig. 1 Simplified cross-sectional, top view of cryogenic facility

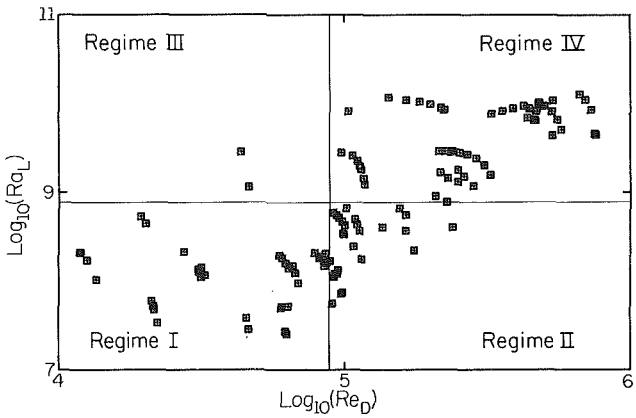

Fig. 2 Combined convection regimes with locations of test points

The model used in the study is a right circular cylinder with a diameter of 0.14 and a height of 0.28 m. The cylinder is hollow with a wall thickness of 5 mm and is made out of 6061-T6 aluminum. The heat transfer coefficient is determined by equating the rate of change of the internal energy of this shell to the convective and radiative losses. The model is heated with nichrome strip heaters which were placed between the outer aluminum shell and an inner, urethane foam cylinder. The urethane foam is a low thermal mass, low thermal conductivity insulation which was designed for cryogenic applications. The inactive, adiabatic ends of the cylinder are constructed out of this same insulation and stiffen with thin stainless steel, perforated plates. Twelve 30-gauge, copper-constantan thermocouples are mounted in 3.2-mm-deep holes on the inside surface of the cylinder.

A test series is initiated after sealing the tunnel by purging it with dry nitrogen gas. Liquid nitrogen is then fed into the vaporizer panels, and the chamber is lowered to the desired ambient temperature T_∞. Next the model is heated slightly above the desired model temperature T_w. The heaters are then switched off; the 11.5-kW, d-c motor is turned on and adjusted to the desired speed. After approximately 20 s, the recording of the model and ambient thermocouple voltages is begun. These signals are digitized and stored on magnetic tape. All data are processed and plotted with digital computer programs. For additional details concerning the model, experimental procedure, and data reduction methods, see [5].

Similitude Considerations

Four flow regimes for combined convection from a vertical cylinder in crossflow were hypothesized [6]. The dividing lines between the regimes are based on the transitional Rayleigh number for pure natural convection, $\mathrm{Ra}_L \simeq 10^9$, and the transitional Reynolds number for pure forced convection, $\mathrm{Re}_D \simeq 10^5$. The regimes are defined as: Regime I (the laminar/subcritical regime); Regime II (the laminar/supercritical regime); Regime III (the turbulent/subcritical regime); and Regime IV (the turbulent/supercritical regime). The regimes are depicted in Fig. 2. The locations of the data from this investigation in this Ra_L–Re_D plane are also indicated in Fig. 2. Finite scales are used in order to show more clearly the experimental data; thus only a portion of each of the four regimes is shown. The pilot plant receiver would typically be operating deeply into Regime IV; hence a turbulent boundary layer is expected over the bulk of the cylinder. Therefore, large Reynolds and Rayleigh numbers are emphasized in this study. In contrast, all available data lie in Regime I at a location far from the boundaries to Regimes II, III, and IV and far beyond the origin of Fig. 2. Hence published data do not appear to be applicable to the combined convective flows of interest. The actual locations of the regime boundaries need to be established. A good understanding currently exists only at the free and forced convection limits.

For a low-speed flow of a perfect gas, Clausing [16] showed that the average Nusselt number in combined convection in a wind tunnel test is dependent on

$$\mathrm{Nu} = f(\mathrm{Re}, \mathrm{Ra}, \mathrm{Pr}, T_w/T_\infty, L/D, \mathrm{Tu}, \mathrm{BR}) \quad (1)$$

where Tu is the turbulence intensity in the wind tunnel and BR is the blockage ratio. It is assumed that the properties, c_p^*, μ^*, and k^* are general functions of only the dimensionless temperature T^*. (The asterisk denotes a dimensionless quantity.) Including the additional group, T_w/T_∞, enables one to arrive at equation (1) without making the Boussinesq approximation. Additional simplifications used in this study follow.

Nomenclature

c_p = specific heat, kJ/kg-K
D = diameter of cylinder, m
f = defined by equation (6)
g = defined by equation (2) or gravitational constant, m/s^2
h = convective heat transfer coefficient, W/m^2 – K
k = thermal conductivity, W/m – K
L = characteristic vertical length, m
T = temperature, K
V = free-stream velocity, m/s
z = defined by equation (10)
β = coefficient of thermal expansion, $1/T_r$, 1/K
ΔT = $T_w - T_\infty$, K
μ = dynamic viscosity, kg/m – s
ρ = density, kg/m^3

Subscripts

B = buoyancy dominated, natural convection limit
D = based on characteristic length, D
f = properties based on film temperature, $T_f = (T_w + T_\infty)/2$
I = inertia dominated, forced convection limit
L = based on characteristic length, L
r = reference temperature: T_f, T_w, or T_∞
rss = root of sum of squares
w = wall
∞ = ambient fluid

Dimensionless Groups

BR = blockage ratio
Gr = Grashof number, $\rho^2 g\beta(T_w - T_\infty)D^3/\mu^2$
Nu = Nusselt number, hD/k
Pr = Prandtl number, $\mu c_p/k$
Ra = Rayleigh number, GrPr
Re = Reynolds number, $\rho VD/\mu$
Ri = Richardson number, $gD\beta(T_w - T_\infty)/V^2$
Tu = turbulence intensity

(*i*) Gases are of interest, and gaseous nitrogen is used in the cryogenic test facility. The Prandtl number Pr is approximately 0.7 for ordinary gases and is essentially a constant—independent of both temperature and pressure. Hence the influence of the Prandtl number is not resolved.

(*ii*) The influences of the turbulence intensity Tu, the blockage ratio BR, and the aspect ratio L/D are not resolved.

Thus the problem reduces to deducing the influence of three variables: the Reynolds number Re, the Rayleigh number Ra, and T_w/T_∞. In our combined convection studies, the Richardson number, $\mathrm{Ri} = \mathrm{Gr}/\mathrm{Re}^2$, is often used in place of Ra. Alternatively, the Froude number, V^2/gD, could also be used. Deducing the influences of even three variables is not an easy task. The task is further complicated by the fact that it is virtually impossible to change any one of the three dimensionless groups over a significant range while holding the other two constant.

A key step, which ultimately led to a successful correlation, was to hypothesize that the influences of temperature-dependent properties on the Nusselt number, a dimensionless temperature gradient at the wall, are not vastly different in combined or forced convection from their influences in pure natural convection. The theory is that the controlling sublayer is similar, when the flow is driven by buoyancy forces, to its form when driven by inertia forces. The general form of the correlation is thus assumed to be

$$\mathrm{Nu} = g(\mathrm{Re}, \mathrm{Ra}) \cdot f(T_w/T_\infty) \tag{2}$$

where g is defined as the constant property correlation, i.e., $f(1) = 1$. The form of equation (2) is not suitable if the variable property influences, which are accounted for with the parameter T_W/T_∞, are dependent on the Reynolds or Rayleigh numbers. Although equation (2) is similar to the property ratio method, the stringent constraint of having to account for variable property influences with a function of a single property ratio is removed.

If the preceeding hypothesis is correct, then the function $f(T_w/T_\infty)$ can be determined from the much simpler, pure natural convection case. This has already been done (see [7]). The results from [7] are summarized in the next section. It should be noted that even in the pure natural convection case, the form $\mathrm{Nu} = g(\mathrm{Ra}) \cdot f(T_w/T_\infty)$ does not follow from the dimensional analysis; its suitability had to be experimentally established. Likewise, the ability to correlate the variable property influences on combined or forced convection data for flow around a cylinder with the function $f(T_w/T_\infty)$, which is derived from results for pure natural convection over vertical surfaces, must also be experimentally demonstrated.

Consider next equation (2) and the form of the function $g(\mathrm{Re}, \mathrm{Ra})$, or $g(\mathrm{Re}, \mathrm{Ri})$, or $g(\mathrm{Ra}, \mathrm{Ri})$, which might be suitable for correlating the constant property, combined convection data. The use of the Richardson number, a ratio of the buoyant force to the inertia force, appears to have merit, especially near the free and forced convection limits. For example, near the forced convection limit, Re has the strongest influence; hence, the form $g(\mathrm{Re}, \mathrm{Ri})$ appears more suitable with Ri accounting only for the perturbation of the weaker buoyancy force. On the other hand, near the natural convection limit, Ra is a more suitable variable with Ri now showing the influences of the secondary, inertia force. For this reason, Clausing [6] proposed a correlation of the form

$$\mathrm{Nu} = [g_I^n + g_B^n]^{1/n} \cdot z(\mathrm{Ri}) \cdot f(T_w/T_\infty) \tag{3}$$

where g_I is the inertia-dominated, pure forced convection correlation, and g_B is the buoyancy-dominated, natural convection correlation. The following points concerning the proposed correlation are to be noted.

(*i*) The limit of equation (3) as $\mathrm{Ri} \to 0$ must be $g_I(\mathrm{Re}) \cdot f(T_w/T_\infty)$; thus the limit of $z(Ri)$ as $Ri \to 0$ is 1. Likewise, the limit of equation (3) as $\mathrm{Ri} \to \infty$ must be $g_B(\mathrm{Ra}) \cdot f(T_w/T_\infty)$; hence the limit of $z(\mathrm{Ri})$ as $\mathrm{Ri} \to \infty$ is also unity.

(*ii*) Although equation (3) contains an additional dimensionless group, it is not as general as equation (2). That is, it cannot be established from dimensional analysis that z is independent of Re or that the product form of equation (3) is acceptable.

(*iii*) The functions $g_I(\mathrm{Re})$ and $g_B(\mathrm{Ra})$ can be determined from the simpler pure forced and pure natural convection cases, respectively. Knowledge of both limits of $z(\mathrm{Ri})$, i.e., $z(0) = z(\infty) = 1$, facilitates its experimental determination.

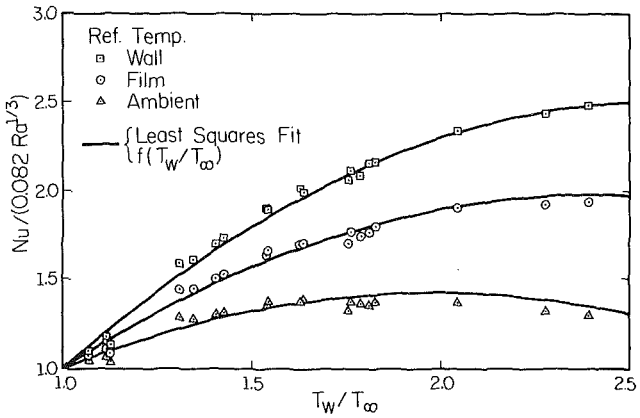

Fig. 3 Variable property correlation—turbulent regime, natural convection data

A value of n of 2 is used in this investigation, and the square root of $(g_I^2 + g_B^2)$ is denoted as g_{rss} for convenience.

Leung [2] studied combined convection from a vertical cylinder in a crossflow in Regime I and correlated his results with a greatly simplified version of equation (3)—$\mathrm{Nu} = g_{rss}$. Leung's data are for a fixed value of T_w/T_∞. Several different cylinder lengths and diameters were used which resulted in a range of L/D between 8 and 16. Clausing [6] reexamined these data in order to determine the reference length in the Richardson number which minimizes the influence of L/D. Based on the criterion set forth in [6], the diameter of the cylinder is the characteristic length which should be used in Regime IV. Hence all dimensionless groups in this study are based on the characteristic length D unless an appropriate subscript indicates otherwise.

Experimental Results

Natural Convection Limit. The UIUC cryogenic facility is an ideal facility for determining the pure natural convection correlation

$$\mathrm{Nu} = g_B(\mathrm{Ra}) \cdot f(T_w/T_\infty) \tag{4}$$

because Ra can be varied by approximately three orders of magnitude simply by changing T_∞. In addition, the influences of radiative heat transfer are greatly reduced especially at large values of T_w/T_∞; hence, it greatly facilitates deducing the variable property influence—$f(T_w/T_\infty)$. The results from the natural convection studies were presented previously in [7] and [8]. The turbulent regime and the influence of T_w/T_∞ are of greatest interest to this study. Equation (4) in this regime was found to be [7].

$$\mathrm{Nu} = 0.082\,\mathrm{Ra}^{1/3} \cdot f, \quad 1.6 \times 10^9 < \mathrm{Ra}_L < 10^{12} \tag{5}$$

If the film temperature, $T_f = (T_w + T_\infty)/2$, is used as the reference temperature, the function f is given by [7]

$$f = -0.9 + 2.4(T_w/T_\infty) - 0.5(T_w/T_\infty)^2, \quad 1 < T_w/T_\infty < 2.6 \tag{6}$$

The reference temperature obviously has no influence on the

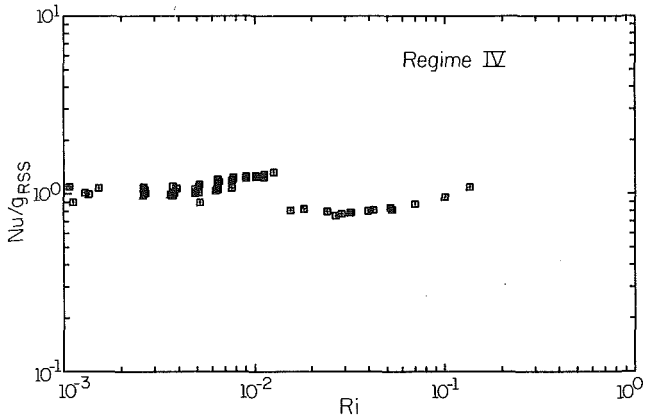

Fig. 4 Data correlated only for influences of Re and Ra—Regime IV

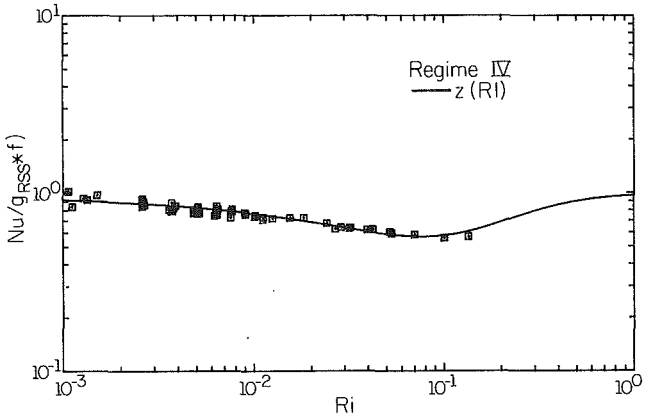

Fig. 5 Richardson number correlation—Regime IV

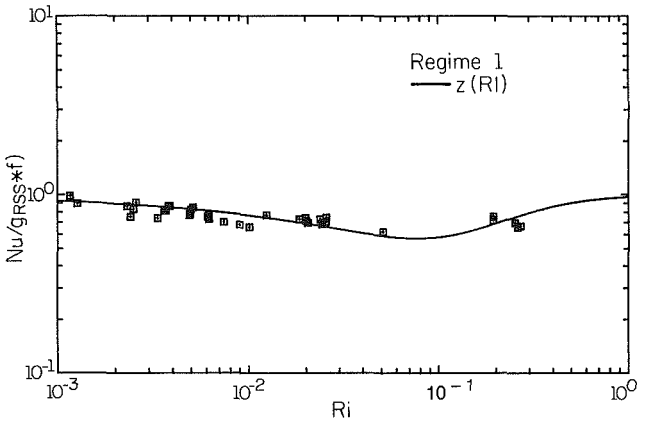

Fig. 6 Correlated data—Regime I

constant property correlation $g_B(\mathrm{Ra})$. Its influence on $f(T_w/T_\infty)$ is shown in Fig. 3.

All the data in the laminar regime, $\mathrm{Ra}_L < 3.8 \times 10^8$, were found to lie within 2 percent of the Schmidt-Beckmann correlation, and $f(T_w/T_\infty)$ was found to be unity in this regime if all properties were based on the film temperature (see [7]). The Schmidt-Beckmann correlation is

$$\mathrm{Nu}_L = 0.52\,\mathrm{Ra}_L^{1/4}, \quad 10^4 < \mathrm{Ra}_L < 3.8 \times 10^8 \tag{7}$$

Thus the film temperature does a remarkably good job of accounting for variable property influences in the laminar regimes but does poorly in the turbulent regime. As expected, the structure of turbulent boundary layers appears to be more strongly dependent on the ambient properties, since most of the temperature drop occurs across the laminar sublayer. Thus in the turbulent regime, $T_r = T_w$ results in the strongest dependence on T_w/T_∞, and $T_r = T_\infty$ results in the weakest dependence. Since the use of the film temperature is more universal and since $f(T_w/T_\infty)$ is unity in the laminar regime with this reference temperature, all thermophysical properties are based on the film temperature in this investigation. $f(T_w/T_\infty)$ in this case is given by equation (6). A correlation for the so-called transitional regime, $3.8 \times 10^8 < \mathrm{Ra}_L < 1.6 \times 10^9$, is also given in [7]. The variable property influence on Nu in this regime is dependent on both Ra and T_w/T_∞. Clausing [7] compared both published data and the UIUC data with these correlations, and the average absolute differences were found to be less than 7 percent in all regimes. The agreement is indeed remarkable, especially considering the ranges of the parameters which the data cover—3.25 mm $\le L \le$ 7,320 mm; $1.03 \le T_w/T_\infty \le 2.53$; 0.97 atm $\le p \le$ 67.7 atm; 9 K $\le \Delta T \le$ 140 K; and 82 K $\le T_\infty \le$ 305 K, $10^4 < \mathrm{Ra}_L < 10^{12}$.

Forced Convection Limit. The limit of the proposed combined convection correlation, equation (3), as Ri $\to$ 0 is

$$\mathrm{Nu} = g_I(\mathrm{Re}) \cdot f(T_w/T_\infty) \tag{8}$$

In the UIUC tunnel, the flow around infinite span cylinders was previously found to be supercritical for the regime $\mathrm{Re} > 9 \times 10^4$ (see [9]). Thus the desired function $g_I(\mathrm{Re})$ for use in Regime IV was derived from a least-squares fit of the lowest Richardson number data ($\mathrm{Ri} < 1.3 \times 10^{-3}$) with $\mathrm{Re} > 9 \times 10^4$. Since the suitability of the function $f(T_w/T_\infty)$, which was derived from the natural convection data, equation (6), is open to question, only data with $T_w/T_\infty < 1.13$ was utilized in order to minimize the correction, $f(T_w/T_\infty)$. Likewise, once $z(\mathrm{Ri})$ was established, an iterative correction was applied which increased the coefficient of g_I from 0.0515 to 0.055. The resulting correlation is

$$g_I = 0.055\,\mathrm{Re}^{0.76}, \quad 9 \times 10^4 < \mathrm{Re} < 10^6 \tag{9}$$

In comparison, the correlation, which was recently proposed by Churchill and Bernstein [10], which reduces to $\mathrm{Nu} = 0.49\,\mathrm{Re}^{1/2} + 0.00092\,\mathrm{Re}$ for Pr = 0.72, lies approximately 40 percent below equation (9) Re = 10^5 or 10^6. However, their corrrelation is for infinite cylinders in flow fields with negligible turbulence intensity. They also state that "the data of Achenback [15] and of Lewis [39] fall above" their correlation.

The following points need to be considered in comparison of equation (9) with published correlations for forced convection over cylinders.

(*i*) Equation (9) is for an aspect ratio L/D of 2, whereas most data in the literature are for $L/D >> 1$. No studies were found which adequately quantify the influence of L/D.

(*ii*) Simonich and Bradshaw's [11] results indicate that a turbulence intensity of 2.3 percent (that of the UIUC tunnel) increases heat transfer coefficients by 12 percent over those obtained in a tunnel with negligible turbulence intensity.

(*iii*) The combined influences of turbulence scale and blockage appear to be of the order of 5 percent, but little agreement exists in the literature concerning these influences.

Combined Convection Regimes. All of the combined convection data are plotted versus the Richardson number since its influence is being deduced. A total of 135 data points were taken in the four regimes (see Fig. 2) with emphasis on Regime IV. The combined convection data cover the following ranges of the dimensionless parameters; $0.001 < \mathrm{Ri} < 0.270$, $10^4 < \mathrm{Re} < 8 \times 10^5$; $1 < T_w/T_\infty < 2.1$ and $2 \times 10^7 < \mathrm{Ra}_L < 3 \times 10^{10}$.

Consider first the data from Regime IV. These data are shown in Fig. 4, which is a plot of $\mathrm{Nu}/g_{\mathrm{rss}}$ versus Ri. Much of the scatter, which would have been present in a graph of Nu versus Ri, has been removed, but appreciable variations still

exist. Next the data are divided by the function $f(T_w/T_\infty)$, equation (6), which was hypothesized to account for the variable property influence. The resulting correlation $z(\mathrm{Ri})$ is shown in Fig. 5 which gives $\mathrm{Nu}/(g_{\mathrm{rss}} \cdot f)$ versus Ri. The effect of $f(T_W/T_\infty)$ on the data is dramatic whenever T_w/T_∞ is large. For example, the data point at Ri = 0.0155 and the adjacent point at Ri = 0.0125 have absolute temperature ratios, T_w/T_∞, of 1.08 and 1.86, respectively. The corresponding values of $f(T_w/T_\infty)$ are 1.11 and 1.83; thus division by $f(T_w/T_\infty)$ shifts these adjacent points from their vastly divergent locations to positions along the smooth correlation, $z(\mathrm{Ri})$.

The function $z(\mathrm{Ri})$, which is shown in Fig. 5, is

$$z(\mathrm{Ri}) = 1 - 0.43 \sin\left\{\frac{\pi \mathrm{Ri}^{1/2}}{(\mathrm{Ri}^2 + 0.09)^{1/4}}\right\}, \qquad (10)$$

$$10^{-3} < \mathrm{Ri} < 0.3$$

The form of equation (10) was chosen such that it satisfies the constraints $z(0) = z(\infty) = 1$. The average deviation of the Regime IV data from the correlation

$$\mathrm{Nu} = [g_f^2 + g_B^2]^{1/2} \cdot z(\mathrm{Ri}) \cdot f(T_w/T_\infty) \qquad (11)$$

where g_f, g_B, z, and f are given by equations (9), (5), (10), and (6), respectively, is 4 percent, and the maximum derivation is only 8 percent.

Consider next the remainder of the data, Regimes I, II, and III. In pure forced convection over an infinite cylinder, the flow field and drag coefficients experience drastic changes as the flow passes from subcritical to supercritical. On the other hand, large changes in the average heat transfer coefficient are not seen. For example, the data from this study with small Richardson numbers and small values of T_w/T_∞ agree well with the correlation $g_f(\mathrm{Re})$ over the complete Reynolds range—$10^4 < \mathrm{Re} < 8 \times 10^5$ (see Fig. 6.11 of [5]). Likewise, the constant property natural convection correlations show no discontinuity at transition, and the laminar and turbulent correlations give similar results in the region $10^8 < \mathrm{Ra}_L < 10^9$ (see Figs. 3 and 7 of [7]). On the other hand, the influence of variable properties is vastly different in the laminar and turbulent regimes. For example, $f(1) = f(2) = 1$ in the laminar regime, whereas $f(1) = 1$ and $f(2) \simeq 2$ on the turbulent regime. Thus the largest uncertainty appears to be the use of equation (6), the variable property correlation, in Regimes I and II.

As expected, the two data points in Regime III agree well with correlation (11). Both points differ by 4 percent. The 38 data points in Regime II also agree well with equation (11), even though the lower range of Ra_L is only 5×10^7. The average deviation is 5 percent and the maximum is 12 percent in Regime II. The Regime I data, which provide the most stringent test, are shown in Fig. 6 after division by equation (6). Again the data are correlated well by equation (11), even though Re extends downs to 10^4 and Ra_L down to 2.7×10^7. The mean and maximum deviations are somewhat larger—6.9 percent and 17 percent, respectively.

Major sources of error in this investigation are the temperature measurements, the determination of the thermal capacitance and emittance of the model, and the velocity determinations. Temperature measurement and thermal capacitance errors were found to be ±2 K and 2.2 percent, respectively. The maximum error in the velocity was estimated to be 3 percent. The error arising from the emittance estimates was determined to be less than 2 percent. An error analysis predicted an experimental uncertainty in the combined convection results of 5 percent. This uncertainty agrees well with the deviations from equation (11) which were indicated.

Conclusions

The following conclusions are drawn from the study. They are applicable only over the ranges of the dimensionless groups which were investigated.

1 The influences of variable properties are correlated well with the additional parameter, T_w/T_∞. When properties are based on the film temperature, the Nusselt number at $T_w/T_\infty = 2$ is approximately 100 percent larger than the corresponding constant property value at $T_w/T_\infty = 1$.

2 The function $f(T_w/T_\infty)$, which was derived from data in the natural convection regime, correlates well the variable property influences in the combined convection regimes. No dependency of these influences on Ri or Re was detectable.

3 The data from this investigation always showed a decrease in heat transfer due to buoyancy influences. That is, $g_{\mathrm{rss}} \cdot z(\mathrm{Ri})$ was always less than $g_f(\mathrm{Re})$. Specifically, $g_f/(g_{\mathrm{rss}} \cdot z)$ lies approximately between 1 and 1.7. It should be noted that the data from this investigation appear to be relatively close to the forced convection limit. For example, the maximum values of the ratio g_B/g_f in Regimes I, II, III, and IV are 0.462, 0.126, 0.319, and 0.234, respectively. The corresponding values of g_f/g_{rss} are 0.908, 0.992, 0.953, and 0.974, respectively.

4 All combined convection data from this investigation (135 data points) correlate well with the correlation

$$\mathrm{Nu} = [g_f^2 + g_B^2]^{1/2} \cdot z(\mathrm{Ri}) \cdot f(T_w/T_\infty) \qquad (11)$$

The average absolute deviation between the data and equation (11) is 5 percent, and the maximum deviation is 14 percent. Although the data were initially divided into four regimes, the results indicate that all data can be placed in a single regime. The data of Leung [2] may lie in a different regime where $\mathrm{Nu} \simeq g_{\mathrm{rss}}$. Since his data are all for a single value of T_w/T_∞, the influence of this variable is not resolvable.

5 Although the limit of $z(\mathrm{Ri})$ as $\mathrm{Ri} \to \infty$ is 1, the function is only valid for the specified range—$10^{-3} < \mathrm{Ri} < 0.3$. The range of Ri clearly needs to be enlarged in both directions. This will not be an easy task. For example, even ambient drafts due to extraneous sources seem to influence natural convection data, and investigators have taken great pain to reduce such influences (see discussions in [7]).

References

1 Oosthuizen, P. H., and Taralis, D. N., "Combined Convective Heat Transfer from Vertical Cylinders in a Horizontal Fluid Flow," ASME Paper No. 78-WA-41, 1976.

2 Leung, R. K., "Combined Convective Heat Transfer from Vertical Bodies in a Horizontal Stream," M.S. thesis, Department of Mechanical Engineering, Queen's University, Kingston, Ontario, Canada, 1975.

3 Oosthuizen, P. H., and Leung, R. K., "Combined Convective Heat Transfer from Vertical Cylinders in a Horizontal Flow," ASME Paper No. 78-WA/HT-45, 1978.

4 Clausing, A. M., "Advantages of a Cryogenic Environment for Experimental Investigation of Convective Heat Transfer," *International Journal of Heat and Mass Transfer*, Vol. 25, No. 8, 1982, pp. 1255–1257.

5 Wagner, K. C., "The Influence of Variable Properties in Combined Convection from a Vertical Cylinder in Crossflow," M.S. thesis, Department of Mechanical and Industrial Engineering, University of Illinois at Urbana-Champaign, Urbana, IL, 1982.

6 Clausing, A. M., "Modeling Requirements for Determination of Convective Losses from Solar Receivers," *Proceedings of the 1981 Annual ISES Meeting*, Vol. 4.1, 1981, pp. 371–375.

7 Clausing, A. M., "Natural Convection Correlations for Vertical Surfaces Including Influences of Variable Properties," ASME JOURNAL OF HEAT TRANSFER, Vol. 105, No. 1, 1983, pp. 138–143.

8 Clausing, A. H., and Kempka, S. N., "The Influences of Property Variations on Natural Convection from Vertical Surfaces," ASME JOURNAL OF HEAT TRANSFER, Vol. 103, 1981, pp. 609–612.

9 Mueller, M. H., et al., "Description of UIUC Cryogenic Wind Tunnel Including Pressure Distributions, Turbulence Measurements, and Heat Transfer Data," University of Illinois Tech. Report, ME-TN-79-9180-1, 1979.

10 Churchill, S. W., and Bernstein, M., "A Correlating Equation for Forced Convection from Gases and Liquids to a Circular Cylinder in Crossflow," ASME JOURNAL OF HEAT TRANSFER, Vol. 99, 1977, pp. 300–306.

11 Simonich, J. C., and Bradshaw, P., "Effect of Free-Stream Turbulence on Heat Transfer Through a Turbulent Boundary Layer," ASME JOURNAL OF HEAT TRANSFER, Vol. 100, 1978, pp. 671–677.

R. Das
Post Doctoral Fellow.

A. K. Mohanty
Professor.
Mem. ASME

Department of Mechanical Engineering,
Indian Institute of Technology,
Kharagpur, India

Laminar Combined Convection in Finite Circular Rod Bundles

Laminar combined free and forced convection in flow through a finite rod array is investigated using a finite difference scheme. The geometrical dimensions simulate those of a CANDU-type pressurized water reactor. The rods are deemed to dissipate heat uniformly, whereas the shell wall is maintained adiabatic. Temperature of the inner rod surface at a non-nodal and nonorthogonal intersection is estimated using a six-point interpolation scheme. Velocity and temperature profiles together with transport rates are presented indicating variations due to buoyancy, power skew, eccentricity, and number of rods in the array.

1 Introduction

The study of thermal-hydraulics in a rod or tube bundle geometry finds extensive practical application in the design of shell and tube heat exchangers. However, recent interests in the rod-bundle investigation stem from the need to predict the transport rates in a nuclear reactor core that model closely with the shell and rod configuration.

The flow regime in the normal operating condition of a reactor is single-phase turbulent, and design information are obtainable by extrapolating the results of simpler internal flow geometries, using the principles of dimensional analysis.

On the other hand, the safety of a reactor is controlled by its adaptability to transients. In the event of a severe transient, such as the loss of coolant accident (LOCA), the coolant flow rate is drastically reduced, causing the degeneration of the flow regime from turbulent to laminar. Reduction of heat transfer rate results in overheating of the fuel rods, and significant buoyancy effects are induced. Ignoring the subsequent two-phase and radiation exchange phenomena, it is realized that the assessment of the accident condition is dependent on the evaluation of the laminar combined free and forced convection transport rates. The laminar rates, being geometry dependent, are not amenable to evaluation by dimensional analysis.

The rod bundle configuration is categorized either as an infinite or a finite array. The influence of the bounding shell is neglected for an infinite array and the results obtained are applicable to only very large-sized reactors. In the smaller designs, e.g., of the CANDU type, and in laboratory simulations, the geometry is finite, and the edge effects are felt all over the cross section. The transport domain is multiply connected.

Fully developed hydrodynamic and thermal conditions are attained at some distance downstream of the entry. The laminar forced convective transprt equations are then of the Poisson's kind. Most of the investigations pertain to solution of Poisson's equation in rod bundle geometries, both infinite [1-3] and finite [4].

Sparrow and coworkers [1, 2] were the earliest ones to study the forced convection through an isothermal infinite bundle by a series solution. The procedure was extended to the uniform heat input condition by Dwyer and Berry [3].

The finite rod bundle geometry, received attention only in the late sixties and seventies. The linear fully developed momentum equation was solved, through a combination of analytical and numerical methods, such as by Mottaghian and Wolf [4], using bipolar coordinate systems: the main one located at the shell center and the auxiliaries at the center of the inner rods.

Benodekar and Date [5] used a difference technique to solve the laminar forced convection equations for finite rod arrays, considering an uniform heat flux boundary. Numerical results for the flow characteristics alone were earlier provided by Gunn and Darling [6] for a 4-rod infinite bundle, and by Zarling [7] for a finite bundle.

Many of the results available through 1977 were summarized by Shah and London [8] and recently updated by Kakac et al. [9].

Combined convection studies have been limited to infinite and semi-infinite rod arrays. Iqbal et al. [10] investigated the influence of buoyancy in an upward flow through triangular and square rod arrays for both constant heat flux and isothermal conditions. A threshold Rayleigh number of 100 was needed before heat transfer was noticeably increased due to buoyancy. Iqbal and coworkers [11] have subsequently considered a conjugate analysis of combined convection.

Ramm and Johannsen [12] observed that buoyancy and power skew cause inversions of velocity and temperature profiles in a semi-infinite hexagonal rod-bundle. The analyses of Yang [13, 14] indicate that heat transfer is decreased and the flow resistance increased, leading to separation, as buoyancy effects are increased in downflow through infinite triangular and square arrays of rods. Yang's results, however, need review because of the assumption that the rod surface is isothermal while dissipating uniform heat flux.

A recent numerical study by Prakash and Patankar [15] of combined convection through a vertical finned tube is of some

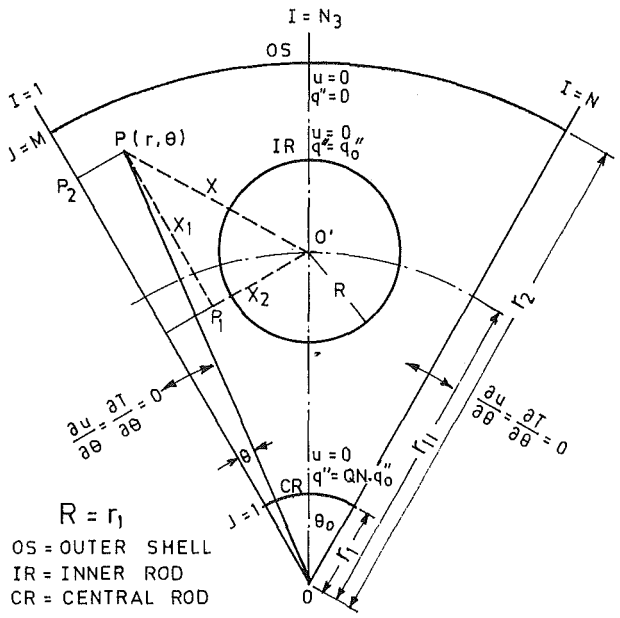

Fig. 1 Physical model

Contributed by the Heat Transfer Division for publication in the JOURNAL OF HEAT TRANSFER. Manuscript received by the Heat Transfer Division May 24, 1984.

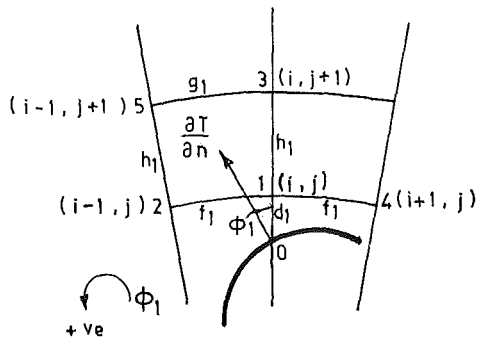

$h_1 = \Delta r$; $d_1 = \alpha \Delta r$

(a) UNCOUPLED INTERSECTION

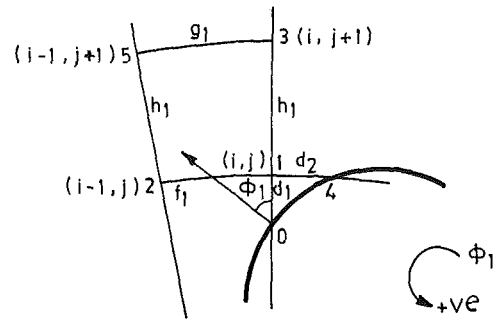

$f_1 = r_j \Delta\Theta$; $d_2 = \beta r_j \Delta\Theta$

(b) COUPLED INTERSECTION

Fig. 2 Gradient interpolation

pertinence to the present investigation in so far as there is a resemblance between the physical models.

The literature on combined convection were critically reviewed by Viskanta and Mohanty [16]. It is their conclusion that the literature information of transport rates through even simpler geometries are not free from contradictions. References to further studies on combined convection in low Reynolds number flow are available in Kakac et al. [9].

The present study is an attempt to provide the transport rate information for a finite rod array taking into account: flow directions, power skew, degree of buoyancy, number of rods, and eccentricity of the rod pitch circle.

2 Physical Model

The finite rod-bundle geometry is subdivided into a number of symmetry sectors and the computation is carried out for any one of these, Fig. 1. The location of a point in the transport field is monitored from both the shell center and the center of the inner rod. The domain of computation is divided into radial and angular grids. The inner rod boundary is not always intersected by the grid lines at the nodal points. The distances of non-nodal intersections, represented by α and β in Fig. 2(a) and 2(b), are evaluated by geometric considerations, the details of which can be found in [17].

3 Analysis

3.1 Governing Equations. We consider fully developed velocity and temperature fields in a vertical orientation for which the conservation equations are

$$0 = -\frac{dp}{dx} + \mu \nabla^2 u \pm \rho g \text{ (momentum)} \tag{1}$$

$$u \frac{\partial T}{\partial x} = \alpha_T \nabla^2 T \text{ (energy)} \tag{2}$$

where

Nomenclature

A_W = flow area, $\pi(r_2^2 - nr_1^2)$, m^2; $A_W^* = A_W/r_2^2$

C_p = specific heat at constant pressure kJ/kgK

D_H = hydraulic diameter, $4A_W/(2\pi nr_1 + 2\pi r_2)$, m; $D_H^* = D_H/r_2$

f = Fanning friction factor

G = nondimensional pressure gradient, $-(dp/dx)r_2^2/\mu u_{\text{ref}}$

Gr = Grashof number, $(q_o'' r_2^4/k)(\beta_T g/\nu^2)$

g = gravitational acceleration, m/s^2

k = thermal conductivity of the fluid, W/m°C

M = number of divisions in the radial direction

N = number of divisions in the angular direction

Nu = Nusselt number, $\bar{h}D_H/k$

n = number of rods in the finite array

P_q = heat transfer perimeter, m; $P_q^* = P_q/r_2$

p = axial pressure, Pa

p_d = hydrodynamic pressure, Pa

p_s = hydrostatic pressure, Pa

$\frac{dp}{dx}$ = axial pressure gradient, Pa/m

Q = flow rate, m^3/s; $Q^* = Q/(r_2^2 u_{\text{ref}})$

QN = power skew factor defined as the ratio of heat flux on central rod to that on an inner rod

q_o'' = heat flux on the inner rod, kW/m^2

$\bar{q}$ = weighted heat flux, kW/m^2

Re = Reynolds number, $u_{\text{av}} D_H/\nu$

r = radial coordinate, m; $r^* = r/r_2$

r_1 = radius of the central and inner rods, m; $r_1^* = r_1/r_2$

r_2 = radius of the outer shell, m

r_{11} = distance between the centers of the inner rod and the central rod, m; $r_{11}^* = r_{11}/r_2$

$r_j^* \Delta\theta$ = nondimensional angular distance between the nodes

S_N = total number of surface points of the inner rod on one side (left) of I = N_3 line

T = temperature, K; $T^* = (T - \bar{T}_S)/T_{\text{ref}}$

T_B = bulk temperature, K

T_C = temperature of the central rod, K

T_R = surface temperature of the inner rod, K

$T_{\text{ref}} = q_0'' P_q/kA_W^* u_{\text{av}}^*$, K

T_S = shell-wall temperature, K

$\bar{T}_W$ = average temperature of the heated surfaces, K

u = local axial velocity, m/s; $u^* = u/u_{\text{ref}}$

u_{av} = average velocity, m/s; $u_{\text{av}}^* = u_{\text{av}}/u_{\text{ref}}$

u_{ref} = reference velocity, $\mu/r_2^2(-dp/dx)$, m/s

x = axial coordinate, m

Greek Symbols

α = fractional radial distance shown in Fig. 2(a)

α_T = thermal diffusivity, m^2/s

β = fractional angular distance shown in Fig. 2(b)

β_T = coeffcient of thermal expansion, K^{-1}

Δr = radial distance between the nodes, m

ϵ = eccentricity, $r_{11}/(r_2 - r_1)$

ρ = fluid density, kg/m^3

$\bar{\rho}_S$ = fluid density at $\bar{T}_S$, kg/m^3

μ = dynamic viscosity, Pa•s

ν = kinematic viscosity, m^2/s

$$p = p_s + p_d$$

The positive sign for body force in equation (1) is associated with a downward flow, and the negative for upward.

In order that the effects of buoyancy, power skew and the like can be referred to a common base, we consider that the hydrodynamic pressure gradient, expressed nondimensionally through G is maintained constant by an external agency. $G = 1$ affords evaluation of u_{ref}. In a measurement of a pressure differential on the wall of a finite rod bundle, the hydrostatic pressure shall be that due to the fluid density at the shell wall. For convenience of correlation with an experimental situation, we choose to define the hydrostatic pressure through $\bar{\rho}_S$ at the shell wall average temperature, $\bar{T}_S$. By combining with the body force, the local buoyancy force is obtained as

$$-\frac{dp_s}{dx} \pm \rho g = \mp \bar{\rho}_S g \beta_T (T - \bar{T}_S) \tag{3}$$

The momentum equation is now written in nondimensional form

$$\nabla^2 u^* = -G \pm \frac{\beta_T g (T - \bar{T}_S) r_2^2}{\nu u_{\text{ref}}} \tag{4}$$

The right-hand side of equation (4) can be simplified after a reference to the temperature equation.

Overall energy balance for a control volume with fully developed thermal conditions and uniform heat input leads to

$$\frac{\partial T}{\partial x} = \frac{dT_B}{dx} = \frac{q_o'' P_q}{\rho A_W u_{\text{av}} C_p} = \text{constant} \tag{5}$$

Substituting relation (5) and defining $T^* = (T - \bar{T}_S)/T_{\text{ref}}$, the energy equation (2) is reduced to

$$\nabla^2 T^* = \left(\frac{q_o'' P_q}{T_{\text{ref}} k A_W^* u_{\text{av}}^*} \right) u^*$$

The coefficient of u^* is simplified to unity by choosing,

$$T_{\text{ref}} = \frac{q_o'' P_q}{k A_W^* u_{\text{av}}^*} \tag{6}$$

resulting in

$$\nabla^2 T^* = u^* \tag{7}$$

Use of equation (6) and T^* enable rewriting the second term in the right-hand side of the momentum equation (4) as

$$\left(\frac{\text{Gr}}{\text{Re}} \right) \left(\frac{P_q^* D_H^*}{A_W^*} \right) T^*$$

A generalized definition of the heat transfer perimeter is adopted to incorporate the power skew factor QN on the central rod.

$$P_q^* = 2\pi r_1^* [(n-1) + QN] \tag{8}$$

Making the substitutions for the buoyancy term, we obtain the momentum equation in the form

$$\nabla^2 u^* = -G \pm \left(\frac{\text{Gr}}{\text{Re}} \right) \left(\frac{4 r_1^*}{1 + n r_1^*} \right) [(n-1) + QN] T^* \tag{9}$$

recalling that the (+) sign is for downward and (−) for upward main flow.

The condition that buoyancy opposes or supports the mainflow, due to $-G$, depends on whether the composite sign of ($\pm$ Gr/Re T^*) is respectively positive or negative.

The two coupled conservation equations (7) and (9) are solved by a finite difference scheme satisfying the boundary conditions

(*i*) (*i*) $u^* = 0$ on the solid surfaces: the inner rod; $r^* = r_1^*$ and $r^* = 1$

(*ii*) $$\frac{\partial u^*}{\partial \theta} = \frac{\partial T^*}{\partial \theta} = 0$$

as the symmetry conditions at $\theta = 0$, $\theta_o/2$ and θ_o.

(*iii*) $$\frac{\partial T^*}{\partial n^*} = -\left(\frac{q_o'' r_2}{k T_{\text{ref}}} \right)$$

on the inner rod, where n^* is the normal to the rod surface.

(*iv*) $$\frac{\partial T^*}{\partial r^*} = -\left(\frac{q_o'' r_2 QN}{k T_{\text{ref}}} \right)$$

on the central rod.

(*v*) $$\frac{\partial T^*}{\partial r^*} = 0$$ on the shell wall.

$\bar{T}_S^* = 0$ is satisfied iteratively to comply with the definition.

3.2 Difference Equation. The radial and angular distances between two nodes are expressed in a generalized manner as $\alpha \Delta r$ and $\beta r_j \Delta\theta$. α and β differ from unity for nodes in the vicinity of the inner rod. Following Greenspan [18], a central difference scheme is adopted. The form of the difference equation for u^* is

$$u_{i,j}^* = \frac{1}{E} [C u_{i,j+1}^* + D u_{i,j-1}^* + F(u_{i+1,j}^* + \beta u_{i-1,j}^*) - G'] \tag{10}$$

where G' represents the right-hand side of equation (9).

The form of the temperature equations is similar, except that G' is replaced by $u_{i,j}^*$. The coefficients C, D, E, and F have different expressions depending on the location of the nodal points with respect to the inner rod. The expressions are derivable without much difficulty, and are given in [17].

The difference equation and its solution for Dirichlet boundary conditions, as applicable to fluid flow problems, is similar to those earlier elaborated by Mohanty and Ray [19]. The solution for temperature distribution in presence of Neumann boundary conditions is comparatively involved and is discussed subsequently.

3.3 Thermal Condition on the Inner Rod. The evaluation of heat flux under the power skew condition on the central rod or the adiabatic condition on the shell wall is carried out adequately by a three-point interpolation along radial lines, as the main radius is perpendicular to these surfaces.

The evaluation of the heat flux on the inner rod is, however, involved for two reasons: non-nodal intersections and the surface normal not being a grid line.

The temperature gradient on a inner rod surface is evaluated through a six-point interpolation scheme expanding on the method of Greenspan [18]. Consider Fig. 2(*a*), where 0 represents the surface point and 1 to 5 are the neighbouring points. The temperature gradient at 0 is represented through

$$\left. \frac{\partial T^*}{\partial n^*} \right|_0 = \left. \frac{\partial T^*}{\partial r^*} \right|_0 \cos\phi_1 - \left. \frac{\partial T^*}{r^* \partial \theta} \right|_0 \sin\phi_1 = \sum_{i=0}^{5} \eta_i T_i^* \tag{11}$$

The T_i^* are expressed through Taylor series expansion. For example, we would write

$$T_5^* = T_0^* + (d_1 + h_1) \frac{\partial T^*}{\partial r^*} + \frac{(d_1 + h_1)^2}{2} \frac{\partial^2 T^*}{\partial r^{*2}} - g_1 \frac{\partial T^*}{r^* \partial \theta} + \frac{g_1^2}{2} \frac{\partial^2 T^*}{r^{*2} \partial \theta^2} - g_1 (d_1 + h_1) \frac{\partial^2 T^*}{r^* \partial r^* \partial \theta}$$

The coefficients η_i are evaluated by comparing the left-hand and the right-hand side of equation (11). The angle ϕ_1 is known from geometrical consideration, e.g.,

$$\phi_1 = \sin^{-1} \left[\frac{r_{11}}{r_1} \sin\left(\frac{\theta_0}{2} - \theta \right) \right]$$

for Fig. 2(*a*). The expression for T_1^* and η_i differ in similar ways as did the coefficients C to F, equation (10), depending on the location of the surface points with respect to the center

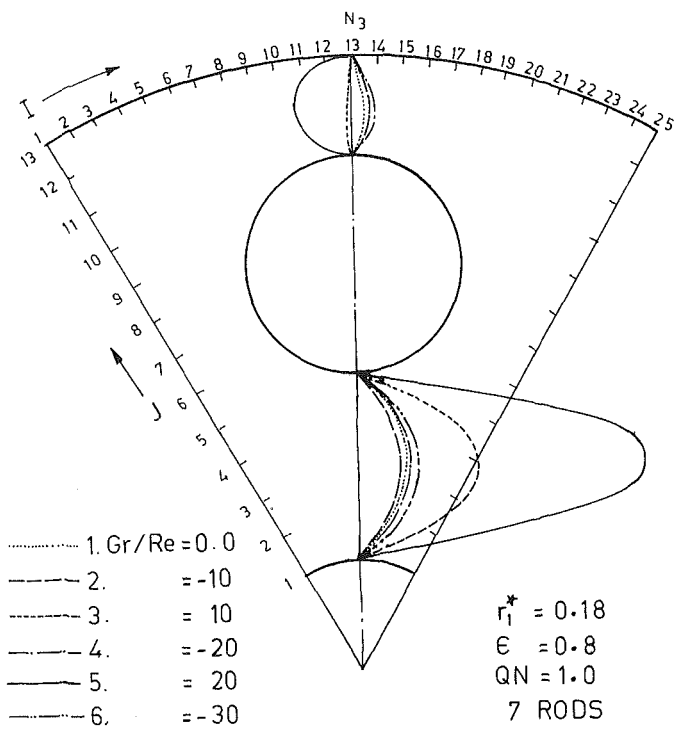

Fig. 3(*a*) Effect of buoyancy on velocity profile at I = N_3

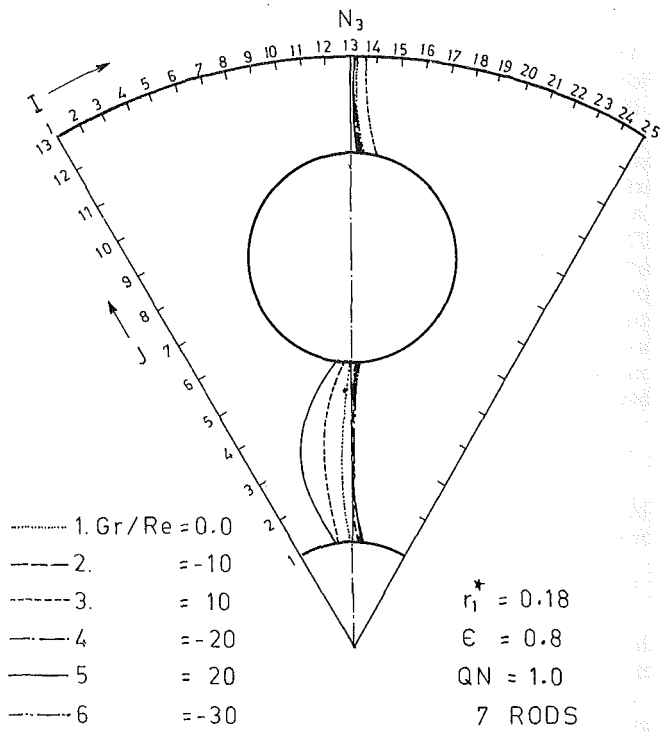

Fig. 3(*b*) Effect of buoyancy on temperature profile at I = N_3

of the inner rod. Figure 2(*b*) is another of the total eight different intersections (four coupled and four uncoupled), details of which can be seen in [17]. The coupled intersections involve both α and β, whereas for the uncoupled ones, only one is different from unity.

The inner rod temperature at an intersecting point is then evaluated as

$$T_0^* = -\frac{1}{\eta_o}\left[\frac{q_o^* r_2}{k\,T_{\text{ref}}} + \eta_1 T_1^* + \eta_2 T_2^* + \eta_3 T_3^* + \eta_4 T_4^* + \eta_5 T_5^*\right] \tag{12}$$

The surface temperature is subsequently used for computing the temperature at the vicinity nodes.

3.4 Method of Iteration and Convergence. Assigning an initial value of unity to a nonzero valued parameter, u^* or T^*, iteration of the momentum and energy equations were carried out simultaneously in a cyclic process. The iterations were begun on $J = 2$ proceeding angularly from $I = 1$ to N_3 till $J = M$ and then returning back to $J = 1$, traversing through the I lines, Fig. 1.

On first reaching $J = M$ midway through the cycle, the nonzero residue of the shell wall average temperature was substracted as correction to the nodal temperatures. The values in the zone $I = N_3$ to N were obtained by reflection of the corresponding left-hand nodal results at the end of every iteration.

The convergence of the iteration was monitored at two nodes: $J = 2$ and $J = M-1$ on $I = N_3$, their importance arising from the proximity of the solid surfaces of the central rod and the shell wall. The convergence was defined as the relative variation of a parameter between the nth and the $(n-1)$th iterations, and a value of 10^{-4} was considered acceptable.

The test case consisted of pure forced convection through a 7-rod assembly of 0.2 radius ratio at $\epsilon = 0.8$, the one investigated by Benodekar and Date [5]. The present results for (13 × 25) grids were within 3 percent of [5].

3.5 Evaluation of Transport Parameters. The parameters of design interest are: cross-sectional flow rate, friction factor, and Nusselt number. These were evaluated in the following manner:

Fanning friction factor

$$f = -\left(\frac{dp}{dx}\right)\frac{D_H}{2\rho u_{\text{av}}^2}$$

results into the expression

$$f\,\text{Re} = \frac{G\,D_H^{*2} A_W^*}{2Q^*} \tag{13}$$

in which all but Q^* are known. The nondimensional flow rate Q^* was evaluated by a trapezoidal averaging of the nodal velocity values weighted by the respective areas.

In any given sector, the heated surfaces are those due to the sector of the central rod and of the inner rod(s). The heat input per unit area accounting for power skew condition is

$$\tilde{q} = \frac{q_o''\,[(n-1)+QN]}{n} \tag{14}$$

The average temperature of the central, or of the shell wall, could be estimated by a simple summation, since the grid sizes are equal. On the other hand, estimation of the inner rod average temperature required weighting through the variable angle ψ_k subtended between two consecutive surface points k and k+1.

$$\tilde{T}_R^* = \frac{\sum_{k=1}^{S_{N-1}} (T_{R_k}^* + T_{R_{k+1}}^*)\psi_k}{2\pi} \tag{15}$$

where S_N is the total number of surface points in the zone $I = 1$ to N_3. The average temperature of the heated surfaces is thus

$$\tilde{T}_W^* = \frac{[\tilde{T}_C^* + (n-1)\tilde{T}_R^*]}{n} \tag{16}$$

The fluid bulk temperature was estimated in the same manner

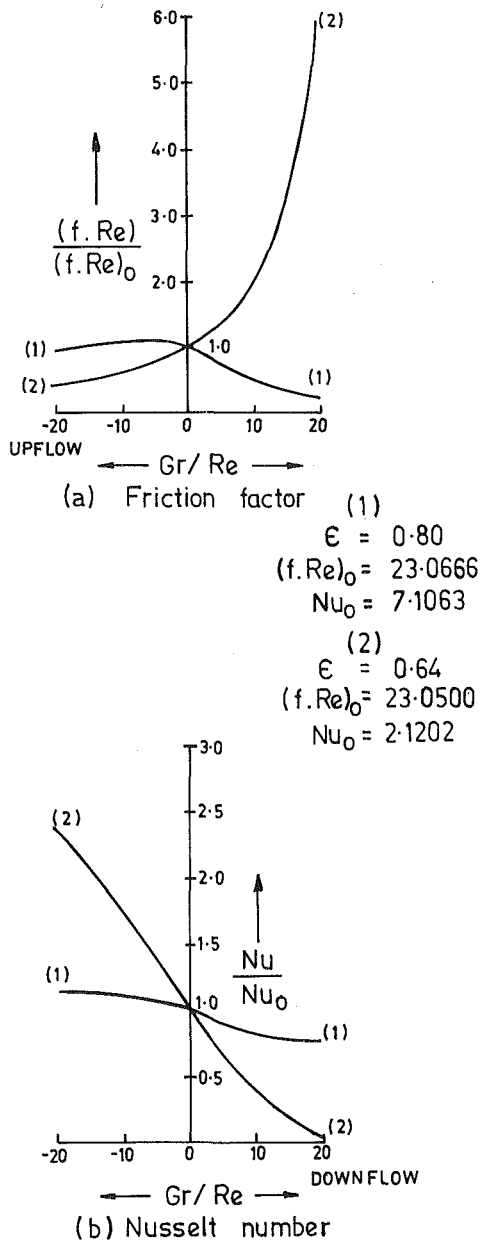

Fig. 4 Effects of eccentricity on transport rates

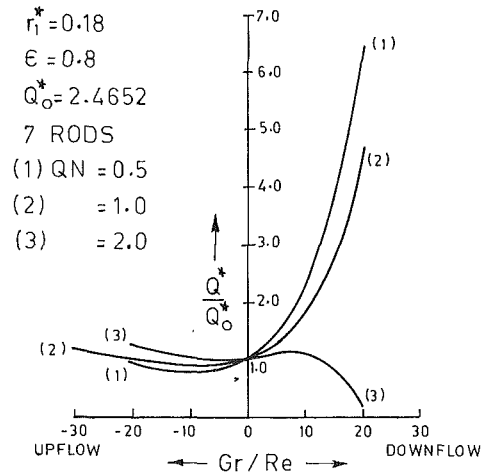

Fig. 5 Effects of buoyancy and power skew on flow rate

and step used for computing the flow rate. Defining the overall heat transfer coefficient as

$$\bar{h} = \frac{\bar{q}}{(\bar{T}_W - \bar{T}_B)}$$

the Nusselt number is written as

$$\bar{\mathrm{Nu}} = \left(\frac{\bar{q} r_2}{k\, T_{\mathrm{ref}}}\right)\left(\frac{D_H^*}{(\bar{T}_W^* - T_B^*)}\right)$$

Upon substitutions for $\bar{q}$ and T_{ref}, we obtain

$$\bar{\mathrm{Nu}} = \frac{Q^* D_{\mathrm{H}}^*}{2\pi n r_1^* (\bar{T}_W^* - T_B^*)} \tag{17}$$

4 Results and Discussions

The expressions of equations (13) and (17) indicate that the influence of buoyancy, and other parameters, on the transport rates can be explained through the variations caused on the velocity and temperature distributions.

The calculations were carried out for a reference set: 7 rods, $r_1^* = 0.18$, $\epsilon = 0.8$, no power skew ($QN = 1.0$) and pure forced convection condition ($\mathrm{Gr/Re} = 0.0$). In a given set of calculations, only one out of these parameters was varied. The velocity and temperature profiles are less nonuniform in the angular zone unoccupied by the inner rod. Reference is, therefore, made to the profiles on $I = N_3$ plane, where the geometric and heat transfer effects are felt most strongly.

We have an "upper zone" between the inner rod and the adiabatic shell, whereas the "lower zone" is between the central rod and the lower surface of the inner rod. Naming of the zones is only for the figures presented in the paper. Physically, both the zones are in the horizontal plane.

It is easy to visualize that the shell wall temperature shall have spatial variation with a crest in the rod region, and a valley between the rods. The crests and valleys combine to produce a zero average.

The high shell temperature on $I = N_3$ and the dissipation of inner rods maintain a positive T^* in the upper zone for all conditions of buoyancy, power skew, and flow direction. At the higher eccentricity of $\epsilon = 0.8$, Fig. 3(*b*), pure forced convection in the lower zone is improved due to the availability of a relativley larger flow area. The fluid temperature is not only below $\bar{T}_S$ ($T^* < 0$), but also less than that of other bounding rod surfaces, curve 1, Fig. 3(*b*).

The downward flow in the upper zone is opposed by a net buoyancy force acting upward due to the local fluid temperature being higher than $\bar{T}_S$ ($T^* > 0$). Flow separation is indicated on the upper surface of the inner rod in downflow at Gr/Re slightly below 10. At still higher values of Gr/Re, flow reversal sets in.

The foregoing physical explanation is the basis for interpreting subsequent results where the sign of $\pm$ (Gr T^*) may simply be referred for brevity. That upward mainflow in the upper zone is assisted by buoyancy follows from $T^* > 0$. It has already been indicated that T^* is lower than zero in the lower zone under forced convection, for $\epsilon = 0$ .8. In other words, the upflow in the lower zone is opposed at low $-\mathrm{Gr/Re} = 10$, curve 1, Fig. 3(*a*). Such opposition, however, results in reduced heat transfer that leads to a reversal, $T^* \geq 0$, at higher values of Gr/Re in upflow. Consequently, the upflow is also assisted in the lower zone for $-\mathrm{Gr/Re} = 20$ or 30.

The picture changes when the inner rods are located closer to the central rod, say with $\epsilon = 0.64$. The flow space in the lower zone is reduced compared to that in Fig. 3(*a*) or 3(*b*). With both the central and inner rod dissipating heat, the lower zone temperature is increased. Both the zones are at temperatures higher than the shell wall average, for all buoyancy conditions in either flow direction. In this case the upflow is

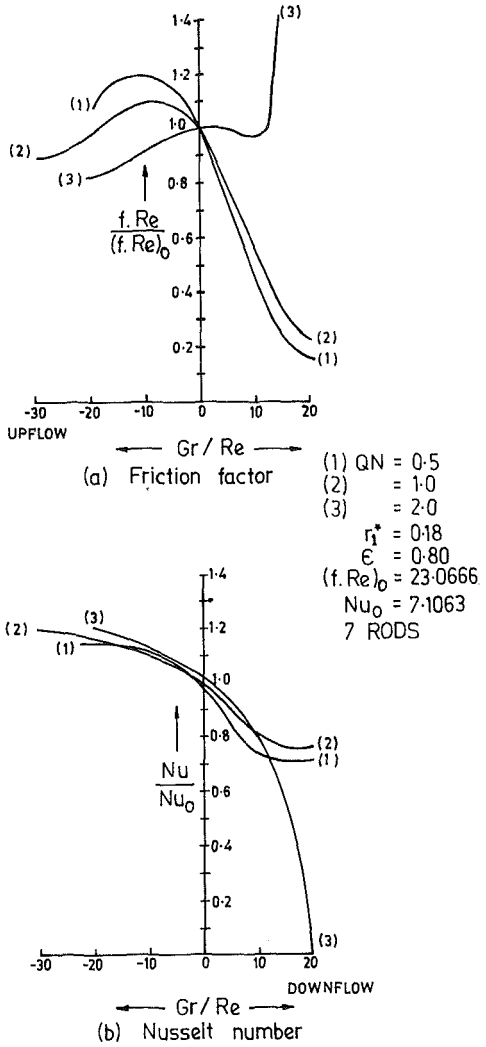

Fig. 6 Effects of buoyancy and power skew on transport rates

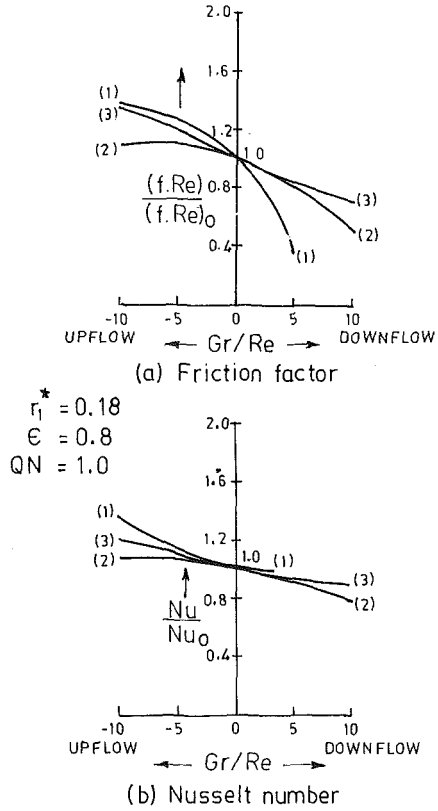

Fig. 7 Variation of transport rates due to number of rods

supported by buoyancy all over the cross section and the downflow opposed.

In comparing the results for $\epsilon = 0.64$ and 0.8, we observe that the phenomena are so critically geometry-dependent that the conclusions for one configuration cannot be generalized to others.

The variations in friction factor (f Re) and heat transfer rate (Nu) for $\epsilon = 0.64$ are shown in Fig. 4. The decrease in flow rate due to buoyancy in downflow is reflected by the increase in friction factor and reduction in Nusselt number. Converse results are observed for upflow.

In a power skew condition, the heat flux on the central rod is QN times that on the inner rod. With $QN = 0.5$, 1, or 2, the variation of total heat input to the flow domain is not significantly different, since the central road surface area is only a fraction of the inner rod (one-sixth for the reference case).

The difference, however, arises due to the variation in local temperature. At $QN = 0.5$, T^* was lower compared to the $QN = 1.0$ condition, for otherwise unchanged parameters. Consequently the local velocities were enhanced in downflow and retarded in upflow, compared to $QN = 1.0$. The reverse effects were observed with $QN = 2.0$. Whereas the influence of power skew on velocity and temperature profiles are given in [17], the overall effects on cross-sectional flow rate can be noted in Fig. 5. The variations of transport rates due both to buoyancy and power skew are presented in Fig 6. An asymptotic rise of friction and a near zero value of the Nusselt number are observed for a highly retarded downflow at $QN = 2.0$ and Gr/Re = 20.

Consider pure forced convection (Gr/Re = 0) due solely to $G = 1$, when the number of rods within the shell is changed from 7 to 5 or 13 for otherwise reference conditions. The flow rate would be proportional to net available area: $Q^* = 5.1877$, 2.4652, and 1.1088, respectively, for 5, 7, and 13 rod assemblies. The decreasing value of Q^* is partially offset by lower values of D_H^* and A_W^* resulting in $(f\,\mathrm{Re})_o$ of 19.7439, 23.0666, and 8.1135.

Greater uniformity of fluid temperature and a lower value of $(\bar{T}_W^* - T_B^*)$ are expected when the number of rods are increased within the shell. The combined effects of low Q^*, D_H^*, and $(\bar{T}_W^* - T_B^*)$ yield Nu_o: 5.2939, 7.1063, and 1.0714 for 5, 7, and 13 rod arrangements.

For completeness, we quote the 7-rod results of Benodekar and Date [5] for a different radius ratio of $r_1^* = 0.2$: $(f\,\mathrm{Re})_o = 24.31$ and $\mathrm{Nu}_o = 5.659$.

It has been already pointed out that the shell wall temperature is spatially periodic, the number of crests or valleys equaling the number of inner rods. The smaller the number of rods, the higher would be the amplitude of variation over zero average $\bar{T}_S$. A high crest of the shell wall temperature combined with the inner rod dissipation result in the maximum value of the positive T^* for the upper zone fluid, when the rod number is minimum. Consequently, an upflow in the upper zone is assisted by buoyancy to the maximum for the minimum number of rods. With increase in number of rods not only does the amplitude of positive T^* decrease in the upper zone, it becomes negative in the lower zone, for $\epsilon = 0.8$. The gross effects of buoyancy on transport rates are noted in Fig. 7.

The variation of the shell wall temperature is shown in the polar diagram in Fig. 8. Both the maximum of the shell wall temperature and that of the upper surface of the inner rod occur in downflow at Gr/Re = 20, corresponding to the reverse flow in the upper zone of Fig. 3(a). The higher surface

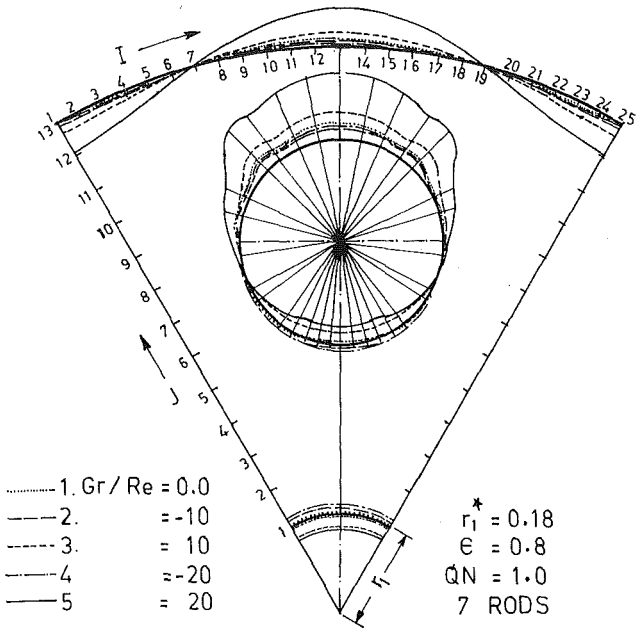

Fig. 8 Polar diagram of surface temperatures

temperatures are due to the reduced local heat transfer rate. On the other hand, the buoyancy enhanced convection in the lower zone, Fig. 3(*a*) and (*b*), explains the "negative" differentials on the central rod and on the lower surface of the inner rod, curve 5, Fig. 8.

5 Conclusions

The present numerical study of combined free and forced convection in a finite rod array was motivated for estimating transport parameter values needed for the thermal-hydraulic safety analysis of a pressurized water reactor. The salient effects of buoyancy, power skew, eccentricity and the number of heat dissipating rods are recalled.

The mainflow caused by impressing an external pressure gradient ($-G$), is not necessarily assisted or opposed by the buoyancy all over the cross section. A downflow is assisted in the location where fluid temperature is below the shell wall average, ($T^* < 0$), and an upflow where T^* is positive.

With the inner rods located at 0.8 eccentricity, a downward flow is opposed by buoyancy in the upper zone. Local flow separation is initiated around Gr/Re = 10. The cross-sectional flow rate is, however, increased due to enhancements in the lower zone with a negative T^*. The effects are reflected by lowering of (f Re) and increase in the heat transfer rate. The downflow is, however, retarded in the lower zone when the eccentricity is reduced to $\epsilon = 0.64$, for which $T^* \geq 0$.

As power skew is increased, the downflow is opposed by the buoyancy in both the zones.

A downflow could be practically stalled all over the cross section for $QN = 2.0$ at $\epsilon = 0.8$, or with $QN = 1.0$ but 0.64 eccentricity, when the buoyancy effect is around Gr/Re = 20. A steeply increasing friction and near zero heat transfer result. On the other hand, for $\epsilon = 0.8$ the variations of Q^* or transport rates in upflow are limited to 20 percent even when $-$Gr/Re = 30, and QN varying from 0.5 to 2.0. The variations are, however, wide for $\epsilon = 0.64$: Nusselt number in upflow is increased by 150 percent at $-$Gr/Re = 20, from its forced convection value.

The extent of local assistance of an upflow, or opposition of a downflow, is higher when the number of rods within the shell is small, consequenting in greater nonuniformity of fluid temperature.

The analysis here has been restricted to one ring of inner rods. In principle, the present method of multiple coordinate analysis is applicable to a geometry having more rings of inner rods. The computation shall, of course, be more involved.

In the vertical orientation of a pressurized water reactor, the coolant flow is upward in the core and downward in the steam generator. The information presented here for both upflow and downflow are, therefore, useful for predicting the rate of cooling of a reactor core following a transient, e.g., a LOCA (Loss of Coolant Accident).

Acknowledgment

The authors gratefully acknowledge the financial support provided for this study by the CSIR, and the Department of Atomic Energy, Government of India.

References

1 Sparrow, E. M., and Loeffler, A. L., Jr., "Longitudinal Flow Between Cylinders Arranged in a Regular Array," *AIChE Journal*, Vol. 5, 1959, pp. 325–329.

2 Sparrow, E. M., Loeffler, A. L., Jr., and Hubbard, H. A., "Heat Transfer to Longitudinal Laminar Flow Between Cylinders," ASME JOURNAL OF HEAT TRANSFER, Vol. 83, 1961, pp. 415–422.

3 Dwyer, O. E., and Berry, H. C., "Laminar Flow Past Transfer for In-Line Flow Through Unbaffled Rod Bundles," *Nuclear Science and Engineering*, Vol. 42, 1970, p. 81–88.

4 Mottaghian, R., and Wolf, L., "A Two-Dimensional Analysis of Laminar Fluid Flow in Rod Bundles of Arbitrary Arrangement," *International Journal of Heat and Mass Transfer*, Vol. 17, 1974, pp. 1121–1128.

5 Benodekar, R. W., and Date, A. W., "Numerical Prediction of Heat Transfer Characteristics of Fully Developed Laminar Flow Through a Circular Channel Containing Rod Clusters," *International Journal of Heat and Mass Transfer*, Vol. 21, 1978, pp. 935–945.

6 Gunn, D. J., and Darling, C. W. W., "Fluid Flow and Energy Losses in Non-Circular Conduits," *Transactions of the Institution of Chemical Engineers*, Vol. 41, 1983, pp. 163–172.

7 Zarlin, J. P., "Laminar-Flow Pressure Drop in Symmetrical Finite Rod Bundles," *Nuclear Science and Engineering*, Vol. 61, 1976, pp. 282–285.

8 Shah, R. K., and London, A. L., "Laminar Flow Forced Convection in Ducts," *Advances in Heat Transfer*, Supplement I, Academic Press, New York, 1978.

9 Kakaç, S., Shah, R. K., and Bergles, A. E., *Low Reynolds Number Flow Heat Exchangers*, Hemisphere Publishing, New York, 1982.

10 Iqbal, M., Ansari, S. A., and Aggarwala, B. D.," Buoyancy Effects on Longitudinal Laminar Flow Between Vertical Cylinders Arranged in Regular Arrays," Paper No. C3.6, *Heat Transfer 1970*, Vol. IV, Elsevier, Amsterdam, 1970.

11 Iqbal, M., Aggarwala, B. D., and Khatmy, A. K., "On the Conjugate Problem of Laminar Combined Free and Forced Convection through Vertical Noncircular Ducts," ASME JOURNAL OF HEAT TRANSFER, Vol. 93, 1971, pp. 52–56.

12 Ramm, H., and Johannsen, K., "Combined Forced and Free Laminar Convection in Vertical Rod Bundles with Longitudinal Flow," ASME Paper No. 77-HT-44, 1977.

13 Yang, J. W., "Analysis of Combined Convection Heat Transfer in Infinite Rod Arrays," *Heat Transfer 1978*, Hemisphere Publishing, Washington, D.C., Vol. 1, 1978, pp. 49–54.

14 Yang, J. W., "Heat Transfer and Fluid Flow in Regular Rod Arrays with Opposing FLow," *Fluid Flow and Heat Transfer Over Rod or Tube Bundles*, edited by S. C. Yao and P. A. Pfund, ASME, New York, 1979, pp. 149–153.

15 Prakash, C., and Patankar, S. V., "Combined Free and Forced Convection in Vertical Tubes with Radial Internal Fins," ASME JOURNAL OF HEAT TRANSFER, Vol. 103, 1981, pp. 566–572.

16 Viskanta, R., and Mohanty, A. K., "TMI-2 Accident: Postulated Heat Transfer Mechanisms and Available Data Base," NUREG/CR-2121, ANL-81-26, 1981.

17 Das, R., "Momentum and Energy Transport in Duct Entrance and in Finite Rod - Bundle Assemblies," Ph.D. thesis, Indian Institute of Technology, Kharagpur, 1982.

18 Greenspan, D., *Introductory Numerical Analysis of Elliptic Boundary Value Problems*, Harper International Edition, New York, 1965.

19 Mohanty, A. K., and Ray, D. K., "Fluid Flow Through a Circular Tube Containing Rod Clusters," *Fluid Flow and Heat Transfer Over Rod or Tube Bundles*, edited by S. C. Yao and P. A. Pfund, ASME, New York, 1979, pp. 121–128.

Jet-Impingement Heat Transfer for a Circular Jet Impinging in Crossflow on a Cylinder

E. M. Sparrow
Fellow ASME.

C. A. C. Altemani

A. Chaboki

Department of Mechanical Engineering,
University of Minnesota,
Minneapolis, Minn. 55455

Quasi-local heat transfer coefficients were measured on a cylinder on which a circular jet impinged in crossflow. The jet diameter and the distance between the initiation of the jet and the cylinder surface were varied parametrically, as was the jet Reynolds number. The measurements showed that the axial distribution of the heat transfer coefficient peaked at the impingement point. For a fixed jet diameter and Reynolds number, the peak heat transfer coefficient increased as the distance between the initiation of the jet and the cylinder surface decreased. The peak coefficient also increased with decreasing jet diameter at fixed values of the jet initiation distance and the Reynolds number. User-oriented correlations of the peak Nusselt number with the geometrical parameters and with the Reynolds number were derived. The dropoff of the heat transfer coefficient with increasing axial distance from the impingement point was more rapid for smaller jet initiation distances (at a fixed jet diameter and Reynolds number) and for smaller jet diameters (at a fixed initiation distance and Reynolds number). The impingement pattern was examined by flow visualization.

Introduction

Jet impingement yields higher heat transfer coefficients than are provided by most other modes of forced convection. It is widely utilized in numerous drying, annealing, tempering, and curing processes and is used to protect surfaces that are exposed to high local heat fluxes. Across this broad spectrum of applications, a variety of impingement surface and jet configurations are employed.

The particular configuration to be investigated here is the crossflow impingement of a circular jet on the surface of a cylinder. A careful examination of the literature, including both the exhaustive 1977 survey article of Martin [1] and more recent papers, did not reveal any published information for this configuration, despite its relevance to practice (e.g., in the manufacture of paper and of glass). There is a modest amount of experimental information for slot jet impingement on a circular cylinder [2, 3], but that is a two-dimensional situation that differs fundamentally from the present three-dimensional problem.

The research described here is experimental in nature. In the main part of the work, measurements were made of the quasi-local heat transfer coefficient as a function of the axial distance along the cylinder. During the course of these experiments, three parameters were systematically varied. Two of these are geometrical. One is the ratio of the jet diameter d to the cylinder diameter D, while the other is the S/d ratio, where S is the distance between the origin of the jet and the cylinder. These ratios spanned the ranges $0.189 \leq d/D \leq 0.424$ and $5 \leq S/d \leq 15$. For each configuration defined by d/D and S/d, the jet Reynolds number was varied from about 4000 to about 25,000.

In the presentation of results, special consideration will be given to the impingement point (actually, impingement region) transfer coefficient, in view of its particular relevance to design. In addition to a multi-viewpoint graphical presentation, an algebraic correlation of the impingement point results is sought involving the geometrical parameters and the Reynolds number. Axial distributions of the transfer coefficient along the cylinder surface are presented from two different viewpoints in order to provide the broadest perspective.

To supplement the transfer coefficient measurements, a flow visualization study was performed to reveal the manner in which the jet spread over the surface. In that study, the oil-lampblack technique was employed.

The Experiments

The heat transfer coefficients to be reported here were obtained from mass transfer experiments involving the naphthalene sublimation technique. The use of the naphthalene technique affords many benefits compared with direct heat transfer experiments. In particular, the experimental apparatus is much simpler while, at the same time, the accuracy of the results is higher. Nonaccountable extraneous losses are virtually nonexistent. In addition, a standard boundary condition (the counterpart of uniform wall temperature in the analogous heat transfer problem) is readily established.

The naphthalene technique has already been used in studying jet impingement [3-5]. However, the existing methods for the preparation of naphthalene surfaces are not suitable for the quasi-local measurements contemplated here. A new napthalene casting technique, developed to provide surface elements that facilitate this type of measurement, will be described shortly.

Experimental Apparatus. The experimental apparatus was housed in a large rectangular test chamber, 1.52 m high, and having a square horizontal cross section of dimensions 0.61 × 0.61 m. The chamber was completely airtight, except for a vertically oriented jet delivery tube that pierced its upper wall and an air exit port that was centered in the lower wall.

The system was operated in the suction mode, with air drawn into the inlet of the jet delivery tube from the laboratory room. During its passage through the tube, the airflow undergoes hydrodynamic development, and at the tube exit, the pipe flow becomes a jet. The jet is aligned to impinge in crossflow on a horizontal cylinder situated at a preselected distance below the tube exit. Upon passing over the cylinder, the air streams toward the bottom of the

Contributed by the Heat Transfer Division for publication in the JOURNAL OF HEAT TRANSFER. Manuscript received by the Heat Transfer Divison November 1, 1983.

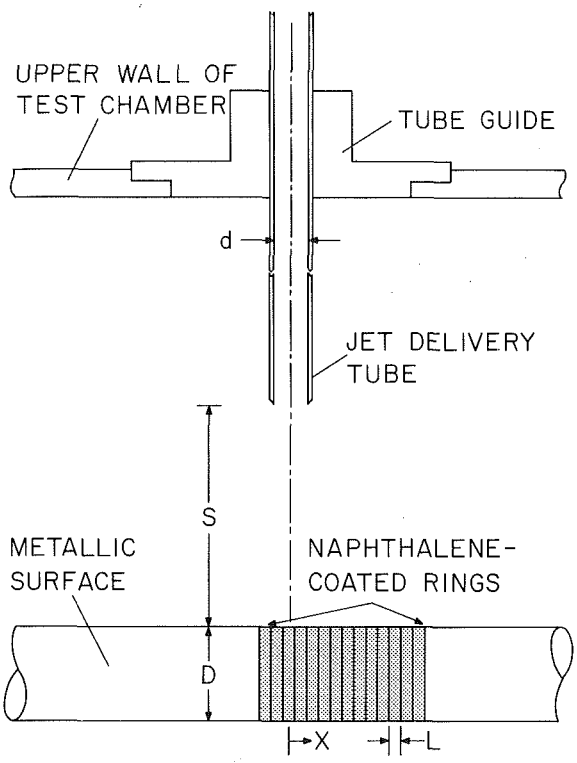

Fig. 1 Schematic diagram showing the main components of the experimental apparatus

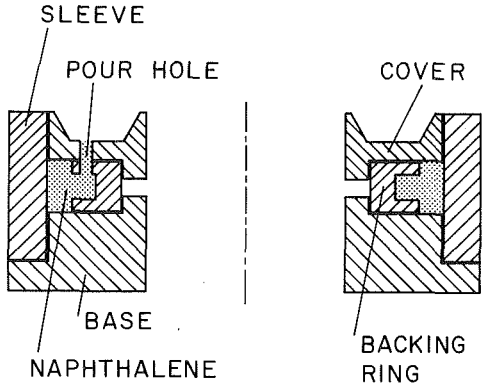

Fig. 2 Mold for casting naphthalene

chamber, from which it exits into an air handling system consisting of a flowmeter (a calibrated orifice), a control valve, and a blower. The blower is located in a service corridor outside the laboratory, and its compression-heated, naphthalene-enriched discharge is vented outside the building. This positioning ensures that the laboratory is free of naphthalene vapor.

Further description of the experimental apparatus is facilitated by reference to Fig. 1. The figure shows the impingement cylinder, the jet delivery tube, and the installation of the tube in the upper wall of the test chamber. The remainder of the test chamber and the air handling system need no further elaboration and are not shown.

As seen in the figure, the jet delivery tube is supported and positioned by a sleevelike fixture (i.e., the tube guide) that rests in a lap in the upper wall of the test chamber. The tube can be slid vertically within the sleeve, so that its exit can be positioned at any desired distance from the impingement cylinder (which is fixed). The distance between the tube exit and the highest point of the cylinder is denoted by the symbol S.

At the lower end, the wall of the delivery tube is beveled back from the exit cross section to minimize possible effects of the finite wall thickness. The upper end of the tube was situated well above the upper wall of the test chamber for all the investigated tube-to-cylinder separation distances S.

Three jet delivery tubes were used during the course of the experiments, with respective inner diameters d given by $d/D = 0.189$, 0.313, and 0.424 (D = impingement cylinder diameter). A different, custom-fitted tube guide was used with each. The respective lengths of the tubes were approximately $80d$, $60d$, and $50d$. These lengths are sufficient to yield well-defined, fully developed velocity distributions and turbulence levels at the exits of the respective delivery tubes.

The impingement cylinder is a composite structure consisting of a 3.81-cm-dia. aluminum core over which are slipped an array of naphthalene-coated rings and aluminum sleeves. When assembled, the outside diameter D of the cylinder is 5.08 cm, and its length is 56 cm. The cylinder is supported at its ends by fixtures attached to the side walls of the chamber. These supports position the cylinder with its axis horizontal and at a fixed elevation in the test chamber.

Figure 1 shows the naphthalene-coated rings as they were deployed during the final data runs. As seen there, a total of 14 rings was employed. One of the rings was centered directly beneath the jet, and it was flanked to one side by 11 rings and to the other side by 2 rings. The centered ring and its set of 11 neighbors yielded the primary data for the axial distribution of the mass transfer coefficient. The other 2 rings served to verify the symmetry of the distribution. In preliminary data runs, performed to investigate symmetry, the rings were deployed more uniformly about the centered ring. The axial length L of each ring was 0.635 cm, which corresponds to $L/D = 1/8$.

Aluminum sleeves of outside diameter identical to that of the naphthalene-coated rings were positioned to either side of the array of rings. Because of the direction of fluid flow over the cylinder, the mass transfer at the naphthalene rings was in no way affected by the nonparticipation of the metal sleeves in the mass transfer process. After the rings and sleeves were assembled, they were pressed tightly together to form a

Nomenclature

A_w = per-ring surface area
C = coefficient in Sh, Re relation
D = diameter of impingement cylinder
d = jet diameter at exit of jet delivery tube
$\mathfrak{D}$ = mass diffusion coefficient
K = per-ring mass transfer coefficient, $\dot{m}/(\rho_{nw} - \rho_{n\infty})$
L = axial length of naphthalene-coated ring
ΔM = per-ring change of mass
$\dot{m}$ = per-ring mass flux
Nu = Nusselt number
$\mathrm{Nu}_{0.7}$ = value of Nu for Pr = 0.7
n = exponent in Sh, Re relation
ORD = ordinate of Fig. 5
Pr = Prandtl number
Re = Reynolds number, $4\dot{w}/\mu\pi d$
S = spacing between exit of jet delivery tube and surface of cylinder
Sc = Schmidt number, $\nu/\mathfrak{D}$
Sh = Sherwood number, $KD/\mathfrak{D}$
$\mathrm{Sh}_{2.5}$ = value of Sh for Sc = 2.5
$\dot{w}$ = flow rate in jet delivery tube
X = axial coordinate
μ = viscosity
ν = kinematic viscosity
ρ_{nw} = naphthalene vapor density at cylinder surface
$\rho_{n\infty}$ = naphthalene vapor density in impinging jet
τ = duration of run

continuous surface by forces imposed at both ends of the cylinder.

Naphthalene Coating Technique. The naphthalene coatings were applied by a casting procedure that utilized a special mold whose description is facilitated by reference to Fig. 2. The basic task was to apply a naphthalene coating of precise dimensions and hydrodynamically smooth surface finish to the outer edge of a metallic ring (hereafter called the backing ring). To this end, the backing ring is incorporated as one part of the four-part mold illustrated schematically in the figure.

As shown there, a stepped disk serves as a base on which are placed the backing ring and a cylindrical sleeve. (Note that the naphthalene coating remaining from the preceding data run is removed from the ring by melting and evaporation prior to its assembly into the mold.) A cover with a stepped lower face and a recessed upper face is situated atop the ring. The steps are precisely machined to positively position all of the mold parts. An annular space bounded by the mold parts serves as the mold cavity into which molten naphthalene is poured through a circular hole in the cover. Another hole in the cover (not shown) serves to vent the air displaced from the mold cavity by the naphthalene.

It may be noted that the outer periphery of the backing ring is grooved in order to provide a footing for the poured naphthalene. The function of the recessed upper face of the cover is to trap excess naphthalene during the pouring process.

Once the naphthalene has solidified, the mold is disassembled by axially displacing the sleeve and rotating the cover. The backing ring with its naphthalene coating is thereby released. The smoothness of the exposed naphthalene surfaces is guaranteed by the high polish of the mold surfaces against which they solidify.

Two of the rings were provided with small access holes to permit calibrated, fine-gage thermocouples to be inserted into the mold cavity and, thereby, to be cast into the naphthalene coating. Each such ring could accommodate two thermocouples, positioned 180 deg apart. The thermocouple lead wires emerge from the bore of the backing ring and are drawn out to one end of the cylinder via axial grooves milled into the aluminum core. The thermocouple-equipped rings were positioned at various stations in the array in order to identify the presence of possible axial and circumferential temperature variations (no such variations were encountered). The temperature data provided by the embedded thermocouples are used in the evaluation of the vapor pressure at the surface of the subliming naphthalene.

Instrumentation and Experimental Procedure. The mass of each of the naphthalene-coated rings was measured immediately before and after each data run as well as after an extraneous-loss accounting procedure (to be described shortly). The mass measurements were made with a Sartorius ultra-precision, electronic analytical balance with a resolution of 10^{-5} g and a capacity of 166 g. Typically, about 0.02 g of naphthalene was sublimed per ring during a data run.

The first step in preparing for a data run was the weighing of the naphthalene-coated rings. Then the rings and the metallic sleeves were assembled on the core and locked into place. An airtight sheath made of aluminum foil and sealed with pressure-sensitive tape was then placed over the array of naphthalene-coated rings to prevent sublimation. The thus-assembled cylinder was installed in the test chamber through an access window, after which the window was sealed and the airflow initiated. During the ensuing period, the outputs of the embedded thermocouples were carefully monitored. When steady temperature readings were attained, the protective sheath was removed from the mass transfer section, and the data run proper was begun.

The duration of the run was selected to limit the average sublimation-related surface recession to approximately 0.0013 cm (0.0005 in.). During the run, the embedded thermocouples were read periodically (a minimum of 10 readings per run). At the conclusion of the run, the cylinder was disassembled, and the naphthalene-coated rings were weighed.

At this point, the experiment was continued in order to determine the amount of mass sublimed between the two weighings during periods other than the data run proper (i.e., during the setup and disassembly of the cylinder). To this end, all aspects of the setup and disassembly operations were repeated (but without an airflow period), after which the rings were weighed once again. The change of mass between this final weighing and the preceding weighing was employed as a subtractive correction.

Results and Discussion

Data Reduction. The mass transfer data for each of the naphthalene-coated rings was processed separately to yield per-ring mass transfer coefficients and Sherwood numbers. Due to the narrow axial extent of each ring (i.e., $L/D = 1/8$), the per-ring results can be regarded as quasi-local with respect to the axial coordinate X (Fig. 1).

The corrected change of mass ΔM for each ring, when divided by the per-ring surface area A_w ($=\pi DL$) and the duration τ of the data run, yields the ring-average mass flux $\dot{m}$ ($=\Delta M/A_w\tau$). With this, the per-ring mass transfer coefficient K and Sherwood number Sh follow as

$$K=\dot{m}/(\rho_{nw}-\rho_{n\infty}),\mathrm{Sh}=KD/\mathfrak{D} \tag{1}$$

The quantities ρ_{nw} and $\rho_{n\infty}$ are, respectively, the naphthalene vapor densities at the subliming surface and in the oncoming jet. The latter is zero in the present experiments. For the former, the vapor pressure/temperature relation of [6] was used to evaluate the equilibrium naphthalene vapor pressure corresponding to the measured surface temperature. Then, with the vapor pressure and the temperature as inputs, ρ_{nw} was obtained from the perfect gas law.

For the Sherwood number, the cylinder diameter D was used as the characteristic dimension. Furthermore, to eliminate the diffusion coefficient $\mathfrak{D}$, the Schmidt number Sc ($=\nu/\mathfrak{D}$) can be employed, which yields

$$\mathrm{Sh}=(KD/\nu)\mathrm{Sc} \tag{2}$$

where Sc = 2.5 [6]. The Sherwood numbers are believed accurate to 2 percent.

The jet Reynolds number Re was evaluated at the exit of the jet delivery tube, so that it is, in effect, a pipe Reynolds number. Therefore,

$$\mathrm{Re}=4\dot{w}/\mu\pi d \tag{3}$$

in which $\dot{w}$ is the flow rate of the air passing through the jet delivery tube.

Heat/Mass Transfer Analogy. The Sherwood numbers determined here can be transformed to Nusselt numbers by employing the well-established analogy between heat and mass transfer. From [1], for jet impingement,

$$\mathrm{Sh}/\mathrm{Sc}^{0.42}=\mathrm{Nu}/\mathrm{Pr}^{0.42}=F(\mathrm{Re},\chi_i) \tag{4}$$

in which χ_i denotes a set of geometrical parameters. Since the present Sherwood number results correspond to a Schmidt number of 2.5

$$\mathrm{Nu}=(\mathrm{Pr}^{0.42}/1.47)\mathrm{Sh}_{2.5} \tag{5}$$

For heat transfer in air ($\mathrm{Pr}\simeq 0.7$)

$$\mathrm{Nu}_{0.7}=0.586\mathrm{Sh}_{2.5} \tag{6}$$

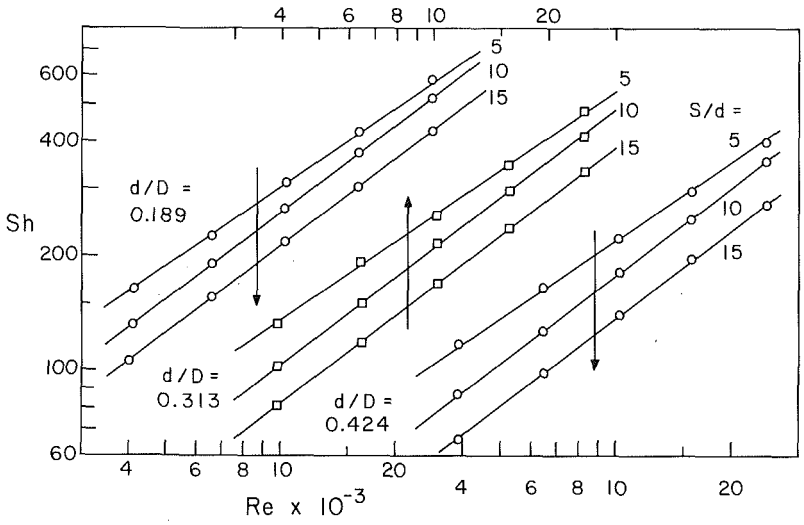

Fig. 3 Peak Sherwood numbers for jets of various diameters and for parametric separation distances between the jet exit and the impingement surface

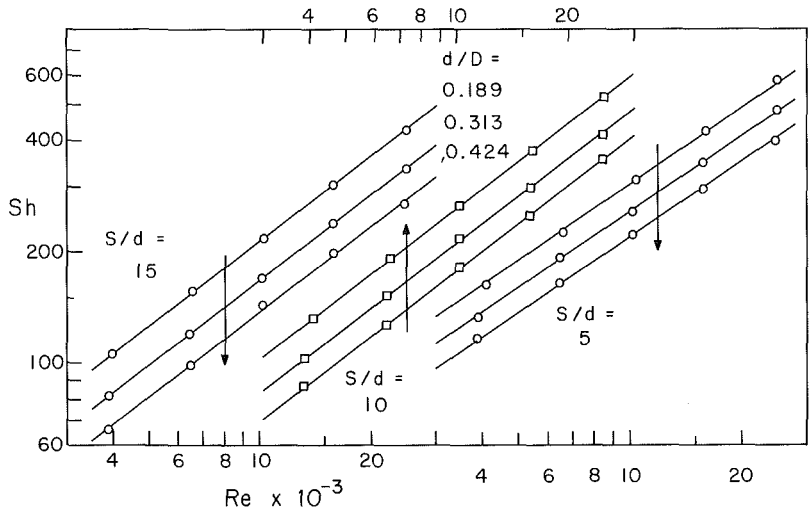

Fig. 4 Peak Sherwood numbers for various separation distances between the jet exit and the impingement surface and for parametric values of the jet diameter

Therefore, by making use of equation (6), the Sherwood numbers to be presented here can be employed in applications involving heat transfer in air. Consequently, in what follows, the phrases mass transfer and heat transfer will be used interchangeably.

Peak Mass (Heat) Transfer Coefficients. As will be demonstrated later, the Sherwood number varies with axial position along the cylinder, with the largest value being attained at the ring that is centered on the symmetry line of the jet (see Fig. 1). The peak value is of particular relevance to practice, and its dependence on the parameters of the problem will now be presented.

In Fig. 3, the peak Sherwood numbers were plotted as a function of the Reynolds number for parametric values of the dimensionless jet diameter d/D and jet exit to cylinder separation distance S/d. The figure is subdivided into three parts. Each part conveys results for a given jet diameter, and the data presented in each part display the effect of varying the separation distance for that jet diameter. The three parts share a common ordinate scale, but each has its own abscissa as indicated by the arrows.

Table 1 C values in Sh, Re Correlations

(a) $\mathrm{Sh} = C\mathrm{Re}^{0.765}$

d/D	S/d	C
0.189	10	0.228
	15	0.186
0.313	10	0.184
	15	0.146
0.424	10	0.155
	15	0.120

(b) $\mathrm{Sh} = C\mathrm{Re}^{0.685}$

d/D	S/d	C
0.189	5	0.555
0.313	5	0.468
0.424	5	0.401

Inspection of Fig. 3 shows that for each configuration (i.e., fixed d/D and S/d), the Sherwood number increases in a regular manner with the Reynolds number, with the Sh, Re relation being very well described by the power law $\mathrm{Sh} = C\mathrm{Re}^n$ (i.e., a straight line on logarithmic coordinates). The

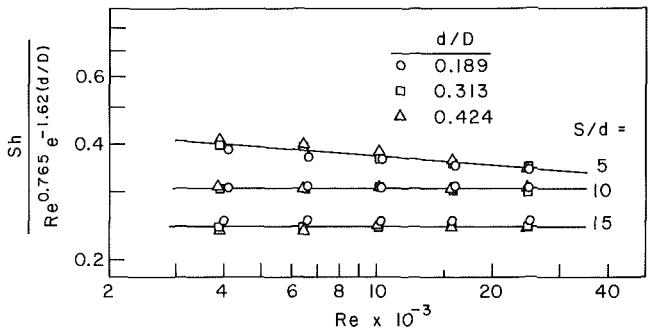

Fig. 5 Correlation of the peak Sherwood number

specifics of the power-law representations will be discussed shortly. Another general trend that is clearly in evidence in Fig. 3 is the drop-off in the Sherwood number with increasing distance between the jet exit and the cylinder. The extent of the drop-off increases as the jet diameter increases. Another effect of jet diameter, which can be seen by comparing the three parts of the figure, is a tendency toward lower Sherwood numbers for jets of larger diameter. This trend will be elaborated in a subsequent figure.

Careful study of Fig. 3 reveals that for all of the investigated jet diameters and for the larger separation distances (i.e., $S/d = 10$ and 15), the Sherwood-Reynolds distributions are all very well correlated by lines of the same slope. These lines are represented by

$$\mathrm{Sh} = C\mathrm{Re}^{0.765}, \text{ all } d/D, S/d = 10 \text{ and } 15 \qquad (7)$$

The constants C, determined by least squares, are listed in Table 1(a).

The straight lines passing through the $S/d = 10$ and 15 data in Fig. 3 correspond to equation (7) and Table 1(a). The excellence with which these lines represent the data and the commonality of their slopes suggests a similarity in the participating physical processes for these cases.

The $S/d = 5$ data are not correlated by equation (7). This is not surprising when consideration is given to the mixing processes to which the jet is subjected after it leaves the delivery tube. For example, as shown in [7], the centerline velocity of a free jet is unaffected by the mixing at a station 5 diameters from the exit, while the centerline velocity is considerably affected (i.e., reduced) at 10 and 15 diameters from the exit. Therefore, there is no reason to expect the $S/d = 5$ results to be correlated with those for $S/d = 10$ and 15.

For $S/d = 5$, a separate least-squares fit to the respective data for $d/D = 0.189$, 0.313, and 0.424 yields slightly different exponents n for the three cases. With a view toward attaining a concise presentation, a single n value was sought and found which correlates the $S/d = 5$ results to high accuracy. The expression

$$\mathrm{Sh} = C\mathrm{Re}^{0.685}, \text{ all } d/D, S/d = 5 \qquad (8)$$

with C from Table 1(b), represents all the $S/d = 5$ data with an extreme error of only 2.4 percent. The straight lines passing through the $S/d = 5$ data in Fig. 3 represent equation (8) and Table 1(b).

An alternate perspective on the peak Sherwood numbers is provided by Fig. 4. This figure is similar in structure to Fig. 3, but now the results are grouped together according to the jet exit to cylinder separation distance S/d. Within each grouping, the curves are parameterized by the dimensionless jet diameter d/D. This presentation highlights the effect of d/D on the Sherwood number results.

As seen in the figure, higher Sherwood numbers are associated with jets of smaller diameter. This finding is physically plausible, since, for a fixed Reynolds number, smaller diameter jets are characterized by higher velocities.

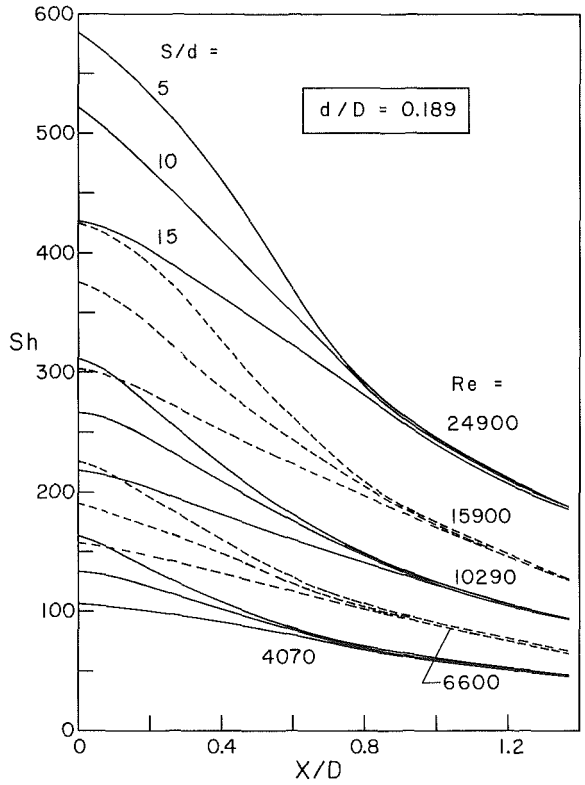

Fig. 6 Axial distributions of the Sherwood number for $d/D = 0.189$

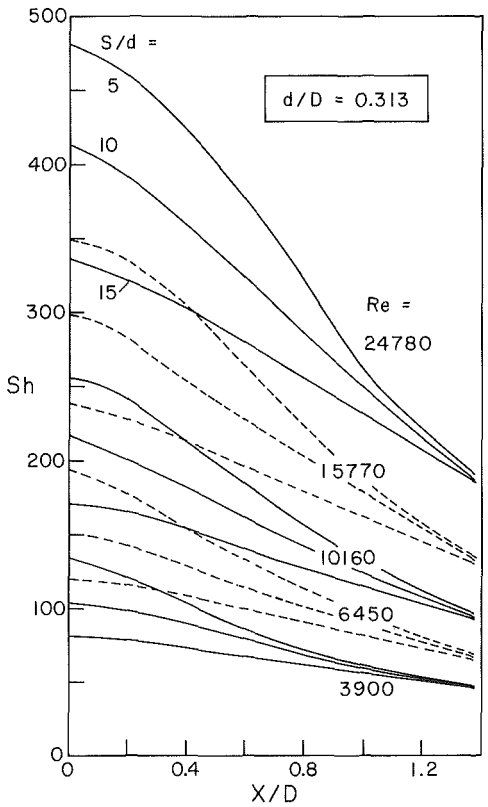

Fig. 7 Axial distributions of the Sherwood number for $d/D = 0.313$

The effect of jet diameter on the Sherwood number diminishes moderately as the separation distance S/d decreases.

To enhance the usability of the results for practical ap-

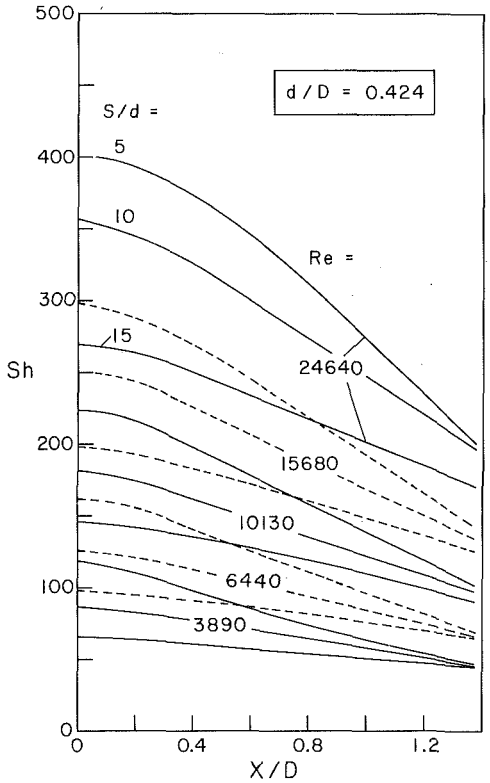

Fig. 8 Axial distributions of the Sherwood number for $d/D = 0.424$

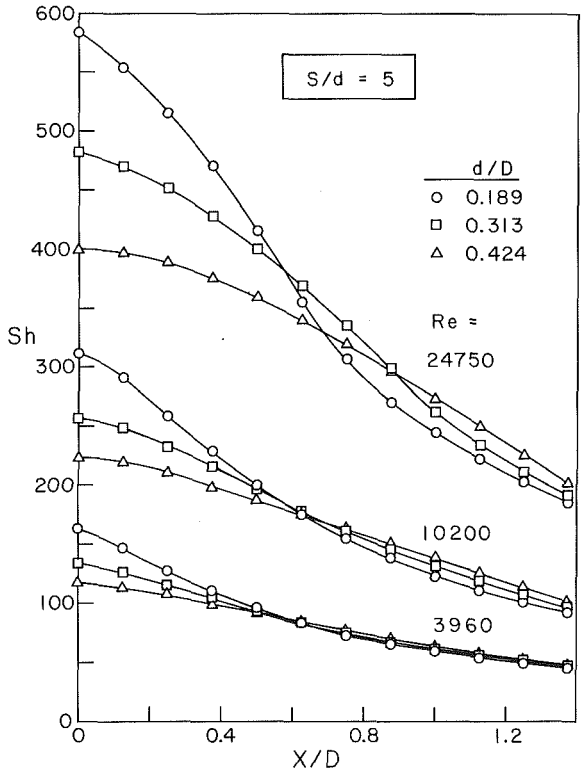

Fig. 9 Axial distributions of the Sherwood number for $S/d = 5$

plications, further correlation of the data was sought. The end result of these efforts is presented in Fig. 5. As can be seen there, the ordinate group includes the Sherwood number as well as functions of Re and d/D, the objective being to render this group virtually independent of Re and d/D. This objective has been fulfilled fairly well, as witnessed by the compact distribution of the data. The compactness of the presentation and the weak dependence of the ordinate group on Re and d/D facilitates easy and accurate interpolation of the results, and invites moderate extrapolation.

If the ordinate group is, for conciseness, designated as ORD, then

$$\text{ORD} = 0.775\text{Re}^{-0.08}, \quad S/d = 5 \tag{9a}$$

$$\text{ORD} = 0.306, \quad S/d = 10 \tag{9b}$$

$$\text{ORD} = 0.244, \quad S/d = 15 \tag{9c}$$

where the residual dependence on d/D is deemed sufficiently small so that it need not be taken into account.

Axial Variation of the Mass (Heat) Transfer Coefficient. Subsequent to its impingement, the jet spreads over the surface. The spreading is characterized by a diminution of velocity and is accompanied by a growth in boundary layer thickness. These processes give rise to an axial decrease in the mass transfer coefficient.

The measured axial distributions of the quasi-local Sherwood number are presented in Figs. 6-8, each of which corresponds to a fixed jet diameter, respectively $d/D = 0.189$, 0.313, and 0.424. In each graph, results are given for five Reynolds numbers ranging from about 4000 to 25,000. Each such Reynolds number is represented by a cluster of three curves which respectively correspond to spacings $S/d = 5$, 10, and 15.

The results for the various Reynolds numbers naturally stack one above the other in each figure. Also the $S/d = 5$, 10, and 15 curves are stacked in that order for each Reynolds number. To avoid unwanted clutter, the S/d designations are affixed only to one set of curves in each figure – that for the highest Reynolds number. As a further measure to avoid what would otherwise be confusing overlap, the data symbols are omitted from Figs. 6-8. The data will be included in subsequent figures.

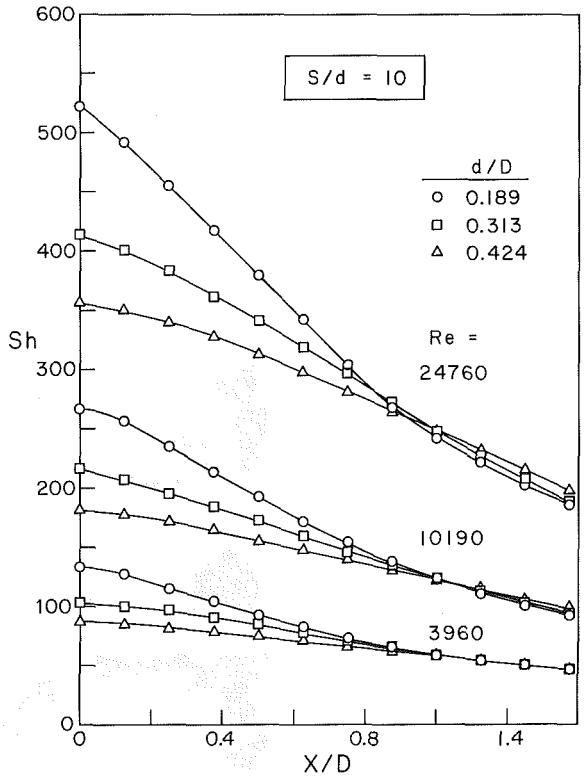

Fig. 10 Axial distributions of the Sherwood number for $S/d = 10$

Attention may first be turned to Fig. 6 (smallest jet diameter). The figure affirms that the peak Sherwood numbers (i.e., at $X/D = 0$) are higher at smaller separation distances S/d between the jet exit and the cylinder. However, the smaller the S/d, the more rapidly does the Sherwood number drop off with increasing axial distance from the impingement point, so that beyond $X/D = 0.8$, the Sherwood number is independent of S/D. This is the main message of Fig. 6. The second key point of the figure is that the drop-off of Sh with X/D is appreciable. Thus, at $X/D = 1.4$, the Sh value is about 30 percent of that at $X/D = 0$ when $S/d = 5$; for $S/d = 15$, the corresponding percentage is 40–45 percent. These percentage drop-offs are almost independent of the Reynolds number.

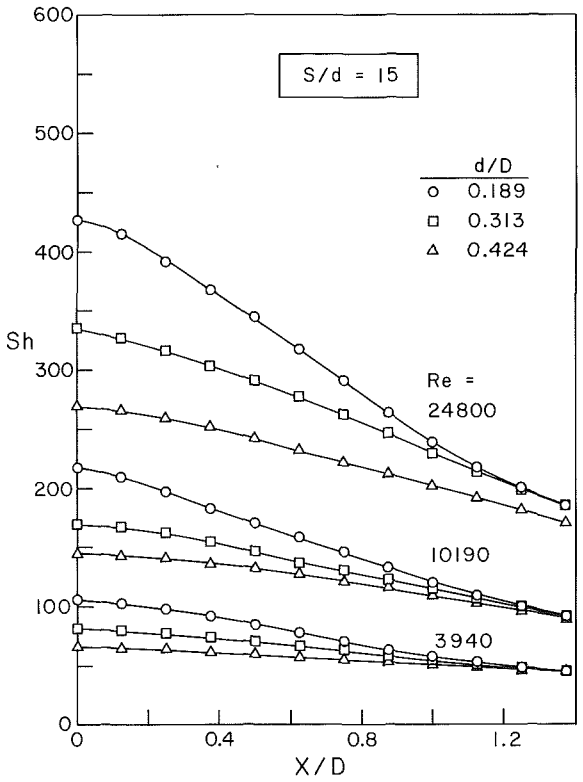

Fig. 11 Axial distributions of the Sherwood number for $S/d = 15$

As evidenced by Figs. 7 and 8, the aforementioned trends are generally preserved, but with modifications, as d/D increases. In particular, although the Sh distributions for smaller S/d continue to drop off more rapidly with X/D than do those for larger S/d, the merging of the curves and their ultimate independence of S/d is attained more slowly (i.e., at larger X/D) for jets of larger diameter. Thus, for example, in Fig. 8, it is seen that at the last measurement station and for Re = 24,640, the curves for the different S/d have not yet merged. Furthermore, the extent of the drop-off of Sh with X/D becomes smaller for jets of larger diameter.

An alternate presentation of the axial distributions is conveyed by Figs. 9–11. Each of these figures is for a fixed separation distance S/d, respectively, 5, 10, and 15. In each figure, Sh distributions are presented for three Reynolds numbers which span the investigated range (two Re values were omitted from these figures to preserve clarity). Each Reynolds number is represented by three curves which respectively correspond to jet diameters $d/D = 0.189$, 0.313, and 0.424.

Figure 9 (the smallest spacing) will be discussed first. The figure shows that although larger Sh values are attained at the impingement point with smaller diameter jets, there is a much more rapid drop-off with X/D when the jet diameter is small. Indeed, the drop-off pattern is such that at a moderate distance from the impingement point, the ordering of the results with jet diameter is reversed so that the largest diameter jet exhibits the highest Sherwood number.

These results may be rationalized by noting that at a fixed Reynolds number, a smaller diameter jet is characterized by a higher velocity but a smaller mass flow. The higher velocity asserts itself in creating higher impingement-point values of Sh, while the lower mass flow is responsible for the more rapid drop-off and the lower values of Sh at larger X/D.

When the distance between the jet exit and the cylinder is increased (i.e., larger S/d), the resulting greater preimpingement jet spreading tends to blur the effect of jet diameter. Thus, in Fig. 10 ($S/d = 10$), although there is a reversal in the ordering of the curves for a given Re as X/D

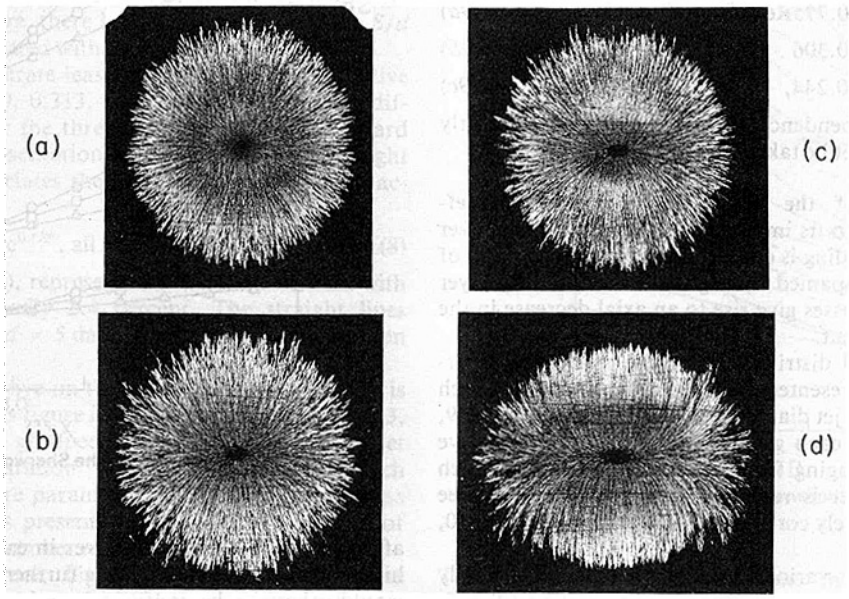

Fig. 12 Flow visualization photographs: (a) $d/D = 0.189$, $S/d = 5$; (b) $d/D = 0.189$, $S/d = 15$; (c) $d/D = 0.424$, $S/d = 5$; and (d) $d/D = 0.424$, $S/d = 15$

increases, it is not nearly as extensive as that in evidence in Fig. 9. For $S/d = 15$ (Fig. 11), the differences in the rapidity of the drop-off for the various S/d have further moderated so that the reversal in ordering has not yet occurred at the last measurement station, although it is incipient.

The results presented in Figs. 6–11, together with the related discussion, suggest that the choice of d/D and S/d for an application will depend on whether a high peak value of Nu (or Sh) is more or less important than uniformity. The former objective is favored by small S/d and small d/D, while the latter is promoted by large S/d and large d/D.

Flow Visualization. As noted in the Introduction, the oil-lampblack technique [8] was used for flow visualization. For this study, the surface of the cylinder was covered with white, self-adhering, plasticized contact paper. Prior to the initiation of the airflow, the contact paper was brushed with a suitable mixture of lampblack powder and oil. When the airflow was activated and maintained, the mixture moved under the action of the fluid shear forces, yielding a pattern of lines which reflect the pattern of fluid flow adjacent to the surface of the cylinder. At the termination of the visualization run, the contact paper was removed from the cylinder, laid flat on a plane backing surface, and photographed.

It was necessary that the mixture was sufficiently stiff so that it did not sag under the action of gravity. On the other hand, such a mixture did not respond to the relatively small shear forces associated with Reynolds numbers in the lower end of the range. Therefore, the visualization work was carried out at the upper end of the investigated Reynolds number range.

The results of the flow visualization are presented in Fig. 12, where four photographs are displayed. Photos (*a*) and (*b*) correspond to the smallest diameter jet, $d/D = 0.189$, and to $S/d = 5$ and 15, respectively. Similarly, photos (*c*) and (*d*) are for the largest diameter jet, $d/D = 0.424$, and for $S/d = 5$ and 15, respectively. For purposes of orientation, a horizontal line may be imagined to be drawn through the black spot in the center of each visualization pattern. Such a line would lie along the upper ridge of the cylinder (facing the oncoming jet), parallel to the axis.

The aforementioned black spot is a stagnation zone, and it marks the position on the surface where the center of the jet impinges. The streak lines which emanate from the stagnation zone show the paths along which the jet spreads over the surface. The pictured streak lines subtend about half the cylinder circumference.

In photograph (*a*), the stagnation zone is a circle, and the streak lines appear to be uniformly radial. Thus, for a small diameter jet and a relatively small jet exit-cylinder separation distance, the jet spreads uniformly over the surface.

The slightly elliptical shape of the stagnation zone in photograph (*b*) is indicative of a modest nonuniformity in the spread of the jet, and this is confirmed by careful study of the streak lines. It appears that fluid particles issuing from the stagnation zone along paths angled slightly away from the axial direction (i.e., the horizontal direction in the photograph) tend to move along slightly curved trajectories. The flow pattern pictured in photo (*c*) is virtually identical to that of photo (*b*). These photos respectively correspond to a small diameter jet which is initiated relatively far from the cylinder and a large diameter jet which is initiated relatively close to the cylinder.

Photograph (*d*) corresponds to a large diameter jet initiated relatively far from the cylinder. The stagnation zone has become more elliptical, and the aforementioned flow path curvature is now more clearly in evidence. The spreading of the jet over the surface is quite nonuniform in this case.

Concluding Remarks

The experiments reported here have provided, seemingly for the first time, mass (heat) transfer coefficients for crossflow impingement of a circular jet on a cylinder. Although the experimental work was performed for mass transfer (i.e., naphthalene sublimation), the results can be employed for heat transfer, as demonstrated by equations (5) and (6).

Two geometrical parameters were varied during the course of the experiments – d/D and S/d, where d is the diameter of the jet at its point of initiation (exit of the jet delivery tube), D is the diameter of the cylinder, and S is the distance between the initiation of the jet and the cylinder surface. The d/D ratio ranged from 0.189 to 0.424, while S/d varied from 5 to 15. For each configuration defined by d/D and S/d, the range of the Reynolds number extended from 4000 to 25,000.

The measurements yielded the circumferential-average mass (heat) transfer coefficient as a function of axial position along the cylinder. The peak transfer coefficients occurred at the section where the jet centerline intersected the surface of the cylinder.

With regard to the peak transfer coefficients, the Sherwood-Reynolds (Nusselt-Reynolds) relation was of identical form ($\mathrm{Sh} \sim \mathrm{Re}^{0.765}$) for all the investigated jet diameters and for both the intermediate and largest jet initiation distances. At the smallest jet initiation distance, the results obeyed a slightly different power law ($\mathrm{Sh} \sim \mathrm{Re}^{0.685}$). A correlation group involving Sh, Re, and d/D was synthesized to enable easy and accurate interpolation of the peak Sherwood number results.

For a fixed jet diameter and Reynolds number, the largest peak Sherwood number occurred for the smallest jet initiation distance. Similarly, for a fixed initiation distance and Reynolds number, the smallest diameter jet yielded the largest peak Sherwood number.

The transfer coefficient decreased with increasing axial distance from the impingement point. The drop-off was accentuated at small initiation distances (at a fixed jet diameter and Reynolds number) and for smaller jet diameters (at a fixed initiation distance and Reynolds number).

The circumferential distributions of the mass transfer coefficient, which would have served to supplement the present results, were not obtained because the special instrumentation needed for their determination was not available.

References

1 Martin, H., "Heat and Mass Transfer Between Impinging Gas Jets and Solid Surfaces," *Advances in Heat Transfer*, Vol. 13, 1977, pp. 1–60.

2 Schuh, H., and Persson, B., "Heat Transfer on Circular Cylinders Exposed to Free-Jet Flow," *International Journal of Heat and Mass Transfer*, Vol. 7, 1964, pp. 1257–1271.

3 Kumada, M., Mabuchi, I., and Kawashima, Y., "Mass Transfer on a Cylinder in the Potential Core Region of a Two-Dimensional Jet," *Heat Transfer—Japanese Research*, Vol. 2, No. 3,1973, p. 53–66.

4 Koopman, R. N., and Sparrow, E. M., "Local and Average Transfer Coefficients Due to an Impinging Row of Jets," *International Journal of Heat and Mass Transfer*, Vol. 19, 1976, pp. 673–683.

5 Sparrow, E. M., and Lovell, B. J., "Heat Transfer Characteristics of an Obliquely Impinging Circular Jet," ASME JOURNAL OF HEAT TRANSFER, Vol. 102, 1980, pp. 202–209.

6 Sogin, H. H., "Sublimation from Discs to Air Streams Flowing Normal to their Surfaces," ASME *Transactions*, Vol. 80, 1958, pp. 61–71.

7 Gardon, R., and Akfirat, J. C., "The Role of Turbulence in Determining the Heat Transfer Characteristics of Impinging Jets," *International Journal of Heat and Mass Transfer*, Vol. 8, 1965, pp. 1261–1272.

8 Merzkirch, W., *Flow Visualization*, Academic Press, New York, 1974, pp. 53–56.

On the Steady-State Temperature Distribution in a Rotating Cylinder Subject to Heating and Cooling Over Its Surface

W. Y. D. Yuen
Research and Technology Centre,
Senior Research Officer,
John Lysaght (Australia) Limited,
Port Kembla, NSW, 2505, Australia

A series solution for the two-dimensional, steady-state temperature distribution in a rotating cylinder, subject to surface heating flux conditions that are at most linear functions of the surface temperature, is applied to strip rolling. An examination of the influence of heat input over the heating region (roll gap) on the peak cylinder (roll) temperature is made. A strip scale layer (which is present in hot rolling) is shown to have a significant effect on roll temperatures through its modification of the heat transfer between strip and roll. The present results indicate that significant errors will arise in estimating the peak roll temperature if insufficient terms are used or if the heat distribution is taken to be uniform in the heating region.

1 Introduction

Much effort has been devoted, over the years, to the understanding of rolling processes in cold and hot strip mills [1]. In particular, the heat transfer and temperature distribution in the work rolls of a rolling stand have been subjects of major interest to rolling mill designers. The studies have been invaluable in determining the strip temperature distribution, in estimating the values of the temperature-dependent parameters, in designing efficient cooling systems to keep the peak temperature and thermal gradient within an acceptable tolerance range, in predicting the roll thermal crown, and in estimating the thermal stresses induced in the rolls, the latter being connected with minimizing the risk of roll spalling.

The thermal processes occurring in the rolls, as a result of strip rolling, are described fundamentally in terms of a rotating cylinder, subject to heating over a small surface area (the roll gap region where the roll is in contact with the strip), and to convective cooling over all or part of the cylinder surface area. Cerni [2] and Cerni et al. [3] have developed a mathematical model to determine the two-dimensional transient temperature distribution in a roll of a rolling stand. Their formulation was based on the assumption that heat transferred in the roll gap from the strip to the rolls, which are subject to uniform circumferential cooling, may be approximated by a line source, and that the decrease in the heat transferred to the rolls, initially at ambient temperature, varies exponentially with time. The transient temperature buildup in the rolls has also been studied experimentally by Stevens et al. [4] and numerically by Parke et al. [5] for specific roll dimensions and speeds. In the latter, a finite difference scheme was used, the work roll was subject to water cooling over a portion of its circumference, and the heat loss to the back-up roll was taken into consideration. Recently, Denisov et al. [6] described experiments which accurately measured the temperature distribution near the roll surface. With this data, the complete roll temperature distribution may be calculated.

In a series of papers, Unger [7, 8], and Unger and Weber [9–11] presented a formulation of the steady-state roll temperature distribution, which included the effects of heat transfer in the roll axial direction. The influence of various parameters on the roll thermal crown in cold rolling was examined from numerical solutions.

Parallel with these numerical investigations, analytical studies have continued. With the assumptions of only radial heat transfer in the roll and a roll surface temperature varying exponentially with time, Pawelski [12] obtained expressions for the transient roll temperature distribution near the roll surface. This work was later extended, with the inclusion of a scale (oxide) layer on the strip surface, to calculations of the steady-state roll temperature near the surface [13]. The analytical detail of this work, however, does not appear to have been published. A more rigorous, two-dimensional analysis of the steady-state temperature has been formulated by Haubitzer [14], the roll temperature being expressed in terms of Kelvin functions in the roll radial direction and Fourier expansions in the circumferential direction, with constants determined from the prescribed surface temperature distribution. Patula [15] extended Haubitzer's work [14] by applying mixed boundary conditions to the same separated form of solution. This was aimed at the application of more practical roll surface conditions, i.e., roll cooling, governed by a uniform convective heat transfer coefficient, was spread over a portion of the roll circumference only. The heat transfer in the finite roll gap was assumed to be uniform (cf. the Cerni et al. [3] formulation of a single line heat source in the roll gap). The roll temperature was expressed in terms of constants determined by the solution of a set of linear simultaneous equations.

This paper presents a more general extension of Haubitzer's formulation [14] to consider prescribed roll surface heat flux conditions that are at most linearly dependent on the roll surface temperature. The solution is then formulated for variable heat input at the roll surface and roll cooling with variable convective heat transfer coefficient. For this, the roll peak temperature is calculated for a variable roll gap heat source, which is obtained from a detailed roll gap analysis [16].

2 Problem Statement and Solution

Under conditions similar to those listed in [15], the temperature, $T(r,\theta)$ (relative to a reference temperature, T_r), within a rotating cylinder is described by

$$\frac{1}{r}\frac{\partial}{\partial r}\left(r\frac{\partial T}{\partial r}\right)+\frac{1}{r^2}\frac{\partial^2 T}{\partial \theta^2}-\frac{\omega}{\alpha_r}\frac{\partial T}{\partial \theta}=0 \qquad (1)$$

where ω is the cylinder angular speed and α_r the thermal diffusivity.

Contriubted by the Heat Transfer Division for publication in the JOURNAL OF HEAT TRANSFER. Manuscript received by the Heat Transfer Division September 23, 1982.

The center temperature (at $r=0$) of the cylinder must be finite and the outer (cylindrical) surface boundary condition (Fig. 1(*a*)) is defined by

$$-k_r \frac{\partial T(R,\theta)}{\partial r} = -q(\theta) + h(\theta)[T(R,\theta) - T_c(\theta)] \qquad (2)$$

where k_r is the thermal conductivity of the cylinder; $q(\theta)$, the heat input distribution at the surface; $h(\theta)$, the convective heat transfer coefficient; and $T_c(\theta)$, the coolant temperature, relative to the reference temperature, T_r.

The solution of equation (1), finite at the origin, is [14, 15]

$$\hat{T}(\hat{r},\theta) = B_o + \sum_{n=1}^{\infty} \left\{ B_n \left[\frac{\mathrm{ber}_n(a_n\hat{r})}{\mathrm{ber}_n(a_n)} \cos(n\theta) - \frac{\mathrm{bei}_n(a_n\hat{r})}{\mathrm{ber}_n(a_n)} \sin(n\theta) \right] + C_n \left[\frac{\mathrm{ber}_n(a_n\hat{r})}{\mathrm{ber}_n(a_n)} \sin(n\theta) + \frac{\mathrm{bei}_n(a_n\hat{r})}{\mathrm{ber}_n(a_n)} \cos(n\theta) \right] \right\} \qquad (3)$$

where $\hat{T}(r,\theta) = T(r,\theta)/(Q_o/h_o)$ is the cylinder temperature, nondimensionalized by the integrated heat input at the cylinder surface, $Q_o = \int_o^{2\pi} q(\theta)d\theta$, and a reference heat transfer coefficient, h_o; $a_n = (n\omega/\alpha_r)^{1/2}R$; $\hat{r} = r/R$; and $\mathrm{ber}_n(x)$ and $\mathrm{bei}_n(x)$ are Kelvin functions that are related to the Bessel function, $J_n(x)$, by $J_n(x \exp[3i\pi/4]) = \mathrm{ber}_n(x) + i\,\mathrm{bei}_n(x)$, where $i^2 = -1$.

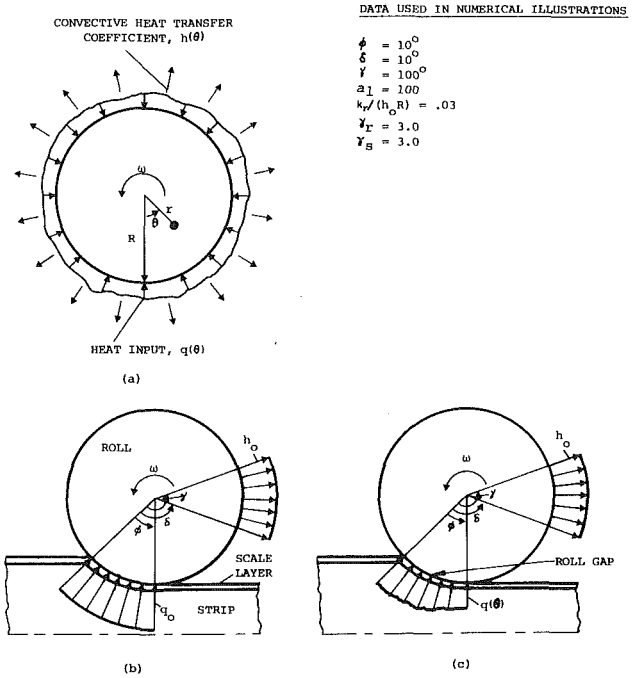

Fig. 1 Boundary conditions at the cylinder surface: (*a*) general; (*b*) uniform heat source and cooling (Patula's formulation [15]); (*c*) actual rolling conditions

Nomenclature

a_n = $(n\omega/\alpha_r)^{1/2}R$
A_1, A_2, A_3 = constants in equation (14)
b_n = $n\hat{\epsilon}$
B_n, C_n = constants in equation (3)
c = specific heat
f_1 = $(\gamma_r - 1)/(\gamma_r + 1)$
f_2 = $(\gamma_s - 1)/(\gamma_s + 1)$
F_d, F_f, F_t = terms defined in equations (19–21)
$h(\theta)$ = convective heat transfer coefficient
h_o = reference heat transfer coefficient
I_1, I_2, I_3 = integrals defined in equations (25–27)
k = thermal conductivity
M_n, λ_n = modulus and phase form of the Kelvin functions (equations (10) and (11))
N = number of terms employed in the truncation of solution (3)
$q(\theta)$ = heat input at the cylinder surface
q_o = uniform heat input intensity in the roll gap
$q_d(\theta), q_f(\theta), q_t(\theta)$ = heat input functions in the roll gap due to the heating components
q_F = average frictional energy generated (per unit area) along the roll/scale layer interface
Q_o = total heat input in the roll gap
Q_d, Q_f, Q_t = integrated heat input in the roll gap due to the heating components
Q_s = average deformation energy (per unit volume) generated in the strip
$r-\theta$ = cylindrical coordinate system as shown in Fig. 1
$\hat{r}$ = r/R
R = cylinder radius
$\hat{t}$ = dimensionless time parameter
t_1 = half-strip thickness
T = cylinder temperature, relative to T_r
$\hat{T}$ = nondimensionalized cylinder temperature, $T/(Q_o/h_o)$
$T_c(\theta)$ = coolant temperature, relative to T_r
T_r = reference temperature
T_{ro} = roll center temperature
T_{so} = mean strip temperature at the roll gap entry
T_o = $T_{so} - T_{ro}$
$\hat{T}_\phi$ = nondimensionalized roll surface temperature at the roll gap exit
$\hat{T}_{\phi p}$ = nondimensionalized "plateau" or "local minimum" roll temperature (equation (14))

Greek Symbols

α = thermal diffusivity
γ_r = $(\rho_r k_r c_r)^{1/2}/(\rho_c k_c c_c)^{1/2}$
γ_s = $(\rho_s k_s c_s)^{1/2}/(\rho_c k_c c_c)^{1/2}$
$\hat{\gamma}$ = γ_s/γ_r
δ, γ = angles given in Fig. 1
ϵ = nondimensionalized scale layer thickness
$\hat{\epsilon}$ = modified scale layer thickness, $\epsilon(\alpha_s/\alpha_c)^{1/2}(\omega t_1^2/\alpha_s)^{1/2}$
ρ = density
ϕ = roll gap angle (Fig. 1)
ω = angular speed of cylinder

Subscripts

c = scale layer
d = due to deformation energy generated in the strip
f = due to friction energy generated at the roll/scale layer interface
r = roll or cylinder
s = strip
t = due to the temperature difference between the strip and the roll

The constants, B_i and C_i, may be determined by expanding the boundary condition (2) in Fourier series and are given by the following infinite set of coupled linear equations

$$B_o\int_0^{2\pi}\frac{h(\theta)}{h_o}\,d\theta+\sum_{n=1}^{\infty}\left[\left(B_n+C_n\frac{\mathrm{bei}_n(a_n)}{\mathrm{ber}_n(a_n)}\right)\times\right.$$

$$\int_0^{2\pi}\frac{h(\theta)}{h_o}\cos(n\theta)\,d\theta+\left(C_n-B_n\frac{\mathrm{bei}_n(a_n)}{\mathrm{ber}_n(a_n)}\right)\times$$

$$\left.\int_0^{2\pi}\frac{h(\theta)}{h_o}\sin(n\theta)\,d\theta\right]=1+\frac{\int_0^{2\pi}h(\theta)\,T_c(\theta)\,d\theta}{Q_o},\ m=0 \tag{4}$$

$$B_o\int_0^{2\pi}\frac{h(\theta)}{h_o}\cos(m\theta)\,d\theta+\sum_{n=1}^{\infty}\left[\left(B_n+C_n\frac{\mathrm{bei}_n(a_n)}{\mathrm{ber}_n(a_n)}\right)\times\right.$$

$$\int_0^{2\pi}\frac{h(\theta)}{h_o}\cos(n\theta)\cos(m\theta)\,d\theta+\left(C_n-B_n\frac{\mathrm{bei}_n(a_n)}{\mathrm{ber}_n(a_n)}\right)\times$$

$$\left.\int_0^{2\pi}\frac{h(\theta)}{h_o}\sin(n\theta)\cos(m\theta)\,d\theta\right]+\frac{\pi k_r}{h_oR}a_m\left[B_m\frac{\mathrm{ber}'_m(a_m)}{\mathrm{ber}_m(a_m)}\right.$$

$$\left.+C_m\frac{\mathrm{bei}'_m(a_m)}{\mathrm{ber}_m(a_m)}\right]=\frac{\int_0^{2\pi}[q(\theta)+h(\theta)\,T_c(\theta)]\cos(m\theta)\,d\theta}{Q_o},$$

$$m=1,2,3,\ldots \tag{5}$$

$$B_o\int_0^{2\pi}\frac{h(\theta)}{h_o}\sin(m\theta)d\theta+\sum_{n=1}^{\infty}\left[\left(B_n+C_n\frac{\mathrm{bei}_n(a_n)}{\mathrm{ber}_n(a_n)}\right)\times\right.$$

$$\int_0^{2\pi}\frac{h(\theta)}{h_o}\cos(n\theta)\sin(m\theta)\,d\theta+\left(C_n-B_n\frac{\mathrm{bei}_n(a_n)}{\mathrm{ber}_n(a_n)}\right)\times$$

$$\left.\int_0^{2\pi}\frac{h(\theta)}{h_o}\sin(n\theta)\sin(m\theta)\,d\theta\right]+\frac{\pi k_r}{h_oR}a_m\left[C_m\frac{\mathrm{ber}'_m(a_m)}{\mathrm{ber}_m(a_m)}\right.$$

$$\left.+B_m\frac{\mathrm{bei}'_m(a_m)}{\mathrm{ber}_m(a_m)}\right]=\frac{\int_0^{2\pi}[q(\theta)+h(\theta)\,T_c(\theta)]\sin(m\theta)\,d\theta}{Q_o},$$

$$m=1,2,3,\ldots \tag{6}$$

where $\mathrm{ber}'_m(x)=\frac{d}{dx}\mathrm{ber}_m(x)$, $\mathrm{bei}'_m(x)=\frac{d}{dx}\mathrm{bei}_m(x)$.

In obtaining a numerical solution of this set of equations, one must truncate the Fourier series but retain sufficient terms to ensure the required accuracy of the approximate solution.

3 Numerical Results and Applications

A computer program (in Fortran) has been written to solve the linear algebraic equations by Gauss elimination with scaled partial pivoting (algorithm due to Conte et al. [17]). In the evaluation of the coefficients, it is useful to note that, as a_n $(n>0)$ is normally large in the case of strip rolling, the Kelvin functions may be expanded asymptotically in modulus and phase form [18], and the ratios of the Kelvin functions can be expressed as follows

$$\frac{\mathrm{bei}_n(x)}{\mathrm{ber}_n(x)}=\tan(\lambda_n) \tag{7}$$

$$\frac{\mathrm{ber}'_n(x)}{\mathrm{ber}_n(x)}=-\frac{n}{x}-\frac{M_{n-1}}{M_n}\frac{\cos(\lambda_{n-1}-\tfrac{1}{4}\pi)}{\cos(\lambda_n)} \tag{8}$$

$$\frac{\mathrm{bei}'_n(x)}{\mathrm{ber}_n(x)}=-\frac{n}{x}\tan(\lambda_n)-\frac{M_{n-1}}{M_n}\frac{\sin(\lambda_{n-1}-\tfrac{1}{4}\pi)}{\cos(\lambda_n)} \tag{9}$$

where

$$M_n=\exp\left\{\frac{x}{\sqrt{2}}-\frac{1}{2}\ln(2\pi x)-\frac{4n^2-1}{8\sqrt{2}x}-\frac{(4n^2-1)(4n^2-25)}{384\sqrt{2}x^3}\right.$$

$$\left.-\frac{(4n^2-1)(4n^2-13)}{128x^4}+\mathrm{O}\left(\frac{1}{x^5}\right)\right\} \tag{10}$$

and

$$\lambda_n=\frac{x}{\sqrt{2}}+\left(\frac{n}{2}-\frac{1}{8}\right)\pi+\frac{4n^2-1}{8\sqrt{2}x}+\frac{4n^2-1}{16x^2}$$

$$-\frac{(4n^2-1)(4n^2-25)}{384\sqrt{2}x^3}+\mathrm{O}\left(\frac{1}{x^5}\right) \tag{11}$$

3.1 Uniform Heat Input Within the Roll Gap—a Study of The Solution Accuracy Near the Heated Region. The number of terms needed to obtain adequate accuracy near the heated region will be examined in this section. It is important to recognize that, if the heat input is over an angle ϕ (the roll bite), the number of terms, N (the upper limit in the summation sign of equation (3)), must be reasonably larger than $2\pi/\phi$ if any precision is to be obtained in the neighborhood of the heated region.

It should be noted, however, that for regions away from the heated region, where the temperature gradients are not large, reasonable accuracy may be obtained with fewer terms (see section 3.4).

For comparison purposes, the conditions specified in Fig. 2 of [15] (see Fig. 1(*b*) of this paper), namely

$$q(\theta)=\begin{cases}-q_0, & 0<\theta<\phi=0.175\ (10\ \text{deg})\\ 0, & \phi<\theta<2\pi\end{cases} \tag{12}$$

$$h(\theta)=\begin{cases}0, & 0<\theta<\delta=0.175\ (10\ \text{deg})\\ h_0, & \delta<\theta<\gamma=1.75\ (100\ \text{deg})\\ 0, & \gamma<\theta<2\pi\end{cases} \tag{13}$$

have been applied to the present solution. (The uniform coolant temperature and convective heat transfer coefficient in the cooling region have been taken as the references, T_r and h_o, respectively.) The evaluation was performed for increasing numbers of terms and the results for the approximate nondimensionalized surface temperature at the end of the heating region (roll gap exit), which is normally the peak temperature in the roll, are shown by the dotted line in Fig. 2.

A close examination of the truncated series for the temperature reveals that the temperature reaches a plateau at multiples of 36 terms: this coincides with the periods needed to describe the roll gap detail. It can be observed that these plateau temperatures, $\hat{T}_{\phi p}$, vary with the number of terms, N, in the manner shown by the dotted curve in Fig. 3. This curve is closely approximated by the equation

$$\hat{T}_{\phi p}=A_1-A_2/(A_3+N) \tag{14}$$

where A_1, A_2, and A_3 are constants. From this equation, it may be concluded that

$$\hat{T}_{\phi p}\to A_1 \text{ as } N\to\infty$$

and that, in order to achieve a 1 percent accuracy, over 500 terms need to be employed. Also, a 40-term solution, which is found to provide sufficient accuracy for regions away from the roll gap (see section 3.4), is predicted to underestimate the peak roll temperature by approximately 9 percent.

3.2 Variable Heat Input Within the Roll Gap. Although

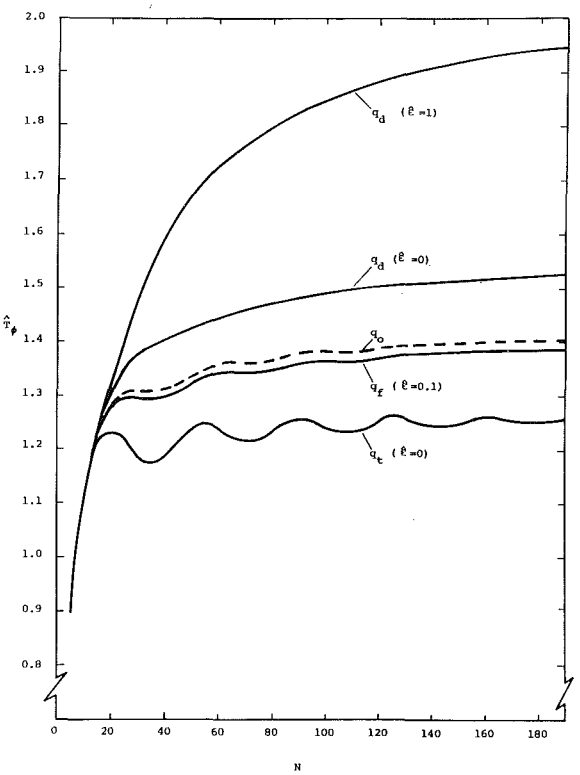

Fig. 2 Variation of the nondimensionalized surface temperature at the roll gap exit, $\hat{T}_\phi$, with the number of terms, N, employed

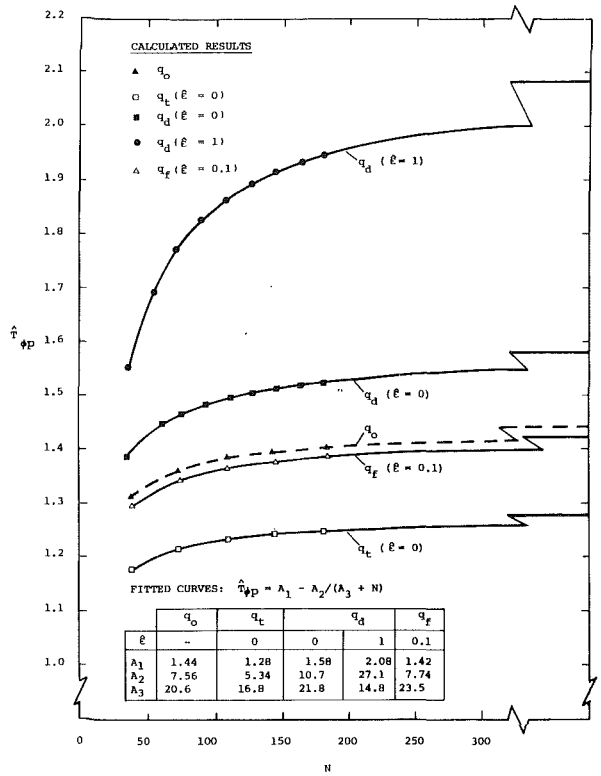

	q_o	q_t	q_d		q_f
$\hat{\epsilon}$	–	0	0	1	0.1
A_1	1.44	1.28	1.58	2.08	1.42
A_2	7.56	5.34	10.7	27.1	7.74
A_3	20.6	16.8	21.8	14.8	23.5

Fig. 3 Variation of the nondimensionalized "plateau" or "local minimum" surface temperature at the roll gap exit, $\hat{T}_{\phi p}$, with the number of terms, N, employed

the roll temperatures derived from a uniform heat input over the roll gap provide useful preliminary information, the fact that the heat input can be far from uniform should be taken into consideration. This is particularly important because the heating distribution will influence both roll peak temperatures and temperature gradients in the neighborhood of the roll gap and, therefore, the locally induced roll thermal stresses which affect roll life.

Details of the heat transfer in the roll gap to the roll may be given [16] in terms of components (because the problem is linear) due to the temperature difference between the strip and the roll ($q_t(\theta)$), plastic deformation energy generated in the strip ($q_d(\theta)$), and friction energy generated at the roll/scale layer interface ($q_f(\theta)$). The function $q(\theta)$, of boundary condition (2), then becomes

$$q(\theta) = \begin{cases} -[q_t(\theta) + q_d(\theta) + q_f(\theta)], & 0 < \theta < \phi, \\ 0, & \phi < \theta < 2\pi \end{cases} \tag{15}$$

These heat components, which were expressed in terms of the dimensionless time parameter $\hat{t}$ in [16], may be written in terms of the angular position θ (using $\theta = \omega(t_1^2/\alpha_s)\,\hat{t}$) as follows

$$q_t(\theta) = F_t \theta^{-1/2} \sum_{n=0}^{\infty} \left\{ (f_1 f_2)^n [i^{-1}\mathrm{erfc}(b_n \theta^{-1/2}) + f_2 i^{-1}\mathrm{erfc}(b_{n+1}\theta^{-1/2})] \right\} \tag{16}$$

$$q_d(\theta) = F_d \theta^{1/2} \sum_{n=0}^{\infty} \left\{ (f_1 f_2)^n \mathrm{ierfc}(b_{n+1/2}\theta^{-1/2}) \right\} \tag{17}$$

$$q_f(\theta) = F_f \sum_{n=0}^{\infty} \left\{ (f_1 f_2)^n [\mathrm{erfc}(b_n \theta^{-1/2}) - f_2 \mathrm{erfc}(b_{n+1}\theta^{-1/2})] \right\} \tag{18}$$

where

$$F_t = \frac{k_r T_{ro}}{2t_1} \frac{T_o}{T_{ro}} \left(\frac{\alpha_s}{\alpha_r}\right)^{1/2} (\omega t_1^2/\alpha_s)^{1/2}/(\gamma_r + 1) \tag{19}$$

$$F_d = \frac{4k_r T_{ro}}{t_1} \frac{Q_s(t_1^2/\alpha_s)}{\rho_s c_s T_{ro}} \frac{k_s}{k_r} \frac{\gamma_r}{(\gamma_r+1)(\gamma_s+1)} (\omega t_1^2/\alpha_s)^{-1/2} \tag{20}$$

and

$$F_f = \frac{k_r T_{ro}}{t_1} \frac{t_1 q_F}{k_s T_{ro}} \frac{k_s}{k_r} \frac{\gamma_r}{\gamma_r + 1} \tag{21}$$

Here $\gamma_r = (\rho_r k_r c_r)^{1/2}/(\rho_c k_c c_c)^{1/2}$, $\gamma_s = (\rho_s k_s c_s)^{1/2}/(\rho_c k_c c_c)^{1/2}$, $f_1 = (\gamma_r - 1)/(\gamma_r + 1)$, $f_2 = (\gamma_s - 1)/(\gamma_s + 1)$, $T_o = T_{so} - T_{ro}$, $b_n = n\hat{\epsilon}$, and $\hat{\epsilon} = \epsilon(\alpha_s/\alpha_c)^{1/2}(\omega t_1^2/\alpha_s)^{1/2}$.

When $\hat{\epsilon} = 0$, equations (16) to (18) reduce to

$$q_t(\theta) = F_t \theta^{-1/2}(\gamma_r + 1)\left(\frac{\hat{\gamma}}{\hat{\gamma}+1}\right) i^{-1}\mathrm{erfc}(0) \tag{22}$$

$$q_d(\theta) = \tfrac{1}{2} F_d \theta^{1/2} \frac{(\gamma_r+1)(\gamma_s+1)}{\gamma_s} \left(\frac{\hat{\gamma}}{\hat{\gamma}+1}\right) \mathrm{ierfc}(0) \tag{23}$$

$$q_f(\theta) = F_f \left(\frac{\gamma_r + 1}{\gamma_s}\right)\left(\frac{\hat{\gamma}}{\hat{\gamma}+1}\right)\mathrm{erfc}(0) \tag{24}$$

where $\hat{\gamma} = \gamma_s/\gamma_r$.

In the foregoing expressions, suffixes r, s, and c refer to roll, strip, and scale layer variables, respectively. T_{ro} is the roll core temperature; T_{so}, the mean strip temperature at the roll gap entry; $2t_1$, the strip thickness at the roll gap entry; ϵ, the scale layer thickness, nondimensionalized by t_1; Q_s, the average deformation energy (per unit volume) generated in the strip; and q_F, the average frictional energy generated (per unit area) along the roll/scale layer interface.

The resulting integrals for $q(\theta)$ on the right-hand side of equations (5) and (6) have forms that are, respectively, the real and imaginary parts of the following integrals

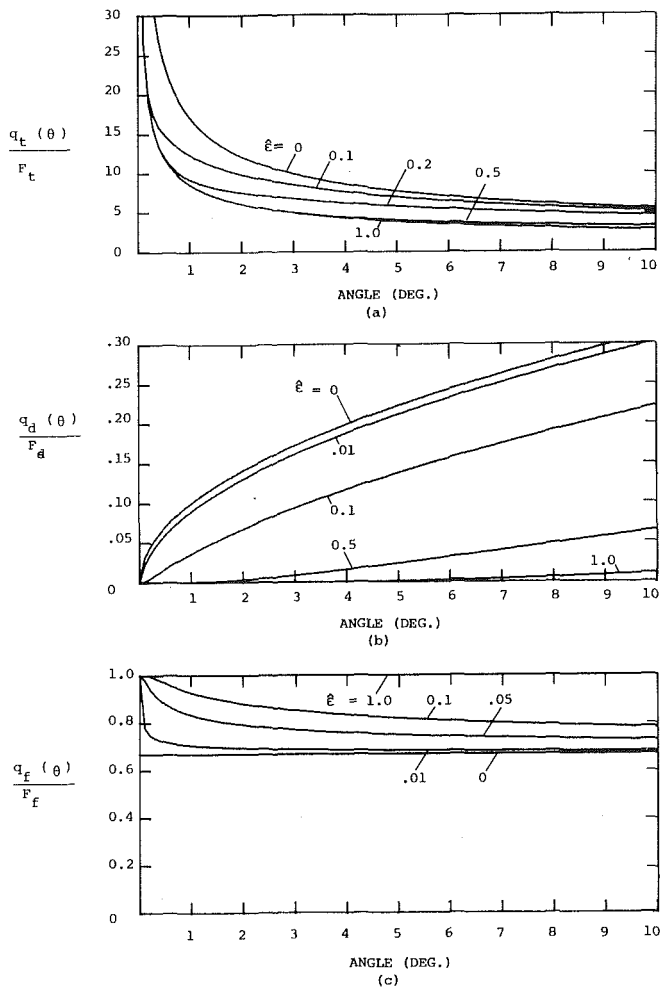

Fig. 4 Variation of heat transfer distribution in the roll gap with modified scale layer thickness, $\hat{\epsilon}$, due to (*a*) a roll/strip temperature difference; (*b*) deformation energy; (*c*) friction energy

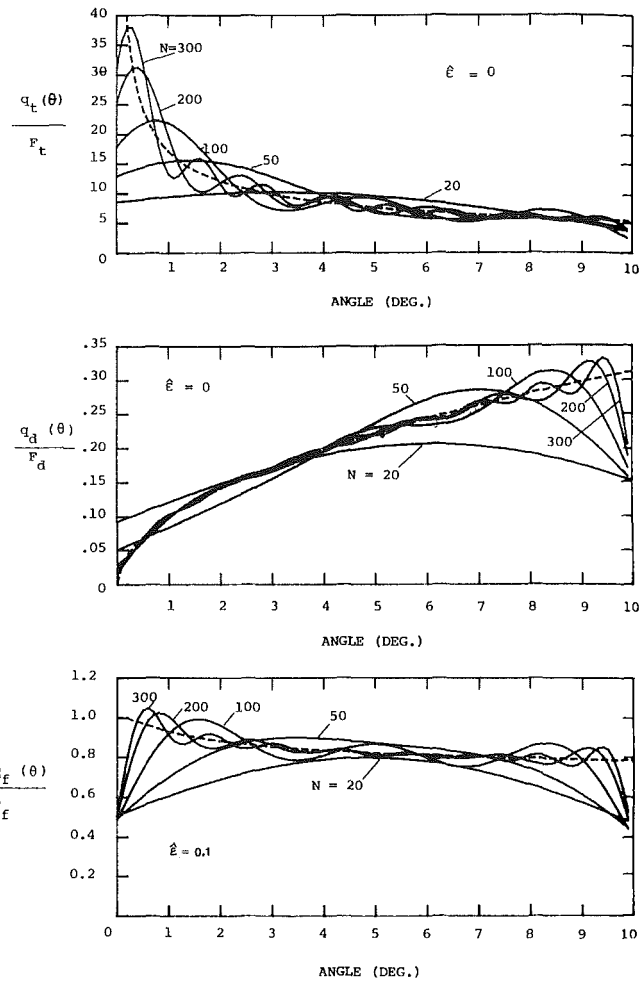

Fig. 5 Truncated Fourier approximation of the heating components ($q_t(\theta)$, $q_d(\theta)$ and $q_f(\theta)$ over an angle of 10 deg) in the roll gap region for varying number of terms, N

$$I_1 = \int_0^{\phi} \theta^{-1/2} i^{-1} \operatorname{erfc}(u\theta^{-1/2}) e^{im\theta} d\theta \tag{25}$$

$$I_2 = \int_0^{\phi} \operatorname{erfc}(u\theta^{-1/2}) e^{im\theta} d\theta \tag{26}$$

$$I_3 = \int_0^{\phi} \theta^{1/2} \operatorname{ierfc}(u\theta^{-1/2}) e^{im\theta} d\theta \tag{27}$$

where u is a function independent of θ, and erfc(z) is the complementary error function (see, for example, [18]). The results of these integrations are given in the Appendix.

The heat transfer distributions within the roll gap ($\phi = 0.175$ rad) due to each heat transfer component for various modified scale layer thicknesses, $\hat{\epsilon}$, are shown in Fig. 4. As an illustration, truncated Fourier expansions for typical heat transfer distributions ($q_t(\theta)$ and $q_d(\theta)$, both with $\hat{\epsilon} = 0$, and $q_f(\theta)$ with $\hat{\epsilon} = 0.1$) are shown in Fig. 5, from which it is clear that many terms, in solution (3), will be required to achieve sufficient accuracy in the heating region.

With the same cooling conditions considered previously, the truncated series for roll surface temperature at the roll gap exit for each heat transfer component, using typical $\hat{\epsilon}$ values, is plotted in Fig. 2 against the number of terms, N, employed in the series solution. Apart from deformation heating, for which there is a monotonic increase with N, the other components show oscillatory behavior with increasing N, although each of them apparently approaches a certain limit as N becomes large. (Although the reason for the nonoscillatory behavior of q_d with N (cf. that of q_t and q_f) is not certain, it is believed that the phenomenon arises from the Fourier series representation of these functions which have different forms: as shown in Fig. 5, q_t and q_f are monotonically decreasing while q_d is monotonically increasing.) The oscillations with increasing number of terms have, at multiples of 36 terms, local minima which again, as shown in Fig. 3, have the form of equation (14). From these results, it may be predicted that, to come within 1 percent of the calculated asymptotes, 400, 650, 1300, and 520 terms are required for $q_t(\hat{\epsilon} = 0)$, $q_d(\hat{\epsilon} = 0)$, $q_d(\hat{\epsilon} = 1)$, and $q_f(\hat{\epsilon} = 0.1)$, respectively. It is also noted that the surface temperature at the roll gap exit is higher due to q_d, and lower due to q_t and q_f, compared to a uniform heat input q_o. This will be elaborated further in the next section.

3.3 Effects of a Scale Layer. The presence of a strip scale layer (which occurs in hot rolling) alters the heat transfer distributions in the roll gap, as shown in Fig. 4. The components of the total heat transfer in the roll gap, Q_t, Q_f, and Q_d, which are found by integration of the respective distributions, are plotted against $\hat{\epsilon}$ in Fig. 6. Reference [16] may be consulted for physical reasoning of the scale layer effect. Suffice it to say that the change in heat transfer distribution and overall heat transfer due to the presence of a scale layer will alter the temperature distribution in the roll gap. The roll temperature at some typical positions is studied below.

With the error estimation process already described and the same boundary conditions, the nondimensionalized surface

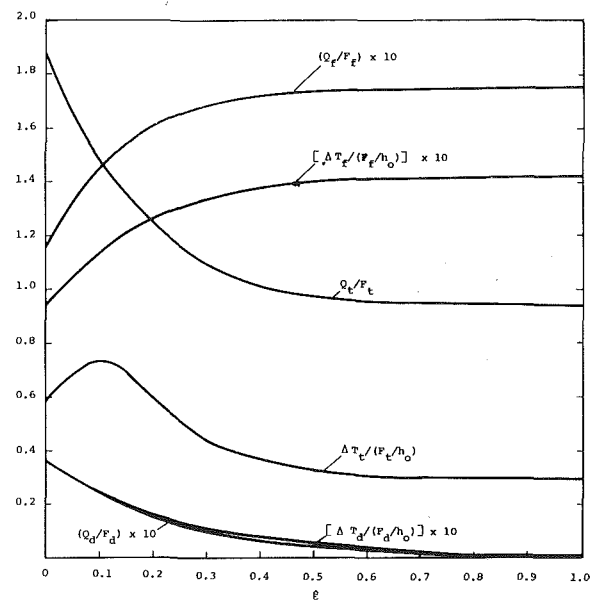

Fig. 6 Variations of the integrated heating components (Q_t, Q_d, Q_f) and temperature difference across the roll gap surface (ΔT_t, ΔT_d, ΔT_f) with the modified scale layer thickness, $\hat{\epsilon}$

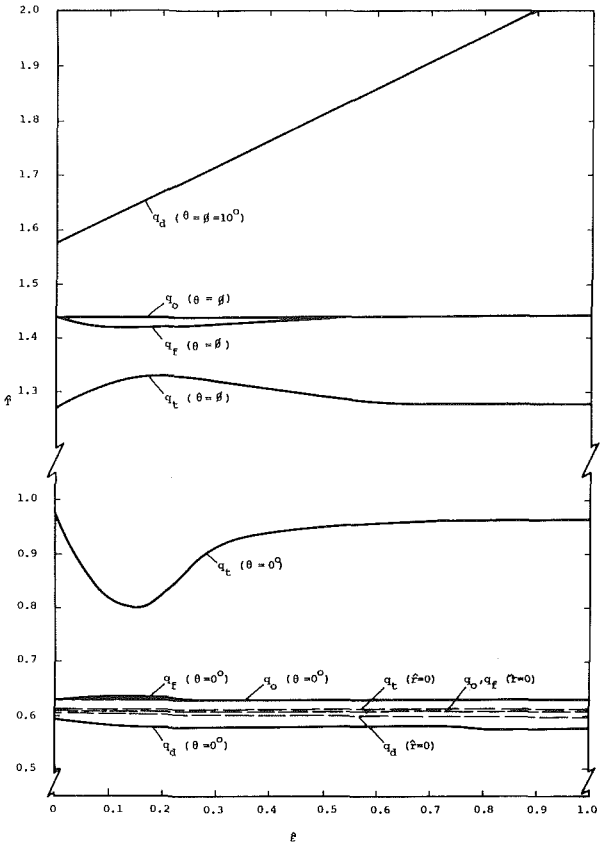

Fig. 7 Variations of the nondimensionalized temperature, $\hat{T}$, at the surface of the roll gap entry and exit (solid lines) and the roll center (dotted lines) with the modified scale layer thickness, $\hat{\epsilon}$

temperature at the roll gap entry and exit were calculated and plotted against $\hat{\epsilon}$ in Fig. 7 (solid lines). It can be seen that, for q_t, the exit temperature reaches a peak at $\hat{\epsilon} \approx 0.2$; for q_d, increases linearly with $\hat{\epsilon}$; and for q_f, remains relatively constant. The entry temperature, however, drops to a minimum at $\hat{\epsilon} \approx 0.15$ for q_t, and remains fairly constant for both q_d and q_f.

It is interesting to observe that the nondimensionalized exit temperature due to the deformation heating, q_d, is always higher than that predicted from the equivalent uniform heat input, q_o, the deviations ranging from 9 percent (at $\hat{\epsilon} = 0$) to 43 percent (at $\hat{\epsilon} = 1$). For q_t, the exit temperature is always lower, the deviations ranging from 8 percent (at $\hat{\epsilon} \approx 0.2$) to 11 percent (at $\hat{\epsilon} = 0$ and 1), and for q_f, the deviations are generally small, reaching a maximum of 1 percent at $\hat{\epsilon} \approx 0.1$. Similar observations were found at the roll gap entry, with the nondimensionalized temperature due to q_d being generally lower than that predicted from q_o, the deviations ranging from 6 percent (at $\hat{\epsilon} = 0$) to 9 percent (at $\hat{\epsilon} = 1$). For q_t and q_f, the entry temperature is generally higher: the deviations range from 27 percent (at $\hat{\epsilon} \approx 0.15$) to 53 percent (at $\hat{\epsilon} = 0$ and 1) for q_t, and have a maximum of 1 percent at $\hat{\epsilon} \approx 0.1$ for q_f.

The actual roll temperatures may be derived from their nondimensionalized values using the total heat transfer components shown in Fig. 6, and it is straightforward to show that the roll gap exit temperature will be a maximum, when the scale layer is absent for q_t and q_d, and when the scale layer becomes very thick for q_f.

The temperature differences across the roll gap surface, ΔT_t, ΔT_d, and ΔT_f, give a fair indication of the average temperature gradient in the roll gap. These, calculated from the entry and exit temperatures (Fig. 7) and the overall heat transfer (Fig. 6), are plotted in Fig. 6.

3.4 Temperature Outside the Roll Gap Region. While the precise shape of the heat input distribution governs the roll temperatures in the roll gap region, its effect on the temperature distribution away from the roll gap should be minimal, provided that the cooling conditions and the total heat input are the same.

The roll core temperatures for the various heating distributions were calculated and plotted against $\hat{\epsilon}$ in Fig. 7 (dotted lines). The results show only a weak dependence on $\hat{\epsilon}$, and there is little variation from one to the other: compared with that predicted from q_o, the roll core temperature is around 1 percent higher for q_t, 1 to 4 percent lower for q_d and, for q_f, the difference is insignificant.

The nondimensionalized surface temperatures (calculated with the error estimation process already described), for the various heat input functions, are compared with those predicted from uniform heating in Table 1, based on the same boundary conditions used previously (Fig. 1). This illustration indicates that for surface angular positions beyond the roll gap angle the deviations are, indeed, small. Thus no significant loss of accuracy of the roll temperature distribution away from the roll gap region occurs with the use of the uniform heat input distribution approximation if the intensity is set equal to the integrated average of the actual heat input function.

Further, for regions outside the roll gap, there are no highly localized effects (in the example of this paper, cooling is over 90 deg, and insulation over 260 deg, compared to heat input over 10 deg in the roll gap), and fewer terms will be needed to determine the accurate temperature distribution in these regions. Table 2 shows the deviations of the temperatures, calculated with only 36 terms, from the predicted asymptotic temperatures for the various heat components. Again the deviations are all small for surface angular positions away from the roll gap. (It is interesting to note that the deviations at $\theta = 100$ deg are higher than their surrounding values, due to the overshoot of the truncated Fourier series at the end of the cooling region.) It is therefore concluded that the 36-term truncated solution will provide reasonable accuracy in describing the roll temperature distribution outside the roll gap region.

Table 1 Comparison of surface temperature ($\hat{T}$), for various heating components (q_t, q_d, q_f), with a uniform heat input (q_o)

Angle, θ	$\hat{T}_{q_o}$	$\Delta\hat{T}/\hat{T}_{q_o}$ (%)					
		q_t		q_d		q_f	
		$\hat{\epsilon}=0$	$\epsilon=0.1$	$\hat{\epsilon}=0$	$\hat{\epsilon}=1$	$\hat{\epsilon}=0.1$	
0	0.629	53.3	7.3	−6.2	−8.7	1.0	roll gap
10	1.438	−14.7	−7.7	9.5	43.5	−1.4	
20	0.835	−0.9	−0.7	0.5	3.4	−0.1	cooling
40	0.649	0.6	−0.6	−0.5	−2.3	−0.1	
80	0.517	1.2	−0.3	−0.8	−3.1	0.1	
100	0.482	1.2	1.8	−0.8	−3.1	0.1	
120	0.560	1.3	−0.3	−0.9	−3.4	0.2	"insulated"
160	0.583	1.4	−0.2	−0.9	−3.4	0.2	
240	0.597	1.5	0.1	−1.0	−3.6	0.2	
280	0.599	1.5	0.3	−1.0	−3.7	0.2	
320	0.599	1.5	0.7	−1.0	−3.9	0.2	
350	0.603	1.8	3.4	−0.9	−2.9	0.2	

Table 2 Comparison of surface temperatures ($\hat{T}$), for various heating components (q_o, q_t, q_d, q_f) using a 36-term truncated solution, with the predicted asymptotic solution

Angle, θ	$\Delta\hat{T}$(36-term)/$\hat{T}$(asymptote) (%)						
	q_o	q_t		q_d		q_f	
		$\hat{\epsilon}=0$	$\epsilon=0.1$	$\hat{\epsilon}=0$	$\hat{\epsilon}=1$	$\hat{\epsilon}=0.1$	
0	15.2	−1.2	7.3	5.5	−6.6	17.4	roll gap
10	−9.1	−7.7	−7.7	−14.8	−24.9	−8.9	
20	0.6	−1.3	−0.7	1.7	−0.1	0.4	cooling
40	0.2	−0.9	−0.6	0.9	1.9	0.0	
80	0.1	−0.4	−0.3	0.6	1.5	0.0	
100	2.1	1.8	1.8	2.4	3.4	2.0	
120	−0.2	−0.3	−0.3	0.1	0.9	−0.2	"insulated"
160	−0.2	−0.1	−0.2	−0.0	0.7	−0.2	
240	−0.2	0.2	0.1	−0.2	0.5	−0.1	
280	−0.2	0.5	0.3	−0.4	0.3	−0.2	
320	−0.1	1.2	0.7	−0.7	0.0	0.0	
350	0.6	4.6	3.4	−1.8	−3.2	1.1	

4 Concluding Remarks

A series solution for the two-dimensional steady-state temperature distribution in a rotating cylinder, subject to surface heat flux conditions that depend at most on linear functions of the surface temperature, has been used to examine the roll heating effects during strip rolling. The large number of terms required to represent the temperature distribution in the heating region has been discussed and, with error estimation methods, accurate predictions of the peak roll temperature have been made. Failure to use sufficient terms or to represent the nonuniform distribution of heat input over the heating region is shown to lead to significant errors in peak roll temperature estimates.

While the present approach is suitable for temperature predictions in the cooling region, it is unrealistic to apply this model to study the temperature distribution within the heating region due to the large number of terms required to achieve sufficient accuracy. (The error estimation process, described in this paper, requires an excessive number of terms to be retained in the Fourier series if finer detail of the temperatures is required within the roll gap region.) Accurate prediction of the temperatures in the heating region may be obtained from the solution given in [16], with correction terms added in localized regions around the leading and trailing edges of the heat source, to account for heat transfer in the circumferential direction. This problem is currently being investigated.

While the formulation of this paper has been sufficiently general to allow for a variable convective cooling heat transfer coefficient around the roll periphery, the results of these applications have been omitted in this paper for the sake of brevity.

Acknowledgments

The author is indebted to Dr. C. H. Ellen for his invaluable comments and interest in this study and wishes to thank the management of John Lysaght (Australia) Limited for permission to publish this paper.

References

1 Pawelski, O., "Contribution of Fundamental Research to Progress in Rolling Technology," *Proceedings of International Conference on Steel Rolling*, Iron and Steel Institute of Japan, Vol. 1, 1980, pp. 27-57.

2 Cerni, S., *The Temperatures and Thermal Stresses in the Rolling of Metal Strip*, Doctoral dissertation, Department of Mechanical Engineering, Carnegie-Mellon University, 1961.

3 Cerni, S., Weinstein, A. S., and Zorowski, C. F., "Temperatures and Thermal Stresses in the Rolling of Metal Strip," *Iron and Steel Engineer Yearbook*, 1963, pp. 717-723.

4 Stevens, P. G., Ivens, K. P., and Harper, P., "Increasing Work-Roll Life by Improved Roll-Cooling Practice," *Journal Iron Steel Institute (London)*, Vol. 209, 1971, pp. 1-11.

5 Parke, D. M., and Baker, J. L. L., "Temperature Effects of Cooling Work Rolls," *Iron and Steel Engineer*, Vol. 49, 1972, pp. 83-88.

6 Denisov, Y. V., Trukhin, B. V., and Kholodov, I. A., "Determination of Temperature at Surface of Rolling Mill Work Rolls," *Steel in USSR*, Vol. 10, 1980, pp. 540-541.

7 Unger, F., "Theoretical Principles for a Mathematical Description of the Thermal Camber of a Cold Rolling Roll Under Static Conditions," *Neue Hütte*, Vol. 22, 1977, pp. 7-10.

8 Unger, F., "Numerical Solution of the Mathematical Expression for the Thermal Convexity of a Cold Roll in Steady State Operation," *Neue Hütte*, Vol. 22, 1977, pp. 72-75.

9 Unger, F., and Weber, K.-H., "Calculation of the Temperature Distribution in Rolls in Steady-State Cold Rolling Operation," *Neue Hütte*, Vol. 21, 1976, pp. 653–657.

10 Unger, F., and Weber, K.-H., "Effect of the Heat Transfer Coefficient and Roll Radius on the Temperature and Thermal Camber of Rolls in Cold Rolling," *Neue Hütte*, Vol. 24, 1979, pp. 138–140.

11 Weber, K.-H., and Unger, F., "Effect of the Barrel Length, Strip Width and Roll Gap Temperature on the Roll Temperature and Thermal Roll Camber During Cold Rolling," *Neue Hütte*, Vol. 24, 1979, pp. 331–336.

12 Pawelski, O., "Calculating the Temperature Field in the Work Rolls of Hot and Cold Rolling Mills," *Arch. Eisenhüttenwes*, Vol. 42, 1971, pp. 713–720.

13 Pawelski, O., and Bruns, E., "Heat Transfer and Temperature Fields in Hot Rolling of Steel With Special Regard to the Influence of Scale," *Stahl und Eisen*, Vol. 96, 1976, pp. 864–869.

14 Haubitzer, W., "The Steady-State Temperature Distribution in Rolls," *Arch. Eisenhüttenwes*, Vol. 46, 1975, pp. 635–638.

15 Patula, E. J., "Steady-State Temperature Distribution in a Rotating Roll Subject to Surface Heat Fluxes and Convective Cooling," ASME JOURNAL OF HEAT TRANSFER, Vol. 103, 1981, pp. 36–41.

16 Yuen, W. Y. D., "On the Heat Transfer of a Moving Composite Strip Compressed by Two Rotating Cylinders," ASME JOURNAL OF HEAT TRANSFER.

17 Conte, S. D., and DeBoor, C., *Elementary Numerical Analysis*, McGraw-Hill, New York, 1972, pp. 132–133.

18 Abramowitz, M., and Stegun, I. A., ed., *Handbook of Mathematical Functions*, National Bureau of Standards, US Department of Commerce, 1972, pp. 297, 299, 304, 382–383.

APPENDIX

The integrals, I_1, I_2, and I_3, defined below, may be integrated and separated into real and imaginary parts using the properties given in [18]:

$$I_1 = \int_o^{\phi} \theta^{-1/2} i^{-1} \operatorname{erfc}(u\theta^{-1/2}) e^{im\theta} d\theta$$

$$= e^{-\sqrt{2mu}} \left[\cos\left(\sqrt{2mu} + \frac{\pi}{4}\right) \{E_R(x_1,y) - 1\} - \sin\left(\sqrt{2mu} + \frac{\pi}{4}\right) E_I(x_1,y) \right]$$

$$+ e^{\sqrt{2mu}} \left[\cos\left(\sqrt{2mu} - \frac{\pi}{4}\right) \{E_R(x_2,y) + 1\} + \sin\left(\sqrt{2mu} - \frac{\pi}{4}\right) E_I(x_2,y) \right]$$

$$+ i\left\{ e^{-\sqrt{2mu}} \left[\cos\left(\sqrt{2mu} + \frac{\pi}{4}\right) E_I(x_1,y) + \sin\left(\sqrt{2mu} + \frac{\pi}{4}\right) \{E_R(x_1,y) - 1\} \right] + e^{\sqrt{2mu}} \left[\cos\left(\sqrt{2mu} - \frac{\pi}{4}\right) E_I(x_2,y) - \sin\left(\sqrt{2mu} - \frac{\pi}{4}\right) \{E_R(x_2,y) + 1\} \right] \right\}$$

$$I_2 = \int_o^{\phi} \operatorname{erfc}(u\theta^{-1/2}) e^{im\theta} d\theta$$

$$= \frac{\sin(m\phi)}{m} \operatorname{erfc}(u\phi^{-1/2}) + \frac{u}{m} \operatorname{Im}(I_{21}) + i\left\{ -\frac{\cos(m\phi)}{m} \operatorname{erfc}(u\phi^{-1/2}) - \frac{u}{m} \operatorname{Re}(I_{21}) \right\}$$

$$I_3 = \int_o^{\phi} \theta^{1/2} \operatorname{ierfc}(u\theta^{-1/2}) e^{im\theta} d\theta$$

$$= \frac{\sin(m\phi)}{m} \phi^{1/2} \operatorname{ierfc}(u\phi^{-1/2}) - \frac{1}{4m} \operatorname{Im}(I_1) + i\left\{ -\frac{\cos(m\phi)}{m} \phi^{1/2} \operatorname{ierfc}(u\phi^{-1/2}) + \frac{1}{4m} \operatorname{Re}(I_1) \right\}$$

where

$$I_{21} = 2\pi^{-1/2} \int_o^{\phi} \exp(-u^2\theta^{-1} + im\theta)\, d(\theta^{-1/2})$$

$$= \frac{1}{2u} \left\{ e^{-\sqrt{2mu}} [\cos(\sqrt{2mu}) \{E_R(x_1,y) - 1\} - \sin(\sqrt{2mu}) E_I(x_1,y)] - e^{\sqrt{2mu}} [\cos(\sqrt{2mu}) \{E_R(x_2,y) + 1\} + \sin(\sqrt{2mu}) E_I(x_2,y)] + i\left[e^{-\sqrt{2mu}} [\cos(\sqrt{2mu}) E_I(x_1,y) + \sin(\sqrt{2mu}) \{E_R(x_1,y) - 1\}] - e^{\sqrt{2mu}} [\cos(\sqrt{2mu}) E_I(x_2,y) - \sin(\sqrt{2mu}) \{E_R(x_2,y) + 1\}] \right] \right\}$$

$$x_1 = -(\tfrac{1}{2}m\phi)^{1/2} + u\phi^{-1/2}$$

$$x_2 = -(\tfrac{1}{2}m\phi)^{1/2} - u\phi^{-1/2}$$

and

$$y = (\tfrac{1}{2}m\phi)^{1/2}$$

Here $E_R(x,y)$ and $E_I(x,y)$ are the real and imaginary parts of $\operatorname{erf}(x+iy)$ and may be expressed in series form [18], and $\operatorname{Re}(z)$ and $\operatorname{Im}(z)$ are the real and imaginary parts of z, respectively.

Optimization of Finned Ducts in Laminar Flow

M. Kovarik
Principal Research Scientist,
Division of Energy Technology,
Commonwealth Scientific and
Industrial Research Organization,
Highett, Victoria,
Australia 3190

A simple necessary condition of optimality for a finned heat exchanger duct in laminar flow is derived. The criterion of optimality is maximum heat transfer from the fin per unit cost of the finned duct. The heat transfer is determined by the conjugate convection-conduction process rather than by the assumption of a given heat transfer coefficient on the fin surface. Both forced and natural convection are considered. Expressions comparing the performance of optimal assemblies of different materials are given. Approximate dimensions of optimal fins are derived. The relations between the present and earlier results are discussed.

Introduction

The development of heat exchanger with optimal performance started with Schmidt's [1] concept of the optimal fin. The theory has been developed since to determine the optimal profiles with extended heat transfer area for either convective or radiative heat transfer [2, 3].

The criterion of optimality was initially minimum mass of the extended heat transfer structure (fin, spike or other). Lately, the consideration has been expanded to include flow characteristics or general thermodynamic performance indicators, such as losses due to friction or the rate of entropy production [4]. A summary of the state-of-the-art is presented by Shah [5].

Optimal distribution of heat conducting material in radiant energy collecting finned pipes has been studied by the present author [6], the consideration including the cost of both the pipes and the fins. Linear heat transfer with a heat transfer coefficient uniform over the fin was assumed.

The assumption of uniformity of the heat transfer coefficient has been experimentally tested by Ghai and Jakob [7], and Stachiewicz [8]; the results indicate wide departures from uniformity in arrays of parallel fins.

Recent numerical analysis, reported by Sparrow et al. [9], Sparrow and Acharya [10], and Sparrow and Chyu [11], confirm that the heat transfer coefficient is not distributed uniformly on the surface of a fin in shrouded fin arrays and in single fins cooled by natural or forced convection with the fluid flow parallel and opposite to the heat flow.

The present author [12] reported a simple result of the optimal design theory for finned duct assemblies that is valid for thin straight fins regardless of nonuniformity of the heat transfer coefficient. The finding is subject to the assumption that the distribution of the heat transfer coefficient along the height of the fin is independent of the scale of the assemblies. This assumption, while less restrictive than that of uniform heat transfer, may not be sufficiently approximate for certain situations of technical importance. In particular, natural convection heat transfer and heat transfer in developing boundary layer flow is known to be strongly scale-dependent.

Even quite simple cases of heat transfer in natural- or forced-convection boundary layer flow are not amenable to analytical solution; however, the governing equations stated in recent works [10, 11] do enable an analytical approach to the problem of optimal design. It will be shown that, by analysis of the governing equations of some heat transfer problems, a necessary condition of optimality may be obtained even if the process of numerical solution is not carried out. By consequence, optimal design may be approached in those problems on the basis of the small amount of relatively accessible information. Due to a partial similarity of the governing equations, it will be possible to consider two problems of optimal design side by side. These are:

(*a*) Vertical fin of uniform thickness in natural convection boundary layer flow

(*b*) Fin of uniform thickness in forced convection laminar boundary layer flow

In both instances, the heat within the fin and the fluid outside are flowing in opposite directions. The problem formulation is adopted from [10] for the natural convection case and from [11] for the forced convection case. The same method of analysis will be applied to both problems, and following the partial similarity of the governing equations, the results obtained will differ only in some numerical factors. Both results will be compared with earlier findings [12] applicable to a fully developed flow along longitudinal fins.

The Thermal Problem

Consider the field of velocity and temperature in the half-space $Y>0$ filled partly by one-half of a thin plate fin, the remainder by a Newtonian fluid, Fig. 1. The fin is connected at one end ($X = 1$) to a source of heat. Following Sparrow and Acharya [10], the hydrodynamic effects associated with the fin root geometry have been neglected; this restricts the validity of the following results to fins whose height L is large compared to the boundary layer thickness at the root.

The fluid in the free stream is moved at a given uniform velocity in the x-direction, or, alternatively, with the fin vertical, the whole fluid is subject to buoyancy forces in a natural convection mode. The flow is laminar and steady.

The temperature and its gradient are continuous in the field and satisfy energy conservation. In the fin, the temperature field is approximated by the one-dimensional heat flow equation, with the outflux proportional to the normal temperature gradient in the adjacent field. Thus, in the fin, using the dimensionless coordinates defined in the Nomenclature,

$$d^2\theta/dX^2 = -N_{cc}\,(\partial\theta/\partial Y)_s \tag{1}$$

where the subscript s denotes the fin surface.

In the fluid, energy conservation is represented by

$$U(\partial\theta/\partial X) + V(\partial\theta/\partial Y) = \mathrm{Pr}^{-1}(\partial^2\theta/\partial Y^2) \tag{2}$$

whereas mass and momentum conservation in the fluid leads to

$$\partial U/\partial X + \partial V/\partial Y = 0 \tag{3}$$

$$U(\partial U/\partial X) + V(\partial U/\partial Y) = \partial^2 U/\partial Y^2 \tag{4}$$

Equations (1-3) hold for both natural and forced convection, equation (4) must be modified for natural convection by the inclusion of the buoyancy force given, in the adopted variables, by the dimensionless temperature θ

Contributed by the Heat Transfer Division for publication in the JOURNAL OF HEAT TRANSFER. Manuscript received by the Heat Transfer Division March 1, 1983.

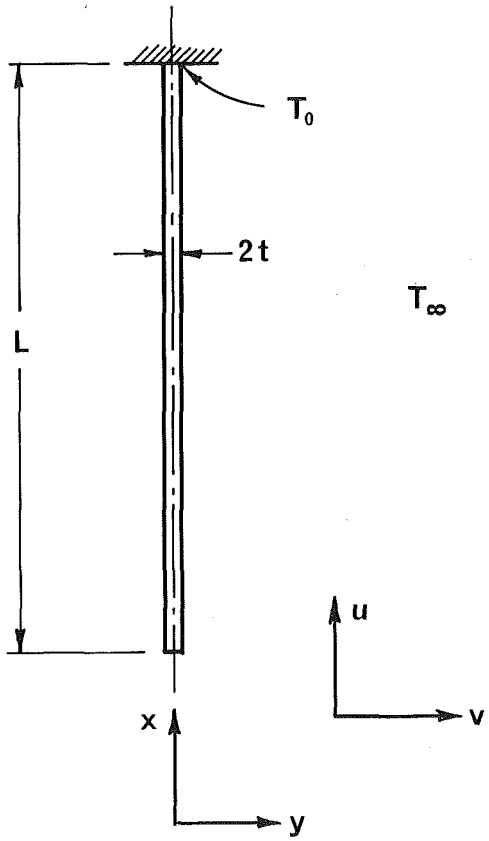

Fig. 1 Plate fin

$$U(\partial U/\partial X)+V(\partial U/\partial Y)=\theta+\partial^2 U/\partial Y^2 \tag{5}$$

The boundary conditions for temperature are, at the fin root ($X = 1$, $Y = 0$) $\theta = 1$, and at the fin tip ($X = 0$, $Y = 0$) $\partial\theta/\partial X = 0$; in the fluid, in addition to the continuity mentioned before, $\theta \to 0$ as $Y \to \infty$.

The velocity components U, V are both equal to zero on the fin surface; in the undisturbed fluid, $U = 1$ in the forced convection case, whereas $U = 0$ in natural convection.

Equations (1–3) and either (4) or (5) with the appropriate boundary conditions determine the dependent variables θ, U, V in terms of the independent variables X, Y and the two parameters of the problem, N_{cc} and Pr.

The total rate of heat transfer from both sides of the fin per unit length of the fin base is given by

$$Q=-2k\int_0^L (\partial T/\partial y)_s dx \tag{6}$$

By substitution of dimensionless variables,

$$Q=2k(T_0-T_\infty)Mz \tag{7}$$

where

$$z=-\int_0^1 (\partial\theta/\partial Y)_s dX. \tag{8}$$

The integral in equation (8) is a function of N_{cc} and Pr only.

While the functional relation between z and its two determining dimensionless parameters remains unknown in general, some properties of optimal finned ducts can nevertheless be obtained, as shown in the following.

Economic Problem

As in [12], the performance index will be defined by the heat transferred by the fin per unit cost of the finned duct assembly

$$J=Q/C \tag{9}$$

A necessary condition for the maximum of J is the simultaneous vanishing of its partial derivatives with respect to the free variables. If these are the fin height L and half-thickness t, then the differentiation of equation (9) leads to

$$\frac{W}{Q}\frac{\partial Q}{\partial W}=\frac{W}{C}\frac{\partial C}{\partial W} \tag{10}$$

where W stands for L or t.

The simultaneous equations expressed by equation (10) can be formed in terms of the parameters M and N_{cc} of Q as

Nomenclature

A = fin cross-sectional area, $2Lt$, m^2
C = cost of assembly per unit length of duct, dollars/m
c_0 = cost per unit length of duct, dollars/m
c_1 = cost per unit volume of fin, dollars/m^3
Gr = Grashof number, $g\beta(T_0 - T_\infty)L^3/\nu^2$, dimensionless
g = acceleration of gravity, m/s^2
h = average heat transfer coefficient, W/m^2 K
J = performance index
k = fluid thermal conductivity, W/mK
k_f = fin thermal conductivity, W/mK
L = fin height, m
M = dimensionless flow parameter, $\mathrm{Re}^{1/2}$ in forced convection, $\mathrm{Gr}^{1/4}$ in natural convection
N_{cc} = conduction-convection parameter, $(kL/k_f t)M$, dimensionless
Pr = Prandtl number, dimensionless
p = heat transfer parameter defined in equations (31) and (41), dimensionless
Q = total rate of heat transfer per unit length of fin base, W/m
Re = Reynolds number, $u_\infty L/\nu$, dimensionless
T = temperature, K
T_0 = fin base temperature, K
T_∞ = temperature of undisturbed fluid, K
t = fin half-thickness, m
U = dimensionless velocity component, u/u_∞ in forced convection, $u/[g\beta(T_0 - T_\infty)L]^{1/2}$ in natural convection
V = dimensionless velocity component, $vL/\nu\mathrm{Re}^{1/2}$ in forced convection, $v/[g\beta(T_0 - T_\infty)\nu^2/L]^{1/4}$ in natural convection
u,v = velocity components, m/s
X = dimensionless coordinate, x/L
Y = dimensionless coordinate, $(y/L)M$
x,y = Cartesian coordinates, m
z = heat transfer parameter defined by equation (8), dimensionless
Z = heat transfer parameter defined by equation (15), dimensionless
β = thermal expansion coefficient, volumetric, °C^{-1}
θ = dimensionless temperature, $(T - T_\infty)/(T_0 - T_\infty)$
ν = kinematic viscosity, m^2/s

$$\begin{bmatrix} \frac{L}{M}\frac{\partial M}{\partial L} & \frac{L}{N_{cc}}\left(\frac{\partial N_{cc}}{\partial L}\right)_t \\ \frac{t}{M}\frac{\partial M}{\partial t} & \frac{t}{N_{cc}}\left(\frac{\partial N_{cc}}{\partial t}\right)_L \end{bmatrix} \times \begin{bmatrix} 1 \\ \frac{N_{cc}}{z}\frac{\partial z}{\partial N_{cc}} \end{bmatrix} = \begin{bmatrix} \frac{L}{C}\frac{\partial C}{\partial L} \\ \frac{t}{C}\frac{\partial C}{\partial t} \end{bmatrix} \tag{11}$$

The elements of the 2 by 2 matrix are all known simple functions of L and t; values of elements of the right-hand side 2 × 1 matrix can be obtained from the definition of the cost C. Thus, if the function $z(N_{cc}, \text{Pr})$ is known, optimal dimensions L and t are obtained by solving the algebraic equation (11). However, z is not known in general; its elimination from equation (11) results in a relation between L and t which is a necessary condition of optimality. Such relations will be obtained for the cases of natural and forced convection in laminar boundary layer flow for a simple cost model.

Simple Cost Model

The cost of the finned duct will depend on its size. The cross-sectional area of the fin will be adopted as an index of its size and the cost of the finned duct is then expressed by

$$C = c_0 + c_1 A \tag{12}$$

If the cost is proportional to mass, this equation is exact; if the cost is a smooth function of mass, equation (12) is valid at least as a first-order approximation in the neighborhood of the optimal point.

In the plate fin case treated here

$$A = 2Lt \tag{13}$$

and both elements of the right-hand side of (11) are $c_1 A/C$.

In the case of natural convection, differentiation of the expressions for M and N_{cc}, as defined in the Nomenclature gives, by substitution into (11)

$$\begin{bmatrix} 3/4 & 7/4 \\ 0 & -1 \end{bmatrix} \begin{bmatrix} 1 \\ Z \end{bmatrix} = \begin{bmatrix} c_1 A/C \\ c_1 A/C \end{bmatrix} \tag{14}$$

where

$$Z = \frac{N_{cc}}{z}\frac{\partial z}{\partial N_{cc}} \tag{15}$$

Elimination of Z leads to

$$c_1 A = 3/8 c_0 \tag{16}$$

as a necessary condition of optimality.

If the constants c_0, c_1 are interpreted as the cost per unit length of duct and per unit volume of fin, respectively, condition (16) can be expressed as: the cost of optimal fin equals three eighths of the cost of the attached duct.

In the case of forced convection, the 2 × 2 matrix in equation (11) is, by reference to the Nomenclature

$$\begin{bmatrix} 1/2 & 3/2 \\ 0 & -1 \end{bmatrix} \tag{17}$$

and the same process leads to

$$c_1 A = 1/4 c_0 \tag{18}$$

with analogous interpretation.

From equations (14, 16), it is evident that Z is a constant for all optimal fins in natural convection; substitution of the matrix (17) into equation (14) proves the same in the case of forced convection. Thus we have

$$Z = -\gamma \tag{19}$$

where $\gamma = 1/5$ in forced convection and $\gamma = 3/11$ in natural convection.

Equation (15) defines Z as dependent on z and N_{cc}; z in turn is defined by equation (8) as a functional of θ. The dimensionless temperature θ is determined by the appropriate subset of equations (1–5) and their boundary conditions. The only parameters in this relationship are N_{cc}, Pr and the constant γ of equation (19). For a constant Pr, equation (19) is equivalent to the ordinary differential equation

$$\frac{N_{cc}}{z}\frac{dz}{dN_{cc}} = -\gamma \tag{20}$$

and, consequently, in the plane (z, N_{cc}) the optimal point lies on the line given by integration of equation (20) as

$$z = D N_{cc}^{-\gamma} \tag{21}$$

where D is the constant of integration, depending on boundary conditions. Since these are identical for all instances of each type of flow (forced or natural), D may have at most two values, one for each type. As noted in connection with equation (8), z is a function of N_{cc} and Pr alone, the dependence of X being eliminated by integration. Thus it follows from equation (21) that for any given Pr, N_{cc} is a constant of optimal design, having a fixed value for each type of flow (forced or natural).

Comparison of Materials

On the basis of results obtained so far, it is possible to make comparisons of dimensions and performance of optimal finned ducts of various materials. Consider two alternative finned ducts, the subscripts A, B denoting parameters of the two materials. As shown in the foregoing discussion, their N_{cc} parameters are equal, provided the Pr of their surrounding fluid is the same.

From the definition of N_{cc}, after substitution for t from the cost equations (16) or (18) and (13) it follows that for optimal fins

$$L^2{}_A M_A / L^2{}_B M_B = c_{1B} c_{0A} k_{fA} / c_{1A} c_{0B} k_{fB} \tag{22}$$

which gives the ratio of their lengths after substitution for M

$$L_A / L_B = (c_{1B} c_{0A} k_{fA} / c_{1A} c_{0B} k_{fB})^{\delta_1} \tag{23}$$

where $\delta_1 = 2/5$ in forced convection and $\delta_1 = 4/11$ in the natural convection case.

Given the same temperature difference $(T_0 - T_\infty)$ and observing that for equal Pr and N_{cc}, the function z has the same value for the different materials, the ratio of total heat transferred is, from (7)

$$Q_A / Q_B = (c_{1B} c_{0A} k_{fA} / c_{1A} c_{0B} k_{fB})^{\delta_2} \tag{24}$$

where $\delta_2 = 1/5$ in forced convection and $\delta_2 = 3/11$ in natural convection.

At optimality, the total cost of finned ducts is proportional to the c_0 cost factor, as evident from equations (16) and (18); therefore, the heat fluxes per unit cost of two optimal systems using materials A and B are related by

$$J_A / J_B = (c_{1B} k_{fA} / c_{1A} k_{fB})^{\delta 2} (c_{0B} / c_{0r})^{(1-\delta_2)} \tag{25}$$

Performance of fins of different materials attached to the same duct ($c_{0A} = c_{0B}$) is compared by

$$J_A / J_B = (c_{1B} k_{fA} / c_{1A} k_{fB})^{\delta_2} \tag{26}$$

If the cost factors c_0 and c_1 of equation (12) are interpreted as weight per unit length of duct and weight per unit volume of fin material, respectively, then results obtained so far

pertain to a finned duct of minimum weight. Thus, for instance, an aluminium fin of minimum weight for a given steel tube, by equation (16) or (18), weighs the same as optimal copper fin and following equation (23) is longer by

$$L_A/L_B = (c_{1B}k_{fA}/c_{1A}k_{fB})^{\delta_1} \tag{27}$$

or 26.6 percent in forced convection, if the densities are 2675 and 8795 kg/m^3 and conductivities 211 and 385 W/mK for Al and Cu, respectively. Their performance index ratio is 1.125, or 12.5 percent higher for Al. In natural convection, the advantage of Al in heat flux is 28.7 percent at optimal design.

Two finned ducts optimized for minimum mass (c_1 = density) and using one material for both fin and duct (c_0 proportional to c_1) compare as

$$J_A/J_B = (c_{1B}/c_{1A})\,(k_{fA}/k_{fB})^{\delta_2} \tag{28}$$

The results of this section are exact in the sense that in their derivation, no assumption was used in addition to those made in the formulation of equations (1–5).

All results so far follow from the conclusion that N_{cc} is constant for all optimal fins. In subsequent sections, the value of the optimal N_{cc} will be found by analysis of published numerical solutions. This will lead to full determination of dimensions of optimal fins.

Approximate Solution for Forced Convection Flow

Among the results reported in [11] is the finding that a "near perfect agreement" exists between the overall rate of fin heat transfer in the solution of equations (1–4) and that obtained from a simple model. The simple model is characterized by a uniform heat transfer coefficient given at Pr = 0.7 by

$$\bar{h} = 0.5854k\mathrm{Re}^{1/2}/L \tag{29}$$

The agreement exists in spite of the highly nonuniform local heat transfer arising from equations (1–4).

Using this coincidence, equation (11) can be solved for both t and L, proceeding as follows:

Conventional plate fin theory as interpreted in [11] for the present case leads to fin efficiency $\eta = (1.307/N_{cc}^{1/2})\tanh(0.5854\,N_{cc})^{1/2}$; this is equivalent in the present Nomenclature to

$$z = 0.5854p^{-1}\tanh p \tag{30}$$

where

$$p = (0.5854N_{cc})^{\frac{1}{2}} \tag{31}$$

Equation (19) in its forced convection form implies that

$$\frac{N_{cc}}{z}\frac{\partial z}{\partial N_{cc}} = -1/5 \tag{32}$$

but from equation (30)

$$\partial z/z\partial p = -p^{-1} + 2/\sinh 2p \tag{33}$$

consequently, in view of equation (31)

$$\frac{N_{cc}}{z}\frac{\partial z}{\partial N_{cc}} = -\frac{1}{2}(1 - 2p/\sinh 2p) \tag{34}$$

Equating the right-hand side of the above to $-1/5$, as in equation (32), leads to the equation for optimal p

$$2p/\sinh 2p = 3/5 \tag{35}$$

with the root $p = 0.919296$.

The corresponding optimal N_{cc}, from equation (31), is

$$N_{cc} = 1.44 \tag{36}$$

This defines the relation between L and t at optimum, by reference to the definition of N_{cc} in the Nomenclature. A further condition for L and t arises from equation (13) in combination with the optimality equation (18).

Combining the two equations with equation (36) gives

$$L = 0.504[c_0k_f\nu^{1/2}/c_1ku_\infty^{1/2}]^{2/5} \tag{37}$$

The corresponding optimal heat transfer rate Q and performance index J are easily obtained from equations (30), (7), and (9).

The half-thickness t follows from equation (18), with $A = 2Lt$. The proportions of optimal fins in forced convection arise from the value of optimal $N_{cc} = 1.44$ and equation (18); the result is

$$t/L = 0.492(c_0/c_1)^{1/5}(k/k_f)^{4/5}(u_\infty/\nu)^{2/5} \tag{38}$$

All conclusions in this section depend on the value of Pr, assumed to be 0.7. Thus they apply to most gases, in particular to air, H_2, He, but not, for instance, to ammonia, steam, and liquids where the Prandtl number is substantially different from 0.7.

Approximate Solution for Natural Convection

Numerical results reported in [10] indicate that "good agreement does prevail" between the values of total heat transfer rate obtained by evaluating equations (1), (2), (3), and (5) and the corresponding values obtained by analytical solution of a simpler problem characterized by uniform heat transfer coefficient on the fin surface. The value of the heat transfer coefficient giving the good agreement is $h = (0.4709\,k/L)\mathrm{Gr}^{1/4}$ for Pr = 0.7. The corresponding total heat transfer rate satisfies, according to [10]

$$Q/k(T_0 - T_\infty)\mathrm{Gr}^{1/4} = (1.372/N_{cc}^{1/2})\tanh p \tag{39}$$

which corresponds to

$$z = 0.4707p^{-1}\tanh p \tag{40}$$

where

$$p = (0.4709\,N_{cc})^{1/2} \tag{41}$$

A procedure analogous to the one followed in the preceding section gives, as a condition for optimal value of p

$$2p/\sinh 2p = 5/11 \tag{42}$$

with the root

$$p = 1.1709 \tag{43}$$

and consequently the optimal value of

$$N_{cc} = 2.91. \tag{44}$$

Substituting for N_{cc} from the Nomenclature and using equations (16) and (13) yields the optimal height as

$$L = 0.802(c_0k_f/c_1k)^{4/11}[g\beta(T_0 - T_\infty)\nu^{-2}]^{-1/11} \tag{45}$$

The optimal value of z corresponding to the p of equation (43) is, in view of equation (40)

$$z = 0.332 \tag{46}$$

The total heat transfer rate is then, by equation (7)

$$Q = 0.562[k^8g^2\beta^2\nu^{-4}(T_0 - T_\infty)^{13}(c_0k_f/c_1k)^3]^{1/11} \tag{47}$$

and the heat transfer rate per unit cost of the fin and duct assembly

$$J = 0.409[(k/c_0)^8g^2\beta^2\nu^{-4}(T_0 - T_\infty)^{13}(k_f/c_1)^3]^{1/11} \tag{48}$$

As in the preceding section, all results are approximate and restricted in application to fluids of Pr = 0.7.

Discussion

The analysis performed here has yielded two kinds of results: the approximate values of optimal fin dimensions and properties in the two sections immediately preceding, and the optimality conditions and relations in the remainder of the paper; these are exact subject to the validity of the assumptions used in constructing equations (1–5).

As in the earlier work, the hydrodynamic effects related to the presence of the base surface are not accounted for. As the authors of [10, 11] state, this should not materially affect the heat transfer results, provided that the fin height L is large compared with the boundary layer thickness at $x = L$.

The condition of zero heat flux from the fin tip is difficult to depart from. If the heat flux through the tip of the fin were to be considered in detail, the integration path in equation (8) would have to extend "around the corner" going through the points (0,0) $(0,t)$, $(1,t)$; as a result, the integral would be a function of t as well as N_{cc} and Pr; this would greatly complicate the optimization procedure without a corresponding improvement in accuracy, as the one-dimensional model basis of equation (1) does not permit any detailed description of the heat flux near the tip. The acceptability of the model chosen depends on its accuracy in the description of overall heat flux; it would be clearly inadequate if the events at the fin tip were to be an important consideration.

The simple relations between the size and the cost factors of an optimal finned duct in equations (16) and (18) are the main results of this work. The rational factors 1/4 and 3/8 are not the consequence of any approximations, but follow directly from the exact values of the logarithmic derivatives of the (2 × 2) matrix in equation (11); these are in turn the consequence of the simple rational powers of the principal dimensions (L, t) as they enter into the definitions of the characteristic dimensionless numbers of the problem (Re, Gr, N_{cc}).

The approximate results agree with the exact ones where these two can be compared. So, for instance, the exact ratios of the optimal values of L, Q, and J for fins of different materials, defined by equations (23-27) are equal to the corresponding ones which can be formed from the approximate results in equations (37), (45), (47), and (48). Thus the approximate results differ from the (unknown) corresponding ones by a multiplicative factor which is independent of material constants.

All results for forced convection heat transfer are independent of temperature, except that the total heat transfer rate is proportional to the difference of temperatures. In natural convection, by contrast, the total heat transfer rate of the optimal fin has a sensitivity of 13/11 to the temperature difference $(T_0 - T_\infty)$. That means that if the temperature difference is changed by 1 percent, other things being equal, the optimal fin designed for the changed conditions will transfer 13/11 percent more heat by equation (47); this increase could be expected. It may be surprising, however, that the height of the optimal fin modified for the increased temperature difference will be 1/11 percent *less* than that of the reference case, as seen from equation (45).

In both natural and forced convection, the optimal fin height is sensitive to the parameter group $(c_0 k_f / c_1 k)$. This sensitivity is slightly higher in the forced convection case (being 0.4), than in the natural convection, where it is 4/11.

The parameter N_{cc} is constant for a given type of optimal fin; therefore the tip dimensionless temperature (θ_0) is also constant. References [10] and [11] give graphs of the distribution of temperature along plate fins, with N_{cc} as a parameter. The tip temperature of an optimal fin may be estimated by interpolation between N_{cc} values given in these references. For the approximately optimal values of N_{cc} reported here as 1.44 and 2.91 in equations (36) and (44), the corresponding tip temperatures are 0.62 and 0.54 for the forced and natural convection, respectively, in dimensionless units. The interpolation leading to these values cannot be considered reliable in the forced convection case, due to sparse data in the neighborhood of the optimal N_{cc}. Recalculation of the results of [11] in the vicinity of $N_{cc} = 1.44$ may be warranted. With a reliable value of the tip temperature, a check on optimality of existing finned ducts is possible, as the tip temperature represents a necessary condition.

Conclusion

The analysis presented here enables the designer to obtain approximate optimal solutions for two simple cases of finned ducts. These solutions are significantly different from the results of earlier analysis, even where the total heat flux prediction is in agreement. The search for the exact optimal solution remains in the domain of iterative numerical techniques. The necessary conditions stated here reduce the search from two variables to one.

Acknowledgment

The author is indebted to his colleagues, in particular P. J. Banks and P. F. Lesse, for helpful discussions during the progress of this work.

References

1 Schmidt, E., "Die Waermeuebertragung durch Rippen," *Zeitschrift des Vereines Deutscher Ingenieure*, Vol. 70, 1926, pp. 885–889.

2 Wilkins, J. E., Jr., "Minimum-Mass Thin Fins and Constant Temperature Gradients," *Journal of Society for Industrial and Applied Mathematics*, Vol. 10, No. 1, 1962, pp. 62–73.

3 Wilkins, J. E. Jr., "Minimum Mass Thin Fins for Space Radiators," *Proc. of the 1960 Heat Transfer and Fluid Mechanics Institute*, Stanford University, 1960, pp. 229–243.

4 Bejan, A., "General Criterion for Rating Heat Exchanger Performance," *International Journal of Heat and Mass Transfer*, Vol. 21, 1978, pp. 655–658.

5 Shah, R. K., "Advanced in Compact Heat Exchanger Technology and Design Theory," *Heat Transfer 1982*, Vol. 1, 1982, pp. 123–142.

6 Kovarik, M., "Optimal Distribution of Heat Conducting Material in the Finned Pipe Solar Energy Collector," *Solar Energy*, Vol. 21, 1978, p. 477–484.

7 Ghai, M. L., and Jakob, M., "Local Coefficients of Heat Transfer on Fins," ASME Paper No. 50-5-18, 1950.

8 Stachiewicz, J. W., "Effect of Variation of Local Film Coefficient on Fin Performance," ASME JOURNAL OF HEAT TRANSFER, Vol. 91, 1969, pp. 21–26.

9 Sparrow, E. M., Baliga, B. R., and Patankar, S. V., "Forced Convection Heat Transfer From a Shrouded Fin Array with and without Tip Clearance," ASME JOURNAL OF HEAT TRANSFER, Vol. 100, 1978, pp. 572–579.

10 Sparrow, E. M., and Acharya, S., "A Natural Convection Fin With a Solution Determined Nonmonotonically Varying Heat Transfer Coefficient," ASME JOURNAL OF HEAT TRANSFER, Vol. 103, 1981, pp. 218–225.

11 Sparrow, E. M., and Chyu, M. K., "Conjugate Forced Convection—Conduction Analysis of Heat Transfer in a Plate Fin," ASME JOURNAL OF HEAT TRANSFER, Vol. 104, 1982, pp. 204–206.

12 Kovarik, M., "Optimal Heat Transfer Assemblies With Thin Straight Fins," ASME JOURNAL OF HEAT TRANSFER, Vol. 105, 1983, pp. 203–205.

Laminar Heat Transfer in a Channel With Two Right-Angled Bends

R. S. Amano
Assistant Professor,
Mechanical Engineering Department,
University of Wisconsin—Milwaukee
Milwaukee, Wis. 53201
Mem. ASME

A numerical study is reported on the flow and heat transfer in the channel with two right-angled bends. The modified hybrid scheme was employed to solve the steady full Navier-Stokes equations with the energy equation. The computations were performed for different step heights created in a long channel. The local heat transfer rate along the channel wall predicted by employing the present numerical model showed good agreement with the experimental data. The behavior of the flow and the heat transfer were investigated for the range of Reynolds number between 200 and 2000 and for step height ratios H/W = *1, 2, and 3. Finally, the correlation of the average Nusselt number in such channels as a function of Reynolds number is postulated.*

Introduction

In the design of a heat exchanger, there are usually two methods of promoting heat transfer rates. The first method is accomplished by inserting obstacles in a duct such as coils, wings, orifices, plates, cylinders, etc., whereas the second method of attaining high heat transfer rates is accomplished by using nonstraight channels or ducts, such as a channel with a corrugated wall or a duct with a backward facing step, which induce complex flow phenomena and subsequently may have a profound influence on the heat transfer results. The former has been studied by many researchers ([1-3], for example) but the latter has not yet been studied extensively. Goldstein and Sparrow [4] reported the local mass transfer rates of the flow in a corrugated wall channel by using the naphthalene sublimation technique. Izumi et al. [5] reported an experimental study on the flow characteristics in a channel with two bends. The channel configuration of Izumi et al. is a simplified flow passage of heat exchanger of a corrugated wall channel. The empirical correlation of Nusselt number obtained by Izumi et al. was suitable for turbulent flow regime; however, the data in laminar flow regime deviate from their empirical correlation.

In this paper, the study of heat transfer is focused on the flow in a corrugated wall channel taking into consideration that the heat exchangers of this type are relatively simple compared to those cases in which obstacles are inserted. As a basic study of this type of heat exchanger, the channel with two right-angled bends is considered. Before the flow of a wide range of Reynolds numbers is studied, it is important to grasp the fundamental flow and heat transfer characteristics in such a channel in a laminar flow regime. A study of turbulent flow in this type of channel can be accomplished without much difficulty if we incorporate a turbulent flow model in the recirculating flow such as that in the work reported by Amano et al. [6] in which the near wall turbulence model was developed for the application to a flow in a pipe with a sudden expansion.

The flow in this channel (in Fig. 1) shows rather complicated behavior accompanying flow separation, flow recirculation, reattachment, impingement, flow deflection, and flow redevelopment downstream from the last bend. In this study, the flow pattern involving these complex phenomena has been investigated numerically for three different step ratios, H/W = 1, 2, and 3 and for Reynolds numbers ranging from 200–2000. Furthermore, the behavior of local heat transfer rates along the channel walls was computed and their characteristics were examined. Finally, the correlation of the average Nusselt numbers in these channels as a function of Reynolds number is postulated.

Contributed by the Heat Transfer Division and presented at the ASME Winter Annual Meeting, Boston, Massachusetts, November 13–18, 1983. Manuscript received by the Heat Transfer Division June 22, 1983. Paper No. 83-WA/HT-10.

Mathematical and Numerical Models

Governing Equations. The equations describing the flow field of the present study are the steady, two-dimensional form of continuity, momentum, and energy equations.

Continuity equation:

$$\frac{\partial(\rho u)}{\partial x}+\frac{\partial(\rho v)}{\partial y}=0 \tag{1}$$

Momentum equations:

$$\frac{\partial}{\partial x}(\rho u^2)+\frac{\partial}{\partial y}(\rho uv)=-\frac{\partial p}{\partial x}+\frac{\partial}{\partial x}\left(\mu\frac{\partial u}{\partial x}\right)+\frac{\partial}{\partial y}\left(\mu\frac{\partial u}{\partial y}\right)+\frac{\partial}{\partial x}\left(\mu\frac{\partial u}{\partial x}\right)+\frac{\partial}{\partial y}\left(\mu\frac{\partial v}{\partial x}\right) \tag{2}$$

$$\frac{\partial}{\partial x}(\rho uv)+\frac{\partial}{\partial y}(\rho v^2)=-\frac{\partial p}{\partial y}+\frac{\partial}{\partial x}\left(\mu\frac{\partial v}{\partial x}\right)+\frac{\partial}{\partial y}\left(\mu\frac{\partial v}{\partial y}\right)+\frac{\partial}{\partial x}\left(\mu\frac{\partial u}{\partial y}\right)+\frac{\partial}{\partial y}\left(\mu\frac{\partial v}{\partial y}\right) \tag{3}$$

Energy equation:

$$\frac{\partial}{\partial x}(\rho c_p uT)+\frac{\partial}{\partial y}(\rho c_p vT)=\frac{\partial}{\partial x}\left(k\frac{\partial T}{\partial x}\right)+\frac{\partial}{\partial y}\left(k\frac{\partial T}{\partial y}\right) \tag{4}$$

These four equations were used to compute flow behavior and heat transfer characteristics in the solution domain shown in

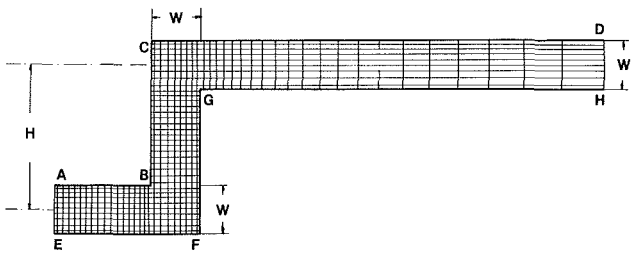

Fig. 1 Typical flow domain and numerical grid (H/W = 3)

Fig. 1. In these equations, the variation of density, viscosity, and thermal conductivity are allowed. However, the flow considered in this research may be assumed to be incompressible. Thus the terms with the coefficient of bulk viscosity were dropped in equations (2) and (3). The viscous dissipation term which has minor influence in the temperature field is also neglected in the energy equation (4). Since the x-, y-coordinates are on the horizontal plane and a two-dimensional assumption is made for simplicity, the buoyant force is also neglected in equations (2) and (3). In the computation, the quantities such as k and μ are evaluated by linear interpolation (the variation of these quantities is important particularly for liquids). In order to compare the results with the experimental data of Izumi et al. [5], air whose Prandtl number is 0.71 is used as a working fluid.

Numerical Solution Procedure. The solution method of equations (1–4) is based on the modified hybrid scheme of Amano et al. [6] in which the combined mode of convection and diffusion is derived by expanding the analytical one-dimensional solution of Spalding [7] up to the fourth-order term. The finite-volume form was derived by integrating the governing equations over the numerical cell. For instance the discretization equation for equation (2) can be put in the following form.

$$a_{ij}u_{ij} = a_{i+1,j}u_{i+1,j} + a_{i-1,j}u_{i-1,j} + a_{i,j+1}u_{i,j+1} + a_{i,j-1}u_{i,j-1} + b \tag{5}$$

where

$$a_{i+1,j} = \frac{\mu}{\delta x} f(R_{i+1,j}) + \max\{-(\rho u)_{i+1,j}, 0\}$$

etc.

and

$$b = S\phi\delta(\mathrm{Vol})$$

$$f(R_{ij}) = \max\left\{0, 1 - \frac{1}{2}|R_{ij}| + \frac{1}{12}|R_{ij}|^2 - \frac{1}{720}|R_{ij}|^4\right\}$$

In the foregoing expression, $S\phi$ is the source term other than the convection and the diffusion in equation (2), and R_{ij} is the cell Reynolds number. Equation (5), which has an elliptic form, is computed by using a line-by-line iterative method. This scheme is comparatively inexpensive to compute and gives improved accuracy, particularly in the range where the cell Reynolds number is between 1 and 4, and in addition switches to the upwind differencing for a cell Peclet number larger than 4. The cell structure of this method has a so-called staggered grid system in which the value of each scalar quantity (pressure and temperature) is associated with every grid node, although the vector quantities (velocity components) are displaced in space relative to the scalar quantities.

The pressure is computed by adopting the SIMPLE Algorithm of Patankar and Spalding [8]. It solves sets of difference equations for fixed pressure fields of both u and v momentum equations by line iteration. After each such sweep over the solution domain, adjustments are made to the pressure field to satisfy the continuity equation along each line of cells. This procedure is repeated until the momentum and continuity equations are simultaneously satisfied to a certain degree of accuracy.

Boundary Conditions. Typically, there are three different types of boundary conditions to be specified for the computation of a flow in the channel shown in Fig. 1: inlet, outlet, and wall boundary conditions.

At the inlet AE (in Fig. 1), all the quantities are specified according to the fully developed condition. Since the inlet locates 2 channel widths upstream of the first bend B, the conditions of inlet flow have minor influences on the rest of the flow field. A test computation with the inlet location of 5 channel widths showed less than a 2 percent change in the Nusselt number when compared with the present geometry.

At the outlet DH, continuous flow conditions are applied where gradients of u, v, p, and T in the flow direction are zero (Neumann conditions), i.e., $\partial\phi/\partial x = 0$, where $\phi = u, v, p$, or T. The position of the outlet is located approximately 20–30 widths from the last bend G; thus the outlet condition will not have much influence on the major portion of the flow.

At the wall boundaries ABCD and EFGH, the velocities and temperature must be specified functionally according to Newton's law of shear stress (Drag Law) and Fourier's law, respectively. For example, the tangential velocity can be expressed in terms of wall shear stress as a functional expression of the boundary condition (Robbin's condition) coupled with the no-slip condition as

$$F = \tau\delta A = \mu u \delta A/\delta y \tag{6}$$

where δA = wall area of the cell.

The expression of (6) is incorporated through the source term $S\phi$ of equation (5) while the coefficient a, representing the wall side is set equal to zero, thus suppressing the diffusive and convective actions towards the wall. The velocity component normal to the wall is set equal to zero. For the computation of the heat transfer coefficient, a condition of a constant heat flux is used at the wall boundary. Then the local Nusselt number is obtained as

$$\mathrm{Nu} = \frac{(\dot{q}_w/k)2W}{|T_w - T_b|} \tag{7}$$

and the bulk temperature T_b is obtained as

Nomenclature

a = coefficient (used in equation (5))
A = area
c_p = specific heat for constant pressure
$\bar{f}$ = average friction factor $(\tau_w/(1/2\rho U^2))$
h = local heat transfer coefficient
H = step height
k = thermal conductivity
Nu = Nusselt number based on $2W$
$\overline{\mathrm{Nu}}$ = average Nusselt number based on $2W$
Nu_{max} = maximum Nusselt number
p = pressure
$\dot{q}_w$ = wall heat flux
R = cell Reynolds number
Re = Reynolds number based on $2W$
s = coordinate along a wall
$S\phi$ = source term
T = temperature
T_b = bulk temperature
T_w = wall temperature
u = velocity component in x-direction
U = average velocity
v = velocity component in y-direction
W = channel width
x = coordinate
y = coordinate

δA = area of numerical cell
$\delta x, \delta y$ = sizes of numerical cell
ρ = density
μ = dynamic viscosity
τ_w = wall shear stress

Subscript

i = node point in x-direction
j = node point in y-direction

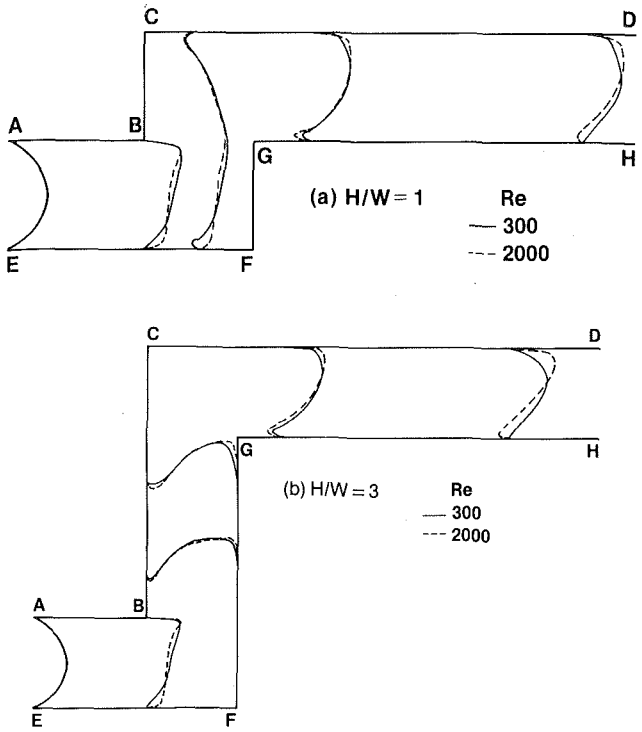

Fig. 2 Streamwise velocity profiles in the channel (*a*) $H/W = 1$, (*b*) $H/W = 3$

$$T_b = \int T|u|dy / \int |u|dy \tag{8}$$

where the integrals are to be carried over the cross-sectional area of the channel. The absolute value of the velocity is taken so that the regions with reverse flow are also properly represented.

The average Nusselt number is defined as done in [5] as

$$\overline{\mathrm{Nu}} = \frac{2W}{Ak} \int hdA \tag{9}$$

Thus the results can be compared with the experimental data of [5].

Computing Details. The computations were performed for three different step ratios $H/W = 1$, 2, and 3, and for Reynolds numbers ranging from 200–2000. The grid numbers employed for the computation were 54 × 18, 54 × 27, and 54 × 36 for step ratios $H/W = 1$, 2, and 3, respectively. As shown in Fig. 1, grid spacings upstream of the corner G are minimal so as to provide fine grid in the flow separating and recirculating regions, while the x-coordinate grid downstream of the corner G expands at a constant rate toward the outlet where the flow characteristics are mostly parabolic. Exploratory tests on grid systems with 30 percent more cells both in x- and y-directions indicated that the present results do not vary more than 3 percent.

The convergence criterion used in this computation is the condition that the summation of the mass flux and momentum flux residuals in the whole domain be less than 1.5 percent of the total mass and momentum fluxes. This condition was attained faster for lower Reynolds number flows and for smaller step ratios; namely, the computation for Re = 200 and $H/W = 1$ converged after 102 iterations. The average central processor time on a UNIVAC 1100 was about 5 min to converge, which was achieved typically after 210 iterations.

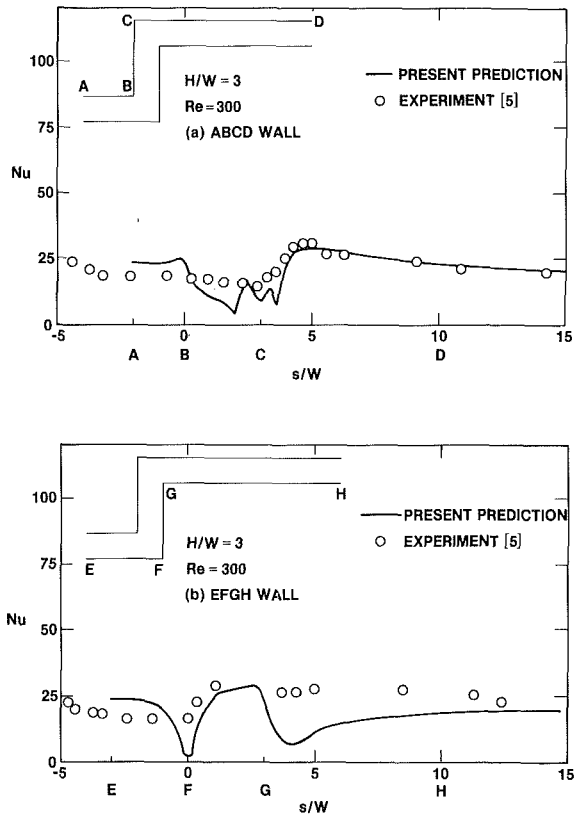

Fig. 3 Local Nusselt number distribution along the channel wall for $H/W = 3$ and Re = 300: (*a*) ABCD wall, (*b*) EFGH wall

Results and Discussion

Flow Field. In Fig. 2, the streamwise velocity profiles are shown in the channels of $H/W = 1$ and 3 for Reynolds numbers of Re = 300 and 2000. For the flow of $H/W = 1$ (Fig. 2(*a*)), the separated flow at the corner B reattaches on the CD wall. Consequently, a recirculating region is formed near the concave corner C. This feature is represented by the negative velocity profile near the corner C. Meanwhile, as is shown in Fig. 2(*b*), the separated flow at the corner B in the channel of $H/W = 3$ reattaches on the wall BC for Re = 300, thus creating two recirculating regions on the BC wall.

The flow also separates at the corner G and reattaches on the wall GH in every H/W case, thus causing a recirculating region beyond the corner G on this wall. This recirculating region on the wall GH increases as Reynolds number becomes larger. This feature is indicated by the velocity profiles at the location 3 channel widths downstream from the corner G; the velocity gradient for Re = 300 is positive but that for Re = 2000 is still negative in every H/W case.

At the cross section of the first bend, B, there is a similar trend in velocity profile for all step ratios; that is, the velocity gradients on the EF wall are steeper for high Reynolds number flows than for low Reynolds number flows. This indicates that the high Reynolds number flow results in stronger deflection on FG wall than the low Reynolds number flow.

It is generally seen that, for all step ratios, the effect of Reynolds number on the wall characteristics may be larger on the BC, EF, and GH walls than on the other walls. Moreover, the effect of Reynolds number on the velocity profile in the redeveloping region (near the section DH) is stronger for larger step ratios.

Local Heat Transfer. Local Nusselt numbers were computed along the channel walls to investigate the local heat

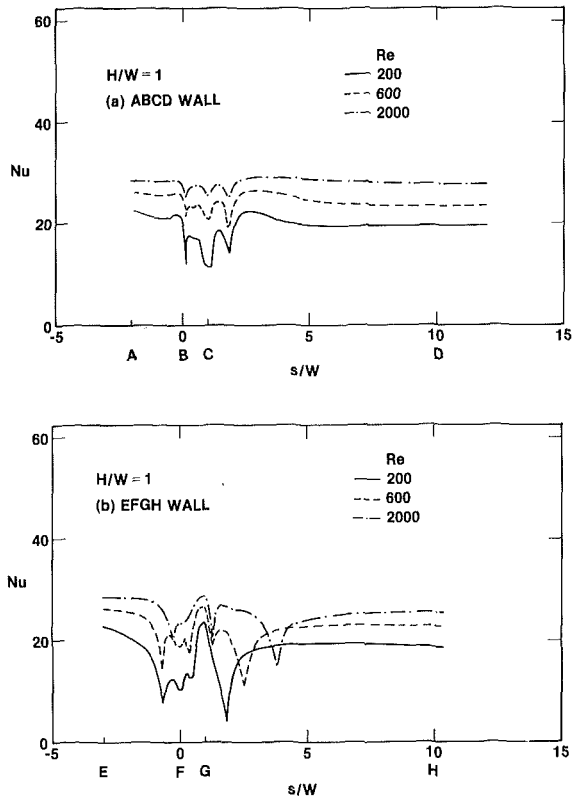

Fig. 4 Local Nusselt number distribution along the channel wall for H/W = 1: (a) ABCD wall, (b) EFGH wall

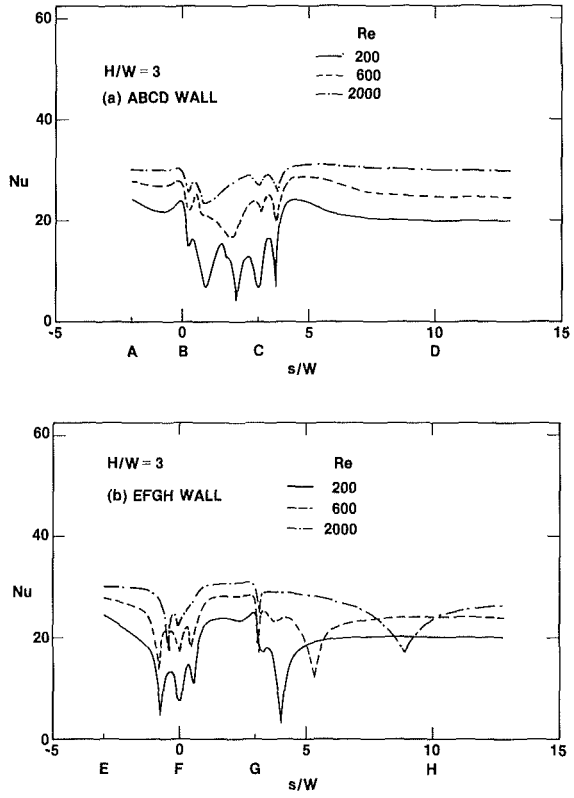

Fig. 5 Local Nusselt number distribution along the channel wall for H/W = 3: (a) ABCD wall, (b) EFGH wall

transfer characteristics affected by the channel bends. In Fig. 3, computed results are compared with the experimental data obtained by Izumi et al. [5] for step ratio $H/W = 3$ and for Re = 300. Along the ABCD wall, the predicted Nusselt number is +20 percent on AB wall, −40 percent on BC wall, and ±2 percent on CD wall, whereas, along the EFGH wall, it is +30 percent on EF wall, −10 percent on FG wall, and −35 percent on GH wall. The agreement is thus relatively good in the inlet and the redeveloping flow regions but a discrepancy is observed near the corners F and G. While the computed results show minimum values at F and at the position one channel width downstream from the corner G, the experimental data do not show this trend clearly. As is shown in Fig. 2, there are recirculating flows at the corner F and at the position slightly downstream from G. The heat transfer rates, therefore, must be minimum in these regions. However, only subtle decreases in heat transfer levels are observed at these positions in the experimental data. These discrepancies may be the result of the departure between the experimental set-up and the numerical model. Albeit the assumption in both cases is two-dimensional, the flow in the experiment is three-dimensional, and this may cause secondary flows near the corners of the channel, which may produce slightly higher heat transfer than that for two-dimensional flow. Another possibility is the experimental error in the measurement of temperature distribution along the channel wall. In the experiment of Izumi et al. [5], Cu-Co thermocouples are mounted to the back of the stainless steel foils to measure temperature. As a result, an inevitable heat conduction in the stainless steel could have smoothed the curves of the Nusselt number throughout the measured domain. The heat conduction effect through the stainless steel is not computed in the present numerical study. A similar discrepancy is observed in Fig. 3(*a*). In this figure, between points B and C, the experimental data show a smooth slope while the computed results show rather abrupt changes in Nusselt number distribution which were attributed to the flow separation, reattachment, and recirculation.

In Figs. 4 and 5, the computed local Nusselt number distributions are drawn for $H/W = 1$ and 3 and for Re = 200, 600, and 2000. As is shown in Fig. 4, the pattern of the local Nusselt number for $H/W = 1$ does not vary much with Reynolds number on the ABCD wall, but it depends strongly on the EFGH wall. This feature accords with the flow pattern shown in Fig. 2; namely, the recirculating region just downstream from the corner G expands toward downstream as Re increases. This is easily seen in Fig. 4(*b*); beyond the corner G, the minimum point moves downstream as Re increases. Generally, a similar trend is observed in Fig. 5, except that the heat transfer variation on the BC wall becomes more distinguishable as Re changes (see Fig. 5(*a*)). This is mainly because, unlike the case of $H/W = 1$, the separated flow at the corner B reattaches on the BC wall for $H/W = 3$. Moreover, the recirculating region on this BC wall expands and eventually merges with the corner recirculating region as Re becomes higher. At the same time the flow deflects and accelerates on the opposite side (FG wall) and that interferes with the recirculating flow on the BC wall. All these effects combine to diminish the minimum points of heat transfer rate on the BC wall for $H/W = 3$ when Re is increased. The heat transfer distribution on the FG wall, however, indicates that a minor change in flow pattern is created as Reynolds number is increased.

Average Heat Transfer. The average Nusselt numbers were computed for three different step ratios and for various Reynolds number flows. The results are compared with the experimental data of Izumi et al. [5] and are represented in Fig. 6. The agreement between the experiment and the computation is fairly reasonable (within 20 percent). Although the agreement is the best at Re = 2000, the experimental data at this Reynolds number deviate from the

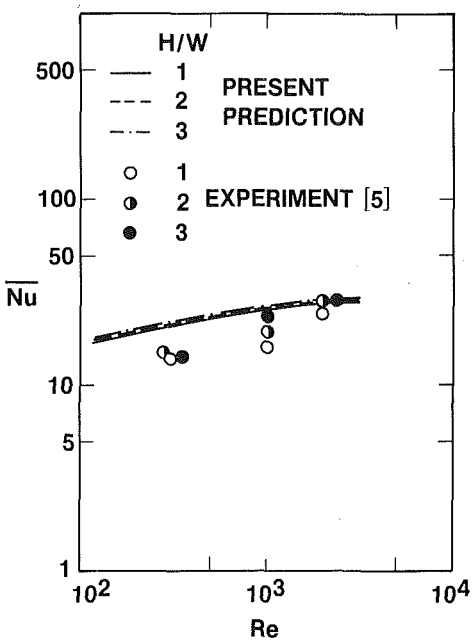

Fig. 6 Average Nusselt number as a function of Reynolds number

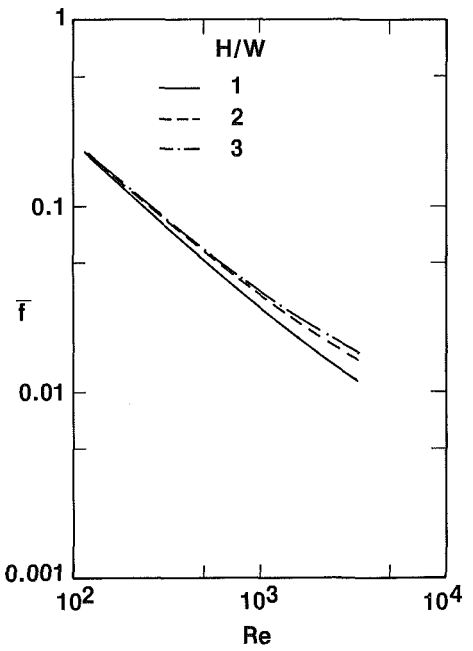

Fig. 7 Average friction factor as a function of Reynolds number

track of the rest of the data points when we compare the slope of the Nusselt numbers. The computed Nusselt number shows a functional dependency on $Re^{0.18}$ in every H/W case, while the experimental data of Nusselt number abruptly increase from the $Re^{0.18}$ relation at Re = 2000. This implies that the flow observed in the experiment is no longer laminar at Re = 2000 but changes over to transition. It is also noticed that the higher the step ratio H/W, the flow regime changes from laminar to turbulent at lower Reynolds numbers. It may be said that a turbulent flow regime may be created at lower Reynolds numbers if the step ratio is made larger. However, this point is beyond the scope of this paper at this stage since a turbulent effect is not considered in the computation. Another feature noticed in Fig. 6 is that the computed Nusselt number is almost independent of the step ratio H/W. This accords

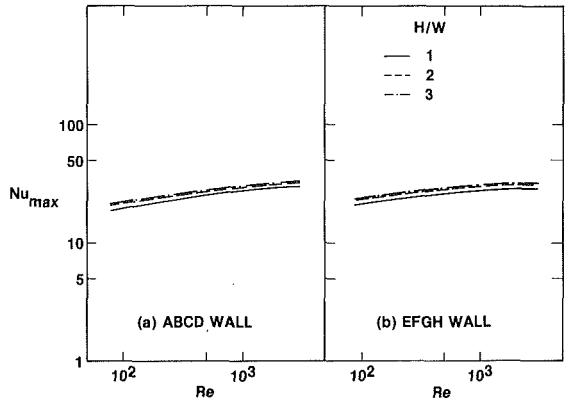

Fig. 8 Maximum local Nusselt number on the channel wall as a function of Reynolds number: (a) ABCD wall, (b) EFGH wall

with the experimental results at Re = 300 and 2000.

From the computed results, the following correlation was obtained.

$$\overline{Nu} = 7.31 Re^{0.18} \tag{10}$$

The computed average friction factors against Re are shown in Fig. 7. The dependency of f on Re changes from $H/W = 1$ to $H/W = 2$, but little change is observed between $H/W = 2$ and $H/W = 3$. This result indicates that a significant change in flow pattern takes place between $H/W = 1$ and $H/W = 2$.

Figure 8 shows the variations of Nu_{max} on both the ABCD and EFGH walls. The maximum value of Nusselt number on the ABCD wall usually occurs at two channel widths downstream from the corner C where the flow is accelerating due to the deflection by the separated flow at the corner G. Meanwhile the maximum point on the EFGH wall occurs at the corner G where the strong convection resulted due to the deflection by the separated flow at the corner B. As was depicted in Fig. 7 for the average friction factor, the levels of Nu_{max} for $H/W = 1$ show lower value than those for $H/W = 2$ and 3, albeit for the same dependency on Re (Fig. 8).

As is pointed out in the foregoing discussion, it was predicted that the effect of the channel step on both Nu_{max} and $\bar{f}$ is greater between $H/W = 1$ and $H/W = 2$. This may be mainly attributed to the flow on the FG wall. For $H/W = 1$, the flow impinging on the FG wall is not accelerating enough when it separates at the corner G; therefore, the strength of the deflection to the opposite wall CD is not higher than for $H/W > 1$, which results in a relatively smaller heat transfer rate at both the corner G and at the maximum deflected point on the CD wall. This result allows us to conclude that the effect of channel step becomes higher between $H/W = 1$ and $H/W = 2$.

Conclusions

A numerical analysis has been performed for the flow in a channel with two right-angled bends. It is found that such a channel creates a complex flow pattern involving separation, impingement, reattachment, recirculating, and flow deflection. The local behaviors of both flow and heat transfer rate were investigated.

The main conclusions to emerge from this study may be summarized as follows:

1 The effect of Reynolds number on the wall characteristics is more distinguishable on the BC, EF, and GH walls than on the other walls for every step ratio.

2 The effect of step ratio is not as remarkable on the average Nusselt number as on the skin friction and the maximum Nusselt number.

3 There is a significant changeover in wall characteristics between $H/W = 1$ and $H/W = 2$.

4 The computed $\overline{\text{Nu}}$-Re correlation is suggested to be

$$\overline{\text{Nu}} = 7.31\text{Re}^{0.18}$$

Finally, it might be suggested that an extensive experimental study of laminar flow in the type of channel studied here is needed before more complicated configurations are studied.

References

1 Bergles, A. E., "Survey and Evaluation of Techniques to Augment Convective Heat and Mass Transfer," *Progress in Heat and Mass Transfer*, Vol. 1, Pergamon Press, 1969, pp. 331–424.

2 Kays, W. M., and London, A. L., "Heat Transfer and Flow Friction Characteristics of Some Compact Heat Exchanger Surfaces—Part 1: Test System and Procedure," ASME *Transactions*, Vol. 72, 1950, pp. 1075–1085.

3 Kays, W. M., and London, A. L., *Compact Heat Exchanger*, 2d ed., McGraw-Hill, New York, 1964.

4 Goldstein, L., and Sparrow, E. M., "Heat/Mass Transfer Characteristics for Flow in a Corrugated Wall Channel," ASME JOURNAL OF HEAT TRANSFER, Vol. 99, 1977, pp. 187–195.

5 Izumi, R., Oyakawa, K., Kaga, S., and Yamashita, H., "Fluid Flow and Heat Transfer in Corrugated Wall Channels," *JSME Journal*, Vol. 47, No. 416, 1981, pp. 657–665.

6 Amano, R. S., Jensen, M. K.,and Goel, P., "A Numerical and Experimental Investigation of Turbulent Heat Transport Downstream from an Abrupt Pipe Expansion," ASME JOURNAL OF HEAT TRANSFER, Vol. 105, 1983, pp. 862–869.

7 Spalding, D. B., "A Novel Finite-Difference Formulation for Differential Expressions Involving both First and Second Derivatives," *International Journal of Numerical Methods in Engineering*, Vol. 4, 1972, pp. 551–559.

8 Patankar, S. V., and Spalding, D. B., "A Calculation for Heat, Mass and Momentum Transfer in Three-Dimensional Parabolic Flows," *International Journal of Heat and Mass Transfer*, Vol. 15, 1972, pp. 1787–1806.

Effects of Wall Conduction on Heat Transfer for Turbulent Flow in a Circular Tube[1]

Y. K. Lin
Graduate Student,
Department of Mechanical Engineering,
University of Houston,
Houston, Texas 77004

L. C. Chow
Assistant Professor,
Department of Mechanical Engineering,
Washington State University,
Pullman, Wash. 99164
Assoc. Mem. ASME

In predicting convective heat transfer for turbulent flow inside a circular tube, the thermal boundary condition at the solid-fluid interface is usually assumed to be known. However, in reality, the thermal boundary condition is normally specified at the outside surface of the tube. The temperature and heat transfer coefficent at the interface are not known a priori. An analytical procedure is used here to obtain the interfacial temperature and the local Nusselt number for turbulent flow with axial and radial wall conduction taken into account. Wall conduction effects are examined by varying four important parameters, namely, the Reynolds number, the Prandtl number, the ratio of thermal conductivity of solid wall to that of fluid, and the nondimensional thickness of the tube wall. Numerical results are obtained to determine their influence on heat transfer.

Introduction

In conventional convective heat transfer problems, it is a common practice to prescribe the temperature, the heat flux, or a combination of the two at the solid-fluid interface. However, in most cases, the boundary conditions at the interface are actually not known a priori, but depend on the coupled conduction-convection mechanism. Therefore, the solution of the energy equations for the solid and fluid media must be obtained simultaneously by considering the temperature and heat flux as continuous functions at the interface. This class of problems is referred to as the conjugated problems.

Siegel and Savino [1] studied the effect of peripheral wall conduction on laminar forced convection in rectangular channels heated on the broad sides. They showed that wall conduction produces substantial decreases in the peak wall temperature and in the temperature gradients along the walls. Davis and Gill [2] analyzed a conjugated problem for parallel plates with one wall at the temperature of the entering fluid and the outside of the other wall at constant heat flux. They found that axial wall heat conduction can significantly affect the fluid temperature field and lower the Nusselt number (Nu_x) relative to that predicted for a uniform heat flux at the solid-fluid interface. Mori et al. [3] analyzed a conjugated problem for parallel plates that was similar to that of Davis and Gill [2]. For the case of specified constant heat flux at the outside wall, again axial heat conduction the wall reduces the Nusselt number. The lowest values of the interface Nu_x correspond to those with constant temperature at the solid--fluid interface as the boundary condition. For the case of specified constant wall temperature at the outside wall, the finite wall resistance increases the interface Nu_x. The highest values of Nu_x correspond to those with constant heat flux at the solid-fluid interface as the boundary condition. They also determined the conditions when the wall conduction is negligible.

Luikov et al. [4] solved the conjugated problem for the circular tube. The solution was presented in closed-form expressions involving complicated functions, integrals, and infinite series. No numerical results were presented. The most comprehensive solution to the conjugated problem of laminar flow in a circular tube was given by Mori et al. [5]. Like their conjugated problems for laminar flow between parallel plates [3], they considered two thermal boundary conditions specified at the outside wall of the circular tube, namely, constant heat flux and constant temperature. They derived essentially the same conclusions as for parallel plates. Faghri and Sparrow [6] considered the simultaneous wall and fluid axial conduction in laminar pipe-flow heat transfer. Depending on a wall conductance parameter and the Peclet number, it was found that axial conduction in the wall can carry a substantial amount of heat upstream into the non-directly heated portion of the tube.

All of the foregoing papers [1-6] dealt with heat transfer in laminar flow only. The conjugated heat transfer problem with turbulent flow is inherently much more complicated. The only significant work in conjugated turbulent flow was done by Sakakibara and Endoh [7]. They dealt with the conjugated heat transfer problem with turbulent flow between parallel plates. The effects of axial wall conduction on the interfacial temperature and the local Nusselt number were determined. They showed that the ratio of thermal conductivity of wall to that of fluid, and the wall thickness to duct length ratio are important parameters to characterize the effects of axial wall conduction. The effects are especially significant for low Prandtl number fluids.

Many practical heat transfer problems, such as in heat exchanger design, are in reality conjugated problems and wall conduction may have significant effects on heat transfer. In this regard, there is a need to assess the effects of wall conduction on heat transfer for turbulent flow in a circular tube. A literature survey shows that the tube geometry has not been considered.

The problem investigated here is the conjugated heat transfer problem with turbulent flow in a circular tube. At the outer surface of the tube, it is assumed that either the heat flux is uniform or the temperature is constant. The influence of the conductivity ratio of solid to fluid and the dimensionless wall thickness on heat transfer for both boundary conditions is predicted.

Definition of System

This analysis is limited to smooth, straight pipes within which the fluid flow is fully developed. In addition, the following assumptions are made:

1 Heat transfer is axiymmetric and steady-state.

[1]This work was done while the authors were at Texas A & M University, College Station, Texas.

Contributed by the Heat Transfer Division for publication in the JOURNAL OF HEAT TRANSFER. Manuscript received by the Heat Transfer Division June 6, 1983. Paper No. 81-HT-30.

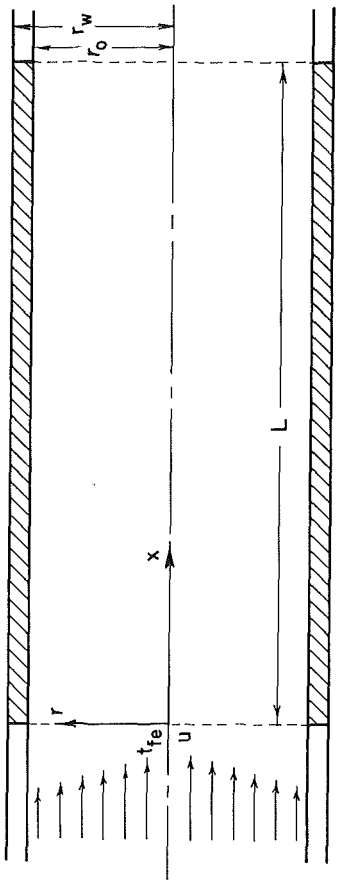

Fig. 1 Schematic model of heat transfer section of circular tube

2 Physical properties are constant.

3 Frictional dissipation is negligible.

4 Axial fluid conduction is negligible with respect to bulk transport.

5 Both the fluid and the tube wall are isothermal for $x \leq 0$, and heat transfer occurs for $x \geq 0$.

It is well known that turbulent flow becomes fully developed at a distance of about 10 dia. Hence the assumption of fully developed flow is adequate. The situation of axisymmetric, steady-state heat transfer does occur in many practical applications. Except for high-speed flows, frictional dissipation is usually negligible. The assumption of constant physical properties, though maybe somewhat unrealistic for low Prantdl number fluids, is necessary to allow the present problem to be solved analytically. For turbulent flow, with the Reynolds number exceeding 10^4, the Peclet number is always greater than 100 even for liquid metal flow. Hence the axial fluid conduction is negligible, and the fluid temperature at the entrance of the tube can be assumed to be isothermal.

Two boundary conditions, uniform wall temperature and uniform wall heat flux on the outside surface of the pipe, are of particular interest and will be considered here. A schematic of the present problem is given in Fig. 1.

With the foregoing assumptions, the energy equation for the fluid can be represented by

$$\frac{1}{r}\frac{\partial}{\partial r}\left[r(\alpha+\epsilon_H)\frac{\partial t_f}{\partial r}\right]=u\frac{\partial t_f}{\partial x} \tag{1}$$

where ϵ_H is the eddy diffusivity of energy. The boundary conditions are

$$\begin{aligned} &x<0: \quad t_f=t_{fe} \\ &x\geq 0: \quad r=r_0,\ t_f=t_{f0}(x) \\ &\qquad r=0,\ \partial t_f/\partial r=0 \end{aligned} \tag{2}$$

The fluid temperature at the solid-fluid interface $t_{f0}(x)$ is not known a priori and will be determined by coupling with the temperature field of the solid wall.

The heat conduction equation in the tube wall is given by

$$\frac{\partial^2 t_s}{\partial r^2}+\frac{1}{r}\frac{\partial t_s}{\partial r}+\frac{\partial^2 t_s}{\partial x^2}=0 \tag{3}$$

The boundary conditions are

$$\begin{aligned} &x=0 \text{ and } L: \ \partial t_s/\partial x=0 \\ &r=r_0 \quad : \ t_s=t_{s0}(x) \\ &r=r_w \quad : \ \partial t_s/\partial r=q_w/k_s \quad \text{--------} (\text{H}) \\ &\qquad\qquad t_s=t_w \quad \text{----------} (\text{T}) \end{aligned} \tag{4}$$

It is perhaps more reasonable to extend the solid region to $-\infty$ and ∞. Instead the temperature gradients are chosen to be zero at $x = 0$ and L. This is because analytical solutions would be impossible otherwise. Also, since it is often desirable

Nomenclature

C_m = coefficent in equation (10)
C_p = specific heat (kJ/kg°C)
D_0 = inner diameter of tube (m)
Gz = Graetz number (= Pe D_0/L)
H_m = $-C_m R'_m(1)/2$
I_0, I_1 = first kind modified Bessel function of 0 and first order
K = k_s/k_f
K_0, K_1 = second kind modified Bessel function of 0 and first order
k = thermal conductivity (kJ/m s°C)
L = length of heat transfer section of circular tube (m)
Nu_x = local Nusselt number defined in equation (22)
Pe = Peclet number (= Re Pr)
P_m = λ_m^2
Pr = Prandtl number (= $C_p\mu/k$)
Q = dimensionless temperature gradient
q = heat flux (kJ/m² s)
R_m = eigenfunction corresponding to λ_m^2
Re = Reynolds number (= $D_0 V/\nu$)
r = coordinate in radial direction (m)
r^+ = r/r_0
t = temperature (°C)
u = velocity of fluid (m/s)
u^+ = u/V
V = mean velocity of fluid (m/s)
x = coordinate in direction of tube axis (m)
x^+ = $2x/(\mathrm{Gz}\,L)$
λ_m^2 = eigenvalues of equation (11)
α = thermal diffusivity (m²/s)
ϵ = dimensionless wall thickness of tube (= $(r_w - r_0)/\mathrm{L}$)
θ = dimensionless temperature used in equation (8)
Θ = dimensionless temperature defined in equation (5)
ρ = density of fluid (kg/m³)
τ = coefficient in equation (14)
(H) = constant heat flux at the outer wall
(T) = constant temperature at the outer wall

Subscripts

e = entrance
f = fluid
s = solid
w = outer surface of tube
0 = solid-fluid interface

Table 1 Typical values for $K = k_s/k_f$

	Air	Liquid sodium	Mercury
Pure copper	15,000	4.4	40
Stainless steel	600	0.2	1.5

to use short passages in a heat exchanger to take advantage of the high heat transfer coefficient, the assumption is therefore acceptable. Again the solid temperature at the interface $t_{s0}(x)$ is not known and will be obtained by matching the temperature and the heat flux at the interface.

Mathematical Analysis

Definition of General Dimensionless Parameters. The temperature can be written in terms of the solutions for a constant interfacial temperature by applying the extended Duhamel's Theorem. The dimensionless variables are defined as

$$r^+ = r/r_0 \; ; \; u^+ = u/V ; x^+ = 2x/(\mathrm{Gz}L)$$
$$\Theta = t/t_{fe} \quad \text{---------- (H)}$$
$$\Theta = (t - t_w)/(t_{fe} - t_w) \quad \text{-------- (T)} \tag{5}$$

Analysis of Energy Equation for the Fluid. The energy equation and boundary conditions are

$$\frac{2}{r^+}\frac{\partial}{\partial r^+}\left(r^+ g(r^+)\frac{\partial \Theta_f}{\partial r^+}\right) = u^+ \frac{\partial \Theta_f}{\partial x^+} \tag{6}$$

where

$$g(r^+) = 1 + \mathrm{Pr}\,\epsilon_H(r^+)/\nu$$

and

$$x^+ < 0 \; : \; \Theta_f = 1$$
$$x^+ \geq 0 \; : \; r^+ = 1, \; \Theta_f = \Theta_{f0}(x^+)$$
$$r^+ = 0, \; \partial\Theta_f/\partial r^+ = 0 \tag{7}$$

First the fundamental turbulent Graetz problem with constant temperature at the solid-fluid interface will be solved. Using a new dimensionless temperature defined as $\theta_f(x^+, r^+) = (t_{f0} - t_f)/(t_{f0} - t_{fe})$, the energy equation and the boundary conditions become

$$\frac{2}{r^+}\frac{\partial}{\partial r^+}\left[r^+ g(r^+)\frac{\partial \theta_f}{\partial r^+}\right] = u^+ \frac{\partial \theta_f}{\partial x^+} \tag{8}$$

$$x^+ < 0 \; : \; \theta_f = 1$$
$$x^+ \geq 0 \; : \; r^+ = 1, \; \theta_f = 0$$
$$r^+ = 0, \; \partial\theta_f/\partial r^+ = 0 \tag{9}$$

By the method of separation of variables, the dimensionless temperature can be written as

$$\theta_f = \sum_{m=0}^{\infty} C_m R_m(r^+) \exp(-\lambda_m^2 x^+) \tag{10}$$

where λ_m^2, R_m are the eigenvalues and eigenfunctions of the Sturm-Liouville problem

$$\frac{d}{dr^+}\left[r^+ g(r^+)\frac{dR_m}{dr^+}\right] + \lambda_m^2 \frac{r^+}{2} u^+ R_m = 0 \tag{11}$$

with boundary conditions $R_m(1) = 0$, $R_m'(0) = 0$.

The solution for the problem with a variable interfacial temperature can be written by applying Duhamel's theorem [8]

$$\Theta_f(x^+, r^+) = 1 + \int_0^{x^+} [1 - \theta_f(x^+ - \xi, r^+)]\frac{d\Theta_{f0}}{d\xi}\, d\xi + \sum_{i=1}^{I} [1 - \theta_f(x^+ - \xi_i, r^+)]\Delta\Theta_{f0,i} \tag{12}$$

where ξ_i are the locations where Θ_{f0} is discontinuous, and $\Delta\Theta_{f0,i}$ are the jumps in Θ_{f0} at the corresponding locations.

The dimensionless temperature gradient at the interface of the tube Q_f is defined by the following equation

$$Q_f = q_f r_0/k_f t_{fe} \quad \text{---------- (H)}$$
$$Q_f = q_f r_0/k_f (t_{fe} - t_w) \quad \text{-------- (T)} \tag{13}$$

If the interfacial temperature is assumed to be given by

$$\Theta_{f0}(x^+) = 1 + \sum_{i=0}^{\infty} \tau_i x^{+i} \tag{14}$$

it can be shown that [9]

$$Q_f = -\left(\frac{\partial \Theta_f}{\partial r^+}\right)_{r^+=1}$$

$$= -2\left[\sum_{m=0}^{\infty}\frac{H_m}{P_m}\left\{\sum_{i=0}^{\infty} b_i x^{+i} - b_0 e^{-P_m x^+} - \sum_{i=1}^{\infty} i b_i F_{i-1}(x^+)\right\} + \tau_0 \sum_{m=0}^{\infty} H_m e^{-P_m x^+}\right] \tag{15}$$

where

$$P_m = \lambda_m^2; \; b_i = (i+1)\tau_{i+1}$$
$$F_0(x^+) = \{1 - \exp(-P_m x^+)\}/P_m$$
$$F_i(x^+) = \{x^{+i} - iF_{i-1}(x^+)\}/P_m$$

Analysis of Energy Equation for the Solid. Using the dimensionless variables, x^+, r^+, and Θ, the heat conduction equation becomes

$$\frac{\partial^2 \Theta_s}{\partial r^{+2}} + \frac{1}{r^+}\frac{\partial \Theta_s}{\partial r^+} + \left(\frac{2r_0}{\mathrm{Gz}L}\right)^2 \frac{\partial^2 \Theta_s}{\partial x^{+2}} = 0 \tag{16}$$

The boundary conditions are

$$x^+ = 0 \; : \; \partial\Theta_s/\partial x^+ = 0$$
$$x^+ = 2/\mathrm{Gz} \; : \; \partial\Theta_s/\partial x^+ = 0$$
$$r^+ = 1 \; : \; \Theta_s = \Theta_{s0} = 1 + \sum_{i=0}^{\infty} \tau_i x^{+i}$$
$$r^+ = r_w/r_0 \; : \; \partial\Theta_s/\partial r^+ = q_w r_0/k_s t_{fe} = Q_w \quad \text{-------- (H)}$$
$$\Theta_s = 0 \quad \text{---------- (T)} \tag{17}$$

The solid temperature at the interface Θ_{s0} is assumed to be the same as the fluid temperature at the interface.

The dimensionless temperature gradient at the interface is defined as

$$Q_s = q_s r_0/k_s t_{fe} \quad \text{---------- (H)}$$
$$Q_s = q_s r_0/k_s (t_{fe} - t_w) \quad \text{-------- (T)} \tag{18}$$

For both cases, $Q_s = -(\partial\Theta_s/\partial r^+)_{r^+=1}$.

(*i*) Constant Heat Flux

The dimensionless temperature gradient at the inner surface of the tube is [9]

$$Q_s = -\left(\frac{\partial \Theta_s}{\partial r^+}\right)_{r^+=1}$$

Table 2 Average percentage difference between Nusselt numbers with and without the effect of wall conduction ($0.25\,L < x < 0.75\,L$, constant heat flux at outer surface of tube, $r_0/L = 0.05$, $\mathrm{Re} = 2 \times 10^5$)

	$(\mathrm{Nu}_H - \mathrm{Nu})/(\mathrm{Nu}_H(\%)$											
Pr	0.01		0.02		0.04		0.06		0.10		0.72	
K \ ϵ	0.01[a]	0.001[b]	0.01	0.001	0.01	0.001	0.01	0.001	0.01	0.001	0.01	0.001
10,000	16.7	4.5	12.5	2.6	8.3	1.7	6.1	1.0	4.0	0.7	0	0
1,000	5.2	0.7	3.0	0.3	2.0	0.3	1.1	0.1	0.8	0	0	0
100	0.8	0	0.4	0	0.3	0	0.1	0	0	0	0	0

[a]For a 1-m-long tube, inside radius 0.05 m, wall thickness 0.01 m.
[b]For a 1-m-long tube, inside radius 0.05 m, wall thickness 0.001 m.

Table 3 Average percentage difference between Nusselt numbers with and without the effect of wall conduction ($0.25\,L < x < 0.75\,L$, constant temperature at outer surface of tube, $r_0/L = 0.05$, $\mathrm{Re} = 2 \times 10^5$)

	$(\mathrm{Nu} - \mathrm{Nu}_T)/\mathrm{Nu}_T(\%)$											
Pr	0.01		0.02		0.04		0.06		0.10		0.72	
K \ ϵ	0.01	0.001	0.01	0.001	0.01	0.001	0.01	0.001	0.01	0.001	0.01	0.001
0.1	26.5	20.7	20.8	17.3	15.9	14.1	12.7	11.5	9.2	9.1	4.2	4.0
1	20.4	6.2	16.2	6.2	13.9	6.2	11.4	5.8	9.1	5.4	3.8	2.5
10	6.7	0.9	6.2	0.9	6.2	0.9	5.6	0.9	5.6	0.8	2.8	0.6

$$= -\frac{r_w}{r_0} Q_w - \mathrm{Gz} \sum_{n=1}^{\infty} \left\{ \left[K_1\left(\frac{n\pi r_w}{L}\right) I_1\left(\frac{n\pi r_0}{L}\right) - I_1\left(\frac{n\pi r_w}{L}\right) K_1\left(\frac{n\pi r_0}{L}\right) \right] \Big/ \left[K_1\left(\frac{n\pi r_w}{L}\right) I_0\left(\frac{n\pi r_0}{L}\right) + I_1\left(\frac{n\pi r_w}{L}\right) K_0\left(\frac{n\pi r_0}{L}\right) \right] \right\} \frac{n\pi r_0}{L} \cos\frac{n\pi \mathrm{Gz}}{2} x^+ \int_0^{2/\mathrm{Gz}} \left(1 + \sum_{i=0}^{\infty} \tau_i x^{+i}\right) \cos\frac{n\pi \mathrm{Gz}}{2} x^+ \, dx^+ \tag{19}$$

(*ii*) Constant Temperature

The dimensionless temperature gradient at the inner surface of the tube is [9]

$$Q_s = -\left(\frac{\partial \Theta_s}{\partial r^+}\right)_{r^+=1} = -\frac{\mathrm{Gz}}{2\ln(r_0/r_w)} \int_0^{2/\mathrm{Gz}} \left(1 + \sum_{i=0}^{\infty} \tau_i x^{+i}\right) dx^+ - \mathrm{Gz} \sum_{n=1}^{\infty} \left\{ \left[K_0\left(\frac{n\pi r_w}{L}\right) I_1\left(\frac{n\pi r_0}{L}\right) + I_0\left(\frac{n\pi r_w}{L}\right) K_1\left(\frac{n\pi r_0}{L}\right) \right] \Big/ \left[K_0\left(\frac{n\pi r_w}{L}\right) I_0\left(\frac{n\pi r_0}{L}\right) - I_0\left(\frac{n\pi r_w}{L}\right) K_0\left(\frac{n\pi r_0}{L}\right) \right] \right\} \frac{n\pi r_0}{L} \cos\frac{n\pi \mathrm{Gz}}{2} x^+ \int_0^{2/\mathrm{Gz}} \left(1 + \sum_{i=0}^{\infty} \tau_i x^{+i}\right) \cos\frac{n\pi \mathrm{Gz}}{2} x^+ \, dx^+ \tag{20}$$

Heat Exchange Between the Fluid and Solid Wall. The following relation is applicable at the solid-fluid interface

$$Q_f = K Q_s \tag{21}$$

where $K = k_s/k_f$. Using Q_f from equation (15), Q_s from equation (19), and the orthogonality properties of cosine functions, the coefficients τ_i for the constant heat flux case be determined from a linear system of simultaneous equations. Similarly, using Q_f from equation (15), Q_s from equation (20), and the orthogonality properties of cosine functions, the coefficients τ_i for the constant temperature case can also be determined. For details, the reader is referred to [9].

If the mean temperature of the fluid at an arbitrary cross section of the tube is designated by t_{fm}, then the local Nusslet number can be defined by

$$\mathrm{Nu}_x = \frac{D_0 q_f}{k_f (t_{f0} - t_{fm})} \tag{22}$$

Through an energy balance and some mathematical manipulations, the Nusselt number can be obtained as [9]

$$\mathrm{Nu}_x = \frac{1}{2}\left[\left(\frac{\tau_1}{8} + \frac{\tau_2}{4} x^+ + \frac{3}{8}\tau_3 x^{+2} + \ldots \right) + \sum_{m=0}^{\infty} H_m \left\{ \tau_0 e^{-P_m x^+} - \frac{\tau_1}{P_m} e^{-P_m x^+} - \frac{2\tau_2}{P_m^2}(1 - e^{-P_m x^+}) - 6\frac{\tau_3}{P_m^2}\left(x^+ - \frac{1}{P_m} + \frac{e^{-P_m x^+}}{P_m} \right) - \ldots \right\} \right] \Big/ \sum_{m=0}^{\infty} H_m \left[\frac{\tau_0}{P_m} e^{-P_m x^+} + \frac{\tau_1}{P_m}(1 - e^{-P_m x^+}) \right.$$

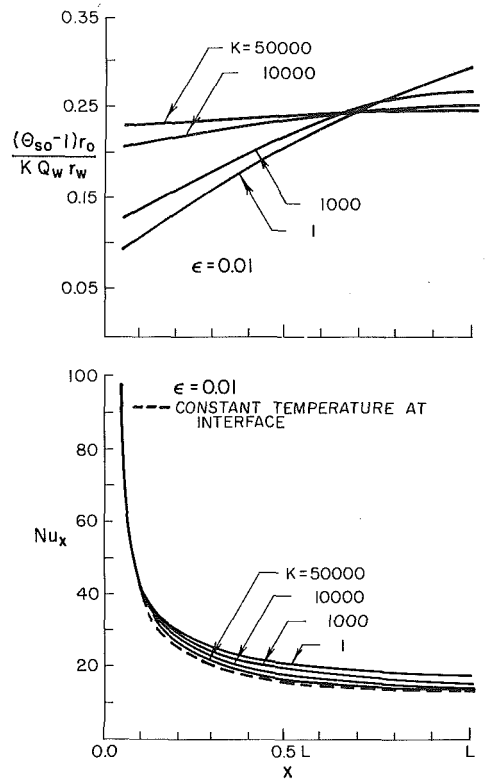

Fig. 2 Effect of ratio of conductivity of wall to that of fluid on interfacial temperature and local Nusselt number (constant heat flux at outer surface of tube, Pr = 0.01, Re = 200,000, r_0/L = 0.05)

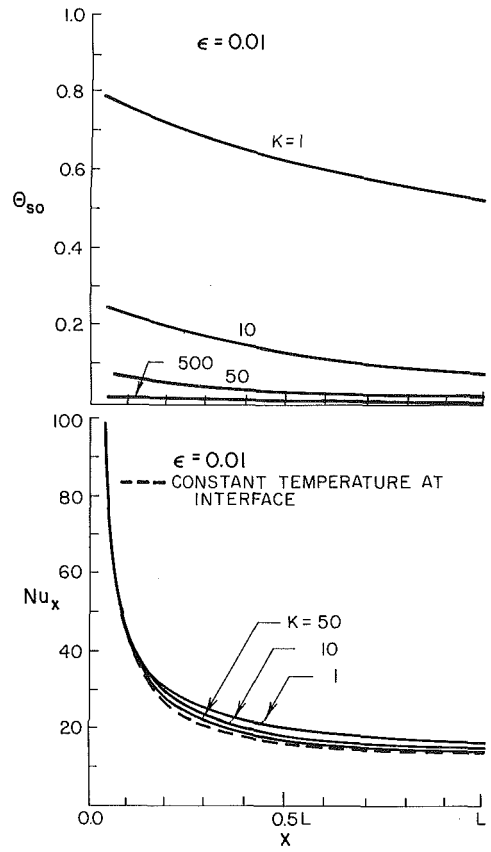

Fig. 3 Effect of ratio of conductivity of wall to that of fluid on interfacial temperature and local Nusselt number (constant temperature at outer surface of tube, Pr = 0.01, Re = 200,000, r_0/L = 0.05)

$$+\frac{2\tau_2}{P_m^2}\left(x^+-\frac{1}{P_m}+\frac{e^{-P_m x^+}}{P_m}\right)+\frac{6\tau_3}{P_m^2}\left(\frac{x^{+2}}{2}\right.$$

$$\left.-\frac{x^+}{P_m}+\frac{1}{P_m^2}-\frac{e^{-P_m x^+}}{P_m^2}\right)+\ldots\Bigg] \qquad (23)$$

Results and Discussions

Before numerical computations are carried out, the eigenvalues, λ_m^2, and constants C_m and H_m for the turbulent Graetz problem for a wide range of Reynolds and Prandtl numbers must be obtained. These values were provided by Sparrow et al. [10], Sleicher and Tribus [11], Notter [12], and Notter and Sleicher [13]. The eigenvalues and constants used in this work are obtained from [12] and [13]. The functional forms of $\epsilon_H(r^+)$ and the details concerning the numerics involved in generating the eigenvalues and constants are given in the same references. The first three or four eigenvalues and constants were obtained numerically, and they are very accurate. However, those with $m \geq 4$ are somewhat inaccurate. This is acceptable because the higher the value of m, the larger the error that can be tolerated. The present results do not depend significantly on the accuracy of the eigenvalues and constants beyond the third or fourth constants. This was confirmed by artifically changing the eigenvalues and constants beyond the third or fourth constants by almost 5 percent; the observed change in the values of the interfacial temperature and Nusselt number was less than 1 percent.

The number of terms used in the expansion of Θ_{f0} in equation (14) was five. This choice is adequate because

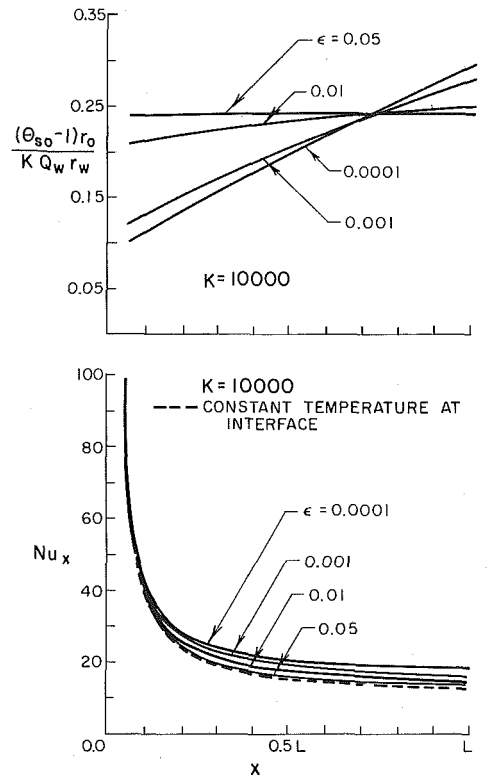

Fig. 4 Effect of wall thickness on interfacial temperature and local Nusselt number (constant heat flux at outer surface of tube, Pr = 0.01, Re = 200,000, r_0/L = 0.05)

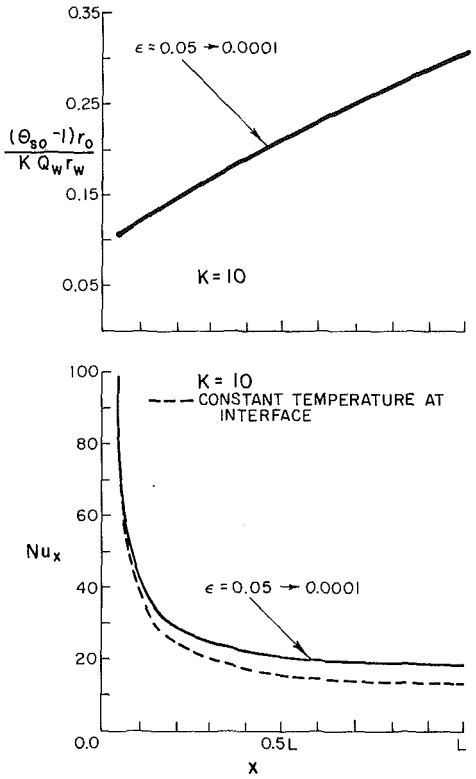

Fig. 5 Effect of wall thickness on interfacial temperature and local Nusselt number (constant heat flux at outer surface of tube, Pr = 0.01, Re = 200,000, r_0/L = 0.05)

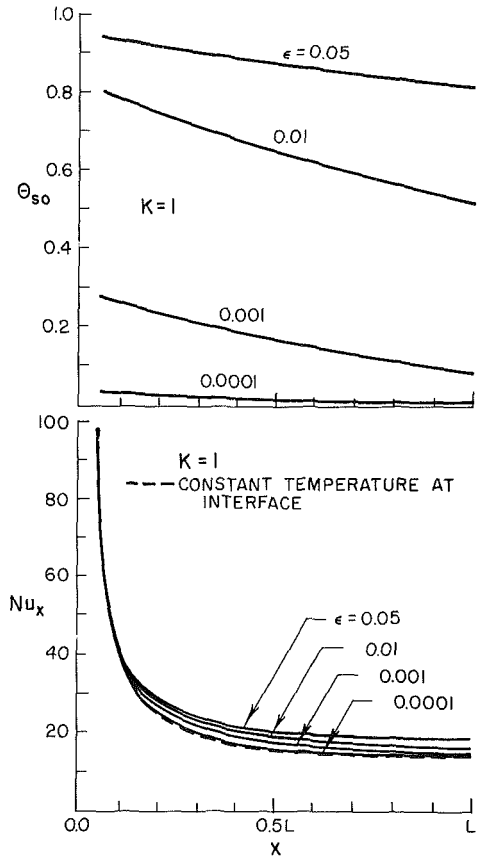

Fig. 6 Effect of wall thickness on interfacial temperature and local Nusselt number (constant temperature at outer surface of tube, Pr = 0.01, Re = 200,000, r_0/L = 0.05)

essentially the same Nusselt number and interfacial temperature were obtained with six terms used in equation (14).

For all cases done in the present work, the ratio of the inner radius of the tube to the heat exchange tube length, r_0/L, was kept at 0.05. Other values of r_0/L should not affect the conclusions of this paper significantly. Computations for a considerable number of combinations of Prandtl numbers, Reynolds numbers, conductivity ratios, and wall thicknesses were made. The present work focused on two different Reynolds numbers, namely, Re = 5×10^4 and Re = 2×10^5. These are two typical Reynolds numbers in practical applications. For each Reynolds number, the Prandtl number was varied from 0.01 to 0.72. Higher values of Pr were not used, because it was observed that the effect of wall conduction is not significant when the Prandtl number is greater than 0.72. The wall thickness was varied from 0.0001 to 0.05. This covers extreme cases of wall thickness. The conductivity ratio K was varied from 0.1 to 5×10^4. In Table 1, some typical values of K are given.

The case of Pr = 0.01 and Re = 2×10^5 was studied extensively. The results for various wall thicknesses and conductivity ratios are given in Figs. 2 to 7.

In Fig. 2, the axial temperature distribution at the interface and the local Nusselt number distribution for various conductivity ratios for constant heat flux at the outer surface of the tube are shown for ϵ = 0.01. The effect of conduction in the wall increases with the increase of the conductivity ratio K. As K increases, the temperature distribution at the interface changes gradually to a constant temperature at the interface. At $K = 5 \times 10^4$, the interfacial temperature distribution becomes uniformly constant and the Nusselt number distribution almost agrees with the result for the constant interfacial temperature case. Conversely, as K

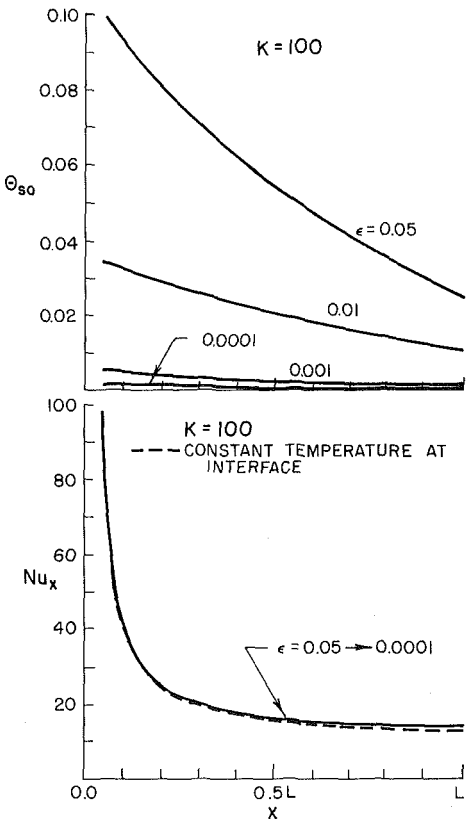

Fig. 7 Effect of wall thickness on interfacial temperature and local Nusselt number (constant temperature at outer surface of tube, Pr = 0.01, Re = 200,000, r_0/L = 0.05)

decreases, the Nusselt number distribution increases. In fact, the $K = 1$ curve is approximately the Nusslet number distribution for constant heat flux with no wall conduction. This is because when K was reduced to 0.1, virtually no difference from the $K = 1$ case was observed. Hence, for $K = 1$, the effect of wall conduction may be neglected. Figures 3 shows the results for constant temperature at the outer surface of the tube for $\epsilon = 0.01$. As K becomes large, the dimensionless temperature $\Theta_{s0} \rightarrow 0$, indicating the interfacial temperature t_{s0} approaches to t_w. For $K > 50$, the Nu distribution almost agrees with the results for constant interfacial temperature. The $K = 0.1$ curve for the Nu distribution is approximately the same as that of the constant heat flux Nu distribution with no wall conduction. However, even though the Nu_x for low K is larger than that for large K, the actual heat transfer is smaller because for small K, $\Theta_{s0} \approx 1$, i.e., $t_{s0} \approx t_{fe}$, indicating that the fluid has gained very little energy.

Now the effect of wall thickness on the interfacial temperature distribution and Nu_x is discussed. Figures 4 and 5 show the results of constant heat flux at the outer surface of the tube for $K = 10000$ and $K = 10$, respectively. In Fig. 4, it is found that $\epsilon < 0.0001$, the effect of wall conduction can be neglected. This can be verified from the identical Nu distribution for $\epsilon = 0.0001$ and $\epsilon = 0.00001$. This Nu distribution is, in fact, the same as the constant heat flux case with no wall conduction. As the wall thickness becomes thicker, the wall conduction becomes more important and the interfacial temperature becomes more uniform. On the other hand, Fig. 5 shows the effect of ϵ depends on the value of K. When $K = 10$, for $\epsilon = 0.0001$ to 0.05, all the interfacial temperature and Nu distributions reduce to the same as those without wall conduction. This indicates that for low K, the effect of wall conduction is unimportant.

Figures 6 and 7 show the results of the case with constant temperature at outer surface for $K = 1$ and 100, respectively. It is found that for small ϵ, the dimensionless interfacial temperature $\Theta_{s0} \rightarrow 0$, that is, $t_{s0} \rightarrow t_w$, and also, the Nu_x approaches asymptotically to the results for the nonwall conduction situation. For larger ϵ, the effect of wall conduction is important for $K = 1$ and insignificant for $K = 100$. This is contrary to the above situation for the case with constant heat flux at the outer surface of the tube.

The case of $Pr = 0.1$ and $Re = 5 \times 10^4$ was also studied extensively. The results are quite similar to those shown in Figs. 2–7 (for $Pr = 0.01$ and $Re = 2 \times 10^5$). However, the effects of wall conduction are more important for the lower Pr case. The relative importance of wall conduction for various Pr's is given in Tables 2 and 3.

Another case that was focused upon is when $Pr = 0.72$ and $Re = 5 \times 10^4$. Again the results are similar to those shown in Figs. 2–7. However, for this higher Pr case, the effects of wall conduction are much less significant compared to the lower Pr cases. In fact, the wall conduction effect is almost negligible (see Tables 2 and 3). This is expected because Siegel and Sparrow [14] showed that for turbulent flow in a tube, the Nusselt number results for uniform wall temperature and uniform heat flux at the interface are nearly identical for $Pr > 0.7$. Hence axial wall conduction, which would yield results between these two, would show little effects.

Figures 2 to 7 revealed similar results for the effects of wall conduction compared to those for laminar flow [5], but to a lesser extent. In other words, the influence of wall conduction is less for turbulent flow than for laminar flow. It is clear that the effects of wall conduction decrease as the Reynolds number increases. The dependence of the effects of wall conduction on the Reynolds and Prandtl numbers can be explained quite easily. For low Prandtl and Reynolds numbers, the fluid conduction near the wall is significant compared to the bulk fluid heat transport, and therefore, the effects of wall conduction should be more significant for lower Prandtl and Reynolds numbers.

For the case of constant heat flux at the outer surface of a tube, Table 2 provides some useful information as to under what conditions the wall conduction is significant. In general, when the heat flux is constant on the outside of the tube, wall conduction is negligible when (*i*) $Pr > 1$, or (*ii*) $K < 10^3$ for a thin wall. It is interesting to note that when wall conduction is important (for low Pr), the results correlate strongly with $K\epsilon$. This indicates that the deviation in the Nusselt number is caused mainly by wall conduction in the axial direction. Similarly, for the case of constant temperatures at the outer surface of a tube, Table 2 provides some useful information as to under what conditions the wall conduction is significant. For this constant temperature case, it can be seen that the wall conduction is negligible when (*i*) $Pr > 1$, or (*ii*) $K > 10$ for a thin wall. However, for this second case, the deviations in the Nusselt number correlate strongly with K/ϵ. This indicates that wall conduction in the radial direction is dominant in this case.

Conclusions

The influence of wall conduction on heat transfer for turbulent flow in a circular tube is analyzed. At the outer surface of the tube, it is assumed that either the heat flux is uniform or the temperature is constant. It is shown that for certain values of Reynolds numbers, Prandtl numbers, conductivity ratios of solid to fluid, and dimensionless wall thicknesses, the wall conduction effect may be important, It was found, as expected, that the effect of conduction in the wall is negligible when the wall is sufficiently thin.

The following conclusions can be drawn from the present analysis:

1 The wall conduction has more influence for laminar flow than for turbulent flow. This is based on comparison of the present results with those for laminar flow in the literature.

2 The effect of wall conduction has a more significant effect on heat transfer for low Pr than for high Pr.

3 For constant heat flux at the outer surface of a tube, the effect of wall conduction on heat transfer increases with the increase of the conductivity ratio.

4 For constant temperature at the outer surface of a tube, the effect of wall conduction on heat transfer increases with the decrease of the conductivity ratio.

5 Depending on the values of various parameters, the wall conduction can change the value of the Nusselt number by almost 30 percent compared to the case when wall conduction is not considered.

References

1 Siegel, R., and Savino, J. M., "An Analytical Solution of the Effect of Peripheral Wall Conduction on Laminar Forced Convection in Rectangular Channels," ASME JOURNAL OF HEAT TRANSFER, Vol. 87, 1965, pp. 59–66.

2 Davis, E. J., and Gill, W. N., "The Effects of Axial Conduction in the Wall on Heat Transfer With Laminar Flow," *International Journal of Heat and Mass Transfer*, Vol. 13, 1970, pp. 459–470.

3 Mori, S., et al., "Steady Heat Transfer to Laminar Flow Between Parallel Plates With Conduction in Wall," *Heat Transfer-Japanese Research*, Vol. 5, 1976, pp. 17–25.

4 Luikov, A. V., Aleksashenko, V. A., and Aleksashenko, A. A., "Analytical Methods of Solution of Conjugated Problems in Convective Heat Transfer," *International Journal of Heat and Mass Transfer*, Vol. 14, 1971, pp. 1047–1056.

5 Mori, S., Sakakibara, M., and Tanimoto, A., "Steady Heat Transfer to Laminar Flow in a Circular Tube With Conduction in the Tube Wall," *Heat Transfer-Japanese Research*, Vol. 3, 1974, pp. 37–46.

6 Faghri, M., and Sparrow, E. M., "Simultaneous Wall and Fluid Axial Conduction in Laminar Pipe-Flow Heat Transfer," ASME JOURNAL OF HEAT TRANSFER, Vol. 102, 1980, pp. 58–63.

7 Sakakibara, M., and Endoh, K., "Effect of Conduction in Wall on Heat Transfer With Turbulent Flow Between Parallel Plates," *International Journal of Heat and Mass Transfer*, Vol. 20, 1977, pp. 507–516.

8 Kays, W. M., *Convective Heat and Mass Transfer*, McGraw-Hill, New York, 1966, p. 136.

9 Lin, Y. K., "Effects of Wall Conduction on Heat Transfer for Turbulent Flow in a Circular Tube," MS thesis, Department of Mechanical Engineering, Texas A & M University, 1980.

10 Sparrow, E. M., Hallman, T. M., and Seigel, R., "Turbulent Heat Transfer in the Thermal Entrance Region of a Pipe With Uniform Heat Flux," *Applied Scientific Research*, Vol. A7, 1957, pp. 37–52.

11 Sleicher, C. A., and Tribus, M., "Heat Transfer in a Pipe With Turbulent Flow and Arbitrary Wall Temperature Distribution," ASME *Transactions*, Vol. 79, 1957, pp. 789–797.

12 Notter, R. H.,. "Matched Asymptotic Expansion Applied to the Turbulent Graetz Problems," PhD dissertation, Department of Chemical Engineering, University of Washington, 1969.

13 Notter, R. H., and Sleicher, C. A., "A Solution to the Turbulent Graetz Problem—III, Fully Developed and Entry Region Heat Transfer Rates," *Chemical Engineering Science*, Vol. 27, 1972, pp. 2073–2093.

14 Siegel, R., and Sparrow, E. M., "Comparison of Turbulent Heat-Transfer Results for Uniform Wall Heat Flux and Uniform Wall Temperature," ASME JOURNAL OF HEAT TRANSFER, Vol. 82, 1960, pp. 152–153.

I. Catton
Professor.
Fellow ASME

J. H. Lienhard V[1]
Research Assistant.
School of Engineering and Applied Science,
University of California,
Los Angeles, Calif. 90024

Thermal Stability of Two Fluid Layers Separated by a Solid Interlayer of Finite Thickness and Thermal Conductivity

Stability limits of two horizontal fluid layers separated by an interlayer of finite thermal conductivity are determined. The upper cooled surface and the lower heated surface are taken to be perfectly conducting. The stability limits are found to depend on the ratio of fluid layer thicknesses, the ratio of interlayer thickness to total fluid layer thickness, and the ratio of fluid thermal conductivity to interlayer thermal conductivity. Results are given for a range of values of each of the governing parameters.

Introduction

Natural convection flows are a common occurrence in technological devices. Buoyancy forces result in fluid motion through a complex relationship between density and velocity fields. A common example might be heat transfer across an unventilated air gap in a building or a solar collector. Under some circumstances, it is desirable to inhibit natural convection. A flat solar collector with a glass cover might be much more efficient with two glass plates or, as suggested by Edwards [1], with multiple thin sheets of a transparent material. The problem then becomes one of knowing when convection will occur. In this work, we address only the case in which there is one interlayer and we generalize this circumstance to arbitrary thickness, thermal conductivity, and location (see Fig. 1). The cooled upper and heated lower surface are assumed to be perfectly conducting.

Thermal stability of a fluid layer heated from below has been the subject of a large number of studies and the state of knowledge of the linear theory is now virtually complete. A history of the subject is found in Chandrasekhar's book [2]. The only work we are aware of that addresses the stability of two fluid layers is that of Gershuni and Zhukhovitskii [3]. Gershuni analyzed the stability of two fluid layers separated by a centrally located interlayer. We will show that allowing the interlayer to be arbitrarily located between the heated and cooled surfaces dramatically increases the complexity of the problem.

Governing Equations

The equations that govern the physical situation to be studied are the steady two-dimensional Oberbeck-Boussinesq equations

$$\nabla \cdot \mathbf{v} = 0 \tag{1}$$

$$\nu \nabla^2 \mathbf{v} - \nabla P/\rho_0 - \rho \mathbf{g}\mathbf{k}/\rho_0 = (\mathbf{v}\cdot\nabla)\mathbf{v} \tag{2}$$

$$\alpha \nabla^2 T = (\mathbf{v}\cdot\nabla)T \tag{3}$$

$$\rho = \rho_0[1-\beta(T-T_0)] \tag{4}$$

Equations (1-4) must be satisfied in both fluid regions, and in the thermal barrier we have

$$\nabla^2 T = 0 \tag{5}$$

The boundary conditions for these equations are

$$\mathbf{v}(y,z_3) = \mathbf{v}(y,-z_1) = \mathbf{v}(y,z_1) = \mathbf{v}(y,z_2) = 0$$
$$T(y,z_3) = T_H, \quad T(y,z_2) = T_C \tag{6}$$

The fluid layers are of infinite extent so periodicity conditions are imposed

$$\mathbf{v}(y,z) = \mathbf{v}(y+\lambda,z)$$
$$T(y,z) = T(y+\lambda,z) \tag{7}$$

The base state, no motion, solutions are

$$\mathbf{v} = 0 \tag{8}$$

and

$$T = T_H - \frac{T_H - T_c}{\left(1 + \frac{L_2}{L_1} + \frac{L_B}{k_B}\frac{k}{L_1}\right)}\left(\frac{z-z_3}{L_1}\right), \quad z_3 \le z \le -z_1 \tag{9a}$$

$$T = T_H - \frac{T_H - T_c}{\left(1 + \frac{L_2}{L_1} + \frac{L_B}{k_B}\frac{k}{L_1}\right)}\left(1 + \frac{k}{L_1}\frac{L_B}{k_B}\frac{(z+z_1)}{L_B}\right),$$
$$-z_1 \le z \le z_1 \tag{9b}$$

$$T = T_H - \frac{T_H - T_c}{\left(1 + \frac{L_2}{L_1} + \frac{L_B}{k_B}\frac{k}{L_1}\right)}\left(1 + \frac{k}{L_1}\frac{L_B}{k_B} + \frac{L_2}{L_1}\frac{(z-z_1)}{L_2}\right),$$
$$z_1 \le z \le z_2 \tag{9c}$$

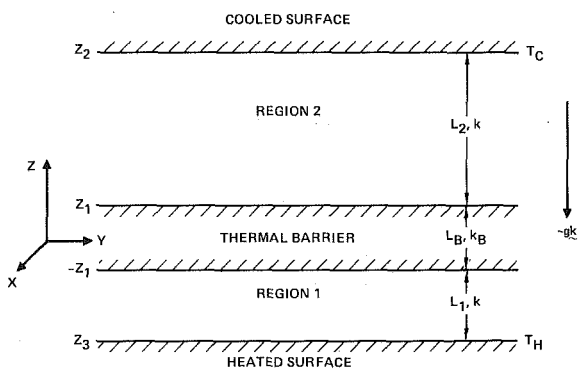

Fig. 1 The physical problem

[1] Presently at the Department of Applied Mechanics and Engineering Science, University of California at San Diego, La Jolla, Calif.

Contributed by the Heat Transfer Division and presented at the ASME-JSME Joint Thermal Engineering Conference, Honolulu, Hawaii, March 1983. Manuscript received by the Heat Transfer Division May 23, 1983.

To obtain the stability equations, we perturb these base state solutions and substitute them in equations (1-3).

Scaling is done separately for each of the fluid regions

$$\mathbf{v}_1' = \mathbf{v}_1^* \alpha / L_1 \qquad T_1' = T_1^* \Delta T_1 \qquad T_B' = T_B^* \Delta T_1$$
$$\mathbf{v}_2' = \mathbf{v}_2^* \alpha / L_2 \qquad T_2' = T_2^* \Delta T_2$$

Analyzing the disturbance quantities into normal modes, substituting them into equations (1-3), and operating in equation (2) with $\mathbf{k} \cdot \mathrm{curl}^2$, we obtain for region 1

$$(D_1^2 - a_1^2)^2 W_1 = a_1^2 \mathrm{Ra}_1 \theta_1$$
$$(D_1^2 - a_1^2)\theta_1 = -W_1$$
$$Z_1 = \frac{z - z_3}{L_1} - \frac{1}{2} \tag{10}$$

for region 2:

$$(D_2^2 - a_2^2)^2 W_2 = a_2^2 \mathrm{Ra}_2 \theta_2$$
$$(D_2^2 - a_2^2)\theta_2 = -W_2$$
$$Z_2 = -\frac{1}{2} + \frac{z_2 - z}{L_2} \tag{11}$$

and for the thermal barrier

$$(D_B^2 - a_B^2)\theta_B = 0$$
$$Z_B = z / L_B \tag{12}$$

where D_i denotes $\dfrac{d}{dZ_i}$.

The wave numbers are all related to a common disturbance wavelength

$$a_1 = 2\pi L_1/\lambda, \quad a_2 = 2\pi L_2/\lambda, \quad a_B = 2\pi L_B/\lambda \tag{13}$$

The boundary conditions for equations (10-12) are

$$W_k(\pm 1/2) = D_k W_k(\pm 1/2) = \theta_2(1/2) = \theta_1(-1/2) = 0, \quad k = 1,2 \tag{14}$$

$$\theta_1(1/2) = \theta_B(-1/2), \quad B\theta_2(-1/2) = \theta_B(1/2) \tag{15}$$

and

$$A(1+B)\frac{k}{k_B} D_1\theta_1(1/2) = D_B\theta_B(-1/2)$$
$$A(1+B)\frac{k}{k_B} D_2\theta_2(-1/2) = D_B\theta_B(1/2) \tag{16}$$

where

$$A \equiv L_B/(L_1 + L_2) \text{ and } B \equiv L_2/L_1.$$

Equations (10-12) with (14-16) form an eigenvalue problem for Ra_1 and Ra_2 with A, B, and k/k_B as parameters. It is important to realize that the appearance of A and k/k_B as a single group in the boundary conditions results from the use of more than one length scale in the nondimensionalization. The natural parameters of the perturbation equation (those obtained using a single length scale) are A, B, and k/k_B. The group $A(1+B)\,k/k_B = L_B k / L_1 k_B$ – the fluid/midlayer conductance ratio – appears only as a parameter for the base state heat transfer, and thus will arise only in the overall Rayleigh number of the system.

More specifically, although the entire system admits an undamped convective disturbance at some point, one may view the thicker layer as becoming unstable and driving convection in the thinner layer. Thus the stability limit of this system is most directly characterized by the Rayleigh number of the thicker of the two layers – by the Rayleigh number of the layer that first becomes unstable. This, in turn, depends on the three parameters, A, B, and k/k_B. The overall Rayleigh number is introduced only as a global design parameter – it does not clearly represent parametric effects on the stability limit. The importance of this fact will be made clear in the discussion of the results.

Some important characteristics of the governing equations are proven in [4]. In particular, solutions for midlayer locations that are symmetric about the center of the layered system are identical – the solution for an upper-to-lower fluid layer aspect ratio of B is identical to that for $1/B$. This indicates that the stability of each fluid layer depends only upon which boundary conditions are imposed on it, not on whether they are imposed at the top or bottom of the layer. This symmetry principle also allows us to solve the problem for midlayer locations to just one side of the center. We have accordingly solved the problem only for $B \le 1$, since solutions for $B > 1$ are the same as those for $1/B$.

The principle of the exchange of stabilities, which we assumed here at the outset, is also proven in [4].

Stability

The Galerkin method will be used as outlined by Chandrasekhar [2] to obtain solutions to the eigenvalue problem previously mentioned. Beam functions [5] will be used to approximate the vertical velocity, and the energy equation

Nomenclature

a_i = dimensionless disturbance wave number for region i, $(2\pi/\lambda)L_i$
A = midlayer/total fluid layer aspect ratio, $L_B/(L_1+L_2)$
B = upper/lower fluid layer aspect ratio, L_2/L_1
C_i = even beam function
g = body force/unit mass (constant and uniform)
k = fluid thermal conductivity
k_B = midlayer thermal conductivity
$\mathbf{k}$ = unit vector in the z-direction
L_i = thickness of layer i
p = fluid pressure
Ra_i = Rayleigh number for region i, $g\beta\Delta T_i L^3/\nu\alpha$
Ra_T = overall Rayleigh number, $g\beta(T_H - T_C)(L_1 + L_B + L_2)^3/\nu\alpha$
S_i = odd beam function
T = temperature
T_C = temperature of the cold upper isothermal surface
T_H = temperature of the hot lower isothermal surface
$\mathbf{v}_i$ = vector fluid velocity in region i
W_i = dimensionless amplitude of normal mode fluid velocity disturbance in region i
x,y,z = Cartesian coordinates
Z_i = dimensionless z-coordinate in region i

Greek Letters

α = fluid thermal diffusivity
β = fluid coefficient of volume expansion
ΔT_i = temperature difference across region i
θ_i = dimensionless amplitude of normal mode temperature disturbance in region i
λ = disturbance wavelength
λ_i, μ_i = eigenvalues of even, and odd, beam functions
ν = fluid kinematic viscosity
ρ = fluid density

Subscripts and Superscripts

$1,2,B$ = a variable or parameter in fluid regions 1 or 2, or the thermal barrier, respectively
$'$ = a disturbance quantity
$*$ = a nondimensionalized variable
$=$ = a two-dimensional matrix
0 = a reference state quantity for the Boussinesq approximation

will then be solved for the temperature perturbations. The beam functions C_i and S_i are themselves eigenfunctions of the problem $y^{[IV]} = b^4 y$, $y(\pm 1/2) = y'(\pm 1/2) = 0$, and thus meet the boundary conditions on W_i identically. Satisfying the momentum equations using the Galerkin method yields the determinant that must be zero.

The series representations assumed for the velocity are

$$W_1 = \sum_i A_i^1 \psi_i^1(Z_1), \quad W_2 = \sum_i A_i^2 \psi_i^2(Z_2) \tag{17}$$

where:

$$\psi_i^1(Z_1) = \begin{cases} C_m(Z_1), & m = (i+1)/2 \text{ and } i = 1,3, \ldots \\ S_m(Z_1), & m = i/2 \text{ and } i = 2,4, \ldots \end{cases} \tag{18}$$

$$\psi_i^2(Z_2) = \begin{cases} C_m(Z_2), & m = (i+1)/2 \text{ and } i = 1,3, \ldots \\ S_m(Z_2), & m = i/2 \text{ and } i = 2,4, \ldots \end{cases} \tag{19}$$

The corresponding temperature profiles obtained as solutions to

$$D_i^2 \phi_i^k - a_i^2 \phi_i^k = -\psi_i^k, \quad k = 1,2 \tag{20}$$

are

$$\phi_i^k = \frac{-\cosh \lambda_m Z_k}{(\lambda_m^2 - a_k^2)\cosh(\lambda_m/2)} - \frac{\cos \lambda_m Z_k}{(\lambda_m^2 + a_k^2)\cos(\lambda_m/2)} + D_i^k \cosh a_k Z_k + E_i^k \sinh a_k Z_k, \quad m = (i+1)/2 \text{ and } k = 1, 2 \tag{21}$$

for $i = 1, 3, \ldots$ and

$$\phi_i^k = \frac{-\sinh \mu_m Z_k}{(\mu_m^2 - a_k^2)\sinh(\mu_m/2)} - \frac{\sin \mu_m Z_k}{(\mu_m^2 + a_k^2)\sin(\mu_m/2)} + D_i^k \cosh a_k Z_k + E_i^k \sinh a_k Z_k, \quad m = i/2, \; k = 1,2 \tag{22}$$

for $i = 2, 4, \ldots$. The disturbance temperature then becomes

$$\theta_k = \sum_i A_i^k \phi_i^k(Z_k) + D^k \cosh a_k Z_k + E^k \sinh a_k Z_k \tag{23}$$

The disturbance temperature in the barrier or interlayer – the solution to equation (13) – is

$$\theta_B = M \cosh a_B Z_B + N \sinh a_B Z_B \tag{24}$$

The constants of integration are found by satisfying the boundary conditions on θ at the heated and cooled surfaces and the matching conditions at the interlayer. The result is

$$\theta_k(Z_k) = \sum_i A_i^k \Phi_i^{kk}(Z_k) + \sum_i A_i^j \Phi_i^{kj}(Z_k), \begin{cases} j = 2, \; k = 1 \\ j = 1, \; k = 2 \end{cases} \tag{25}$$

where the functions Φ_i^{kk} and Φ_i^{kj} are given in the Appendix.

Substituting the derived expressions for θ_k and the assumed series for W_k into equations (10*a*) and (11*a*), and then weighting and integrating over the regions ($k = 1$ and 2) yields the following matrix equation

$$\begin{bmatrix} \bar{\bar{L}} - a_1^2 \mathrm{Ra}_1 \bar{\bar{N}} & -a_1^2 \mathrm{Ra}_1 \bar{\bar{I}} \\ -a_2^2 \mathrm{Ra}_2 \bar{\bar{J}} & \bar{\bar{M}} - a_2^2 \mathrm{Ra}_2 \bar{\bar{K}} \end{bmatrix} \cdot \begin{bmatrix} A^1 \\ A^2 \end{bmatrix} = 0 \tag{26}$$

where

$$\bar{\bar{L}} = \int_{-1/2}^{1/2} \psi_j^1 (D_i^2 - a_1^2)^2 \psi_i^1 dZ_1 \qquad \bar{\bar{N}} = \int_{-1/2}^{1/2} \psi_j^1 \Phi_i^{11} dZ_1$$

$$\bar{\bar{I}} = \int_{-1/2}^{1/2} \psi_j^1 \Phi_i^{12} dZ_1 \qquad \bar{\bar{J}} = \int_{-1/2}^{1/2} \psi_i^2 \Phi_j^{21} dZ_2 \tag{27}$$

$$\bar{\bar{M}} = \int_{-1/2}^{1/2} \psi_j^2 (D_2^2 - a_2^2)^2 \psi_i^2 dZ_2 \qquad \bar{\bar{K}} = \int_{-1/2}^{1/2} \psi_i^2 \Phi_j^{22} dZ_2$$

Noting that

$$\mathrm{Ra}_2 = B^4 \mathrm{Ra}_1 \quad \text{and} \quad a_2^2 = B^2 a_1^2 \tag{28}$$

and applying the requirement for nontrivial solutions, we obtain from equation (26)

$$\left| \begin{bmatrix} \bar{\bar{L}} & \bar{\bar{0}} \\ \bar{\bar{0}} & \bar{\bar{M}} \end{bmatrix} - a_1^2 \mathrm{Ra}_1 \begin{bmatrix} \bar{\bar{N}} & \bar{\bar{I}} \\ B^6 \bar{\bar{J}} & B^6 \bar{\bar{K}} \end{bmatrix} \right| = 0 \tag{29}$$

which has the form of a generalized eigenvalue problem. The choice of an N-term approximation for the velocity yields a $2N$ by $2N$ matrix, whose eigenvalues must be found.

To find the minimum Rayleigh number, values of A, B, and k/k_B are selected. Then values of Ra_1 are obtained for three values of a_1 (a first guess is made for a_1, and the second and third values are chosen by increasing and decreasing the first value by 1 percent.) A parabola is fit through the three points, $\mathrm{Ra}_1 = c_1 + c_2 a_1 + c_3 a_1^2$.

Subsequent values are determined from the requirement

$$\frac{d\mathrm{Ra}_1}{da_1} = 0 \tag{30}$$

and the sets of three are updated so that the value of a_1 associated with the smallest value of Ra_1 is always chosen. Iterations are conducted until further iteration results in less than a 0.01 percent change in Ra.

Results

The stability of two fluid layers separated by a finite thickness, finite thermal conductivity interlayer has been determined. The results are presented in Table 1, where the overall critical Rayleigh number

$$\mathrm{Ra}_T = \frac{g\beta(T_H - T_C)(L_1 + L_2 + L_B)^3}{\nu\alpha}$$

is given for $0.01 \le A \le 1.0$, $0.125 \le B \le 1$, and $0 \le k/k_B \le 100$. The critical Rayleigh number of either layer is related to Ra_T by

$$\mathrm{Ra}_T = \mathrm{Ra}_1 (1+B)^4 (1+A)^3 (1 + kA/k_B) \quad \text{and} \quad \mathrm{Ra}_2 = B^4 \mathrm{Ra}_1 \tag{31}$$

In all cases, a six-term approximation was used in conjunction with a 101 point Simpson's rule quadrature of the integrals. (The computations were made in double-precision arithmetic on an IBM 3033 computer.) Eight term approximations showed a decrease in the Rayleigh number of only about 0.01 percent, and no significant change was noted as the number of quadrature points was increased. Hence the values given in Tables 1 and 2 should be accurate to at least four significant figures.

Results are presented only for $B \le 1$ – that is, for the midlayer lying at or below the center of the layered system. Solutions for $B > 1$ are given by the symmetry principle. The maximum Rayleigh number always occurs when the layer is centered. For a thin layer (say, $A = 0.01$) that is perfectly conducting ($k/k_B = 0$), the critical value of the Rayleigh number for $B = 1$ is about 16 times that of a single layer, as we would expect. Likewise, as B tends to zero (or infinity), the limiting value is on the order of that for a single layer. Calculations were also performed for $B = 2$, 4, and 8 to verify that the numerical solutions were consistent with the symmetry principle. In all cases, an exact agreement between Ra_T for B and $1/B$ provided verification of our numerical procedure.

Figure 2 shows the variation of Ra_T with the midlayer location and conductivity for a thin layer. For a given k/k_B, Ra_T drops off rapidly as the midlayer is moved away from the center – a result of the decreasing stability of the thicker layer.

Table 1 The overall Rayleigh number at which convection initiates

$A = 0.01$

$B \backslash k/k_B$	0	0.2	1	5	10	20	100
0.125	2819	2641	2646	2704	2784	2960	4566
0.25	4296	3910	3909	4007	4140	4423	6906
0.5	8909	7943	7910	8115	8400	9000	14189
1.0	28156	22221	21854	22595	23650	25780	42853

$A = 0.1$

$B \backslash k/k_B$	0	0.2	1	5	10	20	100
0.125	3641	3452	3625	4586	5909	8629	30687
0.25	5550	5208	5423	6910	8942	13098	46729
0.5	11509	10777	11096	14160	18385	27016	96769
1.0	36373	32603	32292	42114	55727	83226	303938

$A = 0.3$

$B \backslash k/k_B$	0	0.2	1	5	10	20	100
0.125	6011	6082	6898	12106	18882	32525	141951
0.25	9161	9258	10452	18387	28718	49517	216303
0.5	18997	19215	21597	37981	59400	102527	448377
1.0	60039	60090	66475	117816	185539	321887	1414980

$A = 1.0$

$B \backslash k/k_B$	0	0.2	1	5	10	20	100
0.125	21887	25144	38266	104485	187471	353516	1682111
0.25	33359	38324	58318	159237	285716	538794	2563776
0.5	69173	79469	120924	330171	592435	1117217	5316218
1.0	218620	251119	381996	1043082	1871908	3530419	16801358

Table 2 The thicker layer Rayleigh number at which convection initiates

$A = 0.01$

$B \backslash k/k_B$	0	0.2	1	5	10	20	100
0.125	1708.0	1596.8	1587.2	1560.3	1533.7	1494.5	1383.2
0.25	1708.0	1551.3	1538.6	1517.0	1496.3	1465.3	1372.8
0.5	1708.0	1519.7	1501.5	1481.7	1464.1	1437.9	1360.2
1.0	1708.0	1345.3	1312.6	1305.4	1304.2	1303.2	1299.8

$A = 0.1$

$B \backslash k/k_B$	0	0.2	1	5	10	20	100
0.125	1708.0	1616.0	1545.6	1433.9	1385.7	1349.1	1308.5
0.25	1708.0	1599.6	1517.2	1417.8	1375.9	1343.6	1307.3
0.5	1708.0	1596.2	1497.0	1401.0	1364.2	1336.5	1305.6
1.0	1708.0	1527.9	1378.5	1318.4	1308.4	1302.7	1297.5

$A = 0.3$

$B \backslash k/k_B$	0	0.2	1	5	10	20	100
0.125	1708.0	1630.6	1507.9	1376.0	1341.3	1320.3	1301.2
0.25	1708.0	1628.3	1498.9	1371.2	1338.5	1318.8	1300.9
0.5	1708.0	1629.8	1493.7	1365.9	1335.2	1316.9	1300.4
1.0	1708.0	1612.7	1454.7	1340.7	1319.6	1308.1	1298.5

$A = 1.0$

$B \backslash k/k_B$	0	0.2	1	5	10	20	100
0.125	1708.0	1635.1	1493.1	1359.0	1330.0	1313.7	1299.7
0.25	1708.0	1635.1	1492.9	1358.8	1329.9	1313.6	1299.7
0.5	1708.0	1635.2	1492.9	1358.7	1329.9	1313.6	1299.7
1.0	1708.0	1634.9	1492.2	1358.2	1329.5	1313.4	1299.6

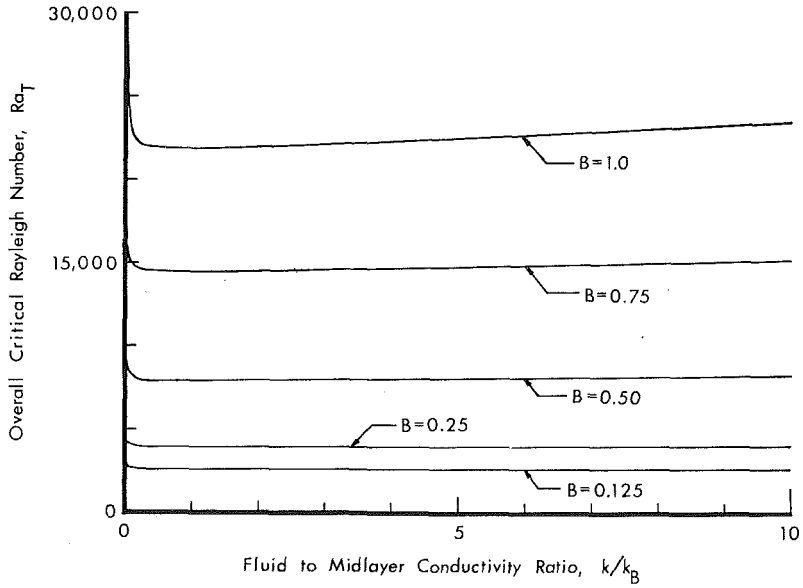

Fig. 2 The effect of midlayer location and conductivity upon fluid stability: $A = 0.01$

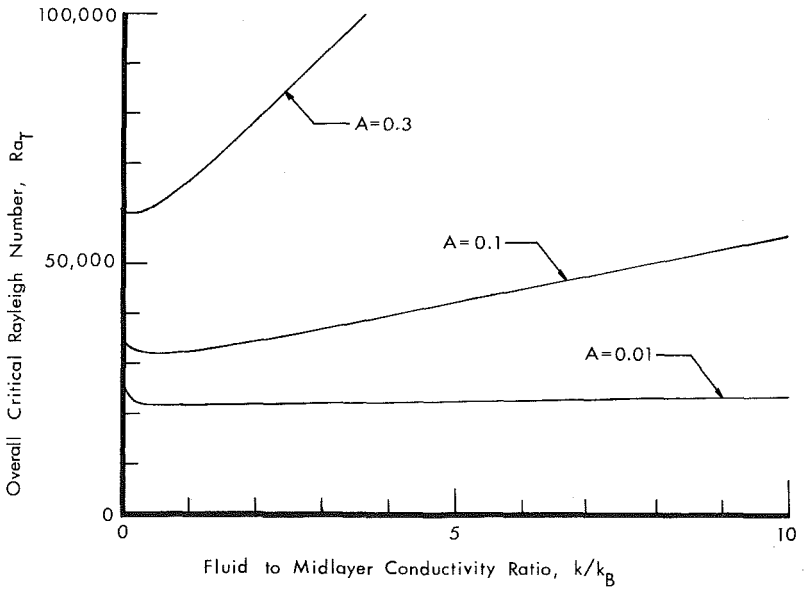

Fig. 3 The effect of midlayer thickness and conductivity upon fluid stability: $B = 1$

As $k/k_B \to \infty$ for a given B, Ra_T continues to rise almost linearly, because of the increasing resistance of the thermal barrier and the corresponding decrease of the ΔT over each fluid layer (for a given $T_H - T_c$). The abrupt drop in Ra_T, as k/k_B is increased from zero, results from decreasing damping of the thermal disturbance in the midlayer. This drop can be better interpreted in terms of the thicker layer's Rayleigh number, below. The drop is smoother for larger values of A, since a thicker layer provides more damping for a given conductivity ratio.

Figure 3 shows the effect of midlayer thickness and conductivity upon Ra_T for fluid layers of equal height. It also shows that as the midlayer becomes thin – as A decreases – there is an increasingly wide range of k/k_B for which there is little effect of interlayer resistance on the overall stability. This rather surprising result implies that the interlayer resistivity does little to supress convection when the fluid is relatively nonconductive.

Figure 3, like Fig. 2, shows that Ra_T increases linearly as $k/k_B \to \infty$, although it does so more steeply for larger A. Again, this is the result of the increasing resistance of the thermal barrier. For $k/k_B = 0$, Ra_T increases as $(1+A)^3$ – an effect of geometry on the layer ΔT's. As k/k_B increases from zero, Ra_T drops in thin midlayers and remains constant for thicker midlayers. This is again the consequence of reduced disturbance damping in the midlayer.

The unusual variation of Ra_T for smaller values of k/k_B obscures parametric effects upon fluid stability. To clarify such effects, it is better to consider the Rayleigh number of the thicker individual layer (see Table 2).

Figure 4 shows the individual layer Rayleigh number, Ra_i, as a function of k/k_B for $B = 1$ and various values of A. Several important limits are apparent here:

- $k/k_B = 0$: The midlayer is ideally conducting and the disturbance does not travel into it. We have two independent layers with isothermal walls – a standard Benard problem. The computed Ra_i is 1707.97 as compared to the exact value of 1707.76.
- $k/k_B \to \infty$: The problem again decouples because no disturbance is carried from one layer to the other. As this limit

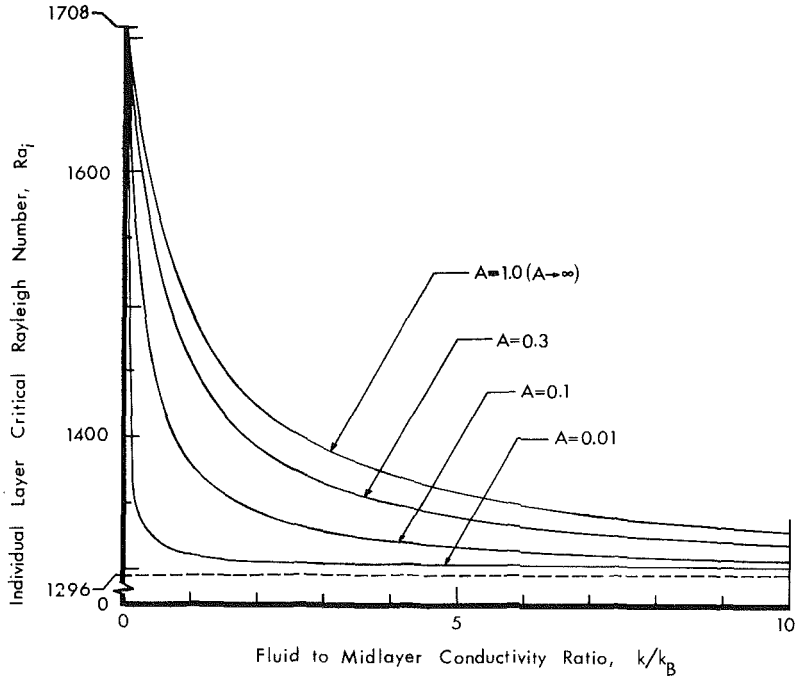

Fig. 4 The effect of midlayer thickness and conductivity upon thicker layer stability: $B = 1$

is approached, the boundary condition at the midlayer approaches that for a fixed heat flux – that is, the wall temperature gradient resists perturbations (see equation (16).) Sparrow et al. [6] obtained a limit value corresponding to $Ra_i = 1295.78$. (Of course, the case $k_B = 0$ has no real meaning, since there can be no temperature gradients.)

• $A \to 0$: In this limit the solution becomes discontinuous. For $k/k_B = 0$, we still obtain the Benard solution, but for $k/k_B > 0$, Ra_i quickly drops toward the limiting value for $k/k_B \to \infty$. As before, the midlayer temperature gradient is not easily perturbed (see equation (16)), and we approach the case of a fixed wall heat flux. Some additional discussion of this limit is given in [4].

In view of these limits, the parametric trends in the individual layer Rayleigh numbers are clear. Thicker midlayers increase individual layer stability because of higher disturbance damping. Higher conductivity midlayers lead to increased stability for the same reason. The small k/k_B behavior of Ra_T is easy to explain once we have this information: the abrupt drop apparent in Fig. 2 corresponds to that region where the Rayleigh number for the thicker layer decreases to its limiting value. Thereafter, Ra_T grows linearly with k/k_B (see equation (31).)

Figure 5 shows how the Rayleigh number of the thicker layer varies with k/k_B for $A = 0.01$ and several values of B. We again draw attention to the limiting values as k/k_B approaches 0 and ∞, since the two layers decouple in these limits and the midlayer location can no longer affect stability. When $B = 1$, the individual layer stability is now at its minimum since the opposing layer has reached its most unstable point. Here the least energy is needed for one layer to drive convection in the other. The Rayleigh number of the thicker layer increases rapidly as the midlayer is moved off-center. As $B \to 0$ the stability curve approaches that for a single layer with a thermally resistive coating over one isothermal wall. The latter problem was considered by Nield [7], and our results for $B = 0.125$ are close to his for the larger values of A and k/k_B.

Table 2 shows that the effect of midlayer position on the Rayleigh number of the thicker layer is strongest when A is small. As $A \to \infty$, the layers will again decouple and are not affected by differences in their respective thicknesses.

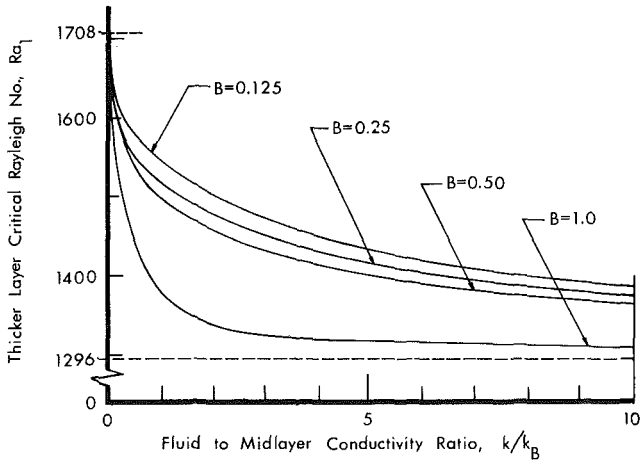

Fig. 5 The effect of midlayer location and conductivity upon thicker layer stability: $A = 0.1$

One can clearly make Ra_T large by increasing A, if the midlayer is to be used to inhibit convection. However, the midlayer thickness will be limited by other factors. For example, the midlayer in a solar collector must be thin enough to keep the transmittance high. Centering the midlayer by setting $B = 1$ also serves to maximize the stability, which decreases strongly as the midlayer is moved off center. For $B = 1$ and $A \to 0$, $Ra_T = 16 \cdot 1300 = 20{,}800$ is the minimum Rayleigh number obtained for any k/k_B, so the benefit of even a single midlayer is quite high.

Our results are compared with those of Gershuni and Zhukhovitskii in Table 3. Our values are all slightly lower as we would expect. They used a one-term approximation of a somewhat crude form. It is surprising that there is not more difference between the results.

As an example of the use of these results, we consider the following problem: a covered, horizontal, flat-plate solar collector has a 1.27 cm air layer partitioned along its horizontal center plane by a 0.013 cm thick Teflon film. The stability parameters are $A = 0.01$, $B = 1$, and $k/k_B \cong 0.10$.

Table 3 A comparison of results from this work with those of Gershuni:[a] Ra_i for $B=1$

	k/k_B				
	0	0.2	1	5	100
$A=0.01$					
This work	1708.0	1345.3	1312.6	1305.4	1299.8
Gershuni	1708.1	1345.7	1313.0	1305.9	1304.2
$A=0.1$					
This work	1708.0	1527.9	1378.5	1318.4	1297.5
Gershuni	1708.1	1528.1	1379.2	1321.3	1305.0
$A=0.3$					
This work	1708.0	1612.7	1454.7	1340.7	1298.5
Gershuni	1708.1	1613.0	1456.5	1345.9	1306.4
$A=1.0$					
This work	1708.0	1634.9	1492.2	1358.2	1299.6
Gershuni	1708.1	1635.4	1495.0	1364.5	1307.6

[a] computed from Gershuni's equations

The overall critical Rayleigh number given in Fig. 2 is $Ra_T \cong 22{,}500$.

Naturally, the present results are not exhaustive. More extensive modeling might include the effect of sidewalls, which should increase the stability of a horizontally small layer; or it might deal the effect of finite outer wall conductivity which will yield a reduction of stability.

Conclusions

1 Critical Rayleigh numbers are presented in Tables 1 and 2 for a system of two horizontal layers separated by a midlayer of finite thermal resistance.

2 The partitioned fluid layer is most stable when the midlayer is centered.

3 The overall stability for relatively thin midlayers is not significantly affected by the midlayer conductivity.

4 Gershuni and Zhukhovitskii give a reasonable approximation to Ra_i for $B=1$. Moreover, their statement that the critical Rayleigh number of the thicker fluid layer is bounded above by its isothermal midlayer value (1708) and below by its constant heat flux value (1296) proves to be true for all midlayer locations.

References

1 Edwards, D. K., personal communication, University of California, Irvine, July 21, 1982.

2 Chandrasekhar, S., *Hydrodynamic and Hydromagnetic Stability*, Oxford, Clarendon Press, 1961.

3 Gershuni, G. Z., and Zhukhovitskii, E. M., *Convective Stability of Incompressible Fluids*, Israel Program for Scientific Translations, Jerusalem, 1976.

4 Lienhard, J. H., V, "Thermal Instability and Heat Transfer in a Singly Partitioned Horizontal Fluid Layer," Master's thesis in Engineering, UCLA, 1984.

5 Harris, D. L., and Ried, W. H., "On Orthogonal Functions Which Satisfy Four Boundary Conditions: Parts I & II," *Astrophysical Journal Supplementary Series*, Vol. 3, 1958, pp. 429–452.

6 Sparrow, E. M., Goldstein, R. J., and Jonsson, V. K., "Thermal Instability in a Horizontal Fluid Layer: Effect of Boundary Conditions and Nonlinear Temperature Profile," *J. Fluid Mech.*, Vol. 18, No. 4, 1964, pp. 513–528.

7 Nield, D. A., "The Rayleigh-Jeffreys Problem with Boundary Slab of Finite Conductivity," *J. Fluid Mech.*, Vol. 32, No. 2, 1968, pp. 393–398.

APPENDIX

Temperature Basis Functions

To properly formulate the eigenvalue problem, we must eliminate the six constants D^k, E^k, M, and N from the expressions defining the temperature basis functions. We proceed from equations (23) and (24) with conditions (14), (15), and (16).

The constants D^k may be removed by applying the condition of zero temperature disturbance at the outer bounding surface. Equation (24) then becomes

$$\theta_k = \sum_i A_i^k \left(\phi_i^k(Z_k) - \phi_i^k(Z_0) \frac{\cosh a_k Z_k}{\cosh a_k Z_0} \right) + E^k \left(\sinh a_k Z_k - \frac{\sinh a_k Z_0}{\cosh a_k Z_0} \cosh a_k Z_k \right) \equiv \sum_i A_i^k \beta_i^k(Z_k) + E^k \gamma^k(Z_k) \tag{A1}$$

where Z_0 is equal to $-1/2$ for $k=1$ and $1/2$ for $k=2$, and where β_i^k and γ^k are defined as indicated in equation (A1).

We may eliminate the constants E^k by matching the fluid and interlayer temperatures to obtain

$$\theta_k = \sum_i A_i^k \left(\beta_i^k(Z_k) - \beta_i^k(-Z_0) \frac{\gamma^k(Z_k)}{\gamma^k(-Z_0)} \right) + \left(M \cosh\left(\frac{a_B}{2}\right) + \frac{C_1}{C_0} N \sinh\left(\frac{a_B}{2}\right) \frac{\gamma^k(Z_k)}{\gamma^k(-Z_0)} \right) \equiv \sum_i a_i^k \delta_i^k(Z_k) + \left\{ M \cosh\left(\frac{a_B}{2}\right) + \frac{C_1}{C_0} N \sinh\left(\frac{a_B}{2}\right) \right\} \frac{\gamma^k(Z_k)}{\gamma^k(-Z_0)} \tag{A2}$$

where C_0 is equal to 1 for $k=1$ and B for $k=2$, and where C_1 is equal to -1 for $k=1$ and $+1$ for $k=2$. The function δ_i^k is defined as indicated in equation (A2).

By matching the fluid and interlayer heat fluxes at either side of the interlayer, we obtain a pair of linear equations for M and N. Defining the constants M_k and N_k as

$$M_k = C_1 a_B \sinh\left(\frac{a_B}{2}\right) - A(1+B) \frac{k}{k_B} \cosh\left(\frac{a_B}{2}\right) D_k \{ \ln[\gamma^k(-Z_0)] \} \tag{A3}$$

$$N_k = a_B \cosh\left(\frac{a_B}{2}\right) - A(1+B) \frac{k}{k_B} \frac{C_1}{C_0} \sinh\left(\frac{a_B}{2}\right) D_k \{ \ln[\gamma^k(-Z_0)] \} \tag{A4}$$

where D_k denotes $d(\ )/dZ_k$ for $k=1, 2$. Then we find

$$N = (k/k_B) \left(\sum_i A_i^2 D_2 \delta_i^2(-Z_0) \right.$$

$$-\frac{M_2}{N_1}\sum_i A_i^1 D_1 \delta_i^1(-Z_0)\Big)\frac{M_1}{M_1N_2-M_2N_1}$$

$$\equiv \sum_i A_i^1 \eta_i^1 + \sum_i A_i^2 \eta_i^2 \tag{A5}$$

and

$$M=\sum_i A_i^1\Big\{D_1\delta_i^2(-Z_0)\frac{1}{M_1}\frac{k}{k_B} + \frac{k}{k_B}\left(\frac{N_1}{M_1N_2-M_2N_1}\right)D_1\delta_i^1(-Z_0)\frac{M_2}{M_1}\Big\} - \sum_i A_i^2\Big\{D_2\delta_i^2(-Z_0)N_1\frac{k}{k_B}\frac{1}{M_1N_2-M_2N_1}\Big\}$$

$$\equiv \sum_i A_i^1 \xi_i^1 + \sum_i A_i^2 \xi_i^2 \tag{A6}$$

Substituting equations (A5) and (A6) into (A2), we obtain the final form for θ_k

$$\theta_k = \sum_i A_i^k\Big\{\delta_i^k(Z_k) + \cosh\left(\frac{a_B}{2}\right)\frac{\gamma^k(Z_k)\,\xi_i^k}{C_0\gamma^k(-Z_0)} + \sinh\left(\frac{a_B}{2}\right)\frac{C_1}{C_0}\frac{\gamma^k(Z_k)}{\gamma^k(-Z_0)}\eta_i^k\Big\} + \sum_i A_i^j\Big\{\cosh\left(\frac{a_B}{2}\right)\frac{\gamma^k(Z_k)}{C_0\gamma^k(-Z_0)}\xi_i^j + \sinh\left(\frac{a_B}{2}\right)\frac{\gamma^k(Z_k)}{C_0\gamma^k(-Z_0)}\eta_i^j\frac{C_1}{C_0}\Big\}$$

$$\equiv \sum_i A_i^k \Phi_i^{kk}(Z_k) + \sum_i A_i^j \Phi_i^{kj}(Z_k), \quad \begin{cases} j=2, & k=1 \\ j=1, & k=2 \end{cases} \tag{25}$$

This gives the form of the temperature basis functions, Φ_i^{kk} and Φ_i^{kj}.

M. M. Razzaque
Assistant Professor
Iowa State University
Ames, Iowa 50011

J. R. Howell
E.C.H. Bantel Professor
of Professional Practice.
Fellow ASME

D. E. Klein
Associate Professor.
Mem. ASME

Department of Mechanical Engineering,
The University of Texas
at Austin,
Austin, Texas 78712

Coupled Radiative and Conductive Heat Transfer in a Two-Dimensional Rectangular Enclosure With Gray Participating Media Using Finite Elements

A numerical solution of the exact equations of coupled radiative/conductive heat transfer and temperature distribution inside a medium, and of the heat flux distribution at all the gray walls of a two-dimensional rectangular enclosure with the medium having uniform absorbing/emitting properties, using the finite element method, is presented. The medium can also have distributed energy sources. Comparison is made to the results of the P-3 approximation method.

Introduction

The finite element method is used to solve numerically the exact expressions of radiative heat transfer coupled with the conductive mode to predict the temperature profile in the medium and the heat flux distributions at all the bounding surface of a two-dimensional rectangular enclosure with a gray absorbing/emitting medium. The walls of the enclosure are considered to be either black or diffuse gray with any specified temperature distribution. Internal heat generation within the medium can also be considered. The exact governing energy balance equation is a highly nonlinear partial integro-differential equation which was solved using the Galerkin finite element method (FEM) with isoparametric, biquadratic, quadrilateral elements and coupled with an iterative technique.

Due to the complexity of coupled radiative/conductive heat transfer problems in the two-dimensional geometry, most of the work that has been reported in this area is confined to the one-dimensional pure radiative case. A finite element approach to combined conductive and radiative heat transfer in one-dimension [1-3] has been attempted. Numerically, both the Monte Carlo method [4, 5] and Hottel's zonal method [6, 7] have been applied to multidimensional computations, and approximation methods [8-14] have been developed for some selected cases of radiative heat transfer. A finite element solution of radiative heat transfer in a two-dimensional rectangular geometry is presented in [15].

The present work is the only numerical analysis of the exact equations of combined radiative-conductive heat transfer in a two-dimensional rectangular geometry with a gray participating medium performed to date. Ratzel [16] has used the spherical-harmonics approach to develop an approximation method to predict the temperature distribution in a medium and the heat flux distribution at all the bounding surfaces of a rectangular enclosure for the combined radiation-conduction case. The FEM results computed in the present study for some similar cases are compared with those of Ratzel.

Analysis

The objective of this analysis is twofold. First, to formulate the exact heat balance equation for the system, and then to write mathematical expressions for the heat fluxes at the bounding surfaces of the enclosure. Second, to apply the finite element technique for solution of the heat balance equation to predict the temperature distribution within the medium and to calculate the heat flux distributions along all the bounding surfaces.

In order to write the heat balance equation for the system, an energy balance is made on a differential volume element within the enclosure. To account for all the incoming radiant energy from the surrounding medium and from the four surrounding walls to the differential element, the interior of the rectangular enclosure is divided into four triangular regions. This configuration is shown in Fig. 1.

Considering radiation and conduction as the modes of heat transfer and with internal heat generation within the medium, the heat balance can be written as follows:

$$-k\nabla^2 T + 4a\sigma T^4 = \int_{4\pi} ai'\,d\omega + Q''' \qquad (1)$$

where the first term is the net conduction heat transfer out of the differential element, the second term is the radiant energy emitted from the differential element, the third term is the total radiant energy absorbed by the differential element that originates from the surrounding medium and the surrounding walls, and the fourth term is the heat generated within the differential element due to internal heat sources. The incoming radiant energy from the medium and the walls can be obtained by integrating the directional radiation intensity i' over all solid angles ω. In this particular geometry, the domain can be divided into four triangular regions as mentioned earlier, and then the incoming radiant energy is obtained by integrating piecewise on each of these triangular regions over the solid angle and summing the results. Thus, in mathematical notation, it can be written as

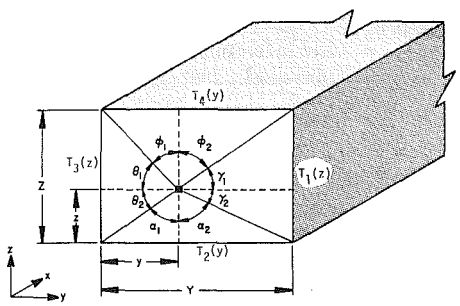

Fig. 1 Rectangular enclosure with the differential volume element and the surrounding triangular regions

Contributed by the Heat Transfer Division and presented at the ASME-JSME Joint Thermal Engineering Conference, Honolulu, Hawaii, March 1983. Manuscript received by the Heat Transfer Division March 14, 1983.

$$\int_{4\pi} i'\,d\omega = \int_{4\pi} i'_{\text{upper}}\,d\omega + \int_{4\pi} i'_{\text{lower}}\,d\omega + \int_{4\pi} i'_{\text{left}}\,d\omega + \int_{4\pi} i'_{\text{right}}\,d\omega \tag{2}$$

Each of the four integals on the right-hand side of equation (2) is again composed of the two integral terms: one being the radiant energy incoming from the wall and the other from the medium. Therefore, the third term in equation (1) is the sum of eight integral terms: four are due to the emission from the four walls and the other four are due to the emission from the four triangular regions of the medium. Deriving these integral terms for this particular geometry and introducing these in equation (1) and nondimensionalizing, one gets the following equation for a gray absorbing/emitting gas with constant absorption coefficient

$$\begin{aligned}
&-2\pi N\nabla^2 u + 2\pi u^4 \\
&= \int_{-\alpha_1}^{\alpha_2} \psi_{o,lo} S_1\left(\frac{z}{\cos\alpha}\right) d\alpha \\
&+ \int_0^z \int_{-\alpha_1}^{\alpha_2} u^4 \frac{1}{\cos\alpha} S_0\left(\frac{z-z^*}{\cos\alpha}\right) d\alpha\, dz^* \\
&+ \int_{-\phi_1}^{\phi_2} \psi_{o,u} S_1\left(\frac{Z-z}{\cos\phi}\right) d\phi \\
&+ \int_z^Z \int_{-\phi_1}^{\phi_2} u^4 \frac{1}{\cos\phi} S_0\left(\frac{z^*-z}{\cos\phi}\right) d\phi\, dz^* \\
&+ \int_{-\theta_1}^{\theta_2} \psi_{o,l} S_1\left(\frac{y}{\cos\theta}\right) d\theta \\
&+ \int_0^y \int_{-\theta_1}^{\theta_2} u^4 \frac{1}{\cos\theta} S_0\left(\frac{y-y^*}{\cos\theta}\right) d\theta\, dy^* \\
&+ \int_{-\gamma_1}^{\gamma_2} \psi_{o,rt} S_1\left(\frac{Y-y}{\cos\gamma}\right) d\gamma \\
&+ \int_y^Y \int_{-\gamma_1}^{\gamma_2} u^4 \frac{1}{\cos\gamma} S_0\left(\frac{y^*-y}{\cos\gamma}\right) d\gamma\, dy^* + S
\end{aligned} \tag{3}$$

where, the nondimensional outgoing radiative heat fluxes for lower, upper, left, and right walls are given for diffusively emitting and reflecting gray surfaces by

$$\psi_{o,lo} = 1 - \left(\frac{1-\epsilon}{\epsilon}\right)\psi_{r,lo} \tag{4}$$

$$\psi_{o,u} = u_4^4 - \left(\frac{1-\epsilon}{\epsilon}\right)\psi_{r,u} \tag{5}$$

$$\psi_{o,l} = u_3^4 - \left(\frac{1-\epsilon}{\epsilon}\right)\psi_{r,l} \tag{6}$$

and

$$\psi_{o,rt} = u_1^4 - \left(\frac{1-\epsilon}{\epsilon}\right)\psi_{r,rt} \tag{7}$$

The boundary conditions for equation (3) are as follows

$$\begin{aligned}
&(i) \quad u(y,0) = 1 \\
&(ii) \quad u(y,Z) = u_4 \\
&(iii) \quad u(0,z) = u_3 \\
&(iv) \quad u(Y,z) = u_1
\end{aligned} \tag{8}$$

The S_o and S_1 functions in equation (3) are defined as

$$S_o(g) \equiv \int_g^\infty K_o(s)\,ds = \int_1^\infty \text{Exp}(-gt)\frac{dt}{t\sqrt{t^2-1}} \tag{9}$$

where K_0 is the modified Bessel function of zero order and

$$S_1(g) \equiv \int_1^\infty \text{Exp}(-gt)\frac{dt}{t^2\sqrt{t^2-1}} \tag{10}$$

The general form of S-functions can be written as

$$S_n(g) = \int_1^\infty \text{Exp}(-gt)\frac{dt}{t^{n+1}\sqrt{t^2-1}} \tag{11}$$

and the recurrence relation is

$$S_n(g) = \int_1^\infty \frac{dt}{t^{n+1}\sqrt{t^2-1}} - \int_0^g S_{n-1}(g^*)\,dg^* \tag{12}$$

where $n = 1,2,3, \ldots\ldots$

The radiative heat flux for the lower wall is given by

$$q_{r,lo} = q_{o,lo} - q_{i,lo} \tag{13}$$

Nomenclature

a = absorption coefficient, 1/m
f = right-hand-side of equation (3)/2π
i = radiation intensity, W/(m^2 – sr)
k = thermal conductivity, W/(m°C)
q = energy flux, energy per unit area and time, W/m^2
Q''' = energy generation per unit volume and time, W/m^3
T = absolute temperature, K
σ = Stefan-Boltzmann constant, W/(m^{2}K^4)
$\alpha_1,\alpha_2,\phi_1,\phi_2,$ $\theta_1,\theta_2,\gamma_1,\gamma_2$ = circumferential angles, radians (Fig. 1)
ω = solid angle, steradian (sr)

Dimensionless Parameters

N = conduction-radiation parameter, $ka/4\sigma T_2^3$
S = heat source, $\pi Q'''/2a\sigma T_2^4$
u = temperature, T/T_2
x = optical thickness coordinate in Cartesian system
y = optical thickness coordinate in Cartesian system
z = optical thickness coordinate in Cartesian system
Y,Z = optical length and height of the rectangular enclosure
ϵ = surface emissivity
ϕ = shape function
ψ = energy flux, $q/\sigma T_2^4$
η,ξ = fractional optical thickness, y/Y, z/Z

Subscripts

i = incoming
l = left
lo = lower
o = outgoing
r = radiative
rt = right
u = upper
1 = surface 1
2 = surface 2
3,4 = surface 3 or 4

Superscripts

$*$ = dummy variable of integration
$'$ = directional quantity

where, $q_{o,lo}$ and $q_{i,lo}$ are the outgoing and the incoming radiative heat fluxes at the lower wall, respectively. Substituting in equation (13) the exact expression for the incoming radiative heat flux for the lower wall of the rectangular enclosure and then introducing the functions S_1 and S_2 and nondimensionalizing, one gets the dimensionless radiative heat flux at the lower wall as

$$\psi_{r,lo}(y,z=0) = \psi_{o,lo}(y,z=0) - \frac{2}{\pi}\left[\int_{-\phi_1}^{\phi_2} \psi_{o,u}\cos\phi S_2\left(\frac{Z}{\cos\phi}\right)d\phi + \int_0^Z \int_{-\phi_1}^{\phi_2} u^4 S_1\left(\frac{z^*}{\cos\phi}\right)d\phi dz^* + \int_0^{\theta_1} \psi_{o,l}\sin\theta S_2\left(\frac{y}{\cos\theta}\right)d\theta + \int_0^y \int_0^{\theta_1} u^4 S_1\left(\frac{y-y^*}{\cos\theta}\right)\tan\theta dy^* + \int_0^{\gamma_1} \psi_{o,ri}\sin\gamma S_2\left(\frac{Y-y}{\cos\gamma}\right)d\gamma + \int_y^Y \int_0^{\gamma_1} u^4 S_1\left(\frac{y^*-y}{\cos\gamma}\right)\tan\gamma d\gamma dy^*\right]. \quad (14)$$

The total heat flux distribution at the lower wall in dimensionless form is given by

$$\psi_{lo}(y,z=0) = -4N\frac{\partial u}{\partial z}\bigg|_{z=0} + \psi_{r,lo}(y,z=0) \quad (15)$$

where,

$-4N\dfrac{\partial u}{\partial z}\Big|_{z=0}$ is the conduction heat flux at the lower wall.

Similarly, the dimensionless radiative heat flux can be derived for the upper wall as

$$\psi_{r,u}(y,z=Z) = \psi_{o,u}(y,z=Z) - \frac{2}{\pi}\left[\int_{-\alpha_1}^{\alpha_2} \psi_{o,lo}\cos\alpha S_2\left(\frac{Z}{\cos\alpha}\right)d\alpha + \int_0^Z \int_{-\alpha_1}^{\alpha_2} u^4 S_1\left(\frac{Z-z^*}{\cos\alpha}\right)d\alpha dz^* + \int_0^{\theta_2} \psi_{o,l}\sin\theta S_2\left(\frac{y}{\cos\theta}\right)d\theta + \int_0^y \int_0^{\theta_2} u^4 S_1\left(\frac{y-y^*}{\cos\theta}\right)\tan\theta\, d\theta\, dy^* + \int_0^{\gamma_2} \psi_{o,ri}\sin\gamma S_2\left(\frac{Y-y}{\cos\gamma}\right)d\gamma + \int_y^Y \int_0^{\gamma_2} u^4 S_1\left(\frac{y^*-y}{\cos\gamma}\right)\tan\gamma\, d\gamma\, dy^*\right] \quad (16)$$

and the total heat flux distribution at the upper wall in dimensionless form can be expressed as

$$\psi_u(y,z=Z) = -4N\frac{\partial u}{\partial z}\bigg|_{z=Z} + \psi_{r,u}(y,z=Z) \quad (17)$$

The dimensionless radiative heat flux for either side wall is given by

$$\psi_{r,l}(y=0,z) = \psi_{o,l}(y=0,z) - \frac{2}{\pi}\left[\int_{-\gamma_1}^{\gamma_2} \psi_{o,ri}\cos\gamma S_2\left(\frac{Y}{\cos\gamma}\right)d\gamma + \int_0^Y \int_{-\gamma_1}^{\gamma_2} u^4 S_1\left(\frac{y^*}{\cos\gamma}\right)d\gamma dy^* + \int_0^{\alpha_2} \psi_{o,lo}\sin\alpha S_2\left(\frac{z}{\cos\alpha}\right)d\alpha + \int_0^z \int_0^{\alpha_2} u^4 S_1\left(\frac{z-z^*}{\cos\alpha}\right)\tan\alpha d\alpha dz^* + \int_0^{\phi_2} \psi_{o,u}\sin\phi S_2\left(\frac{Z-z}{\cos\phi}\right)d\phi + \int_z^Z \int_0^{\phi_2} u^4 S_1\left(\frac{z^*-z}{\cos\phi}\right)\tan\phi d\phi dz^*\right] \quad (18)$$

and the dimensionless total heat flux distribution for either side wall can be given by the following

$$\psi_l(y=0,z) = -4N\frac{\partial u}{\partial y}\bigg|_{y=0} + \psi_{r,l}(y=0,z) \quad (19)$$

$\psi_{o,lo}$, $\psi_{o,u}$, $\psi_{o,l}$, and $\psi_{o,ri}$ in all the preceding heat flux equations are given by equations (4), (5), (6), and (7), respectively.

Finite Element Solution

The Galerkin finite element formulation is applied to equation (3) by writing it in the form

$$-A\nabla^2 u + B(u^3)u = f(y,z,u^4);\ 0\le y\le Y,\ 0\le z\le Z \quad (20)$$

where the left-hand side has been modified from equation (3) by a factor of 2π.

The standard application of the Galerkin method results in the set of nonlinear algebraic equations

$$\sum_{j=1}^{N} K_{ij}\alpha_j = f_i;\quad i=1,2,\ldots N \quad (21)$$

where

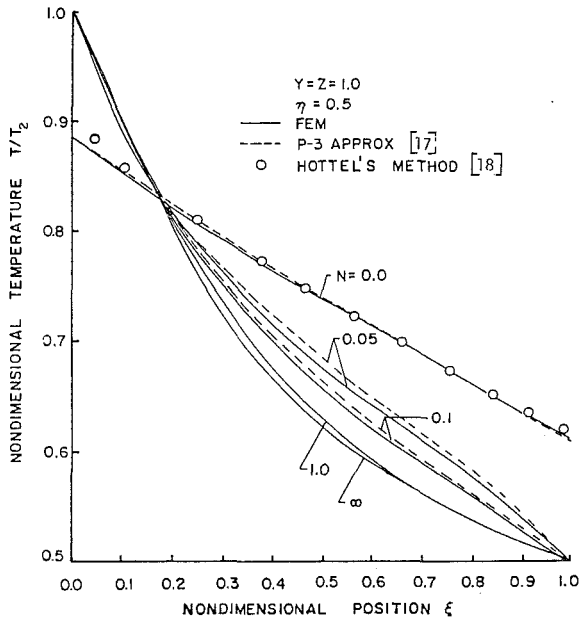

Fig. 2 Nondimensional centerline temperature profiles for different values of N with black walls, bottom wall nodes at nondimensional temperature, u = 1.0, lower corner nodes at u = 0.75, other wall nodes at u = 0.5, S = 0

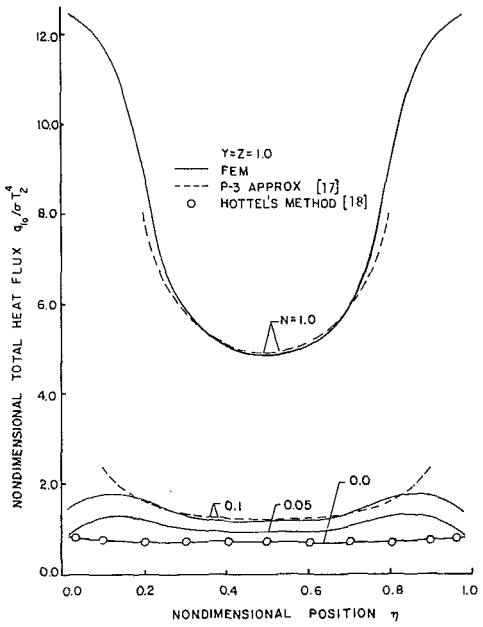

Fig. 3 Nondimensional total heat flux at the lower wall for different values of N with black walls, bottom wall nodes at nondimensional temperature, $u = 1.0$, lower corner nodes at $u = 0.75$, other wall nodes at $u = 0.5$, $S = 0$

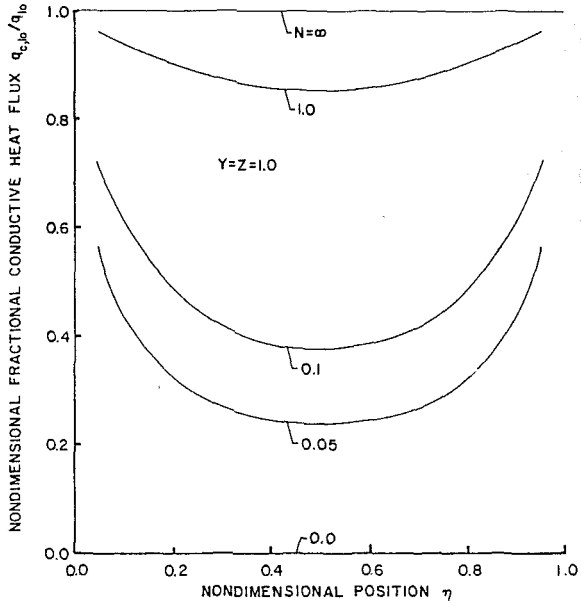

Fig. 5 Fractional conductive heat flux at the lower wall for different values of N with black walls, bottom wall nodes at nondimensional temperature, $u = 1.0$, lower corner nodes at $u = 0.75$, other wall nodes at $u = 0.5$

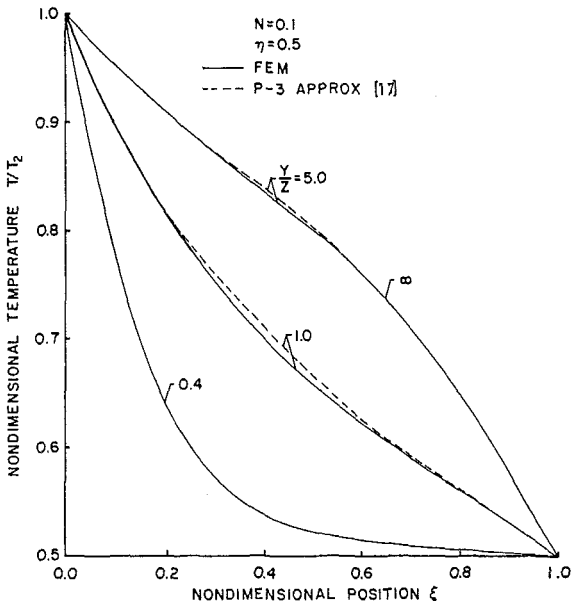

Fig. 4 Nondimensional centerline temperature profiles in rectangular enclosures of different aspect ratio with black walls, bottom wall nodes at nondimensional temperature, $u = 1.0$, lower corner nodes at $u = 0.75$, other wall nodes at $u = 0.5$, $S = 0$

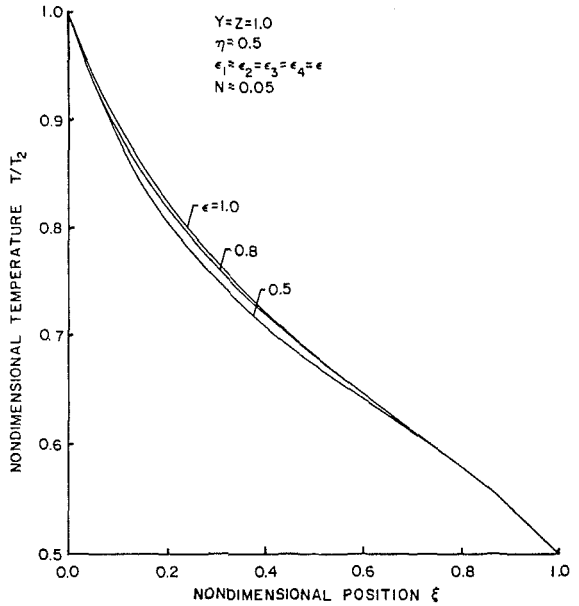

Fig. 6 Nondimensional centerline temperature profiles in a square enclosure with gray walls, bottom wall nodes at nondimensional temperature, $u = 1.0$, lower corner nodes at $u = 0.75$, other wall nodes at $u = 0.5$, $S = 0$

$$K_{ij} = \int_\Omega [A \nabla \phi_j \cdot \nabla \phi_i + B(U^3)\phi_j \phi_i] d\Omega; \quad i,j = 1,2, \ldots N \tag{22}$$

and

$$f_i = \int_\Omega f(y,z,U^4)\phi_i d\Omega; \quad i = 1,2, \ldots N \tag{23}$$

and α_j are unknown coefficients to be found by solution of equation (21) iteratively. The ϕ's are the "shape functions." After completion of solution of equation (21), u is given by

$$u(y,z) \approx U(y,z) = \sum_{j=1}^{N} \alpha_j \phi_j (y,z) \tag{24}$$

In this analysis, the system domain was subdivided into isoparametric, biquadratic, quadrilateral elements having 9 degrees of freedom (or nodes) per element. Sixteen elements in a square enclosure of unit optical thickness gave good results. The shape function was chosen to be a Lagrangian tensor product biquadratic. The numerical integration was performed using a second-order Gaussian quadrature integration scheme. In all cases, the relative change in u between the final iterations was less than 0.001 at all nodes. The computer time requirement for solution was strongly dependent on the values

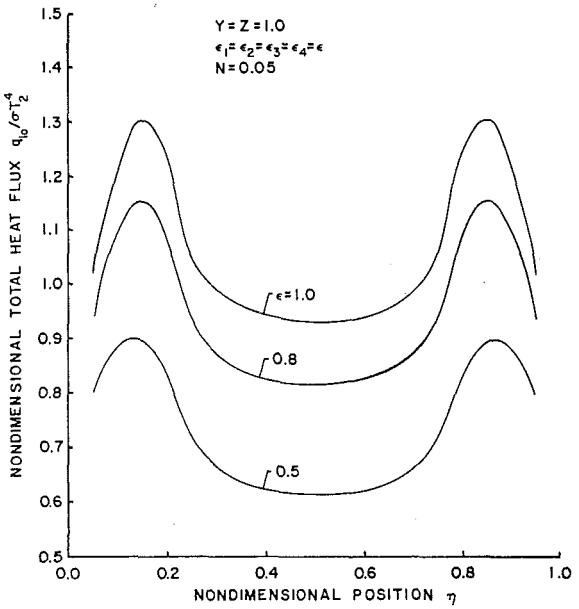

Fig. 7 Nondimensional total heat flux at the lower wall in a square enclosure with gray walls, bottom wall nodes at nondimensional temperature, $u = 1.0$, lower corner nodes at $u = 0.75$, other wall nodes at $u = 0.5$, $S = 0$

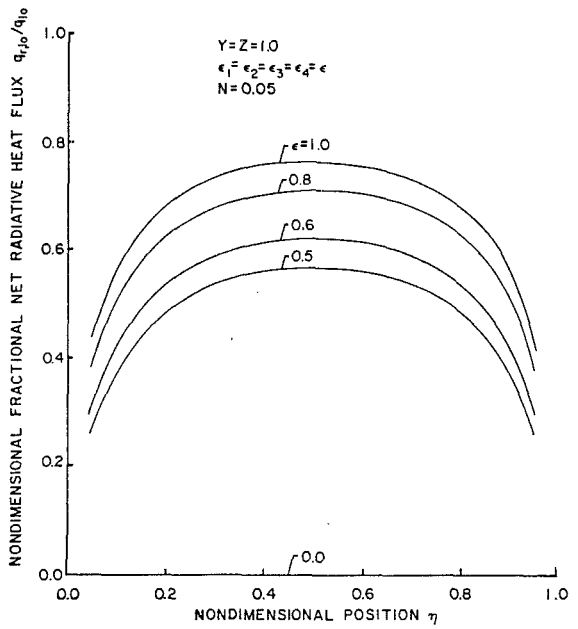

Fig. 8 Fractional net radiative heat flux at the lower walls in a square enclosure with gray walls, bottom wall nodes at nondimensional temperature, $u = 1.0$, lower corner nodes at $u = 0.75$, other wall nodes at $u = 0.5$, $S = 0$

Table 1 Radiation-conduction results

Nondimensional total heat fluxes, bottom wall nodes at nondimensional temperature, $u = 1.0$, lower corner nodes at $u = 0.75$, other wall nodes at $u = 0.5$: $Y = Z = 1.0$, $\epsilon_1 = \epsilon_2 = \epsilon_3 = \epsilon_4 = 0.5$, $S = 0.0$

Nondimensional position η	Bottom (hot) wall nondimensional heat flux		
	$N = 1.0$	$N = 0.1$	$N = 0.05$
0.1	11.382	1.447	0.887
0.2	8.488	1.243	0.831
0.3	5.528	0.922	0.657
0.4	4.687	0.843	0.621
0.5	4.508	0.828	0.614
	Side (cold) wall nondimensional heat flux		
	$N = 1.0$	$N = 0.1$	$N = 0.05$
0.1	−10.789	−1.222	−0.685
0.2	−7.413	−0.926	−0.558
0.3	−4.017	−0.565	−0.367
0.4	−2.662	−0.419	−0.288
0.5	−1.892	−0.330	−0.237
0.6	−1.332	−0.260	−0.195
0.7	−0.906	−0.201	−0.158
0.8	−0.592	−0.152	−0.126
0.9	−0.302	−0.097	−0.086
	Top (cold) wall nondimensional heat flux		
	$N = 1.0$	$N = 0.1$	$N = 0.05$
0.1	−0.275	−0.112	−0.102
0.2	−0.479	−0.156	−0.136
0.3	−0.641	−0.185	−0.156
0.4	−0.740	−0.203	−0.168
0.5	−0.775	−0.209	−0.172
	Total nondimensional heat fluxes		
	$N = 1.0$	$N = 0.1$	$N = 0.05$
Bottom wall	7.398	1.089	0.730
Side wall	−3.440	−0.470	−0.301
Top wall	−0.536	−0.164	−0.140
Total	−0.018	−0.015	−0.012
% error	0.240	1.300	1.600

of conduction/radiation parameter (N) of the medium and the wall emissivity (ϵ). For the 16-element solutions and for the range of values of N and ϵ chosen in this analysis, about 100–1000 s of CPU time on the CDC Dual Cyber computer were required for convergence. More details of the method are available in [16].

Because convergence of the solutions probably takes fewer iterations as the number of elements is increased, the com-

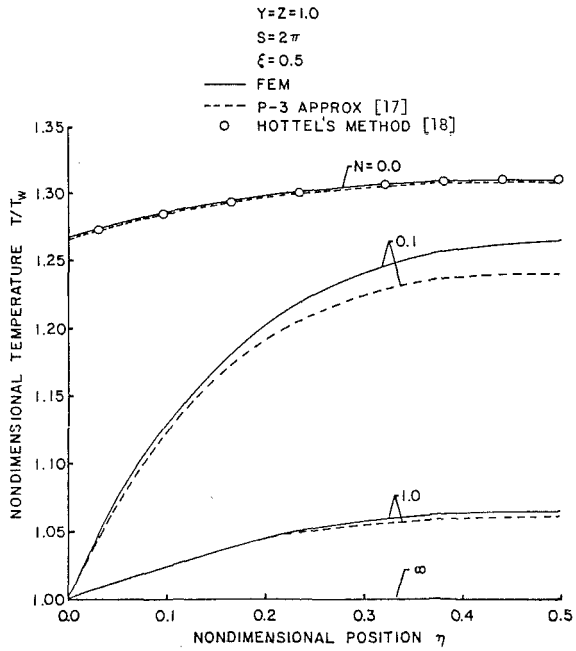

Fig. 9 Nondimensional centerline temperature profiles in a square enclosure for different values of N with internal heat generation and black walls at nondimensional temperature, $u = 1.0$

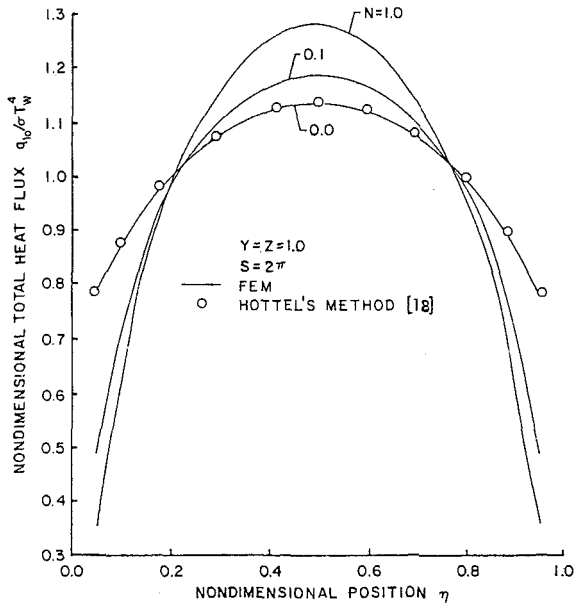

Fig. 10 Nondimensional total heat flux at the lower wall in a square enclosure for different values of N with internal heat generation and black walls at nondimensional temperature, $u = 1.0$

puter time required is not expected to be proportional to the number of elements chosen. However, the method, while exact, may be slower than other more approximate techniques. The computer program was not optimized to reduce computer CPU time.

Results and Discussion

The centerline temperature and the bottom (hot) wall heat flux distributions for a square enclosure with different values of conduction/radiation parameter N are shown in Fig. 2 and Fig. 3, respectively. Figure 4 presents the centerline temperature distributions of the medium for different aspect ratios (Y/Z) and with $N = 0.1$. The peaks in the heat flux curve near the corners are due to the fact that the lower corner nodes are at a lower temperature than the rest of the bottom wall nodes. Comparison of the temperature profiles with those from the P-3 approximation [17] shows good agreement. The P-3 approximation results for heat flux agree reasonably well in the midregion of the lower wall, but deviate considerably from that of FEM near the side (cold) walls. For this physical model, exact solutions do not exist. Since the FEM is a numerical solution of the exact governing equation, it should be the most exact solution within the usual limits of numerical accuracy. The P-N methods are inaccurate near boundaries and at small optical thickness.

Figure 5 shows the fractional conductive heat flux (ratio of conductive to total heat flux) distributions at the bottom wall for various values of N. These results show the relative importance of conductive heat transfer as a function of N. One can see that for $N > 1$, the system is conduction dominated because more than 85 percent of the heat transfer is due to the conduction mode. For $N < 0.05$, the contribution to heat transfer by the conduction mode is < 25 percent and thus radiative heat transfer plays the dominant role.

Temperature profiles of the medium and bottom (hot and gray) wall heat transfer rates for various wall emissivities ϵ and with $N = 0.05$ are shown in Fig. 6 and Fig. 7, respectively. All the walls are assumed to have the same radiative properties (diffuse emissivity, ϵ). Figure 8 presents the fractional net radiative heat flux (ratio of net radiative heat flux to total heat flux) at the bottom wall for wall emissivities ranging from 1 to 0. As ϵ decreases, the net radiative heat flux through the wall also decreases and becomes zero at $\epsilon = 0$.

The heat flux profiles have the peaks near the corners of the hot wall because the temperature $U(y,0)$ is forced to approach the corner temperature at $y = 0, Y$. This is necessary because the shape functions chosen require a continuous temperature profile around their boundary.

Table 1 shows the heat flux distributions on the bottom (hot and gray), the top (cold and gray) and the side (cold and gray) walls. It also shows the total heat transfer through the walls, their energy balance, and the percent error.

Figure 9 shows the centerline temperature profiles in the medium for different values of N with uniform internal heat generation and Fig. 10 presents the total heat flux distributions at the bottom wall. The integrals under the curves in Fig. 10 must be equal since the total amount of heat energy leaving the system for any value of N must be the same as the total heat generated within the enclosure at steady state. Comparison of the temperature profiles with those from the P-3 approximation shows fairly good agreement.

Conclusion

The method developed in the current study of coupled radiative/conductive heat transfer in a multidimensional geometry can provide accurate temperature distributions in the medium as well as wall heat flux distributions near corners and in media with very small opacities where approximation methods break down. Although this paper presents results limited to two-dimensional rectangular enclosures, the method used can be applied to any two- or three-dimensional enclosure using other shape functions. As with all methods, it may be quite difficult to carry through the numerical integrations in such cases; however, within those limitations, the method will provide exact solutions within the bounds of numerical accuracy. The drawback of the current method, as for most others, is that for very low values of wall emissivity and conduction/radiation parameter the method requires a substantial amount of computer time to achieve convergence. This difficulty may be overcome by using a good initial guess of the temperature field and the outgoing radiative heat flux values at the walls.

As discussed in [15, 19–20], the use of the biquadratic finite element shape function was found to be the best compromise between the accuracy of results and the computer time requirement.

References

1 Wu, S. T., Ferguson, R. E., and Altgilbers, L. L., "Application of Finite Element Techniques to the Interaction of Conduction and Radiation in Participating Medium," *Heat Transfer and Thermal Control*, edited by A. L. Crosbie, Vol. 78 of *Progress in Astronautics and Aeronautics*, AIAA, New York, 1980, pp. 61–91.

2 Fernandes, R. L., Francis, J., and Reddy, J. N., "A Finite-Element Approach to Combined Conductive and Radiative Heat Transfer in a Planar Medium," *Heat Transfer and Thermal Control*, edited by A. L. Crosbie, Vol. 78 of *Progress in Astronautics and Aeronautics*, AIAA, New York, 1980, pp. 92–109.

3 Fernandes, R. L., and Francis, J. E., "Combined Radiative and Conductive Heat Transfer in a Planar Medium with a Flux Boundary Condition Using Finite Elements," AIAA Paper 82-0910, St. Louis, June 7, 1982.

4 Siegel, R., and Howell, J. R., *Thermal Radiation Heat Transfer*, 2d ed., McGraw-Hill, New York, 1981.

5 Taniguchi, H., "The Radiative Heat Transfer of Gas in a Three-Dimensional System Calculated by Monte Carlo Method," *Bull. JSME*, Vol. 12, 1969, pp. 67–78.

6 Hottel, H. C., and Sarofim, A. F., *Radiative Transfer*, McGraw-Hill, New York, 1967.

7 Hottel, H. C., and Cohen, E. S., "Radiant Heat Exchange in a Gas-Filled Enclosure: Allowance for Non-uniformity of Gas Temperature," *AICHE Journal*, Vol. 4, No. 1, 1958, pp. 3–14.

8 Breig, W. F., and Crosbie, A. L., "Two-Dimensional Radiative Equilibrium," *Journal of Mathematical Analysis and Applications*, Vol. 46, No. 1, 1974, pp. 104–125.

9 Modest, M. F., "Two-Dimensional Radiative Equilibrium of a Gray Medium in a Plane Layer Bounded by Gray Nonisothermal Walls," ASME JOURNAL OF HEAT TRANSFER, Vol. 96, No. 4, 1974, pp. 483–488.

10 Yuen, W. W., and Tien, C. L., "A Successive Approximation Approach to Problems in Radiative Transfer with a Differential Approximation," ASME JOURNAL OF HEAT TRANSFER, Vol. 102, No. 1, 1980, pp. 86–91.

11 Glatt, L. and Olfe, D. B., "Radiative Equilibrium of a Gray Medium in a Rectangular Enclosure," *J. Quantitative Spectroscopy and Radiative Transfer*, Vol. 13, No. 9, 1973, pp. 881–895.

12 Modest, M. F., "Radiative Equilibrium in a Rectangular Enclosure Bounded by Gray Walls," *J. Quantitative Spectroscopy and Radiative Transfer*, Vol. 15, No. 6, 1975, pp. 445–461.

13 Yuen, W. W., and Wong, L. W., "Radiative Transfer in a Rectangular Enclosure with a Gray Medium," ASME Paper No. 80-HT-101, 1980.

14 Siddall, R. G., and Selcuk, N., "Evaluation of a New Six-Flux Model for Radiative Transfer in Rectangular Enclosure," *Trans. I. Chem. E.*, Vol. 57, No. 13, 1979.

15 Razzaque, M. M., Howell, J. R., and Klein, D. E., "Finite-Element Solution of Radiative Heat Transfer in a Two-Dimensional Rectangular Enclosure with Gray Participating Media," ASME Paper No. 82-WA/HT-51, ASME Winter Annual Meeting, Phoenix, Ariz., Nov. 1982; accepted as Note for ASME JOURNAL OF HEAT TRANSFER.

16 Razzaque, M. M., "Finite Element Analysis of Combined Mode Heat Transfer, Including Radiation in Gray Participating Media," Ph.D. dissertation, Department of Mechanical Engineering, The University of Texas at Austin, May 1982.

17 Ratzel, A. C., "P-N Differential Approximation for Solution of One- and Two-Dimensional Radiation and Conduction Energy Transfer in Gray Participating Media," Ph.D. dissertation, The University of Texas at Austin, 1981.

18 Larsen, M., "Hottel Zone Code," developed for Ph.D. research at The University of Texas at Austin, Aug. 1981.

19 Razzaque, M. M., Howell, J. R., and Klein, D. E., "Finite Element Solution of Combined Radiative, Convective and Conductive Heat Transfer Problems," *Trans. Am. Nucl. Soc.*, Vol. 38, 1981, pp. 334–336.

20 Razzaque, M. M., Howell, J. R., and Klein, D. E., "Finite Element Solution of Heat Transfer for Gas Flow through a Tube," *AIAA Journal*, Vol. 20, No. 7, July 1982, pp. 1015–1019.

Transient Response of the Counterflow Heat Exchanger

F. E. Romie
Palos Verdes Estates, Calif. 90274
Assoc. Mem. ASME

The exit fluid temperature responses are presented for a unit step increase in the entrance temperature of either of the fluids of a counterflow heat exchanger. The exit temperature response histories are functions of four parameters, three of which are commonly used to define the steady-state temperature distributions in the exchanger. The responses are found using a finite difference method and are represented by simple empirical equations for a range of the four parameters believed appropriate for many technical applications.

Introduction

Knowledge of the transient behavior of the temperatures of fluids leaving heat exchangers is required for process control applications. The purpose of this paper is to present, for the counterflow heat exchanger, the exit fluid temperatures that obtain in response to a unit step change in the entrance temperature of either fluid. The exit temperature response histories are found to be dependent on four parameters, three of which are commonly used to define the steady-state temperature distributions of the exchanger core and the two fluids. The responses are found by use of a finite difference method and are represented by two empirical equations for a range of the four parameters believed to be appropriate for a large number of technical applications.

London and co-workers in several papers summarized in [1] give the counterflow heat exchanger exiting gas temperatures for a unit step change in the entrance temperature of either gas. Their responses were found by use of a thermal-electric analog and are restricted to gas-to-gas exchangers in which the capacity rates of the two gases are equal. These two restrictions are not used in this paper: the fluids can be liquids or gases and can have different capacity rates.

The Differential Equations

The counterflow heat exchanger analyzed is shown schematically in Fig. 1 and is defined by the following idealizations:

1 The thermal conductances, $(hA)_a$ and $(hA)_b$, are uniform and constant as are the fluid capacity rates, $(wc)_a$ and $(wc)_b$, and the thermal capacitance, WC, of the exchanger core.

2 No heat is conducted in the axial direction in the exchanger core or in the two fluids. The core wall offers no thermal resistance to flow of heat from one fluid to the other.

3 The exchanger shell or shroud is adiabatic and influences neither the steady-state nor the transient behavior of the fluid temperatures.

Three partial differential equations are required to define the behavior of the exchanger. An energy balance on an elemental length of the exchanger core gives the first equation.

$$WC\frac{\partial T}{\partial t} = (hA)_a(\tau_a - T) + (hA)_b(\tau_b - T) \tag{1}$$

The remaining two equations relate the heat flow from the exchanger core element to the change in temperature of the two fluids.

$$(hA)_a(T-\tau_a) = L(Ax\rho c)_a\left[\frac{\partial \tau_a}{\partial t} + u_a\frac{\partial \tau_a}{\partial x}\right] \tag{2}$$

$$(hA)_b(T-\tau_b) = L(Ax\rho c)_b\left[\frac{\partial \tau_b}{\partial t} - u_b\frac{\partial \tau_b}{\partial x}\right] \tag{3}$$

These three equations will be written using the following dimensionless variables and parameters.

$$\theta = (t - x/u_a)\frac{(wc)}{WC}, X = \frac{x}{L}, \frac{1}{Ntu} = (wc)\left(\frac{1}{(hA)_a} + \frac{1}{(hA)_b}\right)$$

$$E = \frac{(wc)_b}{(wc)_a}, R = \frac{(hA)_b}{(hA)_a}, V = \frac{(wc)}{WC}\left(\frac{L}{u_a} + \frac{L}{u_b}\right)$$

$$N_a = \left(\frac{hA}{wc}\right)_a, N_b = \left(\frac{hA}{wc}\right)_b$$

For the definitions of V, θ, and Ntu (number of transfer units), (wc) is the lesser of $(wc)_a$ and $(wc)_b$. The parameters N_a and N_b are not independent of Ntu, E and R: from the definitions of the five parameters.

$$N_a = E\,Ntu\left(\frac{1+R}{R}\right), N_b = Ntu(1+R), \qquad (E \le 1) \tag{4}$$

$$N_a = Ntu\left(\frac{1+R}{R}\right), N_b = \frac{Ntu}{E}(1+R), \qquad (E > 1) \tag{5}$$

Introduction of the variable θ requires a change of variable in equations (1), (2), and (3). With the change in variable and the continuity relations, $(wc)_a = (\rho cA_x)_a u_a$ and $(wc)_b = (\rho cA_x)_b u_b$, the equations become

$$\frac{\partial T}{\partial \theta} = Ntu\left(\frac{1+R}{R}\right)(\tau_a - T) + Ntu(1+R)(\tau_b - T) \tag{6}$$

$$N_a(T-\tau_a) = \frac{\partial \tau_a}{\partial X} \tag{7}$$

$$N_b(T-\tau_b) = -\frac{\partial \tau_b}{\partial X} + V\frac{\partial \tau_b}{\partial \theta} \tag{8}$$

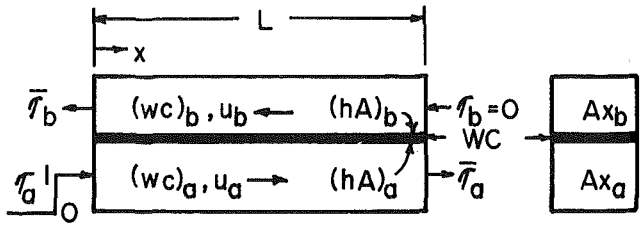

Fig. 1 Schematic of the counterflow heat exchanger

Contributed by the Heat Transfer Division for publication in the JOURNAL OF HEAT TRANSFER. Manuscript received by the Heat Transfer Division April 18, 1983.

These equations have been solved, using an explicit finite difference (FD) method, with the following conditions $\tau_a = \tau_b = T = 0$ for $\theta < 0$ and $\tau_a\ (x = 0) = 1$, $\tau_b\ (x = 1) = 0$ for $\theta > 0$.

The solution for τ_a at $\theta = 0$ can be found by following the first cross-sectional lamina of fluid a which enters the exchanger at $x = 0$ and $t = 0$ with a temperature of unity and flows through the core with a velocity u_a. This first lamina sees the wall at zero temperature during its travel through the exchanger. Therefore its temperature, from equation (7), is exp $(-N_a\ x/L)$. At time $t = x/u_a$ $(\theta = 0)$, it reaches the location x with a temperature exp $(-N_a\ x/L)$. The exit temperature, $\bar{\tau}_a$ of fluid a $[\bar{\tau}_a = \tau_a\ (x = L)]$ is thus zero for $t < L/u_a$ $(\theta < 0)$ and jumps to exp $(-N_a)$ when $t = L/u_a$ $(\theta = 0)$. The time L/u_a is the delay in the response of the fluid a exit temperature. The exit temperature $\bar{\tau}_b$ of fluid b $[\bar{\tau}_b = \tau_b\ (x = 0)]$ has no delay and no discontinuity in its response. Note that θ is always $(t - L/u_a)\ (wc)/WC$ when associated with $\bar{\tau}_a$ and $t(wc)/WC$ when associated with $\bar{\tau}_b$.

The temperatures τ_a, τ_b, and T are seen to be the responses to a unit step increase in the inlet temperature of fluid a. (The subscripts a and b always designate the stepped and unstepped fluids, respectively. Either fluid of an exchanger can be the a fluid and is thus the stepped fluid.) Equations (6), (7), and (8) are linear with constant coefficients and therefore the fact that the responses are initially zero implies nothing about the operating conditions of the exchanger at the time of the transient: the exchanger may be operating in the steady state or may be responding to other disturbances of the inlet fluid temperatures. Superposition is applicable.

The Steady-State Responses

The steady-state responses are obtained as θ increases without limit. In the steady state, the derivatives with respect to θ are zero, and equations (6), (7), and (8) become ordinary differential equations which can be solved for the steady-state exit temperature $\bar{\tau}_{b\infty}$ of fluid b.

$$\bar{\tau}_{b\infty} = \frac{1 - e^{\frac{(E-1)N_b}{1+R}}}{1 - E\, e^{\frac{(E-1)N_b}{1+R}}} \tag{9}$$

Using equations (4) or (5) as appropriate,

$$\bar{\tau}_{b\infty} = \frac{1 - e^{(E-1)Ntu}}{1 - E\, e^{(E-1)Ntu}} \quad , \quad (E<1) \tag{10}$$

$$\bar{\tau}_{b\infty} = \frac{Ntu}{1 + Ntu} \quad , \quad (E=1) \tag{11}$$

$$\bar{\tau}_{b\infty} = \frac{1 - e\left(1 - \frac{1}{E}\right)Ntu}{1 - E\, e\left(1 - \frac{1}{E}\right)Ntu} \quad , \quad (E>1) \tag{12}$$

And, for all E,

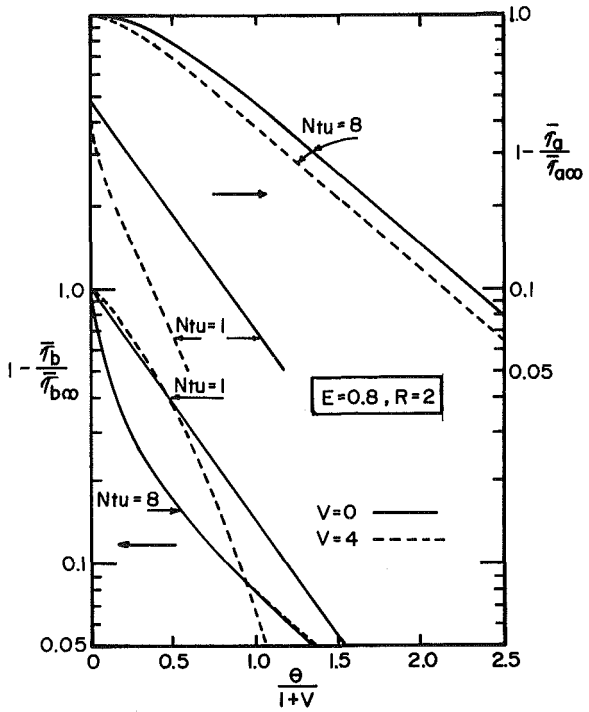

Fig. 2 Complements of the normalized responses for typical cases

Nomenclature

A = heat transfer area, m^2; also coefficient in equation (15)
Ax = cross-sectional area for fluid flow, m^2
a = coefficient in equation (15)
B,b = coefficients in equation (15)
C = unit heat capacity of core material, J/°C kg; also coefficient in equation (16)
c = unit heat capacity of fluid, J/°C kg; also coefficient in equation (16)
D,d = coefficients in equation (16)
E = $(wc)_b/(wc)_a$, capacity rate ratio, dimensionless
h = thermal conductance per unit heat transfer area, W/C m^2
K_0 = function defined following equation (23)
L = fluid flow length of exchanger, m
N = hA/wc, dimensionless
Ntu = number of transfer units, defined following equation (3), dimensionless
R = $(hA)_b/hA)_a$, conductance ratio, dimensionless
s = Laplace parameter
t = time, s
T = core temperature, °C
u = fluid velocity in core, m/s; also argument of function
V = defined following equation (3), dimensionless
v = argument of function
W = mass of exchanger core, kg
w = mass flow rate of fluid, kg/s
(wc) = lesser of $(wc)_a$ and $(wc)_b$, W/°C
X = x/L, dimensionless; also transfer function
x = distance from fluid a entrance, m
θ = $(t-x/u_a)\ (wc)/WC$, dimensionless
ρ = fluid density, kg/m^3
τ = fluid temperature, °C
$\bar{\tau}$ = fluid exit temperature, °C

Subscripts

a = stepped fluid
b = unstepped fluid
∞ = steady-state response

$$\bar{\tau}_{b\infty}(Ntu,E) = \frac{1}{E}\bar{\tau}_{b\infty}\left(Ntu,\frac{1}{E}\right) \quad , \quad (\text{all } E) \tag{13}$$

When $E \ll 1$, $\bar{\tau}_{b\infty}$ is the thermal effectiveness of the exchanger (see, for example, [2]).

A simple energy balance that equates, in the steady state, the heat flow from fluid a to the heat flow to fluid b gives $(wc)_a\,(1-\bar{\tau}_{a\infty}) = (wc)_b\,\bar{\tau}_{b\infty}$.

$$\bar{\tau}_{a\infty} = 1 - E\,\bar{\tau}_{b\infty} \quad , \quad (\text{all } E) \tag{14}$$

Equations (13) and (14) apply to exchangers of all configurations (counterflow, parallelflow, crossflow, etc., single and multipass).

Results of Calculation

The preceding equations show that the exit temperature response histories, $\bar{\tau}_a(\theta)$ and $\bar{\tau}_b(\theta)$, are expressible in terms of four parameters: Ntu, E, R, and V. Figure 2 shows typical responses for several values of the parameters. The responses are normalized by dividing them by their final values to give $\bar{\tau}_a/\bar{\tau}_{a\infty}$ and $\bar{\tau}_b/\bar{\tau}_{b\infty}$, which approach unity as θ increases. The shape of the curves in Fig. 2 suggests that the responses can be represented in a compact empirical form.

$$\frac{\bar{\tau}_a}{\bar{\tau}_{a\infty}} = 1 - A\,e^{-\frac{a\theta}{1+V}} - B\,e^{-\frac{b\theta}{1+V}} \tag{15}$$

$$\frac{\bar{\tau}_b}{\bar{\tau}_{b\infty}} = 1 - C\,e^{-\frac{c\theta}{1+V}} - D\,e^{-\frac{d\theta}{1+V}} \tag{16}$$

For $\theta = 0$, $\bar{\tau}_a = \exp(-N_a)$, and $\bar{\tau}_b = 0$. Therefore, $A + B = 1 - \exp(-N_a)/\bar{\tau}_{a\infty}$ and $C + D = 1$. The term $(1 + V)$ is introduced as a divisor of θ because it is found that this procedure effectively gives the complete dependence of the $\bar{\tau}_b$ responses on V when Ntu is 2 or greater.

Table 1 for $V = 0$ and Table 2 for $V = 4$ give the coefficients A, a, B, b, and C, c, D, d for the 36 combinations of the following parameter values: $Ntu = 1, 2, 4, 8$; $E = 0.8, 1, 1.25$; and $R = 0.5, 1, 2$. In addition, for $E = 1$ and $R = 1$, Table 1 gives the coefficients for the 16 combinations of $Ntu = 1, 2, 4, 8$ and $V = 1, 2, 4, 8$. Table 3 gives $\bar{\tau}_{a\infty}$ and $\bar{\tau}_{b\infty}$ for the values of Ntu and E used in Tables 1 and 2.

Equations (15) and (16) represent the normalized temperature histories computed by the FD method with an accuracy adequate for most application purposes. (The accuracy of the FD solutions is treated in a following section.) For the 168 temperature responses represented in Tables 1 and 2, the maximum absolute difference, at any time, between the response histories given by equations (15) and (16) and by the FD solutions is $\leqslant 0.005$ for 86 cases, $\leqslant 0.01$ for 100 cases, $\leqslant 0.02$ for 144 cases, $\leqslant 0.043$ for 165 cases, and $\leqslant 0.065$ for all cases. The three cases for which the maximum difference is greater than 0.043 but 0.065 or less occur in $\bar{\tau}_a/\bar{\tau}_{a\infty}$ with $V = 0$ and $Ntu = 8$. Reference to Table 3 shows that $\bar{\tau}_{a\infty}$ is small compared to the excitation (unity) for $Ntu = 8$, so that the actual temperature differences for the three cases are quite small. (The differences were evaluated at $\theta/(1 + V) = kn$ $(n = 0, 1, 2 \ldots N)$ in which N is the first value of n for which the normalized temperature response is greater than 0.95. The value of the constant k in most cases was 0.2, but 0.1 was used as necessary to insure that N was seven or greater.)

For most application purposes the normalized temperature responses, $\bar{\tau}_b/\bar{\tau}_{b\infty}$, for the unstepped fluid can be considered to be independent of E and R ($E = 0.8$ to 1.25, $R = 0.5$ to 2.0). In addition, for $Ntu \geq 2$, the $\bar{\tau}_b$ response is not a function of V, except as indicated by the term $(1 + V)$ in equation (16). Therefore, for $Ntu \geq 2$, the coefficients C, c, D, and d can be treated as functions of Ntu only.

Ntu	2	4	8
C	0.748	0.500	0.274
c	2.15	1.70	1.12
D	0.252	0.500	0.726
d	4.71	7.59	8.63

For all of the parameter combinations ($Ntu \neq 1$) represented in Tables 1 and 2, these values of the coefficients give normalized temperature responses that differ, in the worst case, from the FD temperature responses by a maximum absolute difference of 0.032. Interpolation of the coefficients for intermediate values of Ntu is conveniently carried out by plotting the coefficients versus log (Ntu).

The numerical work shows that

$$\frac{\bar{\tau}_b}{\bar{\tau}_{b\infty}}(\theta,Ntu,E,R,V) = \frac{\bar{\tau}_b}{\bar{\tau}_{b\infty}}(\theta,Ntu,1/E,1/R,V) \tag{17}$$

When first one fluid of an exchanger is the stepped fluid and then the other fluid of the exchanger is the stepped fluid, the values of E and R in the two cases are reciprocals, but the values of Ntu, V, and the factor wc/Wc of t in θ are unchanged. Thus the interpretation of equation (17) is that the normalized exit temperature history of the unstepped fluid will be the same irrespective of which fluid of the exchanger is the stepped fluid. Equation (17) is reflected in Tables 1 and 2 by the fact that C, c, D, and d are the same, for example, for $Ntu = 4$, $E = 0.8$, $R = 2$, $V = 4$ and $Ntu = 4$, $E = 1.25$, $R = 0.5$, $V = 4$. Combining equations (13) and (17) shows that

$$\bar{\tau}_b(\theta,Ntu,E,R,V) = \frac{1}{E}\bar{\tau}_b(\theta,Ntu,1/E,1/R,V) \tag{18}$$

Equation (17) also applies [3] to the gas-to-gas ($V = 0$) crossflow heat exchanger. Therefore it seems evident that the interpretation of equation (17) applies to exchangers of all configurations. As previously noted, equation (13) applies to exchangers of all configurations, and therefore equation (18) should apply to exchangers of all configurations. Specifically, when the entrance temperature of first one fluid and then the other fluid of an exchanger is stepped, the responses $\bar{\tau}_b$ of the unstepped fluids in the two cases will differ only by the factor E.

The value of V can be considered to be zero when both fluids are gases. This can be shown by using the continuity relations, $(wc)_a = (\rho cAx)_a\,u_a$ and $(wc)_b = (\rho cAx)_b\,u_b$, to write alternate forms of the definition of V.

$$V = \frac{(\rho cAx)_b L}{WC}\left(1 + \frac{u_b}{u_a}\right) \quad , \quad (E > 1) \tag{19}$$

$$V = \frac{(\rho cAx)_a L}{WC}\left(1 + \frac{u_a}{u_b}\right) \quad , \quad (E < 1) \tag{20}$$

The two velocities will generally be of the same magnitude, so the terms in parentheses sum to roughly two. The factors of the parentheses terms are the ratios of the thermal capacitance of the fluids contained, at any instant, in the exchanger to the thermal capacitance of the exchanger core. This ratio is typically very small ($\lesssim 0.01$) if the fluid is a gas and thus V can be equated to zero when both fluids are gases. The smallness of the capacitance ratio for gases also means that gas a must be replaced many times (t must be many times L/u_a) to effect an appreciable change in the temperature of the core. Consequently, the delay time L/u_a is very small compared to the duration of the transient and can be set equal to zero when fluid a is a gas.

Transfer Functions

The form of equations (15) and (16) permits simple expression of the transfer functions (see, for example, [4]) $X_a(s)$ and $X_b(s)$ of $\bar{\tau}_a(t)$ and $\bar{\tau}_b(t)$ for the counterflow heat exchanger.

Table 1 Coefficients for equations (15) and (16)

E	R	V	A C	a c	B D	b d	A C	a c	B D	b d	A C	a c	B D	b d	A C	a c	B D	b d
			Ntu = 1				Ntu = 2				Ntu = 4				Ntu = 8			
0.8	0.5	0	1.154	1.96	-0.311	3.82	1.760	2.16	-0.780	4.40	2.122	1.82	-1.122	3.88	2.282	1.28	-1.282	2.90
			0.937	2.01	0.063	4.41	0.734	2.20	0.266	6.17	0.479	1.86	0.521	7.90	0.276	1.36	0.724	9.24
0.8	1.0	0	0.686	1.83	-0.034	4.31	1.119	2.02	-0.213	5.08	1.567	1.74	-0.572	4.59	1.878	1.23	-0.878	3.29
			0.913	1.87	0.087	4.24	0.712	2.07	0.288	5.74	0.472	1.77	0.528	7.55	0.278	1.31	0.722	9.02
0.8	2.0	0	0.476	1.93	0.005	3.20	0.827	2.07	-0.038	5.42	1.220	1.72	-0.246	5.56	1.584	1.20	-0.585	3.76
			0.977	1.94	0.023	5.02	0.749	2.08	0.251	5.81	0.487	1.75	0.513	7.48	0.283	1.28	0.717	8.85
1.0	0.5	0	1.346	1.76	-0.446	3.50	2.003	1.86	-1.010	3.82	2.245	1.48	-1.245	3.28	2.245	0.97	-1.245	2.26
			0.926	1.82	0.074	4.05	0.701	1.88	0.299	5.61	0.441	1.49	0.559	6.99	0.255	0.99	0.745	8.15
1.0	1.0	0	0.807	1.69	-0.077	3.78	1.248	1.80	-0.399	4.39	1.676	1.45	-0.678	3.74	1.885	0.95	-0.885	2.49
			0.889	1.73	0.111	4.00	0.680	1.83	0.320	5.52	0.462	1.51	0.538	7.73	0.270	1.02	0.730	8.44
1.0	2.0	0	0.554	1.81	-0.001	7.84	0.922	1.86	-0.071	5.37	1.305	1.47	-0.317	4.85	1.641	0.96	-0.641	2.88
			0.926	1.82	0.074	4.05	0.701	1.88	0.299	5.61	0.441	1.49	0.559	6.99	0.255	0.99	0.745	8.15
1.25	0.5	0	1.327	1.85	-0.432	3.76	2.108	2.07	-1.117	4.05	2.450	1.75	-1.450	3.59	2.550	1.20	-1.550	2.45
			0.977	1.94	0.023	5.02	0.749	2.08	0.251	5.81	0.487	1.75	0.513	7.48	0.283	1.28	0.717	8.85
1.25	1.0	0	0.788	1.81	-0.074	4.20	1.315	2.04	-0.379	4.51	1.800	1.76	-0.802	4.24	2.115	1.25	-1.115	2.92
			0.913	1.87	0.087	4.24	0.712	2.07	0.288	5.74	0.472	1.77	0.528	7.55	0.278	1.31	0.722	9.02
1.25	2.0	0	0.533	2.01	-0.003	3.98	0.900	2.18	-0.072	5.79	1.316	1.84	-0.333	5.51	1.730	1.30	-0.730	3.40
			0.937	2.01	0.063	4.41	0.734	2.20	0.266	6.17	0.479	1.86	0.521	7.90	0.276	1.36	0.724	9.24
1	1	1	0.701	2.61	0.028	13.75	0.989	2.28	-0.440	12.03	1.293	1.61	-0.295	6.57	1.562	0.98	-0.562	3.39
			1.356	2.61	-0.356	8.42	0.872	2.28	0.128	5.02	0.478	1.61	0.513	7.59	0.273	1.03	0.727	8.59
1	1	2	0.599	3.03	0.130	13.19	0.868	2.45	0.077	12.14	1.157	1.65	-0.158	8.66	1.443	0.99	-0.443	3.66
			1.739	3.06	-0.739	6.24	1.000	2.49	0	--	0.509	1.66	0.491	7.98	0.261	1.01	0.739	8.33
1	1	4	0.478	3.30	0.251	17.80	0.768	2.58	0.177	21.40	1.058	1.68	-0.059	9.10	1.352	0.99	-0.352	4.10
			2.400	3.50	-1.400	5.63	1.000	2.52	0	--	0.518	1.68	0.482	8.12	0.262	1.01	0.738	8.32
1	1	8	0.422	3.53	0.307	31.79	0.698	2.65	0.256	36.56	0.998	1.70	0	--	1.313	1.00	-0.313	4.13
			2.750	3.74	-1.750	5.62	1.144	2.66	-0.144	2.87	0.522	1.69	0.478	8.19	0.262	1.01	0.738	8.29

Table 2 Coefficients for equations (15) and (16), $V = 4$

E	R	V	A C	a c	B D	b d	A C	a c	B D	b d	A C	a c	B D	b d
			Ntu = 1				Ntu = 2				Ntu = 4			
0.8	0.5	4	0.469	3.53	0.374	13.34	0.760	2.86	0.220	14.29	1.000	1.91	0	--
			3.790	4.09	-2.790	5.55	1.323	2.92	-0.323	4.65	0.581	1.92	0.419	8.67
0.8	1.0	4	0.397	3.40	0.255	18.52	0.702	2.83	0.204	34.18	0.979	1.89	0.015	8.48
			3.000	3.80	-2.000	5.62	1.223	2.83	-0.223	5.31	0.578	1.90	0.422	8.53
0.8	2.0	4	0.331	3.27	0.149	27.93	0.635	2.80	0.154	42.77	0.936	1.89	0.038	99.00
			3.620	3.95	-2.620	5.40	1.334	2.89	-0.334	4.55	0.574	1.88	0.426	7.90
1.0	0.5	4	0.554	3.35	0.346	10.62	0.841	2.59	0.151	7.50	1.122	1.68	-0.122	11.85
			2.800	3.67	-1.800	5.38	1.074	2.58	-0.074	3.67	0.520	1.68	0.480	8.16
1.0	1.0	4	0.478	3.30	0.251	17.80	0.768	2.58	0.177	21.40	1.058	1.68	-0.059	9.10
			2.400	3.50	-1.400	5.63	1.000	2.52	0	--	0.518	1.68	0.482	8.12
1.0	2.0	4	0.400	3.24	0.153	33.89	0.698	2.58	0.152	40.36	0.999	1.68	-0.012	4.87
			2.800	3.67	-1.800	5.38	1.074	2.58	-0.074	3.67	0.520	1.68	0.480	8.16
1.25	0.5	4	0.518	3.54	0.377	10.79	0.795	2.82	0.196	8.62	1.083	1.90	-0.083	38.40
			3.620	3.95	-2.620	5.40	1.334	2.89	-0.334	4.55	0.574	1.88	0.426	7.90
1.25	1.0	4	0.417	3.41	0.298	16.13	0.720	2.83	0.216	23.48	1.013	1.91	-0.015	5.51
			3.000	3.80	-2.000	5.62	1.223	2.83	-0.223	5.31	0.578	1.90	0.422	8.53
1.25	2.0	4	0.343	3.34	0.187	25.12	0.645	2.85	0.183	36.40	0.982	1.95	0	--
			3.790	4.09	-2.790	5.55	1.323	2.92	-0.323	4.65	0.581	1.92	0.419	8.67

E	A C	a c	B D	b d	A C	a c	B D	b d
	Ntu = 8							
0.8	1.364	1.21	-0.364	4.91				
	0.280	1.23	0.720	8.55				
1.0	1.311	1.20	-0.311	4.99				
	0.324	1.32	0.676	9.50				
0.8	1.268	1.19	-0.268	5.03				
	0.282	1.22	0.718	8.50				
1.0	1.405	1.00	-0.405	3.96				
	0.262	1.01	0.738	8.30				
1.0	1.352	0.99	-0.352	4.10				
	0.262	1.01	0.738	8.32				
1.0	1.307	0.99	-0.307	4.23				
	0.262	1.01	0.738	8.30				
1.25	1.396	1.20	-0.396	4.75				
	0.282	1.22	0.718	8.50				
1.25	1.367	1.22	-0.367	4.53				
	0.324	1.32	0.676	9.50				
1.25	1.295	1.22	-0.295	4.83				
	0.280	1.23	0.720	8.55				

Table 3 Values of $\bar{\tau}_{a\infty}$ and $\bar{\tau}_{b\infty}$. ($\bar{\tau}_{b\infty}$ is the lower entry)

E	Ntu 1	2	4	8
0.8	0.580	0.471	0.312	0.239
	0.525	0.711	0.860	0.952
1.0	0.500	0.333	0.200	0.111
	0.500	0.667	0.800	0.889
1.25	0.475	0.289	0.140	0.048
	0.420	0.569	0.688	0.761

$$X_a(s) =$$

$$\bar{\tau}_{a\infty} s\, e^{-\frac{L}{u_a}s}\left(\frac{1}{s} - \frac{A}{s+\dfrac{a(wc)}{WC(1+V)}} - \frac{B}{s+\dfrac{b(wc)}{WC(1+V)}}\right) \quad (21)$$

$$X_b(s) = \bar{\tau}_{b\infty} s\left(\frac{1}{s} - \frac{C}{s+\dfrac{c(wc)}{WC(1+V)}} - \frac{D}{s+\dfrac{d(wc)}{WC(1+V)}}\right) \quad (22)$$

If $\tau_{a0}(s)$ is the Laplace transform of an arbitrary variation of the inlet temperature of fluid a, then the products $\tau_{a0}(s)\, X_a(s)$ and $\tau_{a0}(s)\, X_b(x)$ are Laplace transforms of the two exit temperatures, $\bar{\tau}_a(t)$ and $\bar{\tau}_b(t)$.

Accuracy of the FD Solutions

A check of the internal consistency of the finite difference solutions is afforded by equation (17) for which each side corresponds to a different computer run. For all corresponding computer runs represented in Tables 1 and 2, the two sides of equation (17) differed by not more than 0.0002.

Two analytical solutions, corresponding to $E = 0$ and $E = \infty$, provide accuracy tests that do not depend only on the internal consistency of the program. The configuration of the exchanger is immaterial for both solutions.

When E increases, the temperature change of fluid b decreases, and in the limit with $E = \infty$, the temperature of fluid b becomes uniform and constant. With $E = \infty$, the FD solution thus gives the exit temperature of fluid a in response to a unit step change in its entrance temperature when the temperature of fluid b is uniform and constant ($\tau_b = 0$). The solution for this case is given by Myers, Mitchell, and Norman [5]. For $t < L/u_a$ ($\theta < 0$), $\bar{\tau}_a = 0$ and for $t \geqslant L/u_a$ ($\theta \geqslant 0$)

$$\frac{\bar{\tau}_a}{\bar{\tau}_{a\infty}} = 1 - K_0\left(\theta(1+R)^2\frac{Ntu}{R}, \frac{Ntu}{R}\right) \quad , \quad (E=\infty) \quad (23)$$

In this equation $\bar{\tau}_{a\infty} = \exp(-Ntu)$, from equations (12) and (14), and

$$K_0(u,v) = \int_0^v e^{-(u+\eta)} I_0(2\sqrt{u\eta})\, d\eta$$

$$= e^{-(u+v)}\left\{v + \frac{v^2}{2!}(1+u) + \frac{v^3}{3!}\left(1+u+\frac{u^2}{2!}\right) + \ldots\right\}$$

I_0 is the modified Bessel function of the first kind, zero order.

When E decreases, the temperature change of fluid a decreases, and in the limit with $E = 0$, the temperature of fluid a becomes uniform. For this case, a unit step change in the inlet temperature of fluid a corresponds to a unit step change in the uniform temperature of fluid a. An example is an exchanger in which fluid a is an evaporating or condensing fluid which, at $t = 0$, experiences an abrupt change in pressure sufficient to increase the saturation temperature by one unit. With $E = 0$, the FD solution thus gives the exit temperature response of fluid b when the uniform temperature of fluid a increases by a unit step.The analytical solution for this case is given by Tan and Spinner [6].

$$\bar{\tau}_b = 1 - \frac{\beta}{\beta-\alpha} e^{-\alpha\theta Ntu\frac{(1+R)}{R}} + \frac{\alpha}{\beta-\alpha} e^{-\beta\theta Ntu\frac{(1+R)}{R}} - S,(E=0) \tag{24}$$

For $\theta \leqslant V$ $(t < L/u_b)$; $S = 0$

For $\theta > V$ $(t > L/u_b)$;

$$S = e^{-Ntu} K_0\left[R\,Ntu, \frac{Ntu}{R}(1+R)^2(\theta - V)\right]$$

$$- \frac{\beta}{\beta-\alpha} e^{-\alpha\frac{Ntu}{R}(1+R)(\theta-V)} e^{-\frac{(1-\alpha)Ntu(1+R)}{1+R-\alpha}}$$

$$K_0\left[\frac{Ntu\,R(1+R)}{1+R-\alpha}, Ntu\frac{(1+R)}{R}(1+R-\alpha)(\theta-V)\right]$$

$$+ \frac{\alpha}{\beta-\alpha} e^{-\beta\frac{Ntu}{R}(1+R)(\theta-V)} e^{-\frac{(1-\beta)Ntu(1+R)}{1+R-\beta}}$$

$$K_0\left[\frac{Ntu\,R(1+R)}{1+R-\beta}, Ntu\frac{(1+R)}{R}(1+R-\beta)(\theta-V)\right]$$

In these equations

$$\alpha = \frac{R + V(1+R) - \sqrt{R + V(1+R))^2 - 4RV}}{2V}$$

and $\beta = R/\alpha V$. For $E = 0$, $V = ((wc)/WC)\ L/u_b$ and equation (10) gives $\bar{\tau}_{b\infty} = 1 - \exp(-Ntu)$.

Comparison of the analytical solutions and the normalized FD solutions for several cases showed a maximum absolute difference of 0.0056 for the worst case. The maximum difference was, for all other cases, much less and was halved when $\Delta\theta$ and ΔX were both halved, thus increasing the solution time fourfold. Good accuracy for the FD solutions is therefore indicated.

Comparison With Other Data

London and co-workers report in several papers summarized in [1], the use of a thermal-electric analog to find the exit temperature responses to a unit step change in inlet temperature for gas-to-gas ($V = 0$) counterflow heat exchangers having equal capacity rates ($E = 1$) for both gases. Figures 3 and 4 compare the FD solutions and their data for $R = 1$. For $\bar{\tau}_a/\bar{\tau}_{a\infty}$ (Fig. 3), their data generally agree with the FD solutions within their stated accuracy of ± 0.04 for $\bar{\tau}_a/\bar{\tau}_{a\infty}$, except for the $Ntu = 1.5$ curve at $\theta = 0$. (The initial jump in $\bar{\tau}_a$ was not incorporated in their figure.) However, for $\bar{\tau}_b/\bar{\tau}_{b\infty}$ (Fig. 4), the FD solutions and their solutions differ by more than their stated accuracy of ± 0.03 for $\bar{\tau}_b/\bar{\tau}_{b\infty}$. They also present the $\bar{\tau}_b/\bar{\tau}_{b\infty}$ response for $Ntu = 8$ (not shown). The $Ntu = 8$ response was obtained using a FD method and in this case their data agree with the FD response of this paper to the accuracy with which their graph (Fig. 3 of [1]) can be read.

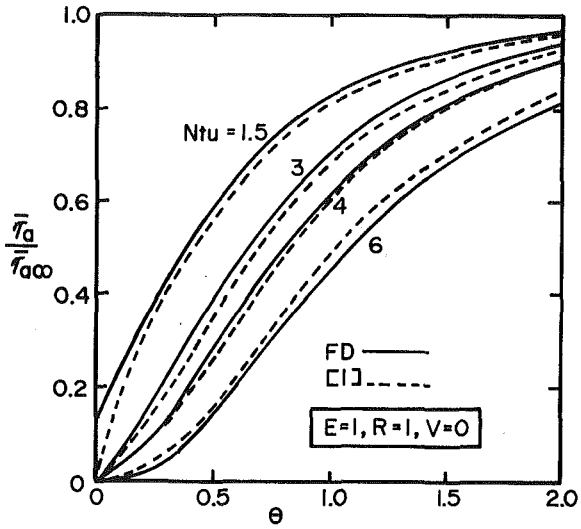

Fig. 3 Comparison of $\bar{\tau}_a/\bar{\tau}_{a\infty}$ responses

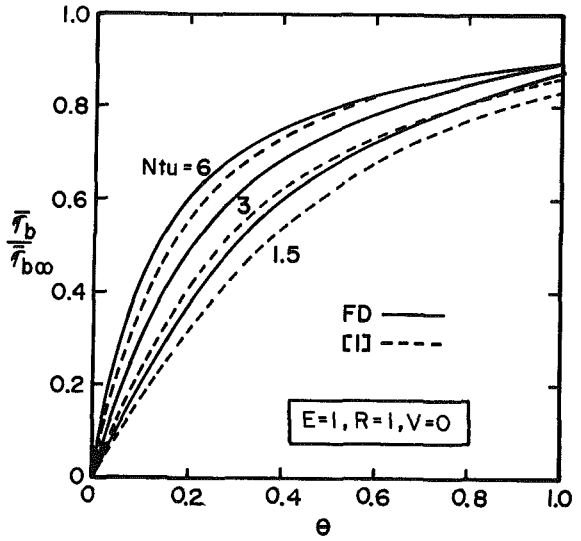

Fig. 4 Comparison of $\bar{\tau}_b/\bar{\tau}_{b\infty}$ responses

Table 4 Table of equivalents

Nomenclature Used In This Paper	Nomenclature Used In [1, 2, 7][1]
Always:	
Ntu	Ntu_o
R	$\frac{1}{R^*}$
V	$\frac{1}{C_w^*}\left(1 + \frac{1}{\theta_d^*}\right)$
θ (for $\bar{\tau}_b$)	$\frac{\theta^*}{C_w^*}$
Step is on C_{min} side:	
θ (for $\bar{\tau}_a$)	$\frac{\theta^* - 1}{C_w^*}$
E	$\frac{1}{C^*}$
Step is on C_{max} side:	
θ (for $\bar{\tau}_a$)	$\frac{\theta^*\theta_d^* - 1}{C_w^*\ \theta_d^*}$
E	C^*

(1) R^* as defined in [1].

Their data for $\bar{\tau}_b/\bar{\tau}_{b\infty}$ are stated to be applicable for all R, which is consistent with the results of this paper for $R = 0.5$ to 2. For $\bar{\tau}_a/\bar{\tau}_{a\infty}$ (Fig. 3), they relabel the abscissa with $\theta - K(1 - R)/(1 + R)$, which they found made the response curves applicable for $R = 0.25$ to 4. Their value for the constant K is 0.4 but a value of 0.53 better represents the data of this paper for $R = 0.5$ to 2.0.

The dimensionless groups used in this paper differ from those used in [1, 2, 7]. In these references, an asterisk is used to denote dimensionless groups and the subscript "min" is used to indicate quantities associated with the fluid having the lesser capacitance rate, e.g., $C_{\min} = (wc)$. The definitions of the groups in [1, 2, 7] in terms of the nomenclature of this paper are as follows: $\theta^* = tu_{\min}/L$, $\theta_d^* = u_{\max}/u_{\min}$, $\bar{C}_w^* = WC/(\rho cA_x L)_{\min}$, $C^* = (wc)_{\min}/(wc)_{\max}$ and $R^* = (hA)_{\min}/(hA)_{\max}$ if the step input is on the $C_{\min}$ side of the exchanger, otherwise $R^* = (hA)_{\max}/(hA)_{\min}$. (These definitions of R^* are given in [1]. The data of [1] are reproduced in [2, 7] but the accompanying definitions of R^* are not consistent with [1].) Table 4 relates the preceeding dimensionless groups to those used in this paper.

Concluding Remarks

The normalized exit temperature responses to a unit step increase in the entrance temperature in either of the fluids of a counterflow heat exchanger have been presented for a range of the governing parameters, Ntu, E, R, and V, appropriate to many applications of the results. Some relationships which should apply to all configurations of heat exchangers have been described.

The second idealization listed states, in part, that the core material offers no thermal resistance to flow of heat from one fluid to the other. However, this requirement is readily relaxed by adding, for example, half the wall resistance to the convective resistance, $1/(hA)_a$ and the other half to the other convective resistance, $1/(hA)_b$. This procedure will give two modified values of the conductances, $(hA)_a$ and $(hA)_b$ to use in evaluating Ntu and R.

References

1 London, A. L., Sampsell, D. F., and McGowan, J. G., "The Transient Response of Gas Turbine Plant Heat Exchangers—Additional Solutions for Regenerators of the Periodic-Flow and Direct-Transfer Types," ASME *Journal of Engineering for Power*, Vol. 86, 1964, pp. 127–135.

2 Kays, W. M., and London, A. L., *Compact Heat Exchangers*, 2d ed., McGraw-Hill, New York, 1964.

3 Romie, F. E., "Transient Response of Gas-to-Gas Crossflow Heat Exchangers with Neither Gas Mixed," ASME JOURNAL OF HEAT TRANSFER, Vol. 105, 1983, p. 563–570.

4 Cheng, D. K., *Analysis of Linear Systems*, Addison-Wesley Co., Reading, Mass., 1959.

5 Myers, G. E., Mitchell, J. W., and Norman, R. F., "The Transient Response of Crossflow Heat Exchangers, Evaporators, and Condensers," ASME JOURNAL OF HEAT TRANSFER, Vol. 89, 1967, pp. 75–80.

6 Tan, K. S., and Spinner, I. H., "Dynamics of a Shell and Tube Heat Exchanger with Finite Tube-Wall Heat Capacity and Finite Shell-Side Resistance," *Industrial and Engineering Chemistry Fundamentals*, Vol. 17, 1978, pp. 353–358.

7 Shah, R. K., "The Transient Response of Heat Exchangers," *Heat Exchangers Thermal-Hydraulic Fundamentals and Design*, edited by S. Kakac, A. E. Bergles, and F. Mayinger, Hemisphere Publishing Corp., Washington, D.C., 1981, pp. 915–953.

Performance of One- and Two-Row Tube and Plate Fin Heat Exchangers

E. C. Rosman

P. Carajilescov

F. E. M. Saboya

Department of Mechanical Engineering,
Pontificia Universidade
Catolica do Rio de Janeiro,

Heat exchangers consisting of finned tubes are commonly employed in air conditioning systems, air heaters, radiators, etc. Local measurements of mass transfer coefficients on fins, obtained by Saboya and Sparrow, are very nonuniform. In the present work, an experimental apparatus was set up to measure overall heat transfer coefficients for two-row tube and plate fin heat exchangers. The obtained results, together with Shepherd's results for one-row exchangers, are used to transform the local mass transfer coefficients into local heat transfer coefficients. A numerical two-dimensional heat transfer analysis has been performed in order to obtain the temperature distribution and fin efficiency. The influences of the Reynolds number and fin material are also analyzed.

Introduction

Heat exchangers consisting of tubes and plate fins with air as one of the fluids have many engineering applications, such as to air conditioning systems, air heaters, radiators, etc. The performance of the surface of these heat exchangers, and in some cases the row by row performance, has been evaluated by "backing out" a uniform surface heat transfer coefficient under the assumption of constant fin efficiency. Experiments performed by Saboya and Sparrow [1], using the naphthalene sublimation technique, show that the mass transfer coefficients present abrupt variations from point to point due to the creation of vortex systems induced by the tube restriction of the flow area. Since there is a close analogy between the processes of heat and mass transfer, those same abrupt variations are present in the local heat transfer coefficients. In the present work, the possible error in fin efficiency, hence row by row heat transfer coefficient, resulting from the uniform heat transfer coefficient assumption is evaluated for several cases and shown to be significant.

To accomplish this, a two-dimensional heat transfer analysis is performed in order to obtain the plate fin temperature distribution, the air bulk temperature distribution along the stream path and the fin efficiency, for several Reynolds numbers and fin materials. The local heat transfer coefficients were obtained by transforming the local mass transfer coefficients, measured by Saboya [2, 3], into local heat transfer coefficients with the use of the heat/mass transfer analogy. In order to establish the analogy, for one-row tube and plate fin heat exchangers, the heat transfer results obtained by Shepherd [4] were used. For two-row exchangers, an experimental apparatus was set up to measure the overall heat transfer coefficients. The analogy is described in the section where the experimental data are analyzed.

Theoretical Analysis

One-centered-row and two-row tube and plate fin heat exchangers are shown in Fig. 1, and the unit cells (the smallest symmetrical sections) are defined.

In the steady state, the heat balance in the fin plate is given by

$$\frac{\partial^2 T}{\partial X^2}+\frac{\partial^2 T}{\partial Y^2}-\frac{2h}{Kt}(T-T_b)=0 \tag{1}$$

where

T_b = air bulk temperature
h = local heat transfer coefficient
K = plate material thermal conductivity
t = fin plate thickness

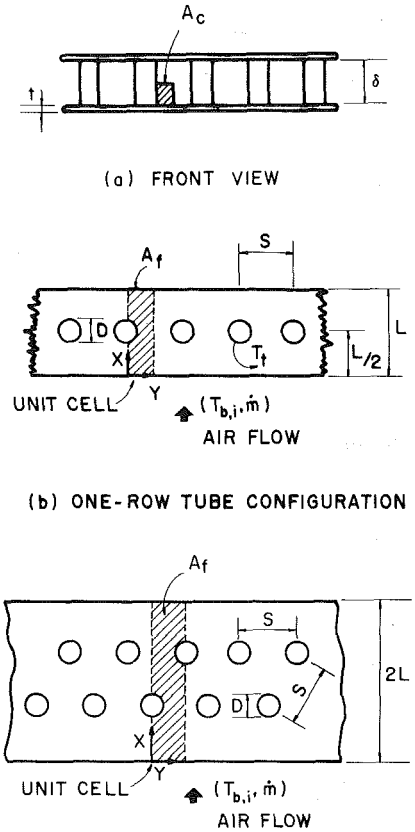

Fig. 1 Schematic of one- and two-row tube and plate fin heat exchangers

Contributed by the Heat Transfer Division for publication in the JOURNAL OF HEAT TRANSFER. Manuscript received by the Heat Transfer Division October 8, 1982.

The heat balance in the air can be written in the form

$$\dot{m}c_p(T_b - T_{b,i}) = \int_0^X d\xi \int_0^{S/2} dY h(T - T_b) \tag{2}$$

where

$T_{b,i}$ = air bulk temperature at the inlet
$\dot{m}$ = air flow rate
c_p = air specific heat at constant pressure

In nondimensional form, equations (1) and (2) can be reduced to

$$\frac{\partial^2\theta}{\partial X^{*2}} + \frac{\partial^2\theta}{\partial Y^{*2}} - 2\mathrm{Nu}\frac{K_a/K}{D_h^* t^*}(\theta - \theta_b) = 0 \tag{3}$$

and

$$\theta_b = \frac{1}{\mathrm{Re\,Pr} A_c^*}\int_0^X d\xi^* \int_0^{S^*/2} dY^* \mathrm{Nu}(\theta - \theta_b) \tag{4}$$

with

$$\theta \equiv \frac{T - T_{b,i}}{T_t - T_{b,i}}$$

where

T_t = tube temperature
K_a = air thermal conductivity
A_c^* = A_c/L^2
Nu = hD_h/K_a = local Nusselt number
Pr = $\mu c_p/K_a$ = air Prandtl number
Re = $\dot{m}D_h/\mu A_c$ = Reynolds number

The superscript (*) denotes dimensionless geometrical parameters. The linear dimensions were made dimensionless dividing by L. The hydraulic diamter D_h was defined as $D_h = (4A_cL)/(A_f + \pi D\delta/4)$, as suggested by Kays and London [5]. As boundary conditions, zero normal temperature gradients were imposed along the unit cell perimeter, except in the region in contact with the tube where $\theta = \theta_t = 1$. Then the fin efficiency is defined by the following ratio

$$\eta = \frac{\theta_{b,e}}{\theta_{b,e}^i} \tag{5}$$

where $\theta_{b,e}$ is the actual dimensionless air bulk temperature at the outlet section and $\theta_{b,e}^i$ is the outlet dimensionless bulk temperature of the air if the fin plate were isothermal at the tube temperature, i.e., $\theta = \theta_t = 1$.

In the analysis, the heat exchanged by the tube surface was neglected. The tube surface area is only 6.5 percent of the fin surface area. Also is should be noticed that, although the tube surface is 100 percent efficient, the local heat transfer coefficients are very low on the back surface of the tube. The nonparticipation of the tube surface in the transfer process does not introduce a significant error in the ratio expressed by equation (5). This assumption causes a systematic error which equally affects $\theta_{b,e}$ and $\theta_{b,e}^i$. Therefore the error on the fin efficiency is very small (the errors on $\theta_{b,e}$ and $\theta_{b,e}^i$ are mutally compensated).

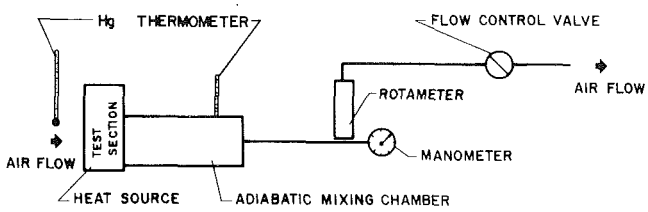

Fig. 2 Experimental apparatus

Defining the average Nusselt number $\overline{\mathrm{Nu}}$ for an isothermal plate fin by the expression

$$\overline{\mathrm{Nu}} = \frac{1}{A_f^*}\int_0^1 dX^* \int_0^{S^*/2} dY^* \mathrm{Nu} \tag{6}$$

the air outlet bulk temperature, for such an isothermal plate fin, is given by

$$\theta_{b,e}^i = 1 - \exp\left[-\frac{\overline{\mathrm{Nu}}}{\mathrm{Re\,Pr}}\frac{A_f^*}{A_c^*}\right] \tag{7}$$

In equation (6), Nu is the local Nusselt number based on the bulk and wall temperature difference, and $\overline{\mathrm{Nu}}$ is the average Nusselt number based on the log-mean temperature difference.

Knowing $\overline{\mathrm{Nu}}$, it is possible to obtain $\theta_{b,e}^i$ by using equation (7). Knowing η, equation (5) gives $\theta_{b,e}$ which is directly related to the actual rate of heat exchanged by the heat exchangers ($\dot{m}c_p(T_{b,e} - T_{b,i}) = \dot{m}c_p\theta_{b,e}(T_t - T_{b,i})$).

Experimental Method

Since experimental data for overall Nusselt numbers for isothermal two-row tube and plate fin heat exchangers are not available in the literature, the experimental apparatus, shown in Fig. 2, was set up. The test section is heated by hot water at constant temperature, as shown in Fig. 3. Air is drawn into the heated test section. Upon traversing the length of the channel, the air passes through an adiabatic mixing chamber, shown in Fig. 4. The inlet and homogenized outlet air temperatures are carefully measured. The air is finally ducted to a rotameter, a blower, and discharged to the atmosphere. The experimental data were reduced by utilizing the following

Nomenclature

A_c = minimum flow area for a unit cell, Fig. 1, m^2
A_f = transfer area for a unit cell, Fig. 1, m^2
D = tube diameter, Fig. 1, m
D_h = hydraulic diameter, $(4A_cL)/(A_f + \pi D\delta/4)$, m
h = local heat transfer coefficient, W/m^2 K
$\bar{h}$ = average heat transfer coefficient, W/m^2 K
K = plate material thermal conductivity, W/m K
K_a = air thermal conductivity, W/m K
L = streamwise length of channel for one tube row, Fig. 1, m
$\dot{m}$ = air flow rate, kg/s
Nu = local Nusselt number, hD_h/K_a
$\overline{\mathrm{Nu}}$ = average Nusselt number, $\bar{h}D_h/K_a$
Pr = Prandtl number
Re = Reynolds number, $\dot{m}D_h/A_c\mu$
S = distance between tube centers, Fig. 1, m
Sc = Schmidt number
Sh = local Sherwood number
$\overline{\mathrm{Sh}}$ = average Sherwood number
t = fin plate thickness, Fig. 1, m
T_b = air bulk temperature, °C
$T_{b,e}$ = exit air bulk temperature, °C
$T_{b,i}$ = inlet air bulk temperature, °C
T_t = tube temperature, °C
X, Y = surface coordinates, Fig. 1, m
δ = spacing between plates, Fig. 1, m
η = fin efficiency, equation (5)
θ = dimensionless temperature, $(T - T_{b,i})/(T_t - T_{b,i})$
θ_b = dimensionless air bulk temperature, $(T_b - T_{b,i})/(T_t - T_{b,i})$
μ = coefficient of viscosity, N s/m^2

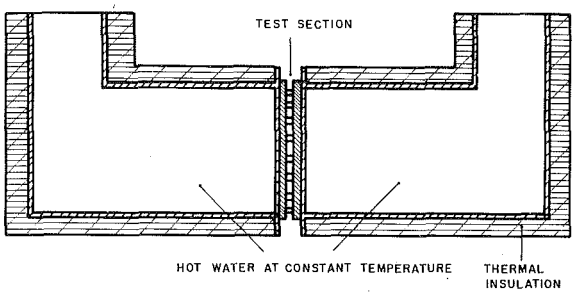

Fig. 3 Test section heating system

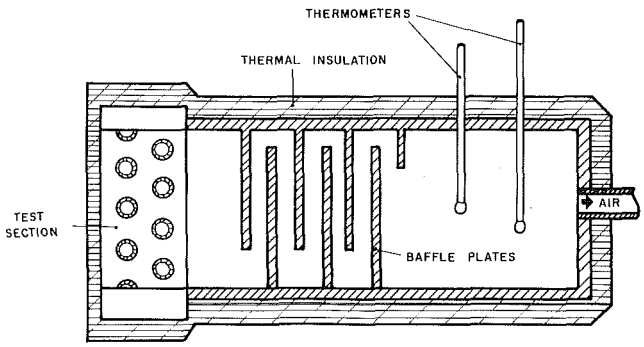

Fig. 4 Test section and adiabatic mixing chamber

equation for the average Nusselt number for an isothermal heat exchanger

$$\overline{\mathrm{Nu}} = \mathrm{Re}\,\mathrm{Pr}\,\frac{A_c^*}{A_f^*}\ln\left(\frac{T_t - T_{b,i}}{T_t - T_{b,e}^{i}}\right) \tag{8}$$

Since this expression requires that the test section be isothermal, it was made of 4-mm-thick copper plate. Its temperature was measured on the external side of each plate in 5 different positions by copper-constantan thermocouples. Since no temperature differences were observed from the readings, it was concluded that the plates were isothermal as required. The dimensional ratios for the present test section were $S/L = 1.1534$, $D/L = 0.4622$ and $\delta/L = 0.0894$. These values are typical of present-day heat exchangers encountered in air conditioning applications. The actual values of the dimensions are: $S = 25.84$ mm, $L = 22.40$ mm, $D = 10.35$ mm, and $\delta = 2.00$ mm. Results for the average Nusselt number are plotted on Fig. 5 as a function of the Reynolds number over the range from $\mathrm{Re} = 200$ to $\mathrm{Re} = 1700$. A curve has been fitted through the points to provide continuity. The measurements of $\overline{\mathrm{Nu}}$ were made within a maximum experimental error of 8.4 percent. Typically, the error was 6 percent. These errors were evaluated by the response of $\overline{\mathrm{Nu}}$ to changes on each of the variables of equation (8) that was used in the data reduction procedure.

For comparison, average Sherwood number results, taken from [3] for similar geometry, are plotted in Fig. 5. The growing contributions of the vortex systems with increasing Reynolds numbers are similar for both heat and mass transfer processes as it should be. The different magnitudes of $\overline{\mathrm{Nu}}$ and $\overline{\mathrm{Sh}}$ are due to differences in the values of Prandlt ($\mathrm{Pr} = 0.7$) and Schmidt ($\mathrm{Sc} = 2.5$) numbers.

For one-row exchanger, similar results are presented in Fig. 6. They are obtained from [1, 2] for mass transfer and from [4] for heat transfer experiments. Differences in behavior could be attributed to the fact that Shepherd [4] presents straight lines on log-log plots of Nu versus Re which, presumably, represent a smoothing of the data points. A detailed analysis of the local mass transfer coefficients reported in [2] shows that, in the range $600 < \mathrm{Re} < 700$, a second horseshoe vortex starts to develop, changing the flow regime and imposing a nonlinearity in the $\overline{\mathrm{Nu}}$–Re plot that

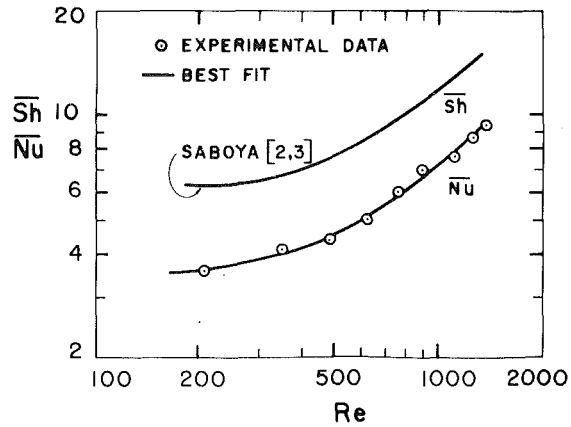

Fig. 5 Average Nusselt and Sherwood number as a function of Reynolds number for two-row tube configuration

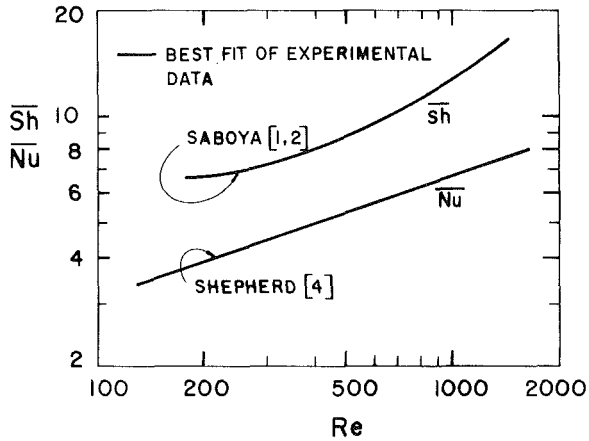

Fig. 6 Average Nusselt and Sherwood number as a function of Reynolds number for one-centered-row tube configuration

was not apparent in Shepherd's results. However the level of agreement between the present results and those of Shepherd is very satisfactory.

Reduction of Experimental Data

The analogy between the Sherwood and Nusselt numbers can be written in the form

$$\mathrm{Nu} = \mathrm{Sh}\left(\frac{\mathrm{Pr}}{\mathrm{Sc}}\right)^n \tag{9}$$

$$\overline{\mathrm{Nu}} = \overline{\mathrm{Sh}}\left(\frac{\mathrm{Pr}}{\mathrm{Sc}}\right)^m \tag{10}$$

where Sc is the Schmidt number and Pr is the Prandtl number. Since, by analogy, the Sherwood number obeys an equation similar to expression (6), it is easy to show that n must be equal to m, as long as the equations (9) and (10) hold. From Figs. 5 and 6, the value of m was calculated for several Reynolds numbers. The results are presented in Figs. 7 and 8 for one-row and two-row tube configurations, respectively. It can be observed that m remains approximately equal to 0.40. Departure from this value, observed for $\mathrm{Re} > 700$, in the one-row tube configuration, can be attributed to Shepherd's linearity representation. So m was taken as 0.40, for all values of Re and both configurations.

Also, the average Nusselt numbers, for an isothermal fin, were correlated in the form

$$\frac{\overline{\mathrm{Nu}}}{\mathrm{Pr}^{0.4}} = 4.18 + 1.50 \times 10^{-3}\mathrm{Re}^{1.15} \tag{11}$$

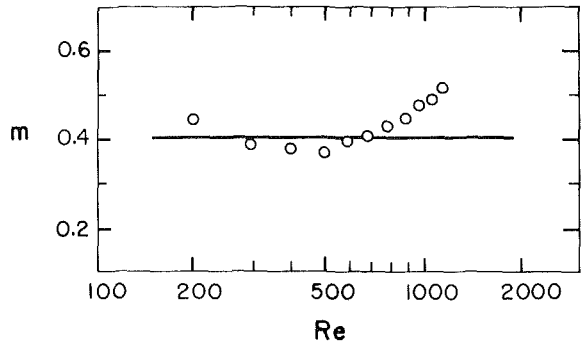

Fig. 7 Exponent m for heat mass transfer analogy for one-row tube configuration

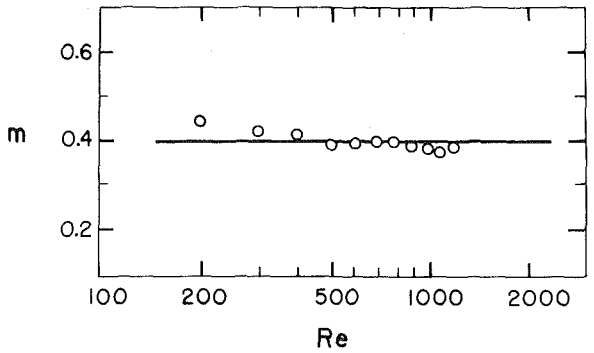

Fig. 8 Exponent m for heat mass transfer analogy for two-row tube configuration

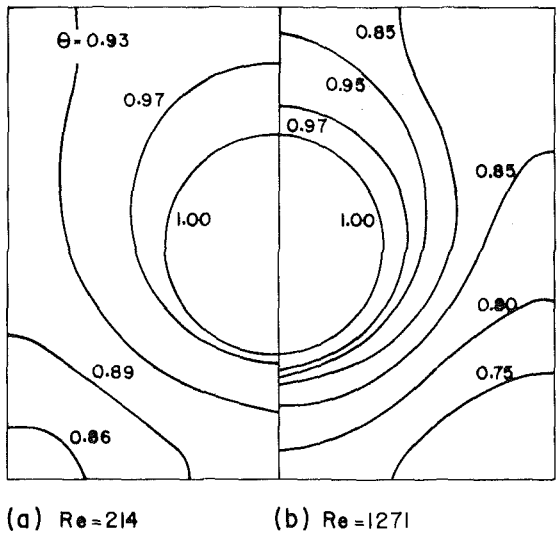

Fig. 9 Effect of the Reynolds number on the temperaure distributions of a one-row tube configuration for $K = 202$ W/m K

for the one-row tube configuration, and

$$\frac{\overline{Nu}}{Pr^{0.4}} = 3.58 + 8.46 \times 10^{-4} Re^{1.24} \qquad (12)$$

for the two-row tube configuration. These average Nusselt numbers are based on the log-mean temperature difference. Equations (11) and (12) were obtained by least-square fitting of experimental data. The average dispersion was only 2.5 percent.

Results

The integral-differential set of equations expressed by equations (3) and (4) was solved numerically. The local Nusselt numbers, required for the solution, were obtained by transforming the local Sherwood numbers, measured by Saboya [2], with the use of the heat/mass transfer analogy and taking m equal to 0.40.

The effects of the Reynolds numbers and fin plate materials were investigated for one- and two-row tube configurations, for $t/L = 0.0082$.

One-Row Tube Results. Figure 9 shows the comparison between the temperature distributions for $Re = 214$ and $Re = 1271$ for the plate fins made of aluminum ($K = 202$ W/m K). It can be observed that, as Re increases, the temperature decreases more rapidly as you move away from the center of the tube, departing more rapidly from the ideal isothermal situation. The efficiency decreases from 92.4 to 82.7 percent as the Reynolds number increases from 214 to 1271.

Figure 10 shows a comparison between the plate fin temperature distributions for $Re = 214$ for two different plate materials. As the thermal conductivity increases, the fin thermal resistance decreases and the fin presents less variations in temperature as you move away from the center of the tube, increasing the fin efficiency.

Dimensionless cumulative heat transfer rates as function of the axial position are shown in Fig. 11 for different Reynolds numbers. It can be observed that the wake region downstream

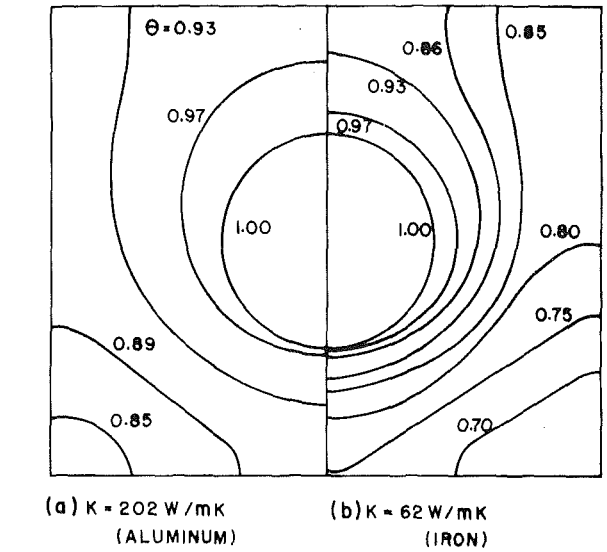

Fig. 10 Effect of the fin plate material on the temperature distributions of a one-row tube configuration for $Re = 214$

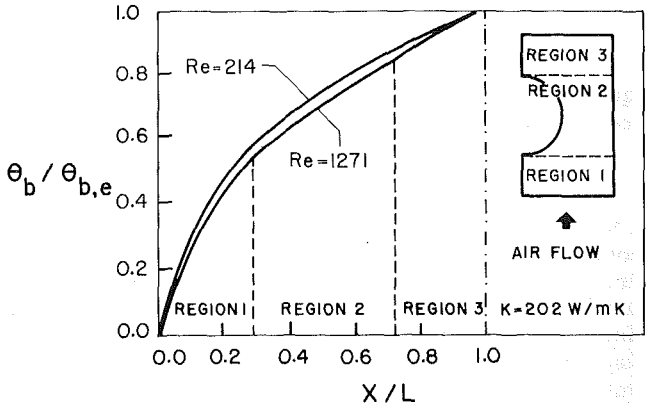

Fig. 11 Dimensionless cumulative heat transfer rates as a function of axial position for one-row tube configuration

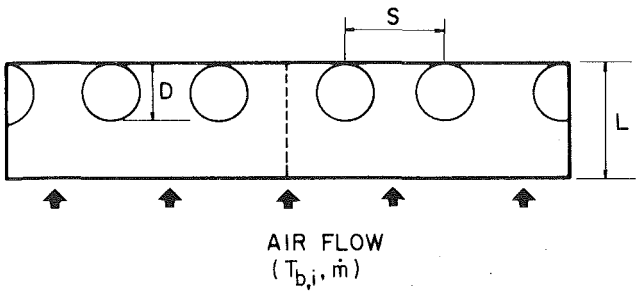

Fig. 12 Plan view of rear-tube row configuration

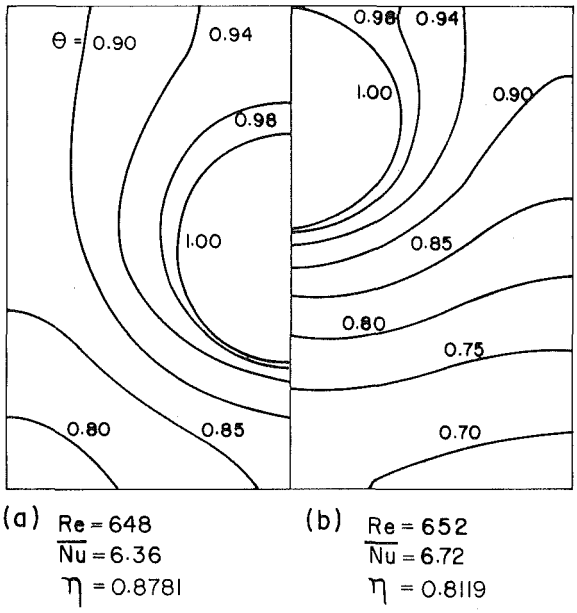

Fig. 13 Effect of the tube displacement on the temperature distribution (K = 202 W/m K)

of the tube row is responsible for only 13 to 14 percent of the total heat transferred by the fin (in the range of Re = 200–1200).

Considering the poor performance of the wake region, it was reasonable to suppose that the transfer capability of the heat exchanger could be improved by relocating the tube row toward the rear of the fin as shown in Fig. 12. This configuration was analyzed using the mass transfer data reported by Saboya and Sparrow [6] for Re = 650 and transforming them into local heat transfer coefficients as mentioned earlier.

Figure 13 shows the comparison between the temperature distributions for Re = 650 for plate fins made of same material (K = 202 W/m K) with central-tube and rear-tube row configurations. It can be observed that the entrance region is greatly affected by the tube displacement. Considering that the transfer coefficients are much higher in the entrance than in the wake region, the fin efficiency decreases 7 percent due to the tube relocation, although the average Nusselt number is higher for the rear tube configuration for isothermal fins.

Dimensionless bulk temperatures for both cases were evaluated at several axial stations. The results are presented in Fig. 14. It is seen that the curve corresponding to the back-row fin does not intercept the central-row fin curve. Since the total heat transfer rate is proportional to θ_b, at the exit station, Fig. 14 shows that this rate for the centered-tube configuration is 4 percent higher.

Two-Row Tube Results. Figure 15 shows the comparison between the temperature distributions for Re = 211 and Re = 1089 for the plate fin made of iron (K = 62 W/m K). Similar to the one-row tube results, as Re increases, the

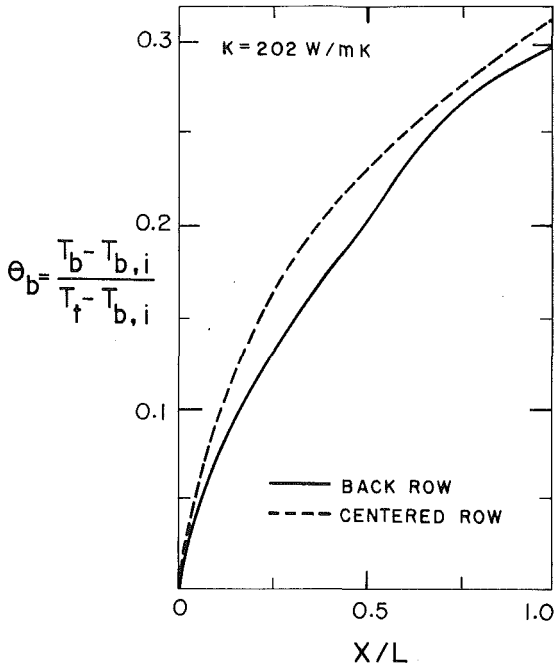

Fig. 14 Dimensionless air bulk temperatures as a function of axial position

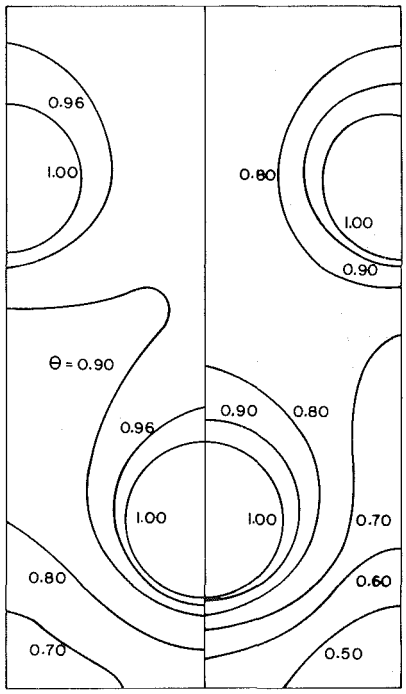

Fig. 15 Effect of the Reynolds number on the temperature distributions of a two-row tube configuration for K = 62 W/m K

temperature decreases more rapidly as you move away from the tube. Although the local heat transfer coefficients are higher in front of the second tube than in front of the first one, which is due to the air flow restriction imposed by the first row of tubes provoking an acceleration of the air, the fin plate presents higher temperature variations near the first tube. This can be attributed to the fact that the air is colder in that region and the temperature differences between plate and air are higher, inducing higher removal rates.

Figure 16 presents the effect of the fin plate material on the temperature distribution for Re = 211. As the thermal conductivity decreases, the departure of the fin plate tem-

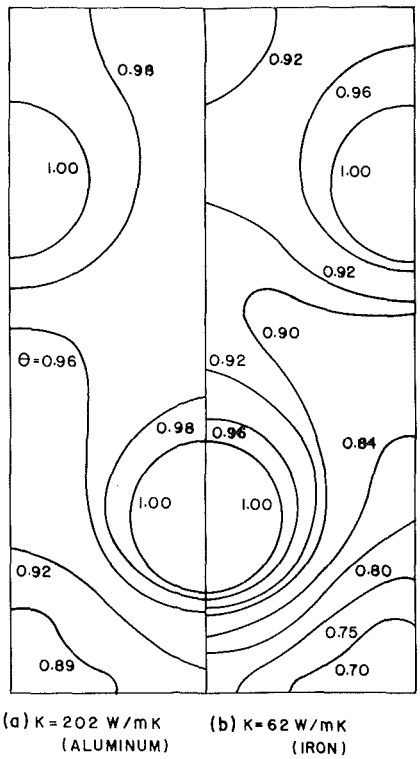

Fig. 16 Effect of the fin plate material on the temperature distributions of a two-row tube configuration for Re = 211

peratures from the ideal isothermal situation increases, leading to lower efficiencies.

Fin Efficiency. Fin efficiencies were calculated with the use of equation (5). Figure 17 shows the effects of the Reynolds numbers and fin plate materials for one- and two-row tube configurations. As the Reynolds number increases, the fin plate temperature departs from the isothermal situation, yielding lower efficiencies. This same effect is produced by materials with low thermal conductivity. It can be observed that, for the same material and Reynolds number, configurations with two-row of tubes lead to higher efficiencies. On the other hand, the conventional analysis assuming uniform heat transfer coefficient on the fin and constant air bulk temperature seems to be inadequate. Fins with one and two rows of tubes would have about the same efficiencies, since the average heat transfer coefficients are about the same for $900 < Re < 1200$.

Concluding Remarks

Heat transfer experiments were run on a two-row exchanger, and the results for the overall Nusselt numbers are reported in Fig. 5 and compared to the overall Sherwood numbers obtained by Saboya [2, 3].

Starting with the heat/mass transfer analogy expressed by equations (9) and (10), the exponents m and n were determined to be equal to 0.4. This value was used to transform the local mass transfer coefficients from [2] into local heat transfer coefficients, and a numerical analysis was made for one and two-tube row configurations for two fin plate materials and different Reynolds numbers. The utility of the mass transfer method of determining local heat transfer coefficients is clearly demonstrated in this analysis.

The results shown in Fig. 17 indicate that the fin efficiency is higher for the two-tube row configuration. This can be attributed to the strong effect of the air entrance region where

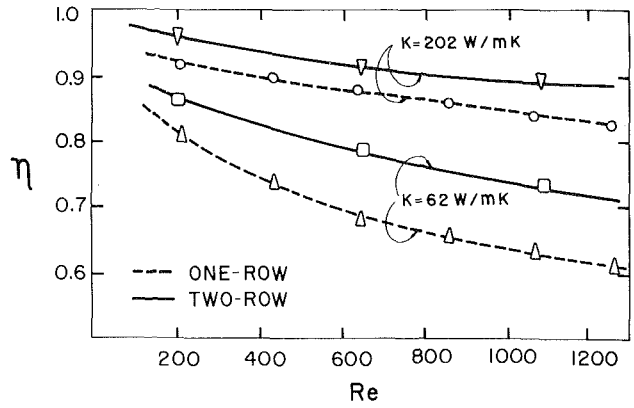

Fig. 17 Fin efficiencies as a function of the Reynolds number

the highest departures from the isothermal situation were observed. This effect is not present in the second tube row region yielding a higher overall fin efficiency. Examination of Fig. 17 reveals that, for $900 < Re < 1200$, the error associated with assuming a uniform heat transfer coefficient can be greater than 8 percent. In this range of Reynolds number, fins with one and two rows of tubes would have about the same efficiencies if the heat transfer coefficients were assumed uniform. For the one-tube row configuration, the displacement of the tube row toward the rear region of fin plate was observed to lead to lower efficiencies, although the isothermal Nusselt numbers are higher in such configuration. The fin efficiency decreases 7 percent due to the tube relocation for fins made of aluminum ($K = 202$ W/m K).

It should be noticed that, knowing the fin efficiency (given by Fig. 17) and the average Nusselt number (provided by equations (11) and (12)), for an isothermal fin, it is possible to obtain $\theta^i_{b,e}$ and $\theta_{b,e}$ using equations (7) and (5); $\theta_{b,e} = (T_{b,e} - T_{b,i})/(T_t - T_{b,i})$ is proportional to the actual heat transfer rate.

As a final remark, the authors call attention to the fact that the increase in the average Nusselt number obtained by tube relocation does not lead to improved thermal performance when compared to a centered tube row. Although transfer coefficients can be used as an orientation, a careful heat transfer analysis, using local heat transfer coefficients, has to be done in order to obtain the fin efficiency before any change of an established fabrication process is undertaken. The performance of the heat exchanger depends on the Nusselt number for an isothermal exchanger and fin efficiency. The assymetric tube location would yield even lower relative performance as the fin thermal conductivity is reduced.

References

1 Saboya, F. E. M., and Sparrow, E. M., "Local and Average Transfer Coefficients for One-Row Plate Fin and Tube Heat Exchanger Configurations," ASME JOURNAL OF HEAT TRANSFER, Vol. 96, 1974, pp. 265-272.

2 Saboya, F. E. M., "Local and Average Transfer Coefficients in a Plate Fin and Tube Exchanger Configuration," Ph.D. thesis, Department of Mechanical Engineering, University of Minnesota, 1974.

3 Saboya, F. E. M., and Sparrow, E. M., "Transfer Characteristics of Two-Row Plate Fin and Tube Heat Exchanger Configurations," *Int. J. Heat Mass Transfer*, Vol. 19, 1976, pp. 41-49.

4 Shepherd, D. G., "Performance of One-Row Tube Coils With Thin-Plate Fins, Low Velocity Forced Convection," *Heating, Piping and Air Conditioning*, Vol. 28, 1956, pp. 137-144.

5 Kays, W. M., and London, A. L., *Compact Heat Exchangers*, 2d ed., McGraw-Hill, New York, 1964.

6 Saboya, F. E. M., and Sparrow, E. M., "Effect of Tube Relocation on the Transfer Capabilities of a Fin and Tube Heat Exchanger," ASME JOURNAL OF HEAT TRANSFER, Vol. 96, 1974, pp. 421-422.

Dimensioning of Spiral Heat Exchangers to Give Minimum Costs

A. B. Jarzębski
Polish Academy of Sciences,
Institute of Chemical Engineering,
Gliwice, Poland

Simple expressions are presented for calculating approximate dimensions of spiral heat exchangers to give minimum annual cost of heating surface plus energy required to pump the fluids. The case of spiral-spiral flow is considered. Equations are derived for exchangers with and without distance holders between plate strips and for two sets of input data: (i) both volumetric fluid flow rates V_1, V_2 and all inlet and appropriate outlet temperatures are given; (ii) the flow rate of the process fluid V_1 and the effectiveness e_1 are imposed, while the flow rate of the working fluid V_2 is an additional variable subject to optimization. For the latter case, appropriate optimum values of V_2 can readily be found from the graphs provided.

Introduction

Due to the complexity of heat exchanger optimization, designers with little experience in that area often find it difficult to determine operating conditions and heat exchanger dimensions ensuring optimum economy. Poor choce of these can lead to significant rise in annual charges, which, of course, is hardly acceptable. One possible remedy is to list all permissible solutions to the given problem, within a broad range of variables, and next is to select the most suitable solution. This is conceptually simple, but due to the number of variables and poor knowledge of the possible optimum variant it is not usually practical. The more effective and up-to-date approach employs numerical methods of nonlinear programming.

Shah et al. [1] and Hedderich et al. [2] provide an extensive review of various, nonlinear programming methods applied to this problem during the seventies. They also indicate the most recent and effective methods designed for air-coolers optimization.

The values of design and operating parameters, optimum for the given problem, are standard output of computer routines. However, there are no simple, approximate methods that could give optimum results using pocket calculators. Moreover, little is known of the effect of various factors on the possible location of the optimum solution. Further analytical investigations in this area could give a better overall understanding of the problem and, hopefully, permit the development of practical guidelines for optimum dimensioning. Clearly, the rough analytical methods for optimum dimensioning can also give useful starting values for more accurate iterative nonlinear programming routines.

Spiral heat exchangers (SHE), shown schematically in Fig. 1, are successfully used in cases of severe fouling or corrosion and details of design features and performance can be found in [3, 4]. Since the effective width b of SHE can range from 0.1 to 1.5 m, the channel spacings s_1, s_2, from 0.005 to 0.025 m, and any arbitrary combination of the two can, at least theoretically, be envisaged within certain limits, and usually several alternatives may be found that meet the imposed data [4, 5]. Annual costs for these design variants may differ significantly, and there are few indications in the literature on the choice of optimum dimensions to achieve minimum costs. The general guideline given by Jenssen states that, for economic optimum, the ratio of capital costs to power cost should be equal to 3 [4, 5]. The object of this paper is to give expressions and also more general guidelines for assessing SHE dimensions at optimum economic heat exchanger costs.

Mathematical Formulation of the Problem

Assuming that the total annual cost C of the heat exchanger comprises the capital charges proportional to the heat transfer area $2bl$ plus the costs of power required to pump the fluids, the problem may be formulated in mathematical terms [4]

$$\min[C = A_1(2bl) + B_1 V_1 \Delta p_1 + B_2 V_2 \Delta p_2] \tag{1}$$

subject to the constraint

$$Q = U(2bl)\,\Delta t_m \tag{2}$$

Factor A_1 takes into account the costs of unit heating surface, allowing for interest and depreciation coefficient, while the factors B_1, B_2 account for the costs of power and time of operation but allow also for pumps efficiencies and utilization factor (details can be found in [4, 5]). Additional constraints supplementary to equation (2) are sometimes imposed depending on the problem statement.

Initial data most often include:

Version 1

Volumetric flow rates V_1, V_2; inlet and outlet temperatures $t_{11}, t_{21}, t_{12}, t_{22}$; and also factors A_1, B_1, B_2

Version 2

Flow rate V_1; temperatures t_{11}, t_{12}, t_{21}; and factors A_1, B_1, B_2

In the second case, the volumetric flow rate V_2 and the related outlet temperature t_{22} are additional variables to be found.

Due to nonlinearity of both the objective function and the constraint, the fair number of variables, and also the discrete character of those permissible s and b, the problem can on the whole be resolved numerically. To find a practical solution,

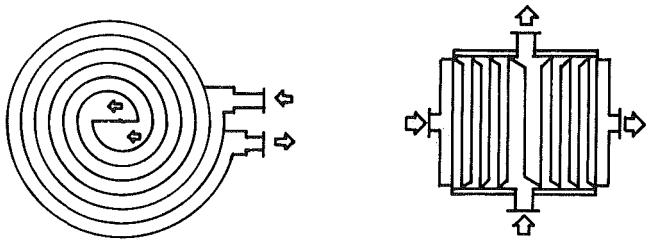

Fig. 1 Schematic representation of SHE's

Contributed by the Heat Transfer Division for publication in the JOURNAL OF HEAT TRANSFER. Manuscript received by the Heat Transfer Division February 3, 1984.

certain simplifications are made without distorting the principal features of the problem so as to render it suitable for analytical attack.

The Simplified Approach

It has been assumed that:

1 b, s_1, s_2, and l may take arbitrary positive values.
2 The performance of a SHE may be approximated to that of a straight (nonspiral) counterflow device with similar passages and the same heat transfer area [6].
3 Overall heat transfer coefficient U is given by the expression $U = Kv_1^{a_1}v_2^{a_2}$ or by its more developed form, i.e., $U = K_1 v_1^{a_1} v_2^{a_2} s_1^{-a_3} s_2^{-a_4}$ [4].
4 Pressure drop may be calculated from the simplified form of the Sander equation [3], i.e.,

$$\Delta p_i = \rho_i v_i^2 l\left(\frac{E_1}{\mathrm{Re}_i^g s_i} + E_2\right) \quad i = 1,2 \tag{3}$$

where an inlet and exit effects are neglected.

Assuming that the equivalent hydraulic diameter of the slit channel is equal to $2s_i$, and introducing equation (3) into equation (2), the objective function takes the form

$$C = 2A_1 bl + lb^{g-2}E_1 2^{-g}\sum_{i=1}^{2} B_i \rho_i^{1-g}\mu_i^g V_i^{3-g} s_i^{-3}$$

$$+ lb^{-2}E_2\sum_{i=1}^{2}\rho_i V_i^3 s_i^{-2} B_i \tag{4}$$

and the constraints are

$$Q = 2KV_1^{a_1}V_2^{a_2}s_1^{-a_1}s_2^{-a_2}b^{1-a_1-a_2}l\Delta t_m \tag{5}$$

$$Q = 2K_1 V_1^{a_1}V_2^{a_2}s_1^{-a_1-a_3}s_2^{-a_2-a_4}b^{1-a_1-a_2}l\Delta t_m \tag{6}$$

depending whether a simpler or more developed expression approximating overall heat transfer coefficient is adopted.

Substituting for l from equation (5) or equation (6) into equation (4), the problem is effectively reduced to finding the minimum of the new objective function over s_1, s_2, b, and V_2. A solution is given here for the cases of a SHE without and with distance holders between the plate strips, i.e., when $E_1 \neq 0$ and $E_2 = 0$ or $E_1, E_2 \neq 0$, respectively.

SHE Without Distance Holders. Analysis of the appropriate objective function obtained by substituting equation (6) into equation (4) showed that there is no minimum of C over feasible s_1, s_2, and b but that there is, for given b, a minimum of C over positive s_1, s_2.

For the first set of imposed data (V_1, V_2, t_{11}, t_{12}, t_{21}, t_{22}), the optimum spacings are

$$s_{1\mathrm{opt}}^{-3} b^{g-3} = \frac{2A_1(a_1+a_3)}{(3-a_1-a_2-a_3-a_4)B_3 V_1^{3-g}} \tag{7}$$

$$s_{2\mathrm{opt}}^{-3} b^{g-3} = \frac{2A_1(a_2+a_4)}{(3-a_1-a_2-a_3-a_4)B_4 V_2^{3-g}} \tag{8}$$

where $B_3 = B_1 E_1 2^{-g}\rho_1^{1-g}\mu_1^g$, $B_4 = B_2 E_1 2^{-g}\rho_2^{1-g}\mu_2^g$.
The ratio of the optimum of s is therefore

$$\frac{s_{2\mathrm{opt}}}{s_{1\mathrm{opt}}} = \left[\frac{B_4 V_2^{3-g}(a_1+a_3)}{B_3 V_1^{3-g}(a_2+a_4)}\right]^{1/3} \tag{9}$$

and for similar liquids is equal to $(B_2 V_2^{3-g}/B_1 V_1^{3-g})^{1/3}$.

The appropriate first derivatives of C are zero at points given by equations (7) and (8), and the Hessian matrix is also positive definite. The equations presented therefore satisfy the necessary and sufficient conditions for a minimum of the objective function [7].

For practical reasons the value of the ratio $s_2/s_1 = m$ is sometimes assumed a priori. Introducing this relationship into the objective function and solving it for optimum s_1 gives

$$s_{1opt}^{-3} b^{g-3} = \frac{2A_1(a_1+a_2+a_3+a_4)}{(3-a_1-a_2-a_3-a_4)(B_3 V_1^{3-g} + B_4 V_2^{3-g} m^{-3})} \tag{10}$$

Substituting for $s_{1\mathrm{opt}}^{-3} b^{g-3}$ and $s_{2\mathrm{opt}}^{-3} b^{g-3}$ from equations (7) and (8) in C, we obtain

$$C_{\mathrm{opt}} = 2A_1 bl\left(1 + \frac{a_1+a_3}{3-a_1-a_2-a_3-a_4} + \frac{a_2+a_4}{3-a_1-a_2-a_3-a_4}\right) \tag{11}$$

The formulation of the basic problem for the second version of the imposed data (V_1, t_{11}, t_{12}, and t_{21}), has also been supplemented with the constraint $s_2/s_1 = m$.
$V_{2\mathrm{opt}}/V_1$ is then given by the equation

$$B\left(\frac{V_{2\mathrm{opt}}}{V_1}\right)^{g-3} m^3 = \frac{3(a_1+a_3+a_4) - g(a_1+a_2+a_3+a_4) - 3V_{2\mathrm{opt}}\dfrac{\Delta t_m'}{\Delta t_m}}{3\left(a_2 + V_{2\mathrm{opt}}\dfrac{\Delta t_m'}{\Delta t_m}\right)} \tag{12}$$

where $B = B_3/B_4$, $\Delta t_m' = \partial \Delta t_m/\partial V_2$, and the optimum value of s_1 is given by equation (10).

As the mean driving force in SHE's usually differs only insignificantly from that for counterflow [6], Δt_m therefore may be assumed to be given by log-mean, which can be ex-

Nomenclature

A_1 = cost per unit surface area, dollars/m^2
a = exponent, dimensionless
B_1, B_2 = cost per unit of fluid pumping power multiplied by annual operation time, dollars/J
B_3, B_4 = given in equation (8)
B = B_3/B_4, dimensionless
b = effective width of heating surface and channel, m
C = overall annual cost of heat exchanger operation, dollars
c = specific heat, J/kgK
E_1 = constant, equation (3), dimensionless
e_1 = thermal effectiveness, dimensionless
g = exponent, equation (3), dimensionless
h = heat transfer coefficient, W/m^{2}K
l = spiral channel length, m
m = spacing ratio = s_2/s_1, dimensionless
Δp = pressure drop, N/m^2
Q = heat transfer rate, W
Re = Reynolds number, dimensionless
s = spacing between plate strips, m
t = temperature, K
Δt_m = mean temperature difference, K
U = overall heat transfer coefficient, W/m^{2}K
V = volumetric flow rate, m^3/s
v = mean axial velocity, m/s
μ = dynamic viscosity, Ns/m^2
ρ = density, kg/m^3

Subscripts

1 = inlet temperature
2 = outlet temperature
opt = optimum value

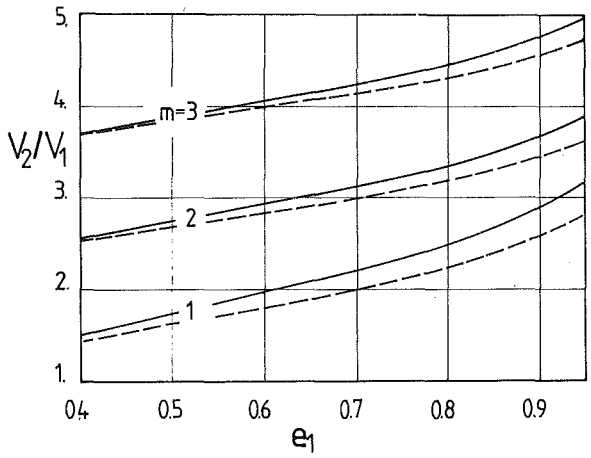

Fig. 2 Optimum V_2/V_1 versus e_1 for $B = 1$, $a_1 = a_2 = 0.27$ (solid lines) and $a_1 = a_2 = 0.37$ (dashed lines)

pressed in terms of the effectiveness $e_1 = (t_{11} - t_{12})/(t_{11} - t_{21})$ and of the fluid heat capacity ratio $R = V_2\rho_2 c_2/V_1\rho_1 c_1$. Therefore, optimum V_2/V_1 depends on four variables: e_1, B, m and the ratio $\rho_2 c_2/\rho_1 c_1$.

As may be seen from Fig. 2, $V_{2\text{opt}}/V_1$ rises sharply with rising e_1 and m but is less affected by a. Obviously, it is also markedly dependent on $\rho_2 c_2/\rho_1 c_1$ and B. Graphs similar to that given in Fig. 2 effectively illustrate the general trends but have less practical application. To provide a simple quantitative method for finding optimum V_2, the graphical solution to equation (12), for given a, was developed. It is shown in Fig. 3 and Fig. 4 for $m = 1$ and $m = 2$, respectively. The procedure is as follows:

- For the given e_1 and assumed $V_{2\text{opt}}/V_1$, and hence R, find the right-hand side ordinate.
- Transfer the right-hand side ordinate to the left-hand side and for the given B check the correctness of the initial assumption.

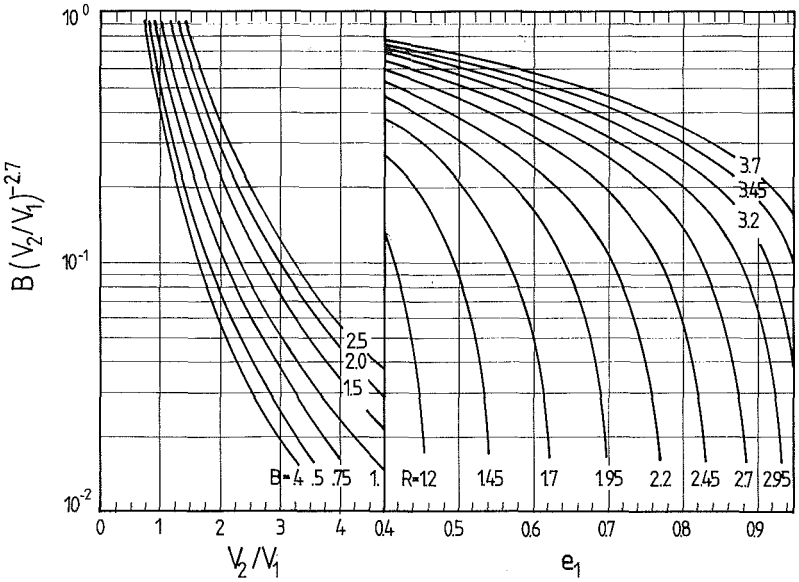

Fig. 3 Graphical solution to equation (12), $m = 1$, $a_1 = a_2 = 0.27$, $a_3 = a_4 = 0.065$, $g = 0.3$

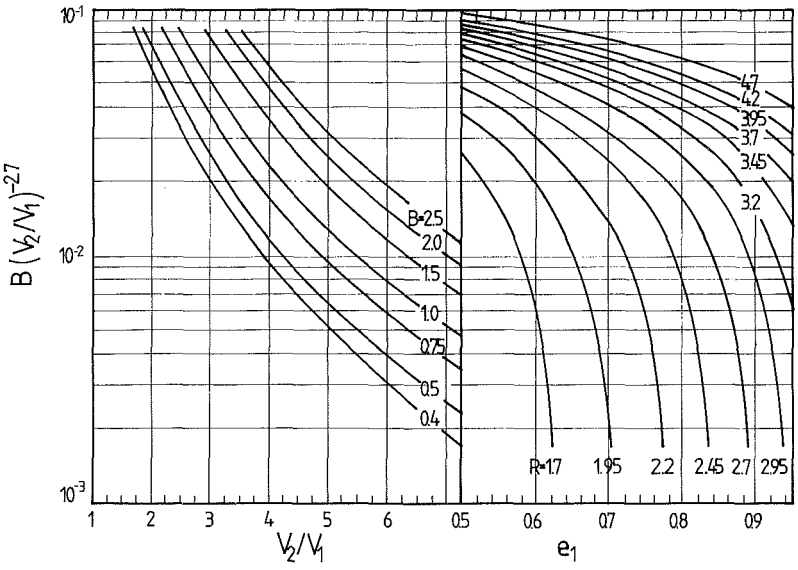

Fig. 4 Graphical solution to equation (12), $m = 2$

Two or three iterations give a good approximation to the value of V_{2opt}.

SHE With Distance Holders. The analysis has been performed assuming that $U = Kv_1^{a_1}v_2^{a_2}$ and $s_2/s_1 = m$. An inspection of the objective function obtained by substituting equation (5) into equation (4) showed that there is a minimum of C over s_1, s_2, and b. The optimum values of b and s_1 are

$$b_{opt} = \left\{ \frac{(B_5 V_1^3 + B_6 V_2^3 m^{-2})^3 [3 - a_1 - a_2 + g(2 - a_1 - a_2)]}{2A_1(a_1 + a_2)g^3 (B_3 V_1^{3-g} + B_4 V_2^{3-g} m^{-3})^2} \right\}^{\frac{1}{3+2g}} \tag{13}$$

$$s_{1opt} = \frac{b_{opt}^g g (B_3 V_1^{3-g} + B_4 V_2^{3-g})}{B_5 V_1^3 + B_6 V_2^3 m^{-2}} \tag{14}$$

where $B_5 = B_1 E_2 \rho_1$ and $B_6 = B_2 E_2 \rho_2$.

It may be proved that equations (13) and (14) satisfy the necessary and sufficient conditions for minimum of the objective function. The more general case of the problem, i.e., without additional constraint on s, cannot be resolved analytically and numerical techniques must be employed to sort out the appropriate set of highly nonlinear algebraic equations.

It may be anticipated that the optimum value of s_2/s_1 should be constrained as follows

$$(B_4 V_2^{3-g} a_1 / B_3 V_1^{3-g} a_2)^{1/3} < (s_2/s_1)_{opt} < (B_6 V_2^3 a_1 / B_5 V_1^3 a_2)^{1/2}$$

Equations (13) and (14) also give the optimum values of b and s_1 for the second set of imposed data. The optimum value of V_2 is then given by the equation

$$[3 + g(2 - a_1 - a_2)]\left(a_2 + V_{2opt}\frac{\Delta t'_m}{\Delta t_m}\right) = \frac{(3-g)(a_1 + a_2)}{B\left(\frac{V_{2opt}}{V_1}\right)^{g-3} m^3 + 1} + \frac{3g(a_1 + a_2)}{\frac{B_5}{B_6}\left(\frac{V_{2opt}}{V_1}\right)^{-3} m^2 + 1} \tag{15}$$

which due to its nonlinearity can only be solved numerically. Results obtained, not included in this paper, did not differ markedly from those given in Fig. 2. The same conclusion may also be reached by comparing the appropriate values of V_2/V_1 given in Fig. 4 and in Fig. 5 for $m = 2$ and $B_5/B_6 = 1$. From equation (15), it may be inferred that the value of E_2, and hence both the actual number of distance holders per unit area and their characteristics, has no effect on the value of V_{2opt}.

Discussion

The expressions derived provide convenient guidelines for optimum dimensioning of SHE's and for choice of optimum quantity of working fluid, if the cost of the latter is insignificant. The optimum values for spacings obtained from the equations will not normally correspond exactly to those quoted by manufacturers. However, as the curve of C is fairly flat around the economic optimum, the nearest given in catalogues will usually give the required results. This has been checked by calculations which also confirmed the validity of the derived equations and of the whole approach.

Computations confirmed the economic sense of employing optimum, usually larger, throughputs of the working fluid, provided the cost of the latter is negligible, and that this does not cause a drastic increase in the initial investment outlay. Economies due to the employment of optimum throughputs of the working fluid proved to be quite substantial and to increase with e_1. For turbulent flow of waterlike liquids ($a_1 = a_2 \simeq 0.27$) the costs could be reduced to 75 percent (for $e_1 = 0.7$) and to 60 percent (for $e_1 = 0.9$) of those corresponding to the assumption $V_2 = V_1 \rho_1 c_1 / \rho_2 c_2$. To reduce the extra power input, the spacing s_2 should be increased so as to reduce the pressure drop. The increase in mean driving force Δt_m, due to larger fluid heat capacity rate $V_2 \rho_2 c_2$, plus an associated reduction in required heating surface contributing further to reduce pressure drop, makes this pay off. The actual spacings were found to have less impact on costs but one may expect savings of some 5–7 percent for $m = 2$, and for $m = 3$ even more than 10 percent. All these observations can be confirmed by more detailed analytical studies of the costs of optimum SHE's as predicted by the equations derived in the paper.

It may be inferred from equation (11) that the ratio of capital costs to power costs for optimum dimensioned exchangers ranges from 2 to 4, and this is in excellent agreement with Jenssen's earlier observations [4, 5]. The lower value refers to cases when film resistances predominate over wall

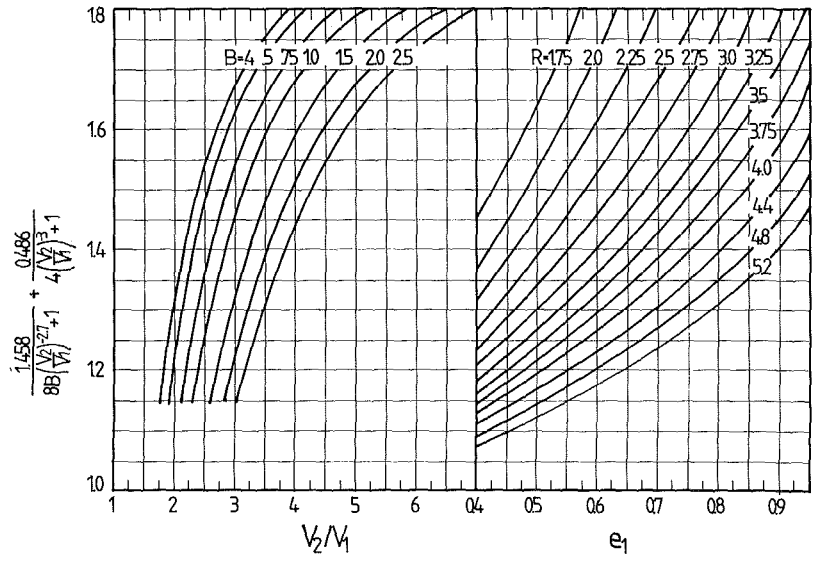

Fig. 5 Graphical solution to equation (15), $m = 2$, $a_1 = a_2 = 0.27$

and fouling resistance. The higher value refers to the cases when all three contributors to the overall heat transfer resistance $1/U$ are of the same order.

For practical application of the equations derived in this paper, it is necessary to know a relevant to the given problem. Their estimation using standard curve fitting routines makes no sense timewise. They can, however, be estimated with fair accuracy from the contributions of the film resistances $1/h_i$ ($i = 1, 2$) obtained for some average velocities, say, of order 0.7 m/s, to the overall heat transfer resistance $1/U$. The values of U/h_i multiplied by 0.8, i.e., by the exponent of Re in the standard heat transfer correlation, give the approximate values of a_1 and a_2 and multiplied by 0.2 the values of a_3 and a_4.

It is worth noting that a similar approach to that outlined here may easily be adopted to provide solutions to related problems concerning heat exchangers with geometrically simple passages, e.g., plate heat exchangers [8].

Conclusions

If certain simplifications are introduced, the problem of optimum dimensioning of SHE's to give minimum costs can be solved analytically. The resulting expressions provide the basis for rapid approximate assessment of optimum spacings between plate strips and also throughput of the working fluid. They also illustrate how and to what extent economic and technical factors and properties of the fluid affect the parameters of the optimum spiral exchangers.

Approximate optimum parameters of SHE's predicted by the equations derived may also be used as starting values in more complete, and hence more accurate, algorithms of computer optimization.

For liquid–liquid mode of operation the overall annual operating cost is markedly dependent on the throughput of the working fluid while the spacings have less effect. The employment of larger throughputs is well justified and leads to economies which increase with thermal effectiveness e_1.

References

1 Shah, R. K., Afimiwala, K. A., and Mayne, R. W., "Heat Exchanger Optimization," *Proceedings of the Sixth International Heat Transfer Conference*, Vol. 4, 1978, pp. 185–191.

2 Hedderich, C. P., Kelleher, M. D., and Vanderplaats, G. N., "Design and Optimization of Air-Cooled Heat Exchangers," ASME JOURNAL OF HEAT TRANSFER, Vol. 104, 1982, pp. 683–690.

3 Hargis, A. M., Beckmann, A. T., and Loiacono, J. J., "Application of Spiral Plate Heat Exchangers," *Chemical Engineering Progress*, Vol. 63, 1967, No. 7, pp. 62–67.

4 *Thermal Handbook*, Alfa-Laval, Stockholm, 1969.

5 Jenssen, S. K., "Heat Exchanger Optimization," *Chemical Engineering Progress*, Vol. 65, 1969, No. 7, pp. 59–66.

6 Brodowicz, K., and Grabowski, M., "Spiral Heat Exchangers. Part 1. Thermal Calculations," (in Polish), *Inzynieria i Aparatura Chemiczna*, Vol. 15, 1976, No. 3 pp. 1–5.

7 Ray, W. H., and Szekely, J., *Process Optimization*, Wiley & Sons, New York, 1973.

8 Jarzębski, A. B., and Wardas-Koziel, E., "Dimensioning of Plate Heat Exchangers to Give Minimum Annual Operating Costs," *Chemical Engineering Research and Design*, submitted for publication.

Effect of Matrix Properties on the Performance of a Counterflow Rotary Dehumidifier

J. J. Jurinak
Assoc. Mem. ASME

J. W. Mitchell
Mem. ASME

Solar Energy Laboratory,
University of Wisconsin-Madison,
Madison, Wis. 53706

A finite difference model of a counterflow rotary dehumidifier is used to determine the effect of six matrix properties of dehumidifier performance. The matrix properties considered are the sorption isotherm shape, the maximum sorbent water content, the heat of sorption, the matrix thermal capacitance, matrix moisture diffusivity, and sorption isotherm hysteresis. The isotherm shapes and the sorption parameter values are selected to be representative of available insoluble desiccants. The results of the finite difference calculations show that the shape of the isotherm has a greater effect on dehumidification than the maximum water content. Large adsorption heat effects or matrix thermal capacitance has a detrimental impact on dehumidification. Hysteresis in the adsorption isotherm significantly impairs dehumidifier performance. The anlaysis shows that commercially available solid desiccants can result in nearly optimal dehumidifier performance.

Introduction

The performance characteristics of a rotary regenerator are largely determined by the physical properties of the porous matrix. Regenerative dehumidifiers, in which maximum moisture transfer is important, utilize a sorbent matrix with large moisture but small thermal capacity. Rotary dehumidifiers are used as industrial air driers [1] and in proposed residential desiccant cooling systems [2, 3].

The simultaneous heat and mass transfer in a rotary dehumidifier has been modeled by both finite difference techniques [4–6] and approximate analytic solutions [7, 8]. In all of these studies, the dehumidifier has been modeled using particular sets of matrix properties. To date, there has been no general study of the effect of matrix properties on the performance of the rotary dehumidifier.

In this paper, a finite difference solution [4, 9] is used to determine the effect of six matrix properties on the steady-state performance of a rotary dehumidifier. The matrix properties considered are the sorption isotherm shape, the maximum sorbent water content, the heat of sorption, the matrix thermal capacity, matrix moisture diffusivity, and sorption isotherm hysteresis. The range of property values was selected to be representative of available solid porous physical adsorbents, such as silica gels or molecular sieves. The results of this study are useful as guides for the selection and appraisal of matrix materials. The results of this study have also been applied to determine the influence of property dependent variations in dehumidifier performance on the performance of an open cycle desiccant cooling system [9].

The Dehumidifier Model

The rotary dehumidifier to be modeled is shown schematically in Fig. 1. The porous matrix of the dehumidifier can be either a packed bed of granular desiccant or a parallel passage wheel formed by spirally winding an adsorbent ribbon on a spoked hub [10]. The two air streams can pass through the matrix in either parallel flow or counterflow paths. A counterflow exchanger with uniform air temperature, humidity ratio, and velocity at the inlet of each period is considered in this study.

Several conventional [4, 5] assumptions are made to focus the model on the dominant flow and transfer processes occurring in the dehumidifier:

1 The air flow in each period is at constant pressure and velocity.

2 The interstitial air thermal and moisture storage capacities are negligible compared to the matrix capacities.

3 Axial heat and mass diffusion in both the air and matrix are negligible.

4 The combined solid diffusion-convective film resistance to heat or mass transfer can be described by composite coefficients.

5 There is no transfer flux coupling through thermal diffusion or Dufor effects.

Under these constraints, the equations of mass and energy conservation in period j of the dehumidifier, written with respect to a coordinate system moving with the rotating matrix, become [4, 5]

$$\frac{\partial w}{\partial x'} + \theta'_j (\mu\kappa)_j \frac{\partial W}{\partial \theta'} = 0$$

$$\frac{\partial i}{\partial x'} + \theta'_j (\mu\kappa)_j \frac{\partial I}{\partial \theta'} = 0 \qquad j = 1,2 \qquad (1)$$

The mass and heat transfer rate equations are

$$\frac{\partial w}{\partial x'} = \Lambda_{w,j} (w_m - w_f)$$

$$\frac{\partial i}{\partial x'} = \Lambda_{w,j} (\mathrm{Le}_o c_f (t_m - t_f) + i_{wv} (w_m - w_f)) \qquad j = 1,2 \qquad (2)$$

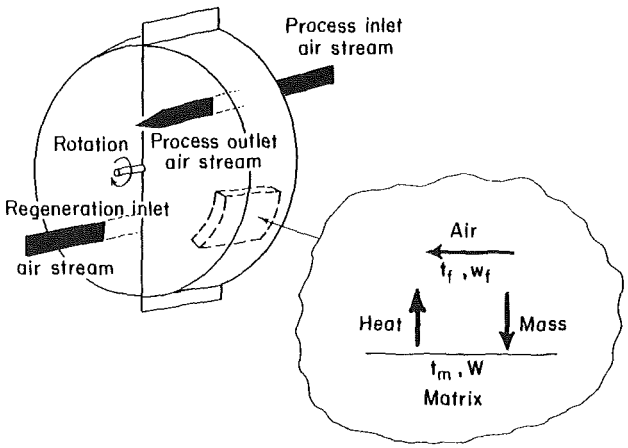

Fig. 1 Counterflow rotary dehumidifier

Contributed by the Heat Transfer Division and presented at the ASME Winter Annual Meeting, Phoenix, Arizona, November 14-19, 1982. Manuscript received by the Heat Transfer Division August 30, 1982.

The independent variables in equations (1, 2) are normalized axial position x' and normalized rotational time θ' (equivalent to circumferential position). The dependent variables are moist air humidity ratio and enthalpy (w,i), and matrix water content and enthalpy (W,I). Because the coordinate system is fixed with respect to the matrix, the rotary nature of the dehumidifier is introduced by imposing periodic boundary conditions. The counterflow condition is represented by a periodic reversal in flow direction. The bulk process outlet state ($t_{p,o}w_{p,o}$) is the average with respect to θ' of the air state distributions at the matrix process period exit.

The finite difference solution of equations (1, 2) utilized in this study employs a method developed by Maclaine-cross [4, 9]. The difference equations, which are of second order, are solved for three space-time grid sizes, and the solutions are quadratically extrapolated to zero grid size. The extrapolated solution is of fourth order. In most cases represented in this study, the lack of closure in the system moisture and energy balances is less than 0.01 percent [9].

The dehumidifier performance is characterized by a dehumidifier moisture efficiency, η_w, defined as

$$\eta_w = \frac{w_{p,o} - w_{p,i}}{w_{p,\text{int}} - w_{p,i}} \tag{3}$$

where $w_{p,\text{int}}$ is the humidity ratio at the intersection point of the line of constant adiabatic saturation temperature through the process inlet state and a relative humidity line through the regenerating inlet state, as shown in Fig. 2. The minimum potential humidity ratio would be $w_{p,\text{int}}$ if the dehumidification process were the reverse of an adiabatic saturation process with air exiting the dehumidifier at the relative humidity of the regenerating state. Because the dehumidification potential lines depend on the matrix properties as well as the moist air properties and are skewed away from wet bulb and relative humidity lines [11], $w_{p,\text{int}}$ is only a convenient normalizing parameter.

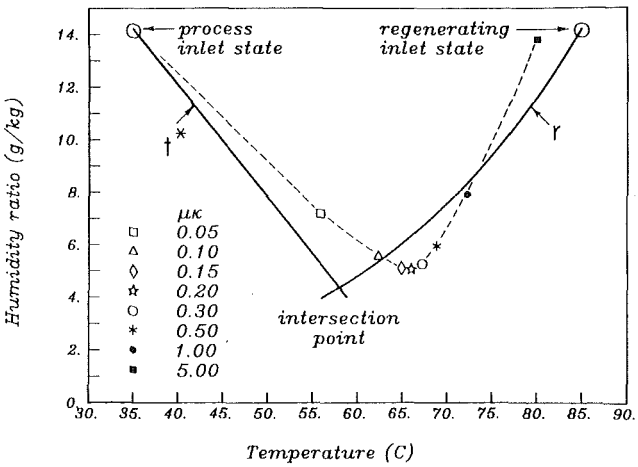

Fig. 2 Variation of the dehumidifier process stream outlet states with $\mu\kappa$, superimposed on a wet bulb (t^*) line through the process inlet state and a relative humidity (r) through the regenerating inlet state

Physical Adsorption and Absorbents

Adsorption is the condensation of a vapor on a surface at a pressure below the normal saturation pressure of the vapor. Thorough discussions of the mechanisms and models of adsorption are found in [12–14]. This study is limited to consideration of the physical adsorption of water vapor on solid sorbents. The characteristics of various physical adsorbents are summarized here to provide perspective for the numerical simulations to be subsequently discussed. This brief description relies heavily on vapor pressure lowering theory and does not mention other factors, such as desiccant surface area and electric field, in proper proportion to their importance [12–14].

Brunauer [13] classified experimentally observed isotherms into five types, illustrated in Fig. 3. The different shapes are generally characteristic of different adsorption mechanisms.

The type 1 isotherm is observed for porous adsorbents with pores that are approximately the size of the sorbate molecules. These ultra-micro pores are filled at low relative pressures, resulting in a plateau in the isotherm. Molecular sieves have a type 1 water adsorption isotherm [12, 15].

Type 2 and type 3 isotherms are associated with multilayer adsorption without capillary condensation. Wool and other biological materials have a type 2 water adsorption isotherm [16, 17]. Type 3 water vapor adsorption isotherms are rare; an example is adsorption on glass [13, 14]. Type 2 materials have a heat of adsorption larger than the heat of vaporization, while the type 3 materials have a heat of adsorption that is less than the heat of vaporization [13].

Types 4 and 5 result for porous materials in which capillary condensation occurs. Type 4 isotherms are characteristic of hydrophilic porous materials, such as silica gels. The plateau in water content at the low relative pressure region of the isotherm is associated with the filling of molecular dimension

Nomenclature

c_d = desiccant specific heat [energy/(dry mass-temp)]
c_f = moist air specific heat [energy/(dry mass-temp)]
c_m = matrix thermal capacitance [energy/(dry desiccant mass-temp)], see equation (8)
c_w = liquid water specific heat [energy/(mass-temp)]
$G(W)$ = isotherm at some temperature t_0 [dimensionless]
h^* = ratio of the isothermal differential heat of adsorption to the heat of vaporization [dimensionless], see equations (4) and (5)
i = moist air enthalpy [energy/dry mass]
$i_s = \left(\frac{\partial i}{\partial w}\right)_t - \left(\frac{\partial I}{\partial W}\right)_t$, isothermal differential heat of adsorption [energy/dry mass]
i_v = heat of vaporization [energy/mass]
i_{wv} = water vapor enthalpy [energy/mass]
I = matrix enthalpy [energy/dry mass], see equation (7)
$J_{t,j}$ = $4h/(\rho' d_h c_f)$, where h is the heat transfer coefficient, ρ' is the dry fluid density, and d_h is the hydraulic diameter. The lumped matrix-transfer coefficient per unit mass of fluid [time^{-1}]
$J_{w,j}$ = $4h_w/(\rho' d_h)$, where h_w is the mass transfer coefficient, ρ' is the dry fluid density, and d_h is the hydraulic diameter. The lumped matrix-fluid mass transfer coefficient per unit mass of fluid [time^{-1}]
Le_o = $J_{t,j}/J_{w,j}$, overall Lewis number [dimensionless]
p_{ws} = saturation pressure of water vapor [force/area]
p_{wv} = equilibrium adsorbed water vapor pressure [force/area]
r = relative humidity (or pressure), ratio of vapor partial pressure to saturation pressure [dimensionless]
t = temperature

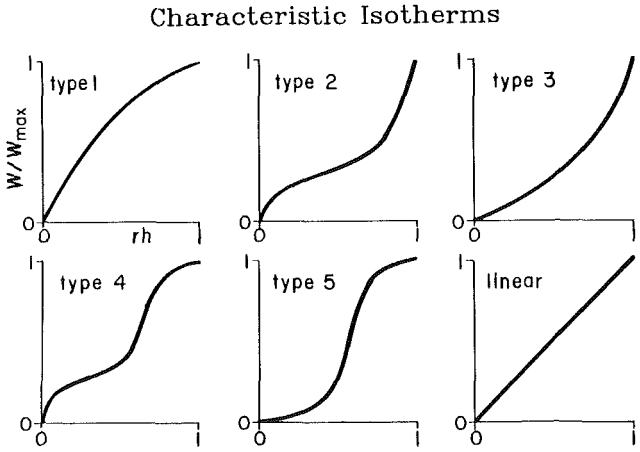

Fig. 3 Brunauer isotherm classification

pores (less than 10A dia), and the rise in water content at a higher relative pressure is due to the filling of capillary pores (10A–500A dia) [12, 13, 18]. The low relative pressure plateau in the type 4 isotherm can be very narrow and indistinct, resulting in an approximately type 1 isotherm. Several microporous (20A mean pore dia) silica gels exhibit approximately type 1 behavior [15, 18, 19]. The type 5 isotherm is characteristic of capillary porous materials in which the solid surface is hydrophobic, an example being the isotherm for water adsorption on activated charcoal [13, 20]. The heat of adsorption for the type 5 adsorbents can be less than the heat of vaporization [13].

The capillary-porous materials (types 4 and 5) frequently exhibit a hysteresis loop in the isotherm. Sorption hysteresis results from changes in the characteristic radii of the adsorbate meniscus in the capillary pores. Hysteresis behavior has been classified according to the irregularities in the pore shapes [21] and can be modeled [12, 22].

Continuum Thermodynamics of Adsorbents

The Clausius-Clapeyron equation relates the water vapor pressure and the saturation pressure to the ratio of the differential heat of sorption to the enthalpy of condensation:

$$\left(\frac{\partial \ln p_{wv}}{\partial \ln p_{ws}}\right)_W = \frac{i_s}{i_v} = h^* \tag{4}$$

Brandemuehl [23] analyzed heat of wetting data for silica gel [24–26] and found that the ratio h^* can be expressed as an exponential function of desiccant water content. The following empirical form is used in this study

$$h^*(W^*) = 1 + \Delta h^* \frac{\exp(kW^*) - \exp(k)}{1 - \exp(k)} \tag{5}$$

where W^* is the water content W, normalized by the maximum water content W_{mx}, $1 + \Delta h^*$ is h^* at $W^* = 0$, and k is a constant.

If the ratio h^* is independent of temperature, equation (4) can be integrated to show that if the adsorption isotherm is a function $G(W)$ at temperature t_0, then at any temperature t

$$r = G(W)\,(p_{ws}(t)/p_{ws}(t_0))^{h^*-1} \tag{6}$$

The form of equation (5) used in this study insures that isotherms given by equation (6) converge to the maximum water content W_{mx} at $r = 1$. This allows W_{mx} to be used as a scaling parameter for the isotherms. The physical assumption implicit in this behavior of the isotherms is that at saturation ($r = 1$), adsorption becomes normal condensation on the matrix.

The enthalpy of the matrix at any temperature and water content with respect to a dry matrix at 0°C is

$$I = c_m t + c_w W t + i_v \int_0^W (1 - h^*)\,dW \tag{7}$$

The dry matrix thermal capacitance, c_m, is related to the bulk desiccant specific heat, c_d, and the specific heats of the nonsorbing matrix materials, c_{Ni}, by

$$c_m = c_d + \sum_i (M_i c_{Ni})/M_d \tag{8}$$

where M_i is the mass of nonsorbing component i and M_d is the mass of the desiccant in the matrix.

The moist air is taken to be an ideal binary mixture of dry air and water vapor, characterized by conventional psychrometric relationships [9, 27].

Matrix Parameters

The intent of this study is to indicate the effect of important matrix properties on the performance of a rotary dehumidifier. Because none of the mechanistic adsorption models is entirely satisfactory [12, 14, 16] and there is considerable scatter in experimental data for common desiccants [15, 19, 28], the approach followed in this work has been to

Nomenclature (cont.)

t^* = thermodynamic wet-bulb temperature
v_j = air velocity in period j [length/time]
w = moist air humidity ratio [dimensionless]
W = matrix water content [dimensionless]
W^* = W/W_{mx} ratio of matrix water content to maximum water content [dimensionless]
W_{mx} = maximum ($r = 1$) matrix water content [dimensionless]
x = axial displacement through matrix measured from period entrance [length]
η_w = dehumidifier moisture efficiency [dimensionless], see equation (3)
θ = time from the beginning of period 1
θ_j = duration of period j [time]
θ' = θ/T, rotational time divided by the time for a complete matrix revolution [dimensionless]
θ'_j = θ_j/T, normalized duration of period j [dimensionless]
κ_j = $L/v_j\theta_j$, carry-over ratio [dimensionless]
$\Lambda_{t,j}$ = $J_{t,j}L/v_j$, dimensionless heat transfer length
$\Lambda_{w,j}$ = $J_{w,j}L/v_j$, dimensionless mass transfer length
μ_j = dry period j matrix mass divided by dry fluid mass contained in matrix in period j [dimensionless]
T = time required for a complete matrix rotation

Subscripts

f = evaluated at fluid state
i = inlet state
int = evaluated at the intersection point of a wet-bulb temperature line through the process inlet state and the relative humidity line through the regenerating inlet state
j = period index
m = evaluated at, or in equilibrium with, the matrix state
o = spatial or rotational average outlet state
p = process period
r = regenerating period
x = relating to maximum dehumidification

Table 1 Dehumidifier flow and matrix parameters

Dehumidifier flow parameters			
$\Lambda_w = 20,\ 0.05 \le \mu\kappa \le 5.0$			
Inlet states pair	Process		Regenerating
1	(35°C, 14.23/kg)		(85°C, 14.2 g/kg)
2	(30°C, 24.5 g/kg)		(100°C, 14.2 g(kg)
Matrix properties			
Variation	Isotherm type (Eq.)	W_{mx}(kg/kg)	$\Delta h^*, k$ (Eq. (5))
Nominal	Linear (9.6)	0.5	0.3, −5.0
Iostherm shape	1 (9.1)	0.5	0.3, −5.0
	2 (9.2)	0.5	0.3, −5.0
	3 (9.3)	0.5	−0.3, −5.0
	4 (9.4)	0.5	0.3, −5.0
	5 (9.5)	0.5	−0.3, −7.5
Maximum W	Linear	0.25	−0.3, −5.0
	Linear	1.00	0.3, −5.0
	1a (9.1*a*)	0.25	0.0
	4a (9.4*a*)	1.125	0.0
Heat ads.	Linear	0.5	0.0
	Linear	0.5	1.0, −1.0
$C_m = 3350 \frac{\text{J}}{\text{kg°C}}$	Linear	0.5	0.3, −5.0
$\text{Le}_o = 4,\ \Lambda_w = 5.0$	Linear	0.5	0.3, −5.0
Hysteresis	Linear-process	0.5	0.0
	1-regenerating	0.5	0.0

Table 2 Isotherm equations

Type		$r = G(W^*)$	Eq.
1		$r = 1 - (1 - W^*)^{1/2}$	(9.1)
1(*a*)		$r = W^*/(1 + 50(1 - W^*))$	(9.1*a*)
2		$r = 0.43194 + 0.43950\tan^{-1}(5.0(W^* - 0.3))$	(9.2)
3		$r = W^*/(1. - 0.75(1 - W^*))$	(9.3)
4	$W^* \le 0.65$	$r = 0.29754 + 0.29437\tan^{-1}(6.37959(W^* - 0.25))$	(9.4)
	$W^* \le 0.65$	$r = 0.65 + 0.06280\tan(3.98089(W^* - 0.65))$	
4(*a*)	$W^* \le 0.1$	$r = 0.35 + 0.30929\tan^{-1}(42.5742(W^* - 0.05))$	(9.4*a*)
	$W^* > 0.1$	$r = 0.85 + 0.069041\tan(3.052(W^* - 0.55))$	
5		$r = 0.50 + 0.10\tan(2.7468(W^* - 0.5))$	(9.5)
linear		$r = W^*$	(9.6)

choose functional variations and ranges of parameter values that are qualitatively representative of a broad spectrum of solid physical adsorbents and matrix configurations. The constraints imposed by continuum thermodynamics are satisfied and the major adsorbent types are all represented.

The reference or base case desiccant is modeled with a simplified representation of Hubard's silica gel data [24]. The isotherm is linear at 60°C, has a maximum water content of 0.5 g/g, and a maximum h^* (at $W = 0.0$) of 1.3.

The counterflow dehumidifier modeled in this study has equal air mass flow rates and flow areas in each period. The reference matrix has a thermal capacitance equal to the bulk specific heat of silica gel (c_m = 921 J/kg°C) and an overall Lewis number of unity. These conditions are representative of a matrix with little nonadsorbent structural materials and in which convection governs the heat and mass transfer rates. The reference value of the dimensionless mass transfer length, Λ_w, is 20, which is representative of high-performance dehumidifiers. The dehumidifier outlet states are influenced by $\mu\kappa$, the ratio of matrix rotational mass flow rate to air mass flow rate, as shown in Fig. 2 for the reference linear isotherm. A range of relative rotational speeds is considered that results in both dehumidifier and enthalpy regenerator operation. The maximum dehumidifier efficiency η_{wx} and the optimum relative rotational speed for dehumidification $\mu\kappa_x$ depend on the matrix properties and the dehumidifier inlet states.

Two pairs of air inlet states relevant to air conditioning are used. One pair has a process inlet state of (35°C, 14.2 g/kg) and a regenerating state of (85°C, 14.2 g/kg). This corresponds to inlet relative humidities of 40 percent and 4 percent, respectively. The other inlet state pair is (30°C, 24.5 g/kg) and (100°C, 14.2 g/kg), with relative humidities of approximately 90 percent and 2 percent, respectively. These inlet state pairs are subsequently referred to as 1 and 2.

The reference matrix properties and the principal variations considered in this study are summarized in Table 1. These variations and their effects on dehumidifier performance are described in the following section.

Results and Discussion

Adsorption Isotherm Shape. Functions $G(W)$ were chosen to qualitatively reproduce the features of the five generic Brunauer types and a linear isotherm. These equations are given as a function of $W^* = W/W_{mx}$ in Table 2. The isotherms qualitatively characterize available desiccants, as illustrated in Fig. 4, where the type 1 and 2 isotherms and normalized data for a microporous silica gel (Davison 03) [15] and wool [17] are shown. Similarly, the types 4, 5, 1(*a*) and 4(*a*) isotherms were chosen to be representative of activated alumina [29], charcoal [20], molecular sieve [15] and macroporous silica gel [15, 28].

The effect of temperature on the isotherm was determined using equations (6) and (5). The values of the constants Δh^* and k (equation (5) and Table 1) were selected on the basis of Brandemuehl's analysis of silica gel data [23]. A negative value of Δh^* is used for the type 3 and type 5 isotherms because the heat of sorption is less than the heat of water vaporization for these absorbents. The temperature at which $r = G(W^*)$ is t_0 = 60°C.

The dehumidifier efficiency was determined for the types 1–5 and linear isotherms with W_{mx} = 0.5 g/g as a function of rotational speed and inlet state. The optimum rotational speed ratio $\mu\kappa_x$, process outlet state, and maximum

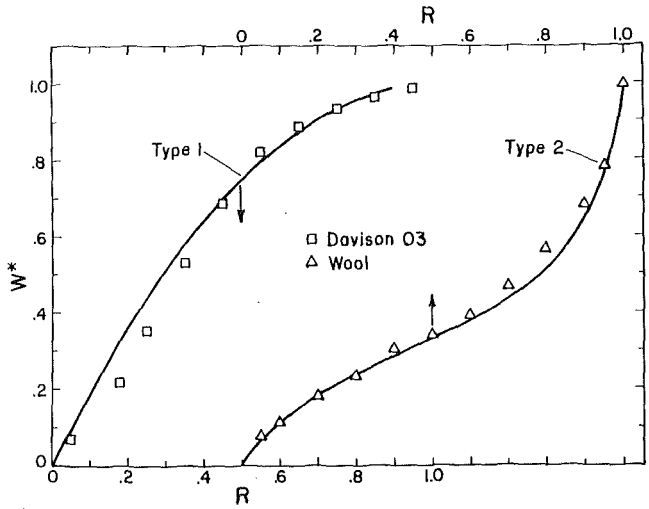

Fig. 4 Type 1 (equation (9.1)) compared to Davison 03 silica gel isotherm [15], and type 2 (equation (9.2)) compared to wool isotherm [17]

dehumidifier efficiency η_{wx} are given in Table 3. These results indicate that the isotherms can easily be classified in two groups, one favorable and the other unfavorable for dehumidification.

The types 1, 2, and 4 and linear isotherms have relatively high η_{wx} and can be considered favorable for dehumidification. The type 1 isotherm η_{wx} are about 5 percent greater than those of the other favorable isotherms. The values of η_{wx} for inlet state pair 1 are about 5 to 7 percent greater than those for inlet state pair 2.

The types 3 and 5 isotherms have η_{wx} that are about 20 percent lower than those for the first group and can be considered unfavorable for dehumidification. For these isotherms, the η_{wx} for inlet state 2 is slightly greater than for inlet state 1.

The results also show that the optimum rotational speed varies with matrix properties and dehumidifier inlet states. The favorable isotherms have a much lower $\mu\kappa_x$ than the unfavorable isotherms, corresponding to a lower optimum matrix rotational speed at a given air flow rate. However, $\mu\kappa_x$ varies more with the change in inlet state for the favorable isotherms than for the unfavorable types. For any of the favorable isotherms, $\mu\kappa_x$ for inlet state 2 is about twice $\mu\kappa_x$ for inlet state 1, representing a double in optimum matrix rotational speed as the inlet states change.

To indicate the effect of operating the dehumidifier at nonoptimal rotational speeds, Table 4 lists the values of $t_{p,o}$, $w_{p,o}$ and η_w at values of $\mu\kappa$ equal to $\mu\kappa_x$ for the alternate inlet state pair. Comparing the results given in Tables 3 and 4, it can be seen that operating at the nonoptimal $\mu\kappa$ results in an average drop in η_w of about 4 percent. This suggests that near optimum dehumidification is obtained over a reasonably broad range of $\mu\kappa$.

Except for the clear distinction between the high-performance favorable isotherms and the low-performance unfavorable isotherms, the variations in isotherms type $\mu\kappa$ and inlet state result in at most 5 to 7 percent variations in η_w. However, measuring these effects as proportional changes in η_w masks the fact that the changes in high-performance dehumidifier design required to offset a 5 percent variation in η_w with matrix properties can be large. For example, Table 5 lists the Λ_w required at optimum rotational speed for the various isotherms to have $\eta_w = 0.95$ for inlet state 1 and $\eta_w = 0.90$ for inlet state 2. The results show that the Λ_w required for a given η_w by the type 2, 4 and linear isotherm dehumidifiers is about twice that of a type 1 isotherm dehumidifier. The type 3 and 5 isotherm dehumidifiers cannot obtain the required η_w at Λ_w more than four times that of the type 1 dehumidifier. Thus other variables being equal, the volume of the type 1 dehumidifier will be at most half that of the alternative designs. The seemingly insignificant performance advantage of the type 1 isotherm dehumidifier and the importance of operating at optimum relative rotational speed are magnified when viewed in this perspective.

Table 3 Effect of isotherm shape on optimum dehumidifier performance

Type	$\mu\kappa_x$	t_o(°C)	$w_o\left(\frac{g}{kg}\right)$	η_{wx}
		Inlet state 1		
1	0.12	63.84	4.729	0.965
2	0.17	65.65	5.154	0.922
3	0.50	66.36	6.678	0.766
4	0.17	65.58	5.124	0.925
5	0.55	67.63	7.096	0.727
linear	0.18	65.64	5.081	0.929
		Inlet state 2		
	$\mu\kappa_x$	t_o(°C)	$w_o\left(\frac{g}{kg}\right)$	η_{wx}
	0.22	82.03	6.918	0.911
	0.30	84.09	7.879	0.862
	0.60	82.35	9.080	0.799
	0.28	83.80	7.620	0.875
	0.70	83.88	10.252	0.739
	0.35	84.02	7.914	0.860

Table 4 Dehumidifier performance at $\mu\kappa$ away from the optimum

Type	$\mu\kappa$	t(°C)	$w_o\left(\frac{g}{kg}\right)$	η_w
		Inlet state 1		
1	0.22	65.26	5.053	0.932
2	0.30	67.34	5.441	0.892
3	0.60	67.99	6.904	0.743
4	0.28	66.99	5.408	0.896
5	0.70	69.85	7.341	0.699
linear	0.35	67.65	5.467	0.890
		Inlet state 2		
	$\mu\kappa$	t_o(°C)	$w_o\left(\frac{g}{kg}\right)$	η_w
	0.12	79.04	7.299	0.892
	0.17	80.67	8.380	0.836
	0.50	79.97	9.229	0.792
	0.17	81.17	7.968	0.857
	0.55	79.86	10.498	0.726
	0.18	79.85	8.413	0.834

Table 5 Λ_w required to obtain $\eta_{wx} = 0.95$ for inlet state 1 and $\eta_{wx} = 0.90$ for inlate state 2

Type	$\mu\kappa_x$	Λ_w	η_w
	Inlet state 1		
1	0.12	16.0	0.950
2	0.17	38.0	0.951
3	0.50	80.0	0.841
4	0.17	35.0	0.949
5	0.50	80.0	0.801
linear	0.18	30.0	0.951
	Inlet state 2		
Type	$\mu\kappa_x$	Λ_w	η_w
1	0.22	17.0	0.899
2	0.30	40.0	0.899
3	0.60	80.0	0.865
4	0.28	30.0	0.900
5	0.75	80.0	0.792
linear	0.35	40.0	0.899

Maximum Water Content. The maximum water content W_{mx} of insoluble desiccants ranges considerably, from ~0.25 g/g for molecular sieves, to 0.35–0.50 g/g for silica gels and activated aluminas, to greater than 1.0 g/g for macroporous gels. A nominal value of $W_{mx} = 0.5$ g/g was used in deter-

Table 6 Effect of W_{mx} on optimum dehumidifier performance

		Inlet state 1		
W_{mx}	$\mu\kappa_x$	t_o(°C)	$w_o\left(\frac{g}{kg}\right)$	η_{wx}
0.25	0.30	67.69	5.591	0.877
0.50	0.18	65.64	5.081	0.929
1.00	0.10	64.20	4.792	0.958
		Inlet state 2		
	$\mu\kappa_x$	t_o(°C)	$w_o\left(\frac{g}{kg}\right)$	η_{wx}
	0.50	85.55	9.044	0.801
	0.35	84.02	7.914	0.860
	0.22	82.67	7.180	0.898

Table 7 Comparison of molecular sieve, microporous gel, and macroporous gel dehumidifier performance

		Inlet state 1		
Desiccant type	$\mu\kappa_x$	t_o(°C)	$w_o\left(\frac{g}{kg}\right)$	η_{wx}
Mole sieve	0.15	64.46	6.153	0.820
Micro gel	0.12	63.84	4.729	0.965
Macro gel	0.30	62.82	6.028	0.832
		Inlet state 2		
	$\mu\kappa_x$	t_o(°C)	$w_o\left(\frac{g}{kg}\right)$	η_{wx}
	0.30	84.89	9.694	0.767
	0.22	82.03	6.918	0.911
	0.50	84.97	8.814	0.813

Table 8 Effect of heat of adsorption on optimum dehumidifier performance

		Inlet state 1		
Δh^*	$\mu\kappa_x$	t_o(°C)	$w_o\left(\frac{g}{kg}\right)$	η_{wx}
0.0	0.18	62.53	5.188	0.918
0.3	0.18	65.64	5.081	0.929
1.0	0.20	72.14	6.217	0.813
		Inlet state 2		
	$\mu\kappa_x$	t_o(°C)	$w_o\left(\frac{g}{kg}\right)$	η_{wx}
	0.30	80.58	7.229	0.895
	0.35	84.02	7.914	0.860
	0.50	89.44	11.306	0.684

mination of the effect of isotherm shape on dehumidifier performance.

The effect on optimum dehumidifier performance of varying W_{mx} of the linear isotherm from 0.25 g/g to 1.0 g/g is shown in Table 6. These data show that as W_{mx} increases, $\mu\kappa_x$ decreases while η_{wx} increases. Because the η_{wx} for $W_{mx} = 1.0$ are approximately 0.95 and 0.90 for inlet states 1 and 2, the results in Table 5 imply that use of the linear isotherm with $W_{mx} = 0.5$ would require the dehumidifier Λ_w to be doubled in order to achieve the same performance as obtained with the $W_{mx} = 1.0$ desiccant. It was determined that the $W_{mx} = 0.25$ isotherm requires the dehumidifier Λ_w to be increased to more than 80 to obtain the same η_{wx} as the $W_{mx} = 1.0$ isotherm dehumidifier with $\Lambda_w = 20$. For the linear isotherm, the Λ_w required for η_w in excess of 90 percent seems to be inversely proportional to W_{mx}.

Although increasing W_{mx} is beneficial to dehumidifier performance, the η_{wx} for the type 1 isotherm with $W_{mx} = 0.50$ (Table 3) are greater than the η_{wx} for the linear isotherm with $W_{mx} = 1.0$. Changing the isotherm shape from linear to type 1 at $W_{mx} = 0.50$ has a greater beneficial effect on η_{wx} than increasing W_{mx} of the linear isotherm from 0.50 to 1.0.

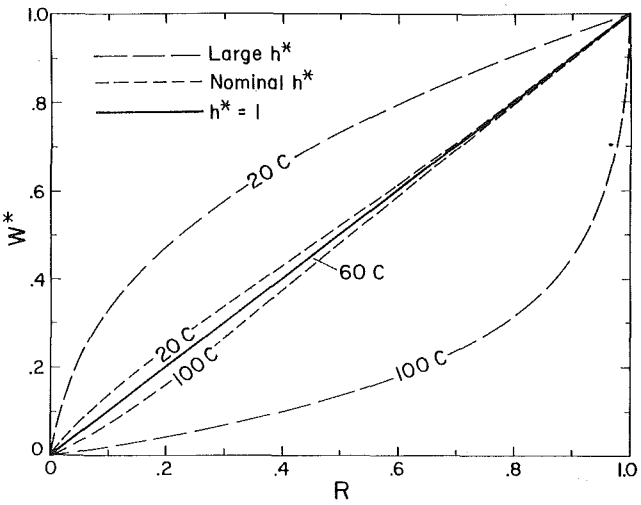

Fig. 5 Temperature variation of the linear isotherm for three different variations of the heat of adsorption

Because variation in the isotherm shape can have as much effect on dehumidifier performances as doubling W_{mx}, the combined effect of isotherm shape and W_{mx} was considered by modeling three generic desiccants. Isotherm type 1(a) with $W_{mx} = 0.25$, type 1 with $W_{mx} = 0.50$, and type 4(a) with $W_{mx} = 1.125$ were used to represent molecular sieves, microporous adsorbents, and macroporous adsorbents. The η_{wx} shown in Table 7 indicates that the microporous adsorbent with the type 1 isotherm has by far the superior performance. The macroporous adsorbent performs slightly better than the molecular sieve, though W_{mx} for the macroporous desiccant is over four times that of the molecular sieve.

Heat of Adsorption. The effect of the heat of adsorption on dehumidifier performance was determined by considering extreme variations in $h^*(W^*)$ for the linear isotherm. The temperature response of the linear isotherm is shown in Fig. 5.

Table 8 shows that a large increase in the heat of adsorption has an adverse effect on dehumidifier performance. For $\mu\kappa$ between 0.10 and 0.50, the strongly temperature sensitive isotherm results in a 6°C to 10°C increase in process outlet temperature and a 10 percent to 25 percent decrease in η_w in comparison to the temperature-independent linear isotherm. The energy liberated on adsorption tends to increase the matrix and air temperatures, adversely affecting the absorptive capacity of the matrix.

The weakly temperature-dependent isotherm also results in dehumidifier process stream outlet temperatures above those obtained with the temperature independent isotherm. However, in this case, for inlet state 1, the outlet humidity ratios are slightly less than those resulting from the temperature-independent isotherm.

These results indicate that the small adsorption heat effects characteristic of common materials such as silica gels have a minor influence on dehumidifier performance. Large latent heat effects, on the other hand, are undesirable.

Matrix Thermal Capacitance. In common matrix configurations, a certain amount of nonadsorbing material is used in the matrix. The bulk specific heat of silica gel, 921 J/(kg-°C) [15], has been used as the reference value of matrix thermal capacitance. A value of $c_m = 3350$ J/(kg-°C), corresponding to a desiccant-substrate system that is 50 percent mylar by volume [10], was used to test the effect of matrix thermal capacitance on dehumidifier performance.

The numerical results show that increasing c_m results in significantly hotter and wetter process stream outlet states. For $\mu\kappa$ between 0.10 and 0.50, the process outlet temperatures

Table 9 Effect of matrix thermal capacitance on optimum dehumidifier performance

c_m $\left(\frac{\text{J}}{\text{kg}-°\text{C}}\right)$	$\mu\kappa_x$	t_o(°C)	$w_o\left(\frac{\text{g}}{\text{kg}}\right)$	η_{wx}
		Inlet state 1		
921	0.18	65.64	5.081	0.929
3350	0.115	69.60	6.285	0.806
		Inlet state 2		
	$\mu\kappa_x$	t_o(°C)	$w_o\left(\frac{\text{g}}{\text{kg}}\right)$	η_{wx}
	0.35	84.02	7.914	0.860
	0.17	86.77	10.409	0.730

Table 10 Effect of Le_o on optimum dehumidifier performance

Λ_t/Le_o	$\mu\kappa_x$	t_o(°C)	$w_o\left(\frac{\text{g}}{\text{kg}}\right)$	η_{wx}
		Inlet state 1		
20/1	0.18	65.64	5.081	0.929
20/4	0.17	63.64	5.836	0.852
		Inlet state 2		
	$\mu\kappa_x$	t_o(°C)	$w_o\left(\frac{\text{g}}{\text{kg}}\right)$	η_{wx}
	0.35	84.02	7.914	0.860
	0.28	80.34	9.193	0.793

and the η_w for the large c_m dehumidifier are, respectively, 5–7°C higher and 10–15 percent lower than for the base case. The data in Table 9 show that the increase in c_m results in a 15 percent decrease in η_{wx} and a reduction in $\mu\kappa_x$.

Comparison of the results for c_m = 3350 J/(kg-°C) in Table 9 to those for Δh^* = 1 in Table 8 shows that the increased sensible heat effects associated with large c_m cause roughly the same decrease in η_{wx} as the large latent heat effects associated with large Δh^*. Increasing c_m has a larger adverse effect on η_{wx} than does decreasing W_{mx}. These results indicate that large latent or sensible heat effects have a significant detrimental impact on the performance of the dehumidifier.

Matrix Moisture Diffusivity. The dehumidifier model is based in part on an assumption that the combined process of diffusion in the matrix and convection at the matrix surface can be described by composite or lumped transfer coefficients. If the resistance to diffusion into the matrix is small, the overall transfer coefficients are governed by the convective film resistances. The convective Lewis number for the air–water vapor system is nearly unity, and Le_o = 1 has been used to this point in this study. However, Banks [30] has estimated that Le_o is at least 2.0 for a parallel passage wheel and van Leersum's results [31] indicate that Le_o = 4 is a lower limit for typical packed bed dehumidifiers.

The results in Table 10 show the effect on the performance of a linear isotherm dehumidifier of increasing Le_o from 1.0 to 4.0 at constant Λ_t = 20, corresponding to an increase in the matrix resistance to water vapor diffusion at constant heat transfer length. Increasing Le_o to 4.0 decreased η_{wx} by about 8 percent. This performance can be obtained by an Le_o = 1 linear isotherm dehumidifier with Λ_w = 9.0. The volume of the Le_o = 4 dehumidifier is therefore about twice that of an Le_o = 1 dehumidifier with the same performance.

Adsorption Hysteresis. An example of the sorption-desorption hysteresis loop in an adsorbent is illustrated by an isotherm for Davison 03 silica gel [28] shown in Fig. 6. This loop was modeled by using the linear isotherm in the adsorbing (process) period of the dehumidifier and the type 1 isotherm in the desorbing (regenerating) period. Because the Clausius-Clapeyron relation (equation (4)) cannot apply in this situation, Δh^* = 0 was used for both branches of the hysteresis isotherm so that the hysteresis loop is independent of temperature.

Table 11 Effect of isotherm hysteresis on dehumidifier performance

Isotherms proc/reg	$\mu\kappa$	t_o(°C)	$w_o\left(\frac{\text{g}}{\text{kg}}\right)$	η_w
		Inlet state 1		
lin/lin	0.10	58.89	5.793	0.857
lin/lin	0.15	61.60	5.260	0.911
lin/lin	0.20	62.99	5.195	0.917
lin/l	0.10	55.28	7.457	0.687
lin/l	0.15	56.70	7.557	0.677
lin/l	0.20	57.57	7.872	0.645
		Inlet state 2		
	$\mu\kappa$	t_o(°C)	$w_o\left(\frac{\text{g}}{\text{kg}}\right)$	η_w
	0.20	77.58	7.616	0.875
	0.25	79.39	7.320	0.891
	0.30	80.58	7.229	0.895
	0.20	72.74	9.832	0.760
	0.25	73.78	10.011	0.751
	0.30	74.56	10.285	0.737

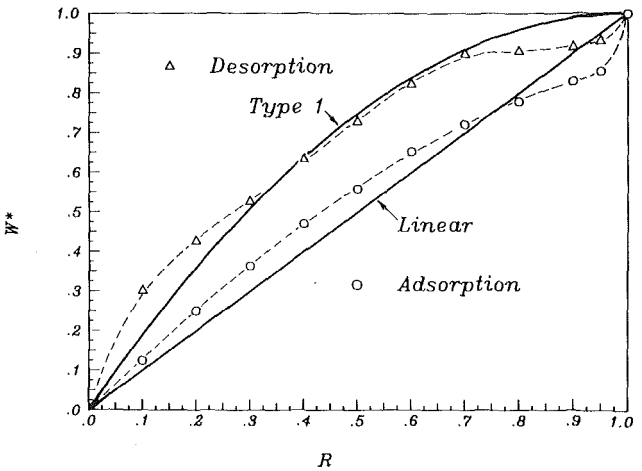

Fig. 6 Adsorption-desorption isotherm hysteresis for Davison 03 silica gel [28]

Modeling the sorption hysteresis isotherm by a simple superposition of two isotherms forces a discontinuous transition at constant W between the sorption and desorption branches of the isotherm and is only a first-order representation of the hysteresis phenomenon [21, 22]. However, this model should provide an upper bound estimate of the effect of adsorption hysteresis on dehumidifier performance.

The performance of a dehumidifier with a linear/type 1 hysteresis isotherm is compared to that with a reversible linear isotherm in Table 11 for values of $\mu\kappa$ that scan the optimum range for the reversible isotherm. The desorption hysteresis loop has a very pronounced adverse effect on the performance of the dehumidifier. The η_w for the hysteresis isotherm are between 15 and 30 percent less than the η_w for the reversible linear isotherm. This corresponds to a decrease in the apparent Λ_w of the dehumidifier from 20 to about 5; i.e., a linear isotherm dehumidifier with Λ_w = 5 (Le_o = 1) has roughly the same η_w as the hysteresis isotherm dehumidifier with Λ_w = 20.

Because an increase in Le_o at fixed Λ_t is equivalent to an increase in mass transfer resistance in the matrix, another way to interpret the effect of the hysteresis isotherm on dehumidifier performance is to determine the apparent Le_o of

Table 12 Le_o required to match the linear isotherm and hysteresis isotherm dehumidifier performance for inlet state 1

	Hysteresis isotherm			
	$\mu\kappa$	t_o(°C)	$w_o\left(\frac{g}{kg}\right)$	η_w
	0.10	55.28	7.457	0.687
	0.15	56.70	7.557	0.677
	0.20	57.57	7.872	0.645
	Linear isotherm			
Le_o	$\mu\kappa$	t_o(°C)	$w_o\left(\frac{g}{kg}\right)$	η_w
9.25	0.10	55.04	7.441	0.689
11.50	0.15	56.51	7.547	0.678
13.00	0.20	57.48	7.863	0.646

a $\Lambda_t = 20$ exchanger that results in the same performance as obtained using the hysteresis isotherm. As shown by the data in Table 12, the effect of the hysteresis isotherm is equivalent to Le_o, ranging from 9.0 to 13.0. Both the outlet temperatures and humidity ratios of the hysteresis isotherm dehumidifier can be closely matched using a single value of Le_o. This implies that if estimates of Le_o are to be obtained by matching predictions of a convective model with experimental data for the dehumidifier outlet states, care must be exercised to avoid confusing the effects of the matrix diffusion resistance and adsorption hysteresis.

Conclusions

The effect of six different matrix properties on the performance of a counterflow rotary dehumidifier has been investigated. The properties considered have been isotherm shape, maximum water content, heat of adsorption, matrix thermal capacitance, matrix moisture diffusivity, and adsorption hysteresis. Results have been obtained for the maximum dehumidification efficiency in each case.

The variation of matrix properties has a profound effect on the design requirements for high-performance dehumidifiers. For example, the dehumidifier Λ_w required for a given level of performance can vary by a factor greater than four as the shape of the adsorption isotherm changes.

The results of this investigation can be summarized in several rough guidelines. For maximum dehumidifier performance, an adsorbent with a near type 1 (weak type 4) isotherm similar to those characteristic of microporous adsorbents should be selected. If an alternate isotherm is considered, the maximum water content must be substantially greater than that of the type 1 adsorbent to realize equivalent dehumidifier performance. The heat of adsorption of the material should be low. It is preferable to design a matrix with low thermal capacitance and $Le_o < 4$ than to have high matrix thermal capacitance and $Le_o = 1$. Isotherms with a major hysteresis loop should be avoided.

Cumulatively these guidelines suggest that commercially available microporous silica gels are attractive materials for dehumidifier construction. Radical changes in desiccant properties would be required to significantly improve dehumidifier performance over that obtainable with these materials.

Acknowledgments

The authors wish to thank Dr. R. K. Collier and Mr. R. Barlow of SERI, who enthusiastically supported this project. Mr. Barlow suggested the tangent and arctangent functional forms used to model several of the isotherms. Dr. D. J. Close, Dr. P. J. Banks, and Dr. J. G. van Leersum of CSIRO, Division of Energy Technology were also very helpful in the early stages of this project. This work was funded by the Solar Heating and Cooling Research and Development Branch, Office of Conservation and Solar Applications, U.S. Department of Energy.

References

1 Product literature, BA-206, BA-297, BA-208, Bry-Air Inc., Sunbury, Ohio.

2 Macriss, R. A., and Zawacki, T. S., "High COP Rotating Wheel Solid Desiccant Systems," *Proc. 9th Energy Technology Conference*, Washington, D.C., Feb. 1982.

3 Jurinak, J. J., et al., "Open Cycle Desiccant Air Conditioning as an Alternative to Vapor Compression Cooling in Residential Applications," *Solar Eng. 1983, Proc. ASME Solar Energy Dir. 5th Annual Conf.*, Orlando, Fl., Apr. 1983.

4 Maclaine-cross, I. L., "A Theory of Combined Heat and Mass Transfer in Regenerators," Ph.D. thesis, Department of Mechanical Engineering, Monash University, Clayton, Vic., Australia, 1974.

5 Holmberg, R. B., "Combined Heat and Mass Transfer in Regenerators with Hygroscopic Materials," ASME JOURNAL OF HEAT TRANSFER, Vol. 101, 1979, pp. 205–210.

6 Mathiprakasam, B., "Performance Predictions of Silica Gel Desiccant Cooling Systems," Ph.D. thesis, Department of Mechanical Engineering, Illinois Institute of Technology, Chicago, Ill., 1980.

7 Maclaine-cross, I. L., and Banks, P. J., "Coupled Heat and Mass Transfer in Regenerators-Prediction Using an Analogy with Heat Transfer," *International Journal of Heat and Mass Trans.*, Vol. 15, 1972, pp. 1225–1242.

8 Mathiprakasam, B., and Lavan, Z., "Performance Predictions for Adiabatic Desiccant Dehumidifiers Using Linear Solutions," ASME *Journal of Solar Energy Engineering*, Vol. 102, 1980, pp. 73–79.

9 Jurinak, J. J., "Open Cycle Solid Desiccant Cooling-Component Models and System Simulations," Ph.D. thesis, Department of Mechanical Engineering, University of Wisconsin, 1982.

10 Barlow, R. S., "An Assessment of Dehumidifier Geometries for Desiccant Cooling Systems," SERI/TR-252-1529, 1982.

11 Banks, P. J., "Coupled Equilibrium Heat and Single Adsorbate Transfer in Fluid Flow through a Porous Medium: 1. Characteristic Potentials and Specific Capacity Ratios," *Chem. Engr. Sci.*, Vol. 27, 1972, pp. 1143–1155.

12 Ponec, V., Knor, Z., and Cerny, S., *Adsorption on Solids*, CRC Press, Cleveland, Ohio, 1974.

13 Brunauer, S., *The Adsorption of Gases and Vapors*, Vol. 1, Princeton University Press, Princeton, 1945.

14 Adamson, A. W., *Physical Chemistry of Surfaces*, Wiley-Interscience, New York, 1960.

15 Product literature, IC-15-1181, IC-221-557, IC-116-881, Davison Chemical Div., W. R. Grace Co., Baltimore, Md.

16 Ngoddy, P. O., and Bakker-Arkema, F. W., "A Generalized Theory of Sorption Phenomena in Biological Materials, Part 1, The Isotherm Equation," *Transactions of the American Society of Agricultural Engineering*, Vol. 13, 1970, pp. 612–617.

17 King, G., "The Interaction of Swelling Agents with Wool and Nylon," *The Structure and Properties of Porous Materials*, edited by D. H. Everett and F. S. Stone, Academic Press, New York, 1958, pp. 322–336.

18 Iler, R. K., *The Chemistry of Silica*, Wiley, New York, 1979.

19 Rosas, F., "Pure Vapor Adsorption of Water on Silica Gels of Different Porosity," M.S. thesis, 2342, Colorado School of Mines, Boulder, Colo., 1980.

20 Kiselev, A. V., in comments on Wynne-Jones, W., "The Surface Characteristics of Carbons," *The Structure and Properties of Porous Materials*, edited by D. H. Everett and F. S. Stone, Academic Press, New York, 1958, p. 51.

21 deBoer, J. H., "The Shapes of Capillaries," *The Structure and Properties of Porous Materials*, edited by D. H. Everett and F. S. Stone, Academic Press, New York, 1958, pp. 68–94.

22 Ngoddy, P. O., and Bakker-Arkema, F. W., "A Theory of Sorption Hysteresis in Biological Materials," *Journal Ag. Eng. Res.*, Vol. 20, 1975, pp. 109–121.

23 Brandemuehl, M. J., "Analysis of Heat and Mass Transfer Regenerators With Time Varying or Spatially Nonuniform Inlet Conditions," Ph.D. thesis, Department of Mechanical Engineering, University of Wisconsin, 1982.

24 Hubard, S. S., "Equilibrium Data for Silica Gel and Water Vapor," *Ind. Engr. Chem.*, Vol. 46, 1954, pp. 356–358.

25 Ewing, D. T., and Bauer, G. T., "The Heat of Wetting Activated Silica Gel," *Journal Am. Chem. Soc.*, Vol. 59, 1937, pp. 1548–1553.

26 Close, D. J., and Banks, P. J., "Coupled Equilibrium Heat and Single Adsorbate Transfer in Fluid Flow through a Porous Medium: 2. Predictions for a Silica-Gel Air-Dryer Using Characteristics Charts," *Chem. Engr. Sci.*, Vol. 27, 1972, pp. 1157–1169.

27 *ASHRAE Handbook 1977 Fundamentals*, Amer. Soc. of Heating, Refrigerating, and Air-Conditioning Engineers, New York, 1977.

28 Mikhail, R. Sh., and Shebl, F. A., "Adsorption in Relation to Pore Structure of Silicas: II. Water Vapor Adsorption on Wide-Pore and Microporous Silica Gels," *Journ. Colloid & Interface Sci.*, Vol. 34, 1970, pp. 65–75.

29 ALCOA Activated Alumina H-15T, cited in Nienberg, J. W., "Modeling of Desiccant Performance for Solar-Desiccant-Evaporative Cooling Systems," M.S. thesis, Engineering, UCLA, Los Angeles, 1979.

30 Banks, P. J., personal communication, CSIRO Division of Energy Technology, Highett, Victoria, Australia, Apr. 1981.

31 van Leersum, J. G., personal communication, CSIRO Division of Energy Technology, Highett, Victoria, Australia, Apr. 1981.

Journal of Heat Transfer

Technical Notes

This section contains shorter technical papers. These shorter papers will be subjected to the same review process as that for full papers.

Anisotropic Heat Conduction With Mixed Boundary Conditions

S. C. Huang[1] and Y. P. Chang[2]

Nomenclature

arg = argument of a complex number
ds = differential element of the boundary, counterclockwise
i = $(-1)^{1/2}$
Im = imaginary part of a complex number
k_{ij} = thermal conductivity of thin plate, $i, j = 1,2$
n_i = x_i component of the outward unit normal of the boundary, $i = 1,2$
n_ξ, n_η = ξ, η components of the outward unit normal of the boundary
q''' = heat generation per unit time-volume
Re = real part of a complex number
T = temperature
T_0 = constant, reference temperature
x,y = $x = x_1, y = x_2$
x_i = cartesian coordinate, $i = 1,2$
β_{12} = $(\nu_{11} - \nu_{12}^2)^{1/2}$
δ = delta function
ν_{ij} = k_{ij}/k_{22}, $i, j = 1,2$
Ω = simply connected domain

Superscript

′ = on the source plane
− = complex conjugate

Introduction

In recent years, owing to their numerous important applications there has been an increasing interest in the study of heat conduction in anisotropic materials. Examples of such materials include crystals, metals undergoing heavy cold pressing, fiber reinforced structures, and many others. As the result of the presence of cross-derivative terms in the energy equation, the problem is nonorthogonal in nature and is difficult to analyze [1-4]. Most available analytical solutions have been restricted to simple geometries with Dirichlet boundary conditions.

In the present study, general shapes of two-dimensional domains are considered. With the proper transformation of coordinates, we will construct Green's function of anisotropic heat conduction through the use of conformal mapping. The boundary condition considered here is of the mixed type, so that the temperature is prescribed on one segment of the boundary while the heat flux is prescribed on the rest of the boundary. Consequently, the Dirichlet boundary condition becomes a special case. The application of the obtained Green's function to an elliptic disk results in an exact solution not reported before.

Formulation and Analysis

Consider the steady-state heat conduction in a thin plate with anisotropic thermal conductivities. The governing energy equation takes the following form

$$\nu_{11}\frac{\partial^2 T}{\partial x^2} + 2\nu_{12}\frac{\partial^2 T}{\partial x \partial y} + \frac{\partial^2 T}{\partial y^2} = -\frac{q'''(x,y)}{k_{22}} \text{ in } \Omega \quad (1)$$

where the notations are explained in the Nomenclature. In this study, we are interested in the problem for which the temperature is specified on the boundary S_1 and the heat flux on the rest of the boundary S_2, i.e.,

$$T = f_1(x,y) \quad \text{on} \quad S_1 \quad (2)$$

$$\frac{\partial T}{\partial n_t} = \nu_{ij} n_i \frac{\partial T}{\partial x_j} = f_2(x,y) \quad i, j = 1,2 \text{ on } S_2 \quad (3)$$

where $\partial/\partial n_t$ is the conormal derivative. The boundary S_1 is assumed to start from the point P_1 and end at the point P_2 in the counterclockwise direction.

The corresponding Green's function $G(x,y|x',y')$ satisfies

$$\nu_{11}\frac{\partial^2 G}{\partial x^2} + 2\nu_{12}\frac{\partial^2 G}{\partial x \partial y} + \frac{\partial^2 G}{\partial y^2} = -\delta(x-x')\delta(y-y') \text{ in } \Omega \quad (4)$$

$$G = 0 \text{ on } S_1 \quad (5)$$

$$\frac{\partial G}{\partial n_t} = 0 \text{ on } S_2 \quad (6)$$

The temperature distribution is related to Green's function by the formula

$$T(x,y) = \frac{1}{k_{22}}\iint_\Omega G(x,y|x',y')q'''(x',y')dx'dy' - \int_{S_1} f_1(x',y')\frac{\partial G(x,y|x',y')}{\partial n_t'}ds' + \int_{S_2} f_2(x',y')G(x,y|x'y')ds' \quad (7)$$

where the primes denote that the integration is carried out in

[1]Department of Mechanical Engineering, Southern University, Baton Rouge, La. 70813, Assoc. Mem. ASME. Present address: Mechanical Technology Inc., 968 Albany-Shaker Road, Latham, N.Y. 12110
[2]Department of Mechanical and Aerospace Engineering, SUNY at Buffalo, Amherst, N.Y. 14260, Mem. ASME
Contributed by the Heat Transfer Division for publication in the JOURNAL OF HEAT TRANSFER. Manuscript received by the Heat Transfer Division November 14, 1983.

the source plane (x',y'). Since $G(x,y|x',y') = G(x',y'|x,y)$, x,y and x',y' can be interchanged.

To obtain Green's function, we first apply the nonorthonormal transformation [2]

$$\xi = (x - \nu_{12}y)/\beta_{12} \tag{8}$$

$$\eta = y \tag{9}$$

The equations (4-6) are transformed into the following system of equations

$$\frac{\partial^2 G}{\partial \xi^2} + \frac{\partial^2 G}{\partial \eta^2} = -\frac{1}{\beta_{12}}\delta(\xi - \xi')\delta(\eta - \eta') \text{ in } \Omega \tag{10}$$

$$G = 0 \qquad \text{on } S_1 \tag{11}$$

$$n_\xi \frac{\partial G}{\partial \xi} + n_\eta \frac{\partial G}{\partial \eta} = 0 \qquad \text{on } S_2 \tag{12}$$

where $1/\beta_{12}$ is the Jacobian of transformation. The left-hand side of equation (10) is easily identified as the Laplace equation in two variables. For the arbitrarily shaped domain Ω, the conformal mapping technique is suitable for the solution.

From the theory of conformal mapping, it can be shown [5] that the Green's function satisfying equation (10) is given by

$$G(\xi,\eta|\xi'\eta') = -\frac{1}{2\pi\beta_{12}} \ln|g(z)| \tag{13}$$

where $z = \xi + i\eta$; $g(z)$ is an analytic function of z in the domain Ω and transforms the source point $z' = \xi' + i\eta'$ to the origin, i.e., $g(z') = 0$.

In order to satisfy the mixed boundary conditions (11) and (12), $g(z)$ is further required to satisfy the following conditions:

(*a*) The boundary S_1 is mapped onto a unit circle centered at the origin, i.e., $|g(z)| = 1$ for points z on S_1.

(*b*) The boundary S_2 is mapped onto a radial cut from the unit circle. To be specific, we shall align the cut along the negative axis of the $g(z)$-plane, i.e., $\arg[g(z)] = \pi$ for points z on S_2.

(*c*) The domain Ω is conformally mapped onto the interior of the unit circle excluding the cut.

The $g(z)$ satisfying the above requirements is given by [5, 6]

$$g(z) = \frac{z_6 - \tan^2\dfrac{\phi+\pi}{8}}{1 - z_6\tan^2\dfrac{\phi+\pi}{8}} \tag{14}$$

where

$$z_6 = -\left(\frac{1-z_5}{1+z_5}\right)^2 \tag{15}$$

$$z_5 = e^{i\frac{\pi}{4}}\left(\frac{e^{i\phi/2} - z_4 e^{-i\phi/2}}{1+z_4}\right) \tag{16}$$

$$z_4 = -e^{-i\psi}z_3 \tag{17}$$

$$z_3 = \frac{z_2 - z_2'}{1 - z_2\bar{z}_2'} \tag{18}$$

In the foregoing equation, ψ is the argument of P_1 in the z_3-plane; ϕ is the argument of P_2 in the z_4-plane; z_2 is the analytic function which maps the domain Ω onto the interior of a unit circle centered at the origin.

The following relations are used in evaluating the conormal derivatives of Green's function

$$\left(\nu_{11}\frac{\partial}{\partial x} + \nu_{12}\frac{\partial}{\partial y}\right)\ln|g(z)| = \text{Re}\left[\frac{\beta_{12} + i\nu_{12}}{g(z)}\frac{\partial g(z)}{\partial z}\right] \tag{19}$$

$$\left(\nu_{12}\frac{\partial}{\partial x} + \frac{\partial}{\partial y}\right)\ln|g(z)| = -\text{Im}\left[\frac{1}{g(z)}\frac{\partial g(z)}{\partial z}\right] \tag{20}$$

If temperature is prescribed on all boundaries of the domain Ω, i.e., Dirichlet boundary condition, we just delete the boundary conditions (3), (6), (12) and the integration along the boundary S_2 in equation (7). In this case, $g(z)$ is simply the z_3 defined in equation (18).

Application to Elliptic Disk

Consider the parametric equation of an ellipse $x = a\cdot\cos\theta$, $y = b\cdot\sin\theta$, where $0 \le \theta < 2\pi$. In this case, we have

$$n_1 = \frac{b\cos\theta}{(a^2\sin^2\theta + b^2\cos^2\theta)^{1/2}}, n_2 = \frac{a\sin\theta}{(a^2\sin^2\theta + b^2\cos^2\theta)^{1/2}} \tag{21}$$

$$ds = (a^2\sin^2\theta + b^2\cos^2\theta)^{1/2}d\theta \tag{22}$$

$$z_1 = \xi_1 + i\eta_1 = \exp(-i\phi_t)z \tag{23}$$

where

$$\phi_t = \frac{1}{2}\tan^{-1}\frac{2\nu_{12}\beta_{12}}{\beta_{12}^2 - \nu_{12}^2 - (a/b)^2} \tag{24}$$

The foregoing ellipse is then transformed onto

$$\frac{(\xi_1)^2}{A^2} + \frac{(\eta_1)^2}{B^2} = 1 \tag{25}$$

in which

$$A^2 = \frac{2}{I - (I^2 - 4D)^{1/2}}, \quad B^2 = \frac{2}{I + (I^2 - 4D)^{1/2}} \tag{26}$$

$$I = \frac{\nu_{11}}{a^2} + \frac{1}{b^2}, \quad D = \left(\frac{\beta_{12}}{ab}\right)^2 \tag{27}$$

The transformation function that maps the interior of the ellipse (25) onto the interior of a unit circle is known [7] to be

$$z_2 = m^{1/2}sn\left(\frac{2K}{\pi}\sin^{-1}\frac{z_1}{(A^2 - B^2)^{1/2}}, m\right) \tag{28}$$

where sn is the Jacobian elliptic function; K is the quarter-period; and m is the modulus

$$m = \left[\frac{\theta_2(q)}{\theta_3(q)}\right]^2 \tag{29}$$

in which θ_2, θ_3 are the theta functions and q is the norm given by

$$q = \left(\frac{A-B}{A+B}\right)^2 \tag{30}$$

In the special case where $A = B$, equation (28) is replaced by

$$z_2 = z_1/A \tag{31}$$

By substituting z_2 into equation (18), $g(z)$ is then completely specified.

Results and Discussion

As a numerical illustration, we take $a = 2b$, $f_1 = 0$ and $f_2 = T_0/a$. The boundary S_1 corresponds to the upper half ellipse, i.e., $0 < \theta < \pi$, and the boundary S_2 corresponds to the lower half ellipse, i.e., $\pi < \theta < 2\pi$. If there is no heat generation, equation (7) becomes

$$\frac{T(x,y)}{T_0} = -\frac{1}{2\pi\beta_{12}}\int_\pi^{2\pi}\ln|g(z)| \Big|_{\substack{x' = a\cos\theta' \\ y' = b\sin\theta'}} \left(\sin^2\theta' + \frac{b^2}{a^2}\cos^2\theta'\right)^{1/2} d\theta' \tag{32}$$

The anisotropic parameters are taken to be $\beta_{12} = 1.2$ and $\nu_{12} = 0.5$. The sn function of complex arguments in equation (28) can be evaluated by expanding it in terms of Jacobian elliptic function of real arguments [8]. The latter is readily available from the IBM Scientific Subroutine Package. Since

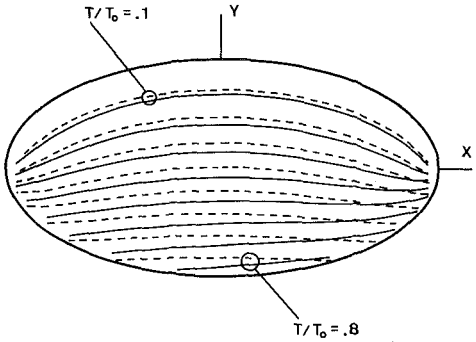

Fig. 1 Temperature distribution in an elliptic disk $a = 2b$. The isotherms shown are at $T/T_0 = 0.1$ intervals. Solid lines are for $\beta_{12} = 1.2$, $\nu_{12} = 0.5$, and dashed lines are for $\beta_{12} = 1$, $\nu_{12} = 0$.

the ln function of complex argument is available in extended Fortran IV, the $\sin^{-1}$ function in equation (28) can be calculated by the formula

$$\sin^{-1} w = -i\ln[iw + (1 - w^2)^{1/2}] \tag{33}$$

The integration in equation (32) can be performed by the Gaussian quadrature.

Figure 1 shows the obtained isotherms by solid lines. While the prescribed boundary conditions are symmetric with respect to the centerline $x = 0$, the isotherms are not symmetric due to the anisotropic thermal conductivities of the material. Since the upper half boundary is maintained at zero temperature and the lower half boundary is supplied with constant heat flux, the high temperature appears on the lower half of the disk. In addition, it is noticed that the right lower side of the boundary has the highest temperature. This is because the thermal resistance from the left lower side to the right upper side of the disk is smaller for the assumed thermal properties. For the purpose of comparison, we also calculate the isotropic case with $\beta_{12} = 1$ and $\nu_{12} = 0$. The resulted isotherms are presented in Fig. 1 by dashed lines. The symmetry of the results with respect to $x = 0$ is as expected. For both isotropic and anisotropic cases, the highest temperature is found to be slightly less than $0.9\ T_0$.

Conclusion

It is demonstrated that the steady-state Green's function for the anisotropic heat conduction in a thin plate with mixed boundary conditions can be constructed by the conformal mapping technique. The advantage of conformal mapping lies in its ability to deal with arbitrarily shaped geometries. The closed-form solution obtained for the elliptic disk proves to be convenient for computation.

References

1 Chang, Y. P., Kang, C. S., and Chen, D. J., "The Use of Fundamental Green's Functions for the Solution of Problems of Heat Conduction in Anisotropic Media," *International Journal of Heat and Mass Transfer*, Vol. 16, 1973, pp. 1905-1918.

2 Chang, Y. P., "Analytical Solution for Heat Conduction in Anisotropic Media in Infinite, Semi-Infinite, and Two-Plane-Bounded Regions," *International Journal of Heat and Mass Transfer*, Vol. 20, 1977, pp. 1019-1028.

3 Poon, K. C., Tsou, R. C. H., and Chang, Y. P., "Solution of Anisotropic Problems of First Class by Coordinate Transformation," ASME JOURNAL OF HEAT TRANSFER, Vol. 101, 1979, pp. 340-345.

4 Huang, S. C., and Chang, Y. P., "Heat Conduction in Anisotropic Wedge and Elliptic Cylinders," ASME JOURNAL OF HEAT TRANSFER, Vol. 105, 1983, pp. 674-677.

5 Kantorovich, L. V., and Krylov, V. I., *Approximate Methods of Higher Analysis*, translated by C. D. Benster, Interscience, New York, 1958.

6 Huang, S. C., "Analytical Solution of Anisotropic Heat Conduction in Simple and Irregular Regions," Ph.D dissertation, SUNY at Buffalo, 1981.

7 Kober, H., *Dictionary of Conformal Representations*, Dover, New York, 1957.

8 Abramowitz, M., and Stegun, I. A., *Handbook of Mathematical Functions*, National Bureau of Standards, 1972.

A New Theory on the Critical Thickness of Insulation

C. K. Hsieh[1] and S. L. Yang[2]

Nomenclature

a = distance to the edge of insulation in x direction
A,B,C,D,E,F = Fourier coefficients
b = half-height of rectangle
e = eccentricity
h = convective coefficient
I = Biot number
k = thermal conductivity
m = eigenvalue
n = number of sides of polygon or normal
N = function of number of sides of polygon or b/a
P = perimeter
Q = heat flow rate
r = radius
r_a = $a/\cos\theta$
r_{ai} = $a/(r_i \cos\theta)$
r_b = $b/\sin\theta$
r_{bi} = $b/(r_i \sin\theta)$
r_e = quantity defined in equation (20)
r_s = quantity defined by equation (20)
r_{si} = r_s/r_i
S = conduction shape factor
T = temperature
w = half-width of one surface of polygon
x,y = axis
α = variable defined in Fig. 1
β = angle between normal and y axis
γ = angle between normal and x axis
θ = angle

Subscripts

c = critical
i = inner circle
m = eigenvalue
o = outside surface
x = x-direction
y = y-direction
∞ = Ambient

Introduction

The critical thickness of insulation was recently determined by Hsieh [1] for a square section. By using a numerical solution, he was able to obtain the critical thickness for the half-width of one side of the square to be 0.79 (k/h). He also noted that, if this half-width was used to find the perimeter of the square and its value compared with that of a circular insulation, they were in good agreement (99.4 percent). Three years later, Aziz [2] commented that the critical thickness given by Hsieh could be derived by using the conduction shape factor in much the same way as one did with a circular insulation. Hsieh [3] responded that, since the use of shape factor was premised on the existence of a uniform surface temperature, which was not the case for the square, Aziz's approach was unconventional. However, Hsieh recalculated the critical perimeter of the square based on Aziz's results and

[1]Professor, Mechanical Engineering Department, University of Florida, Gainesville, Fla. 32611, Mem. ASME

[2]Graduate Research Assistant, Mechanical Engineering Department, University of Florida, Gainesville, Fla. 32611

Contributed by the Heat Transfer Division for publication in the JOURNAL OF HEAT TRANSFER. Manuscript received by the Heat Transfer Division October 5, 1983.

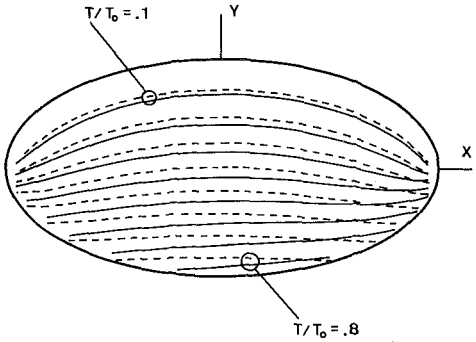

Fig. 1 Temperature distribution in an elliptic disk $a = 2b$. The isotherms shown are at $T/T_0 = 0.1$ intervals. Solid lines are for $\beta_{12} = 1.2$, $\nu_{12} = 0.5$, and dashed lines are for $\beta_{12} = 1$, $\nu_{12} = 0$.

the ln function of complex argument is available in extended Fortran IV, the $\sin^{-1}$ function in equation (28) can be calculated by the formula

$$\sin^{-1} w = -i\ln[iw + (1 - w^2)^{1/2}] \tag{33}$$

The integration in equation (32) can be performed by the Gaussian quadrature.

Figure 1 shows the obtained isotherms by solid lines. While the prescribed boundary conditions are symmetric with respect to the centerline $x = 0$, the isotherms are not symmetric due to the anisotropic thermal conductivities of the material. Since the upper half boundary is maintained at zero temperature and the lower half boundary is supplied with constant heat flux, the high temperature appears on the lower half of the disk. In addition, it is noticed that the right lower side of the boundary has the highest temperature. This is because the thermal resistance from the left lower side to the right upper side of the disk is smaller for the assumed thermal properties. For the purpose of comparison, we also calculate the isotropic case with $\beta_{12} = 1$ and $\nu_{12} = 0$. The resulted isotherms are presented in Fig. 1 by dashed lines. The symmetry of the results with respect to $x = 0$ is as expected. For both isotropic and anisotropic cases, the highest temperature is found to be slightly less than $0.9\ T_0$.

Conclusion

It is demonstrated that the steady-state Green's function for the anisotropic heat conduction in a thin plate with mixed boundary conditions can be constructed by the conformal mapping technique. The advantage of conformal mapping lies in its ability to deal with arbitrarily shaped geometries. The closed-form solution obtained for the elliptic disk proves to be convenient for computation.

References

1 Chang, Y. P., Kang, C. S., and Chen, D. J., "The Use of Fundamental Green's Functions for the Solution of Problems of Heat Conduction in Anisotropic Media," *International Journal of Heat and Mass Transfer*, Vol. 16, 1973, pp. 1905-1918.

2 Chang, Y. P., "Analytical Solution for Heat Conduction in Anisotropic Media in Infinite, Semi-Infinite, and Two-Plane-Bounded Regions," *International Journal of Heat and Mass Transfer*, Vol. 20, 1977, pp. 1019-1028.

3 Poon, K. C., Tsou, R. C. H., and Chang, Y. P., "Solution of Anisotropic Problems of First Class by Coordinate Transformation," ASME JOURNAL OF HEAT TRANSFER, Vol. 101, 1979, pp. 340-345.

4 Huang, S. C., and Chang, Y. P., "Heat Conduction in Anisotropic Wedge and Elliptic Cylinders," ASME JOURNAL OF HEAT TRANSFER, Vol. 105, 1983, pp. 674-677.

5 Kantorovich, L. V., and Krylov, V. I., *Approximate Methods of Higher Analysis*, translated by C. D. Benster, Interscience, New York, 1958.

6 Huang, S. C., "Analytical Solution of Anisotropic Heat Conduction in Simple and Irregular Regions," Ph.D dissertation, SUNY at Buffalo, 1981.

7 Kober, H., *Dictionary of Conformal Representations*, Dover, New York, 1957.

8 Abramowitz, M., and Stegun, I. A., *Handbook of Mathematical Functions*, National Bureau of Standards, 1972.

A New Theory on the Critical Thickness of Insulation

C. K. Hsieh[1] and S. L. Yang[2]

Nomenclature

a = distance to the edge of insulation in x direction
A,B,C,D,E,F = Fourier coefficients
b = half-height of rectangle
e = eccentricity
h = convective coefficient
I = Biot number
k = thermal conductivity
m = eigenvalue
n = number of sides of polygon or normal
N = function of number of sides of polygon or b/a
P = perimeter
Q = heat flow rate
r = radius
r_a = $a/\cos\theta$
r_{ai} = $a/(r_i \cos\theta)$
r_b = $b/\sin\theta$
r_{bi} = $b/(r_i \sin\theta)$
r_e = quantity defined in equation (20)
r_s = quantity defined by equation (20)
r_{si} = r_s/r_i
S = conduction shape factor
T = temperature
w = half-width of one surface of polygon
x,y = axis
α = variable defined in Fig. 1
β = angle between normal and y axis
γ = angle between normal and x axis
θ = angle

Subscripts

c = critical
i = inner circle
m = eigenvalue
o = outside surface
x = x-direction
y = y-direction
∞ = Ambient

Introduction

The critical thickness of insulation was recently determined by Hsieh [1] for a square section. By using a numerical solution, he was able to obtain the critical thickness for the half-width of one side of the square to be 0.79 (k/h). He also noted that, if this half-width was used to find the perimeter of the square and its value compared with that of a circular insulation, they were in good agreement (99.4 percent). Three years later, Aziz [2] commented that the critical thickness given by Hsieh could be derived by using the conduction shape factor in much the same way as one did with a circular insulation. Hsieh [3] responded that, since the use of shape factor was premised on the existence of a uniform surface temperature, which was not the case for the square, Aziz's approach was unconventional. However, Hsieh recalculated the critical perimeter of the square based on Aziz's results and

[1]Professor, Mechanical Engineering Department, University of Florida, Gainesville, Fla. 32611, Mem. ASME
[2]Graduate Research Assistant, Mechanical Engineering Department, University of Florida, Gainesville, Fla. 32611

Contributed by the Heat Transfer Division for publication in the JOURNAL OF HEAT TRANSFER. Manuscript received by the Heat Transfer Division October 5, 1983.

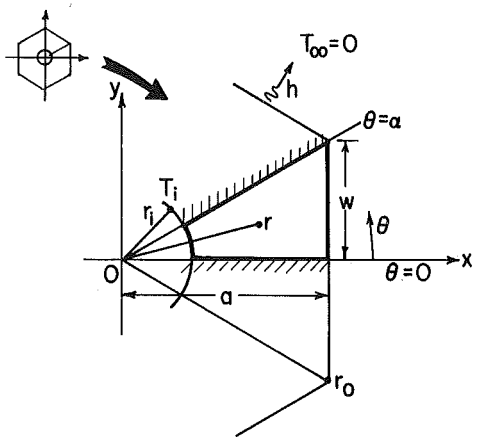

Fig. 1 Geometry of a polygonal insulation

found that the perimeter so calculated was in total agreement with that of the circle [3]. This is truly amazing, since it reveals that something could be missing in the heat conduction theory that has led to this conformity.

This note is offered to uncover this mystery. Specifically, two areas will be investigated. Can the boundary condition be changed from that of a convective condition to that of a prescribed temperature when deriving the critical thickness of insulation? If so, is there a critical perimeter that can be used in place of the critical radius that has been given in the heat transfer literature? As will be shown later, the answers to both questions are positive. In fact, the critical perimeter concept is so general that it is useful to a wide range of configurations, including equilateral polygons and rectangles, as long as their heat sources are centrally located.

Analysis

Consider a two-dimensional system in steady state. The medium is homogeneous and isotropic. There is no heat generation inside the medium, and the convective coefficient is treated as a constant in the analysis. Three separate cases will be studied, with the equilateral polygon examined first.

Equilateral Polygon. For the equilateral polygon depicted in Fig. 1, the temperature T must satisfy

$$\nabla^2 T=0, \qquad \text{where } T=T(r,\theta) \tag{1}$$

The boundary conditions are

$$\frac{\partial T(r,0)}{\partial\theta}=\frac{\partial T(r,\alpha)}{\partial\theta}=0 \tag{2}$$

$$T(r_i,\theta)=T_i \tag{3}$$

$$\left[\frac{\partial T(r_a,\theta)}{\partial r}\cos\theta-\frac{\partial T(r_a,\theta)}{\partial\theta}\frac{\sin\theta}{r_a}\right]+\frac{h}{k}T(r_a,\theta)=0 \tag{4}$$

where equation (4) represents a convective condition imposed at $x=a$ (i.e., $r=r_a=a/\cos\theta$).

A solution to this problem can be derived as

$$\frac{T}{T_i}=1+A\ln\frac{r}{r_i}+\sum_m B_m\left[\left(\frac{r}{r_i}\right)^m-\left(\frac{r}{r_i}\right)^{-m}\right]\cos m\theta \tag{5}$$

where $m=n, 2n, 3n, \ldots$, and n denotes the number of sides of the polygon.

The Fourier coefficients A and B_m are determined by using collocation at $r=r_a$. Hence

$$A(\cos^2\theta+I_a\ln r_{ai})+\sum_m B_m[(r_{ai}^m+r_{ai}^{-m})m\cos^2\theta\cos m\theta$$
$$+(r_{ai}^m-r_{ai}^{-m})(m\sin\theta\cos\theta\sin m\theta+I_a\cos m\theta)]=-I_a \tag{6}$$

where r_{ai} stands for $a/(r_i\cos\theta)$. I_a is the Biot number (ha/k). Equation (6) is used to construct a set of linear equations for solving those Fourier coefficients in equation (5). Once they are found, heat loss can be derived as

$$\frac{Q}{(2n)hT_i}=-\frac{k}{h}\left(\frac{\pi}{n}\right)A-\frac{k}{h}\sum_m mB_m\int_0^{\pi/n}$$
$$[(r_{ai}^m+r_{ai}^{-m})\cos m\theta+(r_{ai}^m+r_{ai}^{-m})\tan\theta\sin m\theta]d\theta \tag{7}$$

The critical thickness of insulation can then be derived by differentiating Q with respect to a and setting the result equal to zero. It follows that

$$\int_0^{\pi/n}[(r_{ai}^m-r_{ai}^{-m})\cos m\theta+(r_{ai}^m+r_{ai}^{-m})\tan\theta\sin m\theta]d\theta=0 \tag{8}$$

This is the necessary condition for the heat loss to be maximized at the critical point. Notice that the Fourier coefficients do not enter into this equation. Study of the polygonal problem with a convective boundary is now complete; attention is now directed to that of a prescribed temperature at the surface.

For a prescribed T_0 at the surface, equation (4) is changed to

$$T(r_a,\theta)=T_o \tag{9}$$

Since this is the only change in the problem, it is expected that a similar solution (equation (5)) will result, with the only exception being those Fourier coefficients that call for use of collocation with a new condition (equation (9)). Consequently, equation (8) is again obtained as the necessary condition for the heat loss to be maximized. This justifies the replacement of the actual convective condition by a prescribed (hypothetical) temperature at the surface when deriving the critical thickness of insulation. Meanwhile, the conduction shape factor can also be used to simplify the derivation.

For a polygon, the conduction shape factor can be expressed as [4–7]

$$S=\frac{2\pi}{\ln(r_o/r_i)-N} \tag{10}$$

where N is a function of the number of sides of the polygon. This N decreases steadily as n increases. Inasmuch as a circle can be considered as the limiting case for the polygon if the number of its sides is increased indefinitely, it is not surprising to see that $N=0$ is indeed the case for the circle.

Using equation (10) to formulate the total resistance for the insulation, and subsequently minimizing this resistance with respect to w, it can be derived that the critical w is

$$w_c=\frac{\pi}{n}\frac{k}{h} \tag{11}$$

It follows that the critical perimeter for the polygon is

$$P_c=(2n)\frac{\pi}{n}\frac{k}{h}=2\pi\frac{k}{h} \tag{12}$$

which is indeed the observation made in Hsieh's paper [1].

Rectangle. Consider a rectangle of size $2a \times 2b$ having one fourth of its section in the first quadrant; w in Fig. 1 is changed to b, and equation (2) is modified to be

$$\frac{\partial T(r,0)}{\partial\theta}=\frac{\partial T(r,\pi/2)}{\partial\theta}=0 \tag{13}$$

Equation (4) is still valid but is useful only for the boundary perpendicular to the x-axis. A similar equation is needed to account for the heat loss from the top surface. Hence

$$\left[\frac{\partial T(r_b,\theta)}{\partial r}\sin\theta+\frac{\partial T(r_b,\theta)}{\partial\theta}\frac{\cos\theta}{r_b}\right]+\frac{h}{k}T(r_b,\theta)=0 \tag{14}$$

where $r_b=b/\sin\theta$.

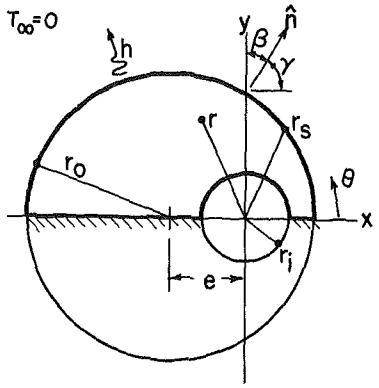

Fig. 2 Geometry of an eccentric circular insulation

The solution is obtained in a similar fashion as before. Consequently,

$$\frac{Q}{4hT_i} = -\frac{k}{h}\left(\frac{\pi}{2}\right)C - \frac{k}{h}\sum_m mD_m\left\{\int_0^\alpha [(r_{ai}^m + r_{ai}^{-m})\cos m\theta + (r_{ai}^m - r_{ai}^{-m})\tan\theta\sin m\theta]d\theta + \int_\alpha^{\pi/2} [(r_{bi}^m + r_{bi}^{-m})\cos m\theta - (r_{bi}^m - r_{bi}^{-m})ctn\theta\sin m\theta]d\theta\right\} \quad (15)$$

where

$m = 2,4,6, \ldots, \alpha = \tan^{-1}(b/a)$, and $r_{bi} = b/(r_i\sin\theta)$

It should be noted here that, when Q is differentiated to find the critical thickness, the aspect ratio of the rectangle b/a will be treated as a constant, while a itself as a variable. This amounts to finding the critical thickness for a class of rectangles that bear geometric similarity. Hence the differentiation of the third term on the right of equation (15) vanishes, and equation (8) is again obtained (with the slight modification that the upper limit of integration is changed to α). This is the necessary condition for Q to be maximized.

By following the procedure previously described for the polygon, it can be proved that, if a prescribed temperature is imposed on the surface, the same necessary condition can be derived for the rectangle. Hence the conduction shape factor can again be used to derive the critical thickness, and in this effort, the shape factor for the rectangle can be arranged to be [4-7]

$$S = \frac{2\pi}{\ln\frac{r_o}{r_i} - \left[2\sum_{m=0}^{\infty}\sum_{n=1}^{\infty}\frac{(-1)^{n+1}}{(2m+1)}\left(\operatorname{sech}\frac{n\pi b}{a}\right)^{2m+1} - \ln\left(\frac{4}{\pi}\cos\alpha\right)\right]} \quad (16)$$

Here $m = n = 0,1,2, \ldots$ Also notice that the expression given inside the brackets in the denominator plays the role of N in equation (10). This bracketed term is a function of b/a.

The critical thickness of insulation can then be derived as a function of α as

$$r_{0,c} = \frac{\pi}{2(\cos\alpha + \sin\alpha)}\frac{k}{h} \quad (17)$$

Correspondingly,

$$P_c = 4r_{o,c}(\cos\alpha + \sin\alpha) = 2\pi\frac{k}{h} \quad (18)$$

which is identical to equation (12).

Eccentric Circle. An attempt was made to see if the foregoing analysis could also be extended to study a circular insulation eccentrically rigged on a pipe, see Fig. 2. As it turns out, for this case the necessary condition for the heat loss to be maximized contains Fourier coefficients that are, of course, different for different conditions imposed on the surface. Hence the conduction shape factor cannot be used to derive the critical thickness. The heat loss equation was thus derived from the temperature equation

$$\frac{Q}{hT_i} = -2\frac{k}{h}\int_0^\pi\left[\frac{E}{r_s}(\cos\theta\cos\gamma + \sin\theta\cos\beta) + \sum_m\frac{mF_m}{r_s}\right.$$

$$\left\{[(r_{si}^m + r_{si}^{-m})\cos\theta\cos m\theta + (r_{si}^m - r_{si}^{-m})\sin\theta\sin m\theta]\cos\gamma\right.$$

$$+\left[(r_{si}^m + r_{si}^{-m})\sin\theta\cos m\theta\right.$$

$$\left.\left.\left.-(r_{si}^m - r_{si}^{-m})\cos\theta\sin m\theta\right]\cos\beta\right\}\right]\frac{r_o r_s}{r_e}d\theta \quad (19)$$

where $m = 1,2,3, \ldots$, and

$$r_s = (r_o^2 - e^2\sin^2\theta)^{1/2} - e\cos\theta = r_e - e\cos\theta \quad (20)$$

This equation (19) will be used later to check if a critical perimeter is still defined for this case.

Results and Discussion

The critical thicknesses of insulation derived for the polygons and rectangles can be verified by substituting them into equation (8). However, this equation cannot be used to derive these thicknesses, because it can be manipulated to contain two intergrals

$$\int_0^\alpha\frac{\cos(m-1)\theta}{\cos^{m+1}\theta}d\theta = 0, \int_0^\alpha\frac{\cos(m+1)\theta}{\cos^{-m+1}\theta}d\theta = 0 \quad (21)$$

which are identically zero. Notice that $\alpha = \pi/n$ for polygons, and $\alpha = \tan^{-1}(b/a)$ for rectangles. The fact that these integrals vanish for $m = n, 2n, 3n, \ldots$ (for polygons) and $m = 2, 4, 6, \ldots$ (for rectangles) serves to reaffirm their being eigenvalues for these geometries. This leads to a paradox in that equation (8) is the necessary condition for the heat loss to be maximized; however, this equation cannot be used to derive the critical thickness. This inconsistency could be attributed to the nature of the boundary value problem, as will now be described.

For the doubly connected system domain considered in the derivation of the critical thickness given in this paper, the condition at the inner boundary is always that of the first kind. Only at the outer boundary conditions are different. Under these circumstances, the temperature equation (5) remains unchanged; only those Fourier coefficients are different for different conditions imposed on the surface. Recall that it was basically equation (5) that was used in the derivation of the necessary condition. Since (5) remains unchanged, the obtaining of the same condition (equation (8)) is really sufficient to prove that, in the extremetization of heat flow, the result is independent of whether a convective condition or a prescribed temperature is imposed on the surface.

That equation (8) cannot be used to derive the thickness could be ascribed to the format of this equation. It is expected that the critical thickness is a function of the ratio k/h which, however, does not appear in this equation. This serves as a clue that this equation is useless in this regard. Fortunately, because the replacement of boundary conditions is now possible, the critical thickness can be derived by means of the conduction shape factor. Whether this can really be done is

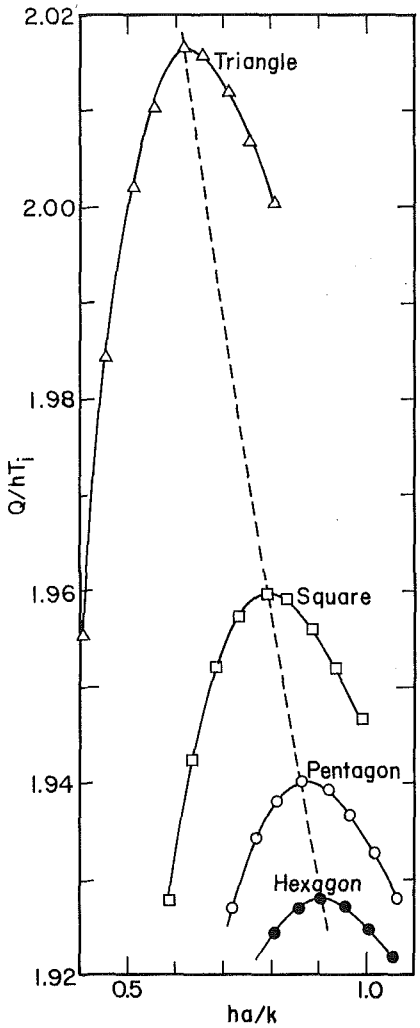

Fig. 3 Heat loss versus Biot number curves for polygonal insulation

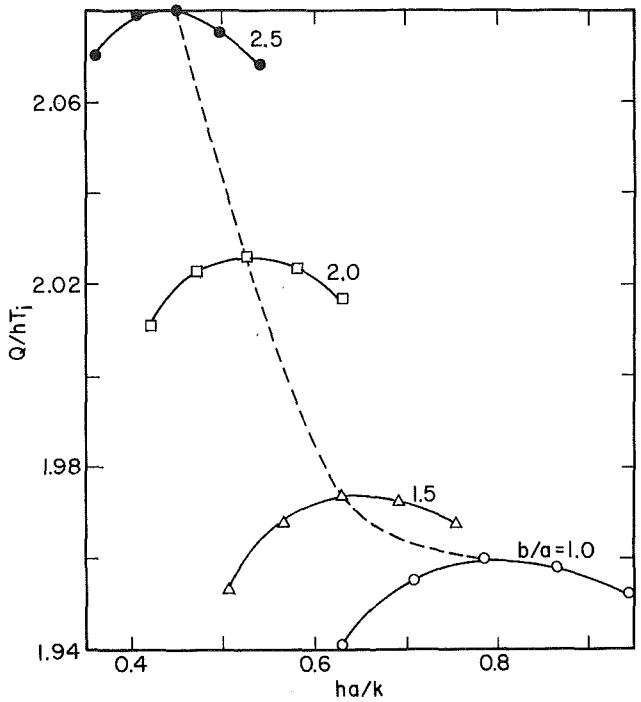

Fig. 4 Heat loss versus Biot number curves for rectangular insulation

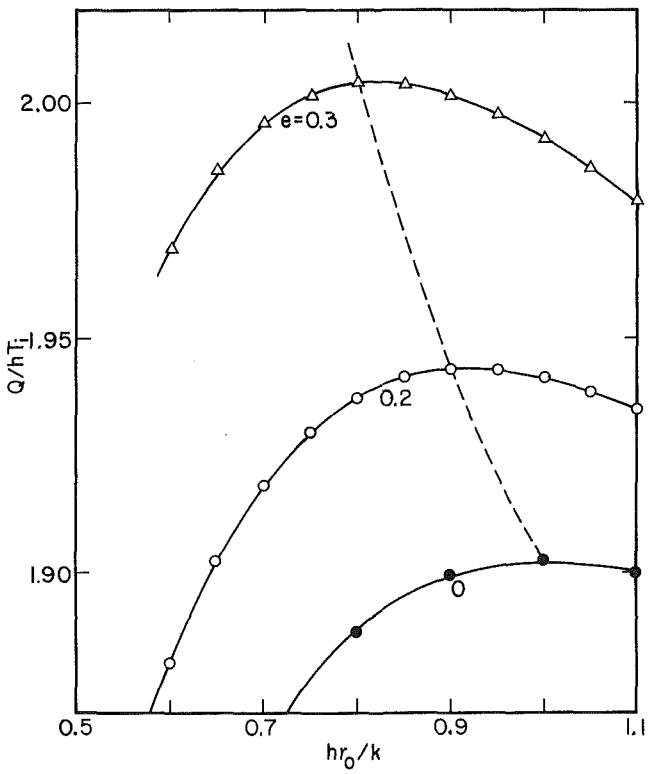

Fig. 5 Heat loss versus Biot number curves for eccentric circular insulation

subject to substantiation, and the whole burden of proof now rests on equations (7), (15), and (19). The data presented in this paper were computed using these equations.

Data for polygons are presented in Fig. 3. The Biot number ha/k is used to plot the x-axis. The critical Biot numbers found from those curves can be related to n by $ha_c/k=(\pi/n)ctn(\pi/n)$, which can also be derived from equation (11). A critical perimeter is thus defined for the polygon. Also notice that the heat loss is increased when the number of sides of the polygon is decreased (see the dash line in the figure). This is because, for a polygon of small n, the tips of the polygon behave like cooling fins.

A plot of the heat loss for the rectangles yields similar results (see Fig. 4). Here the heat loss are peaked at $ha_c/k=(\pi/2)/[1+(b/a)]$. This relationship can also be obtained from equation (17). For the rectangles, the heat loss is increased for large aspect ratios, again a cooling fin effect.

A similar plot is made for the eccentric circles in Fig. 5. This time the critical hr_o/k cannot be related to a critical perimeter. Such a perimeter is thus not defined in this case.

Conclusions

For a cylindrical heat source covered with insulation, the heat loss is maximized when the perimeter of the insulation reaches $2\pi k/h$. This relation is valid if the insulation has the configuration of a circle, an equilateral polygon, or a rectangle as long as their heat sources are centrally located. For these geometries, the extremity of heat loss is independent of whether a convective condition or a prescribed temperature is imposed on the surface. Hence the conduction shape factor can be used to formulate the thermal resistance, which is, in turn, differentiated to maximize the heat flow. The theory breaks down if there is an eccentricity of the heat source.

References

1 Hsieh, C. K., "Critical Thickness of Insulation of a Square Cross Section," *Solar Energy*, Vol. 25, No. 6, 1980, pp. 569–570.

2 Aziz, A., "Comments on 'Critical Thickness of a Square Cross Section'," *Solar Energy*, Vol. 30, No. 5, 1983, pp. 491.

3 Hsieh, C. K., "Response to Prof. A. Aziz's Letter," *Solar Energy*, Vol. 30, No. 5, 1983, pp. 491–492.

4 Hahne, E., and Grigull, U., "Shape Factor and Shape Resistance for Steady Multidimensional Heat Conduction," *International Journal of Heat and Mass Transfer*, Vol. 18, 1975, pp. 751–767.

5 Smith, J. C., Lind, J. E., and Lermond, D. S., "Shape Factors for Conductive Heat Flow," *AIChE Journal*, Vol. 4, 1950, pp. 330–331.

6 Balcerzak, M. J., and Raynor, S., "Steady-State Temperature Distribution and Heat Flow in Prismatic Bars with Isothermal Boundary Conditions," *International Journal of Heat and Mass Transfer*, Vol. 3, 1961, pp. 113–125.

7 Schneider, P. J., "Conduction," section 3, *Handbook of Heat Transfer*, Edited by W. M. Rohsenow and J. P. Hartnett, McGraw-Hill, New York, 1973, pp. 3-120–121.

Interfacial Flow and Evaporation of Sessile Drops on a Vertical Surface

Nengli Zhang[1] and Wen-Jei Yang[2]

Nomenclature

A = cross-sectional area of lens-shaped film (Fig. 3), m^2
B = image of b on screen (Fig. 3), m
b = width of lens-shaped film (Fig. 3), m
Ca = capillary number $= \dfrac{\mu\alpha}{\sigma_0\delta}$
d_i = diameter of ith lens-shaped drop, m
f = focal length of cylindrical segment (Fig. 3), m
f_i = focal length of ith lens drop, m
g = gravitational acceleration, m/s^2
h = height of cylindrical segment (Fig. 3), m
h_i = height of ith lens-shaped drop as defined by equation (1), m
L = image of l on screen (Fig. 3), m
l = length of lens-shaped film (Fig. 3), m
Ma = Marangoni number $= \dfrac{\sigma_1 d_0 \Delta T}{\alpha\mu}$
N = number of segments of lens-shaped drops to form a "tear" drop
n = refractive index of liquid
R = radius of cylindrical segment (Fig. 3), m
R_i = radius of ith lens-shaped drop as defined by equation (1), m
S = arc length of cylindrical segment (Fig. 3), m
T_w = temperature of test plate, K
T_b = boiling temperature of liquid, K
ΔT = $T_b - T_w$, K
t = time, s
V = instantaneous volume, m^3; V_d, of "tear" drop as defined by equation (2); V_{di}, of ith lens-shaped drop as defined by equation (1); V_f, of film as defined in equation (3); V_l, of entire drop (film and "tear"), = $V_d + V_f$
V_0 = initial value of V_l, m^3
α = thermal diffusivity of liquid, m^2/s
δ = equivalent film thickness as defined by $A/(S+b)$, m
ϵ = dielectric constant
η_i = volume fraction of ith lens drop
μ = absolute viscosity, Pa • s
ρ = liquid density, Kg/m^3
σ_0 = mean surface tension, N/cm
σ_1 = negative of temperature derivative of surface tension, N/cm • K
τ = drop lifetime, s
ψ = Nusselt's film thickness parameter $= \left(\dfrac{\rho^2 g}{\mu^2}\right)^{1/3} \delta$

[1]Department of Mechanical Engineering and Applied Mechanics, The University of Michigan, Ann Arbor, Mich. 48109; visiting Scholar on leave from the Department of Thermal Engineering, Tsinghua University, Beijing, China.

[2]Department of Mechanical Engineering and Applied Mechanics, The University of Michigan, Ann Arbor, Mich. 48109, Mem. ASME.

Contributed by the Heat Transfer Division for publication in the JOURNAL OF HEAT TRANSFER. Manuscript received by the Heat Transfer Division March 17, 1983.

Introduction

A comprehensive survey of the literature pertinent to droplet evaporation from solid surfaces is available in [1] and therefore will not be repeated here. Recently, the laser shadowgraphic method [2] was used to experimentally investigate the buoyancy and thermocapillary instability in minute drops evaporating on a horizontal plate, unheated [3] and with various degrees of heating [1]. The direct photographic method was employed to investigate evaporative convection in moving drops [4].

When a droplet is placed or impinged on a vertical surface, the gravitational force causes it to deform into a thin layer with a body of the remaining liquid, called "tears," hanging below, as shown in Fig. 1. The present study employs the laser shadowgraphic method to visualize the interfacial stability of both the thin liquid film and the "tear" and to determine the time histories of the liquid film and "tear."

Experimental Apparatus and Procedure

A schematic diagram of the laser shadowgraphic system is illustrated in Fig. 2. It consisted of a laser light, an achromatic objective, a precision pinhole, a collimating lens, a rectangular aperture, a glass (test) plate, a screen plate, and camera. A minute drop was placed on an optically flat glass plate for evaporation in open air. The light source was a C.W. Radiation Model SP2, 2.5-mW cylindrical helium-neon laser. The collimated laser light passed through the evaporating liquid, both the film and the "tear,' from top to bottom (thus producing a top view of the interfacial activity) and cast a shadow on the screen. The image on the screen was recorded by a 16-mm Bolex H16 EMB movie camera with a Nikon Nikkor 300-mm, 1:45 lens. The drop was carefully placed on the test plate by means of a 50 μl Monoject micro syringe (see [3] for details).

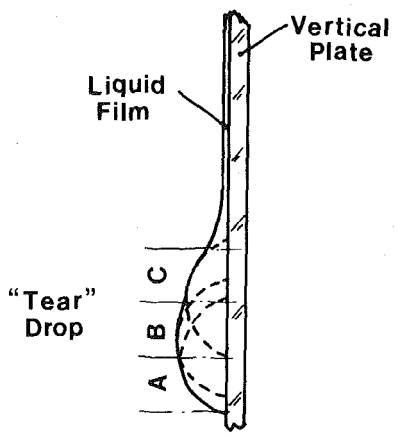

Fig. 1 A schematic of a liquid drop on a vertical plate

References

1 Hsieh, C. K., "Critical Thickness of Insulation of a Square Cross Section," *Solar Energy*, Vol. 25, No. 6, 1980, pp. 569–570.

2 Aziz, A., "Comments on 'Critical Thickness of a Square Cross Section'," *Solar Energy*, Vol. 30, No. 5, 1983, pp. 491.

3 Hsieh, C. K., "Response to Prof. A. Aziz's Letter," *Solar Energy*, Vol. 30, No. 5, 1983, pp. 491–492.

4 Hahne, E., and Grigull, U., "Shape Factor and Shape Resistance for Steady Multidimensional Heat Conduction," *International Journal of Heat and Mass Transfer*, Vol. 18, 1975, pp. 751–767.

5 Smith, J. C., Lind, J. E., and Lermond, D. S., "Shape Factors for Conductive Heat Flow," *AIChE Journal*, Vol. 4, 1950, pp. 330–331.

6 Balcerzak, M. J., and Raynor, S., "Steady-State Temperature Distribution and Heat Flow in Prismatic Bars with Isothermal Boundary Conditions," *International Journal of Heat and Mass Transfer*, Vol. 3, 1961, pp. 113–125.

7 Schneider, P. J., "Conduction," section 3, *Handbook of Heat Transfer*, Edited by W. M. Rohsenow and J. P. Hartnett, McGraw-Hill, New York, 1973, pp. 3-120–121.

Interfacial Flow and Evaporation of Sessile Drops on a Vertical Surface

Nengli Zhang[1] and Wen-Jei Yang[2]

Nomenclature

A = cross-sectional area of lens-shaped film (Fig. 3), m^2
B = image of b on screen (Fig. 3), m
b = width of lens-shaped film (Fig. 3), m
Ca = capillary number $= \dfrac{\mu\alpha}{\sigma_0\delta}$
d_i = diameter of ith lens-shaped drop, m
f = focal length of cylindrical segment (Fig. 3), m
f_i = focal length of ith lens drop, m
g = gravitational acceleration, m/s^2
h = height of cylindrical segment (Fig. 3), m
h_i = height of ith lens-shaped drop as defined by equation (1), m
L = image of l on screen (Fig. 3), m
l = length of lens-shaped film (Fig. 3), m
Ma = Marangoni number $= \dfrac{\sigma_1 d_0 \Delta T}{\alpha\mu}$
N = number of segments of lens-shaped drops to form a "tear" drop
n = refractive index of liquid
R = radius of cylindrical segment (Fig. 3), m
R_i = radius of ith lens-shaped drop as defined by equation (1), m
S = arc length of cylindrical segment (Fig. 3), m
T_w = temperature of test plate, K
T_b = boiling temperature of liquid, K
ΔT = $T_b - T_w$, K
t = time, s
V = instantaneous volume, m^3; V_d, of "tear" drop as defined by equation (2); V_{di}, of ith lens-shaped drop as defined by equation (1); V_f, of film as defined in equation (3); V_l, of entire drop (film and "tear"), = $V_d + V_f$
V_0 = initial value of V_l, m^3
α = thermal diffusivity of liquid, m^2/s
δ = equivalent film thickness as defined by $A/(S+b)$, m
ϵ = dielectric constant
η_i = volume fraction of ith lens drop
μ = absolute viscosity, Pa • s
ρ = liquid density, Kg/m^3
σ_0 = mean surface tension, N/cm
σ_1 = negative of temperature derivative of surface tension, N/cm • K
τ = drop lifetime, s
ψ = Nusselt's film thickness parameter $= \left(\dfrac{\rho^2 g}{\mu^2}\right)^{1/3} \delta$

[1]Department of Mechanical Engineering and Applied Mechanics, The University of Michigan, Ann Arbor, Mich. 48109; visiting Scholar on leave from the Department of Thermal Engineering, Tsinghua University, Beijing, China.

[2]Department of Mechanical Engineering and Applied Mechanics, The University of Michigan, Ann Arbor, Mich. 48109, Mem. ASME.

Contributed by the Heat Transfer Division for publication in the JOURNAL OF HEAT TRANSFER. Manuscript received by the Heat Transfer Division March 17, 1983.

Introduction

A comprehensive survey of the literature pertinent to droplet evaporation from solid surfaces is available in [1] and therefore will not be repeated here. Recently, the laser shadowgraphic method [2] was used to experimentally investigate the buoyancy and thermocapillary instability in minute drops evaporating on a horizontal plate, unheated [3] and with various degrees of heating [1]. The direct photographic method was employed to investigate evaporative convection in moving drops [4].

When a droplet is placed or impinged on a vertical surface, the gravitational force causes it to deform into a thin layer with a body of the remaining liquid, called "tears," hanging below, as shown in Fig. 1. The present study employs the laser shadowgraphic method to visualize the interfacial stability of both the thin liquid film and the "tear" and to determine the time histories of the liquid film and "tear."

Experimental Apparatus and Procedure

A schematic diagram of the laser shadowgraphic system is illustrated in Fig. 2. It consisted of a laser light, an achromatic objective, a precision pinhole, a collimating lens, a rectangular aperture, a glass (test) plate, a screen plate, and camera. A minute drop was placed on an optically flat glass plate for evaporation in open air. The light source was a C.W. Radiation Model SP2, 2.5-mW cylindrical helium-neon laser. The collimated laser light passed through the evaporating liquid, both the film and the "tear,' from top to bottom (thus producing a top view of the interfacial activity) and cast a shadow on the screen. The image on the screen was recorded by a 16-mm Bolex H16 EMB movie camera with a Nikon Nikkor 300-mm, 1:45 lens. The drop was carefully placed on the test plate by means of a 50 μl Monoject micro syringe (see [3] for details).

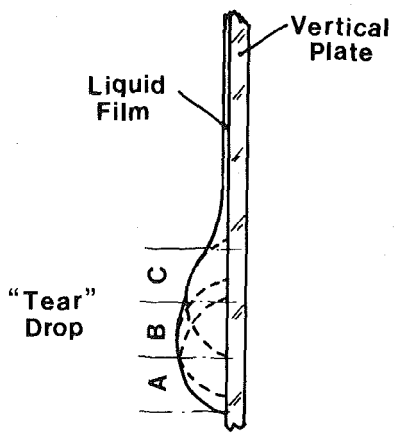

Fig. 1 A schematic of a liquid drop on a vertical plate

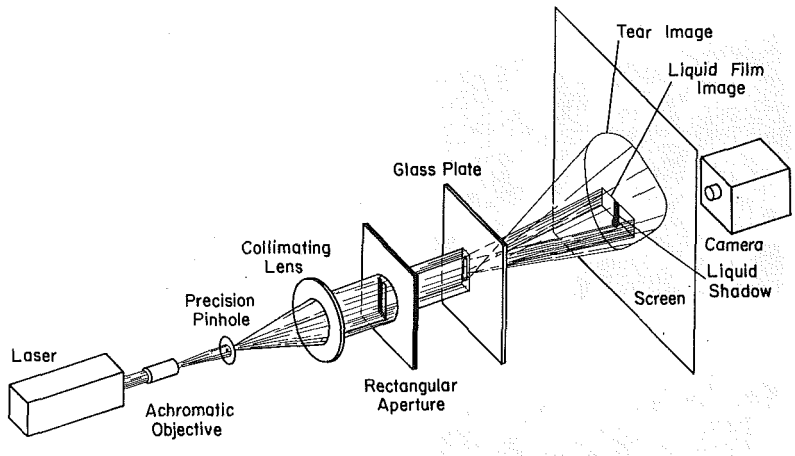

Fig. 2 A schematic of laser shadowgraphic system

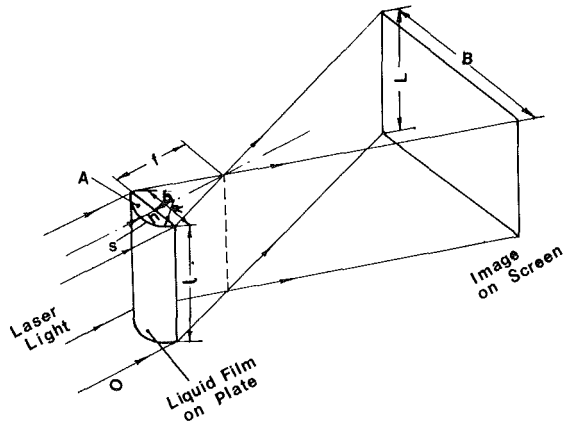

Fig. 3 Geometrical relationship between liquid film and its shadowgraphic image

Photographic Observations

The liquids with a low boiling point being studied include acetone, methanol, ethanol, ethyl acetate, benezene, chloroform, methylene chloride, cyclohexane, carbon tetrachloride, and ethyl ether. Each liquid evaporated on an unheated plate in open air.

Due to the effect of gravity, each drop moved down along the vertical surface, leaving a thin film behind a "tear," the remnant of the drop that stopped moving at the balance of gravitational and surface tension forces. The film and the "tear" evaporated simultaneously. Figure 2 shows the light path and how the liquid bodies cast their shadow and image on the screen. Each photograph exhibited one shadow and two images, inner and outer. The shadow of the entire liquid at the center is surrounded by the inner image for the liquid film and the outer image for the "tear" encircling both. It is simple optical geometry as illustrated in Fig. 2. The inner image depicted the flow pattern at the liquid–solid interface, i.e., liquid–film periphery as shown in Fig. 3. The outer image portrayed the flow structure at the air–liquid and liquid–solid interfaces of the "tear" drop.

Geometrically, one may consider a "tear" drop to consist of segments of multiple lens-shaped drops having various diameters. For example, the "tear" drop illustrated in the lower part of Fig. 1 is composed of segments of three lens-shaped drops, A, B, and C. This concept will be useful in determining the instantaneous size of a "tear" drop from its image on the screen, as will be treated later in the succeeding section. In order to reinforce this idea, a silicon-oil drop was tested as follows. A tiny piece of black paper with a narrow horizontal slit was glued on the back surface of the test plate. As the liquid drifted down the test surface, either the whole or segments of the drop could be observed. In Figs. 4(*a–d*), the vertical rectangle at the photo center was a piece of transparent Scotch tape attached on the screen. This was done to balance the contrast of the inner image (bright portion). The shadow of the slit paper appeared as two horizontal lines (a heavy one over a thin one) with a bright line (slit) in between at the lower end of the rectangle. Figure 4(*a*) showed the image of the whole "tear drop" whose shadow was visible (like a bullet) over that of the slit paper inside the rectangle. Behind the "tear" drop was a trace of liquid film whole image appeared as a bright background surrounding the rectangle. It is to demonstrate that the drop surface in Fig. 4(*a*) can be considered consisting of the three segments, like A, B and C in Fig. 3.

When the front two-thirds of the "tear" drop hid behind the upper piece of the slit paper, the image of its tail end appeared in Fig. 4(*b*). Figure 4(*c*) exhibited the image of the front end, as the drop moved from the upper piece of the slit paper. Finally, Fig. 4(*d*) showed the image of the middle segment when the drop moved halfway through the narrow slit. Figures 4(*b, c, d*) correspond respectively to the lower, upper, and middle segments of Fig. 4(*a*), i.e., to the segments C, A, and B of Fig. 1.

In the case of film evaporation, the naked eye could observe two kinds of film cross sections, as illustrated in Fig. 5: lens shaped as shown by top views a-a and b-b and trough shaped as c-c. Two ridges at the outer edges of the film in case (*c*) were formed with the absorption of water molecules in the air, by the same mechanism as the formation of a torous-shaped periphery in the evaporation of unstable-type drops [3]. The front views in Fig. 5 exhibited the change in shape of the film surface with time. Notice the difference between cases (*a*) and (*b*) near the end of evaporation process. The liquid film in case (*b*) broke up into pieces, while the film in case (*a*) remained a single body throughout the entire evaporation process. At the final stage, the film disappeared leaving a lens-shaped drop. However, the unstable-type liquid failed to form a lens-shaped drop due to the presence of absorbed water molecules in the remaining liquid.

Next, optical observations were performed by means of the laser shadowgraphy. Figures 6(*a–d*) are typical results for the interfacial stability of thin films of various liquids. When a film formed a cylindrical segment with a very smooth surface, the inner image exhibited a near rectangular form as Fig. 3, and Figs. 6(*a, b*) for cyclohexane and carbon tetrachloride, respectively. This type of phase change is classified as "stable-interface-type evaporation" following [3]. It occurred in the liquid films of cyclohexane, carbon tetrachloride, ethyl

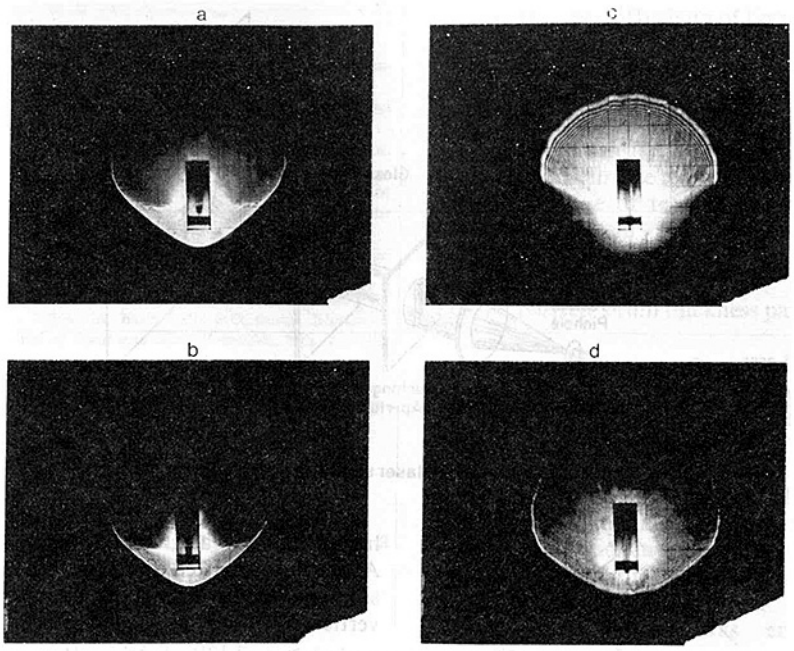

Fig. 4 Instant laser shadowgraphs of a silicon-oil drop on a vertical plate (*a*) entire, drop, (*b*) tail end (c) head end, and (*d*) midsection ($f = 4.5$, time at 1/5, 1/10, 1/2, and 1/5 s, respectively)

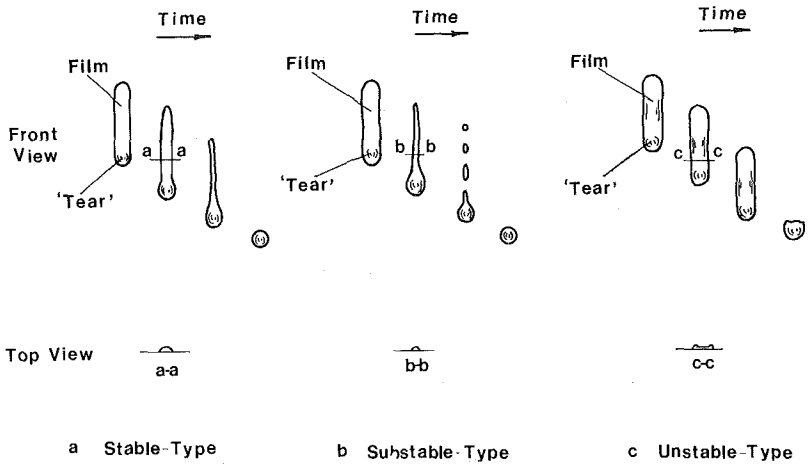

Fig. 5 Schematic illustrations of stable-, substable-, and unstable-interface type evaporation of liquid films on a vertical plate

acetate, and benzene. It is interesting to note the observation of fringes within the image resulting from the Fresnel diffraction of rectangular apertures in Figs. 6(*a*) and 6(*b*). The lower end of the inner image with bent figures portrayed the flow structure on the surface joining the film and the "tear." Should a film surface be slightly rippled, the outer edges of the inner image deviated from a rectangle with short spikes on both sides, see Fig. 6(*c*) for chloroform. The liquid films of chloroform, ethyl ether, and methylene chloride exhibited the behavior, called "subsubstable-interface type evaporation." There is another group of liquids, such as acetone, methanol, and ethanol, that formed a trough-shaped film on a vertical surface. The basin appeared as a bright belt (hidden by the tape in the middle) being sandwiched between the image of the ridges, which had spikes within an arc on both sides, Fig. 6(*d*) for acetone. The Fresnel stripes were nearly concentric. The group is categorized as "unstable-interface type evaporation." The trough-shaped interface could be identified in the shadow which exhibited a lighter stripe sandwiched between two darker stripes in Fig. 6(*d*).

Results and Discussion

A method was developed to determine the liquid volume–time history from the shadowgraph: The liquid is divided into two parts: film and "tear" drop. Then the liquid volume–time history is a superposition of those of the film and drop parts. For the drop part, the image of the "tear" is considered consisting of N segments of multiple lens-shaped drops. The focal length of each drop f_i is calculated using the diameters d_i and D_i of the drop, which were measured from its shadow and image on the screen, respectively, by a simple geometric relationship [3]. Then R_i, h_i, and V_{di} are determined in a subsequent order using the expressions

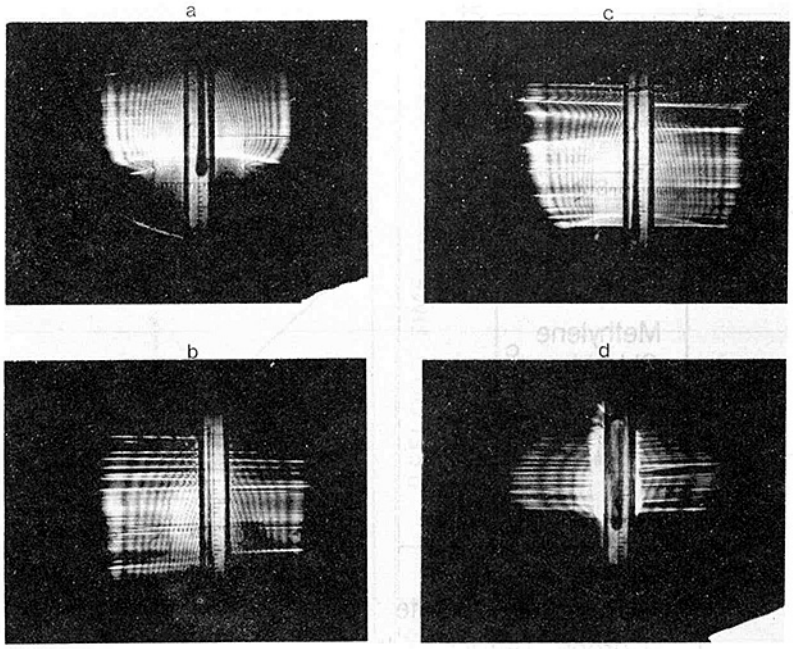

Fig. 6 Instant laser shadowgraphs of (*a*) cyclohexane, (*b*) carbon tetrachloride, (*c*) chloroform, and (*d*) acetone ($f = 5.6$, 1/50 s)

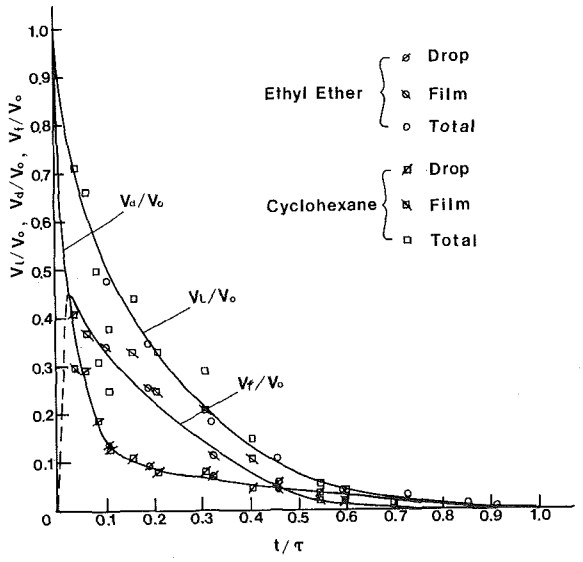

Fig. 7 Volume-time history of film, "tear," and total liquid

$$R_i = (n-1)f_i; h_i = R_i - (R_i^2 - \frac{d_i^2}{4})^{1/2}; V_{di} = \pi h_i^2 (R_i - \frac{h_i}{3}) \quad (1)$$

For the liquids tested here, n varies from 1.3 to 1.5. Then, the volume of the "tear" drop is

$$V_d = \sum_{i=1}^{N} V_{di} \eta_i \quad (2)$$

For the film part, consider a film that has a lens-shaped cross section, i.e., a cylindrical segment, as shown in Fig. 3 *b* and *l* were measured from their shadows (not shown) on the screen. With the distance between the plate and the screen known, the focal length of the lens-shaped film surface f can be calculated by a simple geometric relationship. The radius R, height h, arc length S, cross-sectional area A, and volume V_f of the cylindrical segment can be determined as

$$\left.\begin{aligned} R &= (n-1)f; h = R - \left(R^2 - \frac{b^2}{4}\right)^{1/2} \\ S &= 2R\cos^{-1}\left(\frac{R-h}{R}\right); \\ A &= R^2\cos^{-1}\left(\frac{R-h}{R}\right) - (R-h)(2Rh-h^2)^{1/2} \\ V_f &= Al \end{aligned}\right\} \quad (3)$$

Typical test results for ethyl ether and cyclohexane are presented in graphical form in Fig. 7. Test results for both the stable- (cyclohexane) and substable- (ethyl ether) evaporation cases fall close to a single curve. The evaporation speed of the "tear" drop was extremely rapid during the initial stage t/τ of less than 0.1 and reached an "asymptotic" stage at t/τ of about 0.2. The volume–time history of the unstable type liquids is not available due to difficulty in determining the instantaneous volume of the trough-shaped liquid film.

The ψ/Ca ratio for liquid film was calculated for all liquids tested, using the physical properties in [5–7]. The equivalent film thickness δ used as the characteristic length was defined as $A/(S+b)$, the film cross-sectional area divided by its perimeter. In case of the trough-shaped film, δ was roughly estimated to be 7×10^{-3} mm for all three unstable-type liquids. An interfacial flow map was constructed in Fig. 8 to define the domains of the three basic interfacial flow structure in thin liquid films evaporating on a vertical plate. The figure is a plot of the ψ/Ca ratio versus the dielectric constant ϵ. Unstable-interfacial type liquid films (of trough-shaped cross section) are characterized by high ϵ, while both substable and stable type liquid films (of lens-shaped cross section) have low values of ϵ. A very smooth lens-shaped film surface is formed in the liquids of low ψ/Ca, whereas the liquids with high ψ/Ca have a rippled lens-shaped film surface. This is analogous to the three basic interfacial flow structures observed in minute drops evaporating on a plate. Their domains are defined in an interfacial flow map, a plot of the Marangoni number Ma versus [3]. This map can be applied to the evaporation of "tear" drops. The interfacial instability of liquid films is controlled by deformation of the free surface and the

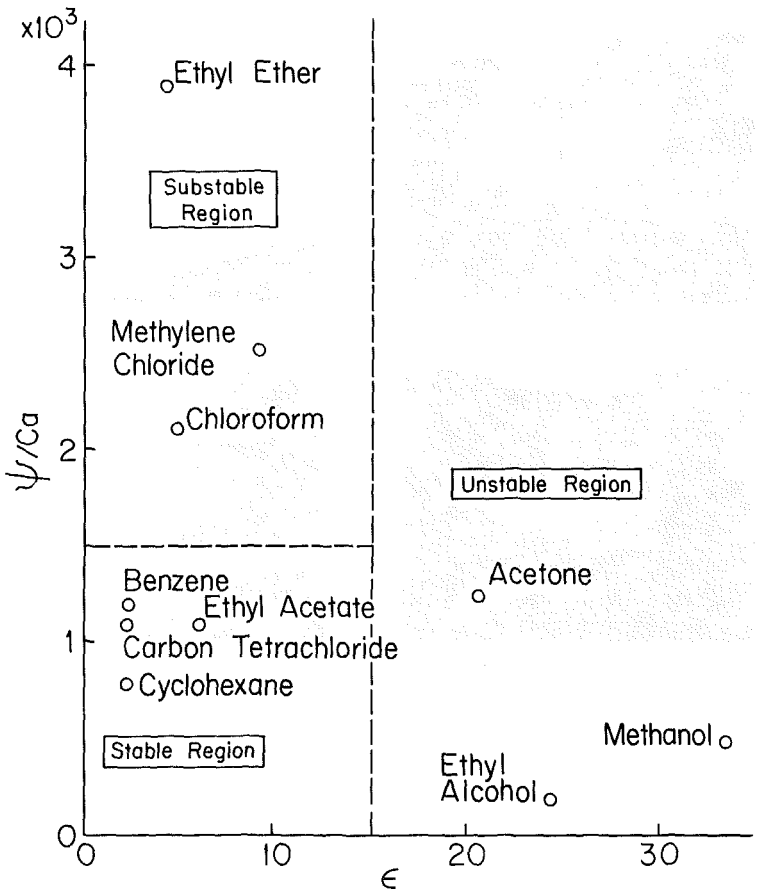

Fig. 8 Interfacial flow map of liquid films on a vertical plate

mechanism of a falling film flow, while the interfacial instability of an evaporating droplet is induced by a thermocapillary mechanism. Hence the ordinates of their interfacial flow maps are different. Most liquids tested are classified into the same category in both flow maps, except ethyl acetate and ethyl ether.

Conclusions

Laser shadowgraphy was employed to investigate interfacial stability in liquid drops evaporating on a vertical plate. Due to gravity, each drop deformed into a thin film trailing behind a "tear" drop. This experiment supports the concept that a "tear" drop consists of segments of multiple lens drops having various diameters. A method was developed to determine the volume-time history of evaporating drops (film and "tear") from shadowgraphic recordings. It is concluded from shadowgraphic visualization that liquid films can be categorized into three types: stable, substable, and unstable evaporation. The interface of stable-type films remains smooth, while that of substable-type films is rippled. However, both interfaces take the shape of a cylindrical segment. The outer edges of unstable-interface type films have ridges, thus forming a trough-shaped geometry for the film cross section. The formation of ridges is caused by the action of surface tension on the film interface mixed with the water molecules that are absorbed from the ambient during the evaporation process. An interfacial flow map for film evaporation is constructed which defines the domains.

References

1 Zhang, N., and Yang, Wen-Jei, "Evaporation and Explosion of Liquid Drops on a Heated Surface," *Experiments in Fluids*, Vol. 1, 1983, pp. 101-111.

2 Zhang, N., and Yang, Wen-Jei, "Visualization of Evaporative Convection in Minute Drops by Laser Shadowgraphy," *Review of Scientific Instruments*, Vol. 54, 1983, pp. 93-96.

3 Zhang, N., and Yang, Wen-Jei, "Natural Convection in Evaporating Minute Drops," ASME JOURNAL OF HEAT TRANSFER, Vol. 104, 1982, pp. 656-662.

4 Zhang, N., and Yang, Wen-Jei, "Evaporative Convection in Minute Drops on a Plate with Temperature Gradient," *International Journal of Heat and Mass Transfer*, Vol. 26, 1983, pp. 1479-1488.

5 Weast, R. C., and Astle, M. J., eds., *Handbook of Chemistry and Physics*, 62nd ed., CRC Press, Boca Raton, Fla., 1981-82.

6 Dean, J. A., ed., *Lange's Handbook of Chemistry*, 12th ed., McGraw-Hill, New York, 1979.

7 National Research Council, U.S.A., *International Critical Tables of Numerical Data, Physics, Chemistry and Technology*, McGraw-Hill, New York, 1933.

The Reflood Time as a Determination for Dryout

C. W. Somerton[1] and I. Catton[2]

Introduction

Following the accident at Three Mile Island, there has been renewed interest in the dryout of a volume-heated particulate bed. The activity generated by this interest has included both the development of theoretical models of the dryout process

[1]Mechanical Engineering Department, Louisiana State University, Baton Rouge, La. 70803, Assoc. Mem. ASME

[2]Nuclear Energy Laboratory, University of California, Los Angeles, Calif. 90025, Mem. ASME

Contributed by the Heat Transfer Division for publication in the JOURNAL OF HEAT TRANSFER. Manuscript received by the Heat Transfer Division July 18, 1983.

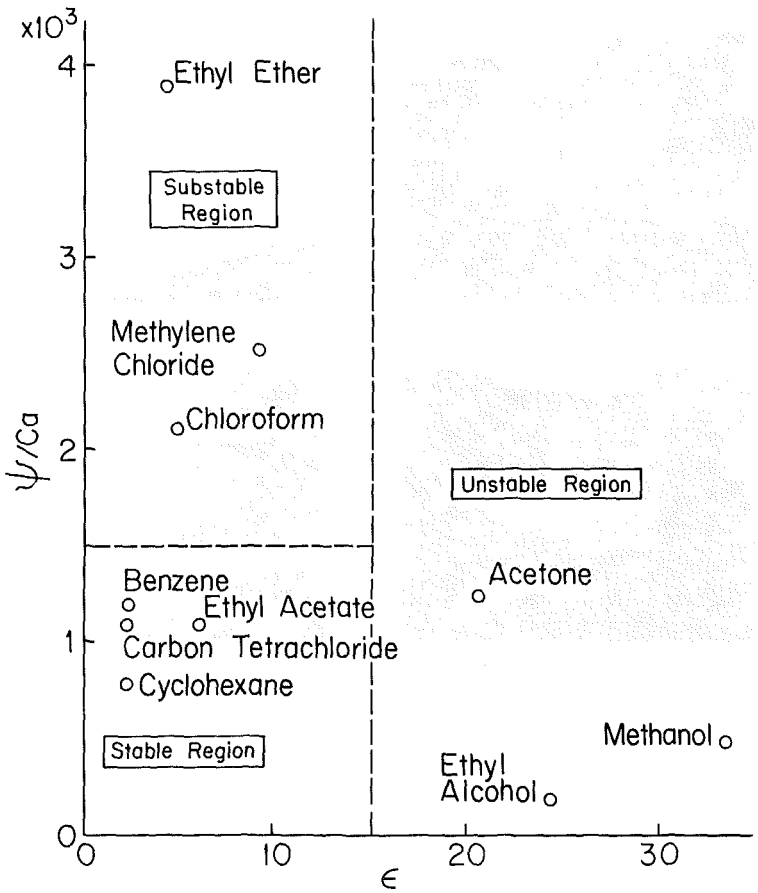

Fig. 8 Interfacial flow map of liquid films on a vertical plate

mechanism of a falling film flow, while the interfacial instability of an evaporating droplet is induced by a thermocapillary mechanism. Hence the ordinates of their interfacial flow maps are different. Most liquids tested are classified into the same category in both flow maps, except ethyl acetate and ethyl ether.

Conclusions

Laser shadowgraphy was employed to investigate interfacial stability in liquid drops evaporating on a vertical plate. Due to gravity, each drop deformed into a thin film trailing behind a "tear" drop. This experiment supports the concept that a "tear" drop consists of segments of multiple lens drops having various diameters. A method was developed to determine the volume-time history of evaporating drops (film and "tear") from shadowgraphic recordings. It is concluded from shadowgraphic visualization that liquid films can be categorized into three types: stable, substable, and unstable evaporation. The interface of stable-type films remains smooth, while that of substable-type films is rippled. However, both interfaces take the shape of a cylindrical segment. The outer edges of unstable-interface type films have ridges, thus forming a trough-shaped geometry for the film cross section. The formation of ridges is caused by the action of surface tension on the film interface mixed with the water molecules that are absorbed from the ambient during the evaporation process. An interfacial flow map for film evaporation is constructed which defines the domains.

References

1 Zhang, N., and Yang, Wen-Jei, "Evaporation and Explosion of Liquid Drops on a Heated Surface," *Experiments in Fluids*, Vol. 1, 1983, pp. 101-111.

2 Zhang, N., and Yang, Wen-Jei, "Visualization of Evaporative Convection in Minute Drops by Laser Shadowgraphy," *Review of Scientific Instruments*, Vol. 54, 1983, pp. 93-96.

3 Zhang, N., and Yang, Wen-Jei, "Natural Convection in Evaporating Minute Drops," ASME JOURNAL OF HEAT TRANSFER, Vol. 104, 1982, pp. 656-662.

4 Zhang, N., and Yang, Wen-Jei, "Evaporative Convection in Minute Drops on a Plate with Temperature Gradient," *International Journal of Heat and Mass Transfer*, Vol. 26, 1983, pp. 1479-1488.

5 Weast, R. C., and Astle, M. J., eds., *Handbook of Chemistry and Physics*, 62nd ed., CRC Press, Boca Raton, Fla., 1981-82.

6 Dean, J. A., ed., *Lange's Handbook of Chemistry*, 12th ed., McGraw-Hill, New York, 1979.

7 National Research Council, U.S.A., *International Critical Tables of Numerical Data, Physics, Chemistry and Technology*, McGraw-Hill, New York, 1933.

The Reflood Time as a Determination for Dryout

C. W. Somerton[1] and I. Catton[2]

Introduction

Following the accident at Three Mile Island, there has been renewed interest in the dryout of a volume-heated particulate bed. The activity generated by this interest has included both the development of theoretical models of the dryout process

[1]Mechanical Engineering Department, Louisiana State University, Baton Rouge, La. 70803, Assoc. Mem. ASME

[2]Nuclear Energy Laboratory, University of California, Los Angeles, Calif. 90025, Mem. ASME

Contributed by the Heat Transfer Division for publication in the JOURNAL OF HEAT TRANSFER. Manuscript received by the Heat Transfer Division July 18, 1983.

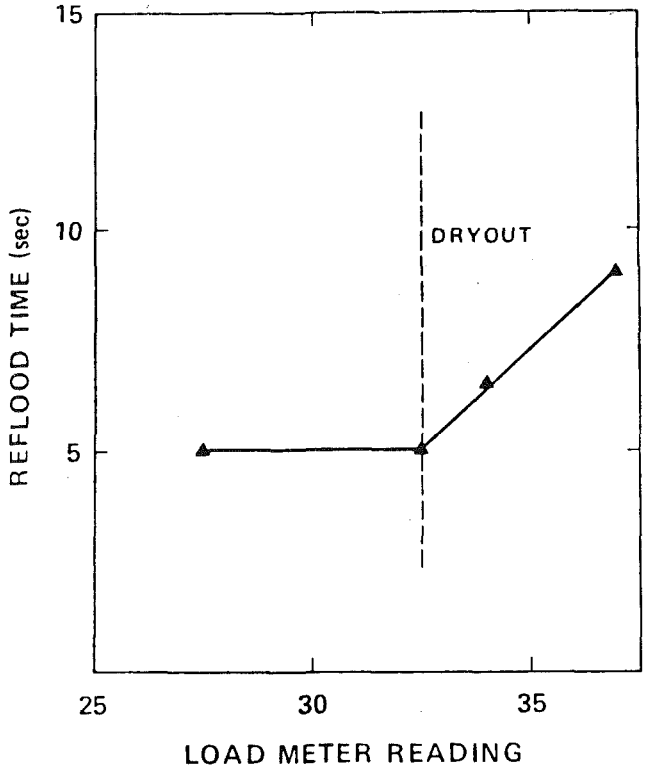

Fig. 1 The reflood time as an indication of dryout

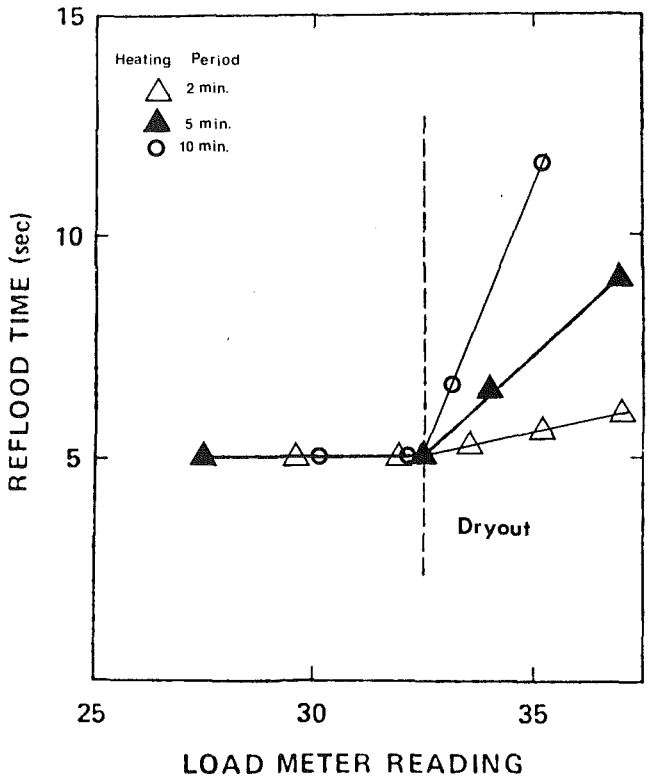

Fig. 2 The effect of heating period on the reflood time

as well as several experimental investigations. In nearly all of the theoretical models it is assumed that the governing mechanism leading to dryout is buoyancy-driven countercurrent flow in a porous medium with phase change, and that dryout occurs when liquid can no longer reach portions of the bed. In practical terms, dryout is defined as the point at which the temperature of the bed will suddenly rise and continue to increase to a very high value. Employing this definition in a laboratory setting has often proved difficult. Several techniques have been used, but all have certain liabilities which can lead to problems with the consistency and reproducibility of the results.

While conducting dryout experiments at UCLA and while faced with the dilemma of determining dryout, the authors developed a method for determining dryout in a consistent and reproducible manner. This technique involves measuring the time required to refill the particulate bed after heating has ceased. This time is termed the reflood time. As will be discussed, the reflood time is an indirect indication of dryout as it is an indirect measure of the temperature, but is found to be a more definitive method of determining the experimental dryout than previous techniques.

Experimental Procedures

Most of the previous experimental work [1–4] used a combination of temperature measurements and visual observations to determine dryout conditions. The drawbacks to both of these techniques involve the local nature of dryout. Visual observations are only good for the outer region of the particulate bed, since one cannot view the inner regions while temperature measurments are obtained with thermocouples, providing very localized temperature readings. If dryout first occurs at a location other than the outside perimeter of the bed or near the thermocouples, then neither technique will give an indication of dryout. Further, if a large number of thermocouples are imbedded in the particulate bed, the physical characteristics of the porous medium could be significantly changed. In particular, the permeability might

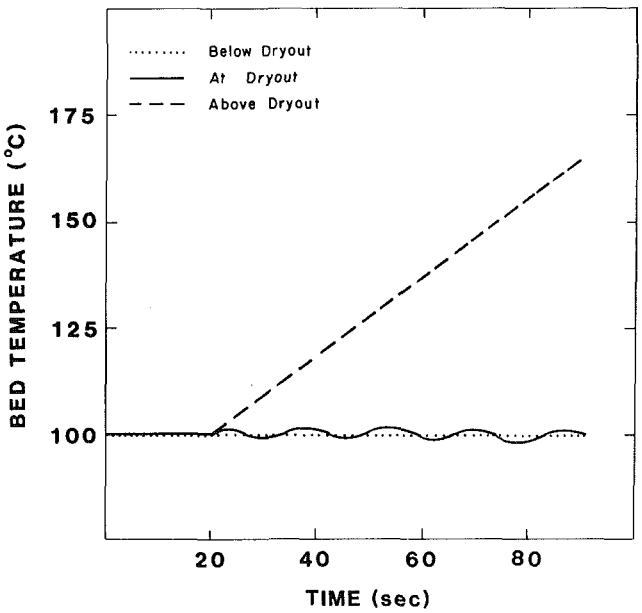

Fig. 3 Bed temperature as a function of time at conditions predicted by the reflood time

change, which has been shown previously [5] to be the key parameter in characterizing the debrid bed in regard to dryout.

Initially, in the experiments conducted by the authors, visual observations and temperature measurements were used as the criteria for dryout. However, consistency and reproducibility became serious problems, and hence it was found that by measuring the reflood time the dryout could be determined in a predictable and consistent manner. Reflood time is defined as the time it takes for liquid phase coolant to totally refill the bed after volumetric heating is stopped. For

heating rates below dryout, the reflood time is constant, but once dryout is achieved, this time increases with increasing power. This is shown in Fig. 1, where the load meter reading is directly proportional to the power. For heating rates below dryout, the bed will be at the saturation temperature. When the power is turned off, liquid that had been displaced to above the bed by vapor production will reflood the bed due to gravity. However, once dryout is reached the particles will attain temperatures above saturation. This superheat is proportional to the heating rate. When the power is turned off and liquid phase coolant begins to reenter the bed, it encounters particles at temperatures above saturation and must then cool them off in order to completely reflood the bed. It is this quenching phenomena that extends the reflood time in a post dryout situation.

In practice, the reflood time was measured as follows. At the moment the power was turned off a timer was started. Liquid would then begin to refill the particulate bed. When the liquid reached a predetermined level near the top of the bed, the timer would be stopped and the time interval recorded. This time interval was used as the reflood time. It was found that this time could be reproduced within ± 0.2 s.

Clearly, the reflood time is actually an indirect measurement of the bed temperature; the higher the bed temperature, the longer the reflood time. The superheat occurring after dryout will not only be a function of the heating rate, but also of the time period over which the heating is applied. The dependence of the superheat on the heating period should also appear in the reflood time, if it is a true indication of the bed temperature. The trend of the reflood time with heating period is shown in Fig. 2. As the heating period increases, the reflood time increases, which is identical to the behavior expected for the superheat.

As final evidence that the sudden increase in reflood time is an indication of the incipience of dryout, a comparison was made between temperature measurements and the reflood time. This comparison is shown in Fig. 3. Note that at a heating rate below the dryout point predicted from the reflood time the bed is at the saturation temperature, while for a heating rate just above the dryout point predicted from the reflood time the bed temperature suddenly rises above saturation and continues to rise, thus indicating dryout has occurred.

From the authors perspective, it is clear that most of the problems associated with identifying dryout can be overcome by employing the reflood time method. The real advantage of using the reflood time is that by careful measurement it allows one to determine the conditions under which dryout was first detected in any part of the particulate bed.

Acknowledgment

The authors gratefully acknowledge the support of the Electric Power Research Institute under Research Project 1931-1.

References

1 Dhir, V. K., and Catton, I., "Study of Dryout Heat Fluxes in Beds of Inductively Heated Particles," NUREG-0262, Nuclear Regulatory Commission, June 1977.

2 Gabor, J. D., Epstein, M., Jones, S. W., and Cassulo, J. C., "Status Report on Limiting Heat Fluxes in Debris Beds," ANL/RAS 80-21, Argonne National Laboratory, Sept. 1980.

3 Barleon, L., and Werle, H., "Dependence of Dryout Heat Flux on Particle Diameter for Volume and Botton-Heated Debris Beds," KfK 3138, Kernforschungszentrum Karlsrche, Nov. 1981.

4 Squarer, D., Pieczynski, A. T., and Hochreiter, L. F., "Effect of Debris Bed Pressure Particle Size and Distribution on Degraded Core Coolability," Paper No. 81-WA/HT-16, ASME Winter Annual Meeting, Washington, D.C., Nov. 1981.

5 Somerton, C. W., and Catton, I., "Using Permeability to Characterize a Debris Bed Under Dryout Conditions," Paper No. 83-WA/HT-40, ASME Winter Annual Meeting, Boston, Nov. 1983.

Vertical Circular Pin With Conjugated Forced Convection–Conduction Flow

Ming-Jer Huang[1] and Cha'o-Kuang Chen[2]

Nomenclature

- f = dimensionless stream function
- h = local heat transfer coefficient
- $\hat{h}$ = dimensionless local heat transfer coefficient, $hL/k\mathrm{Re}_L^{1/2}$
- k = fluid thermal conductivity
- k_f = fin thermal conductivity
- L = fin length
- Nc = conjugated convection-conduction parameter, $(2kL/k_f r_0)\mathrm{Re}_L^{1/2}$
- Pr = Prandtl number
- Q = overall heat transfer rate
- q = local heat flux
- r = radial coordinate
- r_0 = radius of circular pin
- T = temperature
- T_0 = root temperature
- T_f = fin temperature
- T_∞ = ambient temperature
- T_w = surface temperature
- u,v = velocity components
- u_∞ = free-stream velocity
- x = axial coordinate
- $\bar{X}$ = dimensionless coordinate, x/L

Greek Symbols

- α = thermal diffusivity
- η = pseudosimilarity variable
- θ = dimensionless temperature
- θ_f = dimensionless fin temperature
- θ_w = dimensionless surface temperature
- ν = kinematic viscosity
- λ = transverse curvature parameter, $4L/r_0\mathrm{Re}_L^{1/2}$

Introduction

The present paper deals with the analysis of a thin circular fin pin. This type of pin fin is chosen so that one-dimensional condition in the longitudinal direction can be assumed. Physically, the convection heat transfer coefficient is nonuniform over the surface, which is different from the conventional method. In the conventional heat transfer analysis of fins, it is assumed that the heat transfer coefficient for convection at the fin surface is uniform all over the fin. This conventional approach leads to wrong results because, in general, the heat transfer coefficient varies along the fin surface, a condition which has been analyzed by Sparrow and co-workers [1, 2] for a vertical plate fin.

More studies [3-5] had been reported for a vertical cylinder. These analyses were based on the thermal convection processes with the constant temperature along the cylinder. It is well established that the thermal convection boundary layer on a vertical cylinder is thicker than on a vertical plate. This characteristic stems from the finite transverse curvature of the cylinder surface.

[1]Instructor and [2]Professor, Department of Mechanical Engineering, National Cheng Kung University, Tainan, Taiwan, Republic of China

Contributed by the Heat Transfer Division for publication in the JOURNAL OF HEAT TRANSFER. Manuscript received by the Heat Transfer Division April 3, 1984.

heating rates below dryout, the reflood time is constant, but once dryout is achieved, this time increases with increasing power. This is shown in Fig. 1, where the load meter reading is directly proportional to the power. For heating rates below dryout, the bed will be at the saturation temperature. When the power is turned off, liquid that had been displaced to above the bed by vapor production will reflood the bed due to gravity. However, once dryout is reached the particles will attain temperatures above saturation. This superheat is proportional to the heating rate. When the power is turned off and liquid phase coolant begins to reenter the bed, it encounters particles at temperatures above saturation and must then cool them off in order to completely reflood the bed. It is this quenching phenomena that extends the reflood time in a post dryout situation.

In practice, the reflood time was measured as follows. At the moment the power was turned off a timer was started. Liquid would then begin to refill the particulate bed. When the liquid reached a predetermined level near the top of the bed, the timer would be stopped and the time interval recorded. This time interval was used as the reflood time. It was found that this time could be reproduced within ± 0.2 s.

Clearly, the reflood time is actually an indirect measurement of the bed temperature; the higher the bed temperature, the longer the reflood time. The superheat occurring after dryout will not only be a function of the heating rate, but also of the time period over which the heating is applied. The dependence of the superheat on the heating period should also appear in the reflood time, if it is a true indication of the bed temperature. The trend of the reflood time with heating period is shown in Fig. 2. As the heating period increases, the reflood time increases, which is identical to the behavior expected for the superheat.

As final evidence that the sudden increase in reflood time is an indication of the incipience of dryout, a comparison was made between temperature measurements and the reflood time. This comparison is shown in Fig. 3. Note that at a heating rate below the dryout point predicted from the reflood time the bed is at the saturation temperature, while for a heating rate just above the dryout point predicted from the reflood time the bed temperature suddenly rises above saturation and continues to rise, thus indicating dryout has occurred.

From the authors perspective, it is clear that most of the problems associated with identifying dryout can be overcome by employing the reflood time method. The real advantage of using the reflood time is that by careful measurement it allows one to determine the conditions under which dryout was first detected in any part of the particulate bed.

Acknowledgment

The authors gratefully acknowledge the support of the Electric Power Research Institute under Research Project 1931-1.

References

1 Dhir, V. K., and Catton, I., "Study of Dryout Heat Fluxes in Beds of Inductively Heated Particles," NUREG-0262, Nuclear Regulatory Commission, June 1977.

2 Gabor, J. D., Epstein, M., Jones, S. W., and Cassulo, J. C., "Status Report on Limiting Heat Fluxes in Debris Beds," ANL/RAS 80-21, Argonne National Laboratory, Sept. 1980.

3 Barleon, L., and Werle, H., "Dependence of Dryout Heat Flux on Particle Diameter for Volume and Botton-Heated Debris Beds," KfK 3138, Kernforschungszentrum Karlsrche, Nov. 1981.

4 Squarer, D., Pieczynski, A. T., and Hochreiter, L. F., "Effect of Debris Bed Pressure Particle Size and Distribution on Degraded Core Coolability," Paper No. 81-WA/HT-16, ASME Winter Annual Meeting, Washington, D.C., Nov. 1981.

5 Somerton, C. W., and Catton, I., "Using Permeability to Characterize a Debris Bed Under Dryout Conditions," Paper No. 83-WA/HT-40, ASME Winter Annual Meeting, Boston, Nov. 1983.

Vertical Circular Pin With Conjugated Forced Convection–Conduction Flow

Ming-Jer Huang[1] and Cha'o-Kuang Chen[2]

Nomenclature

f = dimensionless stream function
h = local heat transfer coefficient
$\hat{h}$ = dimensionless local heat transfer coefficient, $hL/k\mathrm{Re}_L^{1/2}$
k = fluid thermal conductivity
k_f = fin thermal conductivity
L = fin length
Nc = conjugated convection-conduction parameter, $(2kL/k_f r_0)\mathrm{Re}_L^{1/2}$
Pr = Prandtl number
Q = overall heat transfer rate
q = local heat flux
r = radial coordinate
r_0 = radius of circular pin
T = temperature
T_0 = root temperature
T_f = fin temperature
T_∞ = ambient temperature
T_w = surface temperature
u,v = velocity components
u_∞ = free-stream velocity
x = axial coordinate
$\bar{X}$ = dimensionless coordinate, x/L

Greek Symbols

α = thermal diffusivity
η = pseudosimilarity variable
θ = dimensionless temperature
θ_f = dimensionless fin temperature
θ_w = dimensionless surface temperature
ν = kinematic viscosity
λ = transverse curvature parameter, $4L/r_0\mathrm{Re}_L^{1/2}$

Introduction

The present paper deals with the analysis of a thin circular fin pin. This type of pin fin is chosen so that one-dimensional condition in the longitudinal direction can be assumed. Physically, the convection heat transfer coefficient is nonuniform over the surface, which is different from the conventional method. In the conventional heat transfer analysis of fins, it is assumed that the heat transfer coefficient for convection at the fin surface is uniform all over the fin. This conventional approach leads to wrong results because, in general, the heat transfer coefficient varies along the fin surface, a condition which has been analyzed by Sparrow and co-workers [1, 2] for a vertical plate fin.

More studies [3–5] had been reported for a vertical cylinder. These analyses were based on the thermal convection processes with the constant temperature along the cylinder. It is well established that the thermal convection boundary layer on a vertical cylinder is thicker than on a vertical plate. This characteristic stems from the finite transverse curvature of the cylinder surface.

[1]Instructor and [2]Professor, Department of Mechanical Engineering, National Cheng Kung University, Tainan, Taiwan, Republic of China

Contributed by the Heat Transfer Division for publication in the JOURNAL OF HEAT TRANSFER. Manuscript received by the Heat Transfer Division April 3, 1984.

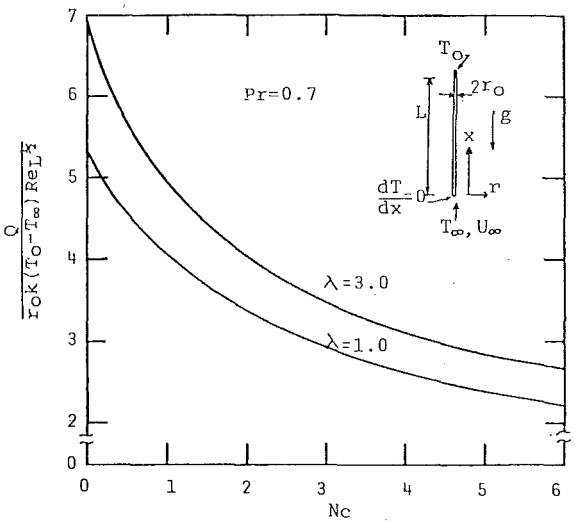

Fig. 1 Total heat transfer rate

The analysis found in the present paper focuses on the vertical circular pin that has a nonuniform temperature. The variations of the pin temperature is strongly affected by the heat transfer coefficient, and the heat transfer coefficient is dependent on the ambient fluid flow. Hence, in order to determine the temperature of the pin, the heat transfer coefficient must be coupled with the convective boundary layer flow, thus making the attainment of results more complicated.

The pin temperature distribution, which is not known a priori, serves as a boundary condition for the thermal boundary layer equation. The solution of the local heat transfer coefficient along the pin surface from the boundary layer equation is resubstituted into the pin energy equation as known, and a search is done for the new temperature of pin surface. This new temperature distribution is then imposed as the surface boundary condition for the boundary layer equation, the solution of which is used to evaluate an updated h, and so on, until the maximum difference of temperature between the successive iterations is less than 10^{-4}.

Analysis

Consider a vertical circular pin of radius r_0, which is extended from a wall at temperature T_0 and situated in a uniform free stream having temperature T_∞ and velocity u_∞, as illustrated in Fig. 1. The axial and radial coordinates are taken to be x and r, with x measuring the distance along the centerline of the pin from its tip end and r measuring normal to the axis of the pin. Since the circular pin considered is very thin, the effect of the stagnation of the flow against the exposed end face of the pin fin has been ignored. By employing the boundary layer approximations, the thermal convection boundary layer equations are

$$\frac{\partial}{\partial x}(ru)+\frac{\partial}{\partial r}(rv)=0 \tag{1}$$

$$u\frac{\partial u}{\partial x}+v\frac{\partial u}{\partial r}=\frac{\nu}{r}\frac{\partial}{\partial r}\left(r\frac{\partial u}{\partial r}\right) \tag{2}$$

$$u\frac{\partial T}{\partial x}+v\frac{\partial T}{\partial r}=\frac{\alpha}{r}\frac{\partial}{\partial r}\left(r\frac{\partial T}{\partial r}\right) \tag{3}$$

where u and v are the streamwise and radial velocity components, respectively, T is the temperature of the fluid, α is the thermal diffusivity, and ν is the kinematic viscosity.

The system of equations (1–3) is subject to the following boundary conditions

$$u=v=0\ ,\quad T=T_w(x)\quad \text{at}\quad r=r_0 \tag{4a}$$

$$u\to u_\infty\ ,\quad T\to T_\infty\quad \text{at}\quad r\to\infty \tag{4b}$$

$$u=u_\infty\ ,\quad T=T_\infty\quad \text{at}\quad x=0,\ r\geq r_0 \tag{4c}$$

Equations (1–3) and boundary conditions (4) do not admit a similarity solution. The nonsimilarity arises from the surface curvature of the pin and the surface temperature $T_w(x)$, which is to be determined. The pseudosimilarity variable η and the dimensionless axial coordinate $\bar{X}$ are introduced as follows

$$\bar{X}=x/L\quad \eta=\frac{r^2-r_0^2}{4r_0L}(\mathrm{Re}_L/\bar{X})^{1/2} \tag{5}$$

which L is the length of the circular pin and Re_L is the Reynolds number, $\mathrm{Re}_L=u_\infty L/\nu$.

The dimensionless stream function $f(\bar{X},\eta)$ and the dimensionless temperature $\theta(\bar{X},\eta)$ are defined, respectively, by

$$f(\bar{X},\eta)=\psi(x;r)/[r_0(\nu u_\infty x)^{1/2}] \tag{6}$$

$$\theta(\bar{X},\eta)=(T(x,r)-T_\infty)/(T_0-T_\infty) \tag{7}$$

where the stream function $\psi(x;r)$ satisfies the continuity equation (1) with

$$ru=\partial\psi/\partial r\qquad rv=-\partial\psi/\partial x \tag{8}$$

Introducing equations (5–7) into equations (2–4), results in

$$(1+\lambda\eta\bar{X}^{1/2})f'''+(\lambda\bar{X}^{1/2}+f)f''=2\bar{X}\left(f'\frac{\partial f'}{\partial\bar{X}}-f''\frac{\partial f}{\partial\bar{X}}\right) \tag{9}$$

$$\frac{1}{\mathrm{Pr}}(1+\lambda\eta\bar{X}^{1/2})\theta''+\left(\frac{1}{\mathrm{Pr}}\lambda\bar{X}^{1/2}+f\right)\theta'$$

$$=2\bar{X}\left(f'\frac{\partial\theta}{\partial\bar{X}}-\theta'\frac{\partial f}{\partial\bar{X}}\right) \tag{10}$$

$$f(\bar{X},0)=f'(\bar{X},0)=0,\quad \theta(\bar{X},0)=\theta_w(\bar{X}) \tag{11a}$$

$$f'(\bar{X},\infty)=2,\quad \theta(\bar{X},\infty)=0 \tag{11b}$$

In the foregoing equations, the primes stand for partial derivatives with respect to η, Pr is the Prandtl number, and λ is the transverse curvature parameter, defined as

$$\lambda=\frac{4L}{r_0\mathrm{Re}_L^{1/2}} \tag{12}$$

The energy equation for the thin pin under a one-dimensional model for the temperature distribution along the longitudinal direction is

$$\frac{d^2(T_f-T_\infty)}{dx^2}=\frac{2h(x)}{k_fr_0}(T_f-T_\infty) \tag{13}$$

where k_f is the pin thermal conductivity, T_f is the pin temperature, and $h(x)$ is the local heat transfer coefficient that can be regarded as known from the current boundary layer solution.

The associated boundary conditions of the energy pin equation are

$$T_f=T_0\qquad \text{at}\quad x=L \tag{14a}$$

$$\frac{dT_f}{dx}=0\qquad \text{at}\quad x=0 \tag{14b}$$

Because the circular pin considered is relatively long compared with its diameter, the amount of heat which passes from the tip of the pin fin to the fluid is negligible. Therefore, the assumption of an adiabatic tip is justified.

Of particular interest is the thermal coupling between the pin and the convective boundary layer. The basic coupling is expressed by the requirement that the pin and fluid temperatures and heat fluxes be continuous at the pin-fluid interface, at all x.

$$\left.\begin{aligned} T_f(x) &= T_w(x) \\ h(T_f - T_\infty) &= -k\frac{\partial T}{\partial r}\Big|_{r=r_0} \end{aligned}\right\} \text{at } r=r_0\text{; and for all } x \qquad (15)$$

Equation (13) was recast in dimensionless form by the substitutions.

$$\bar{X}=x/L \quad \theta_f=(T_f-T_\infty)/(T_0-T_\infty) \qquad (16)$$

and by combining with equation (15), to yield

$$\frac{d^2\theta_f}{d\bar{X}^2} = Nc\hat{h}\theta_f \qquad (17)$$

with

$$\theta_f = 1 \quad \text{at} \quad \bar{X}=1 \qquad (18a)$$

$$\frac{d\theta_f}{d\bar{X}} = 0 \quad \text{at} \quad \bar{X}=0 \qquad (18b)$$

where Nc is the conjugated convection-conduction parameter

$$Nc = \frac{2kL}{k_f r_0} Re_L^{1/2} \qquad (19)$$

The quantity $\hat{h}$ is a dimensionless form of the local forced convection heat transfer coefficient. The value of $\hat{h}$ is obtained by substituting equations (5) and (16) into equation (15)

$$\hat{h} = \frac{1}{2\bar{X}^{1/2}}\left(\frac{-\partial\theta}{\partial\eta}/\theta_f\right)_{\eta=0} \qquad (20)$$

Numerical Results and Discussion

The conservation equations of the laminar boundary layer and the energy equation of the pin are first transformed into a nondimensional form and their solutions are then simultaneously solved by an efficient implicit finite difference method. This method is a modified version of the method described in [7] for solution of uncoupled equations.

To assure the accuracy of present numerical method, its results have been compared in good agreement with those of the nonsimilarity solution [3] for the forced convection flow over the vertical isothermal cylinder.

The pin conduction equation was expressed into finite difference form and solved by using the direct inverse matrix method. Numerical results are presented for $Pr=0.7$ over a conjugated convection-conduction parameter of $Nc=0.0$, 1.0, and 4.0 and a transverse curvature parameter of $\lambda=1.0$ and 3.0.

Numerical results of the overall rate of heat transfer Q from the pin can be obtained from the heat conducted from the wall into the pin base at $\bar{X}=1$ or from the integrating heat convection over the pin surface. The corresponding Q values of these two methods are found to be in agreement. They may be expressed in dimensionless form, as

$$\frac{Q}{r_0 k(T_0-T_\infty)\mathrm{Re}_L^{1/2}} = \frac{2\pi}{Nc}\frac{d\theta_f}{d\bar{X}}\Big|_{\bar{X}=1} \qquad (21)$$

or

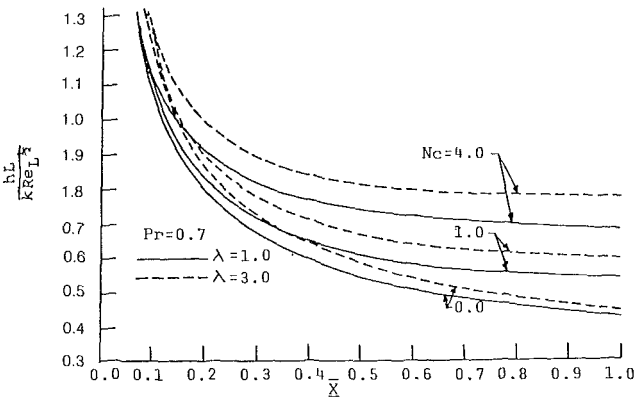

Fig. 2 The local heat transfer coefficients along the pin

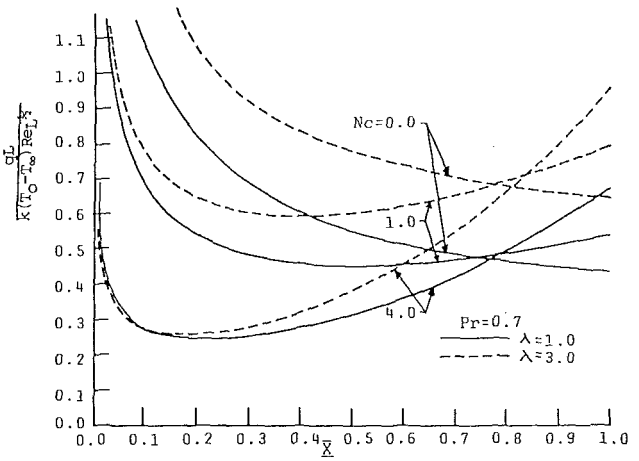

Fig. 3 The local heat fluxes along the pin

$$\frac{Q}{r_0 k(T_0-T_\infty)\mathrm{Re}_L^{1/2}} = 2\pi\int_0^1 \frac{1}{2\bar{X}^{1/2}}(-\partial\theta/\partial\eta)_{\eta=0}d\bar{X} \qquad (22)$$

The results of the overall rate of heat transfer Q from the pin are presented as a function of the conjugated convection-conduction parameter Nc for the fixed transverse curvature parameter λ in Fig. 1. It contains two lines for undergoing the effects of the transverse curvature of the pin. Because r_0 and $\mathrm{Re}_L^{1/2}$ appear in the ordinate, abscissa, and transverse curvature parameter groups, the downsloping trend of the curves indicates that, as expected, the fin heat transfer is increased as the fin conductance k_f increases.

If the ordinate and abscissa coordinates are replaced by the groups

$$\frac{Q}{kr_0(T_0-T_\infty)\mathrm{Re}_L^{1/2}} \Big/ \frac{4L}{r_0\mathrm{Re}_L^{1/2}} = \frac{Q}{4Lk(T_0-T_\infty)} \qquad (23)$$

and

$$\frac{2kL\mathrm{Re}_L^{1/2}}{k_f r_0} \Big/ \frac{4L}{r_0\mathrm{Re}_L^{1/2}} = \frac{k\mathrm{Re}_L}{2k_f} \qquad (24)$$

Since both groups are independent of r_0, it follows that the actual total heat transfer undergoes the effect of the transverse curvature. From the new scale of coordinates, it can be obtained that a smaller transverse curvature of pin, representing a larger radius of the cylinder, has the greater total heat transfer rate.

Figure 2 illustrates respectively the distribution of the local convection heat transfer coefficient along the pin surface as a function of Nc for fixed $\lambda=1.0$ and 3.0. The local heat transfer coefficient can be written, in dimensionless form, as

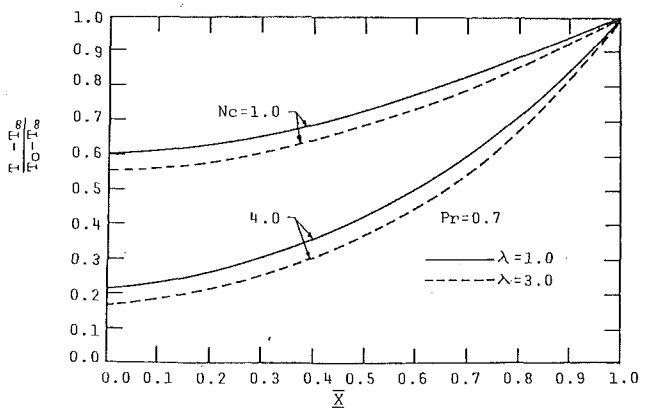

Fig. 4 Temperature distributions along the pin

$$\frac{hL}{k\mathrm{Re}_L^{1/2}} = -\frac{1}{2\bar{X}^{1/2}}\left(\frac{\partial\theta}{\partial\eta}/\theta_f\right)_{\eta=0} \tag{25}$$

The figure, under the fixed transverse curvature, contains three curves $Nc = 0.0$, 1.0, and 4.0. The increasing values of Nc are indicative of smaller conductance of pin. From the figure, it is shown that for a fixed transverse curvature of cylinder the larger Nc, the higher the $\hat{h}$ value and the greater variations of the pin temperature from the tip to the root.

As seen from the figure, for a fixed transverse curvature, $\hat{h}$ decreases monotonically from the tip to the root. Similarly, it can be seen that the larger the transverse curvature of the pin, the greater the $\hat{h}$ value.

Distributions of the dimensionless local convective heat flux at the pin surface are shown in Fig. 3, as a function of $\bar{X}$, with Nc as a parameter and for fixed transverse curvature parameter. The local heat flux can be taken as

$$\frac{qL}{k(T_0 - T_\infty)\mathrm{Re}_L^{1/2}} = -\frac{1}{2\bar{X}^{1/2}}\frac{\partial\theta}{\partial\eta}\bigg|_{\eta=0} \tag{26}$$

This figure shows that at a fixed transverse curvature, the area under the curve of the local heat flux that represents the total heat transfer rate from the pin surface is greater for smaller Nc than that for a larger Nc. It is in agreement with the prediction in Fig. 1.

Representative results for the pin temperature distribution are presented in Fig. 4 for the two different transverse curvatures. Each case contains the pin temperature distribution as a function of Nc. Figure also shows the expected trend whereby the pin temperature decreases monotonically from the root to the tip. The figure also confirms the assertions that larger values of Nc give rise to larger pin temperature variations.

References

1 Sparrow, E. M., and Acharya, A., "A Natural Convection Fin With a Solution-Determined Nonmonotonically Varying Heat Transfer Coefficient," ASME JOURNAL OF HEAT TRANSFER, Vol. 103, 1981, pp. 218–225.

2 Sparrow, E. M., and Chyu, M. K., "Conjugated Forced Convection-Conduction Analysis of Heat Transfer in a Plate Fin," ASME JOURNAL OF HEAT TRANSFER, Vol. 104, 1982, pp. 204–206.

3 Yu, H. S., and Sparrow, E. M., "Local Nonsimilarity Thermal Boundary-Layer Solutions," ASME JOURNAL OF HEAT TRANSFER, Vol. 93, 1971, pp. 328–334.

4 Minkowycz, W. J., and Sparrow, E. M., "Local Nonsimilar Solutions for Natural Convection on a Vertical Cylinder," ASME JOURNAL OF HEAT TRANSFER, Vol. 96, 1974, pp. 178–183.

5 Chen, T. S., and Mucoglu, A., "Buoyancy Effects on Forced Convection Along a Vertical Cylinder," ASME JOURNAL OF HEAT TRANSFER, Vol. 97, 1975, pp. 198–203.

6 Cebeci, T., "Laminar-Free-Convection-Heat Transfer from the Outer Surface of a Vertical Slender Circular Cylinder," *Proc. Fifth Intl. Heat Transfer Conference*, Paper NCl. 4, 1974, pp. 15–19.

7 Cebeci, T., and Bradshaw, P., *Momentum Transfer in Boundary Layers*, Hemisphere Publishing, Washington, D.C., 1977.

On Natural Convection From a Short Conducting Plate Fin Below a Heated Horizontal Cylinder

S. S. Kwon,[1] T. H. Kuehn,[2] and A. K. Tolpadi[3]

Nomenclature

C_F = fin conduction parameter, $k_F t/k_f D$
k = thermal conductivity
L_F = dimensionless fin length, l/D
Nu = Nusselt number, hD/k_f
Q = total heat transfer per unit length of cylinder
r = dimensionless radial coordinate, R/D
Ra = Rayleigh number, $g\beta D^3\Delta T/\nu\alpha$
ΔT = temperature difference, $(T_c - T_f)$
ϵ = fin similarity coordinate, equation (1)
ϕ = dimensionless temperature, $(T - T_f)/\Delta T$
ψ = dimensionless stream function, Ψ/α

Subscripts

c = cylinder
f = fluid
F = fin
o = free cylinder (no fin)

Introduction

Natural convection heat transfer from fins continues to be a subject of investigation due to the challenges created by the interaction of the flow from the fin and its base and the coupling between conduction and natural convection on nonisothermal fins. Interactions between the boundary layers on a fin and its base have been analyzed for isothermal plate fins in air by Aihara [1], who studied vertical fin arrays and separated the fin and baseplate heat transfers to supplement previous investigations, which measured only the total heat transfer from the entire array. A mass transfer experiment conducted by Sparrow and Bahrami [2] on rectangular plate fins mounted on a nonparticipating horizontal cylinder indicated large local mass transfer coefficients near the fin leading edge and a reduction of the mass transfer coefficient near the fin base at the largest fin spacings investigated. The coefficient near the fin base is small due to the overlap of the fin and base boundary layers. Some previous work has been done on the coupling of conduction and natural convection in nonisothermal fins. Lock and Gunn [3] presented a similarity solution valid for a heated downward projecting tapered fin with zero tip thickness. Kuehn et al. [4] developed a similarity solution for infinitely long vertical fins and gave numerical results over a wide range of Prandtl number for plate fins. Sparrow and Acharya [5] performed a numerical boundary layer study on a vertical conducting plate fin in air. Kwon and Kuehn [6] obtained numerical solutions for natural con-

[1] Dean, College of Engineering, Dong-A University, Busan, South Korea, Assoc. Mem. ASME

[2] Associate Professor, Department of Mechanical Engineering, University of Minnesota, Minneapolis, Minn., Assoc. Mem. ASME

[3] Research Assistant, Department of Mechanical Engineering, University of Minnesota, Minneapolis, Minn.

Contributed by the Heat Transfer Division for publication in the JOURNAL OF HEAT TRANSFER. Manuscript received by the Heat Transfer Division April 22, 1983.

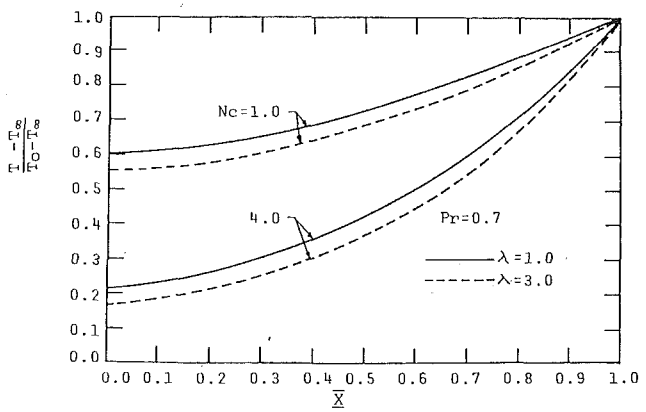

Fig. 4 Temperature distributions along the pin

$$\frac{hL}{k\mathrm{Re}_L^{1/2}} = -\frac{1}{2\bar{X}^{1/2}}\left(\frac{\partial\theta}{\partial\eta}/\theta_f\right)_{\eta=0} \tag{25}$$

The figure, under the fixed transverse curvature, contains three curves $Nc = 0.0$, 1.0, and 4.0. The increasing values of Nc are indicative of smaller conductance of pin. From the figure, it is shown that for a fixed transverse curvature of cylinder the larger Nc, the higher the $\hat{h}$ value and the greater variations of the pin temperature from the tip to the root.

As seen from the figure, for a fixed transverse curvature, $\hat{h}$ decreases monotonically from the tip to the root. Similarly, it can be seen that the larger the transverse curvature of the pin, the greater the $\hat{h}$ value.

Distributions of the dimensionless local convective heat flux at the pin surface are shown in Fig. 3, as a function of $\bar{X}$, with Nc as a parameter and for fixed transverse curvature parameter. The local heat flux can be taken as

$$\frac{qL}{k(T_0 - T_\infty)\mathrm{Re}_L^{1/2}} = -\frac{1}{2\bar{X}^{1/2}}\frac{\partial\theta}{\partial\eta}\bigg|_{\eta=0} \tag{26}$$

This figure shows that at a fixed transverse curvature, the area under the curve of the local heat flux that represents the total heat transfer rate from the pin surface is greater for smaller Nc than that for a larger Nc. It is in agreement with the prediction in Fig. 1.

Representative results for the pin temperature distribution are presented in Fig. 4 for the two different transverse curvatures. Each case contains the pin temperature distribution as a function of Nc. Figure also shows the expected trend whereby the pin temperature decreases monotonically from the root to the tip. The figure also confirms the assertions that larger values of Nc give rise to larger pin temperature variations.

References

1 Sparrow, E. M., and Acharya, A., "A Natural Convection Fin With a Solution-Determined Nonmonotonically Varying Heat Transfer Coefficient," ASME JOURNAL OF HEAT TRANSFER, Vol. 103, 1981, pp. 218–225.

2 Sparrow, E. M., and Chyu, M. K., "Conjugated Forced Convection-Conduction Analysis of Heat Transfer in a Plate Fin," ASME JOURNAL OF HEAT TRANSFER, Vol. 104, 1982, pp. 204–206.

3 Yu, H. S., and Sparrow, E. M., "Local Nonsimilarity Thermal Boundary-Layer Solutions," ASME JOURNAL OF HEAT TRANSFER, Vol. 93, 1971, pp. 328–334.

4 Minkowycz, W. J., and Sparrow, E. M., "Local Nonsimilar Solutions for Natural Convection on a Vertical Cylinder," ASME JOURNAL OF HEAT TRANSFER, Vol. 96, 1974, pp. 178–183.

5 Chen, T. S., and Mucoglu, A., "Buoyancy Effects on Forced Convection Along a Vertical Cylinder," ASME JOURNAL OF HEAT TRANSFER, Vol. 97, 1975, pp. 198–203.

6 Cebeci, T., "Laminar-Free-Convection-Heat Transfer from the Outer Surface of a Vertical Slender Circular Cylinder," *Proc. Fifth Intl. Heat Transfer Conference*, Paper NCl. 4, 1974, pp. 15–19.

7 Cebeci, T., and Bradshaw, P., *Momentum Transfer in Boundary Layers*, Hemisphere Publishing, Washington, D.C., 1977.

On Natural Convection From a Short Conducting Plate Fin Below a Heated Horizontal Cylinder

S. S. Kwon,[1] T. H. Kuehn,[2] and A. K. Tolpadi[3]

Nomenclature

C_F = fin conduction parameter, $k_F t/k_f D$
k = thermal conductivity
L_F = dimensionless fin length, l/D
Nu = Nusselt number, hD/k_f
Q = total heat transfer per unit length of cylinder
r = dimensionless radial coordinate, R/D
Ra = Rayleigh number, $g\beta D^3\Delta T/\nu\alpha$
ΔT = temperature difference, $(T_c - T_f)$
ϵ = fin similarity coordinate, equation (1)
ϕ = dimensionless temperature, $(T - T_f)/\Delta T$
ψ = dimensionless stream function, Ψ/α

Subscripts

c = cylinder
f = fluid
F = fin
o = free cylinder (no fin)

Introduction

Natural convection heat transfer from fins continues to be a subject of investigation due to the challenges created by the interaction of the flow from the fin and its base and the coupling between conduction and natural convection on nonisothermal fins. Interactions between the boundary layers on a fin and its base have been analyzed for isothermal plate fins in air by Aihara [1], who studied vertical fin arrays and separated the fin and baseplate heat transfers to supplement previous investigations, which measured only the total heat transfer from the entire array. A mass transfer experiment conducted by Sparrow and Bahrami [2] on rectangular plate fins mounted on a nonparticipating horizontal cylinder indicated large local mass transfer coefficients near the fin leading edge and a reduction of the mass transfer coefficient near the fin base at the largest fin spacings investigated. The coefficient near the fin base is small due to the overlap of the fin and base boundary layers. Some previous work has been done on the coupling of conduction and natural convection in nonisothermal fins. Lock and Gunn [3] presented a similarity solution valid for a heated downward projecting tapered fin with zero tip thickness. Kuehn et al. [4] developed a similarity solution for infinitely long vertical fins and gave numerical results over a wide range of Prandtl number for plate fins. Sparrow and Acharya [5] performed a numerical boundary layer study on a vertical conducting plate fin in air. Kwon and Kuehn [6] obtained numerical solutions for natural con-

[1] Dean, College of Engineering, Dong-A University, Busan, South Korea, Assoc. Mem. ASME

[2] Associate Professor, Department of Mechanical Engineering, University of Minnesota, Minneapolis, Minn., Assoc. Mem. ASME

[3] Research Assistant, Department of Mechanical Engineering, University of Minnesota, Minneapolis, Minn.

Contributed by the Heat Transfer Division for publication in the JOURNAL OF HEAT TRANSFER. Manuscript received by the Heat Transfer Division April 22, 1983.

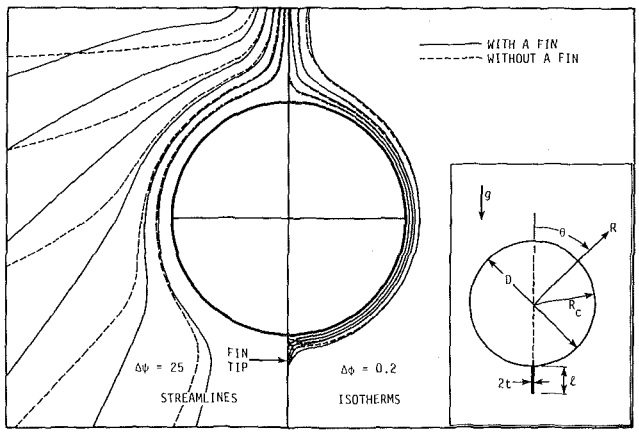

Fig. 1 Schematic of finned cylinder; isotherms and streamlines with and without a short fin, numerical solutions at Ra = 10^6, Pr = 5, C_F = 0.5, L_F = 0 and 0.1

vection from an infinitely long conducting fin mounted vertically on an isothermal horizontal cylinder. The local heat transfer from the fin agreed with the similarity solution [4], except near the cylinder where the boundary layers overlapped. An experimental investigation of natural convection from a single-plate fin attached at various angles to an isothermal cylinder in water was made by Tolpadi and Kuehn [7].

The present study was undertaken to determine the influence of fin length on steady, conjugate, natural-convection heat transfer from an isothermal, horizontal cylinder with one vertical, longitudinal conducting plate fin. The results are compared with the limiting cases of an isothermal free cylinder [8] and a cylinder with an infinitely long conducting fin [6]. A more detailed discussion of this study is given in [9].

Numerical Study

A heated, horizontal cylinder with a short downward projecting plate fin is immersed into a quiescent isothermal fluid of infinite extent. A schematic diagram of this configuration is given in Fig. 1. The cylinder is isothermal with the fin base at the cylinder temperature. The flow is assumed to be steady, laminar, and two-dimensional with a plane of symmetry passing vertically through the centers of the cylinder and fin. The fluid is incompressible, follows the Boussinesq approximation, and is opaque to thermal radiation. The governing equations are written using the stream function vorticity transformation. These equations together with the boundary conditions are given in [6] and will not be repeated here.

The governing equations were written in finite difference form using a successive underrelaxation central difference/upwind hybrid scheme [8] to promote numerical stability. The majority of the solutions were obtained using a 31 × 31 grid. The angular grid spacing was 0.625 deg near the fin and doubled in steps to 10 deg for the majority of the distance around the cylinder. The spacing was then halved in steps to a minimum of 2.5 deg in the plume directly above the cylinder. The radial grid spacing began between 0.003 D and 0.006 D at the cylinder surface. The spacing then doubled in steps as the distance from the cylinder increased, but was halved in steps as the radius of the fin tip was approached. The radial grid spacing at the fin tip varied between 0.004 D and 0.007 D. The spacing was then doubled in steps until the outer boundary was reached, which was located between 3.62 D and 6.76 D. Further details of the numerical technique are given in [6] and [9].

Eighteen numerical solutions were obtained as two of the four dimensionless governing parameters were varied parametrically:

$0 \le L_F \le \infty$, Ra = 10^6, Pr = 5, C_F = 0.5

$0.1 \le$ Pr ≤ 10, Ra = 10^6, C_F = 0.5, L_F = 0.184

Emphasis was placed on the effect of the fin length L_F, as the other parameters had been varied previously (L_F = 0 [8] and $L_F = \infty$ [6]).

Experimental Study

A plain cylinder and a finned cylinder designed to duplicate some of the conditions simulated in the numerical study were constructed for use in a Mach-Zehnder interferometer. An axial slot was machined in one of the 2.54-cm-dia copper cylinders for holding plate fins. Five stainless steel fins of 0.112 cm thickness could be press fitted into the slot to enable the fin length to be changed with C_F remaining constant at approximately 0.60. Each cylinder assembly was supported by thin steel strips welded to washers enabling the cylinder to be rotated about its axis.

A rectangular test cell was constructed of plexiglass to contain the distilled water surrounding the cylinder. A pair of optical grade windows were mounted on the ends of the cell for the interferometric measurements. The cell was placed in one leg of a Mach-Zehnder interferometer which used a 2 mW He-Ne laser as the light source. The interferograms were recorded on 35-mm, fine-grain film. Temperatures and electric power supplied to the heater in the cylinder were measured independently for verification of the optical data.

The refraction errors were found to be too large to obtain optical data at the desired Rayleigh number of 10^6. Therefore, the data were obtained at Ra $\simeq 4 \times 10^5$. This provided enough fringes for adequate local heat transfer determination but did not cause adverse refraction problems. The other parameters were Pr $\simeq$ 5, $C_F \simeq$ 0.6, and L_F = 0.05, 0.10, 0.20, 0.31, and 0.49. Complete details of the apparatus and procedure are given in [7].

Results and Discussion

Streamlines and isotherms from two numerical solutions, a free cylinder at Ra = 10^6, Pr = 5 and a finned cylinder with Ra = 10^6, Pr = 5, C_F = 0.5, and L_F = 0.1, are shown in Fig. 1. The short fin is almost totally surrounded by the cylinder thermal boundary layer. The interaction between the fin and cylinder boundary layers greatly alters the local heat transfer from both the fin and the cylinder from what one would obtain disregarding this coupling, especially near the base of the fin. The fin is immersed into an upflow moving toward the cylinder boundary layer and therefore experiences an aiding mixed convection flow rather than strictly natural convection.

An interferogram from the experimental run with L_F = 0.20 was analyzed in detail and the results compared with the numerical solutions. The data were taken with a cylinder to fluid temperature difference of 0.964°C and a mean temperature between cylinder and water of 32.2°C.

The results in Figs. 2 and 3 are plotted using the fin similarity solution scaling parameters. This should eliminate differences in Ra, Pr, and C_F between the experimental and numerical results, leaving the dimensionless fin length L_F as the sole independent variable.

The equations necessary for the scaling are [4, 6]

$$\epsilon = \frac{r - 0.5}{x_b} + 1 \tag{1}$$

$$\mathrm{Nu}_F{}^* = \frac{\mathrm{Nu}_F \sqrt{2} x_b{}^{1/4}}{\mathrm{Ra}^{1/4} f(\mathrm{Pr})} \tag{2}$$

where

$$x_b = \left(\frac{56\sqrt{2} C_F}{\mathrm{Ra}^{1/4} f(\mathrm{Pr})} \right)^{4/7} \tag{3}$$

$$f(\mathrm{Pr}) \simeq [(2.55\,\mathrm{Pr}^{1/4})^{-2.1} + (1.539)^{-2.1}]^{-1/2.1} \tag{4}$$

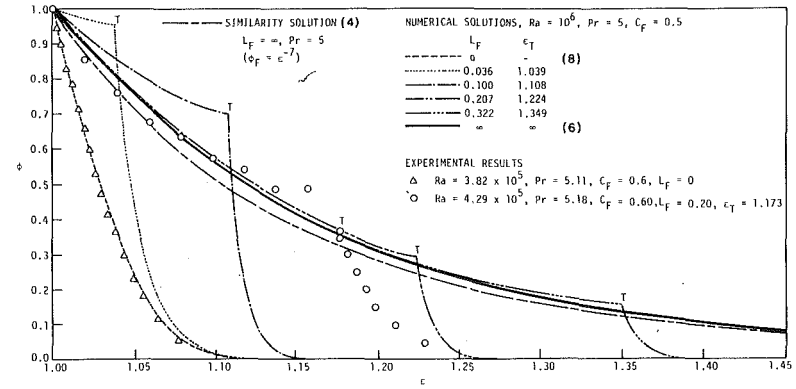

Fig. 2 Dimensionless temperature distributions below the cylinder

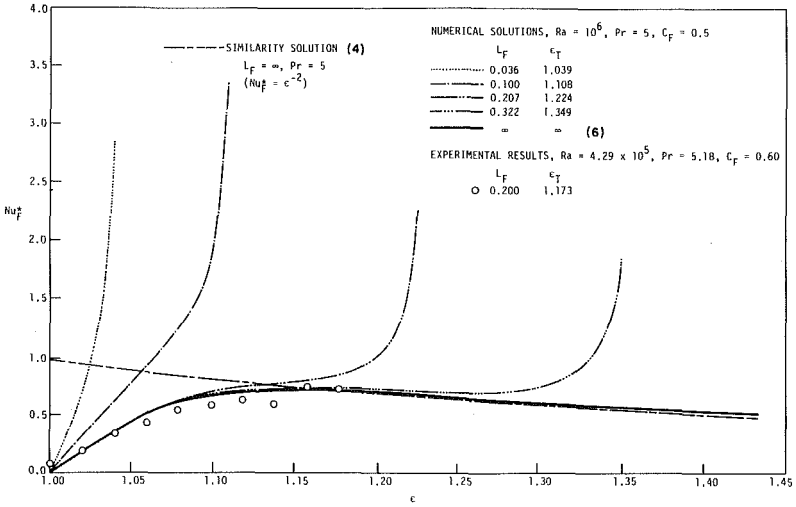

Fig. 3 Local heat transfer coefficient distributions on the fin as a function of fin length

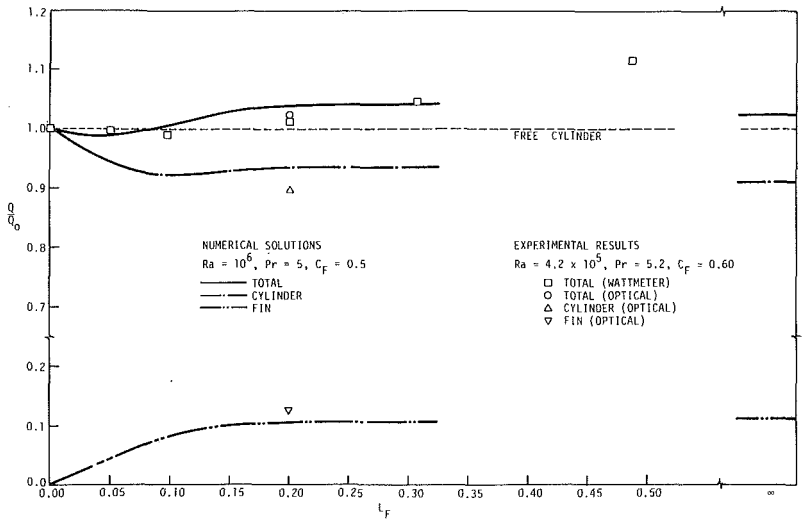

Fig. 4 Numerical and experimental total heat transfer results as a function of fin length

Dimensionless temperature profiles on the vertical symmetry line below the cylinder are plotted in Fig. 2. The shortest fin shown, $L_F = 0.036$, lies entirely within the thermal boundary layer below the cylinder as evidenced by the free cylinder temperature profile, $L_F = 0$. This fin is nearly isothermal with a rapid change in fluid temperature just below the fin tip, which is designated by a "T." As the fin length is increased, the fins become less isothermal and approach the temperature distribution for the infinitely long fin. The temperature distributions for fins with $\epsilon_T \geq 1.2$ can be approximated by the profile from the similarity solution ($\phi_F = \epsilon^{-7}$) with errors less than 20 percent. The experimental fin temperature distribution agrees well with the numerical solutions, although the data exhibit some scatter. The experimental fluid temperature change below the fin tip shows a less abrupt drop than in the numerical solutions.

Dimensionless local heat transfer coefficients on the fin are plotted in Fig. 3. Short fins exhibit large local coefficients

near the tip with a rapid drop to zero at the base.Long fins follow the distribution obtained for the infinitely long fin, except near the tip where the results are higher. The heat transfer coefficients for long fins obtained numerically indicate three regions: (*i*) large local values near the tip, (*ii*) coefficients nearly equal to those predicted by the similarity solution midway between the tip and base, and (*iii*) reduction to zero at the base where the overlap of the fin and cylinder boundary layers causes complete deviation from the similarity solution. The experimental results differ from the numerical solutions in that the sharp increase near the tip is absent. The explanation for this discrepancy is that the fin used in the experiments has a finite thickness, while the fin modeled numerically is treated as being infinitely thin. The finite fin thickness tends to change the flow near the tip, which in turn changes the local heat transfer coefficient there. The short fins studied experimentally, $L_F = 0.05$ and $L_F = 0.10$, showed large refraction near the fin tip, indicating high local heat transfer there, although no quantitative measurements were possible.

The total heat transfer from the fin, cylinder, and fin plus cylinder is plotted in Fig. 4 as a function of fin length. The results are normalized to the free-cylinder heat transfer at the same Ra and Pr to show the enhancement caused by the fin. The most surprising result is the decrease in total heat transfer at short fin lengths. Both the experimental results and the numerical solutions show this behavior. The warm fluid rising from the fin creates a thermal blanket around the cylinder reducing its heat transfer when $L_F < 0.1$. The fin heat transfer increases but is not large enough to compensate so the total heat transfer drops below the free cylinder limit. At longer fin lengths, the increased velocity around the cylinder caused by the fin overcomes the thermal blanket effect so that the total heat transfer from the fin plus cylinder is enhanced over the free cylinder limit. The magnitude of the enhancement is small, within 5 percent for most of the results shown in Fig. 4. The experimental and numerical results agree qualitatively; quantitative discrepancies are caused by experimental and numerical errors and differences in Ra, Pr, and C_F. The heat transfer enhancement divided by fin length reaches a maximum at $L_F \simeq 0.18$, according to the numerical results. This is the fin length at which the fin is most useful per unit length. However, the enhancement achieved is less than 5 percent.

The numerical solutions obtained at Ra = 10^6, $C_F = 0.5$, $L_F = 0.184$, and $0.1 \leq \text{Pr} \leq 10$ indicate the total heat transfer from the fin, cylinder, and cylinder plus fin, closely follow the distributions for a cylinder with an infinitely long fin. Reference [6] contains more details on this Prandtl number effect.

Acknowledgment

This work was performed when the authors were at Iowa State University, Ames, Iowa. The authors wish to acknowledge support from the U. S. National Science Foundation through Grant CME-8003498, the Korean Science Foundation, and the Iowa State University Engineering Research Institute.

References

1 Aihara, T., "Natural Convection Heat Transfer from Vertical Rectangular Fin Arrays, Part 3, Heat Transfer from Fin-Flats," *Bull. JSME*, Vol. 13, No. 64, 1970, pp. 1192–1200.

2 Sparrow, E. M., and Bahrami, P. A., "Experiments on Natural Convection Heat Transfer on the Fins of a Finned Horizontal Tube," *Int. J. Heat Mass Transfer*, Vol. 23, 1980, pp. 1555–1560.

3 Lock, G. S. H., and Gunn, J. C., "Laminar Free Convection from a Downward-Projecting Fin," ASME JOURNAL OF HEAT TRANSFER, Vol. 90, 1968, pp. 63–70.

4 Kuehn, T. H., Kwon, S. S., and Tolpadi, A. K., Similarity Solution for Conjugate Natural Convection Heat Transfer from a Long Vertical Plate Fin," *Int. J. Heat Mass Transfer*, Vol. 26, 1983, pp. 1718–1721.

5 Sparrow, E. M., and Acharya, S., "A Natural Convection Fin with a Solution-Determined Nonmonotonically Varying Heat Transfer Coefficient," ASME JOURNAL OF HEAT TRANSFER, Vol. 103, 1981, pp. 218–225.

6 Kwon, S. S., and Kuehn, T. H., "Conjugate Natural Convection Heat Transfer from a Horizontal Cylinder with a Long Vertical Longitudinal Fin," *Numerical Heat Transfer*, Vol. 6, 1983, pp. 85–102.

7 Tolpadi, A. K., and Kuehn, T. H., "Experimental Investigation of Conjugate Natural Convection Heat Transfer from a Horizontal Isothermal Cylinder with a Nonisothermal Longitudinal Plate Fin at Various Angles," accepted by *Int. J. Heat Mass Transfer*, 1984.

8 Kuehn, T. H., and Goldstein, R. J., "Numerical Solution to the Navier-Stokes Equations for Laminar Natural Convection about a Horizontal Isothermal Circular Cylinder," *Int. J. Heat Mass Transfer*, Vol. 23, 1980, pp. 971–979.

9 Kwon, S. S., Kuehn, T. H., and Tolpadi, A. K., "Conjugate Natural Convection Heat Transfer from a Short Vertical Longitudinal Fin Below a Heated Horizontal Cylinder," ASME Paper No. 83-HT-100, 1983.

Effect of Mass Transfer and Free Convection on the Flow Past a Vertical Porous Plate

M. A. Hossain[1] and R. A. Begum[1]

Nomenclature

C' = species concentration
C_w' = species concentration near the plate
C_∞' = species concentration in the free stream
C_p = specific heat at constant pressure
C = nondimensional species concentration $((C' - C_\infty')/(C_w' - C_\infty'))$
D = chemical molecular diffusivity
Ec = Eckert number $(U_0^2/C_p(T_w' - T_\infty'))$
g = acceleration due to gravity
β = volumetric coefficient of thermal expansion
β^* = volumetric coefficient of expansions with concentration
Gr = Grashof number $(\nu g\beta(T_w' - T_\infty')/U_0^3)$
Gc = modified Grashof number $(\nu g\beta^*(C_w' - C_\infty')/U_0^3)$
γ = suction parameter (ν_0/U_0)
p' = pressure
Pr = Prandtl number $(\mu C_p/K)$
K = thermal conductivity
Sc = Schmidt number (ν/D)
q' = rate of heat transfer
q = nondimensional rate of heat transfer
t' = time variable
t = dimensionless time $(t'U_0^2/4\nu)$
τ' = skin friction
τ = nondimensional skin friction
u', v' = velocity components along x'-and y'-directions
$U'(t')$ = free stream velocity
U_0 = mean of U'
u = nondimensional velocity (u'/U_0)

[1]Department of Mathematics, University of Dhaka, Dhaka-2, Bangladesh.

Contributed by the Heat Transfer Division for publication in the JOURNAL OF HEAT TRANSFER. Manuscript received by the Heat Transfer Division March 30, 1984.

near the tip with a rapid drop to zero at the base.Long fins follow the distribution obtained for the infinitely long fin, except near the tip where the results are higher. The heat transfer coefficients for long fins obtained numerically indicate three regions: (*i*) large local values near the tip, (*ii*) coefficients nearly equal to those predicted by the similarity solution midway between the tip and base, and (*iii*) reduction to zero at the base where the overlap of the fin and cylinder boundary layers causes complete deviation from the similarity solution. The experimental results differ from the numerical solutions in that the sharp increase near the tip is absent. The explanation for this discrepancy is that the fin used in the experiments has a finite thickness, while the fin modeled numerically is treated as being infinitely thin. The finite fin thickness tends to change the flow near the tip, which in turn changes the local heat transfer coefficient there. The short fins studied experimentally, $L_F = 0.05$ and $L_F = 0.10$, showed large refraction near the fin tip, indicating high local heat transfer there, although no quantitative measurements were possible.

The total heat transfer from the fin, cylinder, and fin plus cylinder is plotted in Fig. 4 as a function of fin length. The results are normalized to the free-cylinder heat transfer at the same Ra and Pr to show the enhancement caused by the fin. The most surprising result is the decrease in total heat transfer at short fin lengths. Both the experimental results and the numerical solutions show this behavior. The warm fluid rising from the fin creates a thermal blanket around the cylinder reducing its heat transfer when $L_F < 0.1$. The fin heat transfer increases but is not large enough to compensate so the total heat transfer drops below the free cylinder limit. At longer fin lengths, the increased velocity around the cylinder caused by the fin overcomes the thermal blanket effect so that the total heat transfer from the fin plus cylinder is enhanced over the free cylinder limit. The magnitude of the enhancement is small, within 5 percent for most of the results shown in Fig. 4. The experimental and numerical results agree qualitatively; quantitative discrepancies are caused by experimental and numerical errors and differences in Ra, Pr, and C_F. The heat transfer enhancement divided by fin length reaches a maximum at $L_F \simeq 0.18$, according to the numerical results. This is the fin length at which the fin is most useful per unit length. However, the enhancement achieved is less than 5 percent.

The numerical solutions obtained at Ra = 10^6, $C_F = 0.5$, $L_F = 0.184$, and $0.1 \leq \text{Pr} \leq 10$ indicate the total heat transfer from the fin, cylinder, and cylinder plus fin, closely follow the distributions for a cylinder with an infinitely long fin. Reference [6] contains more details on this Prandtl number effect.

Acknowledgment

This work was performed when the authors were at Iowa State University, Ames, Iowa. The authors wish to acknowledge support from the U. S. National Science Foundation through Grant CME-8003498, the Korean Science Foundation, and the Iowa State University Engineering Research Institute.

References

1 Aihara, T., "Natural Convection Heat Transfer from Vertical Rectangular Fin Arrays, Part 3, Heat Transfer from Fin-Flats," *Bull. JSME*, Vol. 13, No. 64, 1970, pp. 1192–1200.

2 Sparrow, E. M., and Bahrami, P. A., "Experiments on Natural Convection Heat Transfer on the Fins of a Finned Horizontal Tube," *Int. J. Heat Mass Transfer*, Vol. 23, 1980, pp. 1555–1560.

3 Lock, G. S. H., and Gunn, J. C., "Laminar Free Convection from a Downward-Projecting Fin," ASME JOURNAL OF HEAT TRANSFER, Vol. 90, 1968, pp. 63–70.

4 Kuehn, T. H., Kwon, S. S., and Tolpadi, A. K., Similarity Solution for Conjugate Natural Convection Heat Transfer from a Long Vertical Plate Fin," *Int. J. Heat Mass Transfer*, Vol. 26, 1983, pp. 1718–1721.

5 Sparrow, E. M., and Acharya, S., "A Natural Convection Fin with a Solution-Determined Nonmonotonically Varying Heat Transfer Coefficient," ASME JOURNAL OF HEAT TRANSFER, Vol. 103, 1981, pp. 218–225.

6 Kwon, S. S., and Kuehn, T. H., "Conjugate Natural Convection Heat Transfer from a Horizontal Cylinder with a Long Vertical Longitudinal Fin," *Numerical Heat Transfer*, Vol. 6, 1983, pp. 85–102.

7 Tolpadi, A. K., and Kuehn, T. H., "Experimental Investigation of Conjugate Natural Convection Heat Transfer from a Horizontal Isothermal Cylinder with a Nonisothermal Longitudinal Plate Fin at Various Angles," accepted by *Int. J. Heat Mass Transfer*, 1984.

8 Kuehn, T. H., and Goldstein, R. J., "Numerical Solution to the Navier-Stokes Equations for Laminar Natural Convection about a Horizontal Isothermal Circular Cylinder," *Int. J. Heat Mass Transfer*, Vol. 23, 1980, pp. 971–979.

9 Kwon, S. S., Kuehn, T. H., and Tolpadi, A. K., "Conjugate Natural Convection Heat Transfer from a Short Vertical Longitudinal Fin Below a Heated Horizontal Cylinder," ASME Paper No. 83-HT-100, 1983.

Effect of Mass Transfer and Free Convection on the Flow Past a Vertical Porous Plate

M. A. Hossain[1] and R. A. Begum[1]

Nomenclature

C' = species concentration
C_w' = species concentration near the plate
C_∞' = species concentration in the free stream
C_p = specific heat at constant pressure
C = nondimensional species concentration $((C' - C_\infty')/(C_w' - C_\infty'))$
D = chemical molecular diffusivity
Ec = Eckert number $(U_0^2/C_p(T_w' - T_\infty'))$
g = acceleration due to gravity
β = volumetric coefficient of thermal expansion
β^* = volumetric coefficient of expansions with concentration
Gr = Grashof number $(\nu g\beta(T_w' - T_\infty')/U_0^3)$
Gc = modified Grashof number $(\nu g\beta^*(C_w' - C_\infty')/U_0^3)$
γ = suction parameter (ν_0/U_0)
p' = pressure
Pr = Prandtl number $(\mu C_p/K)$
K = thermal conductivity
Sc = Schmidt number (ν/D)
q' = rate of heat transfer
q = nondimensional rate of heat transfer
t' = time variable
t = dimensionless time $(t'U_0^2/4\nu)$
τ' = skin friction
τ = nondimensional skin friction
u', v' = velocity components along x'-and y'-directions
$U'(t')$ = free stream velocity
U_0 = mean of U'
u = nondimensional velocity (u'/U_0)

[1]Department of Mathematics, University of Dhaka, Dhaka-2, Bangladesh.

Contributed by the Heat Transfer Division for publication in the JOURNAL OF HEAT TRANSFER. Manuscript received by the Heat Transfer Division March 30, 1984.

u_0 = mean velocity
u_1 = unsteady part of the velocity
v_0 = suction velocity
T' = temperature of the fluid
T_w' = temperature of the plate
T_∞' = temperature of the free stream
θ = nondimensional temperature $(T' - T_\infty')/(T_w' - T_\infty')$
θ_0 = mean temperature
θ_1 = unsteady part of the temperature
U = nondimensional free stream velocity (U'/U_0)
y = dimensionless coordinate normal to the plate $(y'U_0/\nu)$
μ = viscosity
ρ' = density of the fluid in the boundary layer
ρ_∞' = density of the fluid in the free stream
ν = kinematic coefficient of viscosity
ω' = frequency of oscillation of the free stream
ω = nondimensional frequency $(4\nu\omega'/U_0^2)$

1 Introduction

Free-convection flow past a vertical plate has been studied by Ostrach [1–4] and many others. The effect of viscous dissipation in the convective flow has been neglected in all such studies. However, Gebhart [5] and Gebhart and Mollendorf [6] have shown that the viscous dissipation effect plays an important role in natural convection flow. All the foregoing studies are confined to steady flow. In the case of unsteady flow, Soundalgekar [7] has studied the effects of viscous dissipation and free convection on the oscillatory flow past an infinite vertical porous plate with constant suction directed towards the plate. Somers [8], Wilcox [9], Gill et al. [10], Adams and Lowell [11], Gebhart and Para [12], and many others have studied the effect of mass transfer on the convective flow. In all these studies, the level of concentration of species has been considered very low. Because of these assumptions, the Soret-Dufour (thermal diffusion and diffusion thermo) effect can be neglected. In the free-convective flow, the Soret-Dufour effect has been studied by Sparrow et al. [13]. Soundalgekar & Wavre [14] have very recently studied the effects of mass transfer and suction on the unsteady free convection flow neglecting the Soret-Dufour effects on the energy equation. In this study, the plate temperature is assumed to be oscillatory.

It is of interest to consider the effects of free-convection currents and the presence of foreign masses on the oscillatory flow past a plate with or without Soret-Dufour effects. This situation has not yet been studied. Hence an investigation of the effects of free-convection currents and mass transfer on the oscillatory type of flow of a viscous incompressible fluid past a vertical porous plate with constant suction directed towards the plate is proposed. In this study, the plate temperature is assumed to be constant and the temperature difference $T_w' - T_\infty'$ is considered very large and positive so that free convection can take place in the boundary layer region. Owing to the presence of free convection and mass transfer, the problem is governed by coupled nonlinear equations. The mathematical formalisms are presented under suitable assumptions in section 2, and the results are discussed in section 3.

2 Mathematical Formalisms

For a two-dimensional, unsteady, free-convective flow of a viscous incompressible fluid past an infinite vertical porous plate with constant suction, we take the x'-axis along the plate in the upward direction and y'-axis normal to the plate. Due to the small concentration level, the Soret-Dufour effect is negligible in the energy equation. Hence all the physical variables are functions of y' and t'. Under the usual Bousinesq approximation, the flow is governed by the following system of nondimensional equations [14]:

Momentum equation

$$\frac{1}{4}\frac{\partial u}{\partial t} - \gamma\frac{\partial u}{\partial y} = \frac{1}{4}\frac{dU}{dt} + \mathrm{Gr}\theta + \mathrm{Gc}C + \frac{\partial^2 u}{\partial y^2} \tag{1}$$

Energy equation

$$\frac{1}{4}\mathrm{Pr}\frac{\partial \theta}{\partial t} - \gamma\mathrm{Pr}\frac{\partial \theta}{\partial y} = \frac{\partial^2 \theta}{\partial y^2} + \mathrm{PrEc}\left(\frac{\partial u}{\partial y}\right)^2 \tag{2}$$

Species

$$\frac{1}{4}\mathrm{Sc}\frac{\partial C}{\partial t} - \gamma\mathrm{Sc}\frac{\partial c}{\partial y} = \frac{\partial^2 C}{\partial y^2} \tag{3}$$

The boundary conditions for this problem are

$$\begin{aligned} &u = 0,\ \theta = 1,\ C = 1 \quad \text{at } y = 0 \\ &u = U(t),\ \theta = 0,\ C = 0 \text{ as } y \to \infty \end{aligned} \tag{4a}$$

The free stream velocity is

$$U(t) = 1 + \epsilon e^{i\omega t},\ \epsilon << 1 \tag{4b}$$

The nondimensional quantities Gr, Gc, Pr, Ec, and γ are defined in the Nomenclature.

For small amplitude oscillatory boundary layer flow, we assume the solutions of the equations (1–4) in the following form

$$u(y,t) = u_0(y) + \epsilon u_1(y)e^{i\omega t} \tag{5}$$

$$\theta(y,t) = \theta_0(y) + \epsilon\theta_1(y)e^{i\omega t} \tag{6}$$

$$C(y,t) = C_0(y) + \epsilon C_1(y)e^{i\omega t} \tag{7}$$

Substituting the relations (5–7) into the equations (1–4), we finally obtain

$$u_0'' + \gamma u_0' = -\mathrm{Gr}C_0 \tag{8}$$

$$\theta_0'' + \gamma\mathrm{Pr}\theta_0' = -\mathrm{PrEc}u_0'^2 \tag{9}$$

$$C_0'' + \gamma\mathrm{Sc}C_0' = 0 \tag{10}$$

$$u_1'' + \gamma u_1' - \frac{1}{4}i\omega u_1 = -\left(\frac{1}{4}i\omega + \mathrm{Gr}\theta_1 + \mathrm{Gc}C_1\right) \tag{11}$$

$$\theta_1'' + \gamma\mathrm{Pr}\theta_1' - \frac{1}{4}i\omega\mathrm{Pr}\theta_1 = -2\mathrm{PrEc}u_0'u_1' \tag{12}$$

$$C_1'' + \gamma\mathrm{Sc}C_1' - \frac{1}{4}i\omega\mathrm{Sc}C_1 = 0 \tag{13}$$

with the boundary conditions

$$\begin{aligned} &u_0 = u_1 = 0,\ \theta_0 = 1,\ C_0 = 1,\ \theta_1 = C_1 = 0 \text{ at } y = 0 \\ &u_0 = u_1 = 1,\ \theta_0 = \theta_1 = C_0 = C_1 = 0 \text{ as } y \to \infty \end{aligned} \tag{14}$$

where the primes denote differentiation with respect to y. The equations (8–13) are still nonlinear and hence are difficult to solve analytically. To solve them analytically, we expand the functions u_i, θ_i, and C_i $(i = 0, 1)$ in powers of Ec (as this number, for incompressible fluid << 1). Then

$$u_i(y) = \sum_{j=0}^{\infty}\mathrm{Ec}^j u_{ij}, \theta_i(y) = \sum_{j=0}^{\infty}\mathrm{Ec}^j\theta_{ij}, C_i(y) = \sum_{j=0}^{\infty}\mathrm{Ec}^j C_{ij} \tag{15}$$

Now, substituting equation (15) into equations (8–14) and taking the terms of the θ(Ec) (omitting the higher order terms, which are negligible), we obtain a set of coupled linear

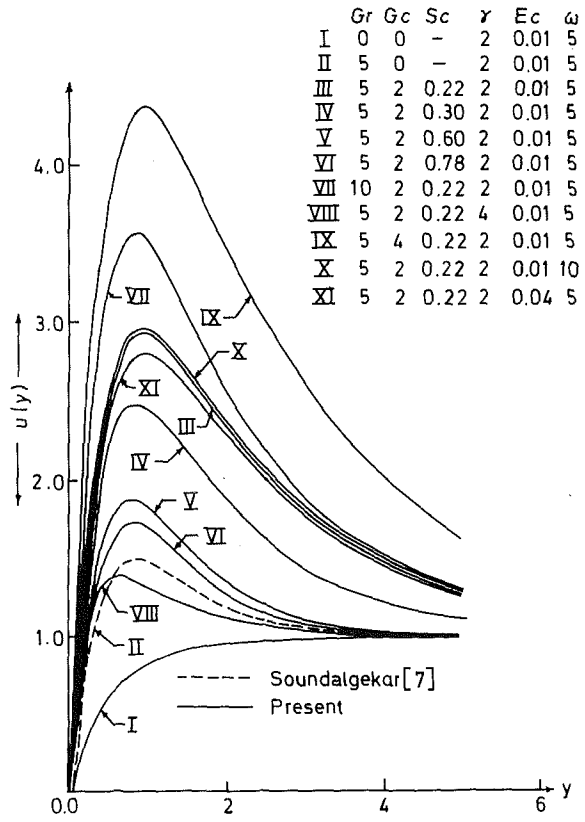

Fig. 1 Transient velocity profiles for Pr = 0.71, $\omega t = \pi/2$, $\epsilon = 0.2$

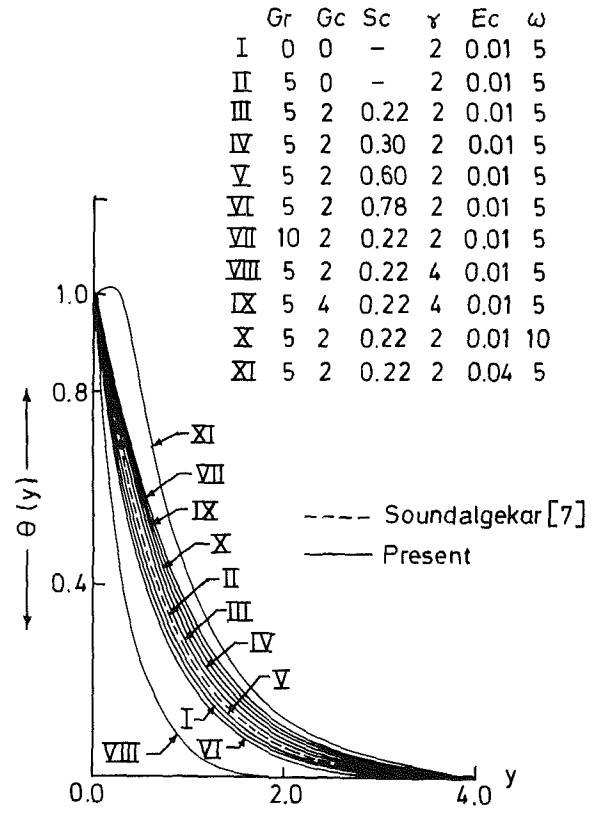

Fig. 2 Transient temperature profiles for Pr = 0.71, $\omega t = \pi/2$, $\epsilon = 0.2$

equations for u_{ij}, θ_{ij}, and C_{ij} $(j = 0, 1)$ only. Solution of the equations satisfying the functions u_{ij}, θ_{ij}, and C_{ij}, together with equation (15), yield

$$u_0(y) = 1 - e^{-\gamma y} + X_1(e^{-\gamma y} - e^{-\gamma \mathrm{Pr} y}) + X_2(e^{-\gamma y} - e^{-\gamma \mathrm{Sc} y}) + \mathrm{Ec}[X_{11}(e^{-\gamma y} - e^{-\gamma \mathrm{Pr} y}) - X_{12}(e^{-\gamma y} - e^{-2\gamma y}) - X_{13}(e^{-\gamma y} - e^{-2\gamma \mathrm{Pr} y}) - X_{14}(e^{-\gamma y} - e^{-2\gamma \mathrm{Sc} y}) - X_{15}(e^{-\gamma y} - e^{-\gamma(1+\mathrm{Pr})y}) - X_{16}(e^{-\gamma y} - e^{-\gamma(1+\mathrm{Sc})y}) - X_{17}(e^{-\gamma y} - e^{-\gamma(\mathrm{Pr}+\mathrm{Sc})y})] \quad (16)$$

$$\theta_0(y) = e^{-\gamma \mathrm{Pr} y} + \mathrm{Ec}[X_4(e^{-\gamma \mathrm{Pr} y} - e^{-2\gamma y}) + X_5(e^{-\gamma \mathrm{Pr} y} - e^{-2\gamma \mathrm{Pr} y}) + X_6(e^{-\gamma \mathrm{Pr} y} - e^{-2\gamma \mathrm{Sc} y}) + X_7(e^{-\gamma \mathrm{Pr} y} - e^{-\gamma(1+\mathrm{Pr})y}) + X_8(e^{-\gamma \mathrm{Pr} y} - e^{-\gamma(1+\mathrm{Sc})y}) + X_9(e^{-\gamma \mathrm{Pr} y} - e^{-\gamma(\mathrm{Pr}+\mathrm{Sc})y})] \quad (17)$$

$$C_0(y) = e^{-\gamma \mathrm{Sc} y} \quad (18)$$

$$u_1(y) = 1 - e^{-my} + Z_5(e^{-my} - e^{-(m+\gamma \mathrm{Pr})y}) + Z_6(e^{-my} - e^{-(m+\gamma \mathrm{Sc})y}) - Z_7(e^{-my} - e^{-(m+\gamma)y}) + Z_8(e^{-my} - e^{-ny}) \quad (19)$$

$$\theta_1(y) = Z_1(e^{-(m+\gamma \mathrm{Pr})y} - e^{-ny}) + Z_2(e^{-(m+\gamma \mathrm{Sc})y} - e^{-ny}) - Z_3(e^{-(m+\gamma)y} - e^{-ny}) \quad (20a)$$

where

$$X_1 = \mathrm{Gr}/(\gamma^2 \mathrm{Pr}(\mathrm{Pr}-1)),\ X_2 = \mathrm{Gc}/(\gamma^2 \mathrm{Sc}(\mathrm{Sc}-1))$$

$$X_3 = 1 - X_1 - X_2$$

$$X_4 = \mathrm{Pr} X_2{}^2/2(2-\mathrm{Pr}),\ X_5 = \mathrm{Pr} X_1{}^2/2,$$

$$X_6 = \mathrm{Pr} X_2{}^2(2\mathrm{Sc}-\mathrm{Pr}),\ X_7 = 2\mathrm{Pr} X_1 X_3/(1+\mathrm{Pr}),$$

$$X_8 = 2\mathrm{PrSc} X_2/(1+\mathrm{Sc})(1+\mathrm{Sc}-\mathrm{Pr}),$$

$$X_9 = 2\mathrm{Pr}^2 X_1 X_2/(\mathrm{Pr}+\mathrm{Sc}),$$

$$X_{10} = X_4 + X_5 + X_6 + X_7 + X_8 + X_9,$$

$$X_{11} = \mathrm{Gr} X_{10}/(\gamma^2 \mathrm{Pr}(\mathrm{Pr}-1)),\ X_{12} = \mathrm{Gr} X_4/2\gamma^2$$

$$X_{13} = \mathrm{Gr} X_5/(\gamma^2 \mathrm{Pr}(\mathrm{Pr}-1)),\ X_{14} = \mathrm{Gr} X_6/(2\gamma^2 \mathrm{Sc}(\mathrm{Sc}-1)),$$

$$X_{15} = \mathrm{Gr} X_7/(\gamma^2 \mathrm{Pr}(\mathrm{Pr}+1)),\ X_{16} = \mathrm{Gr} X_8/(\gamma^2 \mathrm{Sc}(\mathrm{Sc}+1)),$$

$$X_{17} = \mathrm{Gr} X_9/\gamma^2(\mathrm{Pr}+\mathrm{Sc})(\mathrm{Pr}+\mathrm{Sc}-1)$$

$$X_{18} = X_{11} - (X_{12} + X_{13} + X_{14} + X_{15} + X_{16} + X_{17}),$$

$$m = \frac{1}{2}\gamma + \sqrt{\gamma^2 + i\omega},\ n = \frac{1}{2}\gamma \mathrm{Pr} + \sqrt{\gamma^2 \mathrm{Pr}^2 + i\omega \mathrm{Pr}},$$

$$Z_1 = 2m\gamma \mathrm{Ec} \mathrm{Pr}^2 X_1/(m(m+\gamma \mathrm{Pr}) - \frac{1}{4} i\omega \mathrm{Pr})$$

$$Z_2 = 2m\gamma \mathrm{PrEcSc} X_2/((m+\gamma \mathrm{Sc})(m+\gamma \mathrm{Sc}-\gamma \mathrm{Pr}) - \frac{1}{4} i\omega \mathrm{Pr})$$

$$Z_3 = 2m\gamma \mathrm{PrEc} X_3/((m+\gamma)(m+\gamma-\gamma \mathrm{Pr}) - \frac{1}{4} i\omega \mathrm{Pr})$$

$$Z_4 = Z_1 + Z_2 - Z_3$$

$$Z_5 = \mathrm{EcGr} Z_1/\left((m+\gamma \mathrm{Pr})(m+\gamma \mathrm{Pr}-\gamma) - \frac{1}{4} i\omega\right)$$

$$Z_6 = \mathrm{EcGr} Z_2/\left((m+\gamma \mathrm{Sc})(m+\gamma \mathrm{Sc}-\gamma) - \frac{1}{4} i\omega\right)$$

$$Z_7 = \mathrm{EcGr} Z_3/\left(m(m-y) - \frac{1}{4} i\omega\right),$$

$$Z_8 = \mathrm{EcGr} Z_4/\left(n(n-\gamma) - \frac{1}{4} i\omega\right) \quad (20b)$$

Substitution of equations (16–20*a*) into equations (5–7) gives the expressions for the velocity, the temperature, and the concentration profiles. These can now be expressed in terms of fluctuating parts of the unsteady solutions as follows

$$u(y,t) = u_0 + \epsilon(M_r \cos\omega t - M_i \sin\omega t)$$
$$\theta(y,t) = \theta_0 + \epsilon(T_r \cos\omega t - T_i \sin\omega t) \tag{21}$$

where $(M_r, T_r) = \mathrm{Re}(u_1, \theta_1)$ and $(M_i, T_i) = \mathrm{Im}(u_1, \theta_1)$. Hence we can now obtain the expressions for the transient velocity and temperature profiles from equations (21), for $\omega t = \pi/2$ as

$$u(y, \pi/2) = u_0 - \epsilon M_i,\ \theta(y, \pi/2) = \theta_0 - \epsilon T_i \tag{22}$$

The transient velocity and the transient temperature profiles are shown in Figs. 1 and 2, respectively, for different values of the parameter.

Knowing the velocity and the temperature distributions in the flow field, we can now derive the expressions for the skin friction and the rate of heat transfer from the following nondimensional relations

$$\tau = (u_0' + \epsilon e^{i\omega t} u_1')_{y=0} \tag{23}$$

and

$$q = (\theta_0' + \epsilon e^{i\omega t} \theta_1')_{y=0} \tag{24}$$

In terms of amplitude and phase these can be written as

$$\tau = u_0'|_{y=0} + \epsilon |B| \cos(\omega t + \alpha) \tag{25}$$

and

$$q = \theta_0'|_{y=0} + \epsilon |Q| \cos(\omega t + \beta) \tag{26}$$

where, $B = B_r + iB_i$ is the coefficient of $e^{i\omega t}$ in equation (23), $\tan\alpha = B_i/B_r$, $Q = Q_r + iQ_i$ is the coefficient of $e^{i\omega t}$ in equation (24) and $\tan\beta = Q_i/Q_r$. The values of the amplitude and phase of the skin friction are entered in Table 1 and those of rate of heat transfer in Table 2.

In our numerical calculations of the functions representing the velocity and the temperature of the fluid, the amplitude and phase of skin friction and rate of heat transfer, the value of the Prandtl number Pr is taken in such a way that it represents air (Pr = 0.71). The values of Sc are chosen to represent the diffusing chemical species of the most common interest. The values of Sc at 20°C and at 1 atm in air for different species are obtained from Gebhart [15]. The values of Gr and Gc are chosen arbitrarily, whereas, in order to be realistic, the values of the Eckert number, Ec, are chosen as 0.01 and 0.04. The problem reduces to that of Soundalgekar [7] for Gc = 0 and $\gamma = 1$.

3 Discussion and Conclusion

For different values of the parameters, the transient velocity and the transient temperature profiles are shown in Figs. 1 and 2, respectively, and numerical values of the amplitude and phase of the skin friction, and the rate of heat transfer are given in the Tables 1 and 2, respectively. In Fig. 1, the broken curve, labeled by II, represents the transient velocity profile for Gr = 5, Ec = 0.01, $\gamma = 2$, $\omega = 5$, and Gc = 0, which agrees with Soundalgekar [7] qualitatively. Now, comparing the other curves with the curve labeled by II, it is observed that due to presence of H_2 (Sc = 0.22) in air, the transient velocity profile increases (II: III). In the presence of other species (such as He, H_2O, and NH_3) the transient velocity also increases (II: IV, V, VI), but it is not so high for H_2. But at constant Ec and γ and when only H_2 is present in air, an increase of Gr or Gc or ω leads to an increase in the transient velocity (III: VII, IX, X); whereas, at constant Gr, Gc, and ω, the transient velocity decreases with the increase of Ec and γ (III: VIII, XI). In order that these results may be useful for experimental verification, we indicate the percentage increase in the maximum transient velocity. Thus when H_2 is present and for Gr = 5, Gc = 2, Ec = 0.01, and $\gamma = 2$, the transient velocity increases by 654.5 percent. In the presence of He, H_2O, and NH_3, the increase in the transient velocity is 323.3, 61.6, and 30.7 percent, respectively. On the other hand in the presence of H_2, the transient velocity increases by 31.5 or 71.5 or 0.5 percent with the increase of Gr or Gc or of ω, and an increase in Ec or γ leads to a decrease in the transient velocity by 350.0 or 71.5 percent. In Fig. 2, the broken curve, labeled by II, represents the transient temperature profile for Gr = 5, $\gamma = 2$, $\omega = 5$, and Gc = 0, which agrees qualitatively with Soundalgekar [7]. Comparing all other curves, as before, with the curve II, we observe that the transient temperature increases in presence of H_2 and He, and the increase is by 6.09 and 1.68 percent, respectively for $y =$

Table 1 Numerical values of amplitude and phase of the skin friction, $\epsilon - 0.2$

					$\lvert B\rvert$			$\tan\alpha$		
Gc	γ	*Ec*	ω	Sc/Gr	5.0	10.0	15.0	5.0	10.0	15.0
0.0	2.0	.01	5.0	0.00	3.1918			0.1752		
2.0	2.0	.01	5.0	0.22	3.1940	3.1822	3.1600	0.1776	0.1862	0.1992
2.0	2.0	.01	5.0	0.30	3.1910			0.1775		
2.0	2.0	.01	5.0	0.60	3.1894			0.1766		
2.0	2.0	.01	5.0	0.78	3.1896			0.1762		
4.0	2.0	.01	5.0	0.22	3.1963			0.1801		
2.0	2.0	.04	5.0	0.22	3.2192			0.1902		
2.0	4.0	.01	5.0	0.22	3.0412			0.0124		
2.0	2.0	.01	10.0	0.22	3.4953			0.2752		

Table 2 Numerical values of amplitude and phase of the rate of heat transfer, ϵ–0.2

					$\lvert\theta\rvert$			$\tan\beta$		
Gc	γ	*Ec*	ω	Sc/Gr	5.0	10.0	15.0	5.0	10.0	15.0
0.0	2.0	.01	5.0	0.00	0.0303			0.0924		
2.0	2.0	.01	5.0	0.22	0.0581	0.0744	0.0907	0.0829	0.1008	0.1122
2.0	2.0	.01	5.0	0.30	0.0497			0.0920		
2.0	2.0	.01	5.0	0.60	0.0385			0.1042		
2.0	2.0	.01	5.0	0.78	0.0361			0.1054		
4.0	2.0	.01	5.0	0.22	0.0859			0.0795		
2.0	4.0	.01	5.0	0.22	0.0491			0.0169		
2.0	2.0	.04	5.0	0.22	0.2906			0.0831		
2.0	2.0	.01	10.0	0.22	0.0612			0.1011		

1; whereas, at the same distance from the plate the transient temperature decreases in presence of H_2O and NH_3 and the respective decrease is by 1.45 and 1.71 percent. But, in presence of H_2 the transient temperature of the fluid increases due to an increase in Gr, Gc, Ec, ω, or γ (III: VII, VIII, IX, X, XI). When Gr increases from 5 to 10 or Gc from 2 to 4 or Ec from 0.01 to 0.04 or ω from 5 to 10 or γ from 2 to 4, for $y = 1$, the transient temperature increases by 1.25 or 1.58 or 314 percent or by 16.7 percent, respectively.

We now discuss the effects of the parameters Gr, Gc, Sc, Ec, ω, and γ on the amplitude and phase of the skin friction, and the rate of heat transfer, from Tables 1 and 2, respectively. It is observed from Table 1 that due to the presence of H_2 in the fluid, the amplitude $|B|$ of the skin friction increases; but in the presence of heavier species (such as He, H_2O, and NH_3), the value of $|B|$ decreases. To get more insight into the effects of increasing Gr or Gc in presence of the foreign species, we now present these results quantitatively. Thus for Gr = 5, Sc = 0.22, and $\omega = 5$ the value of $|B|$ increases by 0.2 percent when Gc is increased from 2 to 4. Under similar circumstances the value of $|B|$ increases when the value of ω is increased from 5 to 10, or γ from 2 to 4 or Ec from 0.01 to 0.04, respectively; but when Gr is increased from 5 to 10, the value of $|B|$ decreases by 2.5 percent. From the same table it is also observed that the values of $\tan\alpha$, the phase of skin friction, for different values of the parameters are positive and hence there is a phase lead. Finally, we observe from Table 2 that due to the presence of foreign species, the amplitude of the rate of heat transfer $|Q|$ always increases. It also increases due to increase in Gr, Gc, or in ω. But an increase in γ leads to decrease in $|Q|$. To discuss these results quantitatively, we take Gr = 5, Sc = 0.22, $\omega = 5$, $\gamma = 2$, and Ec = 0.01. With these values, when Gc is raised from 2 to 4, the value of $|Q|$ rises by 1.4 percent. The value of $|Q|$ also rises by 0.36, 775, and 0.04 percent when the value of Gr is raised from 5 to 10, Ec from 0.01 to 0.04, and ω from 5 to 10, $|Q|$ falls by 0.5 percent. From the same table we also observe that in presence of the foreign species the values of $\tan\beta$, the phase of the rate of heat transfer, for different values of the parameters are positive, and hence there is always a phase lead.

References

1 Ostrach, S., "New Aspect of Natural Convection Heat Transfer," ASME *Transactions*, Vol. 75, 1953, pp. 1286–1290.

2 Ostrach, S., "Laminar Natural Convection Flow and Heat Transfer of Fluids With or Without Heat Sources in Channes With Constant Wall Temperatures," NACA TN 2863, 1952.

3 Ostrach, S., "Unstable Convection in Vertical Channels With Heating From Below, Including Effect of Heat Sources and Frictional Heating," NACA TN 3458, 1955.

4 Ostrach, S., "Combined Natural and Forced Convection Laminar Flow and Heat Transfer of Fluids With or Without Heat Sources in Channels With Linearly Varying Wall Temperature," NACA TN 3141, 1954.

5 Gebhart, B., "Effect of Viscous Dissipation in Natural Convection," *Journal of Fluid Mechanics*, Vol. 38, 1962, pp. 225–235.

6 Gebhart, B., and Mollendorf, J., "Viscous Dissipation in Natural Convection Flows," *Journal of Fluid Mechanics*, Vol. 38, 1969, pp. 979–107.

7 Soundalgekar, V. M., "Free-Convection Effects on the Oscillatory Flow Past an Infinite, Vertical Porous Plate With Constant Suction—I and II," *Proc. R. Soc. London*, Vol. A333, 1972, pp. 25–36; 37–50.

8 Somers, E. V., "Theoretical Consideration of Combined Thermal and Mass Transfer From a Vertical Flate Plate," *J. Appl. Mech.*, Vol. 23, 1956, pp. 295–301.

9 Wilcox, W. R., "Simultaneous Heat and Mass Transfer in Free Convection," *Chem. Eng. Sci.*, Vol. 13, 1961, pp. 113–119.

10 Gill, W. N., Deleasal, E., and Zec, D. W., "Binary Diffusion and Heat Transfer in Laminar Free Convection Boundary Laminar on a Vertical Plate," *Int. J. Heat Mass Transfer*, Vol. 8, 1965, pp. 1131–1151.

11 Adams, J. A., and Lowell, R. L., "Free Convection Organic Sublimation on a Vertical Semi-Infinite Vertical Plate," *Int. J. Heat Mass Transfer*, Vol. 11, 1968, pp. 1215–1224.

12 Gebhart, B., and Pera, L., The Nature of Vertical Natural Convection Flows From the Combined Buoyancy Effects on Thermal and Mass Diffusion," *Int. J. Heat Mass Transfer*, Vol. 14, 1971, pp. 2024–2050.

13 Eckert, E. R., Sparrow, E. M., and Minkoewycz, W. J., "Transpiration Induced Buoyancy and Thermal Diffusion Termo in Helium-Air Free Convection Boundary Layer," *J. Heat Transfer*, Vol. 86, 1964, pp. 508–514.

14 Soundalgekar, V. M., and Wavre, P. W., "Unsteady Free Convection Flow Past an Infinite Vertical Plate With Constant Suction and Mass Transfer," *Int. J. Heat Transfer*, Vol. 20, 1977, pp. 1365–1380.

15 Gebhart, B., *Heat Transfer*, McGraw-Hill, 2nd ed., 1965.

Numerical Calculation of Natural Convective Heat Transfer Between Horizontal Concentric Isothermal Cylinders – Effects of the Variation of the Fluid Properties

M. Akbar Hessami[1] A. Pollard[2,4] R.D. Rowe[3]

Introduction

A literature survey [1] has indicated that the fluid properties are assumed to be constant in all of the available experimental, analytical, and numerical studies of free-convective heat transfer in horizontal annuli. This assumption is not valid for certain liquids, especially for large temperature differences across the annular gap, and therefore it can provide erroneous heat transfer predictions. In the investigation reported here, the general differential equations of motion and energy with variable fluid properties are solved numerically for laminar natural convection in an annulus.

Different authors have used different methods to include the effects of the variations of the fluid properties on forced and free-convective heat transfer for various geometries. For example, Sparrow and Gregg [2] have defined a "reference temperature" at which the fluid properties should be determined for use in the usual heat transfer correlations. Clausing and Kempka [3] have recently incorporated a temperature ratio correction function in the correlation equation for natural convection from vertical surfaces.

The geometry that is considered for the purpose of the present study consists of two concentric horizontal cylinders; the inner cylinder is kept at a higher (isothermal) temperature than the outer cylinder. The fluids studies are air and glycerin: the former is selected in order to test the accuracy of the computer program against some available experimental data, while the latter is chosen for the significant variation of its properties with temperature to study the effects of the variation of the fluid properties on heat transfer.

The computer program which is used in this study was originally written for solving the *general* three-dimensional continuity, momentum, and energy equations for any geometry and flow regime (see [4]). However, the present computation is carried out for the two-dimensional flow situation, because a review of the pertinent literature suggests that the flow field, away from the side-walls, is two-dimensional. Also, the numerical computations for two-dimensional flow require much less computer time and storage than three-dimensional flow. In order to achieve two-dimensional flow in the computer program, the gradients of the dependent variables in the axial direction in the three-dimensional program were set equal to zero.

Mathematical Statement of the Problem

The governing differential equations that describe the

[1]Graduate Student; [2]Associate Professor, Mem. ASME; [3]Professor; Department of Mechanical Engineering, The University of Calgary, Calgary, Alberta, Canada

[4]Now at Queen's University, Kingston, Ontario, Canada.

Contributed by the Heat Transfer Division for publication in the JOURNAL OF HEAT TRANSFER. Manuscript received by the Heat Transfer Division May 25, 1982.

1; whereas, at the same distance from the plate the transient temperature decreases in presence of H_2O and NH_3 and the respective decrease is by 1.45 and 1.71 percent. But, in presence of H_2 the transient temperature of the fluid increases due to an increase in Gr, Gc, Ec, ω, or γ (III: VII, VIII, IX, X, XI). When Gr increases from 5 to 10 or Gc from 2 to 4 or Ec from 0.01 to 0.04 or ω from 5 to 10 or γ from 2 to 4, for $y = 1$, the transient temperature increases by 1.25 or 1.58 or 314 percent or by 16.7 percent, respectively.

We now discuss the effects of the parameters Gr, Gc, Sc, Ec, ω, and γ on the amplitude and phase of the skin friction, and the rate of heat transfer, from Tables 1 and 2, respectively. It is observed from Table 1 that due to the presence of H_2 in the fluid, the amplitude $|B|$ of the skin friction increases; but in the presence of heavier species (such as He, H_2O, and NH_3), the value of $|B|$ decreases. To get more insight into the effects of increasing Gr or Gc in presence of the foreign species, we now present these results quantitatively. Thus for Gr = 5, Sc = 0.22, and $\omega = 5$ the value of $|B|$ increases by 0.2 percent when Gc is increased from 2 to 4. Under similar circumstances the value of $|B|$ increases when the value of ω is increased from 5 to 10, or γ from 2 to 4 or Ec from 0.01 to 0.04, respectively; but when Gr is increased from 5 to 10, the value of $|B|$ decreases by 2.5 percent. From the same table it is also observed that the values of $\tan\alpha$, the phase of skin friction, for different values of the parameters are positive and hence there is a phase lead. Finally, we observe from Table 2 that due to the presence of foreign species, the amplitude of the rate of heat transfer $|Q|$ always increases. It also increases due to increase in Gr, Gc, or in ω. But an increase in γ leads to decrease in $|Q|$. To discuss these results quantitatively, we take Gr = 5, Sc = 0.22, $\omega = 5$, $\gamma = 2$, and Ec = 0.01. With these values, when Gc is raised from 2 to 4, the value of $|Q|$ rises by 1.4 percent. The value of $|Q|$ also rises by 0.36, 775, and 0.04 percent when the value of Gr is raised from 5 to 10, Ec from 0.01 to 0.04, and ω from 5 to 10, $|Q|$ falls by 0.5 percent. From the same table we also observe that in presence of the foreign species the values of $\tan\beta$, the phase of the rate of heat transfer, for different values of the parameters are positive, and hence there is always a phase lead.

References

1 Ostrach, S., "New Aspect of Natural Convection Heat Transfer," ASME *Transactions*, Vol. 75, 1953, pp. 1286–1290.

2 Ostrach, S., "Laminar Natural Convection Flow and Heat Transfer of Fluids With or Without Heat Sources in Channes With Constant Wall Temperatures," NACA TN 2863, 1952.

3 Ostrach, S., "Unstable Convection in Vertical Channels With Heating From Below, Including Effect of Heat Sources and Frictional Heating," NACA TN 3458, 1955.

4 Ostrach, S., "Combined Natural and Forced Convection Laminar Flow and Heat Transfer of Fluids With or Without Heat Sources in Channels With Linearly Varying Wall Temperature," NACA TN 3141, 1954.

5 Gebhart, B., "Effect of Viscous Dissipation in Natural Convection," *Journal of Fluid Mechanics*, Vol. 38, 1962, pp. 225–235.

6 Gebhart, B., and Mollendorf, J., "Viscous Dissipation in Natural Convection Flows," *Journal of Fluid Mechanics*, Vol. 38, 1969, pp. 979–107.

7 Soundalgekar, V. M., "Free-Convection Effects on the Oscillatory Flow Past an Infinite, Vertical Porous Plate With Constant Suction—I and II," *Proc. R. Soc. London*, Vol. A333, 1972, pp. 25–36; 37–50.

8 Somers, E. V., "Theoretical Consideration of Combined Thermal and Mass Transfer From a Vertical Flate Plate," *J. Appl. Mech.*, Vol. 23, 1956, pp. 295–301.

9 Wilcox, W. R., "Simultaneous Heat and Mass Transfer in Free Convection," *Chem. Eng. Sci.*, Vol. 13, 1961, pp. 113–119.

10 Gill, W. N., Deleasal, E., and Zec, D. W., "Binary Diffusion and Heat Transfer in Laminar Free Convection Boundary Laminar on a Vertical Plate," *Int. J. Heat Mass Transfer*, Vol. 8, 1965, pp. 1131–1151.

11 Adams, J. A., and Lowell, R. L., "Free Convection Organic Sublimation on a Vertical Semi-Infinite Vertical Plate," *Int. J. Heat Mass Transfer*, Vol. 11, 1968, pp. 1215–1224.

12 Gebhart, B., and Pera, L., The Nature of Vertical Natural Convection Flows From the Combined Buoyancy Effects on Thermal and Mass Diffusion," *Int. J. Heat Mass Transfer*, Vol. 14, 1971, pp. 2024–2050.

13 Eckert, E. R., Sparrow, E. M., and Minkoewycz, W. J., "Transpiration Induced Buoyancy and Thermal Diffusion Termo in Helium-Air Free Convection Boundary Layer," *J. Heat Transfer*, Vol. 86, 1964, pp. 508–514.

14 Soundalgekar, V. M., and Wavre, P. W., "Unsteady Free Convection Flow Past an Infinite Vertical Plate With Constant Suction and Mass Transfer," *Int. J. Heat Transfer*, Vol. 20, 1977, pp. 1365–1380.

15 Gebhart, B., *Heat Transfer*, McGraw-Hill, 2nd ed., 1965.

Numerical Calculation of Natural Convective Heat Transfer Between Horizontal Concentric Isothermal Cylinders – Effects of the Variation of the Fluid Properties

M. Akbar Hessami[1] A. Pollard[2,4] R.D. Rowe[3]

Introduction

A literature survey [1] has indicated that the fluid properties are assumed to be constant in all of the available experimental, analytical, and numerical studies of free-convective heat transfer in horizontal annuli. This assumption is not valid for certain liquids, especially for large temperature differences across the annular gap, and therefore it can provide erroneous heat transfer predictions. In the investigation reported here, the general differential equations of motion and energy with variable fluid properties are solved numerically for laminar natural convection in an annulus.

Different authors have used different methods to include the effects of the variations of the fluid properties on forced and free-convective heat transfer for various geometries. For example, Sparrow and Gregg [2] have defined a "reference temperature" at which the fluid properties should be determined for use in the usual heat transfer correlations. Clausing and Kempka [3] have recently incorporated a temperature ratio correction function in the correlation equation for natural convection from vertical surfaces.

The geometry that is considered for the purpose of the present study consists of two concentric horizontal cylinders; the inner cylinder is kept at a higher (isothermal) temperature than the outer cylinder. The fluids studies are air and glycerin: the former is selected in order to test the accuracy of the computer program against some available experimental data, while the latter is chosen for the significant variation of its properties with temperature to study the effects of the variation of the fluid properties on heat transfer.

The computer program which is used in this study was originally written for solving the *general* three-dimensional continuity, momentum, and energy equations for any geometry and flow regime (see [4]). However, the present computation is carried out for the two-dimensional flow situation, because a review of the pertinent literature suggests that the flow field, away from the side-walls, is two-dimensional. Also, the numerical computations for two-dimensional flow require much less computer time and storage than three-dimensional flow. In order to achieve two-dimensional flow in the computer program, the gradients of the dependent variables in the axial direction in the three-dimensional program were set equal to zero.

Mathematical Statement of the Problem

The governing differential equations that describe the

[1]Graduate Student; [2]Associate Professor, Mem. ASME; [3]Professor; Department of Mechanical Engineering, The University of Calgary, Calgary, Alberta, Canada

[4]Now at Queen's University, Kingston, Ontario, Canada.

Contributed by the Heat Transfer Division for publication in the JOURNAL OF HEAT TRANSFER. Manuscript received by the Heat Transfer Division May 25, 1982.

present problem are given in detail in [1]. The boundary conditions for the temperature and velocity fields used in conjunction with these equations are

$$\text{at } r = r_i = D_i/2,\ T = T_i \text{ and } u = v = 0 \tag{1a}$$

$$\text{at } r = r_o = D_0/2,\ T = T_o \text{ and } u = v = 0 \tag{1b}$$

where T_i is the temperature of the inner cylinder of radius $r_i(=D_i/2)$ and T_o is the temperature of the outer cylinder of radius $r_o(=D_o/2)$; u and v are the angular and radial velocity components, respectively. The solution is obtained for only half of the annular gap because of the symmetry condition about the vertical axis; the boundary conditions for this criterion are zero gradient across the symmetry plane for all variables, except angular velocity, which is zero at this plane.

Fluid Properties

The physical properties of the fluids are formulated to vary with temperature using the available equations or experimental properties data. Air density is calculated using the equation of state; other air properties (C_p, μ, and k) are obtained from the equations given in [5] and [6], i.e.,

$$C_P = 1043.66 - 0.31566\,T + 7.0723\times10^{-4}T^2 - 2.7008\times10^{-7}T^3 \tag{2}$$

$$\mu = \frac{1.458\times10^{-6}}{110.4+T}T^{3/2} \tag{3}$$

$$k = 2.6472\times10^{-3}\frac{T^{1/2}}{1+\dfrac{254.4\times10^{-12/T}}{T}} \tag{4}$$

where the temperature T is in K, specific heat C_p is in J/(kg K), dynamic viscosity μ is in kg/(m s) and thermal conductivity k is in W/(m K).

Properties of glycerin are calculated from the following polynomials, which are the best fit for the experimental property data obtained from [7]; it should be noted that these equations may not be valid outside the temperature range of 0–50° C.

$$\phi = a_0 + a_1T + a_2T^2 + a_3T^3 + a_4T^4$$

where ϕ is the fluid property, T is the temperature in ° C and a_0–a_4 are the coefficients given below

ϕ	a_0	a_1	a_2	a_3	a_4
ρ [kg/m^3]	1.276×10^3	-0.6284	2.42×10^{-3}	-4.56×10^{-5}	0
C_p [J/(kg K)]	2.260×10^3	6.134	-4.4×10^{-3}	2.13×10^{-4}	0
μ [kg/(m s)]	10.599	-1.0193	4.174×10^{-2}	-7.993×10^{-4}	5.78×10^{-6}
k [W/(m K)]	0.2819	3.442×10^{-4}	-9.96×10^{-6}	1.019×10^{-7}	0

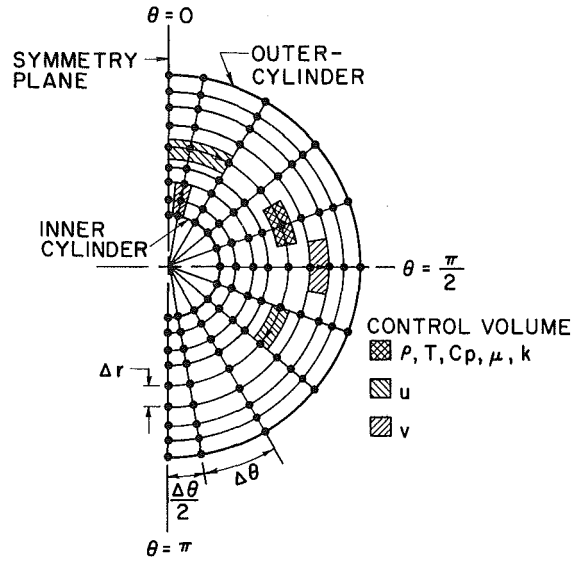

Fig. 1 The (uniform) grid distribution in the r-θ plane

The convergence criteria used in the present study were:

1 The residual for each dependent variable was required to decrease at least three orders of magnitude between the first and the last iteration; this condition was satisfied when additional iterations did not significantly change the dependent variables.

2 The false diffusivity was required to be smaller than the molecular one (kinematic viscosity); if this criterion was not met in addition to the first one, then smaller grid size was used until a satisfactory false diffusivity was found.

Also, the solutions were tested for grid independence, i.e., the grid density was increased until no further significant changes in the dependent variables were observed.

The grid-distribution in r-θ plane and the appropriate control volumes for the dependent variables are shown in Fig. 1. All variables except velocities are stored at the grid nodes; the storage locations for the velocities are at the center of the grid lines.

Computational Aspects

The governing differential equations have been transformed to finite difference equations by using a central differencing scheme, except for the convection term, which has been discretized by employing a hybrid-differencing formulation. The latter equations are solved by a line-by-line interative technique. In every iteration, the updated values of the dependent variables are compared with those from the previous iteration; if the changes between the two consecutive iterations were small enough, the updated values constituted the converged solution, otherwise the iterative computation was continued until the convergence criteria were met. The updating of the dependent variables was done via a pressure-correction equation. Underrelaxation was used in order to avoid probable divergence and/or instability in the computations.

Transformation of the differential equations to finite difference equations via Taylor-series expansion produces false diffusion because of the truncation of the higher-order terms in the series. De Vahl Davis and Mallinson [8] have shown that the false diffusion can be calculated from

$$\Gamma_{\text{false}} = \frac{V(r\Delta\theta)\Delta r\sin(2\psi)}{4[\Delta r\sin^3\psi + (r\Delta\theta)\cos^3\psi]} \tag{5}$$

where ψ is the angle which the resultant velocity V makes with the angular coordinate θ. This equation indicates that the false diffusion can be minimized by aligning the grid lines

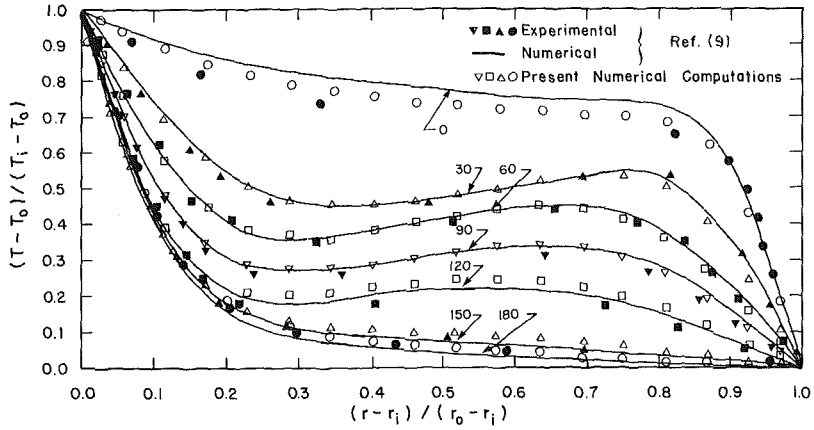

Fig. 2 Temperature distribution for different angular position θ (deg) for air (L/D_i = 0.8)

with the flow direction, and by reducing the grid size. Γ_{false} is maximum when ψ = 45 deg at the point of maximum resultant velocity V_{max}, i.e.

$$(\Gamma_{false})_{max} = 0.707\, V_{max} \frac{(r\Delta\theta)\Delta r}{(r\Delta\theta + \Delta r)} \tag{6}$$

Results and Discussion

The local Nusselt number Nu in the numerical computations is calculated from

$$\text{for inner cylinder } \mathrm{Nu}_{D_i} = \frac{(dT/dr)_i}{(\Delta T/D_i)} \tag{7a}$$

$$\text{for outer cylinder } \mathrm{Nu}_{D_0} = \frac{(dT/dr)_0}{(\Delta T/D_0)} \tag{7b}$$

where $\Delta T = T_i - T_0$. The temperature gradients at the inner and outer surfaces, $(dT/dr)_i$ and $(dT/dr)_0$, respectively, are calculated using the temperature at the four nodes closest to the surface, in a manner similar to that of Kuehn and Goldstein [9].

The accuracy of the computer program used for this study has been tested against the experimental data for air and water of Kuehn and Goldstein [9]; the results for the latter fluid are not included here but can be found in [1]. Kuehn and Goldstein's experimental data have been obtained from the fringes produced by a Mach-Zehnder interferometer; the air data are for the case where L/D_i = 0.8 (D_i = 0.0356m) and $\mathrm{Ra}_{L_f} = 4.7 \times 10^4$ (ΔT = 26.3°C).[5] The temperature field for Kuehn and Goldstein's experimental data for air are compared with our numerical predictions in Fig. 2. It should be noted that although the numerical air data of Fig. 2 are based on the constant fluid properties assumption, the computation for the variable fluid properties case has also been carried out and no significant difference has been observed. The average Nusselt number for the experimental and numerical cases are compared below:

	Numerical (present)	Experimental [9]	Difference (%)
$\overline{\mathrm{Nu}}_{D_i}$	6.52	6.28	3.8
$\overline{\mathrm{Nu}}_{D_0}$	6.09	6.26	2.7

[5] $L = r_0 - r_i$ and Ra_{L_f} is the Rayleigh number based on the gap width L with the fluid properties evaluated at the fluid mean film temperature.

The number of grid nodes was 80 × 70 in the angular and radial directions, respectively; the converged solution was obtained after 680 iterations.

The false diffusivity given by equation (6) for the present numerical results for air at the point of maximum velocity was found to be 1.77×10^{-5} m²/s, in contrast to 1.89×10^{-5} m²/s for the real kinematic viscosity of air at the fluid mean film temperature (ν_f). Because of this relatively large value of $(\Gamma_{false})_{max}$, one would expect a large discrepancy between the numerical and experimental results. However, despite this large numerical diffusion found via equation (6), the agreement between experimental and numerical data, as evident from Fig. 2, is excellent. In view of this agreement, the formulation given by equation (6) appears to be in error when applied to the present annular flow: equation (6) is based on the assumption that the streamlines make a 45 deg angle with the grid-lines in the annulus; in reality, the streamlines are almost parallel to the grid lines, and therefore ψ should be much smaller than 45 deg. Hence, equation (6) overestimates the false diffusivity when it is used for annular flow fields employing cylindrical coordinates.

In order to study the effect of the variation of the fluid properties on the temperature profile and the Nusselt number distribution, heat transfer in glycerin has been investigated for the same geometry and temperature difference across the annular gap, as used above for air. The Rayleigh number for this glycerin case is 9.05×10^4, which is of the same order of magnitude as that for air (4.7×10^4), and therefore the flow patterns are expected to be similar.

The influence of the variation of the fluid properties for glycerin on the temperature profile and Nu field is shown in Figs. 3 and 4. Although the Nusselt number does not change very much between the two different cases, the change in the temperature field is very significant. This variation in the temperature field is due to a temperature difference of only 26.3°C across the annular gap. Larger changes in the temperature profile should occur when the temperature difference between the two cylinders is higher because the variation in the fluid properties increases with temperature difference. The average Nusselt number for these two cases are:

	Variable fluid properties (VFP)	Constant fluid properties (CFP)	Difference (%)
$\overline{\mathrm{Nu}}_{D_i}$	8.22	8.23	0.1
$\overline{\mathrm{Nu}}_{D_0}$	7.82	7.48	4.4

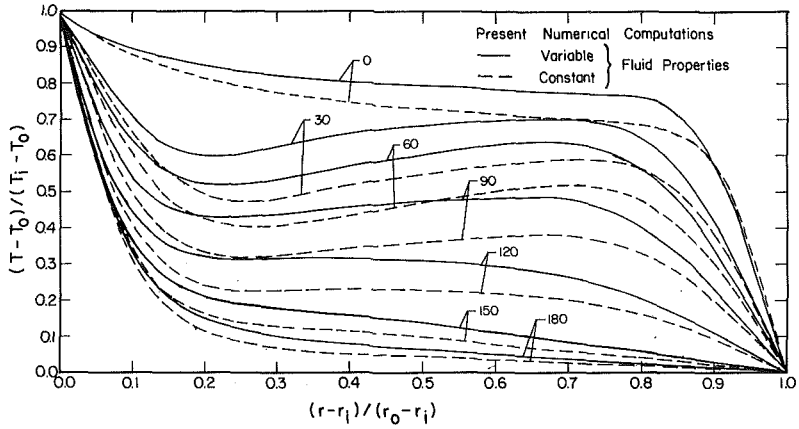

Fig. 3 Temperature distribution for different angular position θ (deg) for glycerin (L/D_i = 0.8)

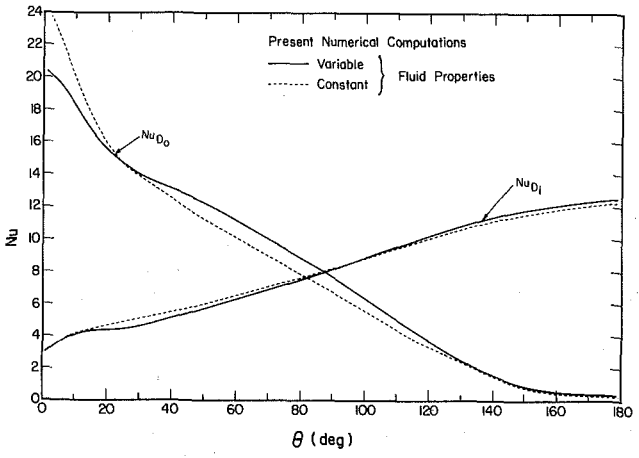

Fig. 4 Nusselt number distribution for glycerin (L/D_i = 0.8)

It is obvious that the difference in $\overline{Nu}$ is small for the two cases, which is an indication of the similar temperature gradients at the surfaces. Figure 3 indicates that the temperature is consistently higher when the VFP assumption is used as compared to the CFP case. Under the former assumption, a lower viscosity region (relative to that at the fluid mean film temperature which is used for the CFP case) exists near the inner cylinder which facilitates a higher velocity field and therefore enhances the heat transfer by convection, which results in a higher temperature field in the near inner cylinder region. The "warmer" fluid moves upward and then along the outer-cylinder. The viscosity of the glycerin near the outer cylinder is higher under the VFP assumption than that for the CFP case. This higher viscosity region reduces the heat transfer by convection, and thus the "warmer" fluid remains warm with a temperature higher than that for the CFP case.

The glycerin solutions were both obtained for a grid density of 70 × 40 after 300 iterations. The false diffusivity for the glycerin numerical computations at the point of maximum velocity was found to be 2.09×10^{-7} m^2/s as compared to $\nu_f = 3.57 \times 10^{-4}$ m^2/s evaluated at the fluid mean film temperature, and thus the numerical error in these results should be insignificant.

Conclusions

The numerical results for natural convective heat transfer in an annulus for air are compared with the available experimental data and excellent agreement was found. The difference between the temperature and Nusselt number field for air for constant and variable fluid properties was found to be negligible. It is therefore concluded that the constant fluid properties assumption is valid for air; because of the similarities in the variation of the properties of gases, the foregoing conclusion should be applicable to all gases. In contrast, the heat transfer results for glycerin indicate a significant difference in temperature field between the constant and variable fluid properties assumptions. This suggests that the variation of the properties of the fluid for glycerin (which can be generalized to all organic compounds) cannot be neglected.

In addition, it is shown that the numerical results are in excellent agreement with the available experimental data for air even when the maximum numerical false diffusivity of de Vahl Davis and Mallinson [8] has almost the same value as the kinematic viscosity. It is believed that the maximum false diffusivity criterion of de Vahl Davis and Mallinson can be relaxed in this situation because the flow is normally closely aligned with the grid lines throughout the flow field, and where the speed has the largest value, in the plane above the inner cylinder, the velocity is almost tangent to the grid lines.

References

1 Hessami, M. A., and Pollard, A., "Numerical Computation of Free-Convective Heat Transfer Between Horizontal Concentric Isothermal Cylinders," Rep. #213, Dept. Mech. Engg., University of Calgary, 1981.

2 Sparrow, E. M., and Gregg, J. L., "The Variable Fluid-Property Problem in Free Convection," ASME JOURNAL OF HEAT TRANSFER, Vol. 80, May 1958, pp. 879-886.

3 Clausing, A. M., and Kempka, S. N., "The Influence of Property Variations on Natural Convection from Vertical Surfaces," ASME JOURNAL OF HEAT TRANSFER, Vol. 103, November 1982, pp. 609-613.

4 Pollard, A., and Spalding, D. B., "Turbulent Flow and Heat Transfer in a Tee-Junction," Paper No. 79-WA/HT-47, ASME Winter Annual Meeting, New York, Dec. 1979.

5 Touloukian, Y. S., *Thermophysical Properties of Matter; Not-Metallic Liquids and Gases*, Vol. 3, IFI/Plenum, New York, 1970, pp. 511-514.

6 Hilsenrath, J., et al., *Tables of Thermodynamic and Transport Properties of Air, Argon, Carbon Dioxide, Carbon Monoxide, Hydrogen, Nitrogen, Oxygen and Steam*, Pergamon Press, New York, 1960.

7 Karlekar, B. V., and Desmond, R. M., *Engineering Heat Transfer*, West Publishing Company, St. Paul, 1977.

8 de Vahl Davis, G., and Mallinson, G. D., "False Diffusion in Numerical Fluid Mechanics," Report #1972/FMT/1, University of New South Wales, School of Mech. and Ind. Eng., 1972.

9 Kuehn, T. H., and Goldstein, R. J., "An Experimental and Theoretical Study of Natural Convection in the Annulus Between Horizontal Concentric Cylinders," *Journal of Fluid Mechanics*, Vol. 74, pt. 4, 1976, pp. 696-719.

Internal Heat Transfer Characteristics of Silicon Carbide Heat Exchanger Tubes

K. O. Smith[1]

Nomenclature

A = heat transfer area, m^2
C_p = specific heat of air, J/Kg°C
d = tube diameter, m
f = Darcy friction factor, dimensionless
g_c = proportionality constant in Newton's second law of motion
h = surface heat transfer coefficient, W/m^2 °C
k = air thermal conductivity, W/m°C
L = tube length, m
$\dot{m}_a$ = air mass flow rate, kg/s
ΔP = pressure drop, Pa
T_w = average tube wall surface temperature, K
T_a = average air temperature, K
ΔT_a = air temperature rise through tube, K
v = air velocity, m/s
ρ = air density, kg/m^3
μ = air dynamic viscosity, Pa•s
Pr = Prandtl number, dimensionless
Re_b = Reynolds number, dimensionless ($\rho vd/\mu$)
Nu_b = Nusselt number, dimensionless (hd/k)

As part of a continuing program to advance ceramic heat exchanger technology, a series of measurements were conducted to determine the internal heat transfer characteristics of SiC tubular specimens. A primary goal was to establish the suitability of forced convection correlations for characterizing the performance of ceramic heat exchangers employing SiC tubes.

Three silicon carbide tube specimens, each from a different ceramic manufacturer, were examined. Two of the tubes were fabricated using siliconized SiC[2]. The third tube was of alpha-sintered SiC[3], which contains no free silicon. All three tube specimens were nominally 2.54 cm (1 in.) o. d., 1.27 cm (0.5 in.) i. d., and 76 cm (30 in.) long.

Internal surface heat transfer coefficients were obtained using the test rig depicted in Fig. 1. Ambient temperature and pressure air flowed through the tube specimens, which were heated using an electric furnace. Tube inner surface temperatures were monitored with five thermocouples embedded in the tube wall at the tube midplane and at the ±20.3 cm (±8 in.) and ±30.5 cm (±12 in.) locations from the midplane. Thermocouple junctions were located within approximately 0.8 mm (0.031 in.) of the tube inner surface. As a result of the relatively high thermal conductivity of the ceramic materials investigated (67 W/m°C for α-SiC at 200°C), temperature gradients through the tube walls were small, and no corrections to the surface temperature measurements for radial conduction were deemed necessary.

Air temperature and total and static pressures were monitored at the tube inlet and exit planes. A mixing chamber was employed at the tube specimen exhaust end to allow an accurate measurement of air exhaust temperature. A sufficiently long straight run was provided upstream of the ceramic tubes to ensure fully developed flow profiles. Average internal heat transfer coefficients were obtained by determining average air and tube surface temperatures and air temperature rise

$$h = \dot{m}_a C_p (\Delta T_a)/A(T_w - T_a)$$

As intermediate air temperature measurements were not conducted, local heat transfer coefficients were not determined.

Friction factors were determined at ambient conditions using

$$f = \frac{\Delta P}{\left(\frac{L}{d}\right)\left(\frac{\rho v^2}{2g_c}\right)}$$

Measurements were conducted over the following ranges:

$3000 < Re_b < 40 \times 10^3$
$360K < T_w < 650\,K$
$290K < T_a < 530\,K$

Assessments of experimental uncertainty indicate that overall surface heat transfer coefficient measurements are accurate to within +5 percent [1]. Friction factor measurements for the turbulent flow regime have a worst-case error of ±7 percent due primarily to the accuracy limits of the manometer used for pressure drop measurements.

Typical heat transfer data are shown in Fig. 2 for the two generic types of SiC materials investigated. In the turbulent regime, the internal surface coefficients of the α-SiC tube are in relatively good agreement with conventional smooth tube correlations [2]. The siliconized SiC material differs from the α-SiC in showing significantly larger surface heat transfer coefficients. The cause of this difference is the extreme internal surface roughness of the siliconized SiC tubes. During the high-temperature phase of the siliconized SiC tube fabrication, excess free silicon in the liquid state diffuses to the tube surface, leaving solidified droplets on the wall of the final product. These solidified drops vary in size from less than a millimeter to several millimeters in their major dimension and are dispersed irregularly along the tube length. In many cases, it appears that droplets have agglomerated before solidifying resulting in significant areas of large scale, irregular surface roughness. In contrast, the inner wall of the alpha-sintered SiC tube appears smooth upon visual examination.

For fully turbulent flows, the surface coefficient data for the two siliconized SiC tubes can be expressed as

$$Nu_b = 0.0103\, Re_b^{0.9} Pr^{1/3} (T_a/T_w)^{0.5}$$

Norton and Coors siliconized SiC ($10{,}000 < Re_b < 35{,}000$)

The heat transfer performance of the siliconized SiC tubes differs significantly from conventional smooth tube correlations in the dependence on Reynolds number to the 0.9 power. In general, the surface coefficients of both siliconized SiC tubes were quite similar in magnitude and significantly larger than the α-SiC coefficients.

A gross characterization of the surface roughness of the three ceramic materials was achieved through friction factor measurements. Test data are shown in Fig. 3 that document the higher degree of surface roughness of the siliconized SiC materials. The two siliconized SiC tubes are characterized in the fully turbulent regime by effective values of ϵ/d on the order of 0.010 to 0.020. However, visual examination of the

[1]Solar Turbines Incorporated, San Diego, Calif. 92101, Mem. ASME.
[2]Norton Company, Worcester, Mass.; Coors Porcelain Company, Golden, Colo.
[3]The Carborundum Company, Niagara Falls, N.Y.
Contributed by the Heat Transfer Division for publication in the JOURNAL OF HEAT TRANSFER. Manuscript received by the Heat Transfer Division April 11, 1983.

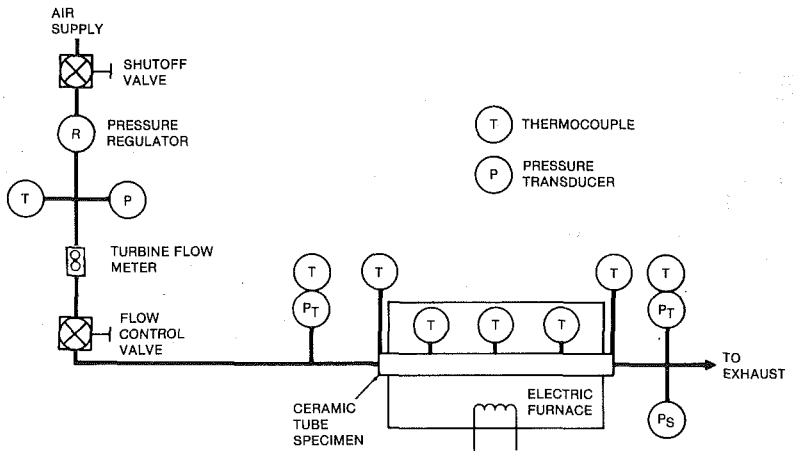

Fig. 1 Test rig for heat transfer and pressure drop measurements

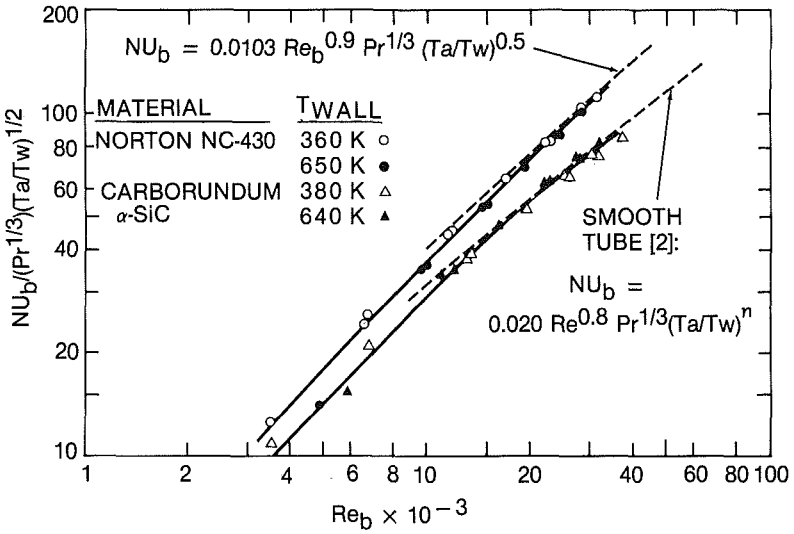

Fig. 2 Comparison of surface heat transfer characteristics of SiC tubes

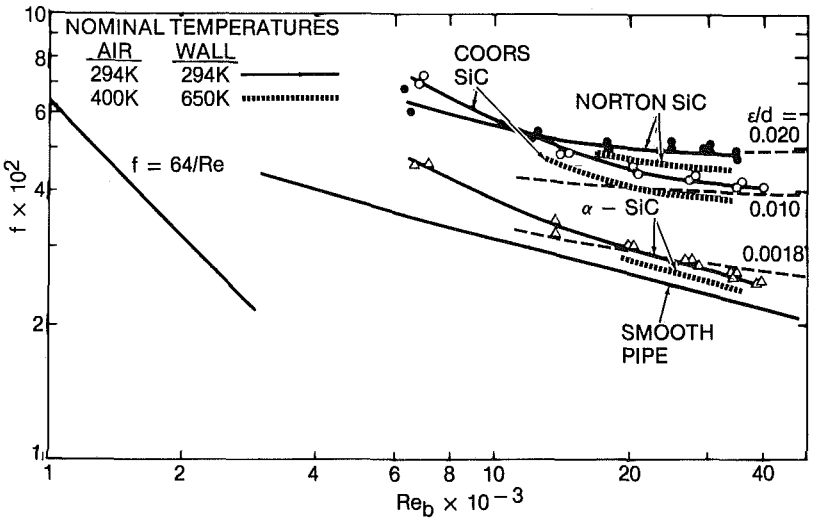

Fig. 3 Friction factor data for SiC tubes

internal tube surfaces indicates that individual surface irregularities can range up to two orders of magnitude larger than suggested by the effective ϵ/d. The α-SiC tube exhibits a low level of surface roughness ($\epsilon/d \simeq 0.0018$), consistent with the similarity of the heat transfer data with smooth tube correlations.

At a fixed Reynolds number in the turbulent regime, friction factor decreased with increasing air and wall tem-

peratures. Over the range of temperatures studied, friction factor decreased approximately 7 percent with increasing temperature for all the materials investigated.

The implications of these test results are significant in terms of advancing the ceramic heat exchanger to a commercially viable component. To predict heat exchanger performance accurately, one of two options will have to be exercised in applications of siliconized SiC tubes. One option is to decrease the tube surface roughness by some processing technique (i.e., grit blasting) to a level where conventional engineering correlations can be applied. Alternatively, modified heat transfer models and correlations must be developed to address the effects of large-scale, irregular surface roughness on the pressure drop and heat transfer characteristics of ceramic heat exchanger tubing.

Acknowledgment

This work was sponsored by the U.S. Department of Energy, Office of Fossil Energy, Division of Coal Gasification and monitored by Argonne National Laboratory.

References

1 Taylor, J. R., *An Introduction to Error Analysis*, University Science Books, Mill Valley, Calif. 1982, pp. 40–59.

2 Kreith, F., *Principles of Heat Transfer*, International Textbook Co., Scranton, Pa., 1968, pp. 379–381.